

The European Spallation Source Project

The ESS Project

Volume III

Technical Report

The European Spallation Source Project

ESS Council

F Barocchi, INFN, Univ. Firenze
A Belushkin, JINR, Dubna
R Cywinski, ENSA, Univ. Leeds
R Eichler, PSI, Villigen
R Feidenhans'l, Risø, Roskilde
F Gounand, CEA, Saclay
H Klein, Univ. Frankfurt/Main
E Koptelov, INR, Moscow
H Rauch, Atominstitut, TU Wien
D Reistad, Univ. Uppsala
D Schildt, CCLRC, Oxfordshire
U Steigerberger (*Secretary*), CCLRC,
Oxfordshire

M Steiner, HMI, Berlin
P Tindemans (*Chairman*), The Hague
A Verkooijen, IRI, Delft
R Wagner, FZJ, Jülich
F Yndurain, CIEMAT, Madrid
M Zoppi, CNR, Firenze
Observers:
C Carlile, ILL, Grenoble
A Fontaine, CNRS, Univ. Paris Sud
T Mason, SNS, Oak Ridge
S Nagamiya, JSNS, Tsukuba
G Ricco, INFN, Univ. Genova
N Williams, ESF, Strasbourg

ESS Project Directorate

K Clausen, Risø, Roskilde
I Gardner, RAL, Didcot

J-L Laclare (*Project Director*), CEA Saclay
D Richter, FZJ, Jülich

ESS Task Leaders and Deputies

Instrumentation:

F Mezei, HMI, Berlin
R Eccleston, CCLRC, Oxfordshire

Target Systems:

G Bauer, FZJ, Jülich
T Broome, CCLRC, Oxfordshire
Ring & Achromat:
C Prior, CCLRC, Oxfordshire

Linac:

A Mosnier, CEA, Saclay

Beam Transport:

R Maier, FZJ, Jülich

Conventional Facilities:

P Giovannoni, CEA, Saclay

ESS Central Project Team

F H Bohn
F Carsughi
A Claver
K Clausen (*Director*)
C Desailly*

P Fabi
Ch Hake
S Palanque*
H Tietze-Jaensch

* members of the staff supporting the project chairman in Saclay.

The European Spallation Source Project

ESS Scientific Advisory Committee

J Colmenero, Univ. of the Basque Country
R Cywinski, Univ. Leeds
W I F David, CCLRC, Oxfordshire
C Fermon, CEA, Saclay
A Furrer, ETHZ & PSI, Villigen
J R Helliwell, CLRC, Daresbury
S Ikeda, KENS/KEK, Tsukuba
G H Lander, IfT, Karlsruhe
H Jobic, Univ. Lyon
T Lorentzen, DanStir ApS,
Frederiksborgvej (until Autumn 2001)
T Mason, SNS, Oak Ridge

R L McGreevy, Univ. Uppsala - CCLRC,
Oxfordshire
F M Mulder, Univ. Delft
H Rauch, Atominstutut, TU Wien
D Richter (*Chairman*), FZJ, Jülich
R Rinaldi, Univ. Perugia
W G Stirling, ESRF, Grenoble
C Vettier, ILL, Grenoble
A Wischnewski (*SAC Assistant*), FZJ,
Jülich
H Zabel, Univ. Bochum

ESS Technical Advisory Committee

Target:

J Carpenter, Argonne National Lab.
M Furusaka, KENS/KEK, Tsukuba
K Jones, Los Alamos National Lab.
J Knebel, FZK, Karlsruhe

Linac:

R Garoby, CERN, Geneva
D Proch, DESY, Hamburg
J Stovall, Los Alamos National Lab.
Y Yamazaki, JAERI/KEK, Tsukuba

Instruments:

M Arai, KENS/KEK, Tsukuba
P Böni, TU, München
G H Lander (*Chairman*), IfT, Karlsruhe
D Myles, EMBL, Grenoble
W Press, ILL, Grenoble

Rings:

H Schönauer, CERN, Geneva
W T Weng, Brookhaven National Lab.

Conventional Facilities:

J Lawson, SNS, Oak Ridge
J-P Magnien, ESRF, Grenoble

The European Spallation Source Project

The ESS Project

**Volume I
European Source of Science**

**Volume II
New Science and Technology
for the 21st Century**

**Volume III
Technical Report**

**Volume IV
Instruments and User Support**

Contents of Volume III

Technical Report

Chapter I Foreword, Introduction and Overview

Chapter 1 The Linac

Chapter 2 Accumulator Rings and Injection Beam Line

Chapter 3 Beam Transfer to Target

Chapter 4 Target Systems

Chapter 5 Instruments and Scientific Utilisation

Chapter 6 Conventional Facilities

Chapter 7 Control Systems, Network and Computers

Chapter 8 Safety and Licensing

Chapter 9 Project Schedule, Organisation, Personnel and Costs

Chapter I

**Foreword,
Introduction and
Overview**

Contents

Foreword, Introduction and Overview

<u>FOREWORD</u>	I-5
<u>I INTRODUCTION AND OVERVIEW</u>	I-6
I.1 HISTORY	I-6
I.2 THE EUROPEAN SPALLATION SOURCE	I-6
I.2.1 LINAC AND RINGS	I-7
I.2.2 TARGET SYSTEMS	I-8
I.2.3 INSTRUMENTS.....	I-9
I.2.4 CONVENTIONAL FACILITIES.....	I-10
I.2.5 SAFETY ASPECTS.	I-10
I.2.6 SCHEDULE AND COSTS.....	I-11
I.2.7 POTENTIAL OTHER USAGES.....	I-12
I.3 CONCLUSION AND NEXT STEPS.....	I-12

FOREWORD

The European Spallation Source (ESS) Project represents the culmination of a decade of intense research, development and design by Europe's leading scientists. The single goal is to provide Europe with the world's most powerful neutron facility. Some 20 laboratories, universities and research organizations plus a large number of scientists from all over Europe, have joined together to develop the science case and the technical design, and to work on the planning and the realization of the ESS project.

This ESS technical design report builds on the ESS feasibility study published in 1996 and subsequent R&D work carried out by the partner laboratories in Europe and through very fruitful collaboration with similar projects Worldwide. New spallation sources in the United States and Japan are already being constructed, with technical solutions, which to a large extent are based on this 1996 feasibility study. The US and Japan sources will produce their first neutrons in 2006. These sources will be superior to the existing European sources. Only by building the ESS will Europe be able to reaffirm its present leading role in the field of neutron research.

The Science Advisory Committee (SAC) of the ESS represents the best neutron scientists in Europe, and the US and Japanese partners in the MW spallation endeavour. A Technical Advisory Committee (TAC) comprising experts from a large number of major facilities all over the world has expressed its confidence in the proposed technical design and the ability of the ESS partners to build it.

The ESS will go one step further compared to the sources under construction in the US and Japan. Not only will its power be higher, which translates directly into more intensity, but the ESS Council has also opted for a source with two complementary targets, a 50 Hz Short Pulse (SP) and a $16\frac{2}{3}$ Hz Long Pulse (LP) target. Each target and the instruments on it can then be optimised to suit different types of experiments.

The combination of a source creating the very best conditions for science in a very wide range of scientific fields, and a challenging technical design based on what will be the world's most powerful proton accelerator, turns ESS into perhaps the most unique and exciting large project for European science. It will be a cornerstone of the European Research Area.

The ESS project acknowledges the advice from our SAC and TAC committees, the very open and mutually beneficial collaboration with institutions and colleagues working on the US and Japanese spallation source projects, financial support from the European Commission through the neutron round-table and last but not least the massive backing by the users organised in the European Neutron Scattering Association.

On behalf of the ESS project:

*The ESS project directorate
Jean-Louis Laclare, Ian Gardner, Dieter Richter and Kurt N Clausen*

I INTRODUCTION AND OVERVIEW

I.1 HISTORY

The story of the ESS started more than 10 years ago. In the Large Facilities Report to the Commission of the European Community (CEC) in 1990, the Neutron Study Panel underlined the continuing need for neutron scattering as a microscopic probe of the condensed state, and recognised that a major initiative was necessary. The Panel recommended that a design study be initiated forthwith for a next generation neutron source.

Forschungszentrum Jülich (FZ-J) and Rutherford Appleton Laboratory (RAL) arranged a series of meetings in 1991 and 1992 to explore options for an advanced high-power accelerator-driven pulsed spallation source. This formed the basis for the specification of the ESS.

This initiative was joined by further laboratories from Austria, Denmark, Germany, Italy, the Netherlands, Sweden, Switzerland and the UK. They all together carried out a two year site-independent feasibility study for a third generation neutron source. A council of representatives from the partners together with observers from France and Spain was formed to oversee the study, which began in June 1993, and continued from December 1994 with CEC support. This feasibility study was published by the end of 1996 and proposed a 5 MW facility with two SP target stations – operating at 50 Hz (4MW) and 10 Hz (1 MW) respectively. The institutions behind this study continued their joint efforts, co-ordinated by the ESS R&D council, on important R&D issues, which had been identified during the feasibility study.

In the late nineties the Organisation for Economic Cooperation and Development (OECD) initiated a discussion among governments, science agencies and scientists worldwide about the strategy that one should follow for the provision of neutrons. A key component in these OECD recommendations, endorsed in 1999 by the science and technology ministers of the OECD countries, was to build a new, high intensity spallation neutron source in each of the major scientific regions of the globe – in North America, in the Asia-Pacific area and in Europe.

Both the US and Japan are now rapidly constructing, their Megawatt Spallation Neutron Sources, each of which will be far more powerful than any existing neutron facility in Europe. The partners in ESS have updated and improved the technical and the scientific proposals for the ESS, the costing has been revisited, and the organisational model has been agreed upon. If a decision is taken by late 2003/early 2004, the ESS can start pre-operation by the beginning of 2012.

I.2 THE EUROPEAN SPALLATION SOURCE

The specification of ESS 2002 builds on the 1996 design but reflects the development in science, the advance in accelerator design and the novel ideas for neutron instrumentation and beam extraction, which has taken place during the last 6 years. The major change concerns the target stations in combination with the overall power level of the accelerator.

Starting from a perspective on the future development of science across the whole range of fields for which neutrons in general and ESS in particular will be important, more than 70 scientists assessed the performance of generic instruments to investigate these scientific problems on three different target stations. One was the 50Hz 5 MW SP station, the second a 10Hz 1 MW SP station and the third a 5 MW $16 \frac{2}{3}$ Hz LP station. The advice from these scientists, which was later strongly endorsed by the ESS SAC, recommended that:

- ESS should be built as a 10 MW facility serving two target stations, a SP 50Hz station and a $16 \frac{2}{3}$ Hz LP station.
- Both target stations should be considered with equal priority.

A perspective view of the ESS reference design is shown in figure I.2-1. It consists of a full energy 1.334 GeV linac, a 5 MW SP target station fed with protons compressed by a factor 800 to pulses of 1.4 μ s duration in a double compressor ring and a 5 MW LP target station fed directly with protons from the linac.



Figure I.2-1: Schematic Layout of the ESS

I.2.1 Linac and Rings

Since 1996 the accelerator architecture has also been revised, due both to the results of R&D activities and to the changed requirements in terms of power and pulse structure.

In the first place work has continued on the Normal conducting (NC) accelerator design of 1996, leading to a modified NC design called the revised 1996 design. Most of the proton accelerators being designed today, however, have a Super Conducting (SC) high-energy part. The ESS project has also embarked on the study of a SC version of the accelerator. The TAC has stated that both solutions are technically feasible. At the present state of the project no clear preference between NC and SC has emerged, neither in terms of cost or performance.

With further development the SC option shows the potential to provide a clearly superior solution. The future efforts will therefore be concentrated on this solution.

For the accumulator, the 1996 two ring design was revised in 1999 to improve the painting scheme and reduce stripping foil heating. This has led to a larger radius of the ring. The main parameters of the linac and rings are given in Table I.2-1.

For linac, rings and beam transport to targets a dominant requirement is to minimise the uncontrolled beam losses to be below 1 Watt per meter and to localise the controlled beam losses in carefully designed serviceable collimators, scrapers or beam dumps. At the targets, an elliptical beam cross-section ($200 \times 60 \text{ mm}^2$) with a parabolic two dimensional density distribution is proposed for both the LP and SP target stations.

Linac	SP	LP
Beam power	10 MW	
Linac beam energy	1.334 GeV	
Linac average current	3.75 mA	3.75 mA
Linac peak current	112.5 mA	112.5 mA
Linac repetition rate	50 Hz	$16 \frac{2}{3}$ Hz
Linac beam pulse duration	$2 \times 0.48 \text{ ms}$	2 ms
Chopping efficiency	70%	no chopping
Linac beam duty cycle	3.4%	3.4%
Two accumulator rings		
Frequency of parallel operation	50 Hz	
Number of circulating protons per ring	2.34×10^{14}	
Revolution frequency	1.2416 MHz	
Bunch length at ring ejection	0.6 μsec	
Peak current	62.5 A	
Mean radius of rings	35.0 m	

Table I.2-1: Main parameters of the accelerator and ring for the reference design.

I.2.2 Target systems

The ESS targets have to withstand a large average beam power, about 30 times that of ISIS the spallation neutron source at RAL. The time structure of the proton beam at the SP target station leads to proton pulses with an energy content of 100 kJ and with a pulse duration of only 1.4 μs . Targets are therefore submitted to a combined load of high radiation damage, large temperature gradients and stress waves. The energy content in the proton pulses for the LP target station is 300 kJ, but delivered in 2 ms pulses. Stress waves will therefore not be an important issue.

Compared to the 1996 study the overall design has been retained, using horizontal injection into a flowing Hg target for both the LP and SP target stations. The number of moderators has been reduced to 2 per target station. The target station will be prepared for advanced cold moderators, when they have been developed. The present design will only use conventional types of moderators – super critical hydrogen and water, but will include novel ideas for pre-moderation and relative positioning of the moderators. The moderators on the SP station consist of:

- One back to back thin cold and thick thermal moderator with one viewed decoupled cold and one viewed decoupled thermal face
- One premoderated coupled cold with 1 viewed cold and 1 viewed multispectral - cold and thermal face

The moderators on the LP station consist of:

- One coupled cold moderator with two viewed cold surfaces
- One multispectral with 2 viewed cold and thermal faces

Recent development in beam optics and in beam extraction systems has led to move the shutters closer to the moderators allowing beam optics to start 1.5 m from the moderator face. The main parameters for the target stations are given in Table I.2-2.

Two target stations	SP Short Pulse	LP Long Pulse
Beam power	5 MW	5 MW
Energy of protons	1.334 GeV	1.334 GeV
Time structure of proton pulse	2 x 0.6 μ s	2.0 ms
Energy content of proton pulses	100 kJ	300 kJ
Repetition rate	50 Hz	16 $\frac{2}{3}$ Hz
Proton beam diameter at target (parabolic 2D-density distribution)	6 x 20 cm ²	6 x 20 cm ²
Target type	Flowing mercury horizontal injection	Flowing mercury horizontal injection
Number of moderators (viewed faces)	2 (4)	2 (4)
Average thermal flux	3.1×10^{14} n/cm ² s	3.1×10^{14} n/cm ² s
Peak thermal neutron flux	1.3×10^{17} n/cm ² s	1.0×10^{16} n/cm ² s
Decay time of flux	150 μ s	150 μ s

Table I.2-2: Main parameters of the target stations.

I.2.3 Instruments

Tremendous progress in neutron scattering research capabilities has been achieved over the past half century primarily by the development of the performance of the instrumentation.

This has involved both new concepts and advances in components, such as detectors. Over the same period of time the brightness of neutron sources only increased by a modest amount. The ESS will offer an unprecedented jump of some two orders of magnitude in a source performance parameter, the instantaneous peak flux compared to the leading neutron sources existing today. In terms of time average flux it will equal the most powerful continuous sources. The pulsed character however allows for a more efficient use of the total number of neutrons produced.

The instrument suite presented in this document is the suite that would be built if the facility were available today. Extensive experience accumulated over the past 5 decades of using continuous reactor sources and nearly 3 decades of progress with pulsed spallation sources combined with the utilisation of innovative concepts provides a solid basis for this effort.

When the facility has been approved the actual instruments will be built sequentially over a period of about 10 years, each based on a detailed science case and state of the art instrumentation capability at the time. Each target station will be able to accommodate 24 instruments. Of the 48 instrumented beam lines, Collaborating Research Groups (CRG) could finance 8.

I.2.4 Conventional facilities

The conventional facilities constitute one of the most critical aspects as regards technical risks, timescale and costs (about 30 % of the construction costs). In the present study on a reference site as described in Chapter 6.2, the targeted level of detail for the main subsystems corresponds to that required to obtain a building permit and sufficiently documented to place an INdustrial Architect (INA) contract just after the go-ahead for the project.

The building programme is based on the 1996 ESS study, the CONCERT study and on recent information from SNS. This building programme was used to study possible technical options for each of the conventional facilities subsystems and to select a reference solution for buildings and general services such as electricity, water, HVAC etc.

Two layouts based on a NC and a SC high-energy section of the linac have been studied. They mainly only differ in the length of the linac. The extra cost of the longer NC linac is compensated by the additional cost of the cryogenic and rf systems for the superconducting version.

I.2.5 Safety aspects.

The radioactivity generated in the target and in other parts of ESS together with the chemical toxicity and volatility of mercury require that considerable effort be spent in safety examinations, shielding calculations and preparation of the formal safety report to meet requirements and procedures for obtaining authorisation to build and operate the ESS.

The primary safety philosophy of ESS is based on defence-in-depth. Main safety features include: Containment by multiple barriers to prevent leakages, the use of high quality material, passive safety features, simple operation, redundancy and diversity in safety systems.

Comparison of licensing requirements in different European countries for a facility like ESS led to the conclusion that for normal operation and beyond design basis accidents similar guidelines concerning radioactivity are applicable (Euratom directive 96/29 respectively ICRP-63), whereas for design basis accidents the national rules differ to some extent. With respect to toxic mercury, rules and intake limits are not very different.

A preliminary safety analysis report (PSAR) now available for the target of the American spallation source SNS was reviewed with the result, that it represents an excellent basis for ESS safety studies. The main conclusion of PSAR, that SNS can be constructed and operated safely with adequate effort on safety measures is also applicable to ESS. However the depth of safety analyses in PSAR is not sufficient for meeting dose criteria under ESS conditions; additional steps in the iterative safety analysis process are undertaken for certain relevant accident events.

Another important safety aspect of ESS is radiation shielding. The shielding calculations from the 1996 ESS study have been updated to comply with the Euratom directive 96/29. The ALARA (As Low As Reasonably Achievable) principle has been respected by assuming a dose rate limit of a half micro Sievert per hour ($0.5 \mu\text{Sv.h}^{-1}$) outside the shield walls (beam loss assumptions of 1 Watt per meter). Because remote handling is foreseen only at specific accelerator positions, beam losses for the linac, rings and transfer lines have to be strictly limited. An active accelerator and radiation monitoring interlock system is mandatory to minimize additional activation from accidental beam losses.

I.2.6 Schedule and costs

The construction of the ESS facility is planned to take 8 years followed by one year of pre-operation. Therefore, assuming that all required decisions are made by January 2004, first user operation could start in January 2012 and full user mode one year later.

10 instruments will be ready at the beginning of pre-operation. New instruments will be introduced at a rate of 5 instruments per year during the first years of operation. When all 48 beam-holes are instrumented, refurbishment will start at a rate of 3 instruments per year.

The construction costs of the ESS facility amount to 1552 Million € at 2000 prices.

This figure includes not only capital investments for all components necessary for the ESS baseline but also the 3300 years of manpower (in-house plus subcontracted staff) required during construction. A contingency of 15 % is included.

With regards to the organisation of the facility, the ESRF model will be chosen with a few minor optimisations. The in-house staff will comprise about 650 including 50 PhD students. The ESS will be a highly user oriented facility operating more than 40 instruments in User Service Mode (USM) for 5.500 hours per year.

The operational budget thus amounts to 142 Million € at 2000 prices.

This budget includes a recurrent investment for developments, completion of the instrument suite and later the systematic refurbishment/enhancement and replacement at a rate of 3 instruments per year.

I.2.7 Potential other usages

The ESS design is rather flexible. It allows using the facility for other purposes. A number of these would not require major new facilities and can be added later if the site layout allows for the physical space. For some applications major financial resources are necessary, the relevant communities should secure these.

The other usages being considered by the respective communities are:

1. An irradiation facility in one of the existing LP or SP target station.
2. A radioactive beam facility.
3. Production of radioisotopes.
4. An Ultra Cold Neutron source.
5. A Muon facility in the transfer line between rings and SP target.
6. A Neutrino facility in a cave below the SP target.

Provision for these other uses are not included in the project proposal and costs.

I.3 CONCLUSION AND NEXT STEPS

The ESS project is backed by a strong science case. It is unanimously supported by the European neutron user community. The timeliness is documented by EC and OECD studies, and the design presents a next step beyond similar projects underway in the US and Japan.

A Technical Advisory Committee consisting of World leading experts in all relevant areas – accelerators, rings, targets, instrumentation and infrastructure, has furthermore reviewed the technical solutions presented in this document. This committee has deemed the ESS project *“a worthwhile project of the greatest importance for European science and technology, whose design and construction is within the competence and capabilities of the collaborating European laboratories”*.

It is of paramount importance that the project maintains its present momentum, starts prototyping of key components and develops the project baseline design, to facilitate site decision and to be prepared for an effective start-up after the project go-ahead. Until the end of 2003, the project team will in particular:

- Continue to advance the engineering study (detailed design, preparation of specifications, etc.) of critical items with regards to timescale or technical risks so as to jump into the construction phase immediately after the decision
- Offer their services for participation in the evaluation of proposed sites
- Prepare the administrative documents to establish the new legal entity
- Be ready to consider amendments to the proposed baseline (scope, timescale, budget profile, etc.)
- Prepare the project baseline report (ESS report volume V) with management concept and project execution plan.

The ministers for science and research of the participating European countries are now invited to decide on the funding and the site of the ESS in late 2003 or early 2004. With their decision the ministers hold the key to the future of modern research and development using neutrons in Europe. The European spallation neutron source, ESS, will be a pillar of European science in the European Research Area.

Volume III Technical Report

Chapter 1

The Linac

Authors and Contributors

The Linac

B Aune¹, P Y Beauvais¹, R Bennett², K Bongardt³, W Bräutigam³, M Desmons¹, G Devanz¹, R Duperrier¹, R Ferdinand¹, D Findlay², I Gardner², R. Gobin¹, H Jones², J L Laclare¹, J M Lagniel¹, A Letchford², A Loulergue¹, M Luong¹, R Maier³, S Martin³, A Morris², A Mosnier¹, M Pabst³, M Painchault¹, J Payet¹, N Pichoff¹, C Prior², G Rees², Y Senichev³, S Schriber⁴, J Sherman⁴, R Stassen³, J Thomason², D Uriot¹, E Zaplatin³

¹CEA, ²RAL/ISIS, ³FZJ, ⁴LANL

The 280/560 MHz NC solution has been worked out under the leadership of the RAL/ISIS team.

The 352/704 MHz SC solution has been worked out under the leadership of the CEA team.

Contents

The Linac

1 THE LINAC.....	1-7
1.1 INTRODUCTION.....	1-7
1.1.1 THE BEAM ACCELERATION REGIMES	1-8
1.2 THE ION SOURCES.....	1-9
1.2.1 INTRODUCTION	1-9
1.2.2 SHORT AND LONG PULSE CONSIDERATIONS FOR H ⁻ ION SOURCES	1-10
1.2.3 PENNING H ⁻ SOURCE	1-10
1.2.4 VOLUME H ⁻ SOURCE.....	1-12
1.2.5 THE ECR H ⁻ SOURCE	1-14
1.2.6 PROTON SOURCES	1-14
1.2.7 CONCLUSIONS.....	1-15
1.3 THE 280/560 MHZ LINAC DESIGN	1-15
1.3.1 INTRODUCTION	1-15
1.3.2 CHOICE OF LINAC FREQUENCIES AND LAYOUTS.....	1-16
1.3.3 LOW ENERGY BEAM TRANSPORT AND RADIO FREQUENCY QUADRUPOLE	1-17
1.3.3.1 LEBT	1-17
1.3.3.2 Three Solenoid Magnetic LEBT.....	1-18
1.3.3.3 Alternative LEBT Designs	1-18
1.3.3.4 RFQs	1-19
1.3.3.5 280 MHz 4-Rod RFQ Parameters.....	1-19
1.3.4 CHOPPER SECTION.....	1-24
1.3.5 280 MHz, 20 MeV DRIFT TUBE LINAC, DTL.....	1-27
1.3.6 FUNNEL	1-30
1.3.7 560 MHZ ACCELERATING STRUCTURES	1-32
1.3.7.1 20 to 100 MeV CCDTL.....	1-32
1.3.7.2 100 to 251.5 MeV CCL1 and 251.5 to 1334 MeV CCL2	1-34
1.3.8 LINAC BEAM DYNAMICS	1-35
1.3.8.1 Coupled Transverse-Longitudinal Coherent Motion.....	1-36
1.3.8.2 Linac Output Energy Error Compensation	1-37
1.3.8.3 Linac Beam Simulations with and without Errors.....	1-37
1.3.9 LINAC BEAM DIAGNOSTICS AND COMMISSIONING	1-41
1.3.9.1 Linac Beam Commissioning.....	1-42
1.3.10 RADIO FREQUENCY AND FIELD CONTROL SYSTEMS	1-43
1.3.10.1 RF Field Control System	1-44
1.3.11 VACUUM SYSTEMS FOR THE LINAC	1-46
1.3.12 BUILDINGS AND TUNNEL	1-49
1.4 THE 352/704 MHZ LINAC DESIGN.....	1-53
1.4.1 INTRODUCTION	1-53
1.4.2 THE LOW ENERGY BEAM TRANSPORT.....	1-54
1.4.2.1 The H ⁻ LEBT	1-54
1.4.2.1.1 Space Charge Compensation	1-54

1.4.2.1.2	Gas stripping of H-	1-55
1.4.2.1.3	The emittance management	1-55
1.4.2.1.4	LEBT with five quadrupoles	1-55
1.4.2.2	The H ⁺ LEBT	1-56
1.4.2.2.1	Space Charge Compensation	1-56
1.4.2.2.2	LEBT with two solenoids	1-56
1.4.2.3	Conclusions.....	1-57
1.4.3	THE RADIO FREQUENCY QUADRUPOLE (RFQ) ACCELERATORS.....	1-58
1.4.3.1	RFQ1.....	1-58
1.4.3.2	RFQ2.....	1-60
1.4.3.3	RFQ3.....	1-62
1.4.3.4	Conclusion	1-64
1.4.4	THE CHOPPER SECTION	1-65
1.4.5	THE DRIFT TUBE LINAC (DTL)	1-67
1.4.5.1	Choice of the focusing scheme	1-68
1.4.5.2	DTL prototype	1-68
1.4.5.3	DTL cell design	1-69
1.4.5.4	H ⁻ DTL Main parameters.....	1-69
1.4.5.5	H ⁺ DTL Main parameters	1-70
1.4.5.6	Diagnostics and commissioning	1-71
1.4.6	THE FUNNEL LINE	1-72
1.4.6.1	Introduction.....	1-72
1.4.6.2	Funnel line concerns	1-73
1.4.6.3	Funnel line characteristics	1-73
1.4.6.4	The funnel cavity	1-74
1.4.6.5	Layout of the funnel line.....	1-76
1.4.6.6	Diagnostics and commissioning	1-77
1.4.7	THE SEPARATED DRIFT-TUBE LINAC (SDTL)	1-77
1.4.7.1	SDTL cavity design	1-78
1.4.7.2	Main parameters	1-79
1.4.7.3	Matching between SDTL sections.....	1-80
1.4.7.4	Diagnostics and commissioning	1-81
1.4.8	THE COUPLED CAVITY LINAC (CCL)	1-81
1.4.8.1	The CCL cavity.....	1-82
1.4.8.2	Main parameters	1-83
1.4.8.3	Diagnostics and commissioning	1-84
1.4.9	THE SUPERCONDUCTING SECTION (SCL).....	1-85
1.4.9.1	General architecture	1-85
1.4.9.2	Longitudinal phase advance	1-86
1.4.9.3	Power coupler capability	1-86
1.4.9.4	Choice of frequency.....	1-88
1.4.9.4.1	Cryogenics aspects	1-89
1.4.9.4.2	RF power sources	1-90
1.4.9.5	Final layout	1-90
1.4.9.6	Cryogenic system.....	1-91
1.4.9.7	The Radio Frequency system.....	1-92
1.4.9.8	The 2-coupler scheme.....	1-96
1.4.9.9	Field control and energy stability	1-97
1.4.9.9.1	One single pulse cycle analysis	1-99
1.4.9.9.2	Multiple pulse cycles analysis	1-101
1.4.9.10	Conclusions.....	1-102

1.4.10 BEAM DYNAMICS	1-103
1.4.10.1.1 Linac characteristics from the beam dynamics point of view	1-103
1.4.10.2 Main beam characteristics in the linac.....	1-106
1.4.10.2.1 Sensitivity to linac element errors	1-110
1.4.10.2.2 Static errors study	1-110
1.4.10.2.3 Dynamic errors study.....	1-112
1.4.10.3 Sources of beam losses	1-115
1.5 ENGINEERING DESIGN AND DEVELOPMENT (ED&D)	1-117
REFERENCES	1-118

1 THE LINAC

1.1 INTRODUCTION

Since the publication of the 1996 ESS Technical Study [ESS-96-53-M], the specification of the target stations has been revised. Instead of two short pulse (SP) target stations driven by a total beam power of 5 MW, there are now a short pulse 50 pps target station and a long pulse (LP) $16 \frac{2}{3}$ pps target station, each driven by 5 MW. To meet this new demand, work has been carried out on accelerator systems in two parallel programmes. In the first programme, the ESS linac design presented in 1996 was refined and has resulted in a 280/560 MHz scheme. Both normal conducting (NC) and superconducting (SC) versions of this scheme were studied in detail [Gardner, 2002], but only the normal conducting version is being presented here. In the second programme, a 352/704 MHz scheme was derived from the 25 MW CONCERT concept [CONCERT, 2000] in which an accelerator-driven neutron spallation source is seen as only one component of a substantially larger accelerator complex based on a superconducting high energy part for the linac.

A key design criterion for the ESS accelerator system is the minimisation of beam losses. To allow maintenance and repair work to be carried out after short cooling times, beam losses must be kept below values of typically 1 nA per metre, and in the proposed accelerator schemes these are achievable. Sufficiently low beam losses can also be achieved in the pulse compression system by adopting the proposed scheme of two compressor rings.

The front ends (i.e. at low energies below 20 MeV) of the two accelerator schemes have similar architecture, as shown in Figures 1.1–1 and 1.1–2 below. Both require state-of-the-art performances from H^- ion sources, choppers and funnel branches. The H^+ branch in the 352/704 MHz scheme represents a contingency measure, which will be implemented only if the H^- ion sources for LP operation are not ready. Between 20 MeV and ~ 200 MeV, both schemes use normal conducting accelerating cavities, although the structures are slightly different.

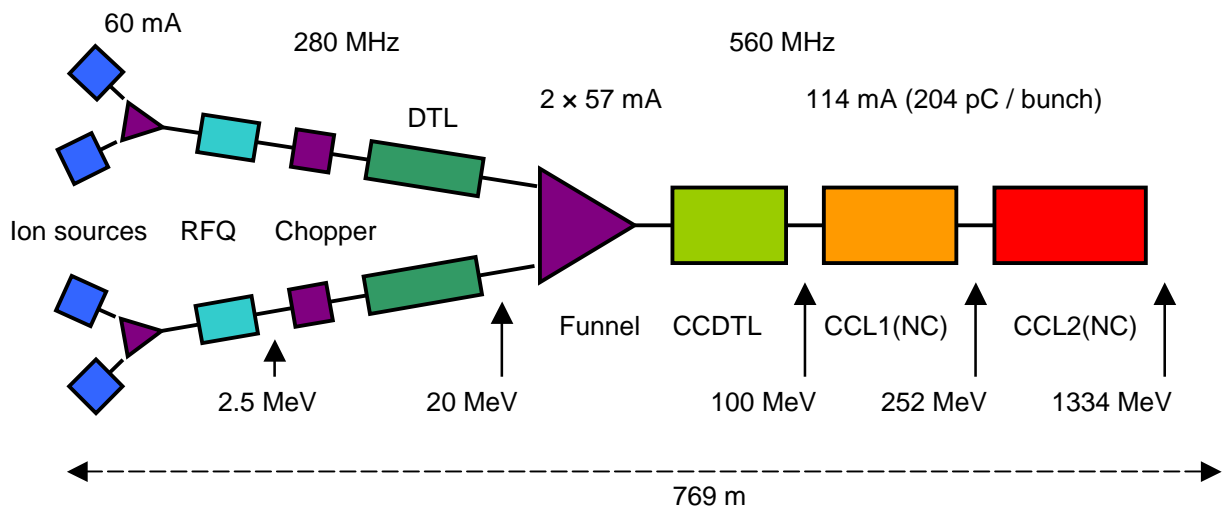


Figure 1.1–1: The 280/560 MHz NC scheme

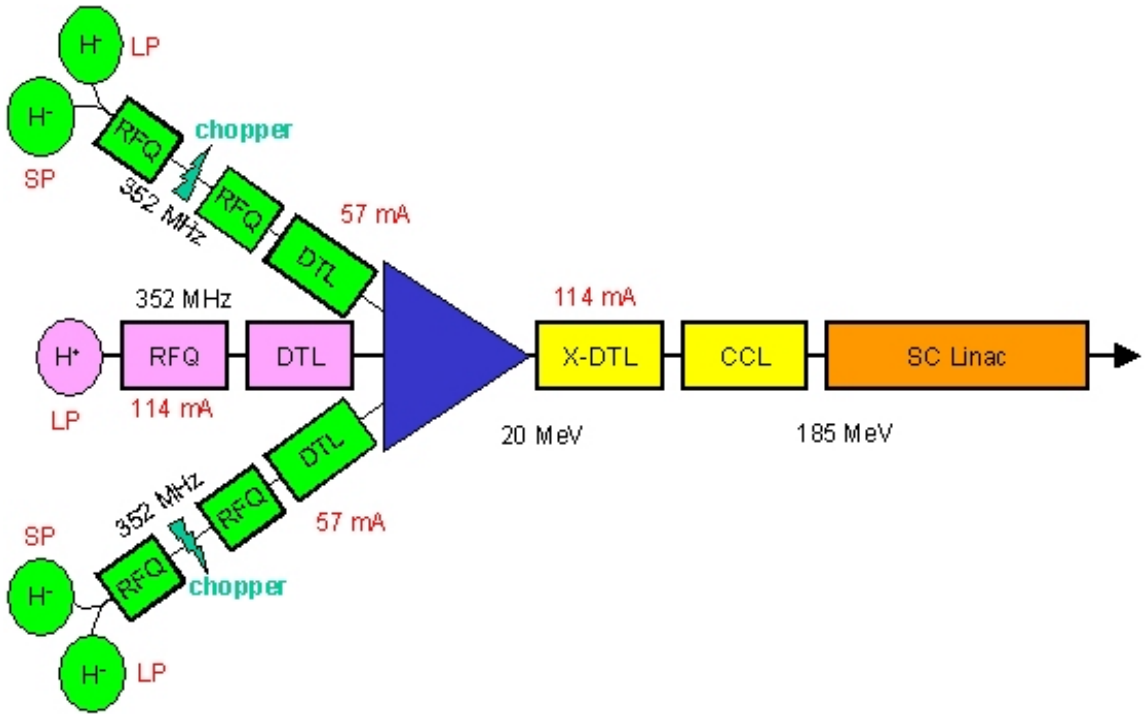


Figure 1.1–2: The 352/704 MHz SC scheme, with the optional LP H^+ contingency measure

The main difference between the two schemes lies in the technology employed between ~ 200 MeV and 1334 MeV. In this energy region the 280/560 MHz scheme uses normal conducting accelerating cavities, whereas the 352/704 MHz scheme uses superconducting cavities. In both the 280/560 MHz and 352/704 MHz schemes the overall accelerating gradients are rather conservative, and in both schemes the designs incorporate the results of detailed analyses of cost, beam dynamics, system robustness, and reliability.

The ESS Technical Advisory Committee (TAC) review [Lander, 2002] of the proposed accelerator schemes did not identify any “show stoppers”. The 280/560 MHz NC scheme “is feasible and can meet the specified performance”, and the 352/704 MHz SC scheme “is a robust and convincing design”. The fact that at this stage two schemes are still under consideration is not seen as anything but a strength.

1.1.1 The beam acceleration regimes

The current ESS specification calls for two neutron-producing targets: a short pulse target to which protons with a mean power of 5 MW are delivered at 50 pps in $1\ \mu s$ pulses, and a long pulse target to which protons with a mean power of 5 MW are delivered at $16^{2/3}$ pps in $2.5\ ms$ long pulses. While short pulse 50 pps specification remains similar to the 1996 specification, the new long pulses at $16^{2/3}$ pps have to be interleaved. Two accumulator rings, fed by two $0.5\ ms$ pulses separated by $0.1\ ms$, produce the short pulses, and it is the outputs from the accumulator rings, which are fed to the short pulse target, whereas the long pulses are delivered directly to the long pulse target. The addition of the new long pulse requirement to the short pulse requirement is a substantial additional demand, and has important implications for the ion sources, the RF systems and the beam dynamics. The specifications of the short pulses (SP) and long pulses (LP) within the acceleration system are given in Table 1.1–1. (Slightly different numbers for beam currents, etc. may be encountered throughout this report;

any differences are likely to be within normal accelerator operating margins and are not material.)

Table 1.1-1: Long and short pulses within the acceleration system

	SP	LP	
PRF (pulses per second)	50	16 ^{2/3}	
Beam pulse half width, 1 ring (ms)	0.48	2.0	
Beam duty factor	4.8%	3.3%	
Non-chopped beam current (mA)	114	114	
Chopping factor	70%	70%	100%
Final energy (MeV)	1334	1334	
Peak beam power (MW)	107	107	152
Mean beam power (MW)	5.1	3.5	5.1
Pulse gaps, ring separation (ms)	0.1		
NC-Linac			
Total linac length (m)	769	769	
Peak RF power (nominal)(MW)	186	236 (100%)	
Wall plug RF power (30 % RF control included) (MW)	34	24	
SC-Linac			
Total linac length (m)	432	432	
Peak RF power (nominal)(MW)	121	167 (100 %)	
Wall plug RF power (30 % RF control included)(MW)	20	15	
Cryo power(MW)	1.5	1.5	

The second section of this chapter describes the ion sources, while in the third and fourth section the 280/560 MHz and 352/704 MHz acceleration schemes are described.

1.2 THE ION SOURCES

1.2.1 Introduction

In order to meet the 5 MW short pulse and 5 MW long pulse ESS beam power specifications, much is required of the ion source(s). Satisfying the requirements with a single ion source implies a considerable extrapolation from present H⁻ ion source performance. However, by combining two beams in a funnel the ion source demands are reduced and brought closer to current source performance.

In this section are described the current states of applicable H⁻ ion sources (*viz* Penning, volume and ECR sources), and also the development work necessary to meet the ESS requirements. The current states of ion sources have been comprehensively reviewed in several fora, most recently [Ferdinand, 2001], and the proposed development strategies have been drawn up on the basis of expert opinion expressed at these fora. On the bases of present ion source operational experience and of development programmes already begun, it is likely that H⁻ ion sources will be produced to meet ESS short and long pulse specifications within 2–3 years. Nevertheless, a fallback strategy exists for long pulses as these are not injected into

the accumulator rings. This is to use a proton source instead of an H⁻ ion source, and proton sources of the required performance already exist. However, accommodating both H⁻ ions and protons within the same acceleration system raises many physics and engineering problems, which might not be easily resolved within the required time scales.

1.2.2 Short and long pulse considerations for H⁻ ion sources

In Table 1.1-2 is presented a summary of the required parameters for the H⁻ ion sources assuming a funnel is used.

Table 1.1-2: The Ion Source Parameters

Parameter	Short pulses	Long pulses
Ion current	60 mA	60 mA
Pulse length (ms)	2×0.48 ms	2.0 ms
Repetition rate (pps)	50 pps	$16^{2/3}$ pps
Duty factor	4.8 %	3.3 %
Required lifetime	≥ 20 days	
Normalised emittance	$\leq 0.3 \pi \text{ mm mrad}$	
Noise	≤ 2 % peak-to-peak	

The long pulses at $16^{2/3}$ Hz have to be interleaved with the short pulses at 50 Hz. It is unlikely that the long pulses could be derived from the same H⁻ ion sources that produce the short pulses because of the very different thermal regimes within the ion sources for short and long pulses. Therefore it is envisaged that the outputs of two sources, one for short pulses, the other for long pulses, would be merged using a switched polarity magnet before each of the two front ends. This design requires a total of four ion sources.

In the next three sections are presented two candidate ion sources, and a third source from which applicable data should become available.

1.2.3 Penning H⁻ source

The Penning source is being developed from the ISIS source currently in operation at the Rutherford Appleton Laboratory (RAL). The source is shown in cross section in. The H⁻ beam is produced from a self-sustained plasma discharge in crossed electric and magnetic fields. It is a surface plasma source that produces energetic H⁻ ions at the cathode surface of the discharge cell. Caesium is used to enhance the production of these H⁻ ions by lowering the work function of the surface.

The extracted H⁻ ion beam is mainly formed from H⁻ ions created near the extraction aperture in a resonant charge exchange reaction between these energetic surface produced H⁻ ions and slow hydrogen atoms thermalised by collisions with gas molecules and the chamber walls.

The resonant charge exchange mechanism results in a low ion temperature ≤ 1 eV. The source operates at high emission current densities $> 1 \text{ A cm}^{-2}$ [Derevyankin, 1994], which is considerably higher than is possible in volume sources. The e/H⁻ ratio is ~ 1 and so a relatively

low electron current is extracted simultaneously with the H^- ion beam. This has important consequences in the design of the optics for the extraction electrode system.

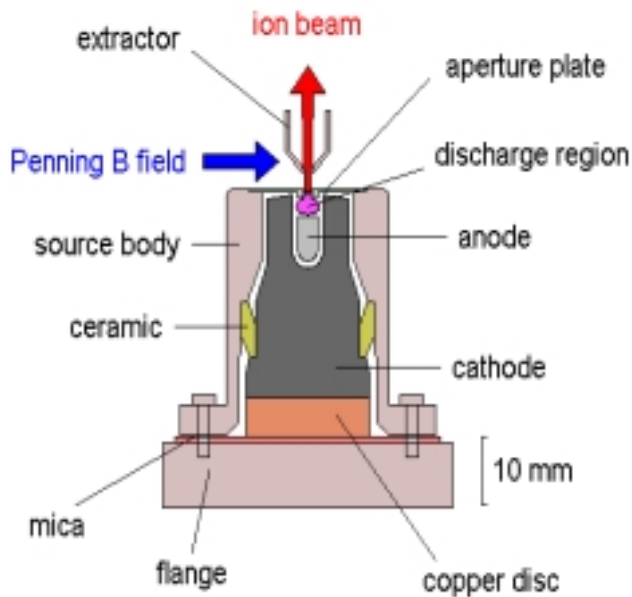


Figure 1.2-1: Schematic cross-section of ISIS Penning H^- ion source

Operational Penning sources have been built with both axially symmetric and slit extraction geometries. Either geometry is acceptable as beam optical matching of the ion beam into the downstream RFQ accelerator can be designed for both geometries. Pulsed Penning sources have a good and well-established track record in an operational environment. Although no existing source can satisfy simultaneously all the requirements of the source for the ESS funnel design, the Penning source currently operating on ISIS and that developed for the Moscow Kaon Factory at Troisk by the Budker Institute in Novosibirsk are the closest in performance.

The ISIS Penning source has slit extraction geometry, but the extracted beam is immediately passed through a 90° sector magnet with an $n = 1$ gradient to separate out electrons and produce an approximately round beam profile. The magnet pole pieces are set into the sides of a stainless steel “cold box”, which is maintained at -5°C to condense excess caesium emitted from the source. In normal operation on ISIS the ion source operates at 35 mA, but the source is deliberately tuned down to this current to match the ISIS linac and multi-turn injection requirements [Sidlow, 1996]. Recently measured normalised RMS emittance values are $\epsilon_H = 0.17 \pi \text{ mm mrad}$ and $\epsilon_V = 0.20 \pi \text{ mm mrad}$.

In non-operational periods of ISIS the source has delivered 55 mA for sustained periods in its present form, which corresponds to a current density of $\sim 1 \text{ A cm}^{-2}$. A dedicated ion source development rig (ISDR) has been constructed and commissioned at RAL, and will allow further development of the source to meet the duty cycle and intensity requirements of the ESS [Thomason, 2002].

The source is very compact, and the primary problem to solve is that of stabilisation of the cathode and anode temperatures at the higher power levels required for the ESS short and

long pulse options by means of controlled cooling. The problem of rapidly establishing stable plasma conditions under pulsed operation is fundamental to all types of ion source and this becomes more difficult with the power levels involved in high duty cycle operation. As part of a research and development programme already begun, the thermal properties of the standard source will be modelled, and this simulation will then be extended to longer duty cycles in order to establish how additional cooling can be introduced most efficiently. If this proves ineffective a scaling approach similar to that previously adopted on the 4X and 8X sources at Los Alamos [Smith, 1994] may be adopted, where increasing component dimensions has been shown to offset heating effects. Predictions based on the experience at Los Alamos suggest that a Penning source producing 100 mA of H⁻ ions with 5 % duty factor and slit extraction geometry should be feasible [Sherman, 2001].

All types of H⁻ ion source rely on the formation of plasma for the generation of the H⁻ ions, and erosion in the source can result from the ions in the plasma and from back-streaming ions formed in the accelerating gap in the ion extraction region. Erosion in the source is probably the limiting factor for source lifetime. In the ISIS Penning source the anode and cathode surfaces erode, and the rate of erosion depends on the electrode material, the uniformity of the Penning discharge and the operating conditions of the source. These are also being studied to maximise the operating life. Continued experience of running the source in an operational environment on ISIS [Thomason, 2000] has already extended the operating life to an average of 26 days and a maximum of 49 days.

Further research and development of the Penning source is needed to meet the ESS specifications, but this is not a large extrapolation from current performance and is considered feasible in the time scale of the ESS.

1.2.4 Volume H⁻ source

The ‘Institut für Angewandte Physik’ (IAP) in Frankfurt is developing a volume ion source. Its low electron temperature and the high achievable current densities make it one of the candidates for the ESS. This type of source has proven its capability for H⁻ ion production, and a design developed at Lawrence Berkeley National Laboratory (LBNL) will be used for the Spallation Neutron Source (SNS) project in the USA [Thomae, 2002]. Such sources may use either filaments or a radio frequency (RF) antenna to generate the plasma. In Frankfurt, 120 mA of H⁻ with caesium has been obtained at 6% duty cycle (1.2 ms, 50 Hz) [Volk, 1998]. The Japan Atomic Energy Research Institute (JAERI) has reported 72 mA of H⁻ with caesium at 5% duty cycle (1 ms, 50 Hz) [Oguri, 2002]. At SNS up to 50 mA of H⁻ with caesium at 6% duty cycle (1 ms, 60 Hz) has been delivered through the low energy beam transport system [Thomae, 2002]. At the ‘Deutsches Elektronen-Synchrotron’ (DESY), 80 mA of H⁻ without caesium has been obtained, but with a very low duty cycle [Peters, 1998].

Several source prototypes have been used in experiments at Frankfurt to test different source geometries and methods of plasma confinement, and to optimise the cathode configuration. The experimental and theoretical investigations have led to a deeper understanding of the complex processes connected with H⁻ production. It has been found that both the H⁻ current and the e/H⁻ ratio are very sensitive even to small changes of the plasma parameters and the source geometry. The cathode configuration of the source has been optimised with regard to position, angular orientation, and polarity. Due to drift in the crossed electric and magnetic fields, the plasma column is displaced perpendicular to these fields. Therefore, the centre of the plasma column does not coincide with the axis of the plasma chamber and the outlet opening has to be appropriately aligned with the centre of the plasma column. It can be shown

that the centred position does not deliver the highest current density and lowest e/H^- ratio [Volk, 1996].

As a result of these experiments, the ion source shown in Figure 1.2-2 has been chosen for further study [Volk, 1998]. The plasma chamber of the ion source is made of a water-cooled copper cylinder 7.0 cm in diameter and 10.0 cm in depth. Ten CoSm magnets surround it in a cusp field arrangement. Near the chamber axis are mounted four tungsten filaments of 1.8 mm diameter. The plasma electrode encloses the front end of the chamber. An electromagnet is installed in the flange of the plasma electrode. Its transverse magnetic field (B_f) acts as an electron filter. An external oven for introducing caesium is mounted on the flange of the plasma electrode. By means of two small pipes the caesium vapour is deposited close to the outlet aperture. The whole system is temperature controlled. In order to extract the H^- ions a single-hole diode extraction system with an aspect ratio of 0.8 is used. A heater is integrated into the ground electrode so that the extractor can be run at temperatures around 250°C. This reduces caesium deposition on the ground electrode and therefore eliminates high voltage breakdowns in the extraction gap.

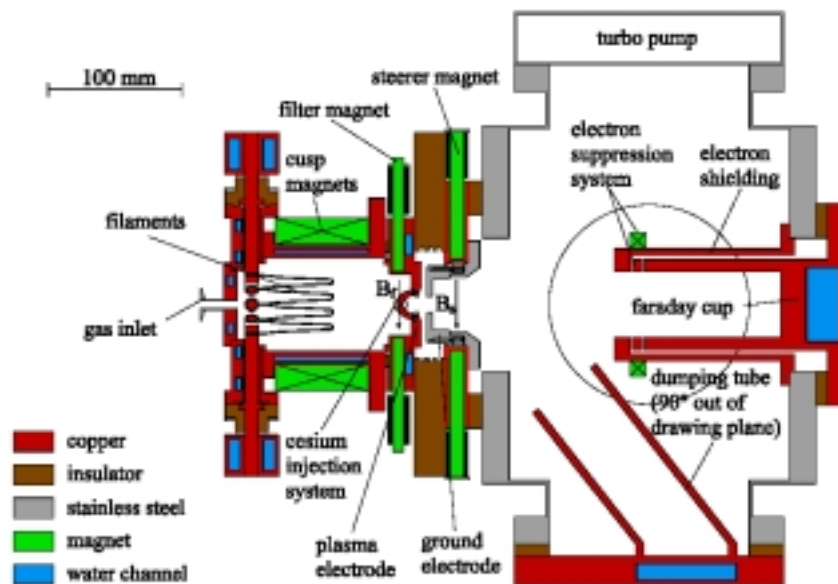


Figure 1.2-2: Schematic cross-section of the Frankfurt volume H^- ion source

Experiments have shown that the ion source is capable of producing 120 mA of H^- beam, measured using a Faraday cup, at an arc power of 47.5 kW (50 Hz, 1.2 ms). In operation with caesium the H^- emission current is up to 4.5 times higher, and for 47.5 kW arc power the e/H^- ratio is about 7. Estimates of $<0.1 \pi \text{ mm mrad}$ have been obtained for normalised RMS emittance.

The source lifetime is limited by wear of the filament, which is roughly inversely proportional to the duty cycle and arc power. With the present filament configuration the ion source has been run for 180 hours at an arc power of 40 kW, during which the diameter of the filaments was reduced from 1.8 mm to 1.5 mm. Since the filaments can be used down to a thickness of about 0.9 mm the ion source lifetime could be expected to be about 15 days. Using thicker filaments could be an advantage, but unfortunately would require operation with a larger power supply. Large arc pulse supplies may be avoided by using RF power to generate the plasma, but this does not form part of the present research at IAP.

Caesium is injected on demand only, so there is wear of the caesium layer, which has to be rebuilt every 10 to 18 hours. To achieve a controlled caesium deposition a specific temperature profile of the plasma generator has to be kept, and hence the arc power has to be reduced for about 15 minutes. A caesium injection system will be developed that will allow caesium injection at higher powers.

The theoretical and experimental investigations accomplished during the first phase of this study have shown that the volume ion source has the potential to fulfil the requirements for ESS, but further research and development is required to improve the lifetime and demonstrate the reliability of the source.

LBNL has suggested a possible agreement between the SNS ion source team and Europe to produce an RF driven volume source similar to that for SNS [Thomae, 2002], but using an external antenna based on the DESY design [Peters, 1998], which has distinct benefits for source lifetime. This research would be subject to funding approval from the USA Department of Energy.

1.2.5 The ECR H⁻ source

ECR H⁻ sources, Figure 1.2-3 on page 1-14, are too distant a possibility to be seriously considered for short pulses for the ESS. Nevertheless, the strong R&D programme currently being carried on such H⁻ sources should allow some results to be available for ESS within the expected time frame. ECR sources should have at least 6 months of availability in CW mode, and this would be ideal for ESS if the extracted H⁻ current can be increased to the required levels.

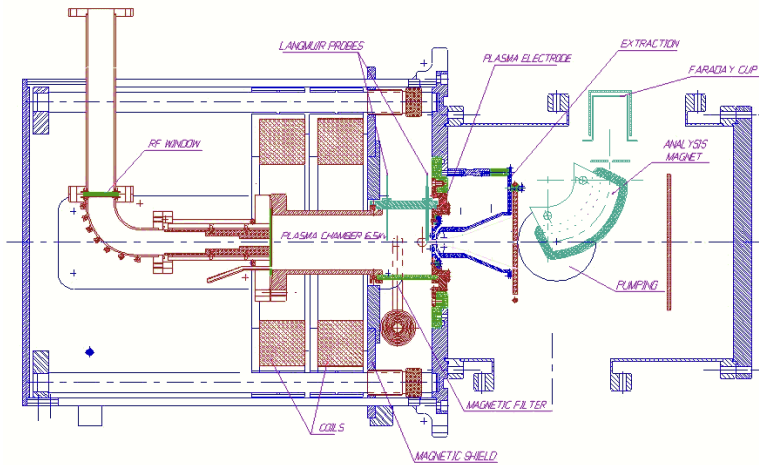


Figure 1.2-3: Schematic cross-section of the ECR H⁻ ion source

1.2.6 Proton sources

Proton ECR sources in different laboratories (LEDA at LANL, SILHI at CEA/Saclay) have already demonstrated capabilities consistent with the ESS requirements [Gobin 2002, Sherman]. In particular, lifetimes in CW mode of the order of 6 months have been achieved with good emittance and high beam currents (>100 mA). They are perfectly suited to long pulses.

1.2.7 Conclusions

It is clear from the above that a programme of ion source development work should be carried out to ensure that suitable ion sources are available for the ESS. In fact, a relevant programme has already begun at the Rutherford Appleton Laboratory where an ion source development rig has been constructed and commissioned. Further, a programme of generic H^- ion source development work has begun, part funded by the European Union. The objective of this programme is to put together all the competence of the European Union to meet the technical challenges raised by the next generation of high power (proton) accelerators.

Neither the Penning source in operation at RAL nor the volume source at Frankfurt has yet met all the ESS requirements, but steady improvements in performance of the sources lead to the expectation that they will meet the requirements.

1.3 THE 280/560 MHZ LINAC DESIGN

1.3.1 Introduction

A different design, from that presented in the 1996 technical study [ESS-96-53-M], has been evolved for the 1.334 GeV H^- linac. There are changes both in the specification and in the linac structures for the new design. Together with the earlier beam power requirements of 5 MW at 50 Hz, an extra 5 MW has to be provided in an interleaved mode at 16.667 Hz. This is more difficult to achieve because of the larger demands that are placed on the H^- ion sources and on key areas of the accelerator such as the choppers, the funnel and the radio frequency (RF) systems.

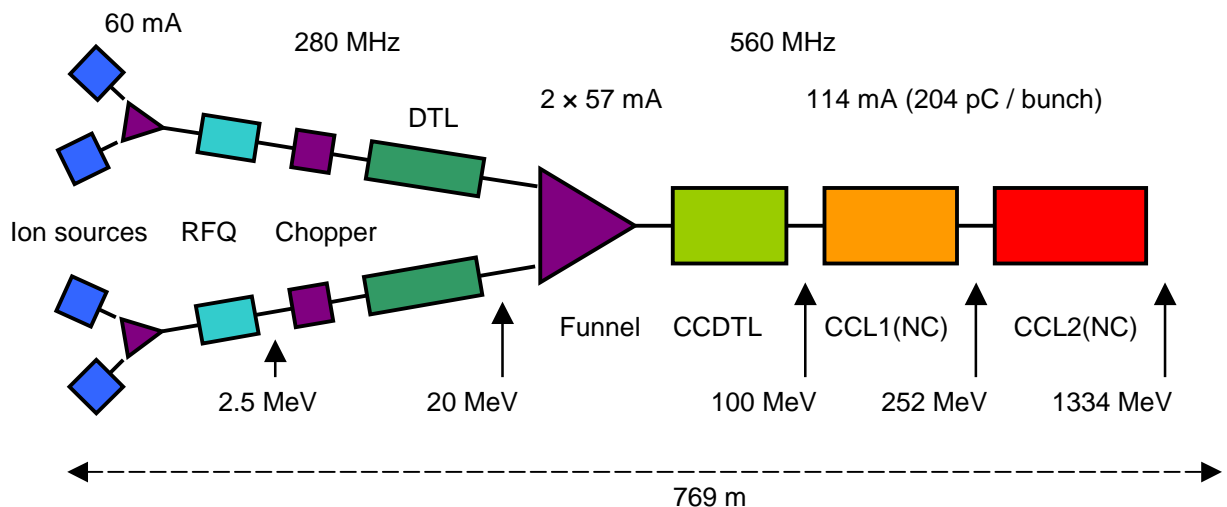


Figure 1.3-1: 280/560 MHz normal conducting linac layout

Changes in frequency have been made for the linac structures, from the previous values of 175, 350 and 700 MHz to the new values of 280 and 560 MHz. The front end is extended to 20 MeV, at which energy two 280 MHz linac sections are funnelled into the high energy 560 MHz stage. Before the funnel, each channel has a 0.075 MeV H^- ion, a solenoid-focussing channel (LEBT), a 2.493 MeV 280 MHz RFQ accelerator, a four-buncher chopper section and a 20 MeV 280 MHz drift tube linac (DTL). Beam currents of 57 mA per channel

are required, chopped at 50 Hz with a duty on-cycle of 5 % and at 16.667 Hz with the added, interleaved duty on-cycle of up to 4.167 %. The corresponding pulse durations are 1.0 ms at 50 Hz and up to 2.5 ms at 16.667 Hz. Further pulse chopping is provided at the ring bunch revolution frequency of 1.24 MHz, to assist in reducing ring losses. Within the pulses, the duty on-cycle is made adjustable in the range 0 to 70 %, and the chopping is included in both the 50 Hz and 16.667 Hz beams to allow initial operation at the same linac current for both targets. The room temperature, high-energy linac sections at 560 MHz consist of a 20 to 100 MeV cavity coupled drift tube linac (CCDL), and a 100 to 1334 MeV cavity coupled linac (CCL).

A variant has also been studied in which a transition is made at 332.8 MeV from a $12\beta\lambda$ FODO normal conducting CCL cavity system to ~ 25 MV/m 560 MHz superconducting $16\beta_g\lambda$ ($\beta_g = 0.75$) cryomodules, within fifty-six of which one hundred and sixty-eight four-cell cavities chosen to give acceptable phase slippages then accelerate the beam up to 1334 MeV (*i.e.* from $\beta = 0.64$ up to $\beta = 0.91$) [Gardner, 2001], [Gardner, 2002]. For the SC version of the 280/560 MHz solution with only one coupler per SC cavity the fraction of the overall superconducting length occupied by accelerating fields is 6/16, and the total linac length is 580.8 m. If the power couplers into the superconducting cavities are limited to 0.64 MW (a little beyond the current state of the art), then because each cavity requires its own RF driver to limit RF errors, one hundred and sixty-eight separate RF systems are called for (and consequently a large number of shielding penetrations are required for the feeders waveguides). This large number has implications for capital and running costs, for linac setting-up times, and for beam dynamics and beam quality (especially if the number has to be increased again to accommodate higher peak RF powers resulting from 2 ms unchopped long pulses). In end-to-end beam simulations with maximum dynamic RF errors of $\pm 1^\circ$ (phase) and $\pm 1\%$ (amplitude) the largest phase offset observed was 12° , resulting in an energy error of 2.4 MeV, which may be compared with the ± 0.7 MeV tolerance for ring injection. The maximum dynamic RF errors in the superconducting cavities should therefore be $< \pm 0.3^\circ$ (phase) and $< \pm 0.3\%$ (amplitude), numbers which may be difficult to achieve, as RF field control is affected by tuning errors due to Lorentz force excitation of mechanical vibration modes in the cavities (the tuning is effected by a combination of mechanical and piezoelectric tuning). Clearly, key tasks should be to develop higher power RF couplers and to prove RF control systems. The in chapter 1.4 presented 352/704 MHz SC linac solution has two couplers per SC cavity in order to keep the peak power per coupler within acceptable limits. Details about the 2-coupler scheme are found in section 1.4.9.

1.3.2 Choice of Linac Frequencies and Layouts

The ESS reference linac design of 1996 was based on three frequencies, 175, 350 and 700 MHz. The reasons for changing to the two new frequencies of 280 and 560 MHz are as follows:

- a) One half of the possible number of bunches are missing in the 700 MHz linac stages, resulting in larger peak currents and space charge effects.
- b) An increase in energy from 5 to 20 MeV has been found necessary for funnelling and, for the original frequencies, this would involve the use, ahead of the funnel, of either large diameter, 175 MHz DTLs or the use of 175 and 350 MHz RFQs with 350 MHz DTLs; preferable to both such arrangements would be a front end entirely at 350 MHz.

- c) Assuming the latter, mechanical tolerances for a 350 MHz RFQ are tighter than for the 280 MHz RFQ proposed.
- d) A cheaper, four-rod design may be adopted for a 280 MHz RFQ, whereas a four-vane design would be required for a 350 MHz RFQ.
- e) Again comparing a 350 and 280 MHz front end, the rise and fall time specification for the important linac chopper section is more difficult for the former than the latter.
- f) Design and matching for the chopper transport line is easier at the new frequency of 280 MHz.
- g) Electromagnetic quadrupoles may be used in a 280 MHz, 2.5 to 20 MeV DTL, allowing flexibility in focussing and matching, whereas permanent magnet units would be needed in a comparable 350 MHz DTL.
- h) A non-dispersive, conceptual funnel design, with very low emittance growth, has been found for the 280 and 560 MHz frequencies, but had proved difficult for the different frequencies of the 1996 design.
- i) Mechanical design for a CCDTL is easier at 560 MHz than 700 MHz.
- j) Smoother matching transitions between linac stages may be obtained for the two, lower frequencies than for the three, higher frequency case.

On the debit side for the proposed change is that engineering costs for the CCL stages will be higher for the larger structures at the new frequency of 560 MHz.

A comparison may also be made between the proposed frequencies and those of 402.5 and 805 MHz selected for the SNS project at Oak Ridge, USA. The arguments presented in favour of the lower frequencies are even stronger in this case, though benefits would ensue from the superconducting developments at the SNS if an SCL option is adopted for the ESS. A further quantification of these advantages/disadvantages remains to be done.

Schematic layouts are given in Figure 1.3–1 for the normal conducting linac (NCL) 280/560 MHz scheme. Smooth focussing transitions are introduced between stages. The FODO focussing pattern adopted for the NCL is $2\beta\lambda$ (RFQ), $4\beta\lambda$ (DTL), $9\beta\lambda$ (Funnel), $10\beta\lambda$ (CCDTL), $11\beta\lambda$ (CCL1) and $12\beta\lambda$ (CCL2), where β is the particle velocity relative to that of light and λ is the free space wavelength at the frequency of 560 MHz. The fractions of the cell lengths with accelerating fields are $6/10$ (CCDTL), $8/11$ (CCL1), and $10/12$ (CCL2). The total linac length is 768.9 m.

1.3.3 Low Energy Beam Transport and Radio Frequency Quadrupole

1.3.3.1 LEBT

The function of the Low Energy Beam Transport (LEBT) is to match the output from the ion source(s) into the RFQ accelerator with minimum emittance growth and minimum loss of beam current. The beam current of 57 mA required in the RFQ is already high for a single aperture H^- source, and so good transmission is necessary between the ion source and the RFQ. Projected normalised RMS emittances from ESS ion sources are typically $\sim 0.1 \pi \text{ mm mrad}$, whereas the projected acceptance of the RFQ is expected to be $\sim 0.2 \pi \text{ mm mrad}$, so tolerable RMS emittance growth is limited to $\sim 100 \%$. The LEBT may also usefully include diagnostics for the beam from the ion source(s); experience at the ISIS

spallation neutron source at the Rutherford Appleton Laboratory shows that information from such diagnostics is very useful operationally [Thomason, 2000].

1.3.3.2 Three Solenoid Magnetic LEBT

As mentioned above, the H^- ion source used for ESS is likely to be either the ISIS-type surface Penning source or the Frankfurt volume source. In order to accommodate the unequal horizontal and vertical transverse emittances from the Penning source, a LEBT for H^- ion sources has been designed with three solenoids [Planner, 1995]. Figure 1.3-2 shows a realisation of the three-solenoid LEBT design, specifically the LEBT on the RFQ test stand at ISIS [Bailey, 2000]. Each of the three identical solenoids has a length of 220 mm and an internal diameter of 72 mm, and incorporates Lambertson coils for steering the beam both horizontally and vertically. A gap between the second and third solenoids provides for vacuum pumping and inclusion of diagnostics. Calculations show that the design accommodates values of space charge compensation between 90 and 110 %.

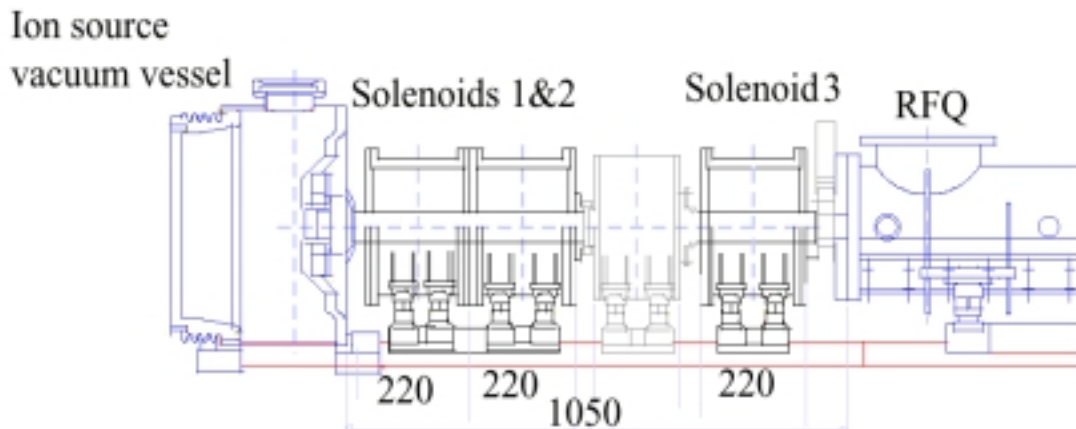


Figure 1.3-2: The ISIS RFQ three solenoid LEBT

With an ISIS-type caesiated surface Penning H^- source running on the ISIS RFQ test stand, the measured vacuum pressures in the LEBT show that pumping the LEBT vacuum between solenoids is effective in de-coupling the RFQ vacuum from the ion source vacuum. Recent beam current measurements on the test stand with the same source have demonstrated that this LEBT performs well, insofar as beam currents of 30 mA have been presented to the RFQ at the end of the LEBT and accelerated through the RFQ from 35 keV to 665 keV with the design beam transmission of 93 %.

Since for the ESS there will not be the same space restrictions as there were for the ISIS RFQ LEBT, it is likely that the length-to-aperture ratio for the ESS LEBT will be larger than that for the ISIS LEBT. Figure 1.3-3 shows emittance measurements of a 30mA, 35 keV H^- beam in the three solenoid ISIS LEBT.

1.3.3.3 Alternative LEBT Designs

It is thought unlikely that in practice an electrostatic LEBT (which assumes there to be no space charge compensation of the beam) would perform as well as a magnetic LEBT (which assumes the beam to be space charge compensated), because, firstly, the required current of 60 mA is high for an electrostatic system, secondly, there is very little space available to fit in

high conductance vacuum pumping ports, and thirdly, there is little or no room for operationally valuable diagnostics.

In the event that a beam for the long pulse target cannot be produced satisfactorily from an H⁻ ion source, the contingency plan is to use an H⁺ source. Suitable two-solenoid LEBT designs are already available [Smith, 1999] [Beauvais, 2000] and have been demonstrated within the Los Alamos LEDA and Saclay IPHI projects.

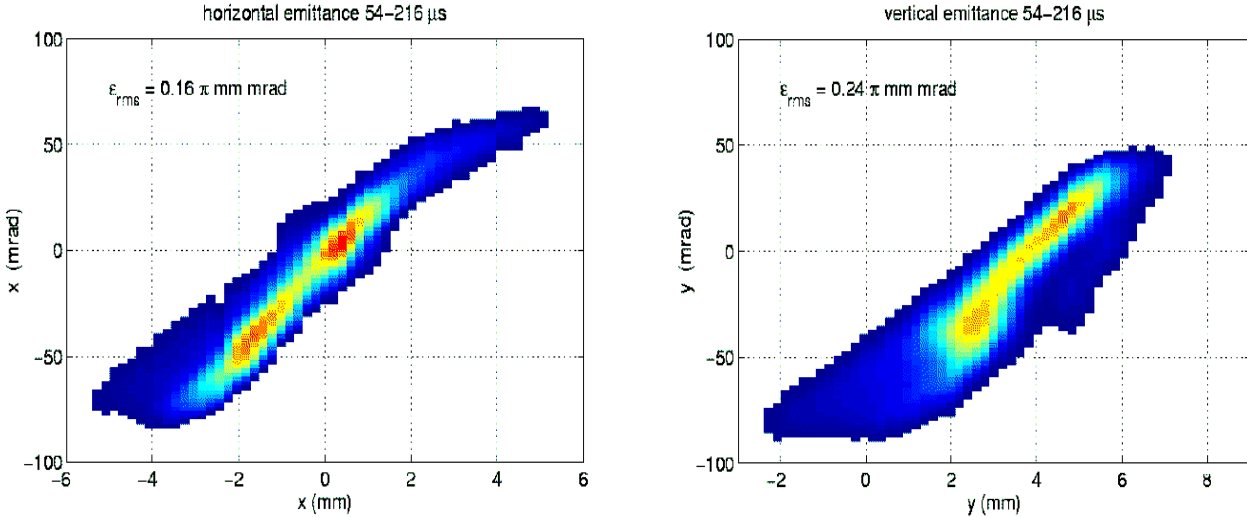


Figure 1.3-3: Emittance measurements of a 30 mA, 35 keV H⁻ beam in the three solenoid ISIS LEBT

1.3.3.4 RFQs

The ESS reference design calls for two Radio Frequency Quadrupole (RFQ) linacs, each one accelerating a 57 mA H⁻ beam. These two beams are then combined at 20 MeV to provide the required power at high energy. As the first accelerating component of the ESS linac the RFQs will play a significant role in determining the quality of the beam in the rest of the accelerator. For this reason beam quality and low emittance growth are the driving forces behind the RFQ design.

1.3.3.5 280 MHz 4-Rod RFQ Parameters

Table 1.3-1 summarises the main parameters of the ESS RFQ design. The RF frequency of 280 MHz is half of the main linac frequency of 560 MHz. At this frequency a 4-rod type resonator has been chosen over the alternative 4-vane type. A great deal of very useful experience has been gained in the design and operation of high power 4-rod RFQs by the injector group at ISIS, the spallation neutron source at RAL, UK and J.W. Goethe university, Frankfurt, Germany [Letchford, 1998][Schempp, 1998][Vormann, 1998][Bailey, 2000][Letchford, 2000][Vormann, 2000]. The final energy of 2.5 MeV is determined by the requirements of the chopping lines that follow the RFQs. A peak electric field of 22 MV/m is modest at a frequency of 280 MHz and poses no significant challenge. A high transmission is desirable to relax the requirements of the ion sources. Very good agreement between computer simulation and measurement on the ISIS-Frankfurt 4-rod RFQ gives confidence that the required transmission can be achieved. Measured emittances of $\sim 0.2 \pi \text{ mm mrad RMS}$ on the RAL Penning H⁻ ion source demonstrate the achievability of the low transverse

emittances [Thomason, 2002] but high machining and alignment accuracy will be needed to maintain these values through the RFQs.

A full design for a 280 MHz, 2.5 MeV 4-rod RFQ has been completed at RAL based on experience with the ISIS high power RFQ. A cold model of the resonator built at RAL has confirmed the resonator properties. Combined RF and thermodynamic modelling studies show that the high power dissipated can be removed from the structure to maintain the required mechanical stability. Figure 1.3-4 shows part of a MAFIA electromagnetic model of the resonator. A corresponding ANSYS heat modelling result is shown in Figure 1.3-5. The output phase space and beam envelope evolution from a beam dynamics simulation of the RFQ are presented in Figure 1.3-6 and Figure 1.3-7 respectively. Negligible emittance growth occurs and the beam shows no dangerous halo or filamentation. A quarter-section outline design is shown in Figure 1.3-8.

Table 1.3-1: Main Parameters of the ESS RFQ Design

RF Frequency	280	MHz
Input Energy	75	KeV
Output Energy	2.5	MeV
Electrode Voltage	100	KV
Total length	4.2	M
Peak electric field	22	MV/m
Transmission	>97	%
Transverse RMS emittance	0.22	π mm mrad
Longitudinal RMS emittance	0.14	π ° MeV
Required structure power	800	kW peak
Required beam power	140	kW peak

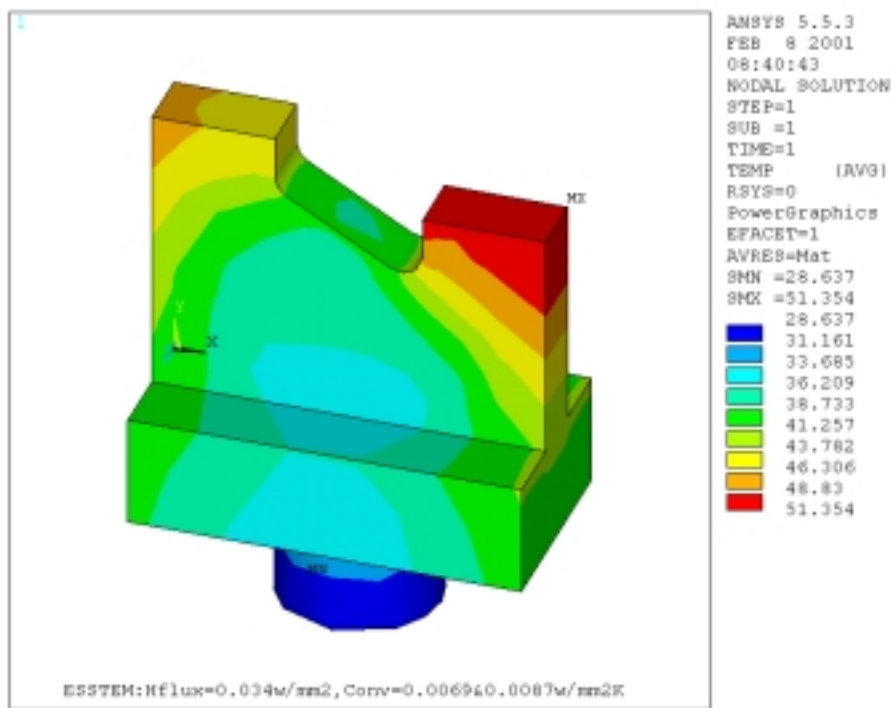


Figure 1.3-4: Surface RF power dissipation from a MAFIA model of the RFQ

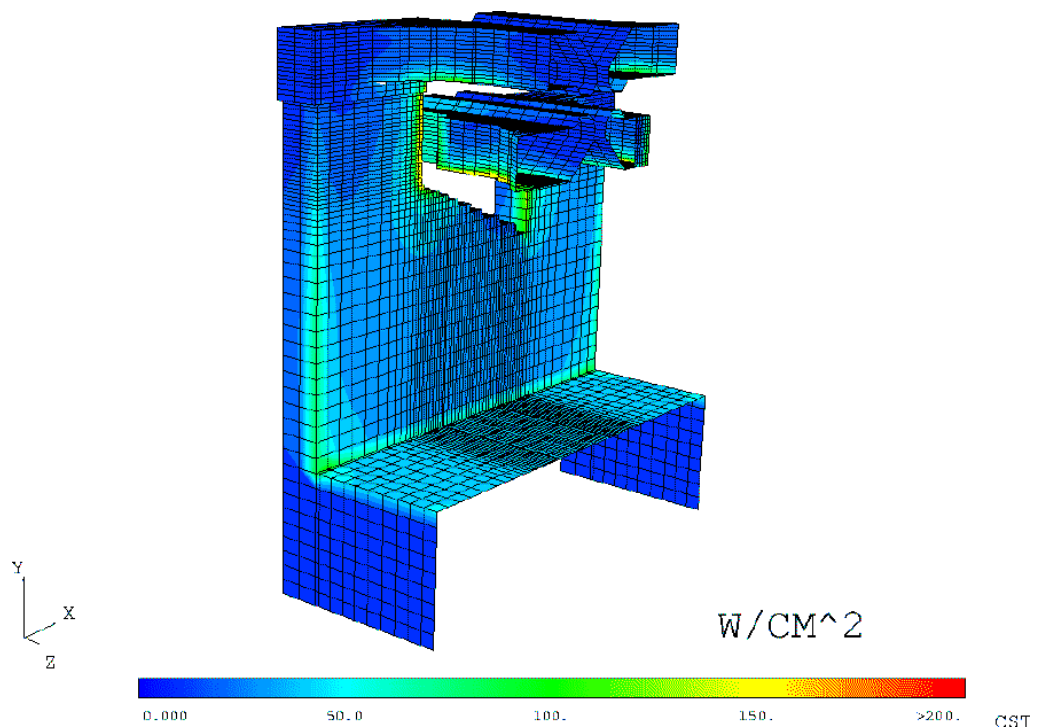


Figure 1.3-5: ANSYS thermodynamic model of an RFQ electrode support stem

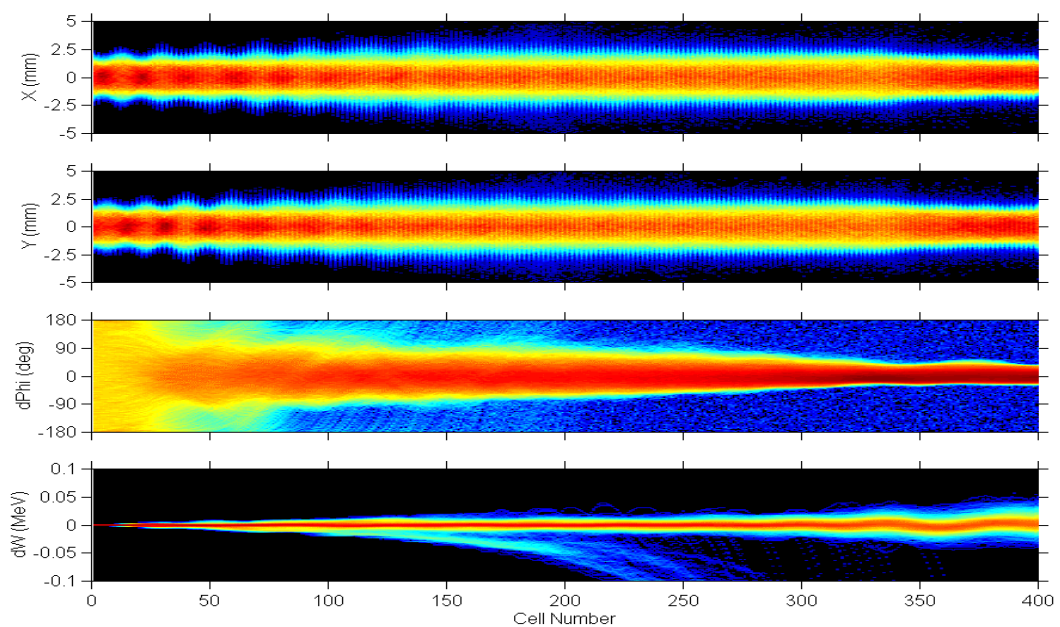


Figure 1.3-6: Simulated evolution of the beam envelopes along the 280 MHz RFQ

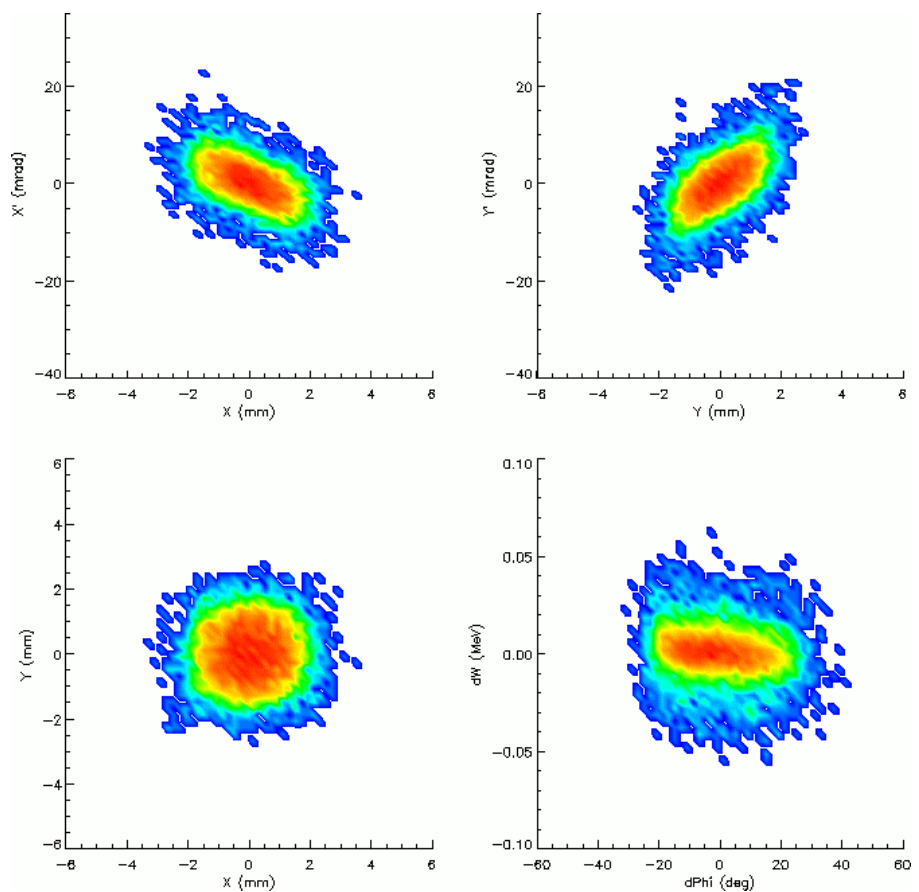


Figure 1.3-7: Simulated output phase space of the 280 MHz RFQ design

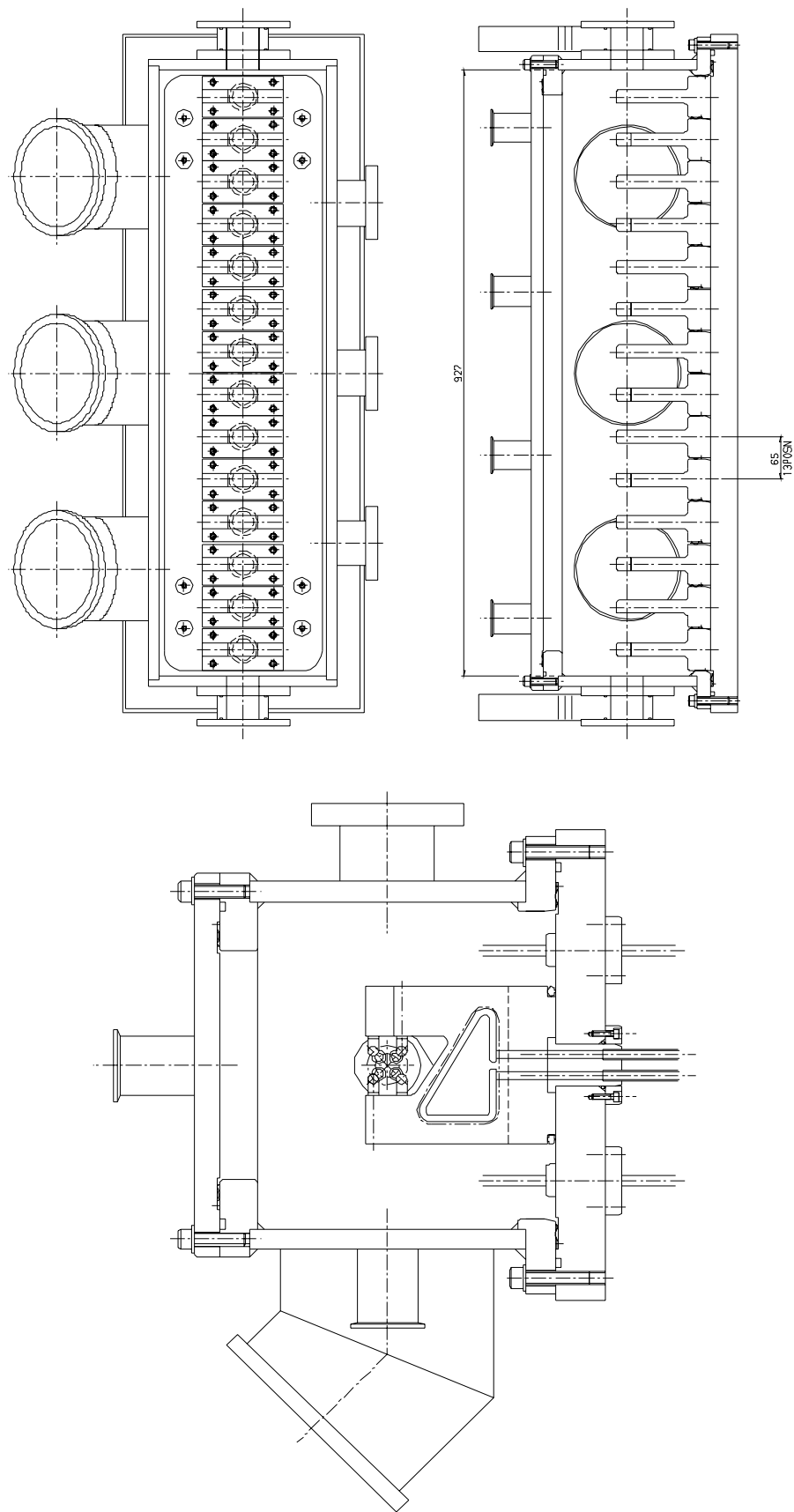


Figure 1.3-8: Quarter-length section of the ESS RFQ

1.3.4 Chopper Section

The H^- output beam from each RFQ passes through a chopper section to the input of a DTL. Matching into the section is simplified by adjusting the output region of the RFQ, and component lengths are reduced, as far as is practical, to restrict the bunch extents during the chopper debunching and rebunching intervals. Chopping is required at a frequency close to the rings' revolution frequency, with beam pulse duty cycles of 0 to 70 %, and with rise and fall times of < 3 ns for the chopper deflection fields. Difficult design areas are: achieving the required rise and fall times, preventing halo growth, and efficiently removing of heat from the loss collectors. Deflected beam powers of up to 5 kW must be removed, and beam current suppression obtained to better than one part in 10^4 for the chopped beam gaps.

Schematic drawings of a chopper line are shown in Figure 1.3-9 and Figure 1.3-10, the latter showing beam sizes under space charge conditions. Lengths may be defined in terms of $\beta\lambda$ where β is the H^- ion velocity relative to that of light and λ is the free space wavelength at 280 MHz. The total length of the chopper section, which is equivalent to $23\beta\lambda$ is about 1.75 m, and the central region has two doublet cells, each having a straight section of length 0.45 m. Travelling wave deflectors are located in the straight sections together with horizontal beam loss collectors. The deflectors may follow the 'meander' design developed at LANL, using microstrip technology and meander separators, though other structures are also of interest. At RAL, R & D is considered necessary before finalising the designs [Clarke-Gayther, 2001].

Deflection within the first unit is accommodated by the decreasing horizontal β -function in the direction of beam motion. Deflection within the second results in beam interception along the collectors, thus distributing the heat load and reducing the power density. Coherent image effects contribute to the deflections. The two central doublet cells have regular lattice functions so keeping equal beam aspect ratios, on average, to inhibit halo growth. Space for vacuum pumping and diagnostics is restricted to the two regions housing the deflectors. Pumping is introduced in both these regions from below and diagnostic units from above. Retractable units are used for beam profile and emittance measurements. Halo scrapers are located ahead of the first quadrupole and a current measuring toroid just ahead of the DTL.

In the channel are nine quadrupoles and four buncher cavities, distributed as in Figure 1.3-9. The design assumes that the space for a buncher gap and its two adjacent quadrupoles is the same as that in the first DTL cell. Input betatron matching from the RFQ makes use of the initial four quadrupoles in the line. The final six-parameter output matching to the DTL makes use of the last two quadrupoles and bunchers together with the first two DTL quadrupoles. The fourth buncher cavity gives flexibility for matching and reduces the voltage needed in the nearby third buncher cavity. An alternative chopper section design is also under study using four, instead of two, central doublet cells. This gives greater scope for chopper and collector designs and for locating scrapers to remove halo and contain partially chopped bunches.

Computer simulations have involved tracking $10^5 H^-$ ions from the chopper input to that of the DTL. Input distributions have their RMS emittances established in RFQ simulations, but with a 6D waterbag distribution of uniform density instead of the actual RFQ output. In the channel, there is some redistribution of the ions in longitudinal phase space but very little halo and emittance growth. At channel entry, the bunch phase extent is $\pm 30^\circ$, and at the entry into the DTL, the extent is reduced to $\pm 18^\circ$. The initial synchronous phase angle in the DTL is chosen at -42° to reduce the non-linear effects on the subsequent longitudinal motion.

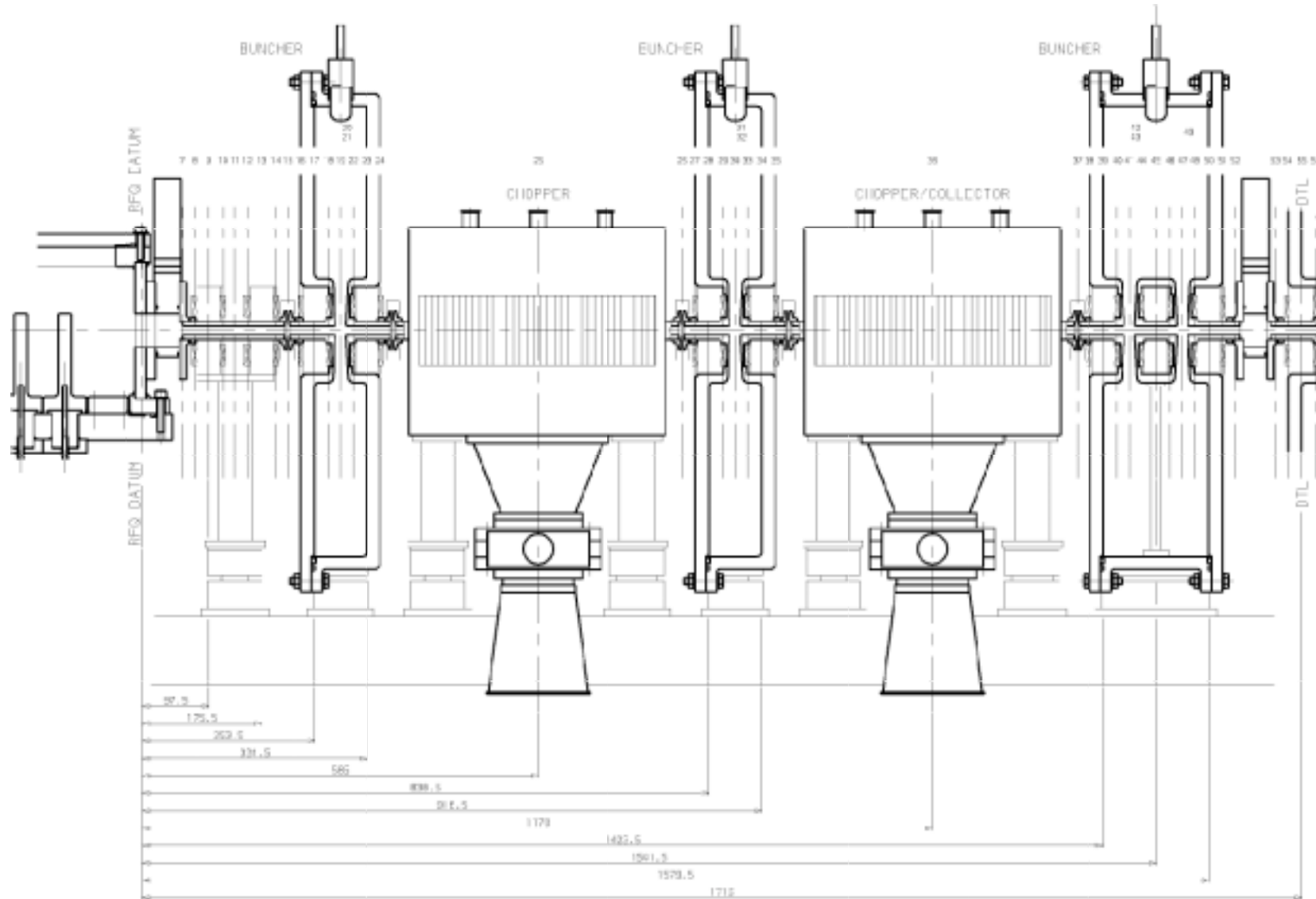


Figure 1.3-9: Schematic view of the 280 MHz Chopper Line

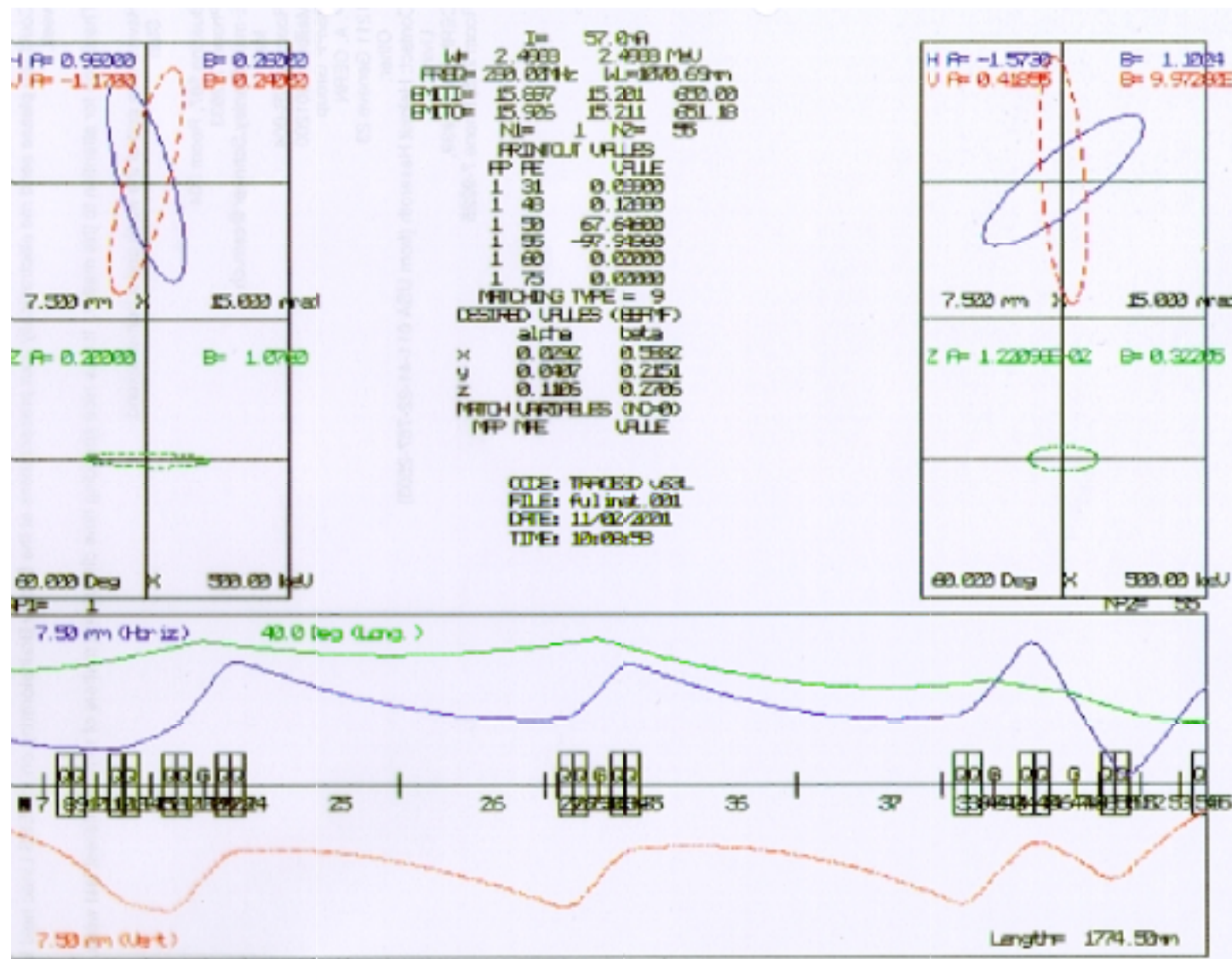


Figure 1.3-10: TRACE3D output of the 280 MHz Chopper Line

1.3.5 280 MHz, 20 MeV Drift Tube Linac, DTL

The DTL is a two tank Alvarez structure, with the first tank, DTL1, accelerating the beam from 2.493 to 11.71 MeV and the second, DTL2, continuing acceleration to 20.0 MeV. DTL1 and DTL2 have, respectively, 42 and 22 drift tube cells, and both are contained in a common vacuum tank to avoid a break in the focussing pattern. An alternative would be to have two separate tanks with a gap between, but with some cells in the transition region shifted in position to reduce the gap mismatch by changing the phase and hence the effect of the RF fields. A suitable tank spacing for this option is $1\beta\lambda$ as this preserves the FODO transverse focussing structure formed by the singlet quadrupole in each drift tube. The initial option of a common vacuum tank for DTL1 and DTL2 is preferred, and the required tank length is then approximately 9.5 m. The layout of the front end is shown in Figure 1.3-11.

The high brightness of the 57 mA H^- beam permits a small bore radius to be selected for the drift tubes, thus enhancing the transit time factors and shunt impedances, and allowing the use of electromagnetic quadrupoles. These follow the design of the adjustable quadrupoles proposed for the JHF-JAERI linac [Yoshino, 2000], and additional steering coils are added to some quadrupole cores to allow H^- beam orbit correction. R & D is required for the design of this quadrupole, whose dimensions are shown in Figure 1.3-12.

The values of radii selected for the tank, the drift tubes and the bore are 325, 75 and 6.5 mm, respectively, and, for the β range 0.07 to 0.02, the transit time factors increase from 0.83 to 0.9 (SUPERFISH value, SV) and the shunt impedances from 51.6 to 65.8 M Ω /m (SV - 10 %). Two linear quadrupole gradient ramps with energy, of different slopes, are used in each tank, with values of 90 and 65.5 T/m at the input and output quadrupoles of DTL1 and with values of 65.5 and 55.2 T/m at the input and output of DTL2.

There is an initial field ramp in DTL1 but for most of DTL1 and DTL2 the accelerating field is set at 2.7 MV/m, with a maximum Kilpatrick level in the tanks of 1.4. The initial value for the synchronous phase angle is -42° , after which it is gradually ramped to -38° and then kept constant. RF power dissipated in the structures is approximately equal to that imparted to the beam, with a total < 1 MW for each tank. An additional 30 % control power is required to meet RF control tolerances of < 1 % maximum in field amplitude and $< 1^\circ$ in RF phase. The klystron power sources for each tank are thus 1.3 MW units. Post couplers are used for stabilisation of the fields in the tanks.

The H^- beam at 2.493 MeV has an input ratio of transverse to longitudinal beam oscillation energies of 0.74, but the ratio is adjusted to become approximately equipartitioned between 8 and 20 MeV. Full current transverse tunes vary from 33.2° to 31.0° in DTL1 and from 31.0° to 27.3° in DTL2 while full current longitudinal tunes vary from 21.6° to 16.3° in DTL1 and from 16.3° to 13.5° in DTL2. The RMS emittance growth is less than 1 %, but a small amount of longitudinal halo develops due to non-linear longitudinal motion in the early stages of DTL1. Six parameter matching is obtained at the entry of the DTL and at the exit from DTL2 to the funnel, with smooth changes of the focussing parameters in the matching regions. The main DTL concern is if the chopper leaves some partly-filled, displaced bunches.

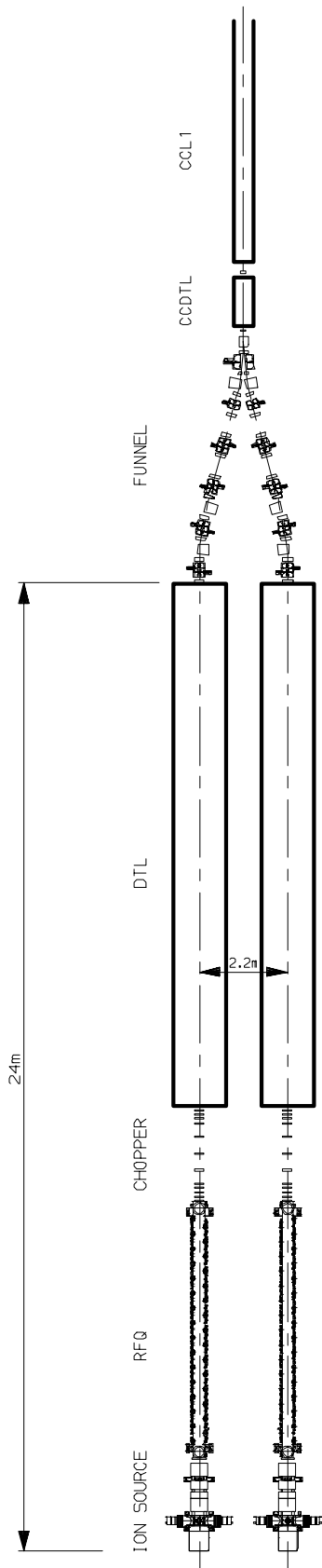


Figure 1.3-11: Injection Front End

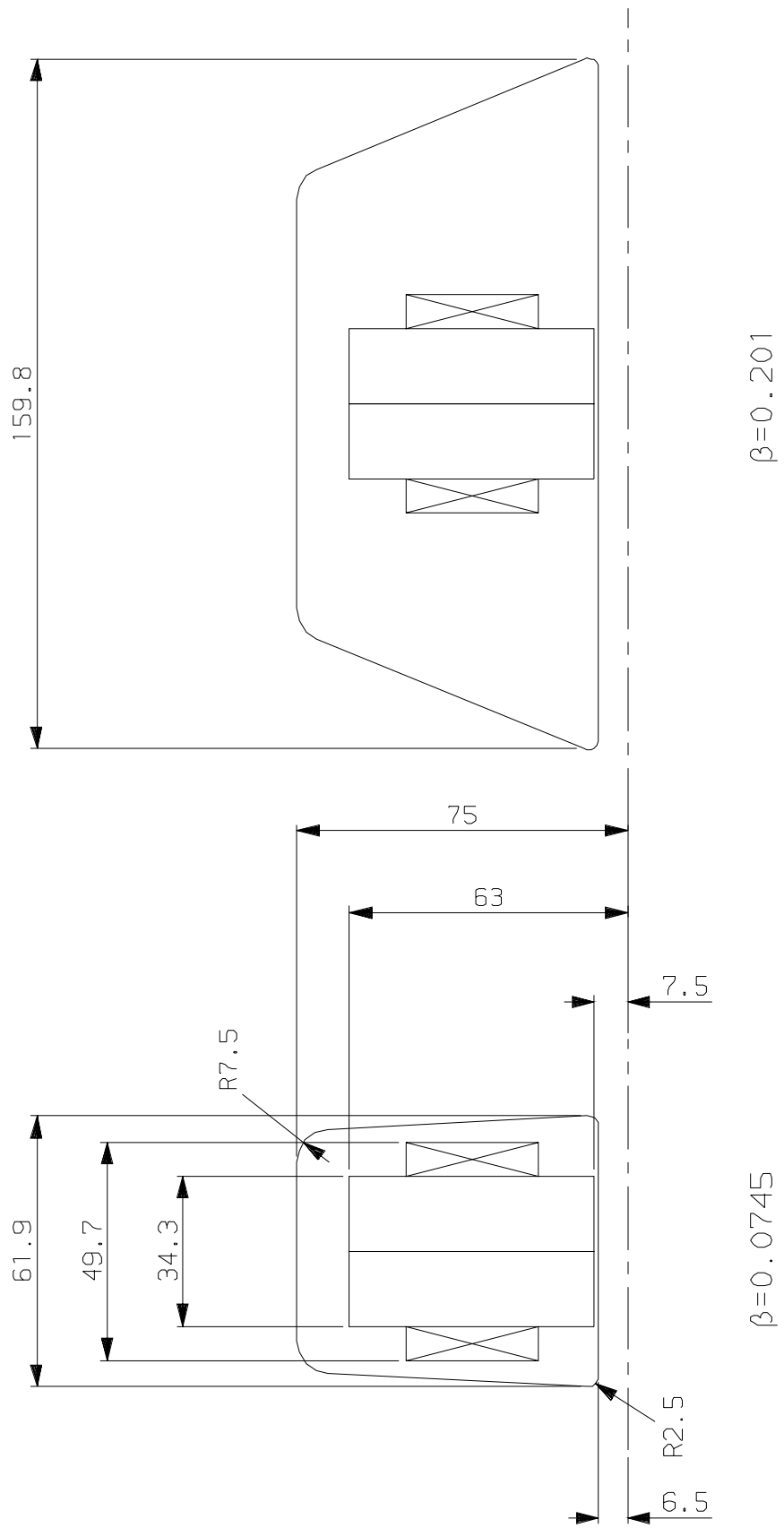


Figure 1.3-12: DTL drift tube and quadrupole dimensions

1.3.6 Funnel

A schematic drawing of the 280-560 MHz funnel is shown in Figure 1.3-13, and a detailed account is given in an ESS report [Prior, 1999]. Each 280 MHz DTL provides a peak pulse current of up to 57 mA and the two beams are interleaved in the funnel section, with a doubling of the peak current for the following 560 MHz CCDTL and CCL (or SCL) stages. The most difficult features for the funnel are the reduction of momentum dispersive effects and the prevention of halo development.

The operating energy of the funnel is 20 MeV and there are six, $9\beta\lambda$, FODO focussing cells in each leg, with a buncher cavity located in the upstream section of each cell. The final (sixth) buncher cavity of the line is common to both legs and requires a special, two channel, asymmetric design. Following it, in the common downstream section of the sixth cell, is a transverse deflection cavity. Frequencies are 840 MHz for the separate cavities in each leg, but 560 MHz for the common sixth unit and 280 MHz for the transverse deflector. The two-beam, buncher cavity and the deflector cavity do not have axial symmetry but, for the pulsed mode of operation, the heat losses are manageable.

In addition to the eleven buncher cavities and the final $\pm 2^\circ$ transverse deflector, there are septum magnets located in the downstream sections of the first, second and fifth cells of each leg. In one leg, the septum magnets bend the beam successively 10° , 2° and -10° , while in the other leg, the equivalent bends are in the opposite direction. The two input DTL beams are in parallel, separated by a horizontal distance of 1.8 m, while the common 280 MHz deflector at the funnel exit bends the beams from each leg alternately in opposite directions, bringing the merged beams on axis for the CCDTL.

The individual cells have length 0.979 m, giving an overall length for the funnel of 5.872 m. Component lengths are 0.06 m for the quadrupoles and 0.23 m for the septum magnets and deflector cavity. Cavity fields are adjusted so that bunches have an upright orientation in longitudinal phase space at the septum magnets and final deflector, with bunches inverted in phase space between one 10° septum magnet and the next, and also between the 2° septum magnet and the 2° deflector. There is a natural matched bunch length for each value of cell length and the chosen $9\beta\lambda$ cell is the most appropriate for the bunches emerging from the DTL. Each leg of the funnel may be regarded as part of an eight-cell structure, with an equivalent superperiodicity of two, but with the final two cells omitted. The mean phase advance per cell under space charge is close to 45° , providing approximately achromatic focussing conditions for the specific bunching and bending that is provided.

The funnel design is optimised for minimum beam halo by adjusting for periodic beam sizes in the cells, compensating the dispersive effects by reduced betatron amplitudes. Diagnostic units and scrapers are included in the two free downstream straight sections of the third and fourth FODO cells. Input matching to the funnel is achieved via the last four quadrupoles of each DTL and the first two buncher cavities in each leg. Output matching from the $9\beta\lambda$ pattern of the funnel to the $10\beta\lambda$ pattern of the CCDTL is obtained in a similar manner, using the last two bunchers of the lines and the first four quadrupoles of the CCDTL. The results of tracking studies for the funnel, which show RMS emittance growths of less than 0.5 %, are given in the listed reference [Prior, 1999].

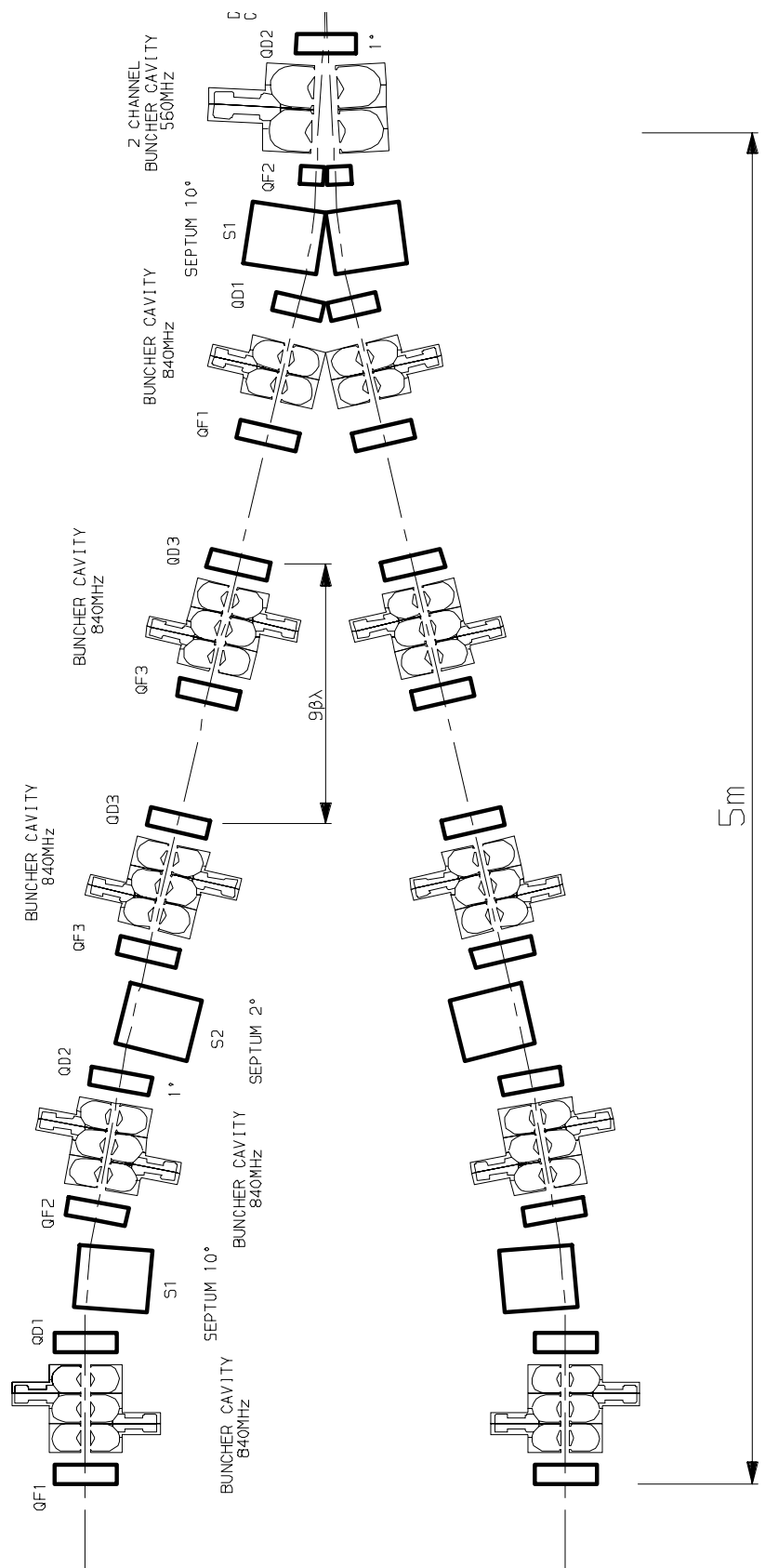


Figure 1.3-13: Schematic layout of the 280 to 560 MHz Funnel

1.3.7 560 MHz Accelerating Structures

Above 20 MeV, all accelerating structures are at 560 MHz, with a CCDTL used from 20 to 100 MeV, and, for the normal conducting scheme, a first CCL (CCL1) from 100 to 251.5 MeV and a second CCL (CCL2) from 251.5 to 1334 MeV. A CCDTL has been chosen in preference to a separated drift tube linac (SDTL) because it allows a smoother matching transition to both the funnel and CCL1.

1.3.7.1 20 to 100 MeV CCDTL

The CCDTL, as its name suggests, is a hybrid accelerating structure combining the advantages of a coupled cavity linac with the features of an Alvarez drift tube linac. There is a standing wave mode along the accelerating and coupling cells, as in the CCL, with the coupling cells nominally unexcited. Each accelerating cell has a single drift tube with two accelerating gaps, and with the electric field in the two gaps in the same direction. The field in the adjacent cell has a phase shift of π so there is a $2\pi-\pi-2\pi$ sequence of accelerating fields. The result is an efficient accelerating structure for ions in the beta range 0.2 to 0.4, with comparable shunt impedances to that for a DTL. There is the added advantage over a DTL (but not over an SDTL) of accessible external quadrupoles allowing both accurate alignment and larger drift tube apertures.

The arrangement proposed for the 560 MHz, ESS CCDTL is a FODO focussing structure of total length $10\beta\lambda$, with two coupled accelerating cells of length $3\beta\lambda$ in each O section and with $2\beta\lambda$ spacings for each of the quadrupoles and associated monitors and steering correctors. This is typical of structures proposed by LANL for APT [Lawrence, 1997]. The $2\beta\lambda$ spaces for the quadrupoles result in a $2\pi-\pi-2\pi-5\pi$ sequence for the accelerating fields, and a long coupling cell is required to span a quadrupole, as shown in Figure 1.3-14.

Typical values for the cavity shunt impedances and the transit time factors are as follows:

Beta	Bore Radius (cm)	Shunt Impedance ($M\Omega/m$)	Transit Time Factor
0.20 to 0.29	1.0	56.2 to 64.2	0.89 to 0.93
0.29 to 0.38	1.25	66.8 to 57.4	0.87 to 0.89
0.38 to 0.43	1.5	56.4 to 45.7	0.84 to 0.85

A single module has four accelerating gaps, and 75 such modules are proposed, many coupled together and fed by single klystrons, with 15 klystrons planned, in total. The accelerating field gradients to be used are 2.25 MV/m, with an initial ramp at low energy. The beam in the CCDTL may be kept approximately equipartitioned by the use of two separate linear ramps with energy for the quadrupole gradients. The quadrupoles are 11 cm in length and are made with an asymmetric core in order to fit above or below the longer coupling cells between modules. The required field gradient ramps are 18.25 T/m at 20 MeV, 17.66 T/m at 36 MeV and 13.76 T/m at 90 MeV.

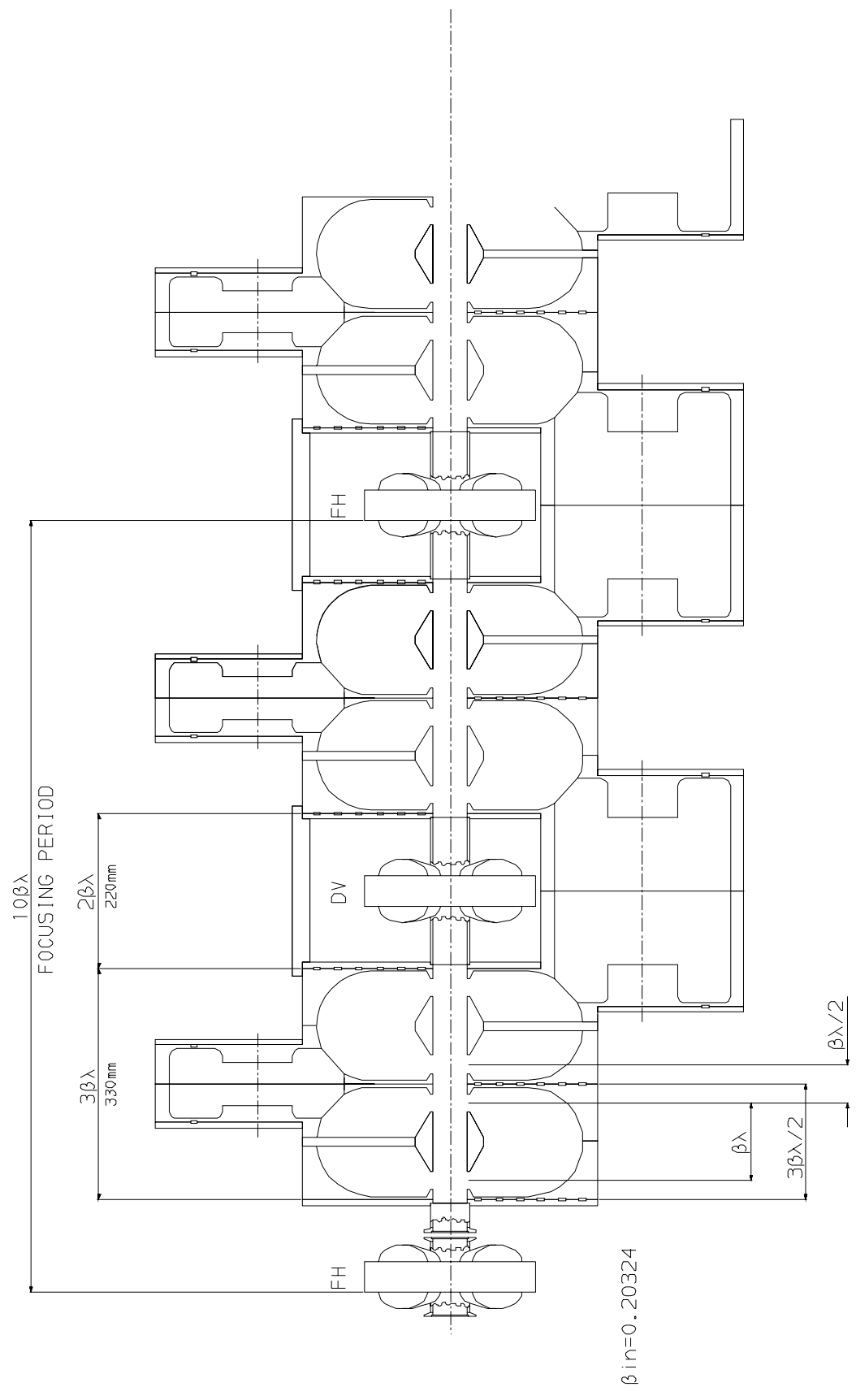


Figure 1.3-14: The 560 MHz CCDTL

1.3.7.2 100 to 251.5 MeV CCL1 and 251.5 to 1334 MeV CCL2

The pulsed, normal conducting, side coupled CCL constitutes the major part of the proposed normal conducting reference design. The first stage, CCL1, accelerates the beam from 100 to 251.5 MeV, while the second, CCL2, continues the acceleration to 1334 MeV. The design follows that of the 805 MHz CCL linacs used reliably at LANL and FNAL. A FODO focussing structure is adopted for both CCL1 and CCL2, with cavities in the O sections, and quadrupoles, monitors and steering correctors at the F and D locations, as shown in Figure 1.3-15.

In CCL1, there are eight cells per tank (cavity) and an inter-tank spacing of $3\beta\lambda/2$ for the magnets, monitors and correctors. Two such tanks and separations span an $11\beta\lambda$ focussing period, and numbers of tanks are coupled together and powered via a bridge coupler. The numbers of coupled tanks are two, four or six depending on the beam energy. The total number of tanks is sixty, and the number of 5 MW klystron power sources, eleven.

In CCL2, the transverse focussing pattern is extended to $12\beta\lambda$, with ten cells per tank and $1\beta\lambda$ tank spacings. Initially, there are units with six coupled tanks and finally, units with four coupled tanks, for a total of 228 tanks and 58, 5 MW klystron power modules. Each cavity contains cells of equal length and the lengths are gradually increased to match the increasing ion velocities. The total CCL length, and associated field gradient, 2.7 MV/m, is optimised for capital and twenty year operating costs.

Transit time corrected shunt impedances per unit length of tank, ZT^2 , have been obtained using the program SUPERFISH. Cell dimensions have been adjusted to optimise the impedances for given bore and outer wall radii. The ZT^2 values decrease as the bore radius and the web and nose-cone thicknesses increase, so these have been kept as small as possible without compromising beam loss tolerances and cooling requirements. Impedances are reduced by 10 %, mostly to allow for the slots of the coupling cells, which introduce 3 % coupling between the accelerating cells.

Typical values for the cavity shunt impedances and the transit time factors are:

Beta	Bore Radius (cm)	Shunt Impedance ($M\Omega/m$)	Transit Time Factor
0.37 to 0.48	1.5	39.8 to 48.2	0.93 to 0.93
0.44 to 0.58	1.75	43.6 to 52.1	0.92 to 0.91
0.50 to 0.91	2.0	45.4 to 62.4	0.90 to 0.84

As noted in the 1996 proposal, it is important to remove TE_{111} or TE_{112} perturbing modes from the pass band of the TM_{010} mode of the bridge couplers used with the CCL cavities [Sande, 1996]. Either a circular resonant post is used at the ends of the coupler for the former, or two rings are used at the maximum field point for the latter, to increase the frequency of the perturbing mode. The TM_{010} mode of the bridge coupler is then returned to 560 MHz and the perturbing modes have been displaced outside the TM_{010} pass band.

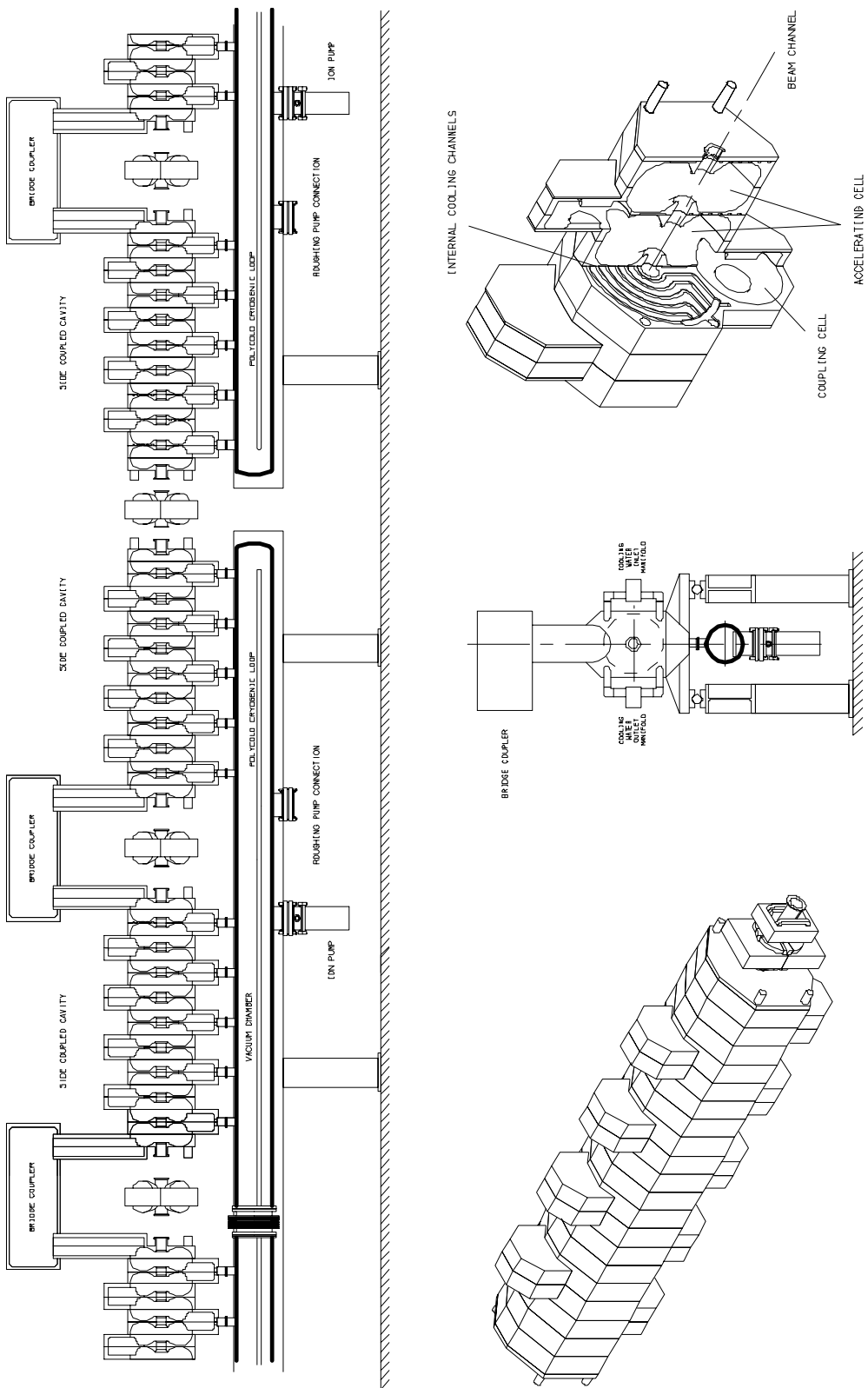


Figure 1.3-15: The 560 MHz CCL arrangement

1.3.8 Linac Beam Dynamics

Linac design starts with studies of the RFQ, the chopper and the funnel. The RFQ and the ion source define the beam parameters and, for the design proposed, the initial RMS normalised

transverse and longitudinal emittances are 0.225 and $1.83 \times 0.225 \pi$ mm mrad, respectively. For these emittances and the 57 mA beam currents, the space charge forces influence the beam dynamics of both the chopper and the funnel. To inhibit halo, an adequate number of buncher cavities are used and beam amplitudes are periodic in regular lattice cells.

Insufficient bunching, and variation from cell to cell of the average beam aspect ratio are avoided as they form halo due to the relative change of the non-linear to the linear forces. Input and output matching is necessary and, in the funnel, the increased beam size due to dispersion must be compensated by a decreased size due to betatron motion. For suitable designs, the chopper channel has two quadrupole doublet cells and four buncher cavities, plus input and output matching, whereas the achromatic funnel section has six FODO cells, six buncher cavities and two septum magnets per channel, plus a final deflection cavity.

Transverse emittance values are similar to those selected for the US SNS project, but the longitudinal emittance is larger due to the choice of the lower RF frequencies. The emittances are < 40 % of those chosen for the 1996 ESS design and need to be reduced the requirements for the chopper and funnel sections. It is also important to restrict emittance growth ahead of the funnel, and the chopper to DTL transition region is thus a crucial design area. A synchronous phase angle of -42° is chosen at the input of the DTL to reduce the nonlinearities in the longitudinal motion, and a fourth buncher cavity is included in the chopper line to assist with the DTL input matching. Emittance growth is then small ahead of the funnel.

The partitioning ratio of transverse to longitudinal beam energies is found to be ~ 0.75 for the chopper design and ~ 1.0 in the funnel. On the input side of the funnel is the DTL and on the output is the CCDTL and in both the focussing is adjusted for equipartitioning, so matching that in the funnel. Smooth changes of partitioning ratio may be made for the following CCL1 and CCL2, provided there is no imbalance at the transitions between stages and provided coupled coherent envelope mode resonances are avoided. Matching is adjusted to avoid any large variations in focussing parameters in the transition regions and, to assist in achieving this, the FODO focussing pattern adopted for the normal conducting scheme is $2\beta\lambda$ (RFQ), $4\beta\lambda$ (DTL), $9\beta\lambda$ (funnel), $10\beta\lambda$ (CCDTL), $11\beta\lambda$ (CCL1) and $12\beta\lambda$ (CCL2).

Emittance growth along the linac is small in the absence of machine errors, with < 5 % (RMS) in the longitudinal plane and < 10 % (RMS) in the transverse. Typical values in CCL2 for the zero and full current phase shifts per cell are then, respectively:

- $36.5^\circ, 15.4^\circ$ (at 251.5 MeV) and $11.4^\circ, 5.3^\circ$ (at 1330 MeV) in the longitudinal plane,
- $57.3^\circ, 28.0^\circ$ (at 251.5 MeV) and $19.7^\circ, 9.8^\circ$ (at 1330 MeV) in the transverse plane.

With predicted error levels, the RMS growth may reach 60 %, but the tune spreads become reduced accordingly and the maximum transverse halo amplitudes are < 9σ .

1.3.8.1 Coupled Transverse-Longitudinal Coherent Motion

Errors in quadrupole settings and RF focussing lead to a combination of three possible coupled transverse-longitudinal coherent envelope modes. There is a pure quadrupole mode, in which the coherent betatron motions in the two transverse planes are out of phase, and a high and a low transverse-longitudinal mode, in each of which the coherent transverse motions are in phase. The oscillation tunes have the units of radians/ 2π for the phase shifts per

cell and resonance effects occur when a sum of integer multiples of the incoherent tunes is equal to an integer, n , or to the tune of a coherent mode, ν_c ,

$$\nu_c \text{ or } n = k\nu_x + l\nu_y + m\nu_z$$

Approximate equations are available for estimating the three coherent tune values. The pure quadrupole mode, $\nu_c = \nu_x + \nu_y$, cannot be avoided, but low order resonances with the high and low coupled modes, or with the focussing periodicity, are avoided when the ESS linac is equipartitioned, with $\nu_x = 1.83 \nu_z$. If not at this condition, the $0 = \nu_x - 2\nu_z$ resonance is best avoided by lowering the transverse and raising the longitudinal tune, rather than vice versa.

1.3.8.2 Linac Output Energy Error Compensation

In the 1996 ESS design, there was no assessment of linac output energy error compensation. Momentum ramping cavities were placed at the linac output and momentum compression (bunch rotation) cavities at a fixed distance downstream. The latter, however, automatically provide some momentum error correction and remove the momentum ramping. A different arrangement is thus adopted, with a momentum enhancement cavity at the linac output, and combined momentum ramping and compression cavities after a suitable debunching distance.

The beam line after the linac thus includes three CCL2 type cavities, one at the input end of the line and two more after an additional distance, l , of ~ 70 m. The first external cavity is powered and phased to give some increase of the beam momentum spread and to hasten the debunching of the beam. In the following section of the line, the beam spreads in phase, tilting in longitudinal phase space, and increasing in $\Delta p/p$ due to the effect of the longitudinal space charge forces. For a total voltage, V , on the second and third cavities, their required distance, l , downstream from the first, for energy compensation, is given by:

$$lV = \beta^3 \gamma^3 \left(\frac{E_0}{e} \right) \left(\frac{c}{2\pi f} \right)$$

Where e , E_0 are the charge and rest energy of the H^- ions, c is the velocity of light and f is the 560 MHz CCL2 frequency. With this arrangement, any error in mean energy of the beam after the first external cavity is cancelled by the subsequent actions of the second and third cavities. If, however, there is an error in phase at the first cavity, this leads to a subsequent error in beam energy due to the effects of the error in the downstream cavities. It is thus the error in the RF phase of the beam at the output of the linac that is an important criterion for assessing the linac performance.

1.3.8.3 Linac Beam Simulations with and without Errors

End to end beam simulations have been made for error-free and error-present versions of the 280/560 MHz scheme. Phase space plots for the error-free machines are shown in Figure 1.3-16 and Figure 1.3-17. Also shown for comparison is the linac output distribution at the end of the 280/560 MHz SC linac.

Random errors assumed for the simulations have been Gaussians, truncated at 2.5σ , with maximum values:

Quadrupole gradients / tilts (% , deg.)	± 0.5 / ± 0.5
Quadrupole displacements (mm)	± 0.1 (slow), ± 0.01 (fast)

Cavity / Monitor displacements (mm)	± 0.25 / ± 0.1 (NCL)
Cavity field phases (deg.)	± 1.0 (systematic), ± 0.5 or 1.0 (dynamic)
Cavity field amplitudes (%)	± 1.0 (systematic), ± 0.5 or 1.0 (dynamic)

The most important errors are those in the phase and amplitude of the RF fields and it is assumed that systematic errors are compensated, but that dynamic errors are not. Coherent longitudinal dipole oscillations develop, with excursions in mean energy and RF phase, as shown in the example of Figure 1.3-18. The output energy excursion is compensated as discussed in Section 1.3.8.2, but the phase excursion remains, creating an energy error in the compensation cavities. The largest phase offset observed in simulations with maximum dynamic RF errors of $\pm 1^\circ$ in phase and $\pm 1\%$ in amplitude is 6° (for the normal conducting machine), resulting in an error of 1.2 MeV in energy. This may be compared with the ± 0.7 MeV tolerance for ring injection. The maximum dynamic errors for the normal conducting machine should therefore be $< \pm 0.6^\circ$ in phase and $< \pm 0.6\%$ in amplitude. These figures may not be easy to achieve in interleaved 50 Hz and 16.667 Hz operation modes if the beam is chopped for the former but not for the latter. Please note that these results relate only to the studied 280/560 MHz SC linac and that such large amplitude oscillations are absent in the 352/704 MHz SC linac presented in chapter 1.4.

Simulations for the linac beam line should also include image force effects [Bongardt, 1996].

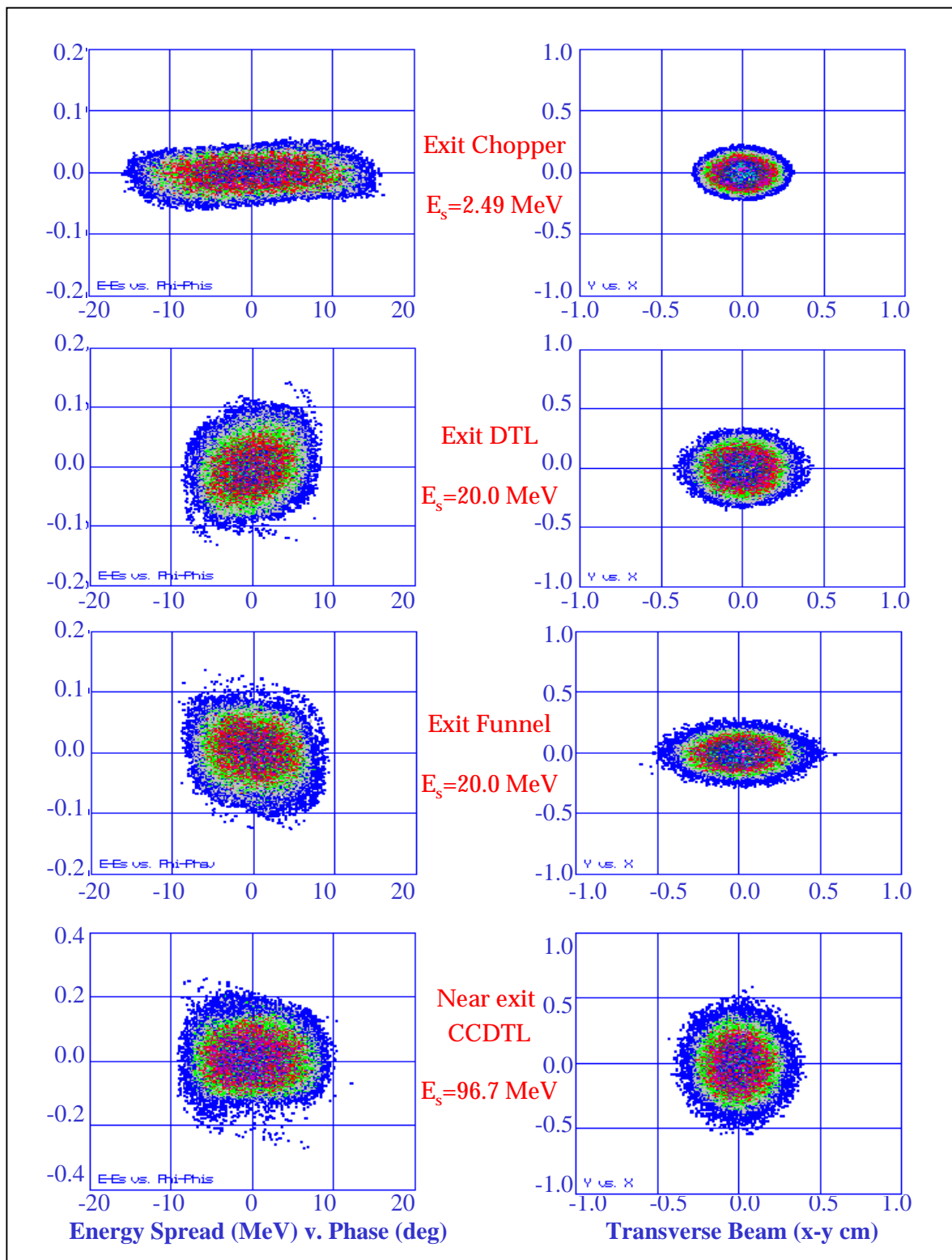


Figure 1.3-16: Beam plots from RFQ output to exit of CCDTL

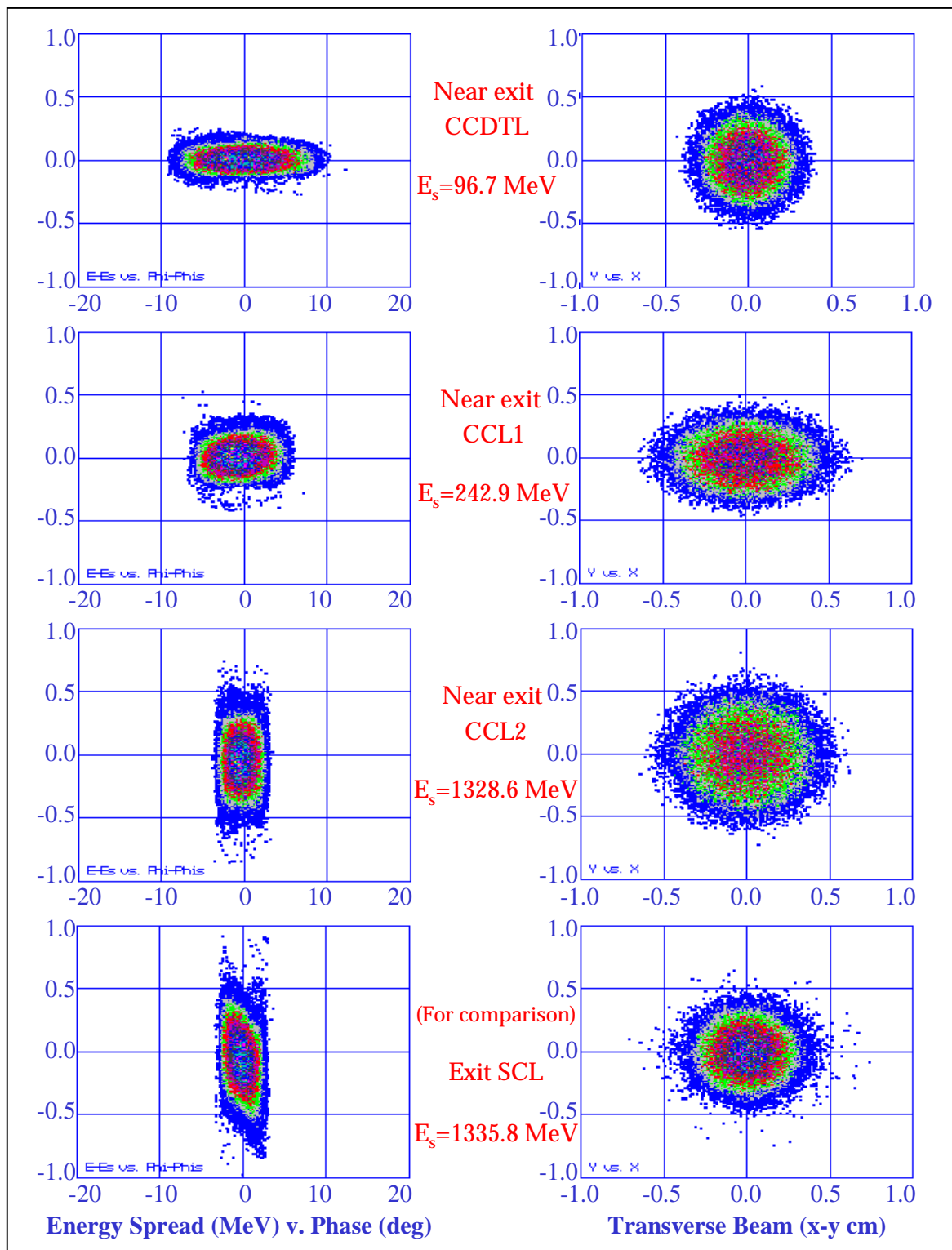


Figure 1.3-17: Beam plots from the exit of the CCDTL to the final output energy

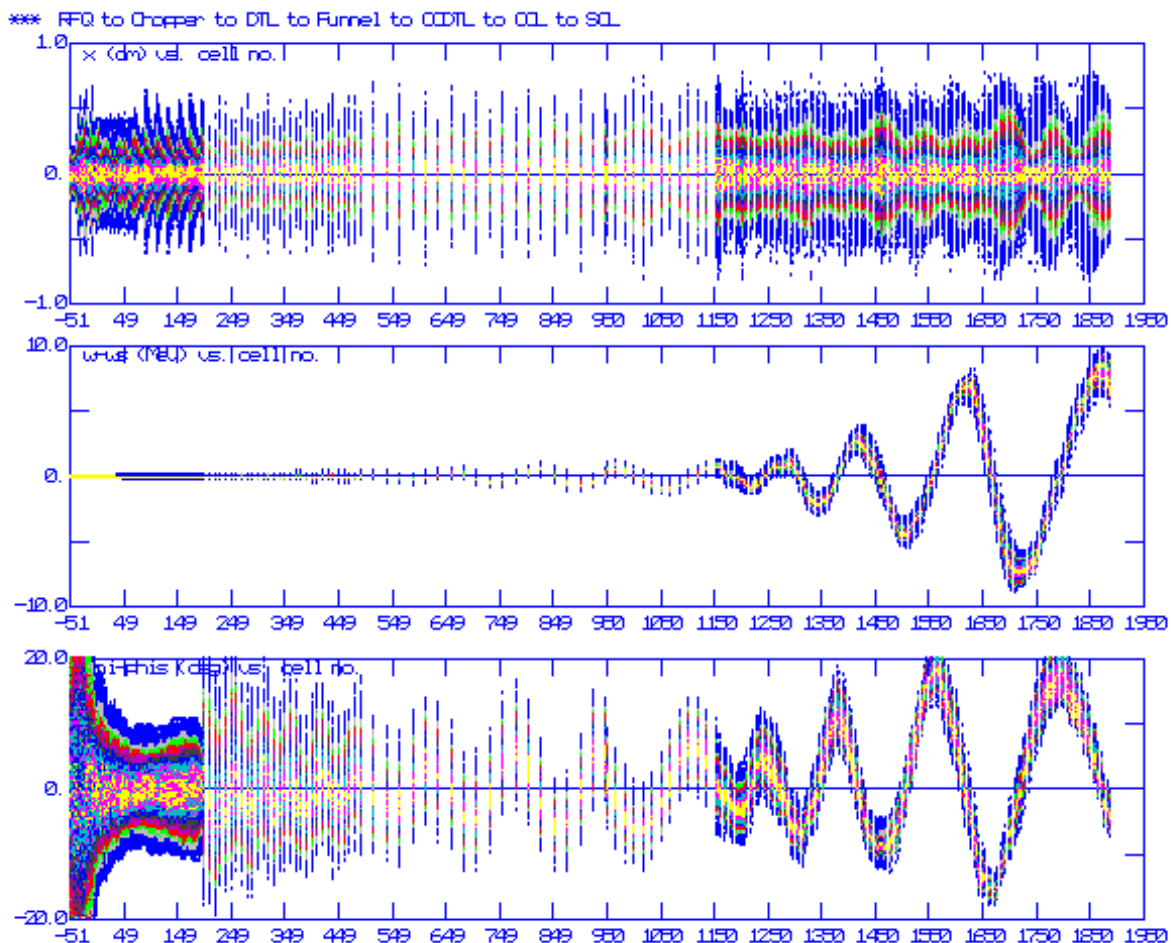


Figure 1.3-18: A superconducting linac beam plot encountered during error studies with 1 % and 1° random field errors. Please note that these results relate only to the studied 280/560 MHz SC linac and that such large amplitude oscillations are absent in the 352/704 MHz SC linac presented in chapter 1.4.

1.3.9 Linac Beam Diagnostics and Commissioning

A combined description of the diagnostics for the linac, the beam lines and the rings is given in the chapter devoted to the accumulator rings. For the linac, the diagnostics include: Faraday cup beam stops (including energy degraders), a slit and collector emittance measuring unit, phosphor screens, a fluorescent light monitor (LEBT), current transformers, strip line and microstrip line position monitors, beam RF phase monitors, HARP and wire scanners profile monitors, laser photo detachment devices and ionisation beam loss monitors. A schematic drawing of the location of these units along the linac is given in Figure 1.3-19.

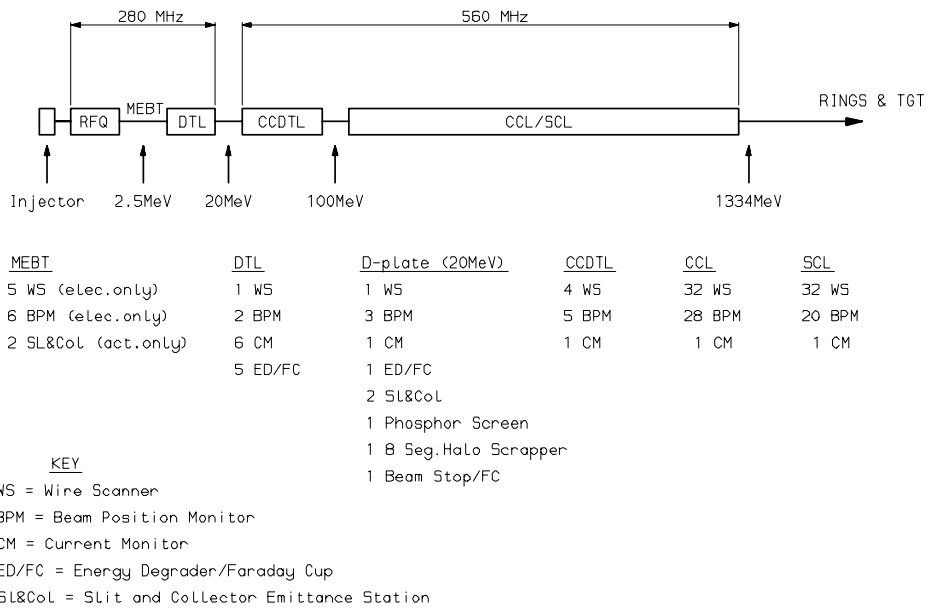


Figure 1.3-19: Location of Linac Beam Diagnostic Units

1.3.9.1 Linac Beam Commissioning

A list is given of the most important stages in beam commissioning for the normal conducting machine:

- a) Ion source and LEBT beam emittance and current measurements,
- b) Beam profile measurement in the LEBT with fluorescent light monitor,
- c) RFQ beam transmission and output emittance measurements,
- d) Chopper input and output matching, beam alignment (BA) and orbit correction (OC) ,
- e) Bunch duration, halo and chopper performance measurements,
- f) DTL beam transmission, BA, OC, input and output emittance measurements,
- g) Input and output matching, BA and OC for the funnel,
- h) Bunch duration and halo measurements in the funnel,
- i) Achromatic properties of the funnel,
- j) CCDTL beam transmission, BA, OC, input & output emittance measurements and halo,
- k) CCL beam transmission, BA, OC, input and output emittance measurements,
- l) Sensitivity of CCDTL and CCL to RF errors,
- m) Sensitivity of CCDTL and CCL to input mismatching,
- n) Linac output energy and RF phase errors, energy compensation and ramping, and
- o) Halo measurements in the achromat for various conditions of the linac.

1.3.10 Radio Frequency and Field control Systems

The RF system consists of a frequency source, a low power distribution system, a phase reference line, power amplifiers, high power distribution systems and the accelerating cavity structures. Three different frequencies are used; the RFQ and DTL operate at 280 MHz, the CCDTL, CCL1, CCL2 and SCL at 560 MHz, and most cavities in the funnel at 840 MHz. The peak RF power required is ~ 260 MW for the normal conducting machine, after including 33 % additional power for control margins and feeder losses. It is proposed to use 1.3 MW peak power klystrons for the 280 MHz stages, and 5 MW peak power klystrons for the CCDTL, CCL1 and CCL2stages. The beam duty on cycles are 5 % at 50 Hz and 4.2 % at 16.667 Hz, with the RF pulse duty cycles ~ 1 % greater for the normal conducting machine to take account of cavity filling and settling times.

There is a 560 MHz master oscillator (MO) that defines the linac frequencies and trigger sources. The MO has a setting accuracy of 10 Hz, a temperature stability of 2.5×10^{-9} at 25°C and multiple one-watt outputs. One output feeds a 10 kW amplifier, which then feeds the 560 MHz power amplifiers via a waveguide feeder system and 40 dB couplers, with the drive to each unit at the one-watt level. A second MO output is frequency divided by two, amplified and used to drive the seven, 280 MHz power modules, and one 280 MHz output is multiplied by three and amplified for the ten, 840 MHz modules.

Self-contained RF power modules, including power supplies, are proposed for the three frequencies. Each RF power module contains, in addition, a low power RF system, a drive amplifier, an RF amplifier, an output feeder system and a control system, including RF cavity field control. The module has three, 50 Hz mains inputs, one of high power for the amplifier power supply, one for the RF drive and ancillary systems and one for the computer control system, which is backed up by an uninterruptible system. The module also has primary cooling water inputs and inputs from the low power RF system and from the phase reference line. The RF output power from each amplifier is fed via a feeder system to its cavity loads, with a circulator used to protect the amplifier from reflected power.

Klystrons are chosen for the 5 MW peak power systems at 560 MHz, but for the remaining lower power units (1.3 MW at 280 MHz, 0.64 MW at 560 MHz and ~ 0.4 MW at 840 MHz), inductive output tubes (IOT) are also to be considered. An IOT can have advantages over a klystron in terms of compactness, a constant efficiency over its working range, and a higher efficiency, ~ 75 % compared with ~ 60 % for a klystron. The disadvantages of an IOT are the increased problem of power dissipation in its collector and its lower power gain (25 dB compared to the ~ 40 dB for a klystron). The IOT therefore requires a drive amplifier and, for the 1.3 MW IOT, the required drive is ~ 4.5 kW. The IOT only draws current when drive is present and so requires a DC power supply. This is in contrast to a klystron, which may draw current when drive is absent, and so requires a pulsed supply. The converter-modulator supply developed for the SNS klystrons [Reass, 2001] is a good design on which to base ESS power supply units. The voltage and mean power levels assumed are 140 kV and 0.8 MW for the 5 MW klystrons, and 100 kV and 0.9 MW for the group of nine, 0.64 MW IOT or klystrons.

The output feeder is nine-inch coaxial line for the 280 MHz systems, WR 1500 (0.3810 m by 0.1905 m) waveguide for the 560 MHz systems and WR 900 (0.2286 m by 0.1143 m) waveguide for the 840 MHz units. At the power amplifier output, there is a circulator, followed by a directional coupler. For the maximum power units, the circulator has to be capable of standing the maximum peak RF voltage level of a 2.5 ms pulse of 5 MW peak

power into a short circuit, and the full mean power of ~ 0.5 MW in its water cooled load. The feeders pass to bridge couplers in the case of the CCDTL and CCL, see Figure 1.3-20.

Each RF module has its own secondary cooling system, with site primary water supplied and a forced air-cooling supply. Cooling is required for the klystron and IOT collectors and for switching devices in the power supply. The power module has its own computer control system, networked to the site control system to allow remote control. All quality assurance (QA) parameters are recorded on the module's history system. The low power RF system contains fast switches to switch off the RF for personnel safety and plant safety reasons, circuits to control the frequency tune of the linac cavities, and RF phase and amplitude controls which are linked to the cavity field control system.

1.3.10.1 *RF Field Control System*

Field tolerances for the accelerating cavities are stringent, $\pm 0.6\%$ for the RF amplitudes and $\pm 0.6^\circ$ for the RF phases along the normal conducting machine. In addition, there is a tolerance of $\pm 0.2^\circ$ for the inlet temperature of the cavity cooling water for the normal conducting cavities. Careful design of the RF field control system is required as the beam power is comparable with the cavity structure power in the normal conducting machine.

Probes in the cavities provide amplitude and phase signals and these are passed to digital signal processors (DSP) to provide composite I and Q control signals, which are derived from the transfer functions of the detuned cavities. Calibration of the probes with beam in the cavities is envisaged. The I and Q signals are passed to the low level RF system to control the amplitude and phase modulation of the currents in the klystrons or IOT. Mainly the DSP units set the bandwidth but, for very fast transients, additional analogue control may be used. The rise time of the cavity fields in each machine pulse causes some initial transients, and adaptive feed-forward control is used to suppress both these and other repetitive or slowly varying transients [Ziomek, 1993], [Simrock, 1996].

For the feedback and feed-forward to be effective, the amplifiers must have adequate available power and $\sim 30\%$ additional power has been allowed for this purpose. Error signals for the tuning control are obtained from measurements of the forward and reverse power in the cavity feed lines. Variations in the mean beam current result in incorrect cavity tuning as the cavities require to be detuned to provide reactive beam loading compensation, and the tuning may only be adjusted slowly, via the water temperature in the case of the normal conducting machine.

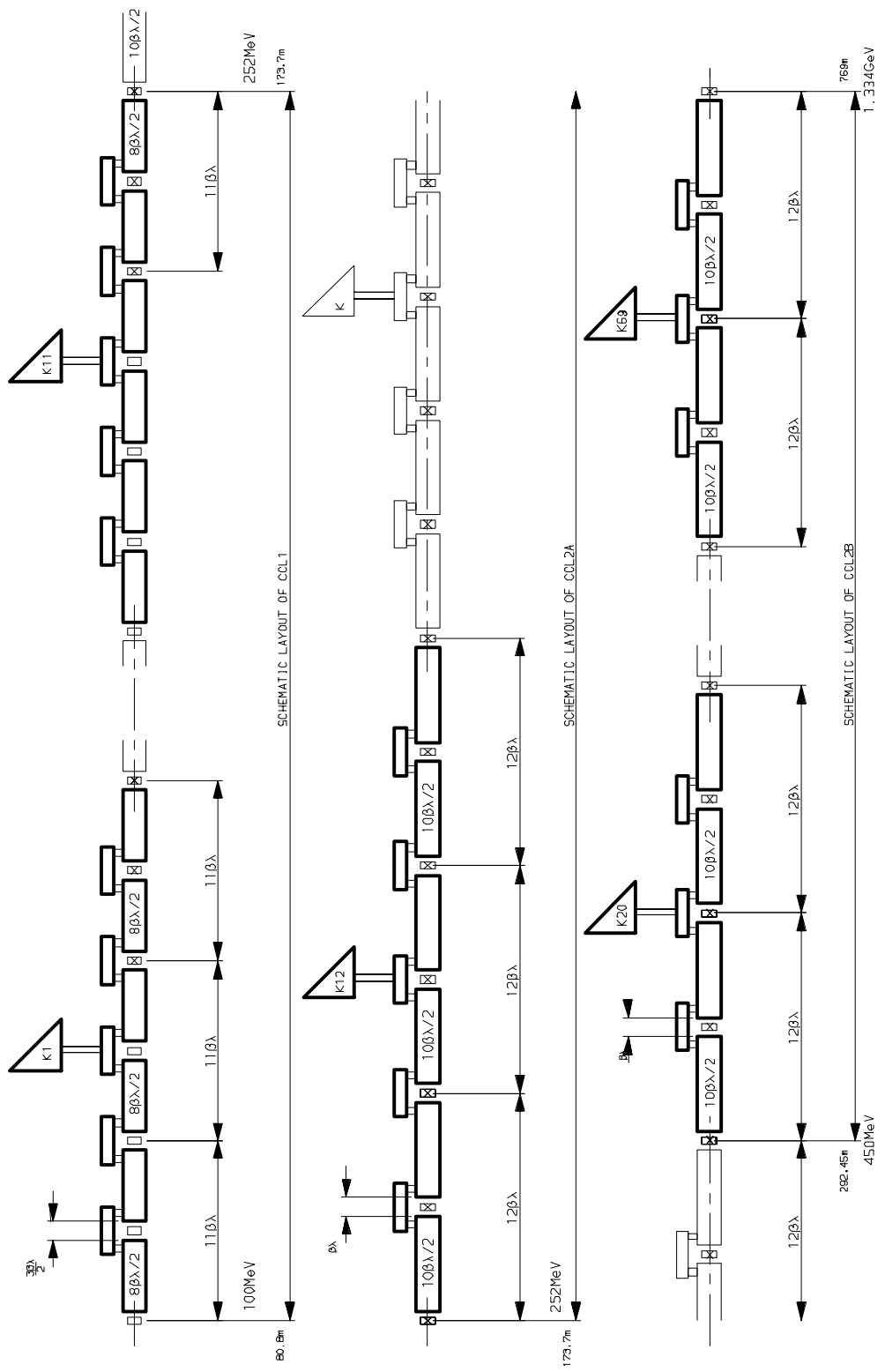


Figure 1.3-20: The room temperature CCL schematic

1.3.11 Vacuum Systems for the Linac

The vacuum pressure required in the machine is based on the desire to keep beam losses to a minimum and to allow “hands on” maintenance ($\sim 10 \mu\text{Sv}/\text{hr}$). At full power of 10 MW and 1.3 GeV this is equivalent to a fractional particle loss of 10^{-7} per metre length or 1 W/m. The largest loss when the beam interacts with the residual gas is due to charge exchange of the H^- ions. In the normal conducting linac the majority of the residual gas will be water vapour. There are few measurements of charge exchange cross sections in water, but the cross sections for oxygen are a near enough approximation, and are shown in Figure 1.3-21 as a function of beam energy [Nakai, 1987]. The calculated cross section from 1 MeV to 1 GeV is also shown [Gillespie, 1977].

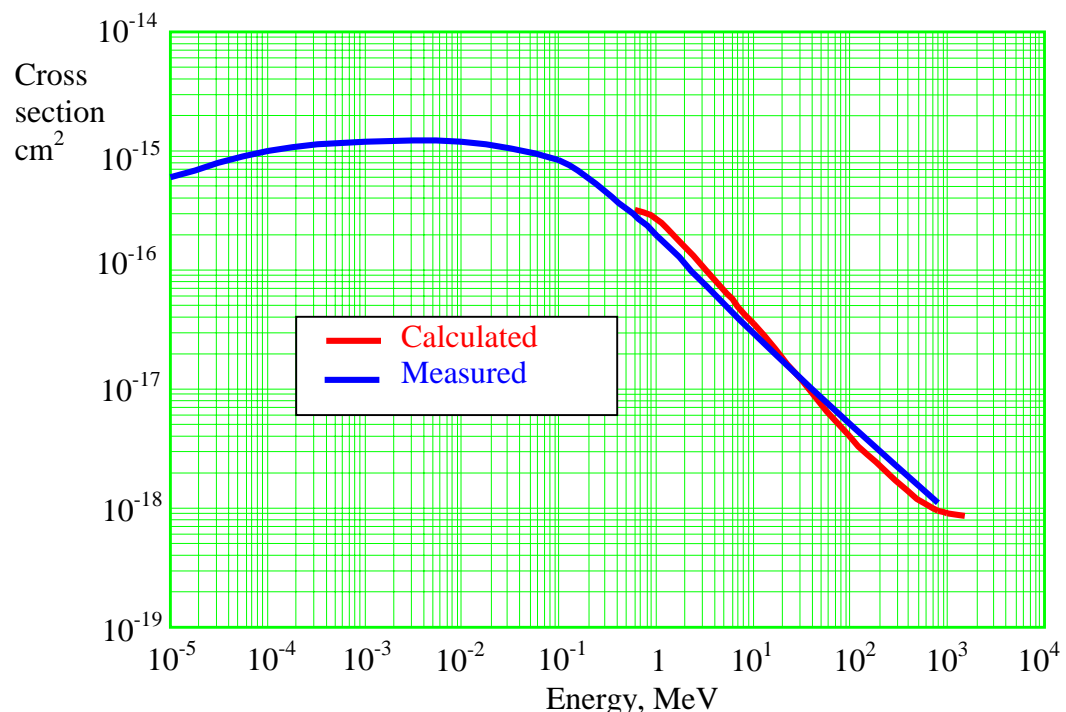


Figure 1.3-21: The total electron loss cross section for H^- ions in oxygen

The induced activity in materials may be characterised by a *danger parameter* [Barbier, 1969]. The danger parameter is defined as the radiation field existing inside a cavity of arbitrary form embedded in an infinite volume of radioactive substance which has been irradiated by a unit flux (one particle per second per square cm). The radiation field in front of an infinite and very thick wall will be half that in the cavity. The danger parameter scales linearly with flux and is a function of the bombarding particle, its energy, the duration of bombardment, the material bombarded and the cooling time after bombardment has ceased. Barbier lists the calculated gamma danger parameter for a number of “target” nuclei for proton bombardment at 50, 100, 600 and 2900 MeV after 5000 days of irradiation and for cooling times of 0 to 360 days. The values are expressed in mrad/hour for unit flux density.

An accelerator structure rarely conforms to a cavity or large thick wall, but the radiation close to the surface of components will approximate to the thick wall case, *i.e.* the radiation field for hands on maintenance will be half the appropriate danger parameter. Figure 1.3-22 shows the danger parameter as a function of beam energy for copper, iron and niobium, the main materials in the normal conducting and room temperature linacs. An infinite irradiation time

and 1 hour cooling time have been chosen as typical worst scenarios. Multiplying the cross section by the danger parameter, a vacuum pressure may be found that allows hands on maintenance, assuming a dose that does not exceed $\sim 10 \mu\text{Sv}/\text{hr}$ (1 mrad/hr).

As the important parameter for activation is the product of the danger parameter and the cross-section, this means that a Niobium cavity operated at 10 times better vacuum will have similar activation as Iron or Copper cavities. To achieve this or better vacuum is standard for SC cavities operated at cryogenic temperatures.

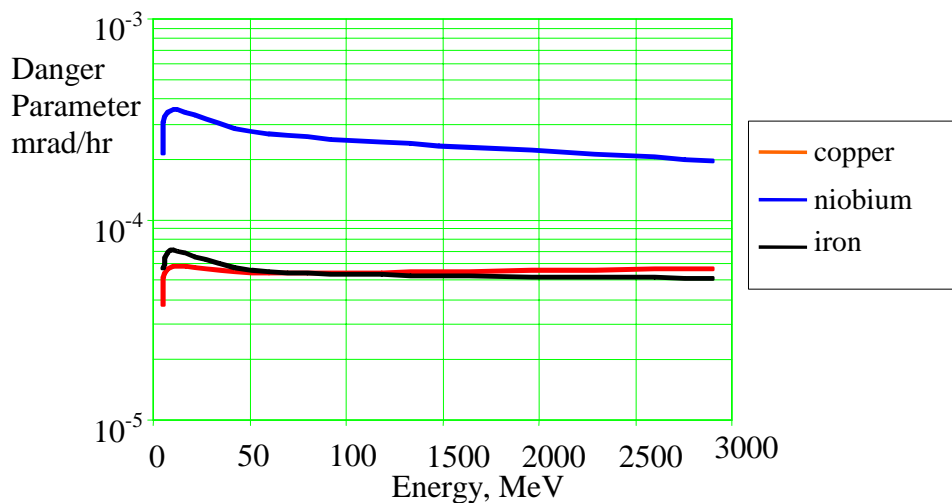


Figure 1.3-22: Danger parameters for copper, niobium and iron versus proton energy. 5000 days irradiation at a flux of $1 \text{ p s}^{-1} \text{ cm}^{-2}$, with 1 hour cooling time.

Figure 1.3-23 on page 1-48 shows this maximum pressure as a function of beam energy. It assumes that the charge exchanged beam hits the vacuum chamber wall adjacent to the point at which the charge change took place. In practice some of these particles will continue down the accelerator or even be accelerated back towards the front end. The value of pressure is conservative and could be perhaps a factor of 2 higher since the material does not form a cavity around the maintenance personnel. However, the whole of the tunnel volume will be activated and the personnel will experience the dose from the surroundings as well as the object being worked upon.

These calculations show that a pressure of $\leq 10^{-8}$ mbar is needed at the front end of the normal conducting CCL1, but relaxes $\leq 10^{-7}$ mbar at the maximum energy of the normal conducting CCL2. Thus, the most difficult region requiring the lowest pressure, between 100 and 300 MeV, is the normal conducting section common to both normal conducting and superconducting options. The pressure requirements are not particularly onerous in the higher energy sections of the normal conducting CCL2. However, the pressure in the room temperature sections between the cryostats in a superconducting option can be quite demanding, although issues of pressure in the cryostats themselves are relatively trivial due to the low temperature. Below 100 MeV the activation falls off sharply, so the pressure at the front end before the CCDTL can be higher; the design pressure is 10^{-6} mbar.

The whole vacuum system will be built to UHV standards using metals and ceramics, including metal seals and all metal valves, to eliminate hydrocarbon contamination, reduce outgassing rates and to be radiation hard. For convenience, valves will divide up the linac into several independent sections.

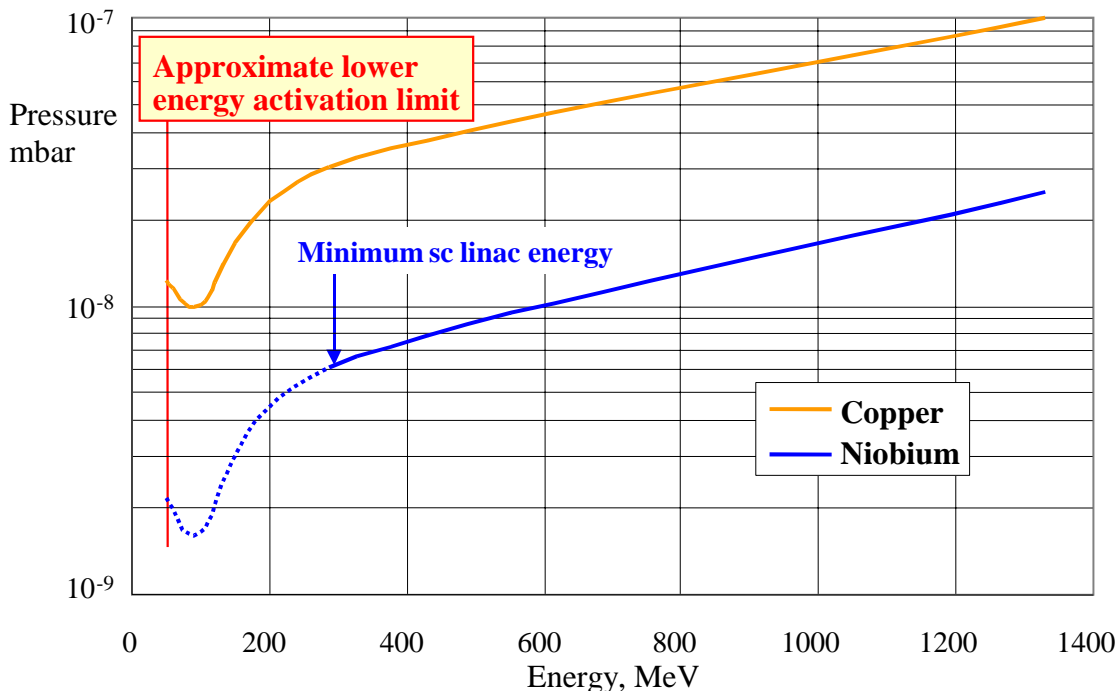


Figure 1.3-23: Maximum vacuum pressure (water vapour) versus H^- energy for a 10 MW proton beam to allow hands on maintenance. To achieve this or even lower pressure is standard for cryogenic operation of SC cavities.

Turbomolecular pumps will pump the RFQ where the gas load from the ion source is likely to be relatively high. The room temperature linac will not be baked, so water vapour will be the main residual gas. High speed *Polycold*^{®1} cryogenic pumps will remove most of the water while noble diode ion pumps will remove the other gases in the room temperature parts of the linac and funnel. Separate units will pump the DTL, but the remainder of the NCL will be pumped via a manifold running the entire length of the system from, and including, the funnel to the CCL. The ion pumps of various speeds will be attached to the manifold at appropriate intervals and the *Polycold* cryocoil will run inside the manifold. The CCDTL and CCL will be connected to the manifold through their side couplers on one side of the cavities. Figure 1.3-24 shows the manifold and pumping system. Since the front end of the CCL requires a lower pressure it will be necessary to pump through every side coupler on both sides of the cavity and two manifolds will be required for the first quarter of the CCL. Even then the pressure is only just attainable with a reasonable margin of safety assuming an outgassing rate of 2×10^{-10} mbar $\ell s^{-1} cm^{-2}$ [Strausser]. The pumping is severely limited by the conductance through the couplers into the cavities (280 MHz). Apart from decreasing the frequency to enlarge the openings, the cavities could be given a light vacuum bake at 80-100°C to reduce the outgassing, particularly of water. Any significant increase in cavity frequency would almost certainly necessitate a bake.

A superconducting linac like the one described in section 1.4 would be effectively pumped by the 2 K surfaces to a pressure of $<<10^{-10}$ mbar, so that beam scattering and charge exchange would be negligible. This is fortunate because a loss of beam at the rate of 1 W/m would add typically ~10 % to the cryogenic power required at 2 K. However, room temperature beam lines between cryomodules would have to be pumped to $\leq 10^{-10}$ mbar, mainly to prevent contamination of the sensitive cavities. These sections would be air baked and then vacuum

¹ Polycold Systems International, San Rafael, California, USA.

baked to achieve outgassing rates of $\sim 10^{-14}$ mbar ℓ s $^{-1}$ cm $^{-2}$ [Bennett, 1992] and then pumped by ion and NEG pumps.

The systems will be roughed by mobile pump sets consisting of carbon vane and wide range turbomolecular pumps. Scroll pumps will back the turbomolecular pumps. Control of the entire vacuum systems will be local with remote monitoring. The systems will automatically shut down in the event of a failure.

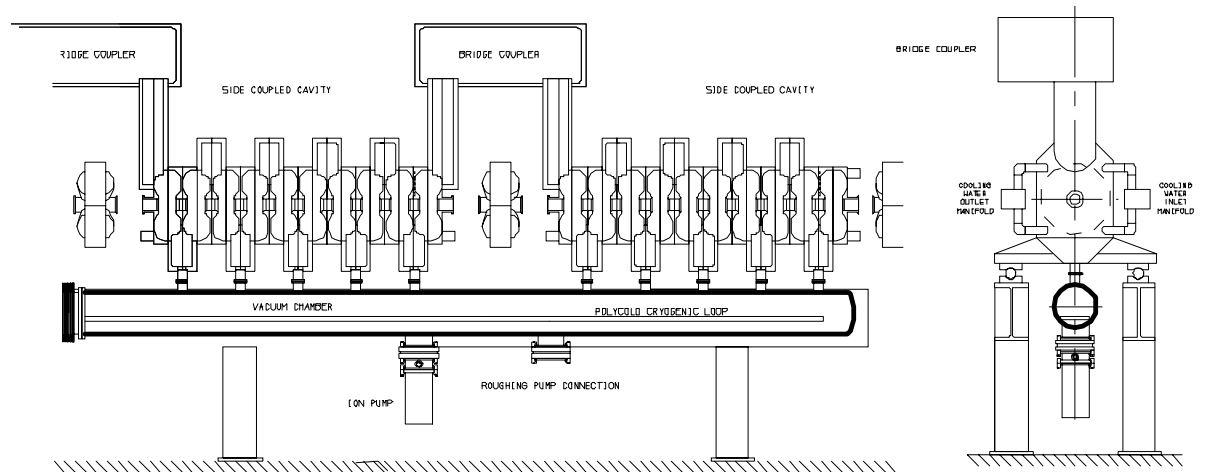


Figure 1.3-24: Sections through a portion of the CCL showing the vacuum manifold

1.3.12 Buildings and Tunnel

Due to the radiation levels present along the linac during operation, it is housed in an underground tunnel. Equipment and services are in ground level buildings along the linac so that wherever possible equipment is outside the radiation shield. A cut and fill earth shielding design has been used to reduce costs. Although the linac has been designed for low beam losses, typically less than 3 nA/m, there will be some unavoidable losses, for example, in the chopper section or due to fault conditions, and active handling techniques will then be required. The shielding is designed for an external radiation level of less than 0.5 μ Sv/hr for normal operation and less than 250 μ Sv/h for full beam loss – in a limited amount of time. The automatic shutdown system will stop the beam in less than a second. The physical basis to radiation protection and to dealing with accidentally activated components is outlined in chapter 8 of this report. Inevitably, the fine details of the linac tunnel layouts will depend on local geology and soil conditions, and the shielding thicknesses will depend on local regulatory regimes. Therefore the following details, which are consistent with the regime prevailing at the ISIS spallation neutron source, should be regarded as representative rather than prescriptive.

The linac is 2.8 m below ground level and 1.2 m above the tunnel floor. The internal tunnel cross section for the normal conducting machine is 5 m wide by 5 m high. The shielding will consist of 1.5 m of concrete and 8 m of earth. Eight tonne travelling cranes are provided for the removal and installation of components. All access is by heavily shielded doors. Figure 1.3-25 shows a section of the tunnel for the normal conducting machine, and Figure 1.3-26 shows a plan view of the tunnel and klystron hall, with the klystrons and modulators

outside the radiation shield. ESS buildings and tunnels are described in full details in chapter 6 of this report.

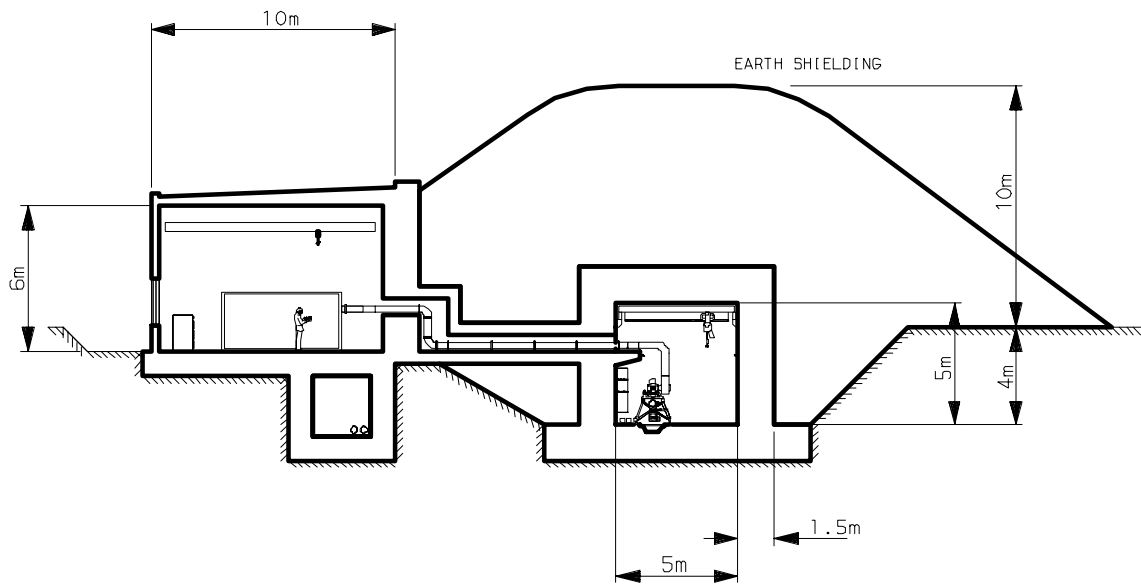


Figure 1.3-25: Cross section of the NCL tunnel and buildings for shielding characteristic prevailing at ISIS in the UK.

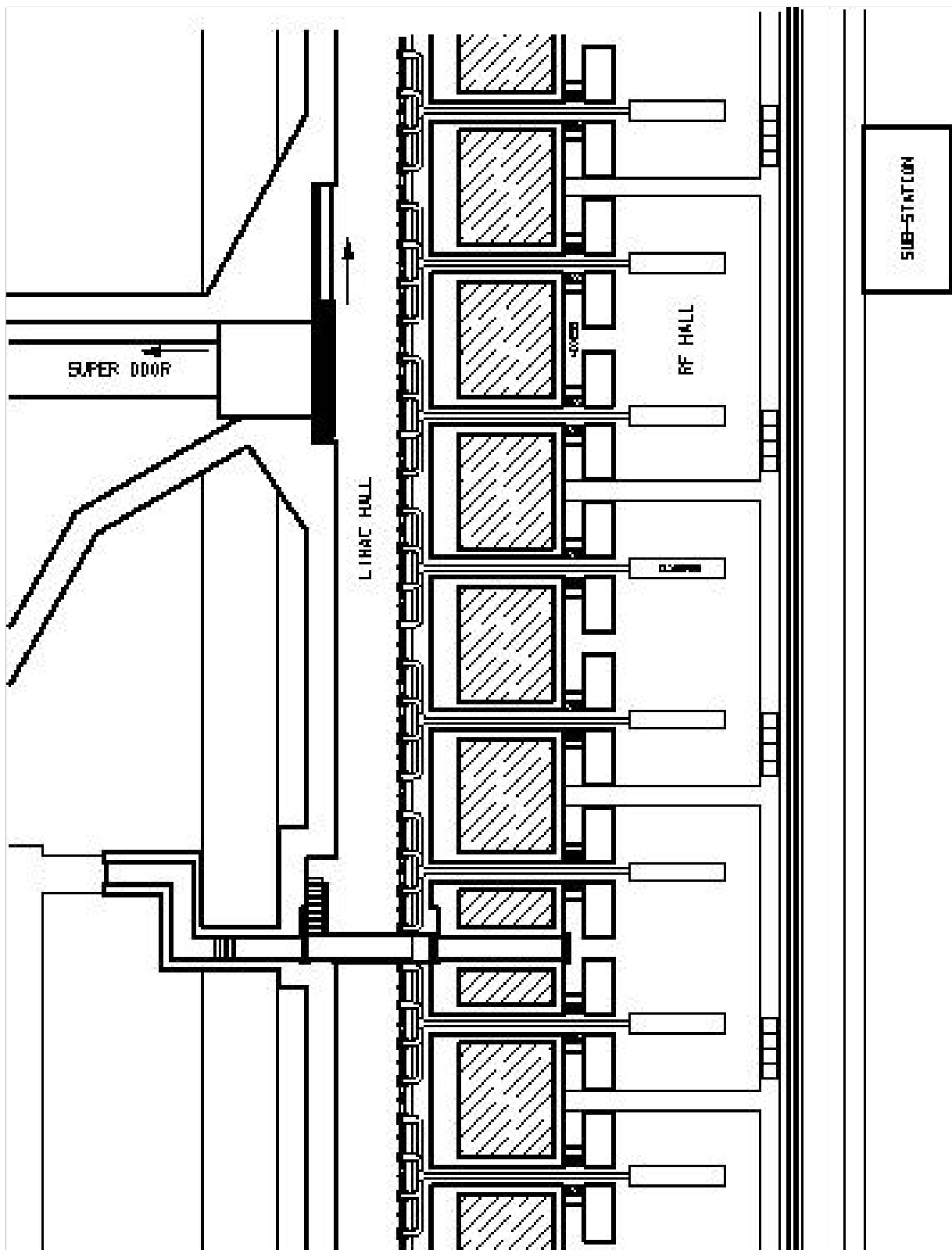


Figure 1.3-26: Plan view of room temperature CCL

1.4 THE 352/704 MHZ LINAC DESIGN

1.4.1 Introduction

The 352/704 MHz design is based on acceleration between 200 and 1334 MeV by means of 704 MHz superconducting RF cavities. The 704 MHz frequency is shown to be a good choice for superconducting (SC) cavities. Initially, two H^- beams are accelerated at 352 MHz to 20 MeV, after which they are funnelled together into a normal conducting 704 MHz separated drift tube linac (SDTL) and accelerated to 100 MeV. Between 100 and 200 MeV, the beam is accelerated by a coupled cavity linac (CCL). Provision has been made in the front end for a proton beam in case long pulse operation proves to be impossible with H^- ions.

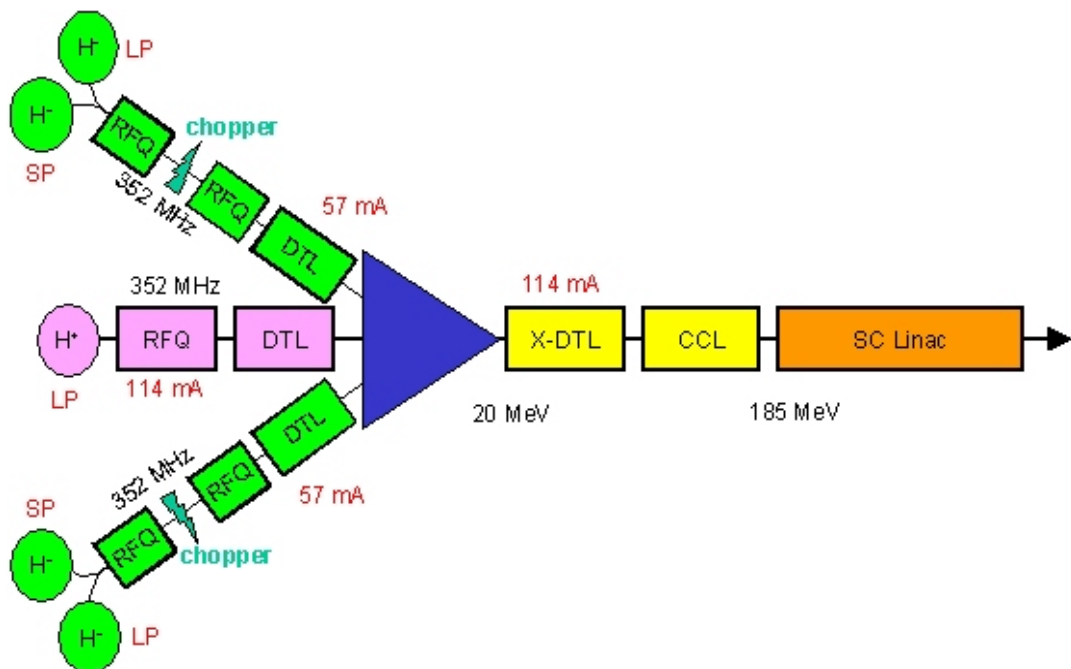


Figure 1.1–2: The 352/704 MHz SC scheme, with the optional LP H^+ contingency measure

The superconducting linac accelerates the beams from 200 MeV to the final energy of 1334 MeV. It is composed of two families of cavities ($\beta_g = 0.66$ and $\beta_g = 0.85$) with accelerating gradients of 10.5 MV/m and 12.5 MV/m respectively (corresponding to 50 mT surface peak magnetic field). The cryostats contain three and four cavities. Two couplers are used for feeding each cavity, allowing a maximum peak power of 1.6 MW. A separate klystron is used for each cavity to guarantee efficient field control and energy stability for all modes of beam operation, and to accommodate cavity detuning effects due to Lorentz forces, microphonics, different beam loadings, *etc.* A single CEBAF-like cryogenic plant is sufficient to take care of the total heat load (2.3 kW at 2 K). Table 1.4–1 shows the main parameters of the 352/704 MHz scheme.

Allowing both H^- ions and protons within the same acceleration system is relatively easy and does not raise physics or engineering problems.

Table 1.4-1: Parameters for the 352.2/704.4 MHz scheme

Linac total length (m)	432
Final Energy (MeV)	H ⁻ /H ⁺ :1348
Pulse length (ms)	SP:2×0.48; LP:2
Peak current (mA)	SP:114;LP:114
Repetition rate (Hz)	SP:50; LP:50/3
Chopping factor	SP:70%; LP:70% to100%
Peak beam power(MW)	107(70%), 152(100%)
Beam average power (MW)	SP:5.1;LP:3.5(70%) to 5.1 (100%)
Wall plug RF power (MW) (30 % RF control included)	SP: 20;LP:15(100%)
Cryo power (MW)	SP: 1.5 ; LP: 1.5

1.4.2 The low energy beam transport

The low energy beam transport (LEBT) line transports and matches the beam from the ion source into the first RFQ of each front end. The main design criterion is the minimization of emittance growth with a minimum loss rate (stripping for H⁻, wall hit for both H⁻ and H⁺). The different species and the different optical performance levels between ion sources imply two different LEBTs for H⁻ and H⁺. The required output current for the H⁻ line is 60 mA with X and Y emittances below $0.3 \pi \text{ mm mrad}$. For the H⁺ line, the goal current is 95 mA in order to ensure 90 mA at the output of the RFQ and an emittance lower than $0.25 \pi \cdot \text{mm.mrad}$. These different values of emittances and currents take into account present state of art in particles sources. In this chapter only magnetic LEBTs incorporating solenoids and quadrupoles will be considered. Electrostatic LEBTS are likely to be inadequate for the currents envisaged (because of issues of non-compensation and aberration) — an electrostatic LEBT like the one being built for the SNS project is not currently being considered for the ESS.

1.4.2.1 The H⁻ LEBT

1.4.2.1.1 Space Charge Compensation

Positive ions and electrons are produced by the collisions of H⁻ with the residual gas molecules in the transport line. In the absence of any other perturbing phenomena, the beam potential traps positive ions well and electrons are repelled towards the vacuum chamber wall. This process continues until the beam is fully neutralised and a dynamic equilibrium is reached. Above a pressure of 10^{-5} hPa , (*i.e.* 10^{-5} mbar) the time required to reach equilibrium is around one hundred microseconds, a value consistent with both experimental measurements and theoretical predictions.

In reality, the neutralisation is often not uniform along the line, and this can happen for several reasons. These include variation of the pipe diameter, divergence of the beam, mirrors effect induces by solenoids, *etc.* which can provoke electron drift. At the present time, there is no universally accepted model or code able to predict variations of compensation along transport lines. Therefore experimental measurements, theoretical work and computer codes are required in the fields of charge distributions, beam transport, emittance growth and associated beams diagnostics.

Experience shows that the H⁻ LEBT may often be considered as fully compensated. This is why only fully compensated beams will be considered in this section. Overcompensated beams have also been observed. This can be explained by the production of relatively high velocity electrons in the ionisation process while heavier positive ions stay around the axis long enough to create such an overcompensated regime. Results of simulation in the ESS Technical Study (vol. III) [ESS-96-53-M] show that, even in 10% overcompensated or undercompensated regimes, matching can still be obtained. It may be added that due to the time constants involved and the detrimental effect of electric fields on compensation, chopping in the LEBT is not recommended.

1.4.2.1.2 Gas stripping of H-

At low energy (up to ~50 keV), the probability of H⁻ stripping has to be considered. Experiments performed at Los Alamos have shown that very short LEBTs are more effective for minimising stripping below 50 keV. These experiments have also shown that stripping was not a great problem around 100 keV. It seems that a LEBT length below 0.5 m is adequate to ensure good efficiency at 60 keV. This reduces the possibility of inserting several diagnostics, pumping and steerers into the LEBT. But once the optical performance of the line has been tested, only steering, current noise and peak current in the pulse are necessary during operation of the linac. As the system is pulsed, a single current transformer can determine both values. The peak current is computed during the pulse rise and the noise by fluctuations in the pulse. These values are more relevant if they are measured in front of the RFQ. The best location for vacuum pump(s) is close to the ion source, which is the main source of gas in the line. Steerers can be inserted into quadrupoles with 100 mm apertures.

1.4.2.1.3 The emittance management

For practical choices of types of ion source (volume, filament or Penning), two cases have to be considered. For the volume or filament source, emittances in the X and Y planes will be very similar and no particular treatment compared to H⁺ LEBT case is necessary. For the Penning source with slit emitters, emittances in the X and Y planes will be different by a factor ~2. In order to equalize emittances and then simplify the linac design, two possibilities may be considered:

- Coupling between X and Y in the RFQ to equalize the emittances. It is relevant if the channel is relatively long and the acceptance large enough (see RFQ section). This choice does not require solenoids, which induce strong coupling. Quadrupoles can then be used to obtain a short LEBT.
- In order to relax the constraints on the RFQ, coupling in the LEBT using solenoids. To be efficient, the line must include three or four solenoids [Planner, 1995]. This choice is the opposite to that of a short LEBT because very short solenoids induce beam aberration [Bailey, 1998]. Anyway, coupling is never perfect, especially with non-linear space charge. Studies have shown that the emittances equalisation can be performed in the RFQ itself [Duperrier, 2001].

1.4.2.1.4 LEBT with five quadrupoles

In this configuration, no coupling is applied. Emittances should be preserved if no additional phenomena occur. With five quadrupoles, it is relatively easy to get the matching into the RFQ (Figure 1.4–1). The design of the quadrupoles can be directly extrapolated from the IPHI DTL quadrupoles. A large aperture is used for the first quadrupole, enabling insertion of the extraction system if needed. The first quadrupole can then be used as a dipole to separate electrons from the beam. The required aperture for pumping can be inserted between two

poles of the first quadrupole. No extra drift in the LEBT is then necessary for pumping. A drift greater than 100 mm is included at the end of the line. It allows inserting a TI for current measurement. Steerers can be inserted in quadrupoles. The obtained line is difficult to build but is not unfeasible. The total length is 43 cm.

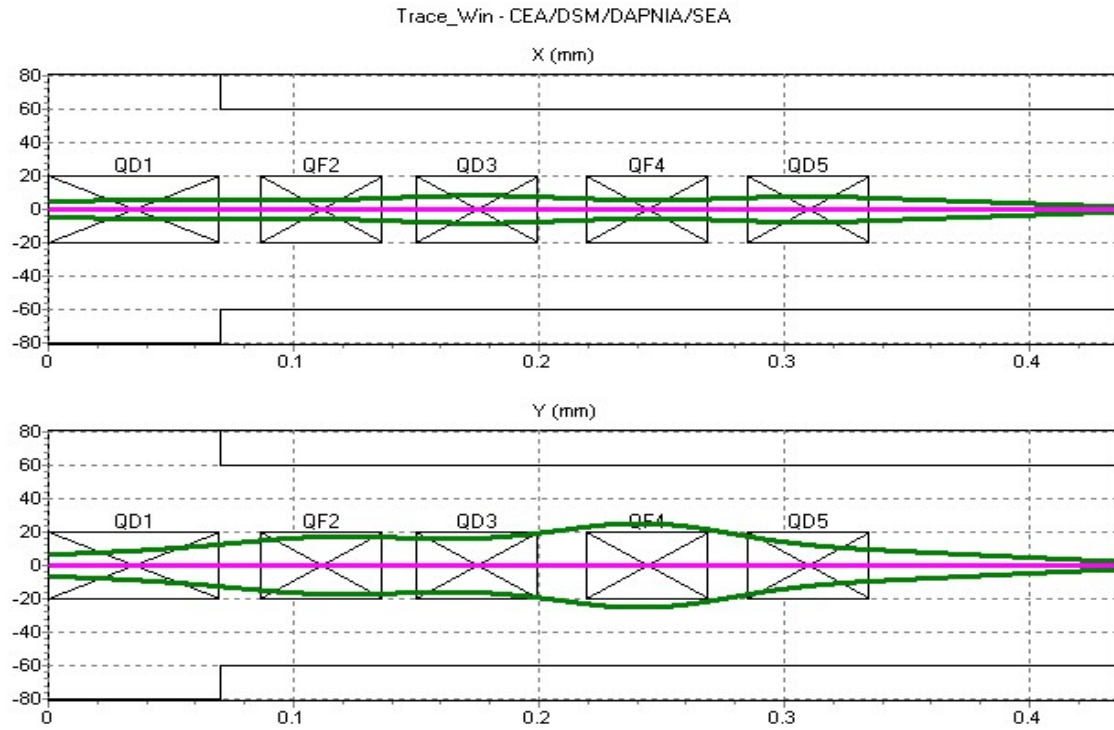


Figure 1.4-1: Beam envelope with full compensation in the quadrupoles LEBT (x-axis in meters).

1.4.2.2 The H⁺ LEBT

1.4.2.2.1 Space Charge Compensation

The mechanism of space charge compensation in the gas-focusing régime is similar to the compensation of H⁻ beams. However, there are a few notable differences. Compensation is obtained by trapped electrons instead of by trapped positive ions, a consequence of which is that the time needed to reach the space-charge compensation steady-state régime at 10⁻⁵ hPa (10⁻⁵ mbar) is a few tens of microseconds for H⁺ compared with around one hundred microseconds for H⁻. Moreover, the steady-state régime is also different. For the same reasons as in the H⁻ LEBT, chopping in the LEBT is not recommended.

1.4.2.2.2 LEBT with two solenoids

In this section, a beam line with two solenoids is described, as seems appropriate in order to match the beam extracted from an ECR source into a RFQ. In such configuration, the beam is mainly axes symmetric. Emittances may be preserved if the beam radius is less than half the solenoid bore radius (thereby avoiding non linearity in focusing). A line with three solenoids is also possible, but the following simulations show that matching requirements can be achieved with two.

Matching to the RFQ has been obtained with two line configurations:

- A compensation of 98% along the line. This value has been measured at Los Alamos and Saclay with high accuracy after the ECR sources (LEDA and IPHI projects). The magnetic field is 0.108 T for the first solenoid and 0.191 T for the second one. Figure 1.4–2 shows beam envelope variation for this configuration.
 - A compensation of 70% along the LEBT, to see if a pessimistic case can be managed. It is interesting to notice that such a value has been measured at Saclay at the LEBT exit. The magnetic field is 0.158 T for the first solenoid and 0.212 T for the second one. The solenoid used for this simulation has the same characteristics as SILHI which can reach fields higher than 0.25 T. Figure 1.4–3 is a diagram of the SILHI LEBT.

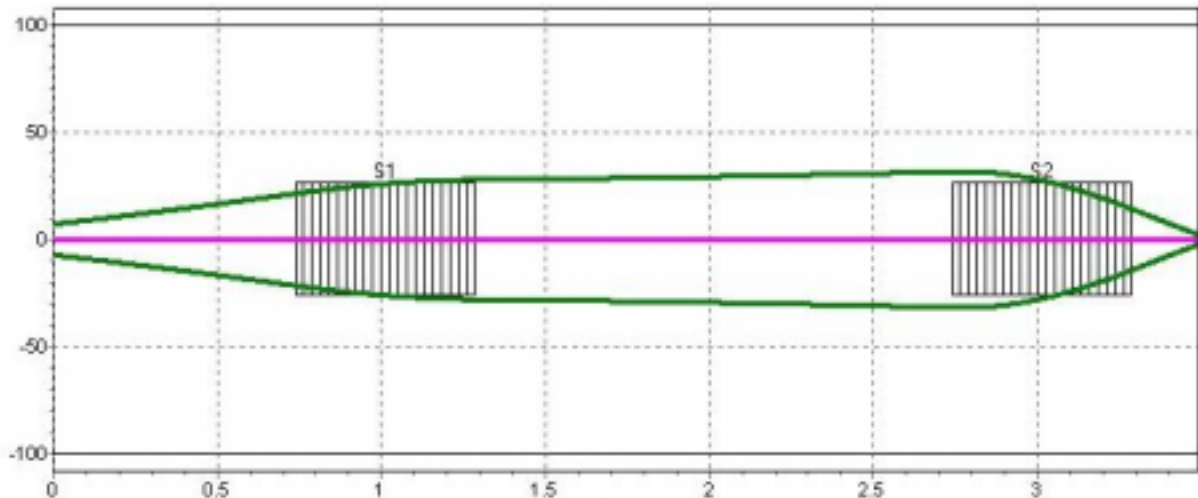


Figure 1.4–2: Beam envelope for 98% compensated case

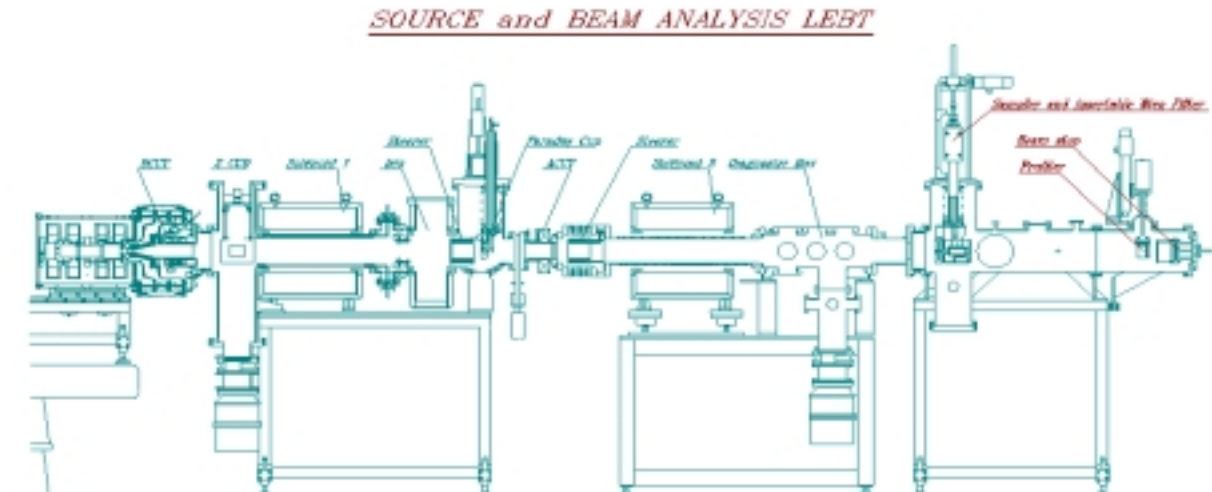


Figure 1.4-3: *The SILHILEBT*

1.4.2.3 Conclusions

With present knowledge, mainly based on experiments and theoretical work, it is likely that a magnetic LEBT will meet the requirements on emittance transmitted current for the ESS project. The advantages compared to an electrostatic LEBT (experience, aberration, space for

diagnostics, space charge) make it the preferred solution. However, experiments have to confirm the performance of the magnetic H⁻ LEBT especially as concerns the space-charge compensation.

The choice of magnetic elements (solenoids or quadrupoles) has to be established for the H⁻ LEBT. Both seem to be feasible and have advantages and drawbacks. For the quadrupoles LEBT, the advantages are: a minimization of the stripping (shorter line), a bigger aperture; and the main drawback is the compactness, which implies complex engineering arrangements to accommodate vacuum pumping and inclusion of beam diagnostics. For the solenoids LEBT, the main advantage is a minimization of the constraints on RFQ (emittances equalisation); the drawbacks are: a higher stripping (longer line), beam filamentation induced by solenoids, a smaller aperture in order to minimize these filamentations (worst margin beam / aperture), and a coupling between X and Y directions that could be hard to compensate. In the work described in this section hereafter, it has been assumed that a quadrupoles LEBT is in use.

For the H⁺ LEBT, it is not obviously necessary to minimize stripping. It is then interesting to use a long line (possible insertions for pumping and diagnostics) with long solenoids (strong focusing and low filamentation).

1.4.3 The radio frequency quadrupole (RFQ) accelerators

The first accelerator cavities after the sources are RFQs. They allow for good bunching with high transmission. The two source beams are then accelerated to 20 MeV where they are funnelled together to provide the required current at high energy. As the first accelerating components of the ESS overall acceleration scheme, the RFQs play a significant role in determining the quality of the beam in the rest of the accelerator. For this reason beam quality and low emittance growth are the driving forces behind the RFQ design.

The 352.2 MHz ESS option requires three different RFQs (a total of five RFQs, of which one is for the H⁺ line). At this frequency, four-vane geometries are used. Each H⁻ RFQ line is split into two sections with the chopping line placed between the two RFQs, at 2 MeV. As a matter of fact, a (p, n) reaction on copper exists with threshold energy of 2.16 MeV (⁶⁵Cu (p, n) ⁶⁵Zn, T_{1/2} = 244 days). This 2 MeV choice will therefore avoid unnecessary beam loss induced activation in the preceding structure and in the chopper line. It implies use of another RFQ after the chopping line. The frequency choice of 352.2 MHz is consistent with present LEDA and IPHI project experience [Smith, 1998], [Lagniel, 1998]. LEDA has demonstrated its ability to accelerate 110 mA with a good efficiency. The IPHI project, which is very similar, enables know-how to be gained for such a structure in Europe. The IPHI R&D is then perfectly relevant for ESS.

Only simulations performed with a 4D-water-bag matched beam at input are shown in this section. It allows each element to be qualified separately. Studies have shown that the impact of filamentation at the input of the RFQ does not imply a different beam at the exit if we consider only RMS matching [Duperrier, 2001]. A re-tuning of the linac is not, then, necessary but extra losses, especially in the RFQ itself, are induced (producing beam halo).

1.4.3.1 RFQ1

The first H⁻ RFQ has been designed to minimize emittance growth in the transverse plane during the bunching and acceleration process while keeping a large acceptance (0.3

$\pi \text{mm.mrad RMS}$). This parameter puts less constraint on the H^- source. At the same time, the bunching has to be very efficient to reduce the constraints on the H^- sources. The more efficient is the bunching, the less is the required source current. The behaviour of the parameters of RFQ1 is shown in Figure 1.4–4. The output distribution is plotted in Figure 1.4–5 and Table 1.4–2 gives the main results.

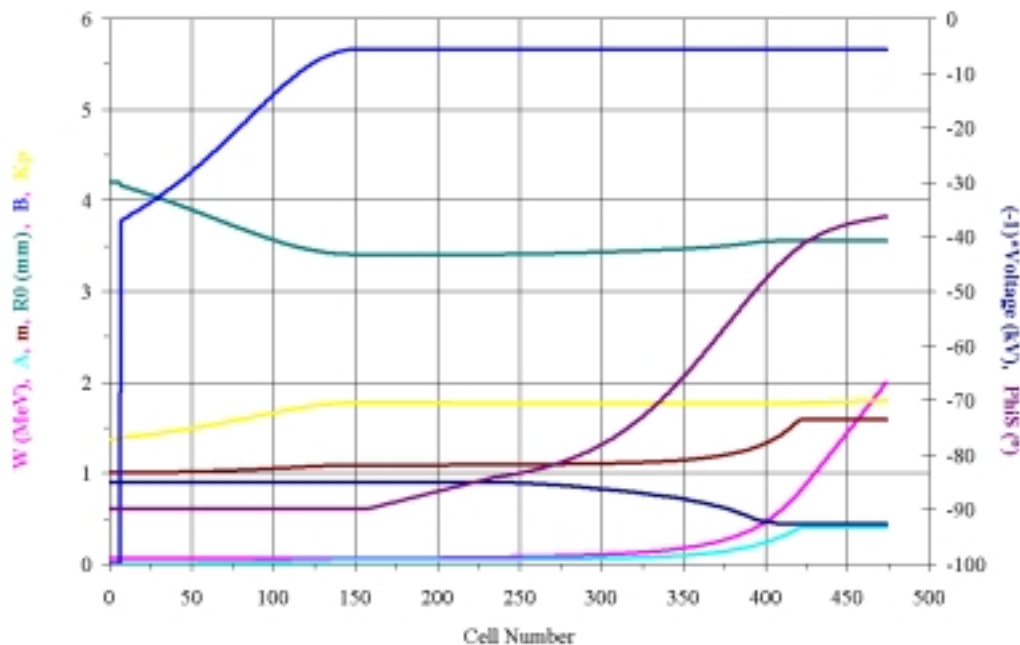


Figure 1.4–4: Behaviour of RFQ1 structure parameters

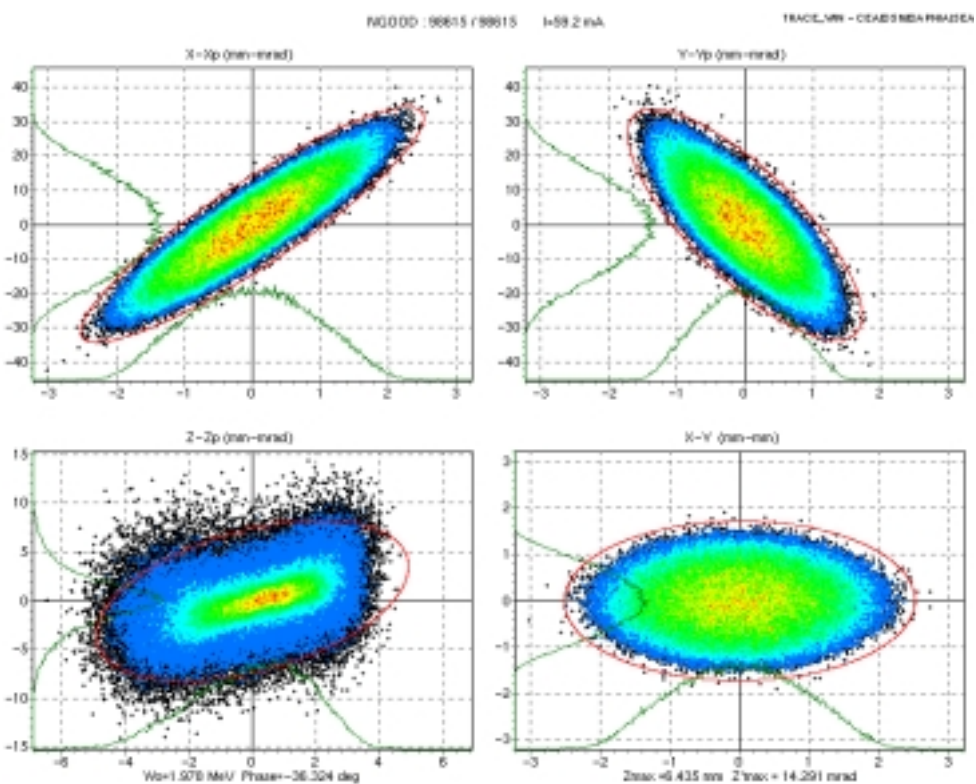


Figure 1.4–5 : RFQ1 output beam distribution

Table 1.4-2: Main parameters and results for RFQ1

RF Frequency	352.2 MHz
Input Energy	65 keV
Output Energy	1.98 MeV
Length	3.92 m
Number of cells	474
Minimum aperture a (mm)	2.74-4.2
Modulation m	1.00-1.59
Mean aperture R_0 (mm)	3.55-4.2
Voltage	85-92.62 kV
Peak field	1.37-1.8 Kp; 25.24-33.17 MV/m
Input transv. rms norm. Emittance	$0.3 \pi \text{ mm.mrad}$ (or 0.2π in X and 0.4π in Y)
Input long. Rms norm. Emittance	$0 \pi \text{ mm.mrad}$
Output transv. rms norm. Emittance	$0.3 \pi \text{ mm.mrad}$
Output long. rms norm. Emittance	$0.3 \pi \text{ mm.mrad}$; 0.14 deg.MeV
Input current	60 mA
Output current	59.2 mA
Transmission	98.6%
Peak power in copper (+20% margin)	0.636 MW
Peak beam Power	0.114 MW
Total peak power	0.750 MW

No emittance growth has been found with this design. The transmission is high (98.6%). Figure 1.4–5 shows that no significant halo has been produced. The cavity can be fed by one single 1 MW klystron (LEP klystron).

1.4.3.2 RFQ2

The second H⁻ RFQ has been designed to minimize emittance growth during the acceleration process, maintaining a longitudinal acceptance that is as large as possible. In order to simplify the DTL design for the H⁺ and H⁻ lines, this RFQ has the same zero current phase advance at exit as RFQ3. The behaviour of the RFQ2 parameters is shown in Figure 1.4–6. The output distribution is shown in Figure 1.4–7 and Table 1.4-3 gives the main results.

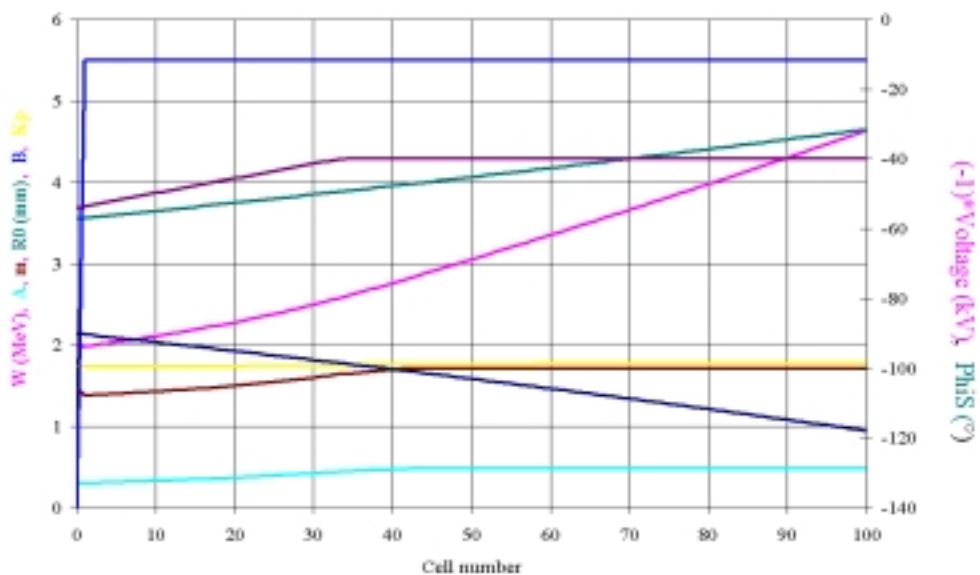


Figure 1.4-6: Behaviour of RFQ2 structure parameters

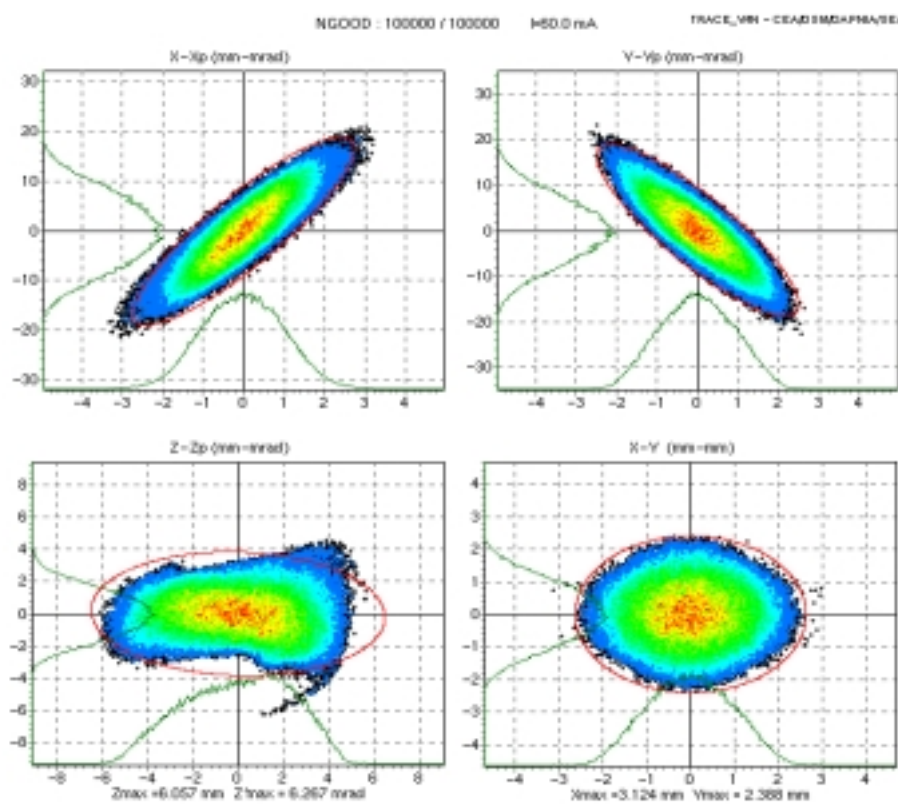


Figure 1.4-7: RFQ2 output beam distribution

Table 1.4-3: Main parameters and results for RFQ2

RF Frequency	352.2 MHz
Input Energy	1.98 MeV
Output Energy	5.0 MeV
Length	4.09 m
Number of cells	113
Minimum aperture a (mm)	2.87- 3.5
Modulation m	1.47-1.71
Mean aperture R_0 (mm)	3.55-4.8
Voltage	90-121.73 kV
Peak field	1.74-1.77 Kp; 32.06-32.62 MV/m
Input transv. rms norm. emittance	$0.3 \pi \text{ mm.mrad}$
Input long. Rms norm. emittance	$0.3 \pi \text{ mm.mrad}$
Output transv. rms norm. emittance	$0.31 \pi \text{ mm.mrad}$
Output long. rms norm. Emittance	$0.32 \pi \text{ mm.mrad}$; 0.14 deg.MeV
Input current	57 mA
Output current	57 mA
Transmission	100 %
Peak power in copper (+20% margin)	0.700 MW
Peak beam Power	0.171 MW
Total peak power	0.871 MW

Emittance growth has been kept below 6%, which is tolerable. The transmission is excellent (100%). This is very important taking into account that threshold copper activation by protons is 2.16 MeV. This cavity can be fed by one single 1 MW klystron.

1.4.3.3 RFQ3

The main goal of proton RFQ3 design is to minimize losses above 2.16 MeV in order to avoid copper activation. The bunching and acceleration process has been kept as adiabatic as possible. The change in the RFQ3 parameters is shown in Figure 1.4-8. The output distribution is shown in Figure 1.4-9 and Table 1.4-4 gives the main results. This RFQ is identical to the IPHI RFQ, which is under construction. Numerous error studies were carried out to ensure the success of this RFQ.

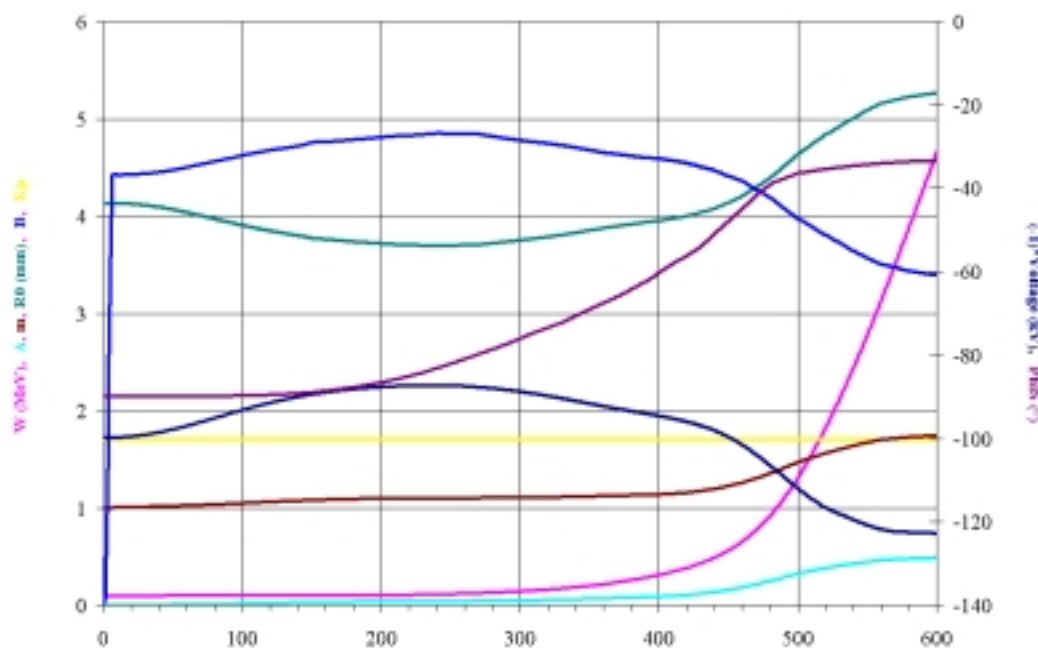


Figure 1.4-8: Behaviour of RFQ3 structure parameters

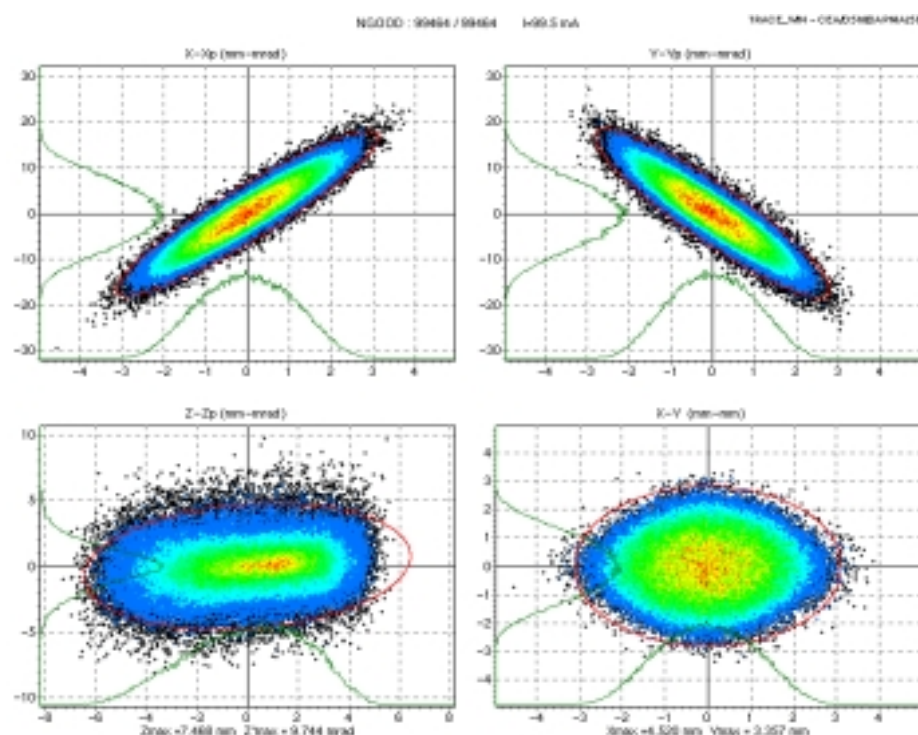


Figure 1.4-9: RFQ 3 output beam distribution

Table 1.4-4: Main parameters and results for RFQ3

RF frequency	352.2 MHz
Input Energy	95 keV
Output Energy	5.0 MeV
Length	8 m
Number of cells	610
Min. aperture a	3.5 - 4.1 mm
Modulation	1.0 - 1.74
Mean aperture R_0	3.7 - 5.27 mm
Peak field	1.7 kp; 31.3 MV/m
Vane voltage	87 - 123 kV
Input Trans. emit.	$0.25 \pi \cdot \text{mm.mrad}$
Input Long. emit.	0
Output Trans. emit.	$0.26 \pi \cdot \text{mm.mrad}$
Output Long. emit.	$0.15 \deg \cdot \text{MeV}; 0.38 \pi \cdot \text{mm.mrad}$
Input current	95 mA
Transmission	99.50%
Peak power in copper (+20% margin)	1.16 MW
Peak beam Power	0.49 MW
Total peak power	1.65 MW

Transverse emittance growth is lower than 4%. Losses are mainly from slow particles. Two 1 MW klystrons are required for this cavity. This can be explained by a higher current (95 mA) and acceleration range (from 0.095 to 5 MeV). Figure 1.4–10 shows an example of electromagnetic computations for IPHI RFQ extremities.

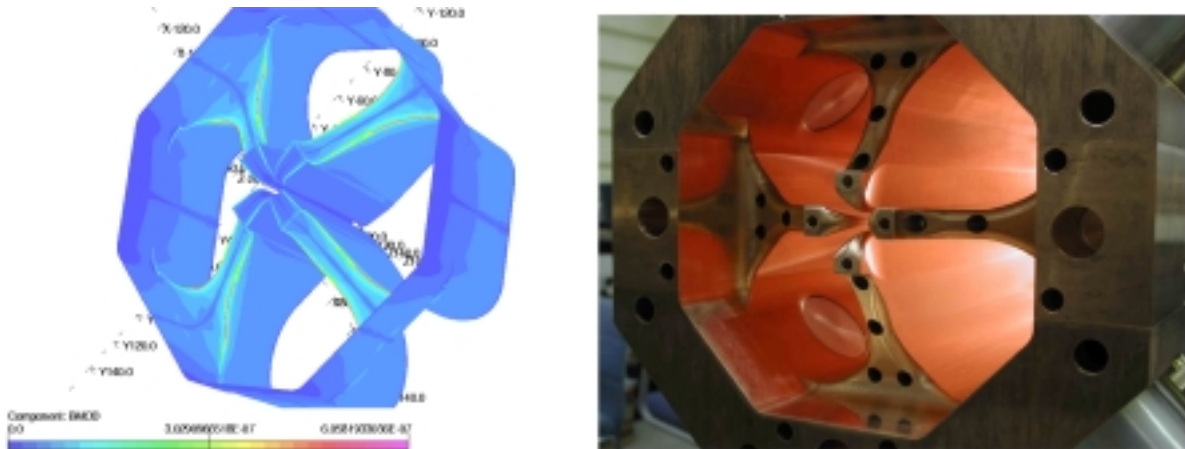


Figure 1.4–10: Magnetic field map at IPHI RFQ exit, and picture of the IPHI RFQ

1.4.3.4 Conclusion

The proposed injector system meets the requirements for the ESS project. This scheme uses present experience with ISIS, LEDA and IPHI project. LEDA has demonstrated its ability to accelerate 110 mA with a good efficiency. The three different RFQs at 352.2 MHz minimize activation and keep emittance growths to an acceptable level (5%), which is very important for reliability aspects.

1.4.4 The chopper section

Time structure is required in the H⁻ beam to enable low loss multi-turn injection into and single turn fast extraction from the accumulator rings. The chopping occurs at 1.242 MHz, the revolution frequency of the rings. A fast chopper is inserted after the first RFQ and must chop the beam cleanly between the RFQ beam bunches (2.84 ns) so as not to generate beam loss on the downstream linac structures. The beam gap in the ring is of the order of 240 ns (30% of the ring circumference).

The beam energy should not be so low that the space charge strongly de-bunches the beam, nor too high such that the beam rigidity imposes a high chopper voltage. The optimised energy is between 2 and 2.5 MeV.

The Los Alamos National Laboratory (LANL) has developed such a chopper structure for the Spallation Neutron Source project, using notched strip lines with separators to avoid coupling between adjacent lines. Very good technical collaboration exists among LANL, CEA-Saclay, CERN-SPL, and RAL on the development of chopper structures.

Although no potential showstoppers are predicted vacuum properties (out-gassing, mechanical deformation under vacuum), distribution of heat losses (possible distortions, cooling) and long-term resistance to irradiation (beam losses) still need to be studied.

The rise time of the chopper power supply will probably be the limiting element. Following a suggestion from RAL, the drive will provide a sinusoidal shape instead of a pulse shape. A series of advantages are expected from this option:

- A frequency corresponding to half the bunch spacing will deviate one bunch in one direction and the next one in the opposite direction. While this scheme doubles the number of beam dumps, each is expected to be easier to build and cool with only half the total chopped beam power.
- A careful choice of the phase synchronisation between the beam and the wave allows for a small spread in the deflection angle. This could help to reduce the power density on the beam stoppers.
- According to “Spice” calculations, the power supply bandwidth can be decreased from about 0-600 MHz to an easier range of 0-300 MHz.
- A higher voltage should be achievable. A reasonable peak value of 1.4 kV (20 kW rms on a 50 Ω load) will be assumed on each plate. The 85% field efficiency leads to an expected equivalent electrical field of about 133 kV/m for an 18 mm gap between the chopper plates.

The chopper line must be kept as short as possible to avoid excessive emittance growth. Careful dynamics design allows for a 10% rms emittance growth, but actual blow-up during daily operation might be higher. Error studies of such a line will certainly help to optimise the robustness of the chopper line.

The proposed chopper line contains 13 quadrupoles, 4 buncher cavities at 352.2 MHz and two 240 mm long choppers located inside two quadrupoles. The chopper plate voltages are ±1150 V and the distance between them is 16 mm. The line is 2.67 m long.

The beam simulations use the previous accelerator output distribution. So, the chopper line simulation uses the RFQ1 output distribution. The beam radii ($\sqrt{5} \times$ rms radii) and the position of the elements are shown on Figure 1.4–11 which also shows the position of the beam collimator and the beam dump. The separation of the chopped and un-chopped beams is very good (the distance between beam centres at beam stop position is 8.5 times the beam rms size at this location). This large separation is needed to reach 0% chopped beam transmission (Figure 1.4–12 and Figure 1.4–13). The line transmission is 96.3% for the un-chopped beam and less than 10^{-6} for the chopped beam. At ± 800 V, the transmission is lower than 10^{-5} (Figure 1.4–13). The emittance growth in the line is very low.

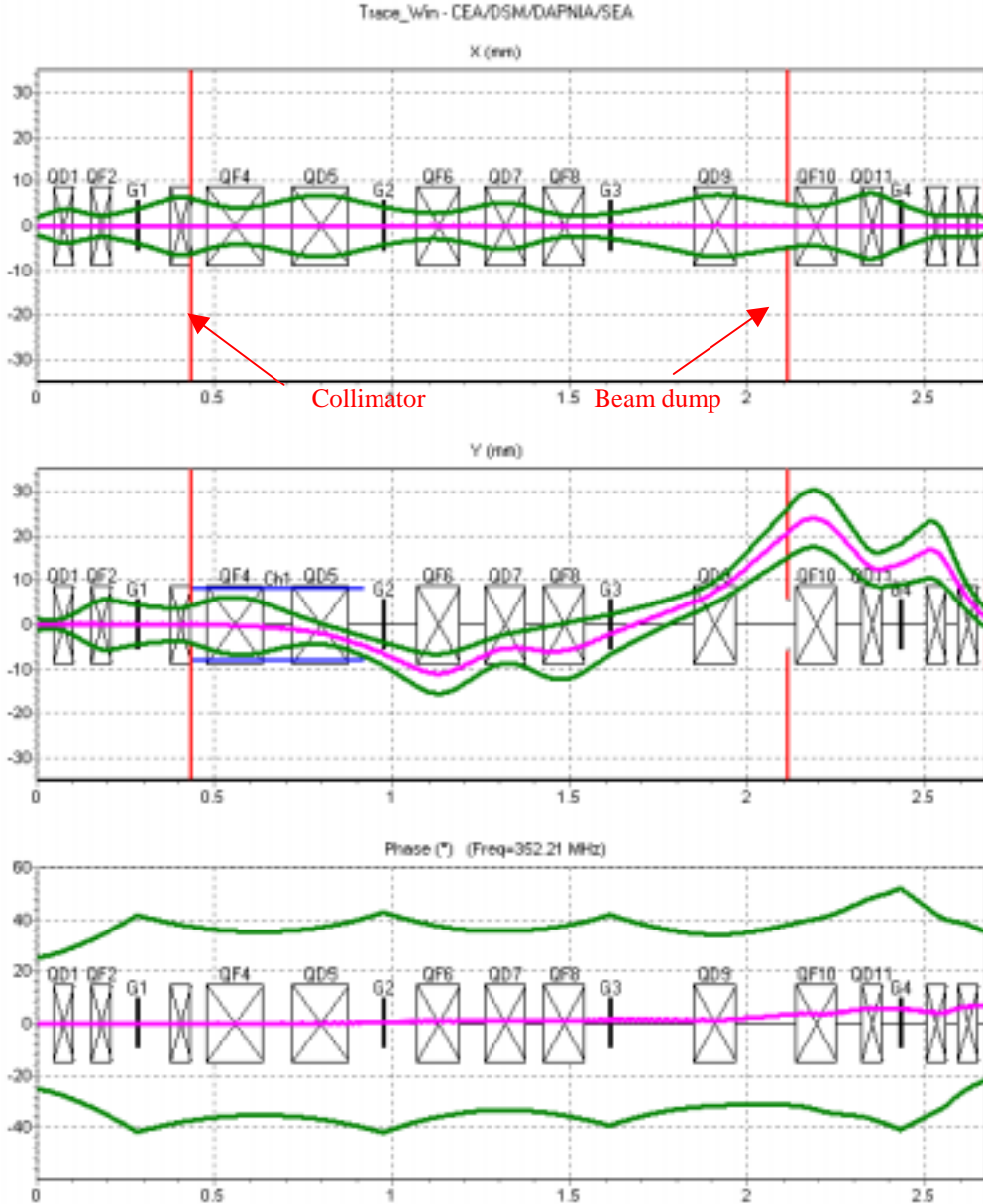


Figure 1.4–11: Beam envelope

The pulse amplitude of the amplifier is 1.4 kV and the pulse jitter must be lower than 0.2 ns. The rise time is 1.9 ns from 1% to 90 % of the pulse amplitude. The fall is obviously the same from 1% to 90 %. The maximum duty cycle is 5%. The pulse train length and the repetition

rate follow the ESS requirements of 1.2 ms and 50 Hz respectively. The chosen load resistance is 50Ω .

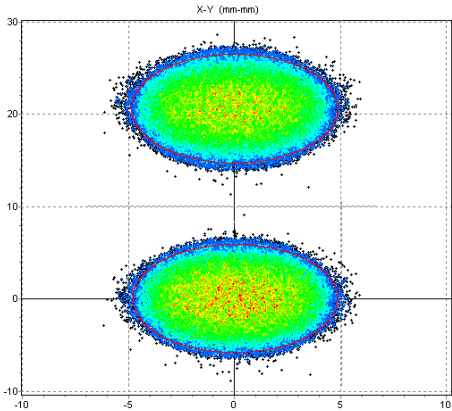


Figure 1.4-12: Separated and non-separated beam at 1150 V

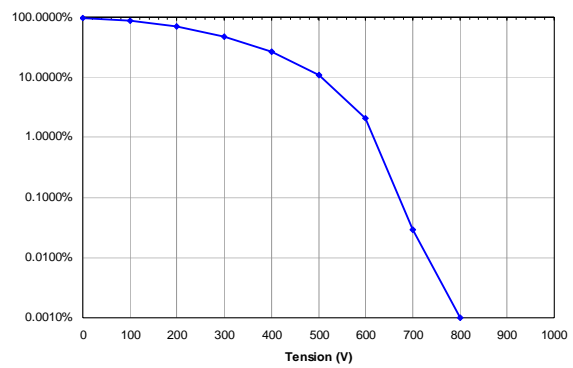


Figure 1.4-13: Particles transmission with chopper voltage

A two-plate meander strip line chopper prototype was built at Saclay in the year 2000 (Figure 1.4-14). Each plate is composed of:

- a metallic ground plate with thin parallel separators
- a printed-circuit board with inside jagged outlines supporting the meander line

A micrometre slide system allows gap adjustment from 10 to 35 mm.



Figure 1.4-14: CEA-Saclay chopper prototype

1.4.5 The Drift Tube Linac (DTL)

DTL tanks are used to increase the energy of the beams to around 20 MeV where they can be funnelled much more easily. This structure is relevant after an RFQ in order to ensure continuity of the focusing scheme. Above 20 MeV a different structure is used to give improved shunt impedance.

The H^- peak current is 57 mA and the ESS-DTL design is based on the IPHI R&D program. A power of 1 MW (1.3 MW klystron) per tank has been chosen. The DTL tank was designed with SUPERFISH allowing a 20% margin on the calculated shunt impedance (including stems). Constraints have been relaxed by setting a deposited power per unit length of less than 120 kW/m, a deposited power density of less than $20W/cm^2$, and a peak electric field of less

than 1 Kp. The same quadrupoles have been used all along the DTL to reduce development cost. The distance between tanks has been set to $1 \beta\lambda$.

1.4.5.1 Choice of the focusing scheme

A 5 MeV input energy into a 352.2 MHz DTL allows the use of conventional electromagnetic quadrupoles, instead of the permanent magnets used in the SNS design. The use of permanent magnets would allow reduction of the drift tube size, and increase of the tank shunt impedance, but it is necessary to be able to tune the DTL to avoid halo development and therefore losses at higher energy, which is not possible with permanent magnets. Moreover, the IPHI project has shown the feasibility of the quadrupoles in the first drift tubes at such a low energy and strong focusing. Electromagnetic quadrupoles are chosen to preserve the beam quality but at the expense of lower shunt impedance.

An FD (one letter per drift tube) focusing scheme is chosen. Alternative schemes with a longer period (the period of FD is $2 \beta\lambda$, that of FODO is $4 \beta\lambda$, and that of FFODDO is $6 \beta\lambda$) would reduce the phase advance per unit length and would prevent staying below 90° per lattice. The phase advance per meter would not be conserved between RFQ output and DTL input and the matching would be more difficult. The price to pay is a higher magnetic field gradient (but IPHI project has shown it is possible), but the beam size is smaller (and then decreasing the tune depression and decreasing the probability of beam losses).

1.4.5.2 DTL prototype

A four-cell prototype is being built at Saclay for the IPHI project [Beauvais, 2000] in order to test various aspects like technological feasibility, quadrupole magnet design, vacuum problems, cooling, mechanical aspects, etc.

All three drift tubes and two magnets have been manufactured. Following copper welding tests, the steel tank of the four-cell prototype is currently being built. Low power and high power tests will be made on the hot model from May of 2002 to the end of summer 2002.

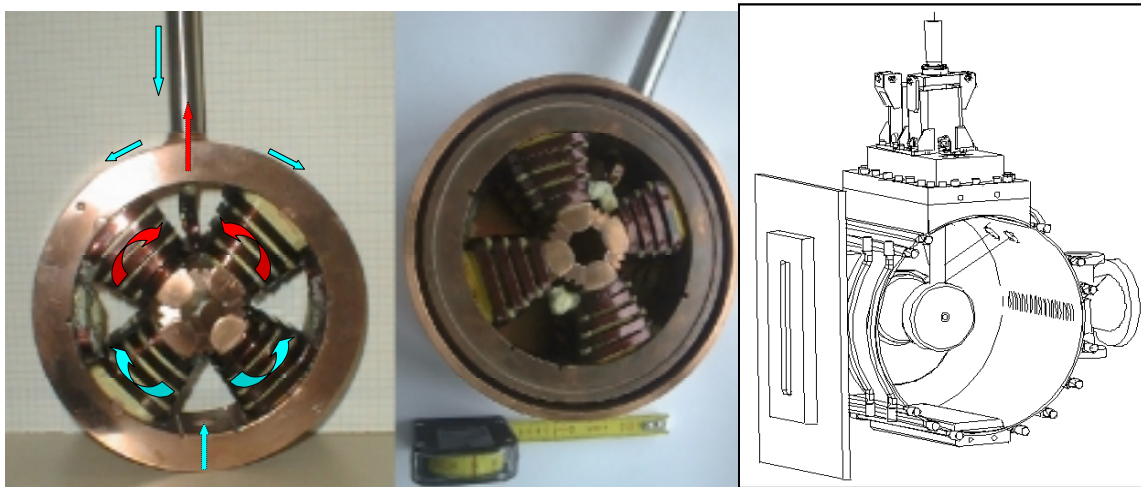


Figure 1.4-15: CEA-Saclay short DTL prototype

1.4.5.3 DTL cell design

The tank diameters are optimised to minimise the power losses in the copper (maximise effective shunt impedance). The 1 cm radius aperture is imposed by the error studies. The geometry of the first and last cells is shown in Figure 1.4–16. The same quadrupole is used.

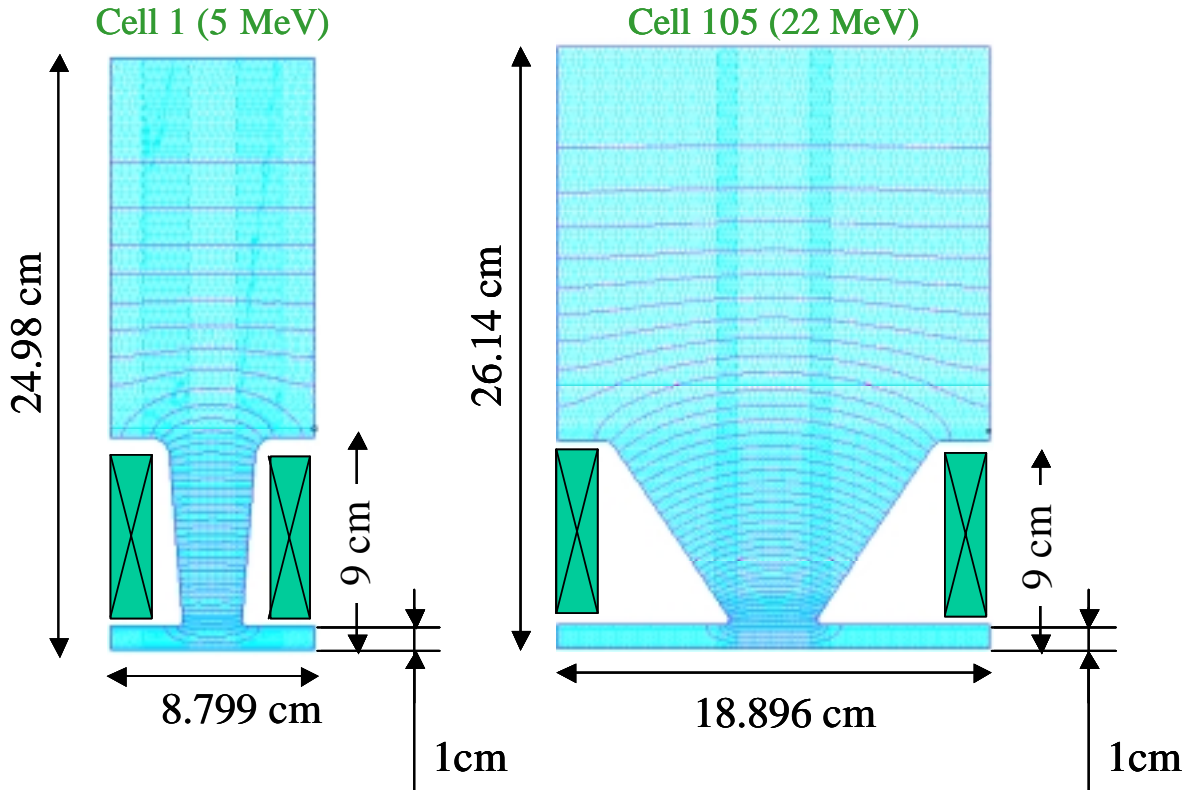


Figure 1.4–16: First and last DTL cell designs

1.4.5.4 H DTL Main parameters

The synchronous phase is ramped from -50° to -30° in the first tank and kept to -30° in the second one. This allows a larger longitudinal acceptance at the DTL input. The longitudinal phase advance per metre is kept continuous with the RFQ (it is $120^\circ/\text{m}$ at RFQ output, see Figure 1.4–17). The mean electric field amplitude E_0 is also ramped in the first tank from 1.2 MV/m to 2 MV/m. The effective shunt impedance is shown in Figure 1.4–18. It is low at low energy ($20 \text{ M}\Omega/\text{m}$) but increased rapidly to $40 \text{ M}\Omega/\text{m}$ at the end. The DTL main parameters are summarised in

Table 1.4-5.

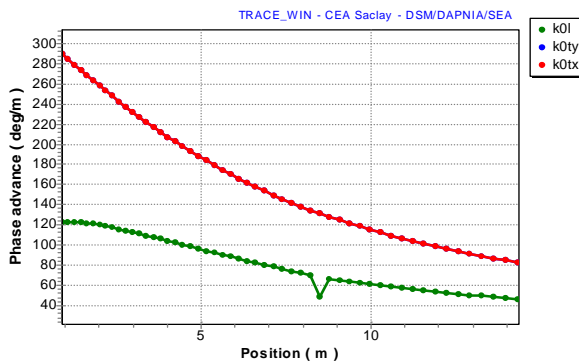


Figure 1.4-17: k_{0L} and k_{0t}

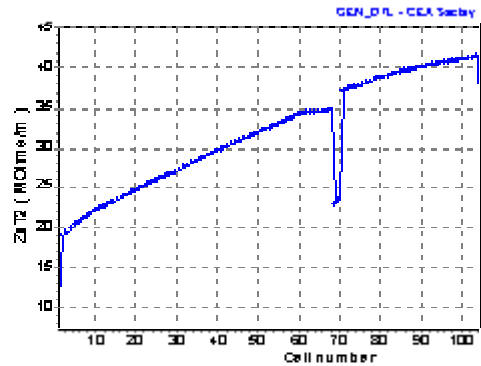


Figure 1.4-18: ZsT^2

Table 1.4-5: H^- DTL main parameters

RF Frequency	352.2 MHz
Length	13.62 m
Input energy	5.00 MeV
Output energy	21.89 MeV
Average ZsT^2 (incl. 20% SF margin)	33 MΩ/m
Number of tanks	2
Number of cells	105
Max peak power per tank (LP)	1 MW
Beam peak power gain	674 kW(SP), 963 kW(LP)
Max total peak power (LP)	2 MW

1.4.5.5 H^+ DTL Main parameters

The H^+ beam peak current is 90 mA. To equal the H^- beam energy after the funnel (21.7 MeV), three tanks are needed (compared to two for the H^- DTL). The constraints on design are identical to the H^- DTL. The synchronous phase is ramped from -50° to -30° in the first tank and kept to -30° in the other ones. This allows a larger longitudinal acceptance at the DTL input. The longitudinal phase advance per metre is kept continuous with the RFQ (it is $120^\circ/m$ at RFQ output, see Figure 1.4-19). The mean electric field amplitude E_0 is also ramped in the first tank from 1.1 MV/m to 2.5 MV/m . The effective cell shunt impedance is shown in Figure 1.4-20. It is low at low energy ($20 \text{ M}\Omega/\text{m}$) but increased rapidly to $40 \text{ M}\Omega/\text{m}$ at the end. The DTL main parameters are summarised in Table 1.4-6.

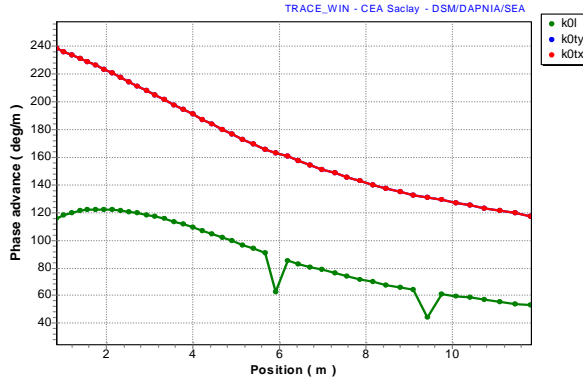


Figure 1.4-19: k_{0L} and k_{0t}

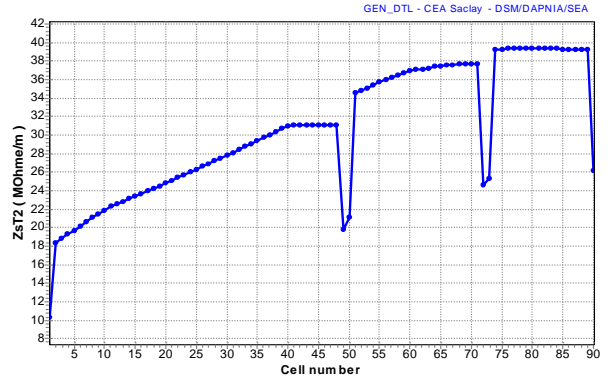


Figure 1.4-20: ZsT^2

Table 1.4-6: Main parameters

RF Frequency	352.2 MHz
Length	11.4 m
Input energy	5 MeV
Output energy	21.73 MeV
Average ZsT^2 (incl. 20% SF margin)	32 MΩ/m
Number of tanks	3
Number of cells	87
Peak power per tank	1 MW
Beam peak power gain	1.51 MW
Total peak power	2.87 MW

1.4.5.6 Diagnostics and commissioning

A $\pm 125 \mu\text{m}$ error on quadrupole positions is assumed in the DTL. This is the value assumed by SNS. In the IPHI project, a $\pm 50 \mu\text{m}$ uncertainty is expected, but it has a cost. Due to the large number of periods per tank and the small linac aperture, it is impossible to guarantee a low loss level with only beam position monitors (BPMs) and horizontal and vertical steering magnets (steerers) outside the tanks. They must be included in the drift tubes.

The following scheme has been chosen:

- A correction-set (CS) consists of two, two-plane steerers associated with two, two-plane BPMs. A set of four equations with four unknowns is solved to obtain the steerer fields that put the beam on axis in the BPMs.
- There is about 90° zero-current, betatron phase advance between two consecutive BPMs in the same correction set.
- BPMs are placed in the drift tubes with the wires running through the tube and the stem.

- The steering magnetic field is obtained by adding one or two windings around the quadrupole poles. The maximum magnetic field needed is estimated at 0.03 T which can be obtained with about 100 A.t per pole.

Six CSs are used along the DTL. The position in the DTL of each steerer and BPM is given in

- Table 1.4-7. The meaning of -X is that the steerer is placed in the RFQ-DTL matching line in the Xth quadrupole placed before the DTL. The first DTL quad (in half the first drift-space) is labelled 0. The meaning of +4 is that the steerer is placed in the funnel line in the fourth quadrupole placed after the DTL. The DTL contains 105 quadrupoles (70 in the first tank and 35 in the second one, including those on both ends).

Table 1.4-7: Positions of the correction-sets in the DTL

	Steer. 1	Steer. 2	BPM 1	BPM 2
CS1	-2	-1	9	13
CS2	14	18	24	28
CS3	29	33	41	46
CS4	47	51	64	69
CS5	70	74	85	90
CS6	91	95	102	+4

1.4.6 The Funnel line

1.4.6.1 Introduction

The peak current achievable with a H⁻ source is estimated at 60 mA. However, the ESS rings require a 114 mA beam to limit the number of injection turns and thus the number of foil hits. Two 57 mA beams, produced by two independent sources, are funnelled to double the beam current.

The funnel line is one of the most complicated sections of the linac. Although the principle was advanced a long time ago, there is no operating piece of equipment in the world today. The energy at which the funnel line operates is a compromise between lower beam rigidity at low energy and lower space-charge effects along the beam transport at high energy. The proposed compromise for ESS sets the funnel energy between 20 and 25 MeV.

The main difficulty is to transport the beam without emittance growth and to prevent halo development. This is obtained by a smooth change of the focusing force from the output of the preceding structure to the input of the following one. To solve the problem of congestion of elements in the line, harmonic cavities have been used as bunchers. A big effort is made to insert the H⁺ beam between the two H⁻ lines. This is made possible by the development of a new deflecting cavity allowing ± 5 degrees deflecting angle. No asymmetric bunching cavities are in use. The induced emittance growth is negligible.

1.4.6.2 Funnel line concerns

To achieve the $\pm 5^\circ$ deflection angle requirement, an attractive new type of funnel cavity is being proposed [Senichev, 2002]. Interesting properties include:

- The amplitude of the field that deflects the beam is close to the cavity peak field. The latter is limited at 1.2 Kilpatrick to avoid spark down.
- A multi-cell cavity allows reaching the desired deflection angle without using dipole magnets.
- The high shunt impedance combined by a nominal operation duty-cycle at only 10% if both short and long pulses are produced with H^- source, or 6% if the long pulse is made of H^+ makes the cooling easier.

Because no dipole is used, the line is not perfectly achromatic. Nevertheless, the chromaticity gives a very small transverse-longitudinal coupling, re-equilibrating itself through space charge forces with a negligible emittance growth. Moreover, a perfectly achromatic line does not exist for space charge driven beams, where the force is non linear and the tune depression low and different from the beam centre to the beam border, whatever the solution of a funnel line.

The funnel line should allow the injection of the H^+ long pulse if needed by injecting the H^+ beam between both H^- branches. Moving quadrupoles and bunchers placed just before entering the deflecting quadrupole does the matching of the H^+ beam to the DTL.

1.4.6.3 Funnel line characteristics

The input and output energies are 21.89 and 21.74 MeV. The angle between both H^- lines is $\pm 10.9^\circ$.

	H^- branch	H^+ branch	Common branch
Number of bunchers:	18	2x4	5
Number of quadrupoles:	54	2x13	10
Total lengths	7 m	14.4 m	7.7m

Quadrupoles

54 quads

quad length (53 quads): 10 cm

min apertures (53 quads): 3 cm

max gradient (53 quads): 40 T/m \rightarrow max Field on pole : 0.6 T

deflecting quad : $L = 20$ cm, $\phi_{\min} = 20$ cm; $G = 5.5$ T/m \rightarrow max Field on pole : 0.55T.

Bunchers

Frequency : 704.4 MHz

3 two-gap, 15 three-gap bunchers.

maximum gap $E_0 TL$: 155 kV ($E_0 T \sim 1.65$ MV/m)

The low energy scheme is shown in Figure 1.4–21. The H^+ line lies between both H^- lines. The funnel line scheme with all elements is shown in Figure 1.4–22. The boxes do not represent the physical size of an element but represent the overall size of it, including water inlet for instance.

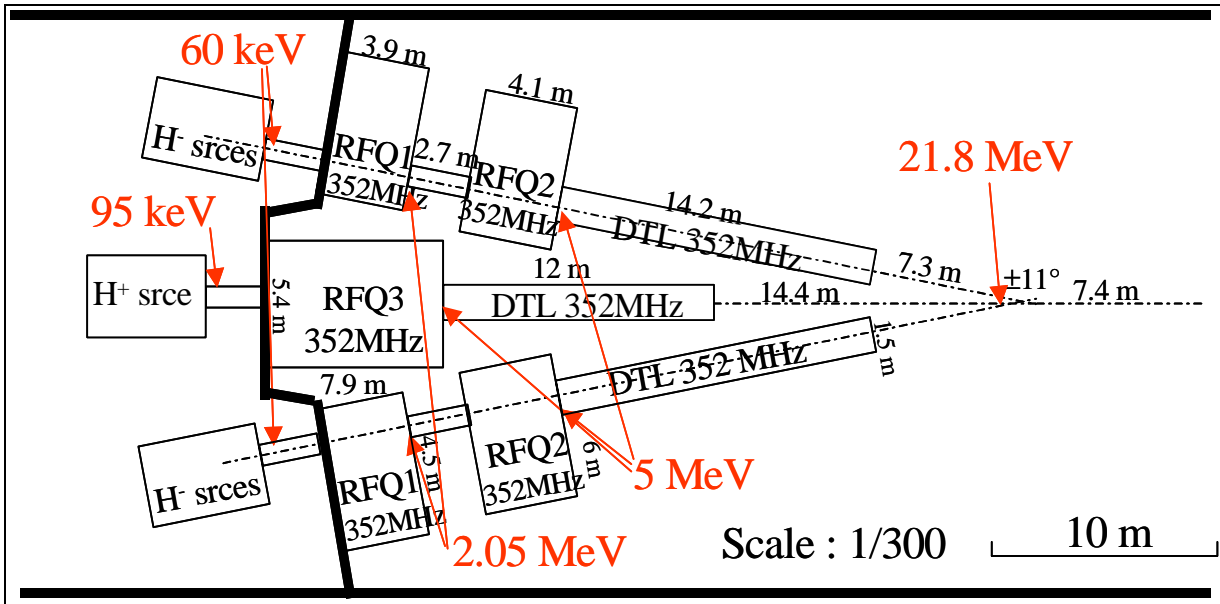


Figure 1.4-21: The low energy scheme

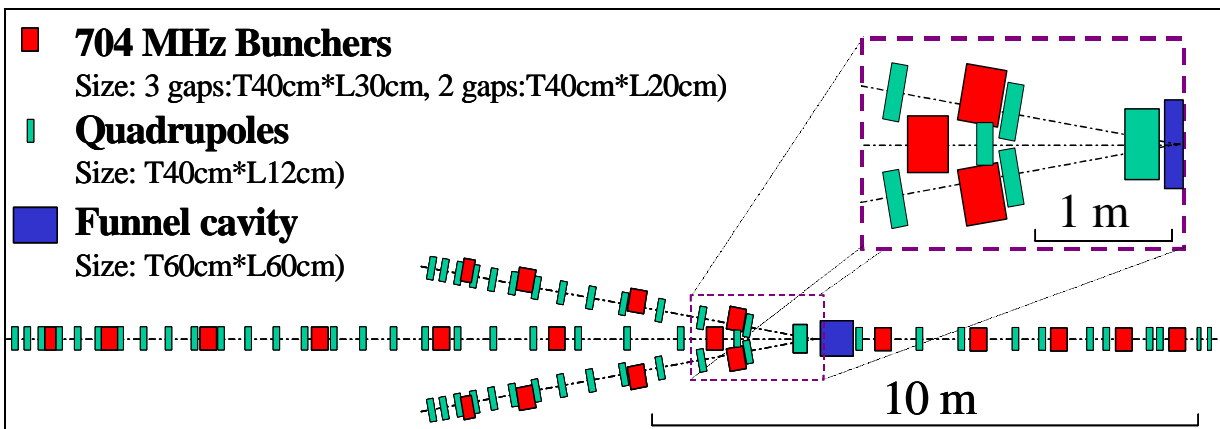


Figure 1.4-22: The funnel line elements

1.4.6.4 The funnel cavity

The funnel device is based on an H cavity with TE101 fundamental mode. A 352.2 MHz, 4-gap, PI transverse mode RF cavity was adopted to deflect the beam transversally by 4.75 degrees [Senichev, 2002], [Barsukov, 2001]. The details are:

- The length is about 0.45 m,
- The deflection angle is about $\pm 4.75^\circ$,
- The maximum distance between plates is 60 mm,
- The transverse electric field is about 15 MV/m.

A 352.2 MHz, tested, prototype cavity, together with its drawing, is shown in Figure 1.4-23a and Figure 1.4-23b.

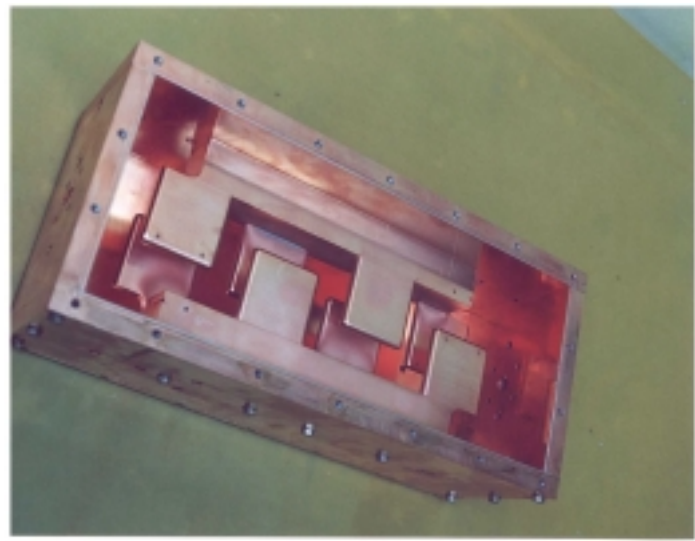


Figure 1.4-23a: Tested prototype deflecting cavity @ 352.2 MHz

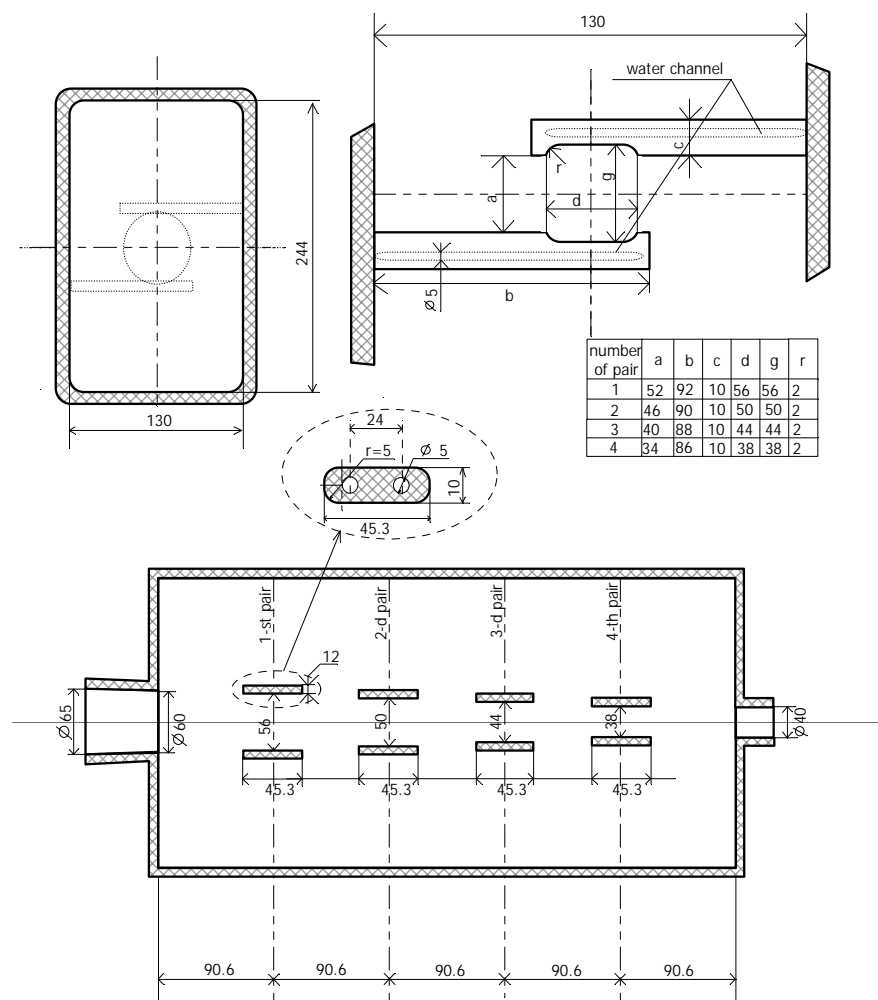


Figure 1.4-23b: Deflecting cavity @ 352.2 MHz (drawing)

The frequency tuning procedure was developed during experimental testing. The field distribution was measured and compared with MAFIA results. The trajectory of the beam centre was integrated in 3D field of MAFIA. In calculation with space charge the calculated angle and space deviations from 3D simulation are represented as one transverse kick per cell. The transverse kicks are assumed the same as they are in reality. This model *does* take into account the coupling between the deflection and the phase of the particle.

1.4.6.5 Layout of the funnel line

The beam deflection in the last metre of the funnel line is shown in Figure 1.4–24. This gives the deflecting quadrupole aperture (200 mm) and the tangent of the deflecting angle ~ 0.194 (11°). The lines in red represent rectangular apertures at each end of the plate (to evaluate the beam losses in the deflecting cavity).

The beam envelope ($\sqrt{5} \times$ rms radii) of the H^- beam along the complete 13 m long funnel is shown in Figure 1.4–25. The deflection is in the x plane. The transverse focusing is progressively modified from a FODO cell (output of the DTL) to a FDO cell (input of the SDTL). Multi-particle simulations exhibit a 10% rms emittance growth in the x -direction during the deflector traversal. 1% in this emittance growth is due to the space charge, 2% is due to the line chromaticity, and the rest is due to the phase-dependent particle transverse deflection. The chromaticity effect seems marginal.

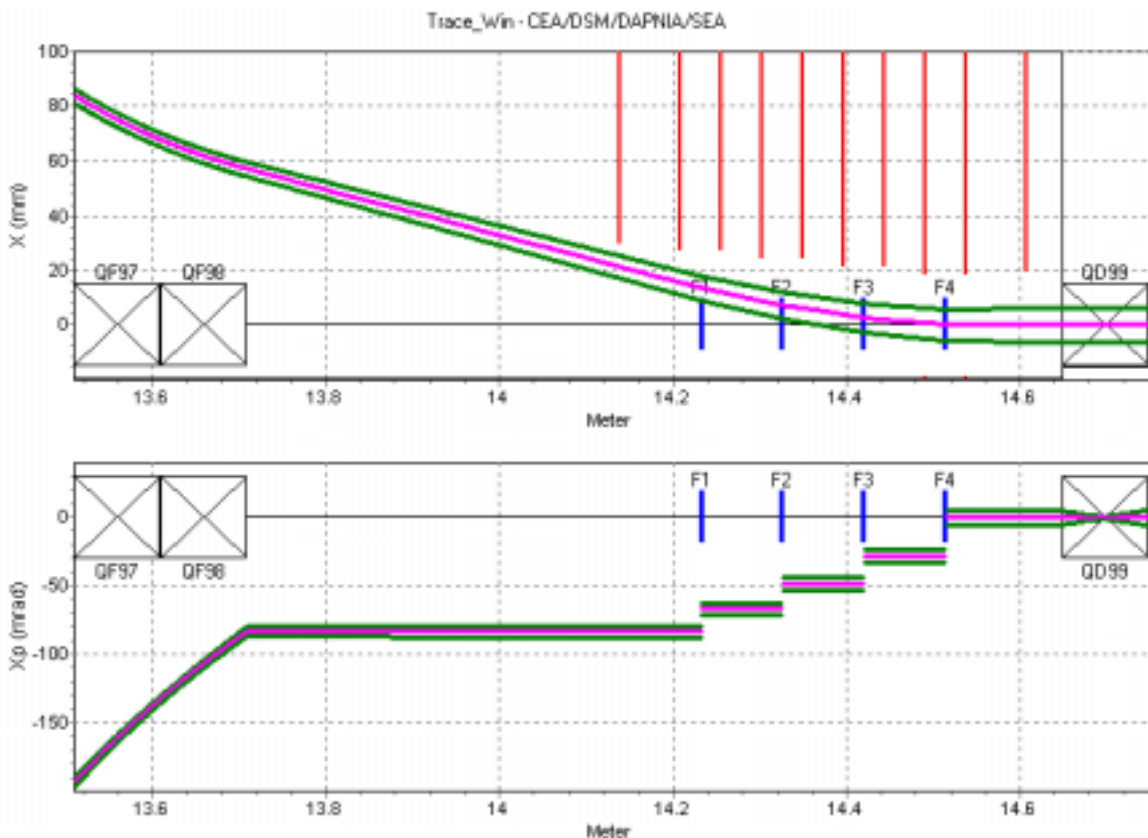


Figure 1.4–24: Deflection of the H^- beam in the cavity and the quadrupole

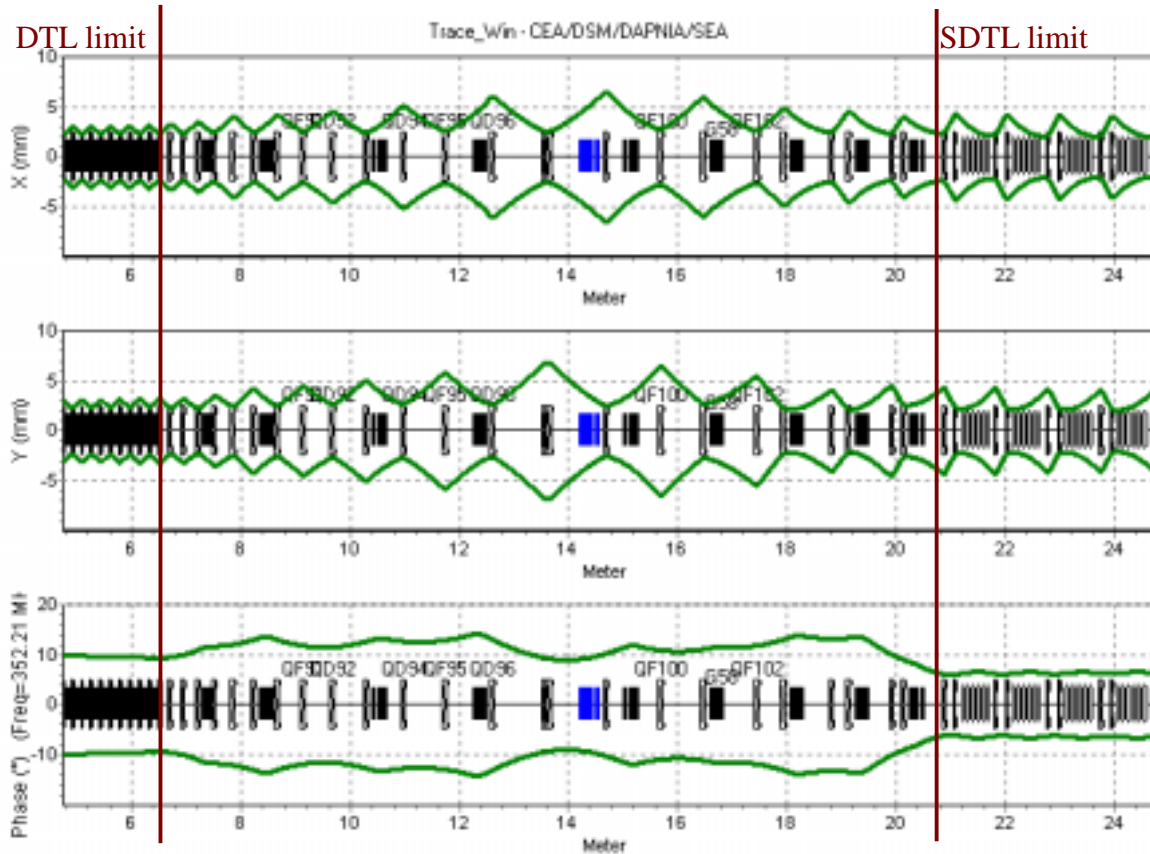


Figure 1.4–25: Beam envelope in the funnel line

1.4.6.6 Diagnostics and commissioning

A correction-set (CS) comprises of two, two-plane steering magnets (steerers) associated with two, two-plane beam position monitors (BPMs). A set of four equations with four unknowns is solved to set the steerer fields to put the beam on axis in the BPMs. Two CSs are used along the line. The position of each steerer and BPM is shown in Figure 1.4–26.

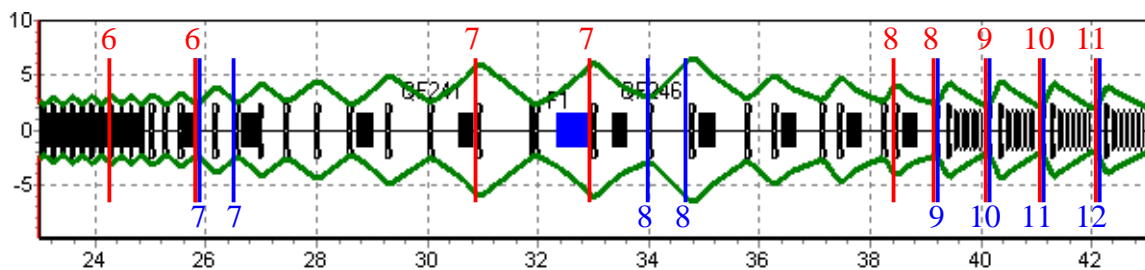


Figure 1.4–26: Correction-sets positions in the funnel line

1.4.7 The Separated Drift-Tube Linac (SDTL)

The beam energy is increased, after the funnel, to about 100 MeV in a SDTL prior to acceleration in a CCL to 185 MeV and then in a superconducting linac to 1334 MeV.

At 20 MeV, a DTL, a separated DTL (SDTL), or a coupled-cavity DTL (CCDTL) can be used.

The SDTL and the CCDTL structures show better beam dynamics characteristics than a DTL and have a lower mechanical complexity. They also have less severe tolerances on quadrupole alignment, a lower number of quadrupoles, and a better RF power efficiency.

However, SDTL and CCDTL are different:

- The CCDTL cavities are shorter (3–5 cells), allowing the use of FODO periods inside the stability limit of 90° phase advance per lattice. This is very convenient for matching a CCL structure with a FODO lattice, which is the 560 MHz normal conducting option.
- The SDTL cavities are longer (6–9 cells). A doublet-focusing lattice is chosen to reduce the period by a factor 2 compared to a FODO lattice. Otherwise, the electric field would have to be reduced in order to keep the longitudinal phase-advance below 90° per lattice. This doublet period is very convenient for matching with a CCL or a SCL with a doublet lattice, which is the 704.4 MHz superconducting option.

Families of power have been used to reduce the rf distribution complexity and cost. Each SDTL cavity design has been optimised to maximise the Shunt impedance, but with the same drift tube nose shape to reduce the construction cost. The cavities were designed with SUPERFISH allowing a 20% margin on calculated shunt impedance, and taking into account the influence of the stems. Some constraints have been imposed on the design. Deposited power per unit length is less than 120 kW/m, deposited power density is less than 20W/cm² and the peak electric field is less than 1.3 kV/m.

1.4.7.1 SDTL cavity design

Each cavity diameter has been optimised in order to minimise the power losses in the copper. The geometry of the first is shown in Figure 1.4–27. The nose shape is the same whatever the cavity.

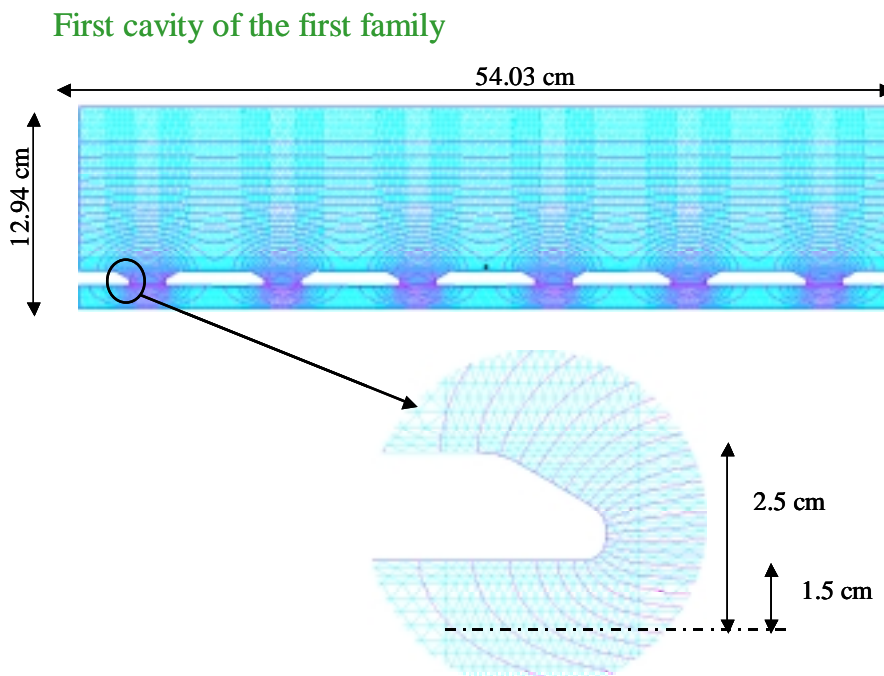


Figure 1.4–27: Design of a SDTL tank

1.4.7.2 Main parameters

The synchronous phase is initially ramped from -40° to -30° to increase the initial longitudinal acceptance. The evolution of the accelerating field is plotted in Figure 1.4–28. The field slopes are explained by the constant power feeding the cavities. The longitudinal phase advance (Figure 1.4–29) is smoothed, and the beam is matched at transition between families by adjusting the synchronous phase.

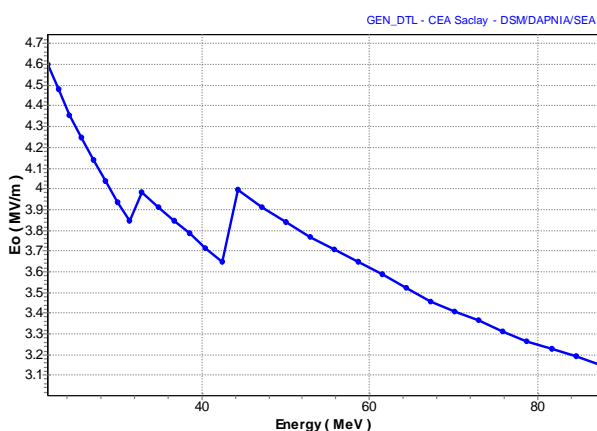


Figure 1.4–28: Average field

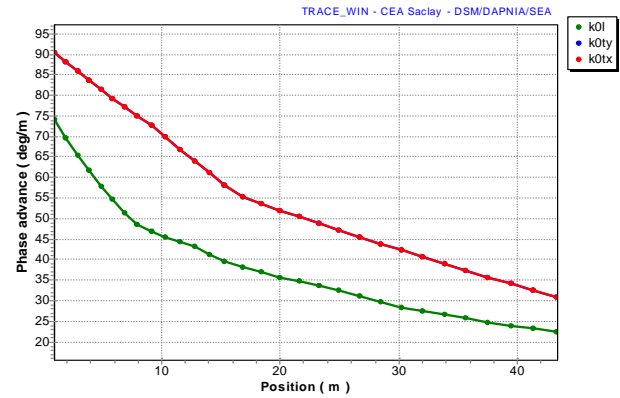


Figure 1.4–29: Zero current phase advances per meter (k_{0l} and k_{0t})

Figure 1.4–30 and Figure 1.4–31 show the evolution of the effective shunt impedance and the power distribution along the SDTL. One klystron supplies two or three cavities. The klystrons are of the same type as those used to supply the superconducting cavities. The power distribution is as follows:

- four 1.1 MW klystrons for the first family (eight 6-cell cavities).
- two 1.6 MW klystrons for the second family (six 7-cell cavities).
- eight 1.6 MW klystrons for the third family (sixteen 9-cell cavities).

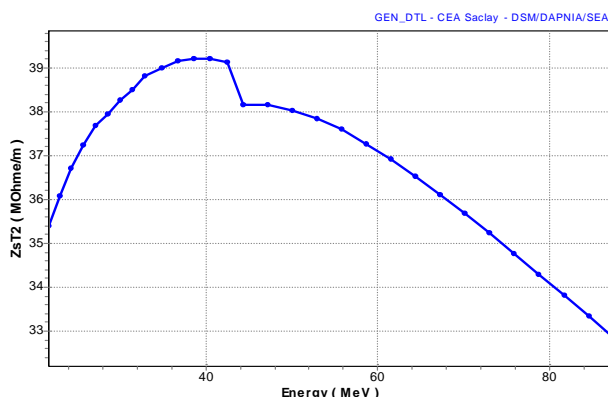


Figure 1.4–30: Effective shunt impedance(Z_{sT}^2)

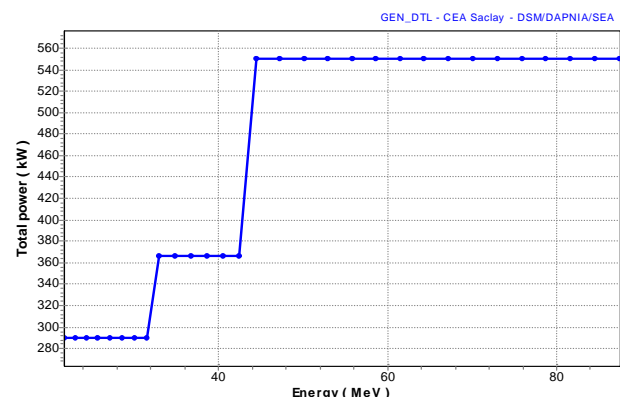


Figure 1.4–31: Total power per cavity

Table 1.4-8: SDTL main parameters

RF Frequency	704.4 MHz
Length	43.3 m
Input energy	21.7 MeV
Output energy	90.5 MeV
Average ZsT^2 (incl. 10% SF margin)	36.6 MΩ/m
Number of families	3
Number of cavities	30
Number of cells	60
Number of quadrupoles	60
Max peak power per cavity (LP-H ⁻)	550 kW
Max total peak power (LP-H ⁻)	13.3 MW

1.4.7.3 Matching between SDTL sections

A schematic view of a lattice is shown in Figure 1.4–32. The distance between quadrupoles is set at 13.3 cm, the quad length is 6.6 cm and the distance between quads and cavities is 6 cm.

Adjusting the first and last two quads and synchronous phases of the adjacent families by a few per cent and a few degrees performs matching between two families.

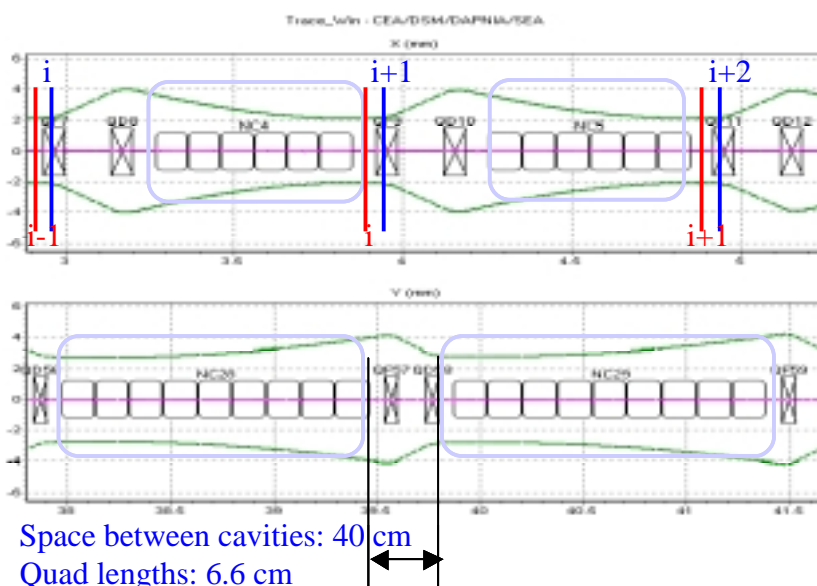


Figure 1.4–32: SDTL lattice

1.4.7.4 Diagnostics and commissioning

A correction-set (CS) comprises one two-plane steering magnet (steerer) associated with one two-plane beam position monitor (BPM). A set of two equations with two unknowns is solved to set the steerer field to put the beam on axis in the BPM. The positions of the CSs are shown in Figure 1.4–32. The BPMs are in red and the steerers in blue.

The details are:

- One CS is used per lattice.
- BPMs are placed ahead of the first quadrupole of the doublet.
- The steering magnetic field is obtained by adding one or two windings around the quadrupole poles.

1.4.8 The Coupled Cavity Linac (CCL)

Above 100 MeV, the effective shunt impedance of the SDTL structure decreases rapidly. A switch is therefore made to the Coupled Cavity Linac (CCL) structure, which is more efficient at high energy. A CCL is used from 90 MeV to 185 MeV.

Because the preceding SDTL and following SCL both use a doublet lattice period, this doublet scheme is also used for the CCL. The matching between the sections is then simpler, smoother and current independent.

All the cavities have different beta values, maximising the transit-time factor. However, in one cavity, all cells have the same cell length. Cavity families could have been used to minimise the construction cost, but the savings, according to LANL lab studies made for the SNS project, should be negligible.

24-cell cavities in a doublet cell have been used. The goal is:

- to keep a doublet focusing scheme between SDTL and SCL,
- to make a transition between the last lattice period of the SDTL (1.95 m) and first lattice period of the SCL (6.15 m),
- to feed each cavity with a 1.6 MW klystron similar to that used for superconducting linac.

1.4.8.1 The CCL cavity

Figure 1.4–33 shows the geometry of one CCL cell. The cavity frequency is 704.4 MHz.

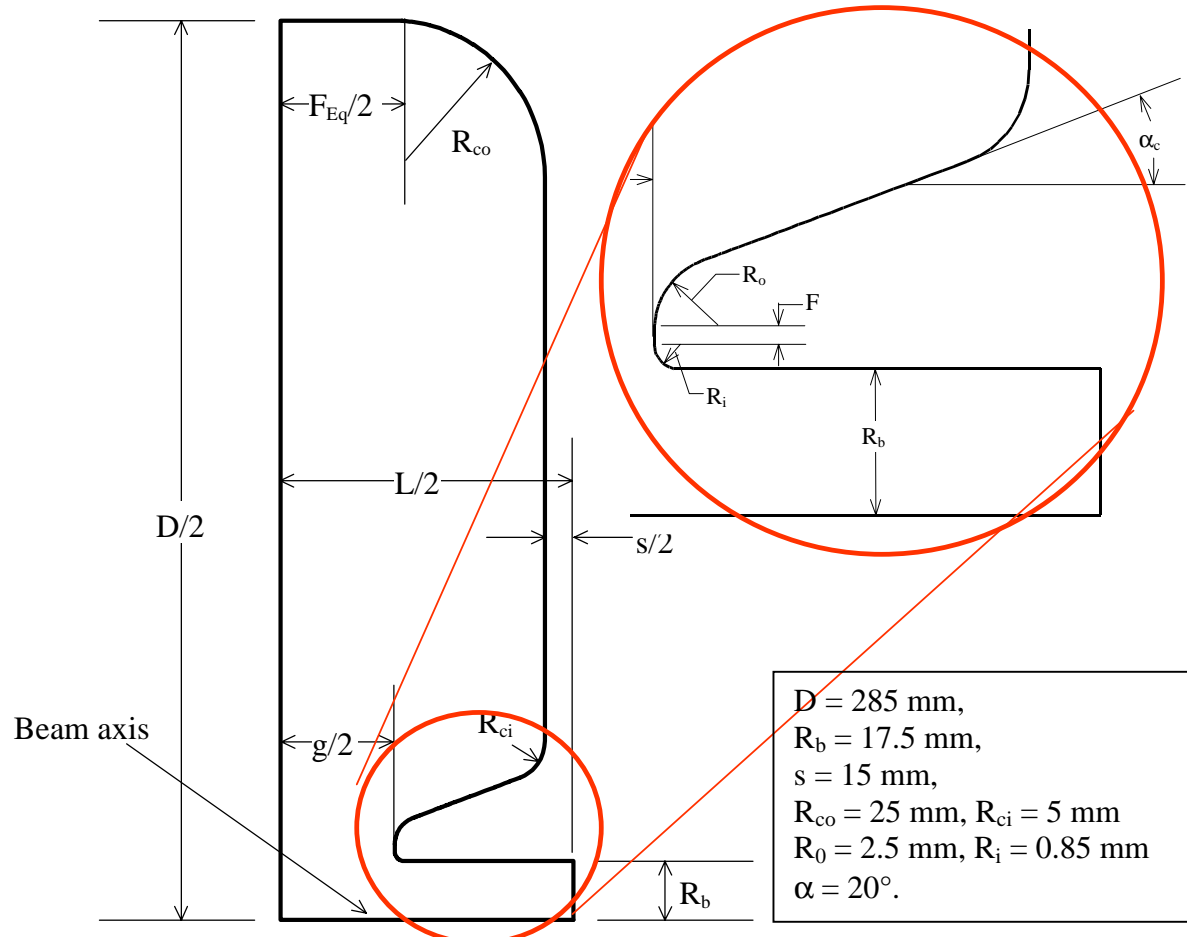


Figure 1.4–33: CCL-cell geometry

To minimize construction costs, the dimensions given above are identical for all the cavities (from 90 MeV to 185 MeV). Their optimisation is not fully completed. The effective shunt impedance of these cavities is shown in Figure 1.4–34 as a function of the cavity and beam beta. A 5% inter-cell coupling is used. The geometry of the coupling cell has still to be calculated.

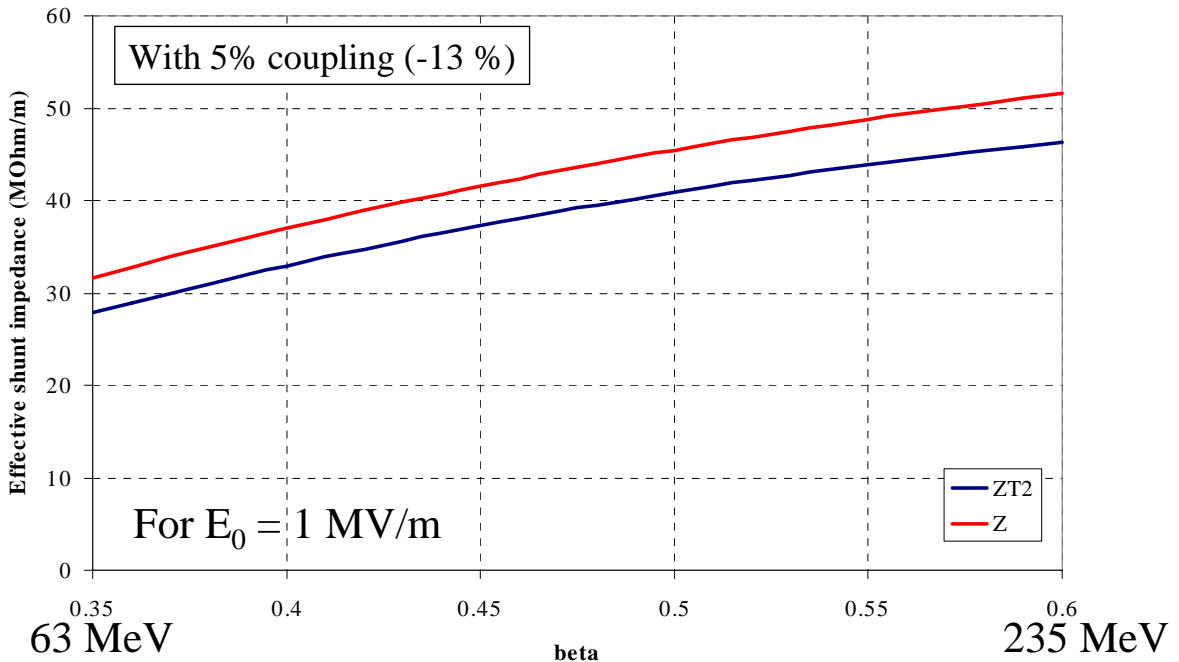


Figure 1.4–34: Shunt impedance (effective or not) of a CCL cavity

1.4.8.2 Main parameters

Cost optimisation shows that the optimum $E_0 T$ is around 2.5 to 3.5 MV/m (in fact, it is very flat between 2 and 4 MV/m), and 1.4 MW klystrons (those used for the superconducting structure) are used. Taking into account RF margins, the effective power that can be injected into the cavities stands at around 1.1 MW per klystron.

From these two considerations, 24 accelerating-cell cavities, fed by one klystron each, have been chosen. The power dissipated in each cavity was calculated with 90% of the cavity shunt impedance given by SUPERFISH. A 5% inter-cell coupling is used. The power efficiency is around 50%. Eighteen cavities (and therefore 18 klystrons) are used.

The maximum peak field is 1.1 Kp (located in the first cavity). The maximum peak power density is 2.2 W/cm² (located in the first cavity). The maximum dissipated power per meter is 25 kW/m (located in the first cavity). The effective electric field ($E_0 T$) varies from 2.6 to 2.4 MV/m.

Table 1.4-9 gives the main parameters of the CCL.

A schematic view of the lattice is given in Figure 1.4–35. The distance between the quadrupoles is set to 20 cm, the quadrupole length is 10 cm the distance between the quadrupoles and the cavities is 10 cm. The quadrupole gradients are about 26 T/m and their aperture is 35 mm.

Table 1.4-9: CCL main parameters

RF Frequency	704.4 MHz
Length	55.3 m
Input energy	90.5 MeV
Output energy	184.5 MeV
Average ZsT ² (incl. 10% SF margin)	39 MΩ/m
Number of cavities	18
Number of cells	432
Number of quadrupoles	36
Max peak power per cavity (LP-H ⁺)	1.1 MW
Max total peak power (LP-H ⁺)	19.8 MW

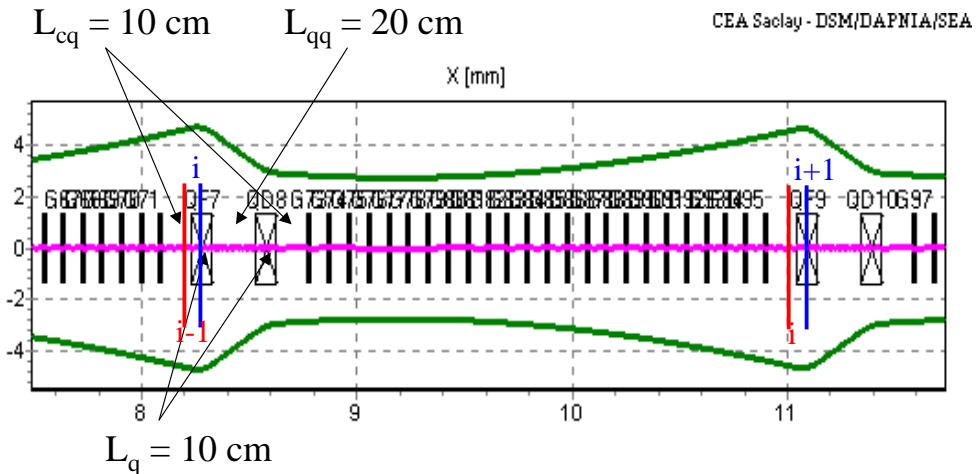


Figure 1.4–35: Schematic view of a CCL lattice

1.4.8.3 Diagnostics and commissioning

A correction-set (CS) is comprised of one two-plane steering magnet (steerer) associated with one two-plane BMP. A set of two equations with two unknowns is solved to set the steerer fields to put the beam on axis in the BPM. The positions of the CSs are shown in Figure 1.4–35. The BMPs are in red and the steerers in blue. The details are:

- One CS is used per lattice as in the SDTL.
- BMPs are placed ahead of the first quadrupole of the doublet.
- The steering magnetic field is obtained by adding one or two windings around the quadrupole poles.

1.4.9 The Superconducting section (SCL)

1.4.9.1 General architecture

As the acceleration efficiency of a given accelerating structure varies with the beam energy, the linac is composed of different types of accelerating sections. Below about 200 MeV, the energy gain per metre of real estate of SC cavities is actually lower than 2 MeV/m, a gradient, which can be easily reached by NC structures. Furthermore, the design of SC cavities for beta values lower than 0.6 is complicated by stiffness and microphonics issues. The transition energy between NC and SC structures is then fixed at 185 MeV. The different cavity types and transition energies are obtained from length and cost optimisation. As a result, two 5-cell cavity families with geometric “beta” values of 0.66 and 0.85 are well suited for the acceleration between 185 MeV and 1330 MeV as we will see later on. The SCL main parameters are summarised in Table 1.4-10.

Table 1.4-10: SCL main parameters

RF Frequency	704.4 MHz
Length	290 m
Input energy	184.5 MeV
Output energy	1348 MeV
Number of cavities	$3 \times 15 + 4 \times 23 = 137$
Number of quadrupoles	$2 \times (15+23) = 76$
Max peak power per cavity [*] (LP-H)	1.6 MW
Max beam peak power gain (LP-H)	133 MW
Max total peak power [*] (LP-H)	176 MW

* including 33% margin for control and losses.

In superconducting RF linacs, the following three constraints have to be taken into account:

- The maximum gradient is determined by the maximum expected peak surface fields,
- The longitudinal phase advance per lattice must be below 90°,
- The power coupler capability.

The maximum peak surface field determines the achievable gradient in SC cavities that we can expect at the niobium cavity walls in a reproducible way and without resorting to sophisticated surface treatment. From the current Superconducting RF state-of-the-art, a peak magnetic field of $B_p = 50$ mT (corresponding to about $E_p = 27.5$ MV/m) can be considered as a conservative value. This value is lower by a factor of two than the surface field aimed at for the TESLA project. A 30% higher field is slightly more ambitious but does not require too much ED&D effort. For example, SNS adopted a peak electric field of $E_p = 35$ MV/m for the high- β cavities. For non-relativistic protons, the lower the “beta” value of the cavity, the larger the ratio of surface field to accelerating gradient. Figure 1.4–36 shows the empirical laws of accelerating field as a function of the cavity “beta” for the two magnetic peak surface fields 50 and 65 mT, referred to respectively as conservative- and high-gradient hereafter. The data for the SNS cavities (corresponding to $E_p = 27.5$ MV/m) and for the Saclay-Orsay-INFN collaboration are also shown.

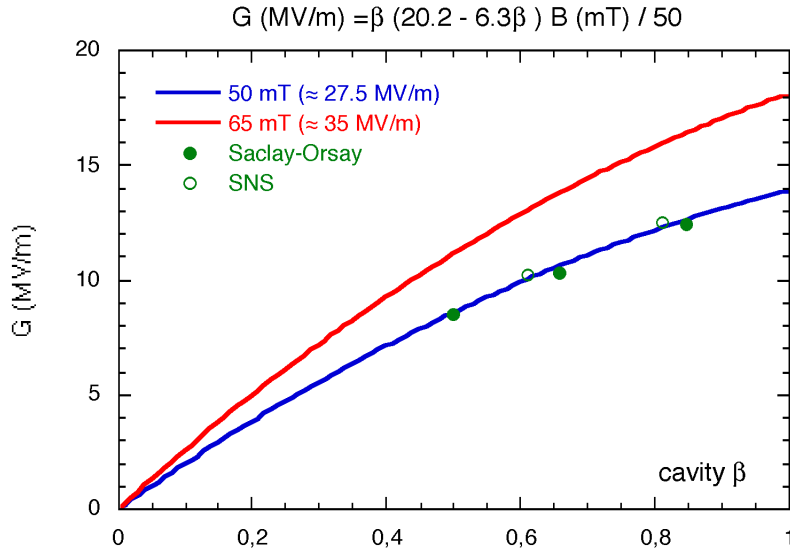


Figure 1.4–36: Empirical laws of accelerating gradient vs. cavity “beta”

With a peak magnetic field of around 65 mT, an accelerating gradient of up to 12.5 and 16.25 MV/m could be chosen for the two geometric “beta” values of 0.66 and 0.85 respectively. Figure 1.4–37 shows for example the results of measurement on single-cell cavities at 700 MHz and on a 6-cell cavity at 805 MHz of SNS. They all achieved an accelerating gradient steeper than 15 MV/m.

1.4.9.2 Longitudinal phase advance

The second constraint, of keeping the phase advance per cell below 90°, must be fulfilled in order to avoid structure instability. As the longitudinal phase advance scales like the square root of the accelerating gradient, the maximum energy gain per lattice is therefore limited, especially at low energy. A good compromise consists in restricting the number of cells per cavity (to five or six) and/or the number of cavities per cryomodule (to three at low energy and to four at high energy).

1.4.9.3 Power coupler capability

RF power as high as 1 MW has been transferred on test stands at different places (DESY, LANL). The highest power currently delivered to the beam is 380 kW CW at KEK-B. The design power of the SNS coaxial coupler, a derived version of the KEK-B coupler, is 500 kW. First power tests at room temperature showed very promising results (around 2 MW), which have to be confirmed at cold temperature. For the ESS linac, we can reasonably rely on a 800 kW coupler. Nevertheless, attention must be paid to the higher duty cycle and pulse length of ESS pulses with respect to SNS ones, demanding an increase of the cold RF window cooling. Besides, two couplers can be mounted on a same cavity without too much mechanical complexity. We will show later on that this 2-coupler scheme is adequate to transfer properly the RF power to the beam. It does not give rise to technical risk, and it only requires a careful mechanical design of the cryostat. In addition to the beam power, the couplers must be capable of transferring extra power due to RF mismatch and field control, estimated at 26%. With two 800 kW couplers, the maximum beam power per cavity amounts then to 1270 kW.

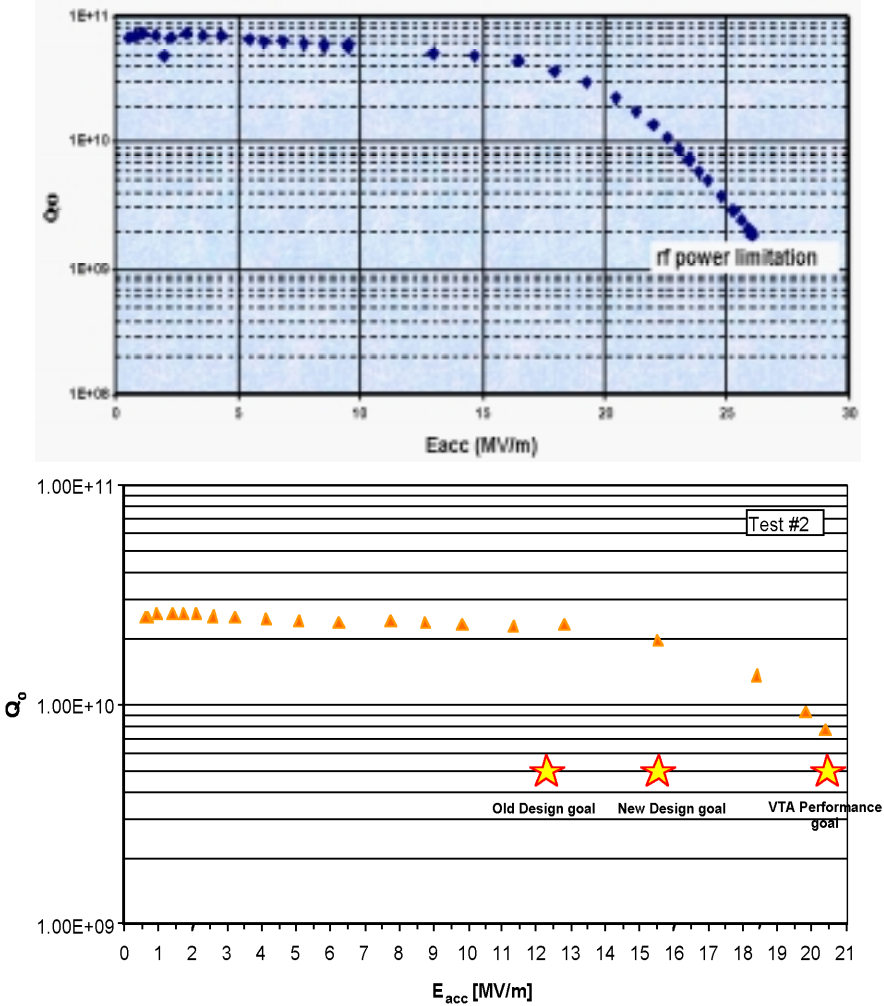


Figure 1.4-37: Excitation curves $Q_o = f(E_{acc})$ Upper: for single-cell $\beta = 0.65$ cavity (Saclay measurement) Lower: for multi-cell $\beta = 0.61$ cavity (JLab measurement)

Once the maximum peak surface fields are given, the linac architecture can be optimised. The optimum transition energy, cavity “beta” and number of cavities per cryomodule which give the minimum linac length while fulfilling the first two conditions — maximum accelerating gradient for each cavity type and phase advance — can be computed as a function of the maximum RF input power. Figure 1.4-38 shows the results for the two sets of maximum peak fields (50 mT / 50 mT and 50 mT / 65 mT for the low- β / high- β sections) and for two numbers of cells per cavity.

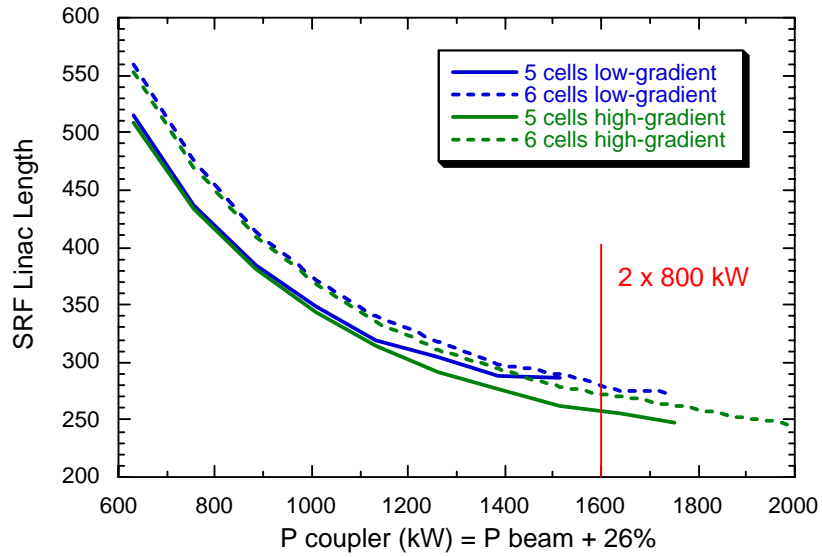


Figure 1.4-38: Minimum SC linac length vs. maximum RF input power

In both cases, the 5-cell cavities give generally shorter linacs. The conservative-gradient option provides a linac length less than 300 m. Above 1200 kW, the high-gradient option is slightly better and can lead to a length less than 250 m, but with a coupler power rising to 2 MW.

Assuming an unchopped beam with a current of 114 mA and superconducting cavities operating at 700 MHz, Figure 1.4-39 gives the beam power for each cavity for the conservative gradient option. The maximum coupler power stays below 1600 kW.

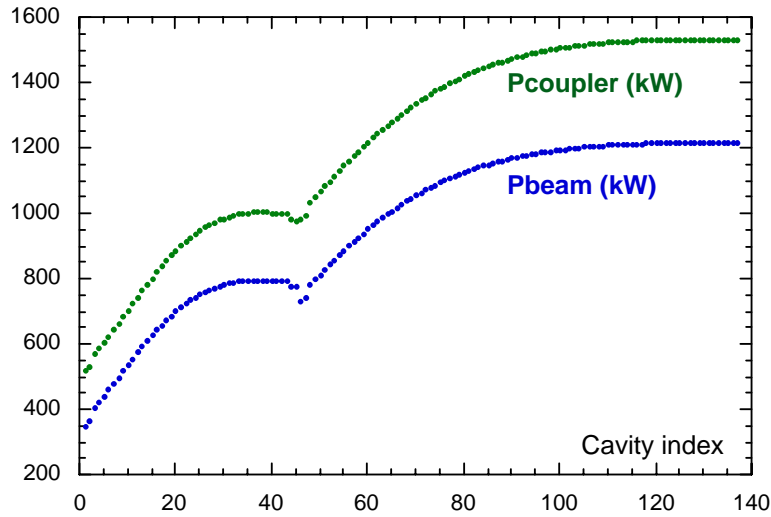


Figure 1.4-39: Beam power and required RF peak power per cavity
(beam current = 114 mA)

1.4.9.4 Choice of frequency

The basic advantage of SC cavities lies in the fact that they can provide much higher fields than NC cavities. Very high peak fields have been achieved at high frequency. For example,

40 MV/m fields are commonly measured in TTF 9-cell cavities at 1.3 GHz without sophisticated surface treatment, single-cell low-beta cavities at 700 MHz from the Saclay-Orsay-INFN collaboration reached more than 50 MV/m and recently, the same peak field was obtained on the 6-cell SNS cavities at 800 MHz. However, such high fields remain to be demonstrated at lower frequency. Smaller cavity area might reduce the probability of particle contamination and material defects, thus decreasing the risk of field emission and quench respectively, at a given accelerating field. High frequency is then preferred, first to guarantee the field but also for cryogenics and cost aspects, and RF power source availability.

1.4.9.4.1 Cyogenics aspects

There is an optimal working temperature, which minimises the helium consumption or the global cryogenic cost (construction and operation). The optimum point will be slightly higher at a lower frequency, simply because the Bardeen-Cooper-Schrieffer (BCS) term of the niobium surface resistance varies with the square of the frequency. The heat load is the sum of the dynamic losses (including cavity dissipation driven by the non-linear surface resistance and all active components such as the power coupler) and the static losses (including the cryostat and the transfer lines). On the other hand, the efficiency of the refrigerator decreases when the working temperature drops. Figure 1.4–40 shows, for example, the required power from the mains, for the cryogenic plant of the ESS SRF linac, as a function of temperature for three different frequencies. The linacs consist of 700 MHz, 5-cell cavities, and 560 and 840 MHz cavities with their cell number multiplied by the ratio 4/5 and 6/5 respectively, while keeping the cavity length and the accelerating gradient constant to retain identical architecture. Although the optimum temperatures are different, the minimum AC power is quite similar. However, because of the more effective thermal properties of superfluid helium, the highest fields are more easily achieved at a temperature $T < T_\lambda = 2.17^\circ\text{K}$. At the expense of greater complexity of the cryogenic system and of a slight increase in operating cost, operation in the superfluid regime below T_λ will then be preferred. However, the extra costs will, of course, be higher at lower frequency because the temperature deviation from the optimum temperature is higher. In conclusion, the choice of around 700–800 MHz is a good compromise.

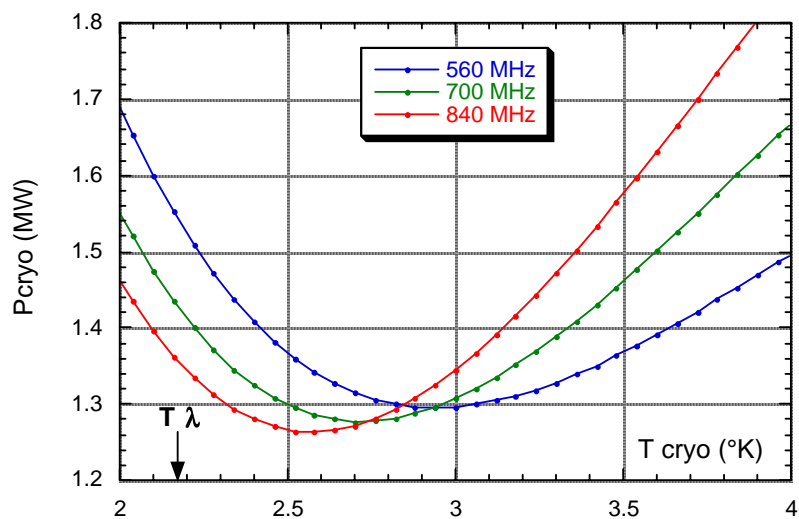


Figure 1.4–40: AC power for the cryogenic plant as a function of the working temperature for three frequencies (cryogenic duty factor = 12%)

1.4.9.4.2 RF power sources

From the point of view of RF power source availability, the pairs of klystrons at 350-700 MHz and 400-800 MHz exist on the market and do not need any large development to accommodate the output power. In addition, the second pair could benefit directly from SNS developments, which use a large number of 400 MHz and 800 MHz klystrons. These klystrons could be used for tests and prototyping for the ESS project and would have to be scaled to higher power for the real ESS linac.

1.4.9.5 Final layout

The present design uses the conservative gradient option, resulting in a total SC linac length less than 300 m. The schematic layout is drawn in Figure 1.4–41. The maximum coupler input power is lower than 800 kW for the beam current of 114 mA. If couplers show a higher RF power capability, choosing higher gradient could further reduce the length. Though the choice between 700 and 800 MHz is still open, the linac, which is presented throughout this document, has been designed at 704.4 MHz (at two times the frequency of the largely used 352.2 MHz klystron). This design can be of course scaled directly to 805 MHz at any time. In that case, the number of cells would be increased to 6 instead of 5. As a result, the required RF power per cavity would be increased by the cavity length ratio, *i.e.* by only 5%.

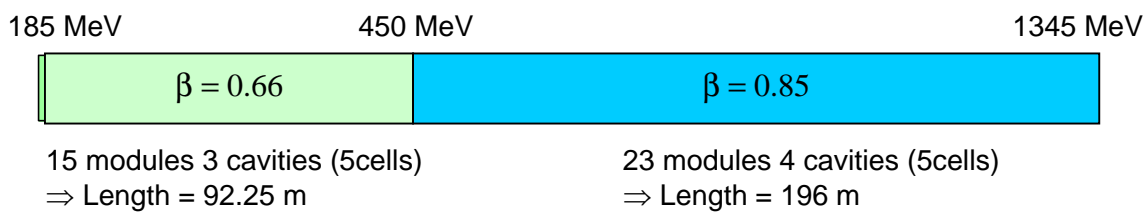


Figure 1.4–41: Schematic layout of the ESS superconducting linac

The linac is composed of 5-cell cavities (Figure 1.4–42). A symmetric cavity was chosen mainly because it maintains field flatness over a wide tuning range, providing an identical deformation of both end-cells, and minimises the risk of inadequate damping for dipole Higher Order Modes, which can be excited by the beam. Stiffening rings are welded between cells in order to minimize the Lorentz force detuning. The main characteristics of both medium- β and high- β cavities are listed in Table 1.4-11.

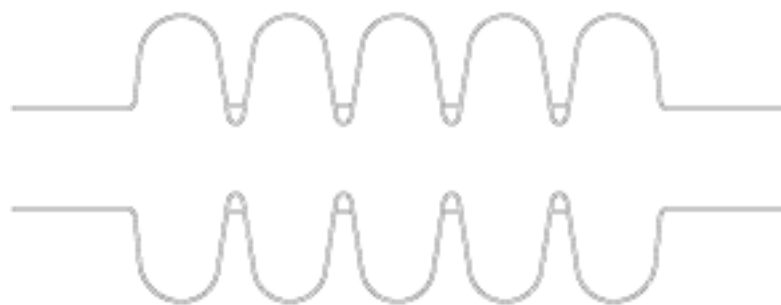


Figure 1.4–42: Geometry of the 5-cell cavity

Table 1.4-11: SRF cavities parameters

	Medium beta	High beta
Cavity beta	0.66	0.85
R/Q (Ohm)	151	242
Iris diameter (mm)	90	100
Cell-to-cell coupling (%)	1.1	1.3
Ep / Eacc	2.6	2.4
Bp / Eacc (mT/MV/m)	4.8	4.0
Eacc (MV/m)	10.5	12.5

Realistic dimensions of the cryostat including all components (cavities, helium vessel, tuner, etc.) and of the warm section between the cryomodules for doublet focusing and diagnostics have been assumed. Figure 1.4-43 shows a sketch of a lattice period composed of one cryomodule and the warm part connecting two adjacent cryostats. The dimensions for both medium- β and high- β sections are listed in Table 1.4-12. The warm quadrupoles have field gradients of 4.2 T/m to 5.5 T/m, and have 10 cm aperture radii.

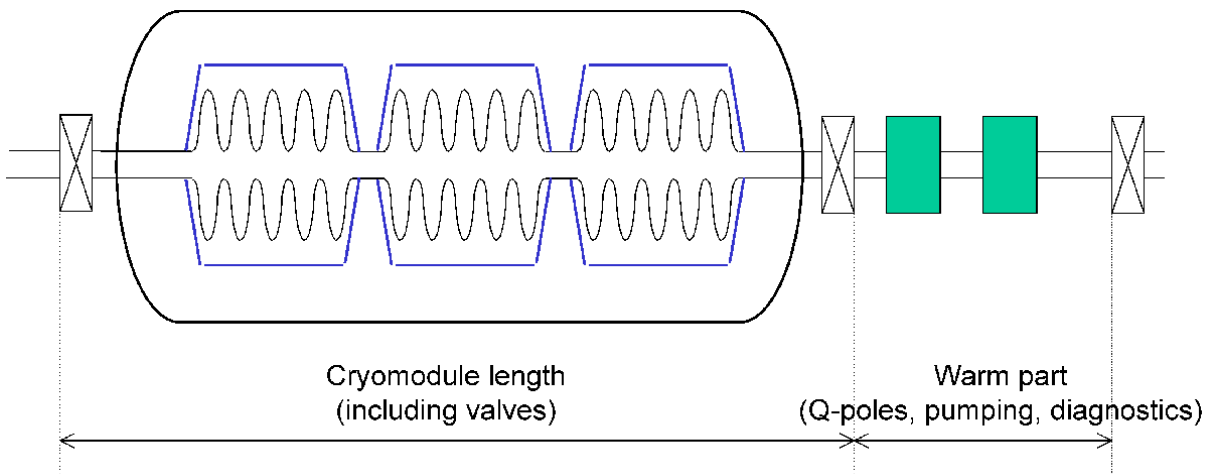


Figure 1.4-43: Schematic drawing of a lattice period of the SC linac

Table 1.4-12: Lengths in SC linacs

	cavity	cryomodule	warm space	lattice period
Medium beta section	0.70	4.30	1.85	6.150 m
High beta section	0.90	6.475	2.05	8.525 m

1.4.9.6 Cryogenic system

Though the optimal temperature is above the lambda point ($T_\lambda = 2.17^\circ\text{K}$) the working temperature is chosen just below, close to 2.1°K , in order to take advantage of the thermal properties of superfluid helium. The cryogenic loads at this temperature are listed in Table 1.4-13 for both sectors and for the total beam pulse structure, including short and long pulses. After addition of the losses in the transfer lines, the total cryogenic load amounts to about 2.3 kW. A CEBAF-like cryogenic plant largely meets the ESS cryogenic requirement. The

refrigerator produces a 3-bar, 4.5°K stream, which feeds the cryomodule cooling loops along the linac. Cold boxes at each end of the cryostats contain heat exchangers and Joule-Thomson valves to cool the cavity at ~2°K and the outer conductor of the power coupler at ~ 4–5°K. Another 4-bar, 35°K stream is used to cool the supply transfer line, the thermal shield of the cryostat and finally the return transfer line. Each cryomodule can be replaced in less than a day without warming-up thanks to a bayonet design for the connections of the helium lines.

Table 1.4-13: Heat load at 2°K

	Medium beta	High beta
Nb cavities / module	3	4
Nb modules	15	23
Qo (10^9)	5	5
Gradient (MV/m)	10.5	12.5
Dynamic load / module (W)	19	37
Static load / module (W)	25	30
Total sector load (W)	660	1540

1.4.9.7 The Radio Frequency system

The short pulse target needs a chopped beam divided into two short pulses (0.48 ms) for proper injection into the rings. The long pulse target does not need a chopped beam, has a maximum duration of 2.5 ms and occurs once every three cycles. One entire cycle is shown in Figure 1.4–44. For the superconducting linac, grouping of the three pulses is preferred for the following reasons:

- There is only one cavity filling at each cycle, thus maximising the RF-to-beam power efficiency
- The field in the cavity is kept constant between the current pulse, keeping the pulsing rate of the cavity to a maximum of 50 Hz, thus alleviating the Lorentz forces issue

The inter-pulse spacing must be larger than the fall/rise time of the pulsed switching dipole, *i.e.* about 100 µs. The forward power per cavity amounts to about the beam power during the filling and beam-on time, and about one quarter of this value between the pulses. The field is kept rigorously constant in-between thanks to the “feedforward” technique which forces a fast change of incident power (in-phase and in-quadrature).

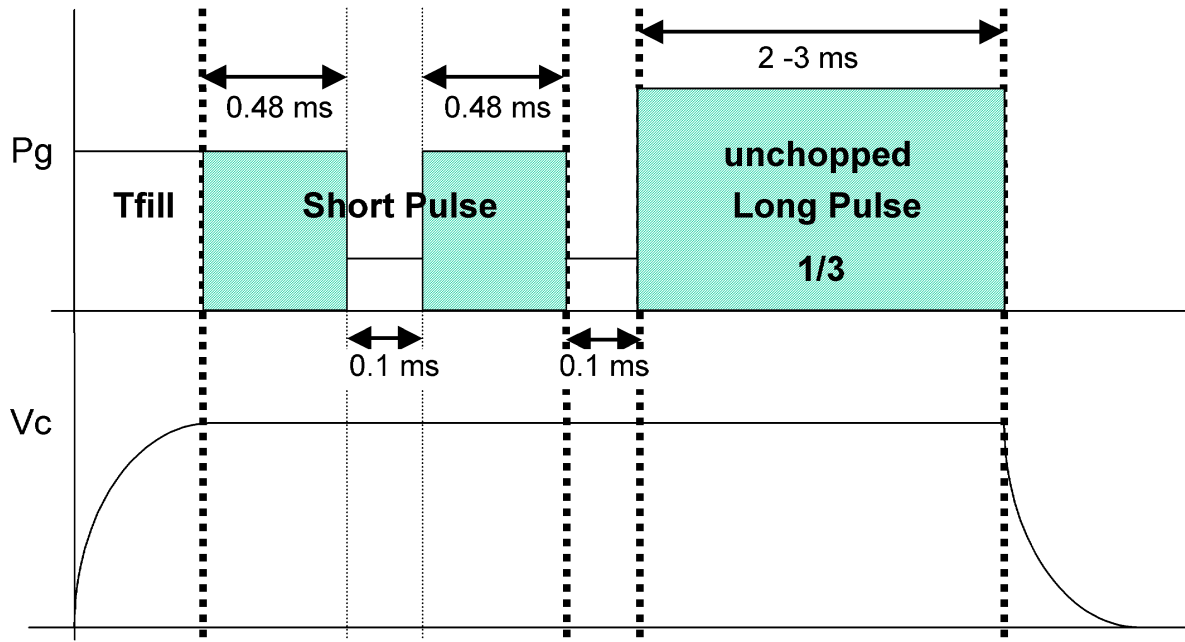


Figure 1.4-44: ESS pulse sequence over one cycle

The bunch charge is the same for both short and long H^- pulses. The beam parameters are listed in Table 1.4-14. We note that for the H^- long pulse operation, the beam power of 5 MW is achieved with a 2.0 ms long pulse, but has a potential of 6.3 MW with a 2.5 ms long pulse. The fallback solution using protons instead of H^- ions, assumes that the linac is able to transport both H^- and H^+ particles. In that case, the proton beam power could start at 3.2 MW with identical bunch charges for both species. The proton beam power would then be progressively increased to 5 MW when H^+ bunch charge is 60% higher than the H^- bunch charge.

Table 1.4-14: Beam parameters for long and short pulses

	SP H^-	LP H^-	LP H^+
Bunch frequency (MHz)	704.4	704.4	352.2
Pulse length (ms)	0.48	2.0	2.5
Nb pulses per cycle	2	1/3	1/3
Beam chopping factor (%)	70	100	100
Bunch charge (nC)	0.162	0.162	0.256
Peak current (mA)	114	114	90
Pulse current (mA)	79.8	114	90
Mean current (mA)	3.83	3.75	3.75
Max beam power (MW)	5.1	5.0	5.0

Each RF source has to deliver a power nearly equal to the beam power during the filling of the cavity (about 200 μ s) and during the current pulses. Only about one quarter of that power has to be delivered during the 100 μ s switching times to maintain the cavity field at a constant value. The “one klystron per cavity” scheme has been chosen because it provides the best RF stability, the simplest operating procedure and the greatest flexibility. Figure 1.4-45 shows the beam and klystron peak powers needed for each cavity for the 114 mA beam. In addition to the beam power, the klystron power includes a total of 32% extra power, to make up for

circulator and waveguide losses (6%), waveguide distribution and coupler mismatches (6%) and to allow for cavity field control (20%).

Due to the large RF power range required from the low energy end to the high-energy end (500 kW to 1600 kW) it is worthwhile considering different tunings of the klystron made at the company in order to maximise the efficiency. A RF efficiency of 65% at rated RF power can be expected for klystrons without modulating anode and up to 4 ms pulse length.. For intermediate RF power, a lower de-rating efficiency was used for estimating the overall electrical consumption.

Furthermore, in order to reduce the cost of the high voltage power supplies (modulators) and to increase the reliability, several klystrons are driven by one power supply and the high voltage setting is adjusted to maximise the overall efficiency of the group of klystrons. The optimisation is performed with two different tunings and two types of modulators, which differ in their output high voltage values.

Maximum efficiency and minimal cost of modulators occur when the tuning change coincides with the transition between the medium- β section and the high- β section. The overall efficiency, the ratio of the beam power to power drawn from the AC mains supply, is 35.7%.

The resulting RF power distribution along the linac is plotted in Figure 1.4–45 and the number of klystrons driven by each power supply in Figure 1.4–46. The number of klystrons and modulators is listed in Table 1.4-15.

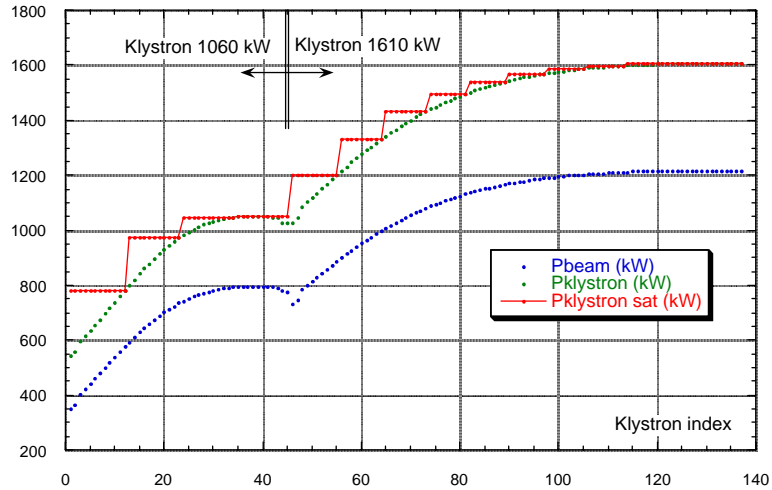


Figure 1.4–45: Power distribution along the SC linac

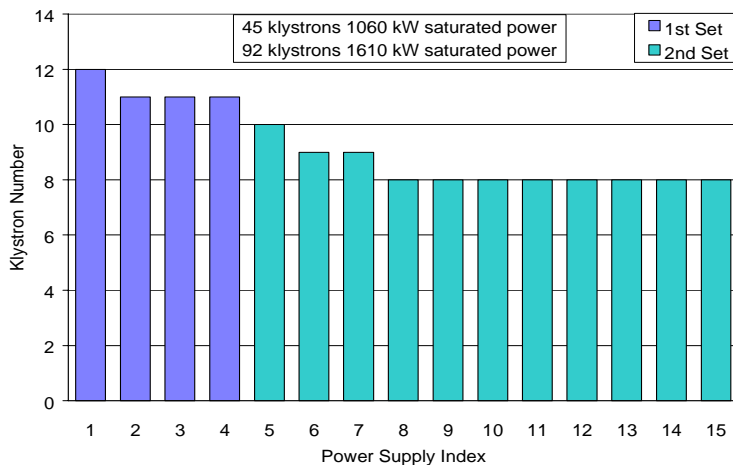


Figure 1.4-46: Number of klystrons driven by each power supply

Table 1.4-15: Power distribution

	1 st set	2 nd set
No. of klystrons	45	92
Klystron peak power (kW)	1060	1610
No. of modulators	4	11
Average power (kVA)	1800	2400

Various power systems have been evaluated to provide, with very high efficiency, the pulsed RF power at a 50 Hz repetition rate and with high peak power levels, which can vary on a pulse-to-pulse basis. The combination of long pulses (4 ms pulse length capability with fast switching times < 30 μ s) with high repetition rates and large duty cycle eliminates conventional solutions, which would be very challenging and expensive. For example, the TTF-like modulator would require a very large pulse transformer with complex bouncer circuitry for voltage drop compensation. The chosen solution is based on power supplies made of series-connected modules with IGBT switches (Figure 1.4-47) operating in pulse width modulation (PWM) mode. The DC-DC high frequency converter using an IGBT inverter, adopted for SNS, is a possible and more compact alternative but with some additional losses in the high frequency high voltage transformer. The modulator is designed to deliver maximum power for up to 4 ms pulse length. Reduced peak RF power or shorter pulse length is obtained by modifying both RF drive and high voltage to keep a high klystron efficiency.

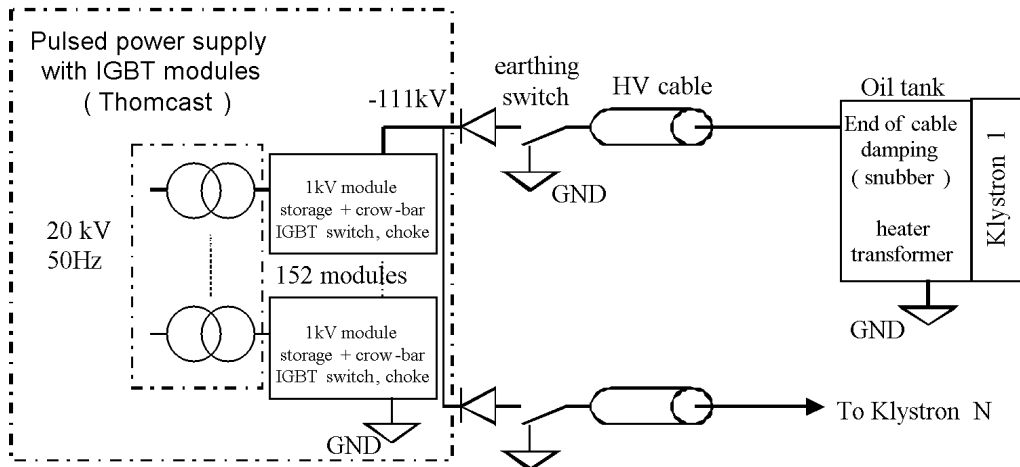


Figure 1.4–47: Sketch of the IGBT power supply

1.4.9.8 The 2-coupler scheme

The klystron is protected from any reflected power by a circulator. A 3-arm RF circuit, composed of a Magic Tee and load, splits the power coming from the klystron to the pair of input couplers, symmetrically mounted on the cavity. This two-coupler arrangement has already been used on copper cavities in both, circular machines and linear accelerators. The behaviour of such a RF system, coupler pairs and superconducting cavity, including some errors and breaking the symmetry, has been checked by means of dedicated RF structures codes. These 3D numerical simulations have demonstrated, by investigating the transient as well as the steady regime, that the behaviour of the 2-coupler scheme obeys the conventional superimposition rule for superconducting cavities in a similar way to normal conducting ones. No excessive sensitivity to coupler asymmetry, amplitude or phase balance was observed and the effects of perturbations such as Lorentz forces, de-tuning or microphonics are the same as in the usual one-coupler scheme. An artificial asymmetry was introduced using 5 mm difference in penetration depth of the inner conductors corresponding to a very pessimistic manufacturing error ($\Delta Q_{ex}/Q_{ex} \approx 30\%$).

For example, the steady-state regimes were investigated with the HFSS code (Agilent Technologies). RF signals are applied with given amplitude and phase at each port. The energy density ($\propto E^2$) for the symmetric and asymmetric cases are drawn in Figure 1.4–48 when the amplitude and phase of the excitations are equal.

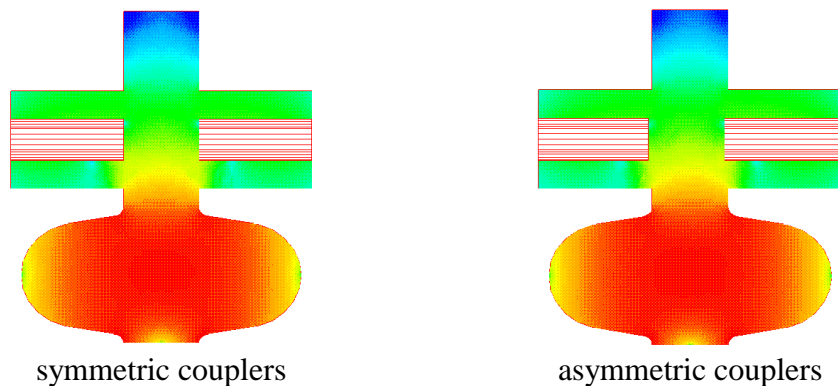


Figure 1.4–48: Energy density in steady regime (colour code in log scale)

No significant difference relating to coupler asymmetry is observed. The field amplitude is much higher in the cell than in the coaxial lines as expected in the steady regime. By monitoring the longitudinal component of the electric field along the beam axis while changing the amplitude and/or phase of the excitations it can be checked that the superimposition rule of the equivalent circuit applies perfectly.

The time domain of the MAFIA code (CST) was used to simulate cavity filling in a transient regime (T3 module). Figure 1.4–49 shows for example the field pattern at the symmetry plane of the cavity 1 μs after the beginning of the excitation. The accelerating mode is easily identified while again no significant differences between perfectly balanced couplers and unbalanced couplers are observed. The ratio of field amplitude inside the cell to the field amplitude inside the coaxial couplers increases as the cavity is being filled.

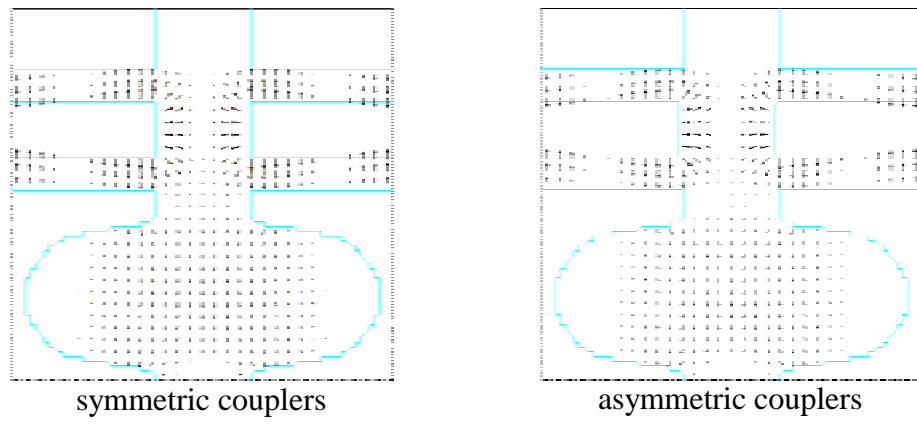


Figure 1.4–49: Electric field pattern 1 μs after excitation

1.4.9.9 Field control and energy stability

Regardless of the source of cavity field fluctuations, the tolerance on amplitude and phase errors can be inferred from Monte Carlo calculations. Assuming random errors of uniform distribution, simultaneous cavity field errors of 1% in amplitude and 1° in phase lead to an rms beam energy fluctuation of 0.8 MeV and a phase fluctuation of 1.2° at the linac exit (Figure 1.4–50).

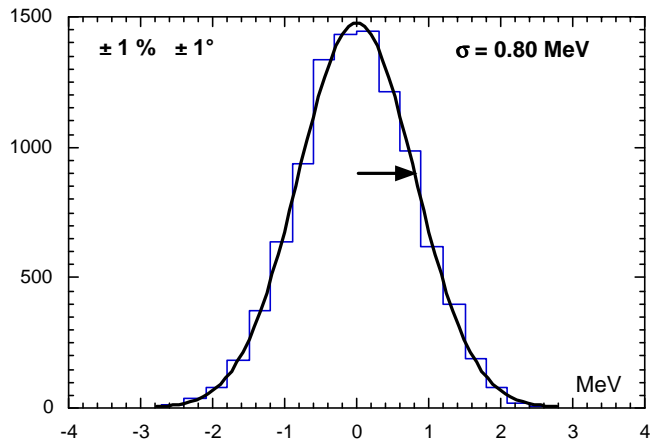


Figure 1.4–50: Energy distribution at SC linac exit (10,000 simulations)

The “one klystron per cavity” scheme, where each cavity has its own feedback/feedforward RF control system, has been chosen because it provides the best RF stability for proton beams, the simplest operating procedure and the greatest flexibility in the event of a sudden RF failure. Due to the narrow bandwidth of superconducting cavities, field fluctuations originate mainly from any slight detuning, induced by the so-called Lorentz forces or by microphonics. In addition, any bunch phase oscillation, induced for example by energy or phase error of the incoming beam, will upset the cavity voltage via beam-loading. A low level RF system with fast feedback loops has been designed and numerical simulations using the PSTAB code showed that the cavity voltages can be efficiently controlled. Since it could be the most troublesome effect, the Lorentz force was carefully studied. First, assuming no cumulative effect from pulse cycle to pulse cycle and second, taking into account multiple cycles.

The pressure exerted by the RF fields on the cavity wall, given by:

$$P = \frac{1}{4}(\mu_o H^2 - \varepsilon_o E^2)$$

induces cell deformation and then resonant frequency shift. This cavity detuning is proportional to the square of the accelerating field and the sensitivity to the Lorentz force is defined by the parameter K :

$$\Delta f = -K E_{acc}^2$$

Because of the higher peak surface fields and of the worse cavity stiffness, this parameter tends to strongly increase as the cavity beta decreases. One of the strategies for reducing the Lorentz force consists in welding rings between cells. This stiffening scheme has two beneficial effects: firstly, it tends to compensate the opposite effects of electric field in the iris region and of the magnetic field in the equator region; and secondly, it tends to lower the resonant frequency of the mechanical modes.

The wall deformation was computed with the finite element code CASTEM. The radiation pressure and the resulting frequency shifts were computed with the cavity code SUPERFISH. Figure 1.4–51 shows an example of cell deformation for the medium- β cavity, for a given position of the rings and with fixed ends as boundary conditions. It is worth noting that the wall deformation, which is symmetric with respect to the middle plane of the cavity, is not identical for all cells because of the different shape of the end-cells.

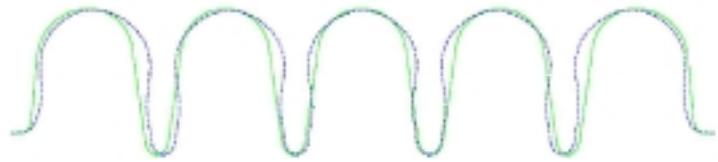


Figure 1.4–51: Initial and deformed (amplified) contour of the medium- β cavity

As the results are very sensitive to the choice of the boundary conditions, which depends on the stiffness of the external structure including the helium vessel and the tuning system, the radial position of the rings was optimised to seek the minimum frequency shift. Figure 1.4–52 shows the Lorentz force parameter as a function of the ring position for fixed end-cells and for a realistic external stiffness of 100 kN/mm. Optimum compensation is achieved for ring stiffeners located at 70 mm, resulting in a parameter K lower than $2 \text{ Hz} / [\text{MV/m}]^2$ for an anticipated external stiffness of 100 kN/mm. Though the K parameter is low enough, a factor of 2 larger will be used in the further simulations. Furthermore, the frequency shift could be efficiently counteracted by a fast piezo-element incorporated in the tuning system. The effectiveness of such a device has been demonstrated on pulsed mode experiments made on a TESLA 1300 MHz cavity at DESY [Liepe, 2001] and on a 500 MHz cavity at FZ-Jülich [Stassen, 2001].

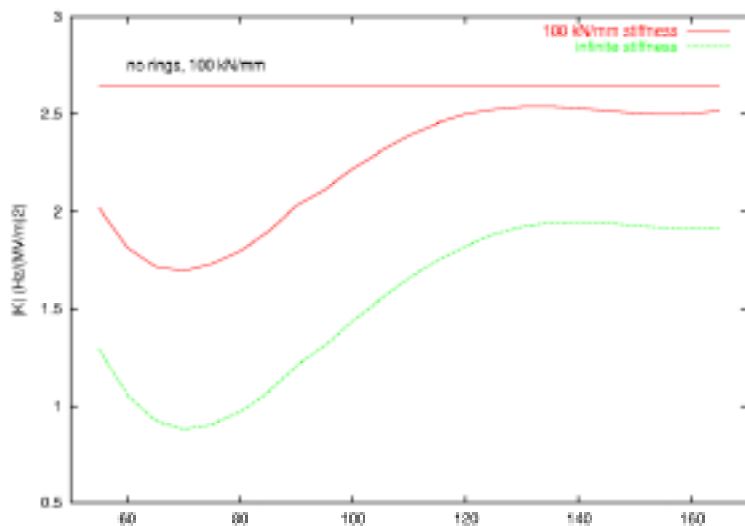


Figure 1.4–52: Lorentz detuning parameter vs. stiffening ring position for the medium- β cavity and for different boundary conditions

1.4.9.9.1 One single pulse cycle analysis

In this study, we consider the multi-pulse beam only during a single cycle, ignoring any cumulative between the successive cycles.

In order to minimize the needed RF power,

- Q_{ex} is set near the optimum coupling (about 2×10^5);
- The cavity is de-tuned to compensate for the reactive beam-loading due to non-zero beam phase.

Figure 1.4–53 shows the effect of Lorentz force de-tuning (4 and 2 Hz/(MV/m)² for the medium- and high-beta cavities) on the field of the last cavity of the SC linac, in amplitude and phase, during the passage of the multi-pulse beam over one cycle (two short chopped beam pulses and one long unchopped beam pulse). A time delay of 2.4 μ s due to the digital system was assumed and a gain of 30 was set for both the I and Q feedback loops. Feedforward (change of the in-phase and in-quadrature drive signals) is used between the successive pulses to compensate for the sudden change in beam loading. The natural amplitude and phase changes due to the beam chopping during the first two short pulses disappear during the last long pulse of unchopped beam. Figure 1.4–54 shows the energy and phase deviations of the multi-pulse beam at the exit of the linac. The maximum deviation is less than ± 0.05 MeV and $\pm 0.2^\circ$ during the short pulses used for ring injection.

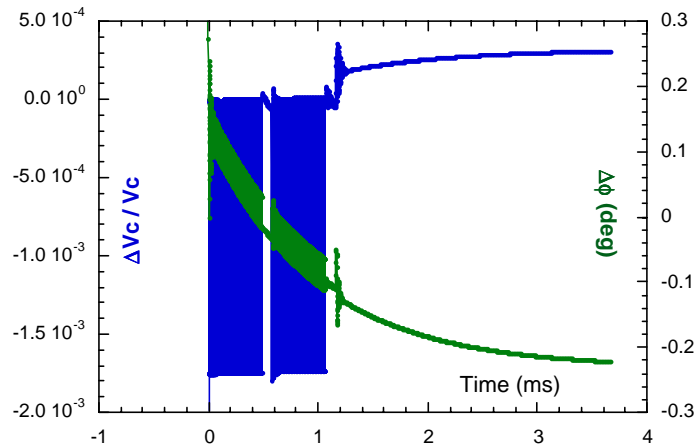


Figure 1.4–53: Field errors of the last cavity (with Lorentz forces effects)

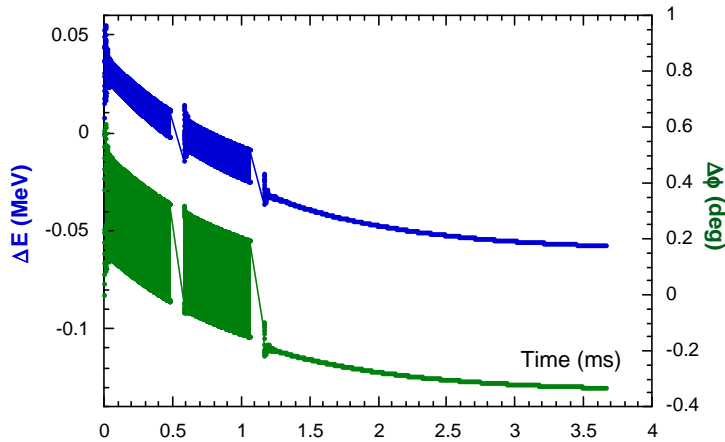


Figure 1.4–54: Energy and phase deviations of the multi-pulse beam at the linac exit (with Lorentz forces effects)

With other additional perturbation sources, such as microphonics (400 Hz oscillation with an amplitude of 100 Hz equivalent to phase fluctuations of $\pm 10^\circ$) and random current fluctuations (5%), the maximum deviations remain small (± 0.2 MeV and $\pm 0.5^\circ$) and the maximum extra power is lower than 5% despite the pessimistic errors chosen.

1.4.9.9.2 Multiple pulse cycles analysis

The pulsing of the RF fields at 50 Hz and even 50/3 Hz (because of the appearance of the long pulse every three cycles) could excite mechanical modes of the cavities and lead then to large amplitude and phase fluctuations. Careful calculations with CASTEM and SUPERFISH were therefore carried out to determine the characteristics of these modes. Figure 1.4–55 gives two examples of mechanical modes for the medium- β cavity.

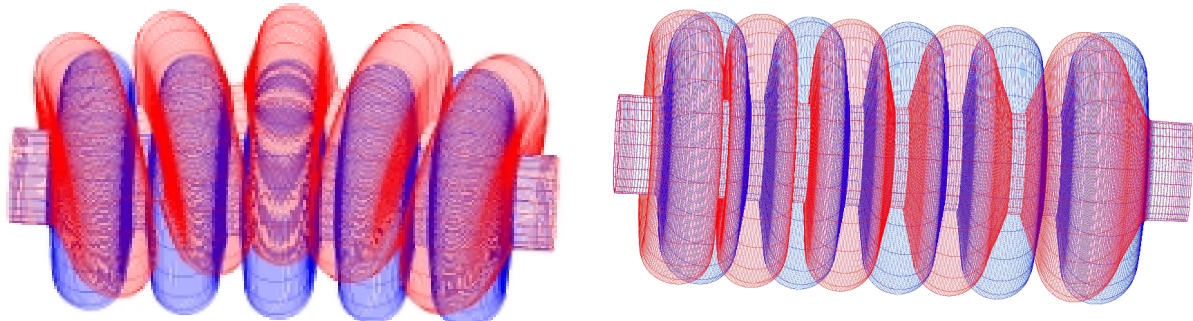


Figure 1.4–55: Two examples of mechanical modes for the medium- β cavity

The underlying mode spectrum is shown in Figure 1.4–56, demonstrating significant contributions from mechanical modes only below 700 Hz.

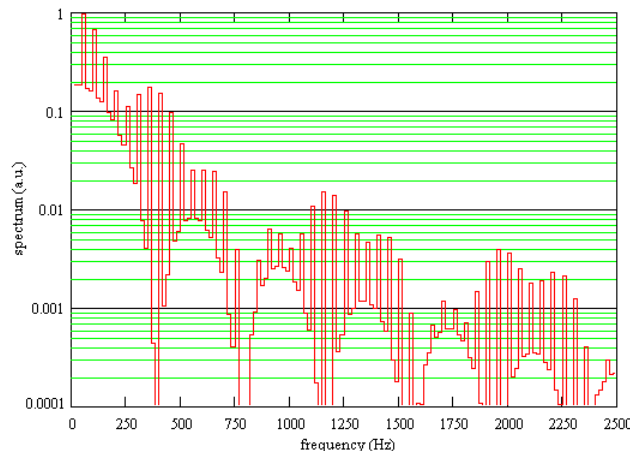


Figure 1.4–56: Power spectrum of the RF pulses

The values of the coupling factors K_m are calculated with the CASTEM and SUPERFISH codes by using the harmonic analysis. The low frequency modes, which could be excited by the RF field pulsing, have a very low K_m coupling coefficient. Only the high frequency modes, having significant K_m values, contribute to the total Lorentz force de-tuning. Assuming a quality factor Q of 100 for all modes, there is no dramatic increase of the fluctuations due to the cumulative effect from cycle to cycle. Even by setting the highest K_m mode at a multiple of the pulsing rate (1400 Hz), the effect is hardly visible except a slight increase of the 1400 Hz oscillation. Figure 1.4–57 shows the dynamic frequency shifts over the 100th cycle and the extra-power required for the feedback loops, which remains below 2%.

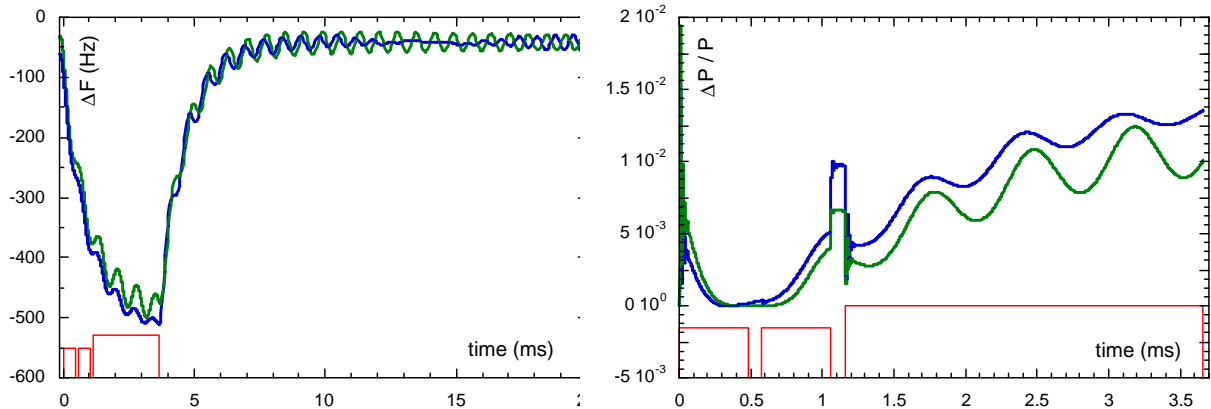


Figure 1.4-57 : Frequency shift (left) and extra-power (right) of the 1st cavity at the steady-state regime with computed mechanical modes (blue curve) and with the highest K_m mode at a multiple of the pulsing rate (green curve)

Finally, Figure 1.4-58 shows the energy and phase deviations of all bunches at the linac exit over one cycle in the steady-state régime. The fluctuations are very similar to the one single cycle analysis (in comparison with Figure 1.4-54) and no significant cumulative effect is expected.

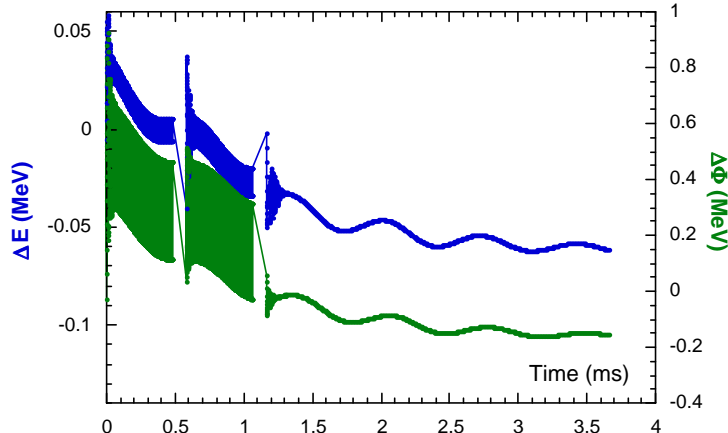


Figure 1.4-58: Energy and phase deviations of the multi-pulse beam at the linac exit at steady-state with computed mechanical modes

In conclusion, no serious trouble as regards mechanical modes of the cavities is expected for the ESS pulsed mode operation, especially when the cavities are equipped with stiffening rings and present low K_m coupling factors for the low frequency modes.

1.4.9.10 Conclusions

Superconducting RF is now a mature technology. While taking into account the critical points of the SC option, like the present state-of-the-art of RF couplers or the Lorentz force detuning, the design is safe and without risk. Conservative values of the accelerating fields have been chosen. The different beam pulses (chopped, unchopped and variable pulse length) can be easily handled by the RF system. Capital costs are similar for NC and SC solutions but

operation cost reduction is expected from the SC solution (electricity consumption and heat release). From the beam dynamics point of view (see below) the SC linac transports the beam from the warm-cold transition without any further degradation nor formation of beam tails and the beam stays far from the vacuum chamber. In particular, the final energy spread and jitter after the bunch rotation cavity are much smaller than the ring injection requirements.

1.4.10 Beam dynamics

The goals of the beam dynamics studies are:

- To serve as guideline for the linac design,
- To estimate the beam output characteristics and show that they fulfil the requirements,
- To test the robustness of the design to errors on input beam or linac elements,
- To estimate the beam losses all along the linac, and at ring injection.

For these reasons, this chapter is divided in four parts.

- In the first part, the linac characteristics are given from a beam dynamics point of view. The “working-point” is described and its choice is explained.
- In the second part, the main beam characteristics (matched beam) along the linac are described. Particular care is given to the analysis of the beam characteristics at linac output.
- In the third part, the influence of linac element errors on the output beam is evaluated.
- In the last part, the expected beam losses along the linac and the associated activation are estimated.

1.4.10.1.1 Linac characteristics from the beam dynamics point of view

To ensure small emittance growth and little halo formation in the beam, both the NC and the SC linac designs use the same philosophy:

- Keep the average phase advance per meter (average beam confinement) as smooth as possible,
- Keep the focusing lattice scheme as continuous as possible,
- Match the rms beam parameters at the transitions,
- Avoid zero current phase-advance per lattice higher than 90° ,
- Avoid equal transverse and longitudinal phase advances in order to prevent emittance exchange,
- Frequencies for the mismatch modes should be outside the beam frequency range
- Keep the tune depression as high as possible,
- Avoid insufficient bunching, and variation from cell to cell of the average beam aspect ratio.

The evolution of the phase advance per metre is represented in Figure 1.4–59. It is kept as smooth as possible through the transitions. A discontinuity in longitudinal focusing can be seen in the funnel line (from the DTL to the SDTL). However, the observed emittance growth in the funnel line is not due to this.

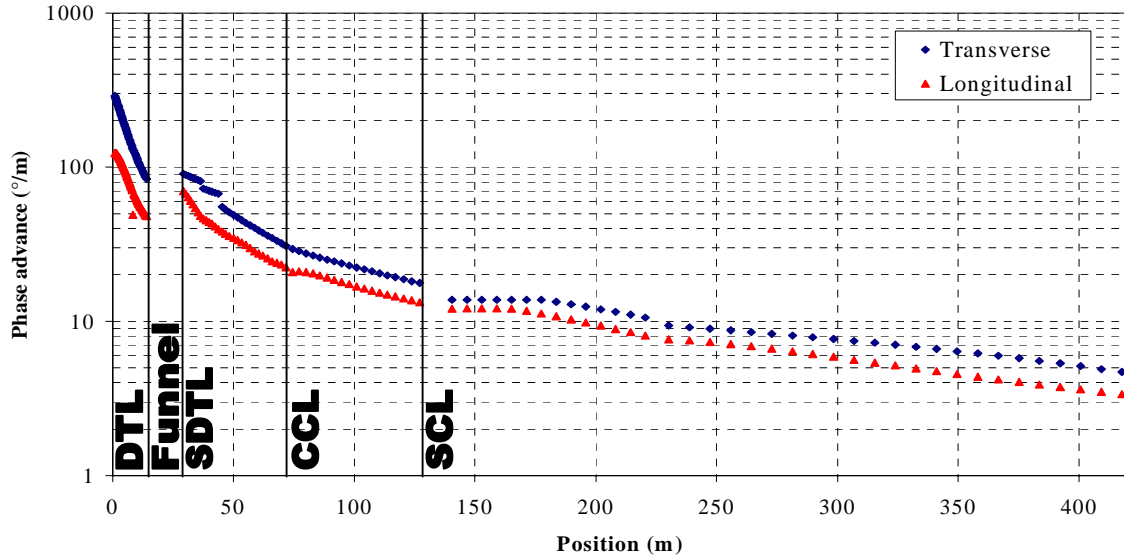


Figure 1.4–59: Zero current phase advance per unit length along the linac

The focusing lattice is FODO before the funnel line (RFQ1, RFQ2, DTL) and doublet after (SDTL, CCL, SCL). The funnel line makes the transition as smooth as possible.

The zero current phase advance per lattice is kept below 85° transversely and below 75° longitudinally. The transverse phase advance is adjusted to stay always 10° to 20° higher than the longitudinal one preventing coupling resonance and crossing of the mismatch modes.

The tune depressions are higher than 0.55 in all directions (Figure 1.4–60) apart from in the DTL. This is made possible in the longitudinal direction by the high frequency and accelerating field (here is one big advantage of the superconducting linac).

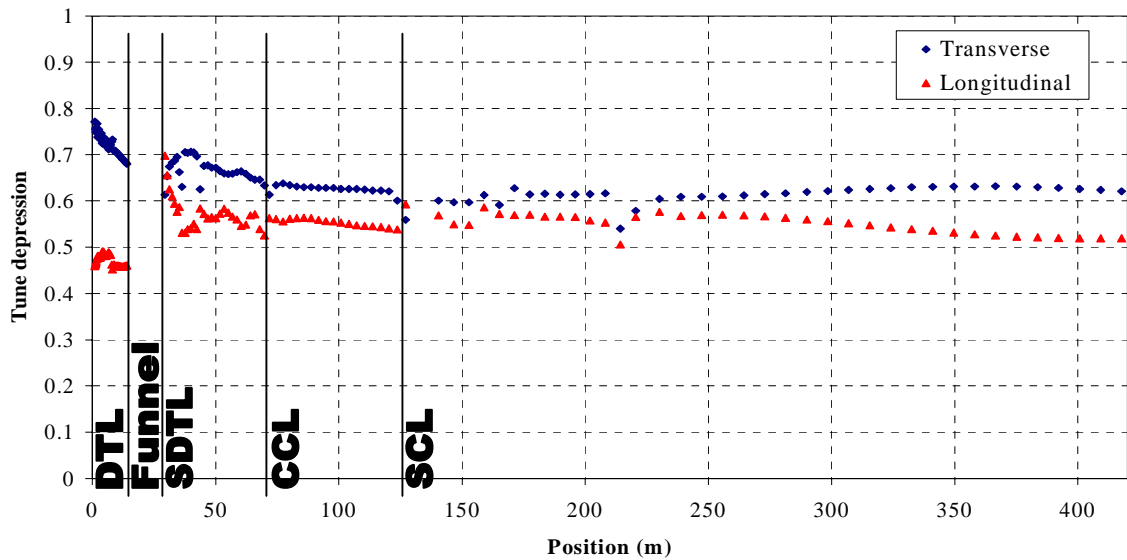


Figure 1.4–60: *Tune depressions along the linac*

The ratios between the linac apertures and the beam maximum rms sizes are plotted in Figure 1.4–61. The longitudinal “aperture” is a function of the synchronous phase. It corresponds, in the harmonic potential approximation of small amplitude, to the phase amplitude of a particle having sufficient energy to exit the bucket. For example, a synchronous phase of -30° gives a “longitudinal aperture” of 35° . Due to the superconducting structure, this ratio is greater than 10 beyond 200 MeV.

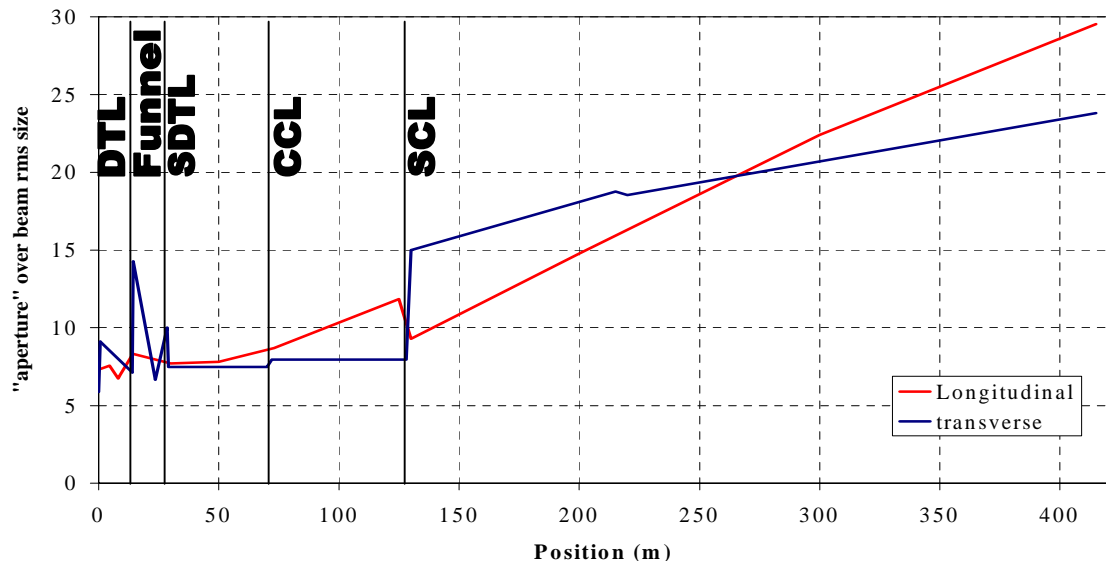


Figure 1.4–61: *Aperture to beam RMS size ratios along the linac*

The working point evolution is plotted on a coupling resonance chart (Hofmann-Lagniel chart, Figure 1.4–62). Emittance exchanges are possible in the DTL through a third order resonance. However, the high and odd order of this resonance and the short length of the DTL make its influence very low.

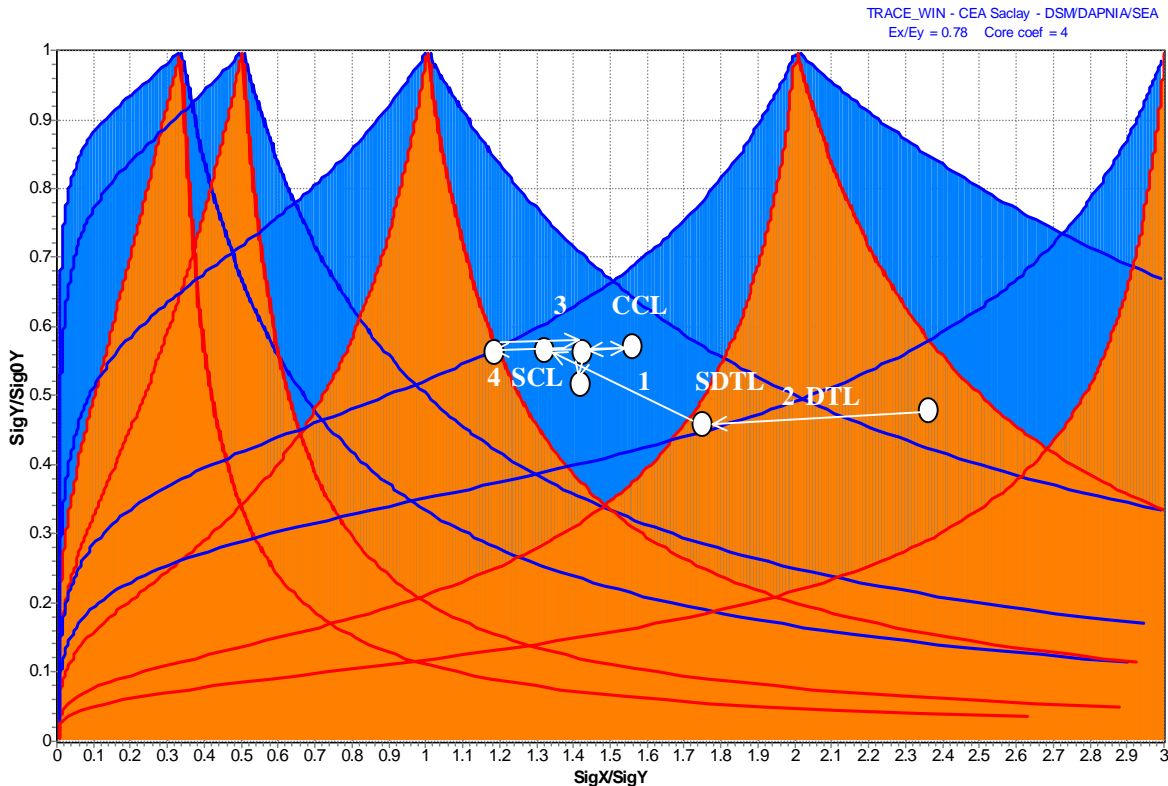


Figure 1.4–62: Beam working point in the coupling resonance chart (Hofmann-Lagniel chart)

1.4.10.2 Main beam characteristics in the linac

A 4D water-bag distribution with a transverse rms normalised emittance of 0.3π mm.mrad is used as the 352.2 MHz RFQ input. The longitudinal emittance is given by the RFQ, and it depends on its frequency. Multi-particle simulations are then run from the RFQ output through the full linac. Studies have shown that the impact of filamentation at the input of the RFQ does not imply a different beam at the exit if we consider only RMS matching [Duperrier, 2001].

The beam is transported from the RFQ input to the end of the linac right after the bunch rotation cavity. The input distributions are:

- H^- : water-bag, 60 keV, 100 000 macro particles, 0.3π .mm.mrad rms normalised transverse emittance, 60 mA beam current.
- H^+ : water-bag, 95 keV, 100 000 macro particles, 0.3π .mm.mrad rms normalised transverse emittance, 95 mA beam current.

The matching at transitions is done with TraceWIN. Transport through the RFQs used TOUTATIS ($64 \times 64 \times 64$). Transport through the rest of the linac is done with PARTTRAN (with PICNIC 3D space charge routine).

Before the funnel, all branches are tuned and matched independently. After the funnel, the linac is tuned and matched for H^- beam and the H^+ beam is just transported though it without

extra tuning or matching. One can note that the H^+ bunch charge is $2 \times 95/114 = 1.67$ time bigger than the H^- bunch charge.

The evolution of the beam envelope is plotted in Figure 1.4–63. Because of the difference in bunch charge, the proton beam is not perfectly matched in the SCL. However, the mismatch is not huge.

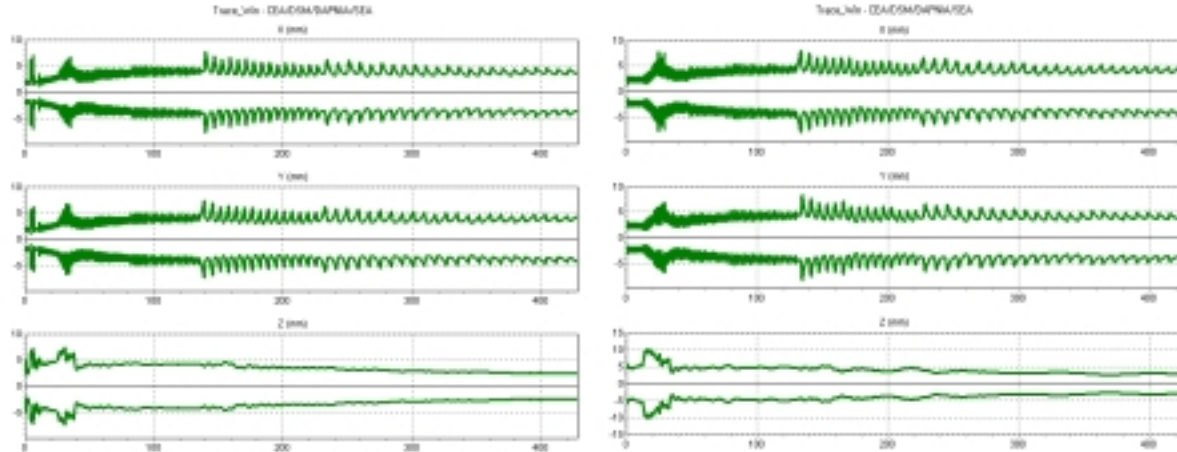


Figure 1.4–63: Beams envelopes. Left: H beam, Right: Proton beam

Beam emittance growth is plotted on Figure 1.4–64 for both beams.

- Longitudinal emittance growth is observed in RFQ2, because the beam is not perfectly matched (this will be corrected),
- Emittance growth occurs in the funnel line. For the H^- beam, it is due to the funnel cavity deflection depending on particle phase (coupling between longitudinal position and transverse deflection). For the proton beam, it is due to the length of the funnel section which is not perfectly tuned.
- Emittance growth occurs at the transition between the CCL and the SCL. This is due to the abrupt change of periodicity and the 3-metre line necessary to pump strongly between the CCL and the SCL.

However, these emittance growths are very small. They represent the emittance growth that will occur in reality where the matching will not be perfect.

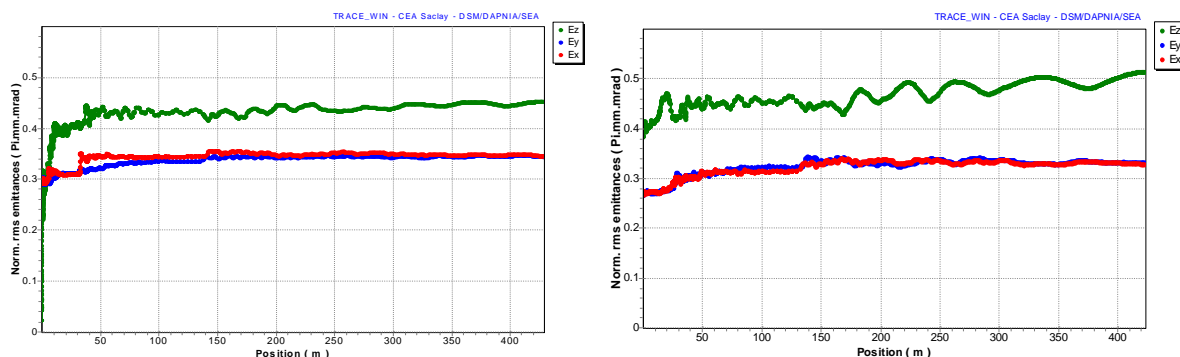


Figure 1.4–64: Beam emittance growth. Left: H^- beam. Right: proton beam

The beam density radii along the linac are plotted in Figure 1.4–65. The bore radius is also plotted to figure out the “danger” for loss. The lower density level is 10^{-5} . A level of 1 W represents of level of 10^{-7} at 1.33 GeV. The proton beam 10^{-5} level is bigger than this level of the H⁻ beam. This is due to the higher current and the small mismatch of the proton beam. The minimum ratio between the bore radius and the 10^{-5} level is approximately:

- 1.45 in the NC linac section for H⁻,
- 2.55 in the SC linac section for H⁻,
- 1.15 in the NC linac section for protons,
- 2.1 in the NC linac section for protons.

The superconducting linac section has much more margin than the normal conducting sections.

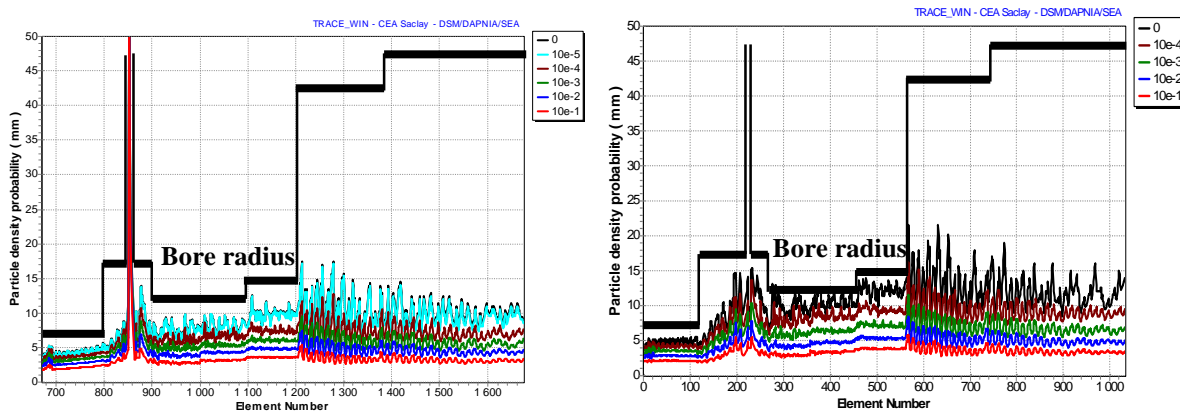


Figure 1.4–65: Beam density radii. Left: H⁻ beam. Right: proton beam

The beam phase space distributions at the linac output are plotted in Figure 1.4–66. The proton beam has more halo than the H⁻ beam. Nevertheless, the tails are very tiny and have rather small amplitude.

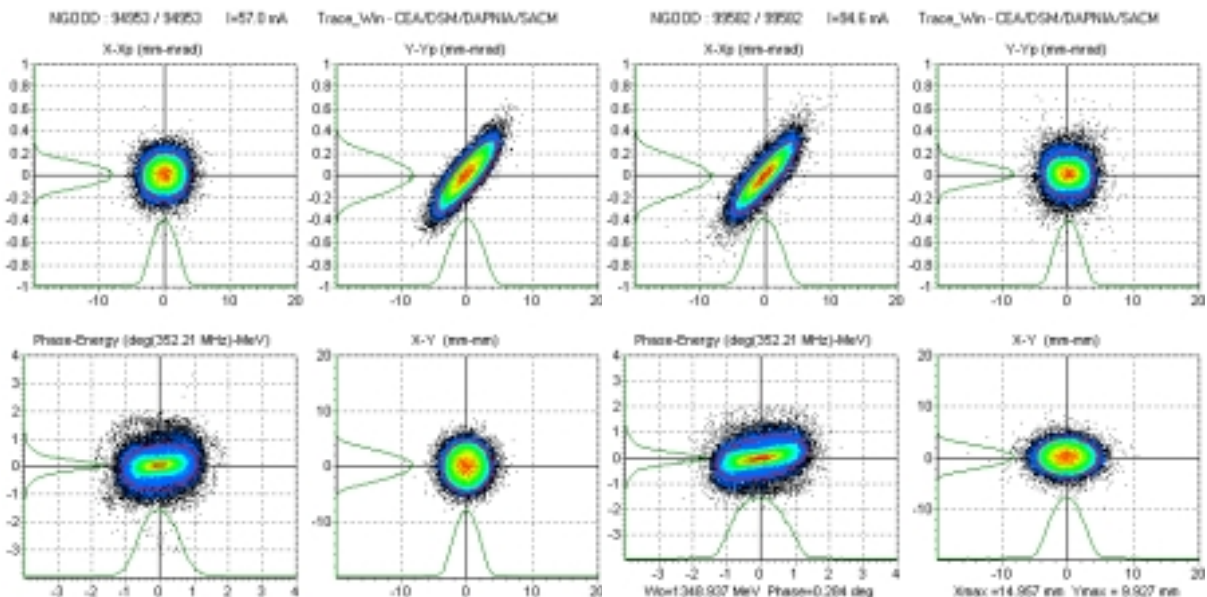


Figure 1.4–66: Beams output distribution. Left: H⁻ beam. Right: proton beam

The beam is then transported through a bunch rotator line. The goal of this line is to reduce the beam energy spread for injection into the ring. The energy-spread requirement at ring injection is about ± 1 MeV (corresponding to $\pm 0.5 \times 10^{-3}$ in dp/p).

In order to verify that the beam can be properly injected into the ring, the transport from the linac end to the exit of the rotation cavity buncher was modelled. The transport line was extrapolated from the 1996 ESS reference design. The only difference is the doublet-focusing scheme, more convenient for the SRF linac, instead of the FODO lattice used for the CCL linac. In this version, no cavity is used at the beginning of the line to increase the beam energy spread for faster debunching (as opposed to the line proposed with the 560 MHz normal conducting option). Should the line length be reduced, a different phase in the last superconducting cavities (for example $+30^\circ$ rather than -25°) could be used. The current line length is ~ 75 meters. The rotation buncher is a 5-cell, $\beta = 0.85$ superconducting cavity with a field of 93.5% of the field of the other cavities. The beam envelopes in the transport line are shown in Figure 1.4–67.

The final longitudinal phase space distribution is plotted in Figure 1.4–68 in phase-energy and $z-dp/p$. The beam rms energy spread is 90.6 keV, and 99.9% of the beam is within ± 500 keV. The fraction of the beam outside $\pm 0.5 \times 10^{-3}$ in dp/p is a few 10^{-5} . This could be improved with better matching in the linac.

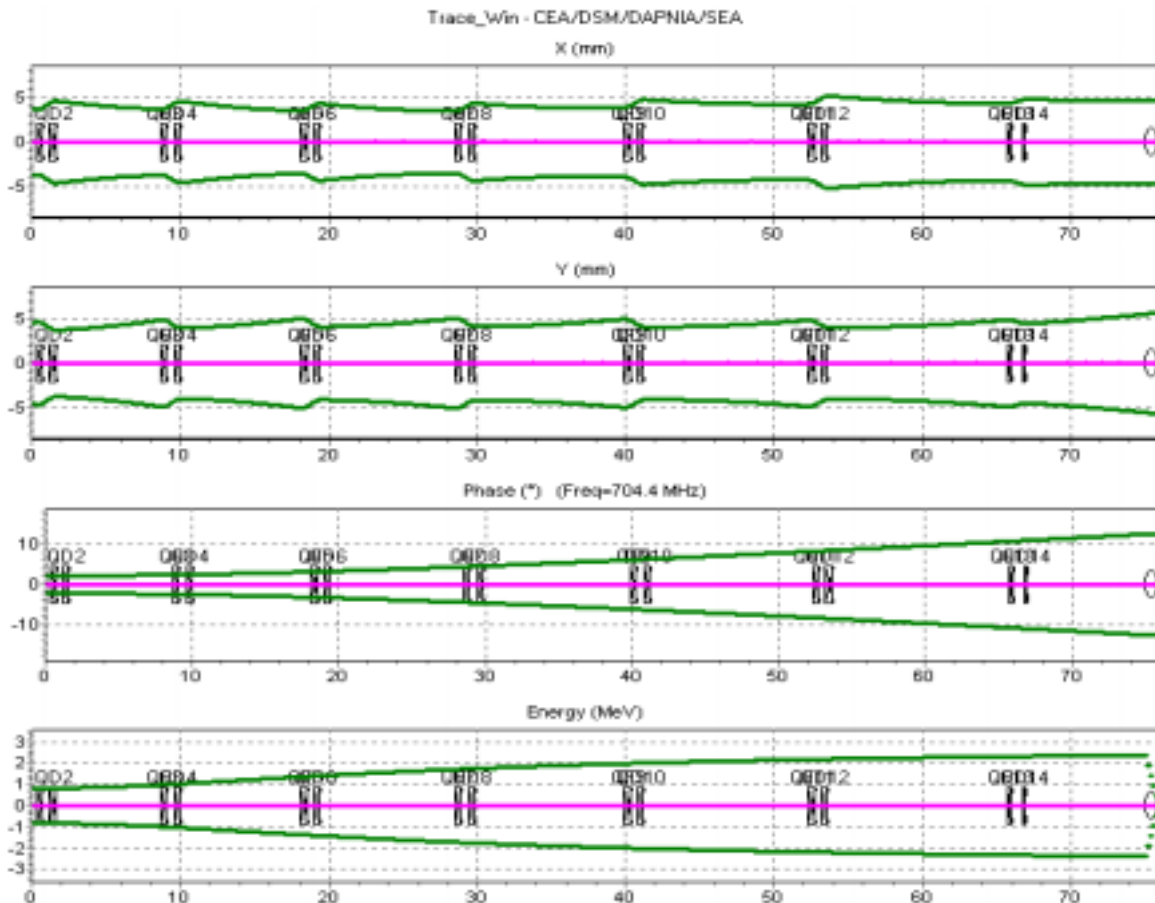


Figure 1.4–67: Envelopes in bunch rotation line

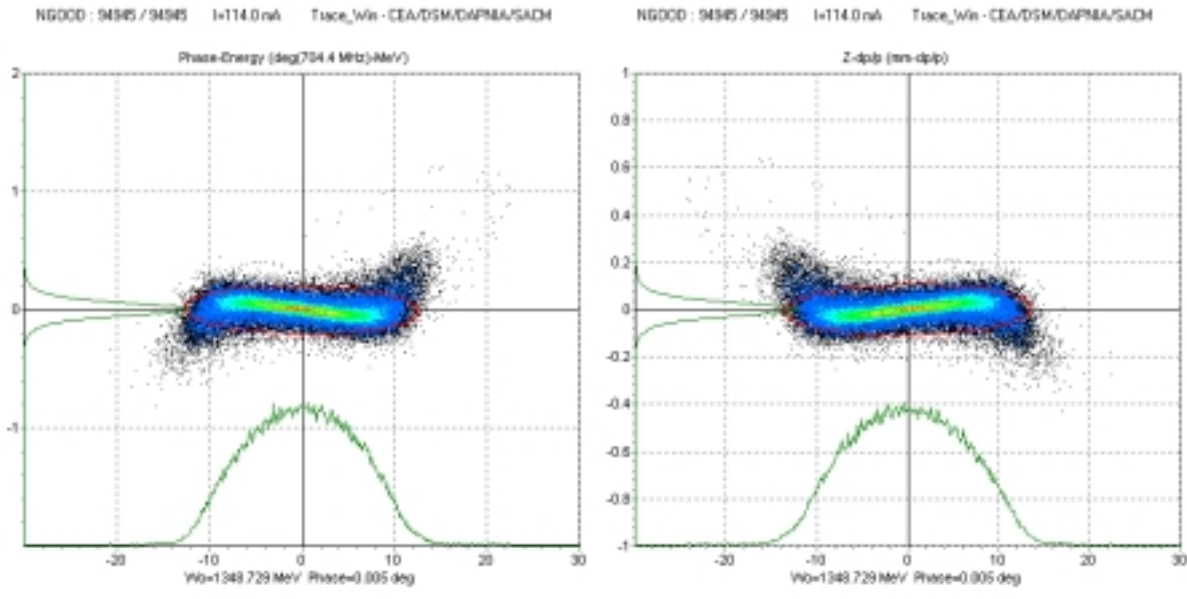


Figure 1.4–68: Longitudinal phase space distribution after the bunch rotation cavity

1.4.10.2.1 Sensitivity to linac element errors

In reality, the linac is not perfect. The linac elements are not quite as expected. Quadrupoles may have the wrong position, be tilted, or have the wrong gradient. Cavities may have the wrong position, be tilted, or have the wrong field (phase or amplitude). Taken together, these are called the errors on elements. Two kinds of errors can occur:

Static errors: The effect of these errors can be detected and corrected with appropriate diagnostic and correctors. For example, beam position measurement coupled with steerers can compensate the quadrupole or cavities misalignments. Correction strategy should be known to be able to estimate their impact on beam dynamics.

Dynamic errors: The effect of these errors cannot be measured and then corrected. Fortunately, they usually have lower amplitude than static errors. They are, for example, the vibrations or the RF field variations (in phase or amplitude). The knowledge of the correction scheme is not needed to study their statistical impact. They are responsible for orbit oscillations around the corrected orbit (this notion of orbit is also extended to the longitudinal motion).

In the following paragraphs, the effects of linac component errors have been studied only on the H^- beam. The H^- beam requirements are indeed much more constraining than for the H^+ beam because of the injection into the ring.

1.4.10.2.2 Static errors study

The effect of the static errors depends on the orbit control system.

A correction scheme has been studied. The positions of the beam position monitors and these of the associated steerers are described in the paragraphs describing the structures. The effect of this correction scheme is described in this paragraph.

Errors with different amplitudes have been used depending on the linac section. The amplitude of the static errors are summarised in Table 1.4-16. For an error amplitude of A , the element error has an equivalent probability to be between $-A$ and $+A$. The rms error is then $A/2$.

Table 1.4-16: Static errors amplitudes used for the errors study

Section	Quads	dx (μm)	dy (μm)	θ_x ($^\circ$)	θ_y ($^\circ$)	θ_z ($^\circ$)	dG/G (%)
	Cavities	dx (μm)	dy (μm)	θ_x ($^\circ$)	θ_y ($^\circ$)	$d\varphi$ ($^\circ$)	dE (%)
RFQ-DTL matching	Quads	125	125	0.2 ¹	0.2	0.2	0.5
	Cavities	125	125	0.2	0.2	1	1
DTL	Quads	125	125	0.2	0.2	0.2	0.5
	Cavities	125	125	0.2	0.2	1	1
Funnel	Quads	125	125	0.1	0.1	0.1	0.5
	Cavities	125	125	0.1	0.1	1	1
Deflection	Quads	125	125	0.05	0.05	0.05	0.5
	Cavities	125	125	0.05	0.05	1	1
SDTL	Quads	125	125	0.2	0.2	0.2	0.5
	Cavities	125	125	0.1	0.1	1	1
CCL	Quads	125	125	0.1	0.1	0.1	0.5
	Cavities	300	300	0.2	0.2	1	1
SCL	Quads	125	125	0.03	0.03	0.03	0.5
	Cavities	2000	2000	0.2	0.2	1	1

¹ Angles have been calculated by assuming an independent motion of element edges with amplitude defined in dx and dy . These correspond to $\sim \arctan\left(\sqrt{2} \cdot \frac{dx}{Le}\right)$ where Le is the element length.

² The errors are coupled for each tank. Quads are assumed to have independent errors.

The RMS value of the residual orbit along the linac is plotted in Figure 1.4-69. It is the result of a statistic over only 10 linacs (the error bar is then 30%). A total number of 94 beam position control sets is used in the linac.

The correction scheme is very efficient after the funnel line (a few 100 μm), but it is less efficient in the DTL (~ 1 mm). This is due to the huge number of quadrupoles between the correctors and the diagnostics. This might probably be improved, if needed.

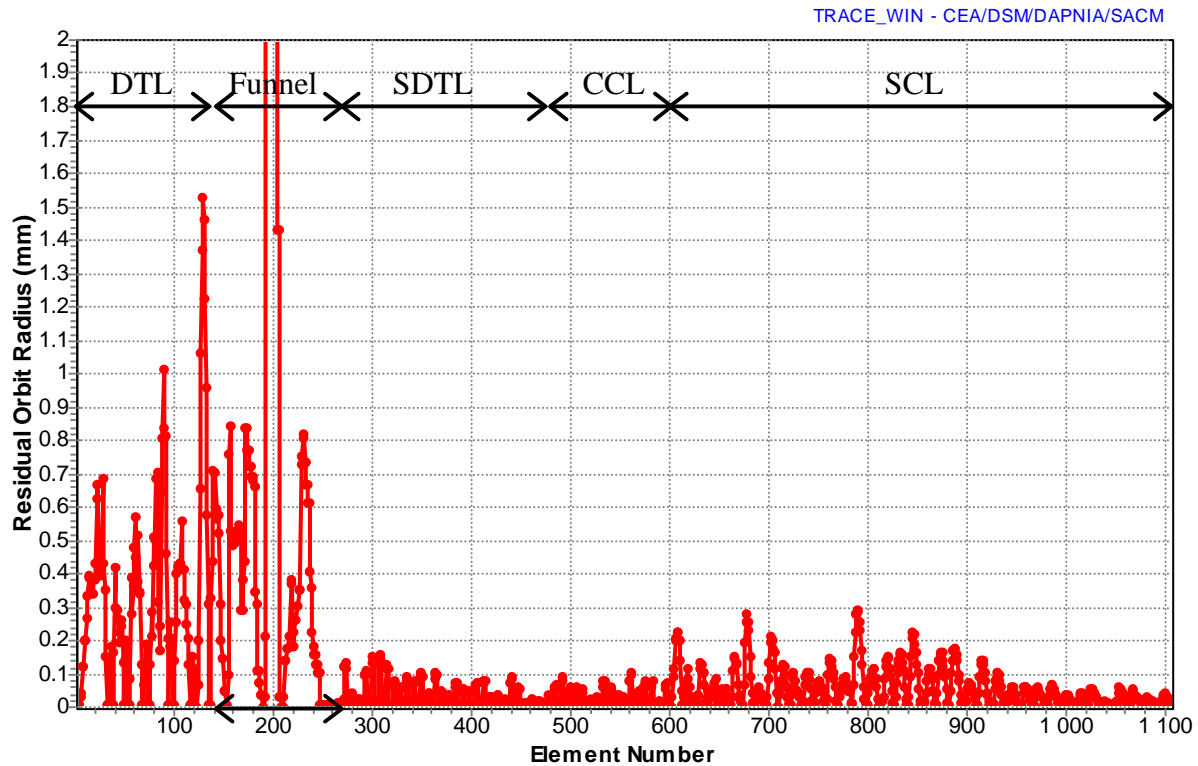


Figure 1.4–69: Residual orbit RMS value along the linac

1.4.10.2.3 Dynamic errors study

Errors with different amplitudes have been used depending on the linac section. The static errors are assumed being corrected. The amplitude of errors are summarised in Table 1.4-17. For an error amplitude of A , the element error has a equivalent probability to be between $-A$ and $+A$. The rms error is then $A/2$.

The transport of a 100,000 particles beam has been simulated in a set of 231 different linacs with errors on each element. The total number of particles used is 23 millions. The simulation begins at RFQ2 exit with the output distribution from RFQ2 as initial distribution. Figure 1.4–70 represents the evolution of the fractional beam radii along the linac. The inner curve is the 90 % level, the outermost one the 100 % level.

A comparison with Figure 1.4–65 shows that the effect of the transverse jitter will not substantially effect the beam losses in the linac. Studies however are continuing to evaluate the consequences in the beam blow-up section in front of the long pulse target station (see the beam transport chapter).

Table 1.4-17: Dynamic errors amplitudes used for the errors study

Section	Quads	dx (μm)	dy (μm)	θ _x (°)	θ _y (°)	θ _z (°)	dG/G (%)
	Cavities	dx (μm)	dy (μm)	θ _x (°)	θ _y (°)	dφ (°)	dE (%)
rfq-dtl matching	Quads	2	2	0.004 ¹	0.004	0.004	0.05
	Cavities	2	2	0.004	0.004	0.5	0.5
DTL	Quads	5	5	0.01	0.01	0.01	0.05
	Cavities	5 ²	5	0.01	0.01	0.5	0.5
Funnel	Quads	2	2	0.002	0.002	0.002	0.05
	Cavities	2	2	0.002	0.002	0.5	0.5
Deflection	Quads	2	2	0.001	0.001	0.001	0.05
	Cavities	2	2	0.002	0.002	0.5	0.5
SDTL	Quads	2	2	0.004	0.004	0.004	0.05
	Cavities	2	2	0.002	0.002	0.5	0.5
CCL	Quads	2	2	0.004	0.004	0.004	0.05
	Cavities	2	2	0.002	0.002	0.5	0.5
SCL	Quads	2	2	0.0005	0.0005	0.0005	0.05
	Cavities	2	2	0.0002	0.0002	0.5	0.5

¹ Angles have been calculated by assuming an independent motion of element edges with amplitude defined in dx and dy. These correspond to $\sim \arctan\left(\sqrt{2} \cdot \frac{dx}{Le}\right)$ where Le is the element length.

² The errors are coupled for each tank. Quads are assumed to have independent errors.

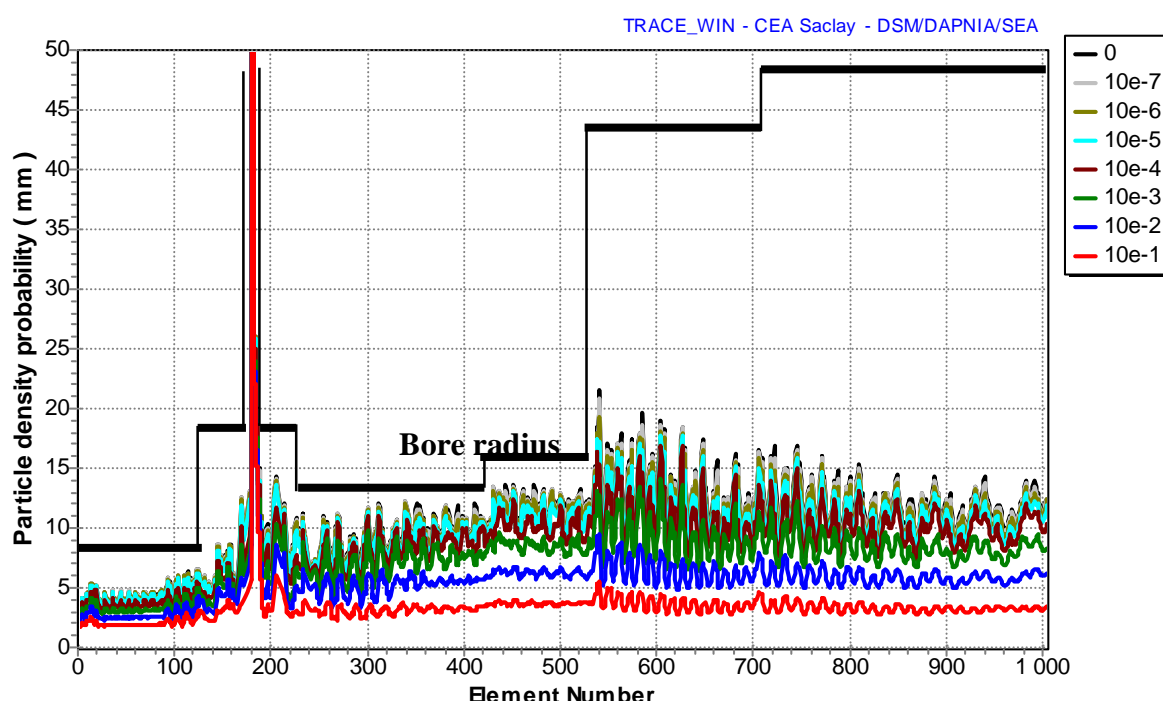


Figure 1.4-70: Fractional beam radii of the ESS H⁻ beam particles with dynamic errors

The position of the beam centre of gravity at the output of each linac in the (x,y), (x,x'), (y,y') and (Phase, Energy) are represented on Figure 1.4–71. The beam motion in transverse phase space is very small (100 μm RMS in both direction). The normalised rms emittances covered by the beam centre of gravity are about $2 \times 10^{-3} \pi.\text{mm.mrad}$ (in X and Y directions) and $0.335 \pi.\text{MeV}$ (@704.4 MHz). The effect is essentially longitudinal. A statistical study [Pichoff, 2002b] has shown that a 0.65% field amplitude error and a 0.65° field phase amplitude are tolerable for proper injection into the compressor rings.

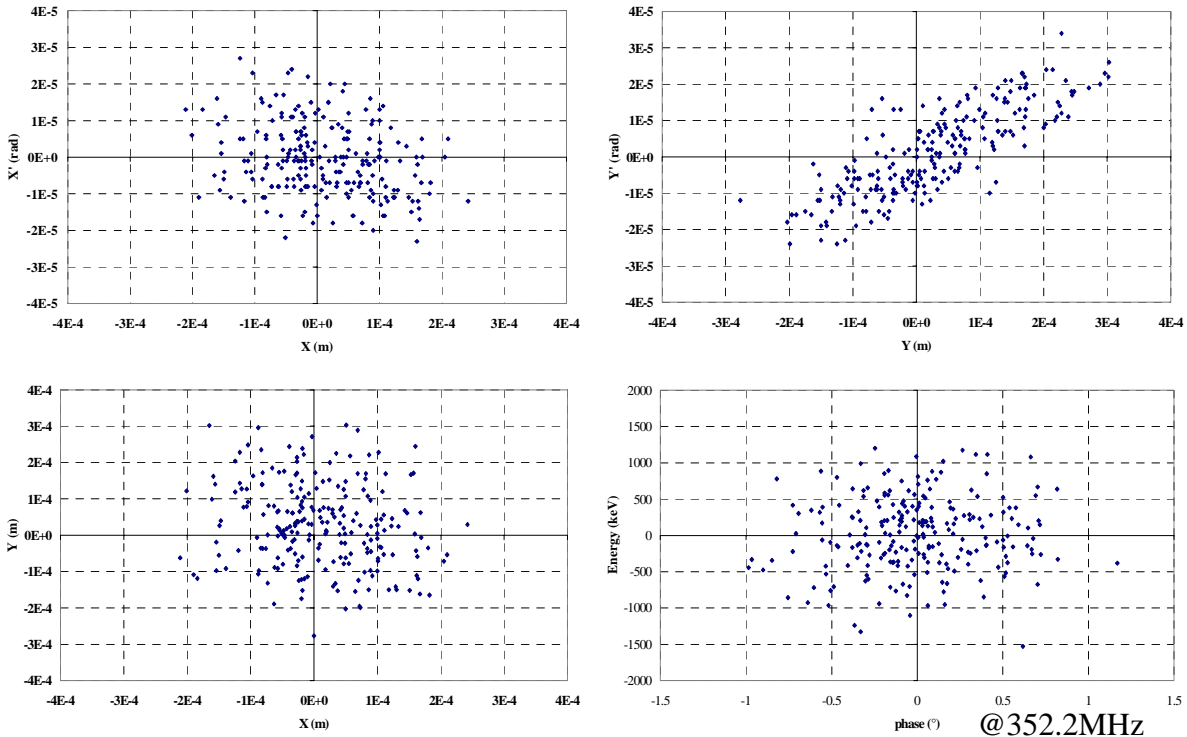


Figure 1.4–71: Positions of beam centre of gravity in phase-spaces for different linacs

The distribution of the final emittances is given in Figure 1.4–72.

The longitudinal rms emittance growth is small (average value: +5.5%). The effect of the non-linear longitudinal force can “reasonably” be decoupled from a study of the centre-of-gravity motion alone.

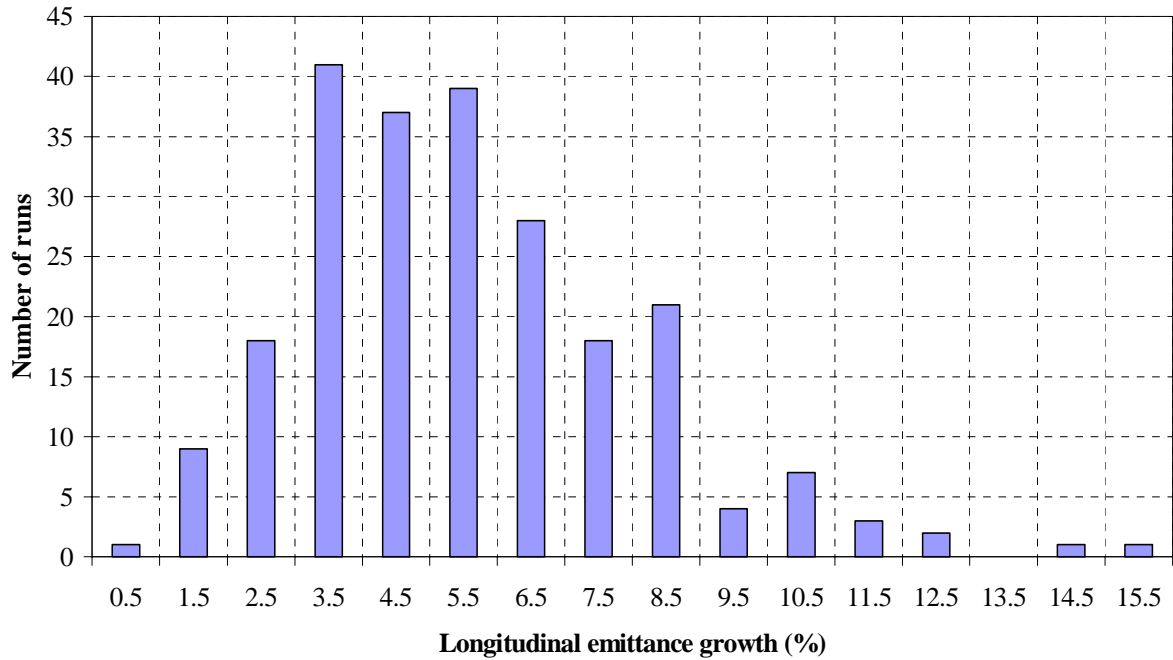


Figure 1.4–72 : Output longitudinal emittance growth histogram

1.4.10.3 Sources of beam losses

The control of beam losses in a high power linac is very important for many reasons:

- High-level losses can have a very bad impact on linac reliability (out-gassing, spark down, radiation damage of cable, electronics, power-supplies, etc.).
- High-level losses can have a very bad impact on linac availability (structure activation, and cooling time before maintenance).
- High-level losses can have a very bad impact on linac radiological protection cost (radiological protection is based initially essentially on the assumed beam losses).

For these reasons, the loss level has to be estimated as well as possible and has to be as low as possible. Many sources of losses are possible:

- Beam misalignment or mismatch.
- Linac elements errors.
- Linac elements failures.
- H- stripping on residual gas.
- H- stripping by magnetic field (Lorentz stripping).
- Scattering on residual gas.

The first two sources are taken into account in the error studies presented before. They have exhibited no significant losses in the linac. Studies are continuing on the beam blow-up system in front of the long pulse target station.

The effect of the last two sources is coupled and amplified by the first two sources (beam off-centring and mismatch). Their induced losses are very low with a matched, centred beam. However, a correlated error study will be done to quantify the exact impact of these errors.

The third type of error (component failure) is more difficult to evaluate. The problem is to estimate the probability of a component failure. This could be done in association with the reliability/availability study. However, beam dynamics studies can help to estimate the impact of a component failure.

The fourth type of error can be quantified very easily. The vacuum pressure required in the machine is based on the desire to keep beam losses to a minimum and to allow “hands on” maintenance. At full power of 10 MW and 1.3 GeV this is equivalent to a fractional particle loss of 10^{-7} per metre length or less than 1 W/m.. The largest loss when the beam interacts with the residual gas is due to charge exchange of the H^- ions. In the normal conducting linac the majority of the residual gas will be water vapour. There are few measurements of charge exchange cross sections in water, but the cross sections for oxygen are a sufficient approximation, and are shown in Figure 1.4–73 as a function of beam energy [Nakai, 1987].

The calculated cross section from 1 MeV to 1 GeV is also shown [Gillespie, 1977].

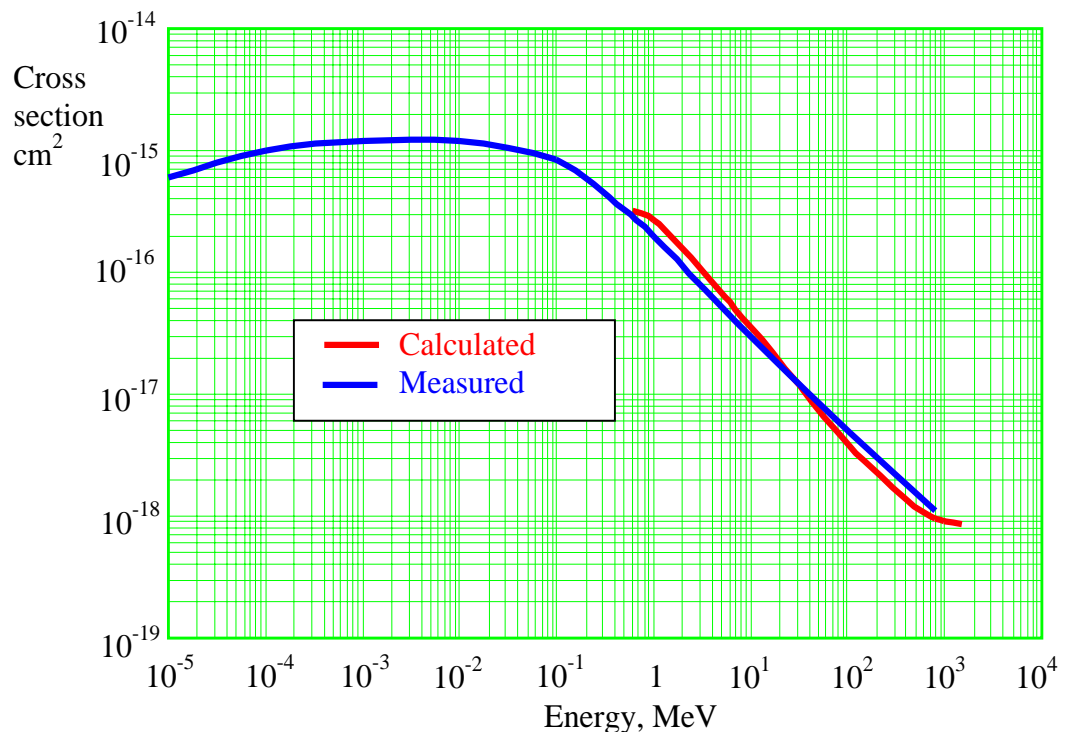


Figure 1.4–73: The total electron loss cross section for H^- ions in oxygen

A recent study [Pichoff, 2002] has shown that the vacuum (H_2O) pressure should be below 4.10^{-8} hPa at high energy to stay below the loss level of 1W/m. An estimation of the residual gas pressure and composition has been done for SNS project. Using this value, an estimation of the beam losses and the associated activation has been calculated for ESS. An estimation of 0.9 W/m, equivalent to an activity of 170 $\mu\text{Sv}/\text{h}$ at 1 foot after 4 hours, is expected in the CCL at 185 MeV.

1.5 ENGINEERING DESIGN AND DEVELOPMENT (ED&D)

Much development work in the field of H⁻ sources is being carried out at present [HPNIS Network]. The ESS SP and LP ion source requirements are expected to meet provided that ED&D activities continue. A contingency measure is in place to the extent that an existing 100 mA proton source could accommodate LP needs.

While the RF sources for both types of linac can be designed on the basis of existing devices at similar frequencies, prototype work (*e.g.* on the low- β front end with its RFQ and chopper elements) will help to achieve gains in performance and reliability. Further items, which will benefit from prototyping work include high-gradient DTL quadrupoles, buncher and deflection cavities, septum magnets and beam diagnostic elements.

RF power couplers relevant to the ESS SC accelerator scheme are being studied at the SNS and at KEK. ESS ED&D work on RF power couplers should build on existing studies, and in particular should address the use of dual couplers necessary to ensure that the RF power per coupler at the ESS pulse length and duty cycle is kept below reasonable limits. Work on RF control for pulsed SC cavities will also be a continuing ED&D item.

Prototyping of major systems, such as the complete front end, will only be undertaken when the construction of the ESS facility is approved.

REFERENCES

- [Bailey, 1998] C P Bailey,
Limits in the design of short solenoids for into matching to RFQs,
Proceedings EPAC 1998, Stockholm, 1998
- [Bailey, 2000] C P Bailey *et al.*
The Rutherford RFQ Test Stand
Proceedings EPAC 2000, Vienna, 2000, p.933
- [Bailey, 2001] C P Bailey *et al.*
Work at RAL towards an Ion Source and RFQ for ESS
'Wissenschaftsrat' Meeting, Jülich, Germany, December 2001
- [Barbier, 1969] M Barbier
Induced Radioactivity
North-Holland Publishing Company, Amsterdam, 1969
- [Barsukov, 2001] A Barsukov *et al.*
Funneling System for the European Spallation Neutron Source ESS
ISSN 1433-559X, ESS 01-119-L, October 2001
- [Beauvais, 2000] P-Y Beauvais *et al.*
Status Report on the High Intensity Injector Project (IPHI)
Proceedings EPAC 2000, Vienna 2000, p. 283
- [Bennett, 1992] J R J Bennet and R J Elsey
Vacuum, 43, 1992, p. 35
- [Bongardt, 1995] K Bongardt and M Pabst
Design Criteria for High Intensity H⁻ Injector Linacs
Proceedings PAC, Dallas, May 1995
- [Bongardt, 1996] K Bongardt, M Pabst
Accelerator Physics of High Intensity Proton Accelerators
Proceedings 5th EPAC, Sitges, Spain, 1996
- K Bongardt, M Pabst, A Letchford, V G Vaccaro and L Verolino
Filamentation Effects and Image Charges in High Beta Transfer Lines
Proceedings 5th EPAC, Sitges, Spain, 1996
- [Boussard, 1996] D Boussard
Operational Experience with The LEP2 SC Cavity System
Proceedings 5th EPAC, Sitges, Spain, 1996

- [Brennan, 1989] J M Brennan *et al.*
A Fast Chopper for Programmed Population of the Longitudinal
Phase Space of the AGS
BNL-41832, PAC89, IEEE Chicago 2669, 1989, p. 1154
- [Clarke-Gayther, 2001] Clarke-Gayther
Modulator Systems for the ESS 2.5 MeV Fast Chopper
Proceedings 2001 IEEE Particle Accelerator Conference, 2001
- [CONCERT, 2000] J-L Laclare *et al.*
B.130, CEA Saclay, F-91191 Gif-sur-Yvette, France
- [Crawford, 1987] J F Crawford (Ed.)
Proposal for a European Hadron Facility
EHF-87-18, May, 1987
- [Derevyankin, 1994] G E Derevyankin
Negative Hydrogen Ions for Accelerators
Proceedings European Particle Accelerator Conference,
pp 1450 - 1452, London, 1994
- [Duperrier, 2001] R Duperrier
CEA Saclay, private communication
- [ESS-96-53-M] The European Spallation Source Study 1996,
Volume III: The ESS Technical study
- [Ferdinand, 2001] R Ferdinand, H Klein and J W G Thomason
ESS Workshop on Sources
28 November 2001, Saclay
ESS report, April 2002
- [Gardner, 1995] I S K Gardner, H Lengeler, G H Rees (Editors)
Outline Design of the European Spallation Source
ESS Report 95-30-M, Jülich, September, 1995
- [Gardner, 2001] I S K Gardner *et al.*
The ESS accelerator and beam lines with the 280/560 MHz linac
ESS-01-1A, December 2001
- [Gardner, 2002] I S K Gardner *et al.*
The ESS 280/560 MHz acceleration system
ESS report, April 2002
- [Gillespie, 1977] G H Gillespie
Physical Review A, 16, 1977, 16, p. 943
- [Gobin, 2002] R Gobin *et al.*
High Intensity ECR Ion Source (H+, D+, H-)
Developments at CEA-Saclay
Review Scientific Instruments 73(2), 2002 (to be published)

- [HPNIS Network] High Performance Negative Ions Sources Network
 HPRI-CT2001-50021
 Supported by European community
- [IFMIF, 1997] IFMIF Conceptual Design Report
 Oak Ridge, to be published
- [Johnson, 1992] K F Johnson, O R Sander, G O Bolmer, J D Gilpatrick, F W Guy,
 J H Marquardt, K Saadatmand, D Dandoval and V Yuan
 A Beam Funnel Demonstration: Experiment and Simulation
 Particle Accelerators, Vols. 37-38 (1992) 261
- [Klein, 1995] H Klein
 Spallation Neutron Sources
 Proceedings LINAC 94, Tsukuba, Japan, 1995
- [Lander, 2002] Report of the first Technical Advisory Committee (TAC) of the European
 Spallation Source (ESS) project
 ESS report, April 2002
- [Lagniel, 1998] J-M Lagniel, *High Intensities linac studies in France*
 Linac 98 conference, Chicago, pp.706.
- [Lagniel, 2001] High Current, High Reliability Negative Ion Sources For Next
 Generation Accelerators
 CEC Contract NO. HPRI-CT-2001-50021
- [Legg, 1996] R Legg
 Operating Experience at CEBAF
 Proceedings of the 5th European Accelerator Conference 1996
- [Lengeler, 1994] H Lengeler
 Proposals for Spallation Sources in Europe
 Proceedings EPAC'94, London, June 1994
- [Letchford, 1998] A Letchford and A Schempp
 Comparison of 4-Rod and 4-Vane RFQ Fields
 Proceedings EPAC 1998, Stockholm, 1998, p. 1204
- [Letchford, 2000] A Letchford *et al.*
 First Results from the ISIS RFQ Test Stand
 Proceedings EPAC 2000, Vienna, 2000, p.833
- [Liepe, 2001] M Liepe *et al.*
 DESY report TESLA-01-03, 2001
- [Magistris, 1996] M de Magistris, V G Vaccaro, L Verolino
 Bunched Beams in Axisymmetric Systems, Il Nuovo Cimento, 1996
- [Nakai, 1987] Y Nakai *et al.*
 Atomic Data and Nuclear Data Tables, 37, 1987

- [Oguri, 2002] H Oguri *et al.*
Development of an H⁻ Ion Source for the High Intensity Proton Linac
Review Scientific Instruments 73(2), 2002 (to be published)
- [Pabst, 1996] M Pabst, K Bongardt and A Letchford
Halo Simulation in a Realistic Proton Linac
Proceedings LINAC96, Geneva, Switzerland.
- [Peters, 1998] J Peters
The Status of DESY H- Sources
Review Scientific Instruments 69(2), 1998
- [Pichoff, 2002a] N Pichoff, R Duperrier, D Uriot
Beam Losses in ESS from H- stripping on residual gas
ESS Linac Technical Note n° ESSLIN-TN-0202-01, 2002
- [Pichoff, 2002b] N Pichoff, R Duperrier, D Uriot
Sensitivity of the ESS linacs to RF field errors
ESS Linac Technical Note n° ESSLIN-TN-0202-02, 2002
- [Planner, 1995] C W Planner
Matching Unequal Transv. Emittances from an H⁻ Ion Source to an RFQ
Particle Accelerators, Vol. 48, pp 243-250, 1995.
- [Prior, 1999] C R Prior
Funnel Studies for the European Spallation Source
Report ESS 99-96-A, September 1999
- [Rode, 2001] C Rode and the Jlab SNS Team
The SNS Superconducting Linac System
Proceedings PAC 2001, Chicago
- [Rüedi, 1995] H Rüedi *et al.*
A new IGBT Gate Unit for High Current, High Voltage IGBT Modules
Proceedings International Power Conversion, Nürnberg, Germany, 1995
- [Sande, 1996] M van de Sande
TUE Internal Report, VDF/NK 96-01, 1996
- [Schempp, 1998] A Schempp *et al.*
A New High Duty Factor RFQ Injector for ISIS
Proceedings EPAC 1998, Stockholm, 1998, p.782
- [Schneider, 2001] W J Schneider *et al.*
Design of the SNS Cryomodule
Proceedings PAC 2001, 18-20 June, 2001-12-17
- [Schröder, 1994] Schröder, Leung, Alonso (Ed.)
Proceedings of Workshop on Ion Source Issues Relevant to a Pulsed SNS
Lawrence Berkeley National Laboratory, USA, 1994

- [Senichev, 2002] Yu Senichev *et al.*
ESS funnel design investigation, EPAC 2002
- [Sherman, 2001] J D Sherman
Scaling of the Penning Surface Plasma Source (SPS) to high duty factor (2.3 – 5 %), 100 mA H⁻ currents with slit emitters
Proceedings 7th ESS General Meeting, Seggau, Austria, September 2001
- [Sidlow, 1996] R Sidlow
Operational Experience of Penning H⁻ Ion Sources at ISIS
Proceedings EPAC96, Sitges, Spain, June 1996
- [Simrock, 1996] S N Simrock, I Altmann, K Rehlich, T Schilcher
Design of the Digital RF Control System for the TESLA Test Facility
Proceedings EPAC, Sitges, June 1996
- [Smith, 1994] H V Smith *et al.*
H⁻ and D⁻ Scaling Laws for Penning Surface-Plasma Sources
Review Scientific Instruments 65(1), 1994
- [Smith, 1998] H V Smith, D Schneider
Status update on the Low Energy Demonstration Accelerator (LEDA)
Proceedings LINAC 98, Chicago, USA, pp.418
- [Smith, 1999] H V Smith *et al.*
Comparison of Beam Simulations with Measurements for the LEDA LEBT H⁺ Beam
Proceedings PAC 99, New York, USA, p.1929
- [Stassen, 2001] R Stassen *et al.*
Proceedings PAC 01, Chicago, USA, p.1080.
- [Strausser] Y Strausser
Review of Outgassing Results, Varian Report, VR-51
- [Thomae, 2002] R Thomae *et al.*
Beam Measurements on the H⁻ Source and LEBT System for the SNS
Review Scientific Instruments 73(2) 2002 (to be published)
- [Thomason, 2000] J W G Thomason and R Sidlow
ISIS Ion Source Operational Experience
Proceedings EPAC 2000, Vienna, Austria, June 2000
- [Thomason, 2002] J W G Thomason *et al.*
H⁻ Ion Source Test and Development Capabilities at ISIS
Review Scientific Instruments 73(2), 2002 (to be published)
- [Volk, 1996b] K Volk *et al.*
An H⁻ source for ESS
Review Scientific Instruments 67(3), 1996

- [Volk, 1998] K Volk, A Maaser, H Klein
The Frankfurt H⁻ Source for the ESS,
Proceedings LINAC 1998,Chicago
- [Vormann, 1998] H Vormann *et al.*
Design of a High Current RFQ Injector with High Duty Cycle
Proceedings LINAC98, Chicago, 1998, p. 791
- [Vormann, 2000] H Vormann *et al.*
Retuning of the ISIS RFQ
Proceedings EPAC 2000, Vienna, 2000, p.869
- [Ziomek, 1993] C D Ziomek *et al.*
Results of Adaptive Feedforward on GTA
Proceedings PAC 1993

Chapter 2

Accumulator Rings and Injection Beam Line

Authors and Contributors

Accumulator Rings and Injection Beam Line

J R J Bennett¹, M Masullo², S Pape Moller³, C R Prior¹, G.H. Rees¹, J V Trotman¹,
V Vaccaro², C M Warsop¹

¹RAL/ISIS, ²Univ. Naples, ³Univ. Aarhus

Contents

Accumulator Rings and Injection Beam Line

2 ACCUMULATOR RINGS AND INJECTION BEAM LINE	2-4
2.1 INTRODUCTION	2-4
2.2 RING BUILDINGS AND TUNNEL.....	2-6
2.3 INJECTION BEAM LINE	2-7
2.4 ACCUMULATOR MAGNET LATTICE	2-12
2.5 RING BEAM DYNAMICS	2-16
2.5.1 BEAM EMITTANCES, ACCEPTANCES AND SPACE CHARGE TUNE SHIFTS	2-16
2.5.2 CLOSED ORBIT DISTORTION AND CORRECTION	2-17
2.5.3 BEAM STABILITY.....	2-18
2.5.4 ELECTRON-PROTON (E-P) INSTABILITY	2-20
2.5.5 PROFILING OF THE VACUUM CHAMBER WALL.....	2-21
2.5.6 INSTABILITY SUPPRESSION.....	2-21
2.5.7 CORRECTION MAGNETS	2-22
2.6 H⁻ CHARGE EXCHANGE INJECTION.....	2-22
2.6.1 LONGITUDINAL PAINTING	2-27
2.6.2 TRANSVERSE PAINTING.....	2-27
2.6.3 STRIPPING FOIL TEMPERATURES	2-29
2.7 RADIO FREQUENCY SYSTEM	2-30
2.8 FAST EXTRACTION SYSTEM	2-34
2.9 BEAM LOSS COLLECTION	2-39
2.10 MAGNETS AND POWER SUPPLIES.....	2-45
2.10.1 ACCUMULATOR RING BENDING MAGNETS AND QUADRUPOLES	2-45
2.10.2 INJECTION BEAM LINE BENDING MAGNETS AND QUADRUPOLES.....	2-45
2.11 BEAM DIAGNOSTICS	2-48
2.12 THE VACUUM SYSTEM FOR THE RINGS AND BEAM LINES.....	2-53
2.13 INSTALLATION AND ALIGNMENT	2-55
2.14 RESEARCH AND DEVELOPMENT.....	2-55
2.15 CONCLUSIONS	2-55
REFERENCES	2-56

2 ACCUMULATOR RINGS AND INJECTION BEAM LINE

2.1 INTRODUCTION

The revised specification for the European Spallation Source (ESS) includes 5 MW of proton beam power to be delivered to a short pulse target at 50 Hz, in pulses of time duration 1.5 μ s or less, and 3.4 MW to a long pulse target in an interleaved mode at 16.667 Hz, with pulses of maximum time extent 2.5 ms. The specification is more difficult to meet than for the earlier ESS design where the total beam power was 5 MW, shared between 50 Hz and 10 Hz short pulse targets.

The specifications are met through the use of two, 50 Hz, 1.334 GeV accumulator rings which are filled and emptied successively once every cycle with $2.34 \cdot 10^{14}$ protons per ring. 5 MW of beam power are developed in the H⁻ linac for this mode of operation, and the two accumulators act to compress the time duration of the linac pulse via a multi-turn charge exchange ring injection process. In addition, for the long pulse target, 3.4 MW of beam power is required in an interleaved 16.667 Hz mode in pulses of maximum duration \sim 2.0 ms. The duty cycle for the linac at 50 Hz is about 5 % and corresponds to < 600 turn injection for each ring, with a through-put power per ring of 2.5 MW, while the added duty cycle at 16.667 Hz is \sim 3.3 %.

The 16.667 and 50 Hz linac beams are chopped with an additional 65-70 % duty cycle at the ring bunch revolution frequency. The chopped 2.0 ms pulses at 16.667 Hz pass directly to the long pulse target, while the chopped 1.0 ms pulses at 50 Hz are transported to the 1.334 GeV accumulator rings. Chopping is required to minimise the ring beam losses but is initially included in the 16.667 Hz beam to limit the reflected power in the linac radio frequency (rf) systems. The single bunch accumulated in each ring is contained by rf systems of harmonic numbers one and two. Subsequently, after fast ring extraction and a switch magnet, the two bunches in each 50 Hz pulse are spaced with bunch and pulse durations of 0.6 and 1.4 μ s, respectively, at the short pulse neutron target.

The 1.5 μ s specification for the proton pulse on the 50 Hz target sets the mean radius of the 1.334 GeV accumulators at \sim 35.0 m, with the ring revolution period at \sim 0.8 μ s and the linac duty cycle at 5 % for \sim 600 turn injection per ring. The average current circulating in each ring is 46.55 A, and the required peak and average linac currents during the pulsing intervals are 114 and 79.8 mA, respectively. A schematic layout detailing the relative positions of the beam lines and accumulators is shown in Figure 2.1.1.

Two areas are of major importance for the accelerators. First, the 1.334 GeV H⁻ linac is at the state of the art for pulsed, high brightness linacs, but is beyond the state of the art for the required H⁻ ion sources. The latter is mainly so due to the interleaved 50 and 16.667 Hz pulsing for the two targets. Secondly, beam loss in the rings has to be much lower than has previously been achieved and this is despite the use of an increased number of injected turns.

Important areas for accelerator R & D are H⁻ ion sources, H⁻ stripping foils, chopping, funnelling and beam loss control. For the ion sources, improvements are required in output current, emittance and duty cycle and, for the foils, adequate lifetimes when cycling over wide temperatures. New methods are proposed to contain and reduce ring beam losses.

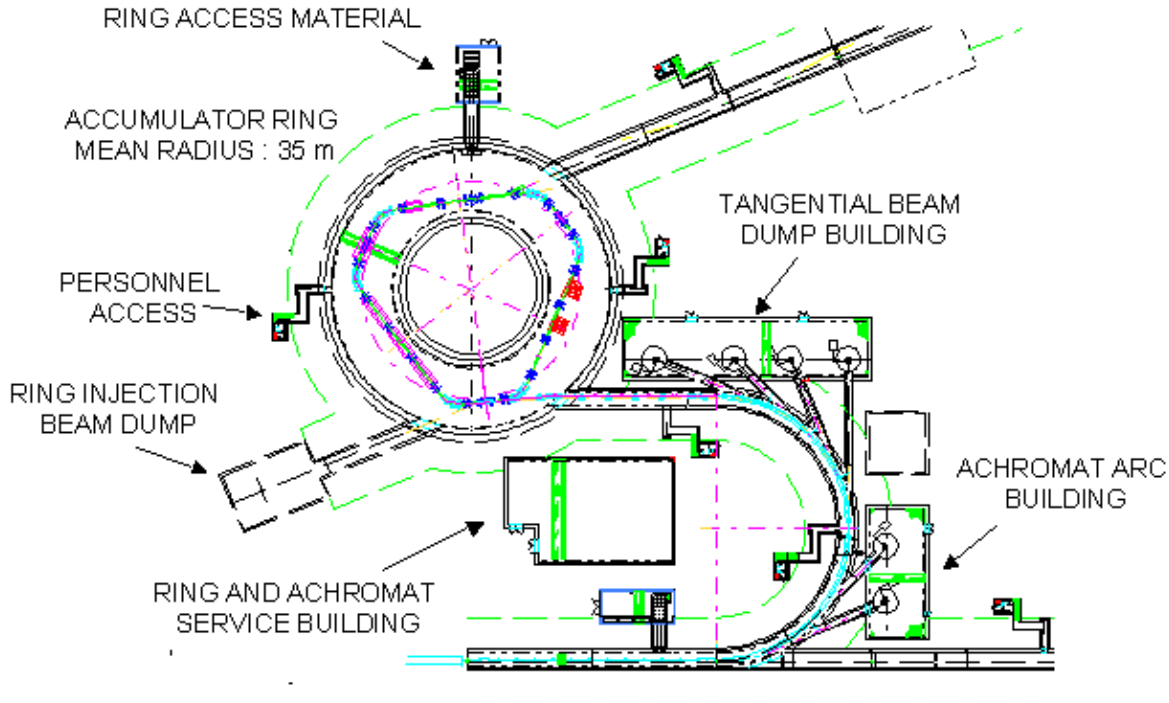


Figure 2.1.1: Relative layout of Achromat, Transfer Lines and Rings

Halo scraping is planned for the linac H^- beam, both for transverse and longitudinal motion, using a number of stripping foils in a large achromatic 180° bending section. The achromat uses low field, C-shaped, combined function magnets and appropriate foils to remove beam halo outside set values of transverse emittances and fractional momentum spread. For the rings, a special injection region is included in the lattice, allowing combined injection painting in all three phase planes. This reduces the number of proton foil transits and the resulting beam loss. Elsewhere in the ring, a beam loss collection system is used to localise the loss.

Table 2.1.1: Parameters for the Accumulator Rings

Ring max. kinetic energy (MeV)	1334.0
Repetition frequency (Hz)	50.0
Accumulator ring mean radius (m)	35.0
Ring rms $\epsilon\beta\gamma$ ($\pi \mu\text{rad m}$)	(2.21) 30.0
Ring average circulating current (A)	46.55
Number of circulating protons (10^{14})	2.34
Revolution frequency (MHz)	1.2416
Main (h) & additional harmonic number	1,2
Peak kV/turn at injection	8 to 26
Ratio V(2h) / (V(h) at injection	0.4 to 0.9
Peak kV/turn during storage	26.0 to 28.0
No of 'h' cavities/ring	3 (single gap)
No of '2h' cavities/ring	1 (double gap)
Length of 'h' and '2h' cavities (m)	1.5, 2.2
Bunch and pulse extent at target (μs)	0.6, 1.4

2.2 RING BUILDINGS AND TUNNEL

The configuration of buildings and tunnels has evolved from geometric, cost, functional, and radiological considerations. Where possible, a cut and fill earth shielding design for beam line tunnels has been used to minimise costs. Buildings are located over ventilated tunnels, with removable steel and concrete shielding to allow regular or active maintenance. Transfer lines and rings are designed for low loss, typically less than 3 nAm^{-1} , allowing hands on maintenance. Unavoidable losses will be concentrated in areas designed for active handling. Shielding is designed for external radiation levels of less than $0.5 \mu\text{Sv h}^{-1}$ for a localised loss of 1% of the design intensity. Monitoring devices will detect unexpected loss and invoke immediate trips when pre-set limits are exceeded.

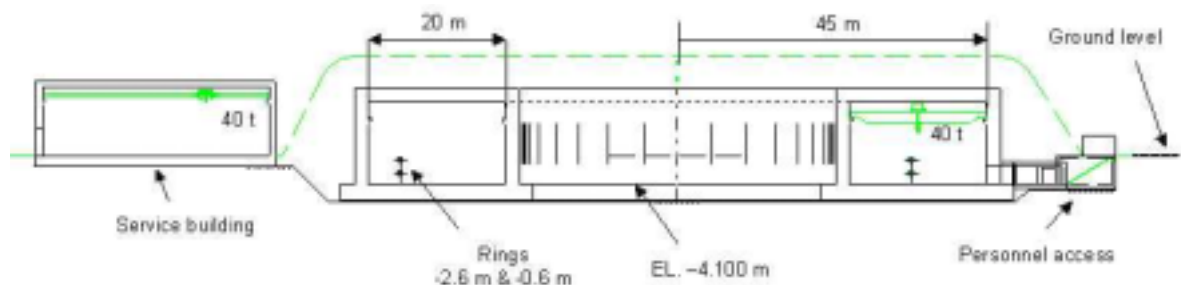


Figure 2.2.1: Ring buildings and tunnel

The linac, transfer lines and rings are 2.6 m below ground level and 1.5 m above floor level. Target beam lines rise to 1.5 m above ground in the experimental hall. The internal tunnel cross section is 4 m high by 5 m wide, allowing adequate space for services, temporary shielding (during maintenance), personnel and equipment access. The tunnels will be surrounded by 1.5 m of concrete and 8 m of earth, and surface tunnels, inside buildings, with 2.4 m of steel and 1 m of concrete. Beam-dump tunnels will be 3 m high by 2 m wide. All main tunnels will have 8 tonne travelling cranes for removal and installation of components and will be accessed by heavily shielded doors.

Five beam dumps serving the stripping foils in the achromat are grouped into two adjacent buildings that provide all the service and handling requirements, as shown in Figure 2.3.2. A large service building is located in the achromat arc for power and water services, equipment preparation, spares, storage and a local workshop.

The rings are in a tunnel, 20 m wide by 10 m high, designed for active handling and hands on maintenance (Figure 2.2.1). The lower ring is at the linac beam height with the upper ring 2 m above. Annular service tunnels are separated from the ring, with sufficient concrete for equipment protection though not for occupation during running. Access is through a shielded and baffled entrance and equipment will be moved using 50 tonne overhead cranes. The beams left unstripped after the foil are transported via a short tunnel to a beam dump in a hall which could be used for either muon or radioactive ion beam research.

The beam switching area is inside a large service building housing close-coupled power and water supplies, local spares, handling facilities and power supplies for the target beam line elements. The switching area tunnel has a removable concrete and steel roof or wall through which damaged modules will be replaced and later removed to a separate repair building.

Target beam lines are underground until they rise into the muon or neutron target halls where they may be serviced using the large overhead cranes. The beam line between the muon and the 50 Hz target will require the development of specialised handling techniques and the use of radiation hard components. Small service buildings are spaced along the 16.667 Hz target beam line to supply water, ventilation and other requirements.

2.3 INJECTION BEAM LINE

A schematic drawing of the injection beam line is shown in Figure 2.3.1, a layout plan of an achromatic bending region in Figure 2.3.2, the vertical separation region in Figure 2.3.3 and focussing parameters of the line in Figure 2.3.4. The initial section of line after the linac is for matching, beam debunching, bunch rotation and injection momentum ramping. The line then divides into a long pulse target beam line and an achromatic bending region. For the former, the H^- beam is deflected on to a foil in the first achromat magnet where it is stripped to protons, which proceed to leave the magnet and expand while in transit to the long pulse target. The 50 Hz H^- beam continues in the achromat where collimators provide momentum and horizontal/vertical betatron selection. Finally, there is vertical beam separation into two ring matching sections, with focussing of the H^- beams to the correct spot sizes at the injection stripping foils.

On leaving the linac, the beam bunches enter a momentum enhancement cavity and then debunch ahead of two cavities which provide both bunch rotation and the momentum ramping appropriate for horizontal and longitudinal injection painting (note section 2.6). The longitudinal space charge forces enhance the beam momentum spread and phase width, with the core increasing in phase extent from $\pm 3^\circ$ (at 560 MHz) to $\sim \pm 11^\circ$ at the rotation-ramping cavities. The phase extent is within the linear range of the sinusoidal cavity fields, even with the phase shifts required for momentum ramping, so allowing a reduction of instantaneous momentum spread by bunch rotation. Errors in mean beam energy after the enhancement cavity are removed at the two downstream cavities by a correct choice of the separation distance. Errors in mean phase, however, lead to subsequent errors in phase, and hence in energy, at the downstream units. A small over-rotation of the bunch phase space ellipse is made ahead of the achromat (where the beam dynamics is as for a circular machine above transition energy, with focussing space charge forces in the longitudinal envelope equation). Ramping is introduced ahead of collimation, and the extent depends on both the beam momentum spread and the injection painting requirements. For example, if the beam momentum spread, $\Delta p/p$, when entering the ring is $\pm 0.5 \cdot 10^{-3}$, the required $\delta p/p$ ramp is from $0.5 \cdot 10^{-3}$ to $3.5 \cdot 10^{-3}$, the average beam momentum is offset from its nominal value by an amount $\Delta p/p$ of $2 \cdot 10^{-3}$, the achromat is centred about this offset value, and the collimators remove beam of momenta outside the $\Delta p/p$ range 0 to $4 \cdot 10^{-3}$. Debunching in the achromat is small, but debunching continues in the line and ring.

Linac beam halo leads to injection losses which are difficult to localise and hence the proposal to collimate ahead of the rings. Transverse and momentum collimation are introduced in the achromat bending magnets by means of stripping foils which separate away the unwanted particles. H^- stripping is a much more appropriate mechanism for collimation than is normal beam interception. The foil locations along the transfer line are shown in Figure 2.3.1. Normalised linac rms output emittances are $< 0.4 (\pi) \mu\text{rad m}$ ($5 \mu\text{eV s}$) transverse, and $7.3 \mu\text{eV s}$ longitudinal. Transverse collimation (3σ) is at $> 3.6 (\pi) \mu\text{ rad m}$.

The quadrupole focussing adopted in the linac is continued into the transfer line though the cell length is made twice that at the end of the linac and the gradients are adjusted to give twice the betatron phase shifts per cell. Transverse space charge tune depressions lead to enhanced β -functions in both linac and beam line but there is a smooth transition between the two focussing regions. Matching is adjusted for the level of the transverse space charge forces.

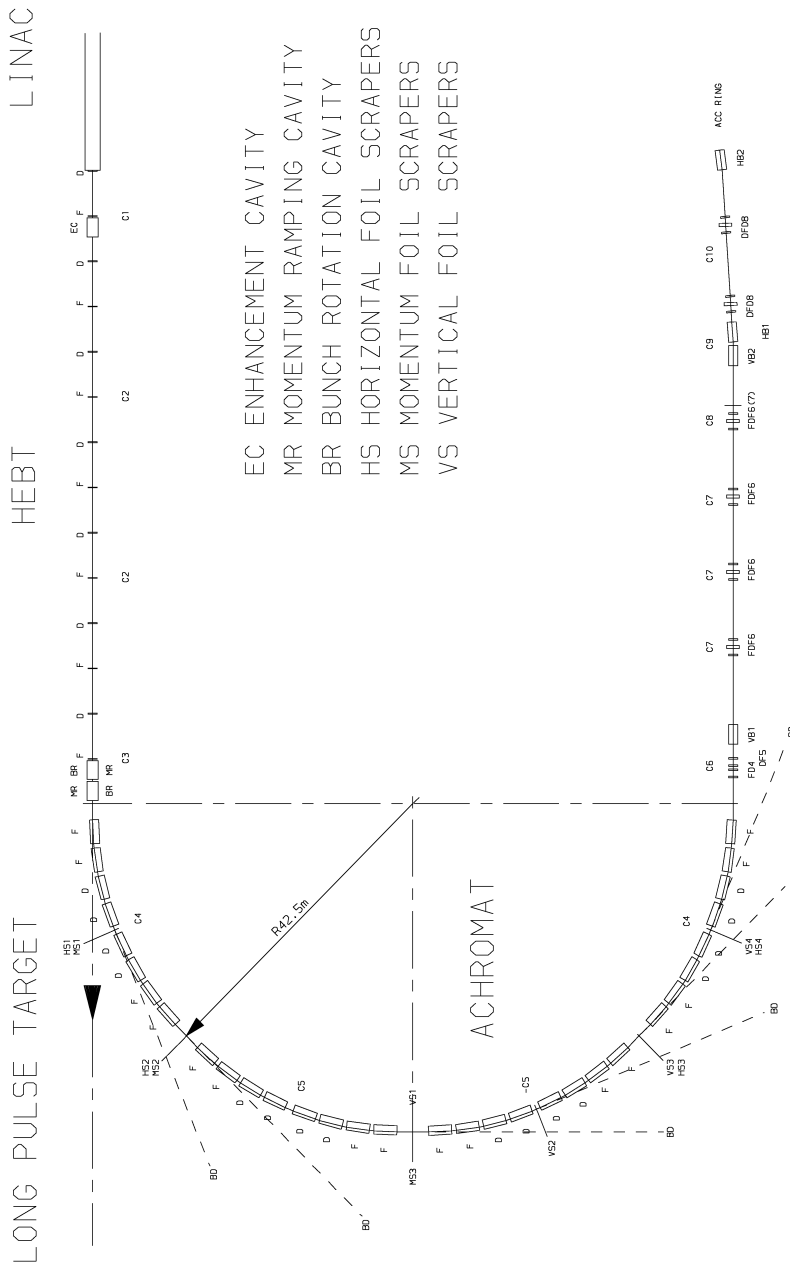


Figure 2.3.1: Schematic layout of the 1.334 GeV injection beam line

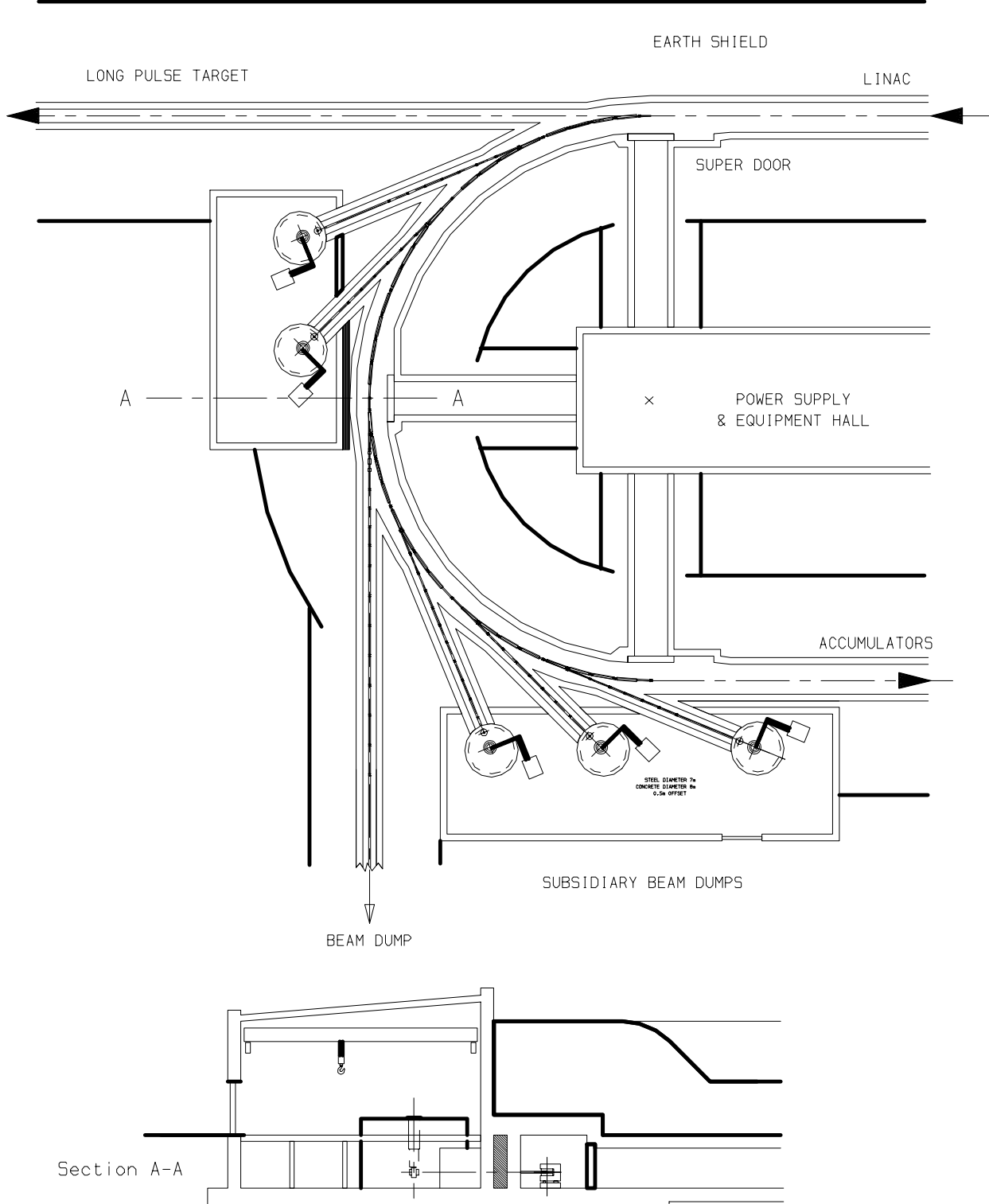


Figure 2.3.2: The Achromat Hall

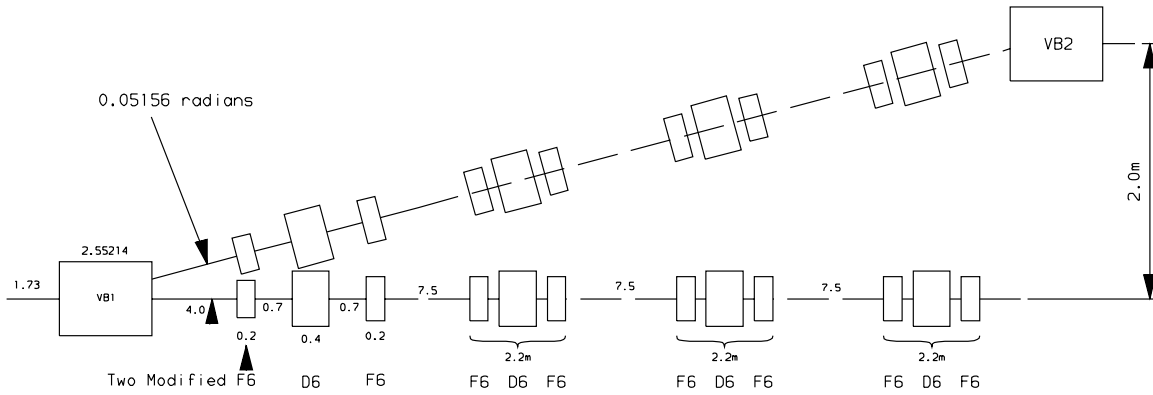


Figure 2.3.3: Vertical separation of the accumulator injection lines

The 180° achromat, of mean radius 42.5 m, has four superperiods, each with a low field triplet of combined function magnets, as in Figure 2.3.1. Betatron parameters, shown in Figure 2.3.4, are matched vertically, but not horizontally, to the adjoining sections. The horizontal dispersion is zero at input and output and a maximum at the central M3 position. The horizontal β function oscillates symmetrically through the four superperiods, with a maximum normalised dispersion at the centre point of $5.5 \text{ m}^{1/2}$. Low fields are used in the magnets to avoid pre-stripping the H^- beam and obtain the high normalised dispersion. Achromatism is obtained by the use of mirror symmetry (C4, C5, -C5, C4) about the arc centre and the use of a horizontal betatron phase shift under space charge of $\sim\pi$ radians over the first two and last two superperiods. Collimation of both sides of the beam occurs at three locations for the longitudinal and four each for the horizontal and vertical motions, as in Figure 2.3.1 which also shows one high power and five low power associated beam bumps. The two regions of momentum pre-collimation, M1 and M2, enable the magnets to have small apertures. C-shaped cores are used, open on the outer radius for ease of exit of the stripped particles. The four vertical collimators are spaced with a phase shift of 45° between each unit.

Downstream of the achromat, the line splits into two accumulator ring matching sections, with a final vertical separation of 2 m. There is initial four quadrupole matching ahead of a vertical splitting magnet, which is a pulsed dipole of fall time 100 μs . The H^- beam is either deflected into the upper vertical line or passes undeflected into the lower line after the fall time of the pulsed field. Both sections have four 90° triplet cells, followed in the upper line by a constant field vertical dipole giving an equal and opposite deflection to that of the pulsed magnet. There is 360° vertical betatron phase difference between the centres of the two vertical bend units, restoring the vertical dispersion to zero in the upper line. The final section of each line consists of a horizontal dipole magnet, two 90° DFD triplet cells and a final horizontal dipole similar to the first. The final dipole for each line is half a ring injection magnet; it acts to restore the horizontal dispersion to zero at the position of the stripping foil.

Focussing parameters under space charge are as in Figure 2.3.4. There are dual betatron waists at the foil, with $\beta_h = 5.5 \text{ m}$ and $\beta_v = 4.2 \text{ m}$, values significantly lower than the corresponding ring lattice parameters so as to optimise the injection painting [Prior,1994]. The longitudinal motion is also mismatched, with zero injection dispersion at the foil but finite ring dispersion. Transverse and longitudinal beam halo are collimated to obtain

acceptable parameters for ring injection. The average momentum offset of the injected beam is related to an equivalent offset of the rf frequency maintained in the rings throughout injection. Subsequently, the frequency is reduced to displace the injected beam from the vicinity of the stripping foil.

There is a deflection kicker just ahead of the first achromat magnet to direct the beam to the long pulse target beam line. This is described in detail in Chapter 3.

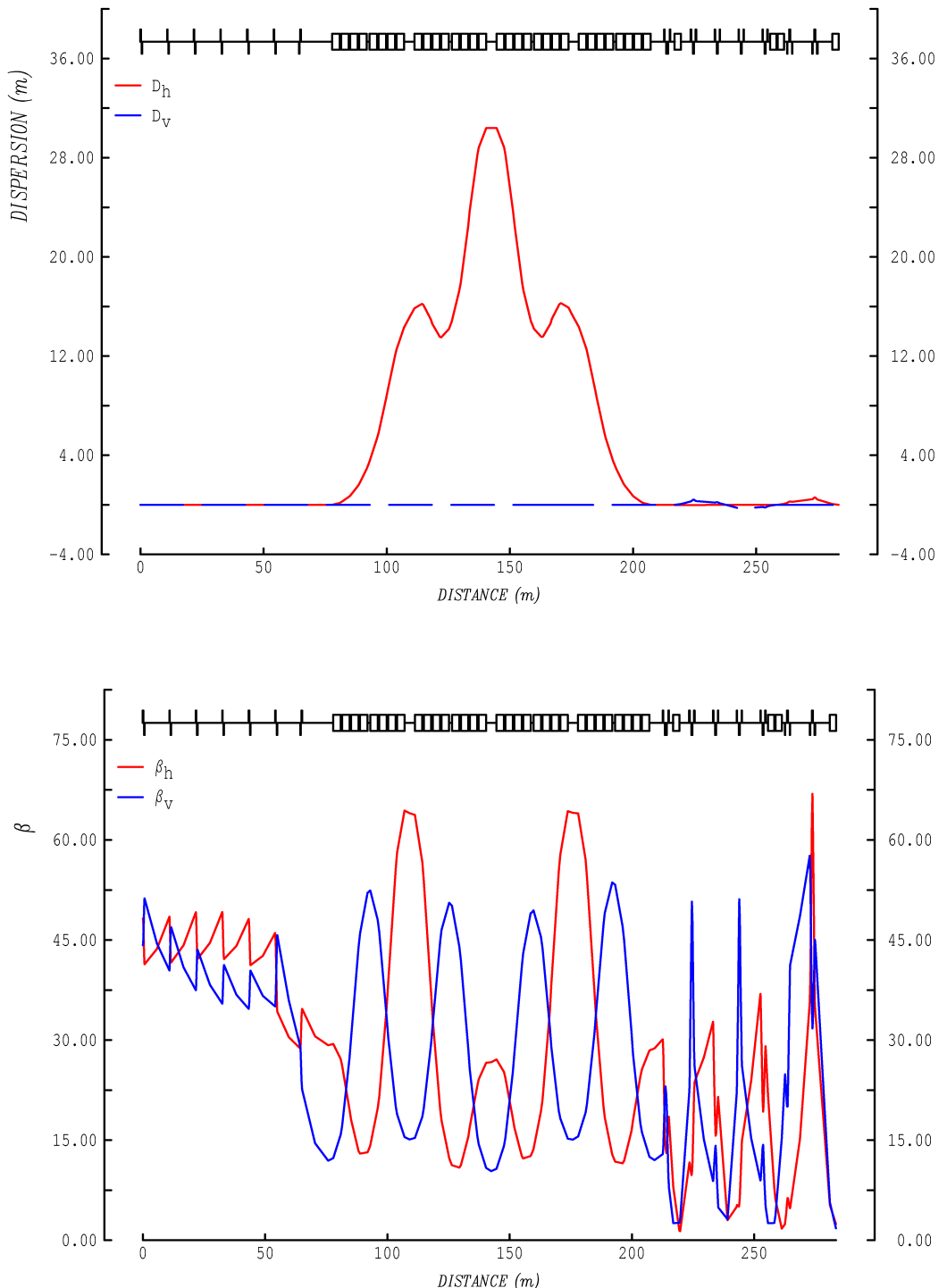


Figure 2.3.4: Focussing parameters for the 1.334 GeV beam line

2.4 ACCUMULATOR MAGNET LATTICE

Important features for the accumulator lattice are the injection and extraction regions and the use of relatively long straight sections. In particular, separate regions of zero dispersion are required for betatron collimation, fast extraction and radio frequency systems, and separate regions of high dispersion for H^- injection and momentum collimation. A bending region of high dispersion is favoured for injection as it simplifies injection and is the better choice for anti-correlated transverse painting (zero dispersion is better for correlated painting). Superperiods with an achromat and a long straight region are appropriate, and a suitable number of such superperiods is three. This is due to the 35.0 m mean radius restriction for the two rings to meet the 1.5 μ s pulse requirements of the 50 Hz spallation neutron target.

Optimised conditions for injection include the presence of a dual betatron waist at the location of the H^- stripping foil, together with a specified value for the normalised dispersion parameters. The simplest way to create these conditions is to base the lattice design around configurations of triplet quadrupoles. A first order achromat may be realised by three triplet cells incorporating dipole magnets, and the related zero dispersion region by three further triplet cells without dipoles. Using this arrangement, there are eighteen cells in the lattice.

The centre cell of the achromat has a long low field dipole, an important component for the H^- injection system, and the outer cells contain the main high field dipoles. Parallel edged units are used and these contribute some vertical edge focussing. The main dipoles are curved to reduce their steel volume, while the low field units are rectangular to satisfy injection requirements. Triplet quadrupoles have a figure of eight design to accommodate the special features of H^- injection and horizontal single turn extraction. The central D quadrupoles have a height of 1.4 m, a width of 1.08 m and a length of 0.63 m, while the outer F quadrupoles are 1.64 m high, 0.92 m wide and 0.34 m long. There are extensive end fields.

Each superperiod has mirror symmetry about the point where stripping foil parameters are specified. Only three of the six triplets in a superperiod are thus independent and only nine of the quadrupoles may be adjusted independently. These nine quadrupole gradients are set to create the zero dispersion region, to determine the betatron tunes and peak β functions and also the normalised dispersion parameters at the foil location. The betatron tunes are 4.19 for Q_h and 4.31 for Q_v . A perspective drawing of the accumulators is given in Figure 2.4.1, a layout of the components in Figure 2.4.2, and the lattice betatron and dispersion parameters in Figure 2.4.3. The β functions are low apart from in the D quadrupoles and the peak β_v value is 24.0 m. The normalised dispersion at the foil is set at $1.6 \text{ m}^{1/2}$, with D_x at 5.88 m and D'_x zero. End fields and the effects of linear space charge are simulated in the lattice programs.

There are some systematic betatron resonances near to the operating points due to the presence of only three superperiods. The most significant of these are the fourth order resonance $2Q_v - 2Q_h = 0$, which is excited by space charge forces, and the third order resonance $3Q_h = 12$, which is excited by sextupole error fields and for which there is a need for sextupole correctors. The natural lattice chromaticities are $\xi_h = -1.19$ and $\xi_v = -1.58$. The use of a large vertical injection orbit bump leads to a reduced lattice superperiodicity of one but, after injection, the bump is removed to restore the basic superperiodicity of three.

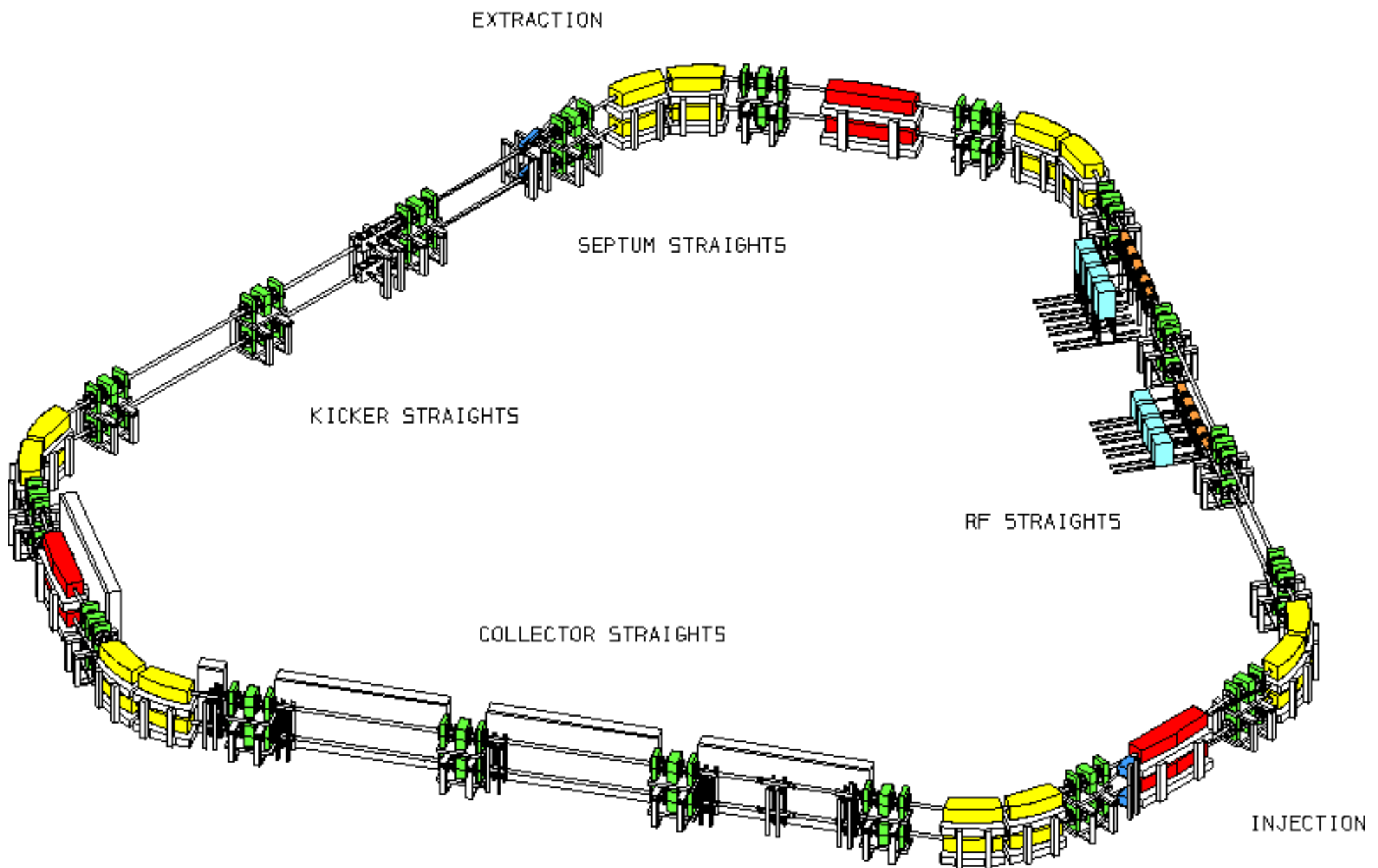


Figure 2.4.1: Perspective of the 1.334 GeV accumulator rings

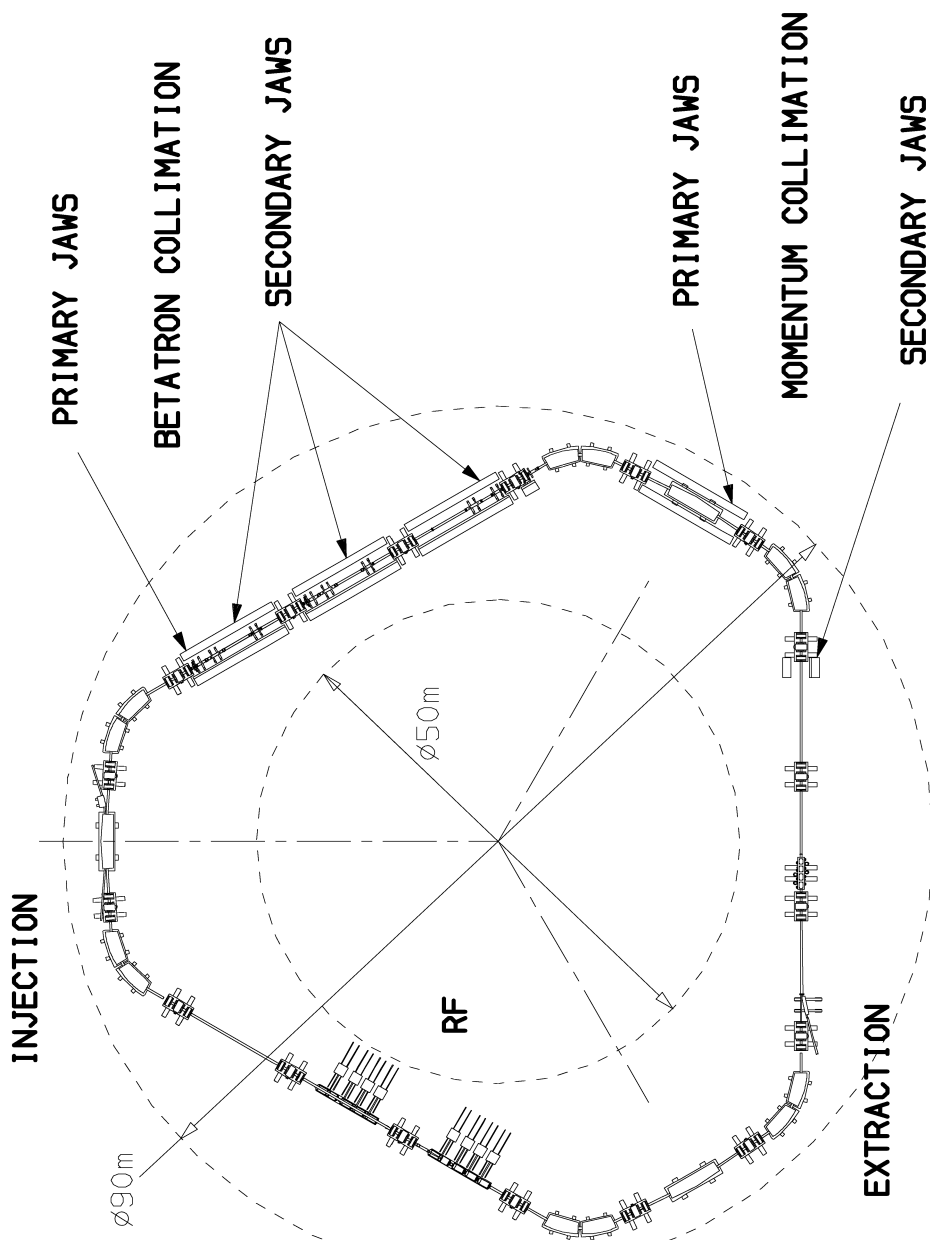


Figure 2.4.2: Layout of the components of the 1.334 GeV accumulator rings

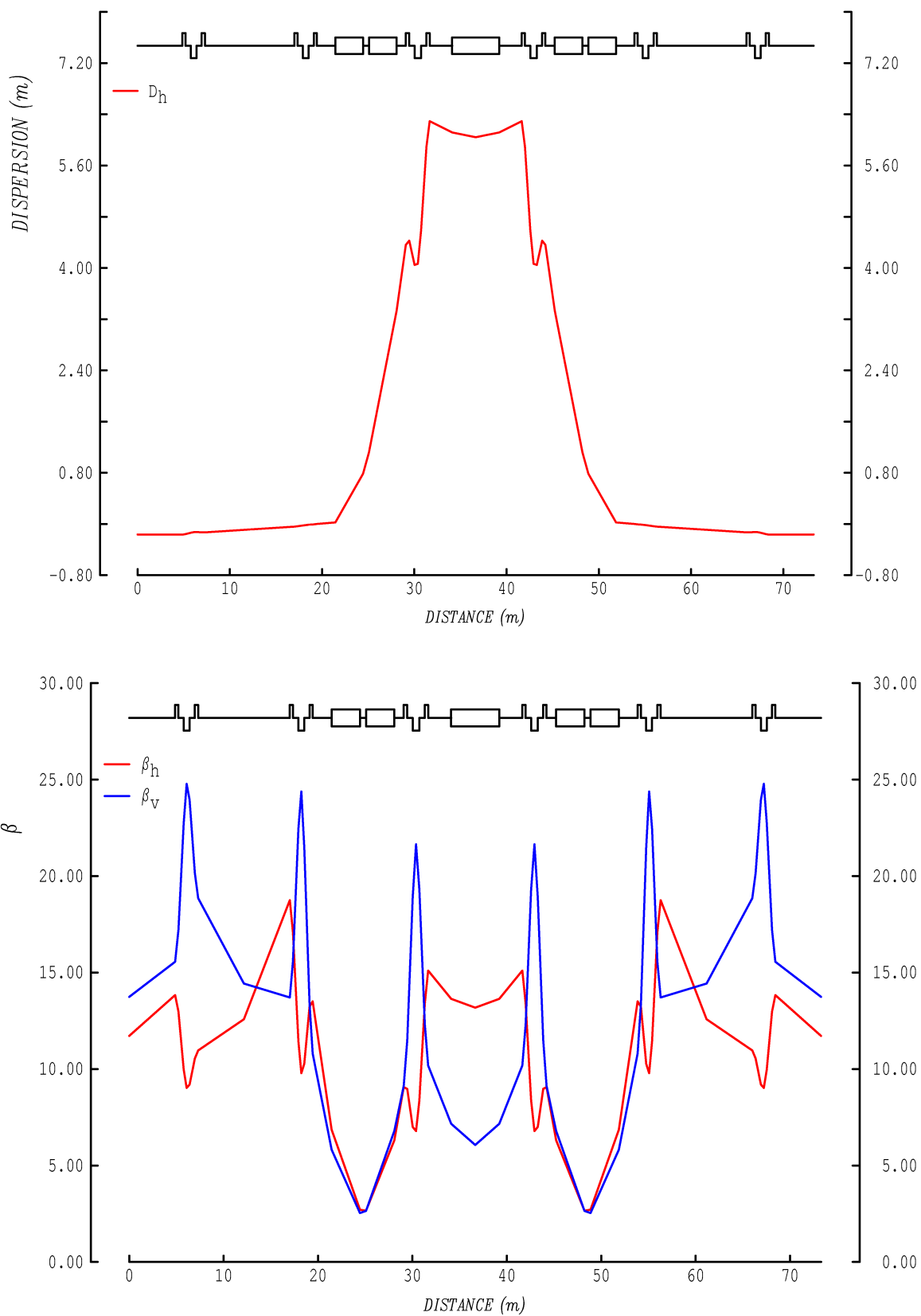


Figure 2.4.3: Focussing parameters for the 1.334 GeV accumulators

2.5 RING BEAM DYNAMICS

The 1.334 GeV linac feeds 5.1 MW of the H⁻ beam at 50 Hz to the two accumulator rings. The main beam dynamics' issues for the accumulators are beam loss effects, beam stability, space charge tune shifts, and orbit misalignments and corrections. [Bongardt, 1996] and [Rees, 1994] A discussion of the main loss effects is deferred to the sections on H⁻ charge exchange injection and on beam loss collection.

2.5.1 Beam Emittances, Acceptances and Space Charge Tune Shifts

Space charge tune shifts are estimated assuming two dimensional elliptic beam density distributions in the ring transverse (x, y) and longitudinal (W,φ) planes. Here x and y are transverse particle co-ordinates, $W = \Delta E/\omega_b$ is a particle angular momentum, φ is the related phase which is defined by a radio frequency (rf) containing system, and ΔE is the difference in energy from that of a synchronous particle of angular revolution frequency, ω_b . The elliptic distributions have the form:

$$\rho(x,y) = \frac{3\lambda}{2\pi ab} \left[1 - \frac{x^2}{a^2} - \frac{y^2}{b^2} \right]^{\frac{1}{2}}$$

$$\rho(W,\phi) = k\lambda \left[W_b^2(\phi) - W^2 \right]^{\frac{1}{2}}$$

with $W_b(\phi)$ the value of W at the beam bunch boundary, λ the line charge density, k a normalising factor, and a, b the transverse semi-axes of an assumed elliptical section.

Large transverse beam emittances are required in the rings to restrict both the transverse space charge tune shifts and the proton foil traversals during injection. The chosen values for the unnormalised rms transverse emittances, the machine acceptances and the collimator acceptances are 30, 480 and $260\pi\mu\text{rad m}$, respectively. Longitudinal emittances for the single bunch in each accumulator are set at $\sim 10\text{ eV s}$. The lattice superperiodicity of three is superior to a choice of two with respect to the proximity of systematic betatron resonances excited by space charge forces. The large emittances are chosen to restrict the maximum transverse space charge tune depressions to less than 0.07.

The tune shifts are estimated as follows. The K-V envelope equations are solved for the lattice under linear space charge for assumed values of peak circulating current and image effects, using a computer code SPACEX. The linear tune shifts are obtained, and estimates are then made for non-linear distributions. Tune shifts and spreads are determined for 2D elliptic and parabolic distributions. The injection process does not produce any particles with small betatron amplitudes in both transverse planes and the calculations reflect this feature. There is a smaller maximum tune shift for the elliptic than the parabolic distribution, but the difference is less than the central beam core densities suggest. More accurate tune shift values are obtained by detailed tracking of the injection process. The limit of 0.07 for the maximum tune depression is set to limit the effect on the charge exchange injection process.

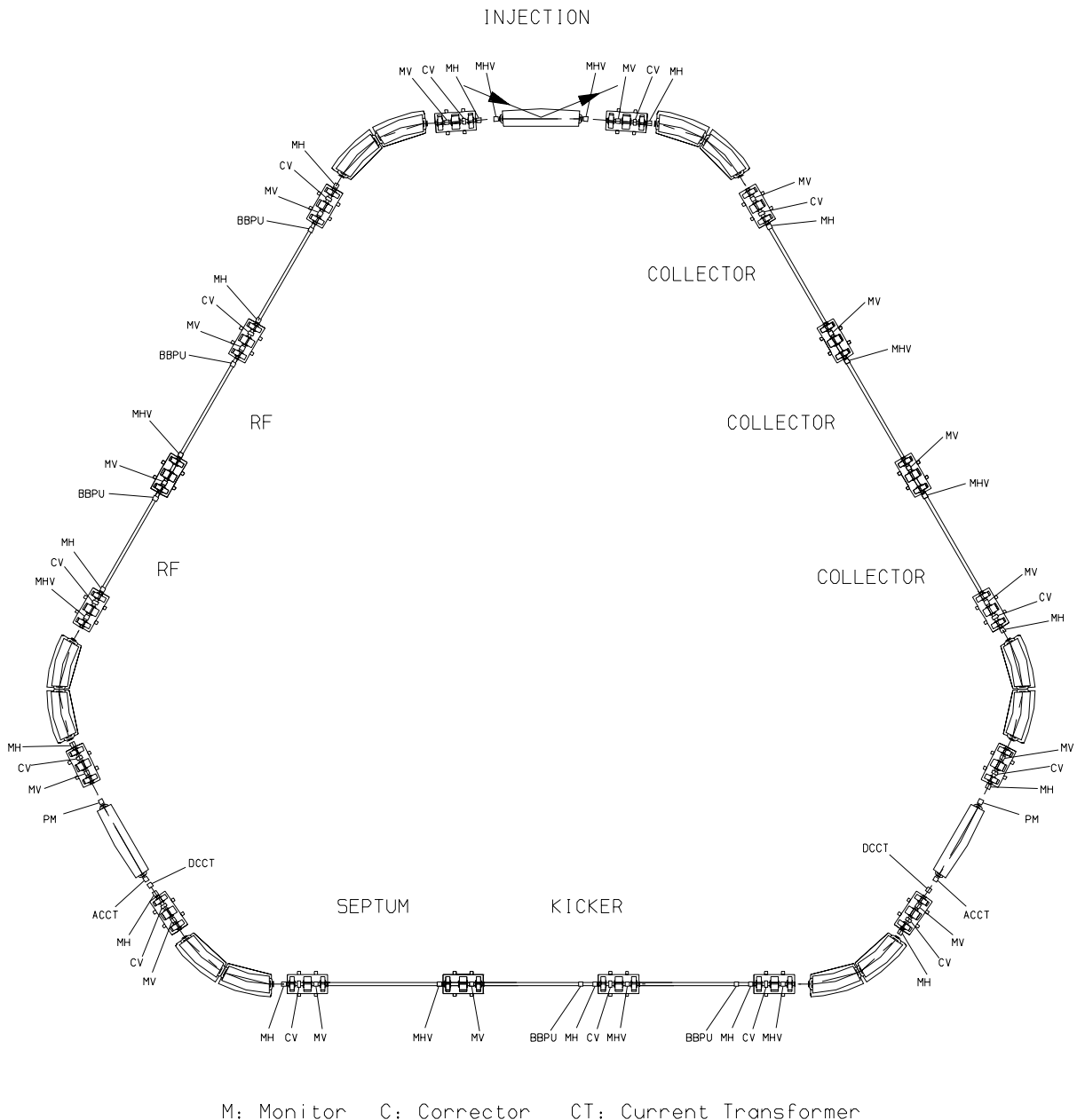


Figure 2.5.1: Closed orbit correction system

2.5.2 Closed Orbit Distortion and Correction

The lattice sensitivity to transverse misalignments, tilts and magnetic field errors has been investigated, together with an orbit correction scheme. Quadrupole transverse misalignments, dipole rotations around the longitudinal axes and dipole field errors have been introduced in the magnetic elements and random horizontal and vertical stray fields in the straight sections. It has been found that the largest effect is due to the quadrupole misalignments and that a

correction scheme may be devised which shows a good balance between the corrected closed orbit deviations and the required correction strengths.

The computer code MAD has been used for generating Gaussian random error distributions in the ring elements and calculating the resulting closed orbit. A number of different error distributions have been used, and the residual and corrected closed orbit deviation found for the monitor and corrector locations indicated in Figure 2.5.1. Each set of triplet quadrupoles in the ring has its own common support, and equal misalignment errors are assigned to the set. Small additional errors have also been assumed for individual quadrupoles within the triplet. The correction scheme uses 15 horizontal and 15 vertical closed orbit monitors, together with 7 additional horizontal-vertical monitors in the injection and extraction regions and the long straight sections. Orbit correctors include 12 horizontal back leg windings on the main lattice dipoles and 15 vertical dipole magnets, each of length 20 cm, installed at 5 cm to one side of each of 15 of the main lattice defocussing quadrupoles.

The rms values assumed for the errors in the computations are $\Delta x = \Delta y = 0.3$ mm for the quadrupole misalignments, $\Delta\phi = 0.1$ mr for the dipole rotations, $\Delta B/B = 3 \cdot 10^{-4}$ for the relative field errors in the dipoles, and 0.1 and 0.2 Gauss, respectively, for the horizontal and vertical stray fields in the straight sections. The related horizontal and vertical closed orbit deviation around the ring, before and after correction, are typically < 2 mm and < 0.2 mm rms before and after orbit correction, respectively, in the absence of monitor errors. In the case of 0.8 mm monitor errors in both transverse planes, the corrected orbits are < 0.8 mm rms, with maximum orbit displacements of up to 2 mm. The related corrector deflection angles, α , are < 0.5 mr in the horizontal plane and < 0.25 mr in the vertical.

2.5.3 Beam Stability

Effects that may disturb beam motion in the accumulators, in addition to foil scattering and betatron resonances, are single bunch longitudinal and transverse instabilities and (or) electron proton instabilities. These appear manageable despite the high ring currents, though there is some conflicting experimental evidence on the instabilities from existing rings.

Bunched beam longitudinal stability may be achieved by profiling the vacuum chamber walls and by appropriate choices for the rf containing fields, the rf control loops and the momentum painting of the injected beam. A dual harmonic rf system is proposed, with a second to first harmonic amplitude ratio, δ , in the range of 0.4 to 0.9. For stability analysis, a convenient distribution is the 2D elliptic of Hofmann and Pedersen [Hofmann, 1979], since it has a constant ratio for the longitudinal space charge to the rf focussing forces along the beam axis, with the ratio, η_{sc} , required to be < 0.4 for longitudinal stability. The ratio may be found from an instability form factor, $f \sim 1$, and the normalising factor of the 2D elliptic distribution, F , [Duke, 1994]:

$$\eta_{sc} = Ne h^2 g / 2\epsilon_0 R \gamma^2 f F V < 0.4$$

$$F = 2(\sin \phi - \phi \cos \phi) - 0.5 \delta (\sin 2\phi - 2\phi \cos 2\phi)$$

where Ne is the charge per bunch, the harmonic number h is one, g is the longitudinal space charge geometry factor, ϵ_0 is the permittivity of free space, R is the mean ring radius, V is the voltage amplitude of the $h = 1$ rf field and ϕ is half the phase extent of the bunch.

The dominant beam coupling impedance, $Z/n = -j gZ_0/2\beta\gamma^2 = -j 62 \Omega$, is that due to the space charge, with $Z_0 = 377 \Omega$, and $g = 1.75$ for the profiled vacuum chamber wall. The negative inductance drops by about one half at the chamber cut off frequency of 1800 MHz. A value of $\eta_{sc} = 0.4$ corresponds to a high frequency single bunch instability, whose growth time depends on the resistive and reactive beam coupling impedances at the instability frequency. The longitudinal instability is avoided by choosing V at 26 kV, when the $\Delta p/p$ value is $\sim \pm 6 \cdot 10^{-3}$ and η_{sc} is well below the threshold level of the instability. A dual harmonic rf system has been selected as it improves both the longitudinal injection painting and the transverse beam bunching factor. The further complexity of a barrier bucket rf system does not appear justified. Operation is below transition, as at ISIS, where it is observed that the residue of the linac bunch structure in the circulating beam during injection is damped in 50 μs even when operating an order of magnitude above the instability threshold. The discrepancy from traditional theory may be due to coupling between slow and fast instability waves.

Transverse bunched beam instabilities are of more concern than longitudinal, and fast instabilities may arise due to the combined effects of transverse space charge forces, transverse wall impedances and coupled electron-proton motion. The space charge forces remove the Landau Damping, and coherent transverse motion may be anti-damped due to both the resistive components of impedance and the delayed effects in the electron-proton interaction.

The dominant ring impedance is that due to transverse space charge and it is larger than the coasting beam threshold impedance for many coasting beam modes, n , at the peak circulating beam current, I , of 95 A and the chosen full $\Delta p/p$ width, at half I peak, of $\sim 6 \cdot 10^{-3}$:

$$RZ_0 \left(\frac{1}{a^2} - \frac{1}{b^2} \right) \frac{|j|}{\beta^2 \gamma^2} > \frac{\pi F Q \beta \gamma E_0}{e I R} \left| (\xi Q + \eta(n-Q)) \frac{\Delta p}{p} \right|$$

where Z_0 (free space impedance) is 377Ω , a and b are the average beam and aperture radii, β and γ are relativistic factors, γ_r is the ring transition energy, η equals $(\gamma_r^{-2} - \gamma^2)$, Q is the relevant The dominant ring impedance is that due to transverse space charge and it is larger than the betatron tune, F is the form factor of the transverse beam distribution and ξ is the ring chromaticity in the relevant transverse plane.

The unstable ($n-Q$) coasting beam modes have n values up to ~ 145 , corresponding to mode frequencies up to 180 MHz. Instabilities grow from noise and the largest noise components are due to the residue of the linac bunch structure in the injected beam. Fortunately, the ESS linac bunch frequency is 560 MHz and the fundamental and higher harmonic components lie in the stable ($n-Q$) mode region. For lower frequency modes, concern exists only if growth times are significantly less than the occupancy time in the ring, which is ~ 1 ms. Underestimates of growth times may be found by neglecting Landau damping through:

$$\tau = \frac{Q e \gamma Z_0}{I r_p R_\perp}$$

where r_p is the classical proton radius and R_\perp the real part of the transverse impedance. The main transverse impedances are (in units of $k\Omega/m$):

Space charge	(-2260 + 50)j
Resistive wall (copper or aluminium)	~ 5j + 5 (maximum)
Extraction kicker (see section 2.8)	~ 25j + 5 (maximum)
Broad band (at 50 Hz)	~ 25j + 10

The estimated growth times are then at the safe level of ~ 1 ms. To these slow growth rates, however, must be added the effect of the electron-proton interaction; hence, space will be made available for the possible inclusion of collimation clearing electrodes and instability damping systems [Galluccio, 1996].

Vertical and horizontal head-tail instabilities are not expected to occur since the beam is in the rings for less than a synchrotron period and, even at reduced chromaticities, there are large chromatic head-tail coherent phase shifts for the long bunch circulating in each ring. At the natural chromaticities, the chromatic phase shifts are:

$$\psi_{v,h} = (\xi Q)_{v,h} \omega_o \tau \eta^{-1} = 2\pi(41), 2\pi(26)$$

where ω_o is the ring angular revolution frequency and τ is the total bunch duration. There is stability against coherent head tail motion for the mode numbers $m < \psi/2\pi$ so vertical modes up to mode number 41 and horizontal modes up to mode number 26 are stable if the rings are operated at the natural values of the chromaticities.

2.5.4 Electron-Proton (e-p) Instability

The e-p interaction is the most serious instability issue for the ESS rings. Electrons are formed by ionisation of the residual gas and by secondary emission at the vacuum chamber walls. The (so-called) electron cloud interacts with the single proton bunches in each ring in a more complex way than if the beam were unbunched. The electrons in or near the beam take time to respond to coherent proton beam motion, and antidamping forces arise because the attractive forces on the protons, due to the electrons, are proportional to the proton displacements of an earlier instant in time. The oscillation frequency of the electrons changes continually and the oscillation amplitudes are greater than those for the protons. Frequencies are at a maximum when the peak of the bunch passes and are small when the gap is adjacent.

An e-p type instability studied at the PSR proton storage ring at LANL has received much attention at recent e-p workshops [Macek, 2001], but the exact instability mechanism remains in doubt. Observations at the PSR include: coherent vertical motion at frequencies in the range up to 250 MHz, with growth times of ~ 50 μ s, a lowering of the instability threshold for reduced rf containing fields, wall conditioning effects, large signals induced on two 4 m, 50Ω deflector plates in the ring, prompt and delayed motion of electrons to the chamber walls after passage of the proton bunch, and the survival of a roughly constant number of electrons at the time the bunch returns after one ring revolution.

Electrons that leave from the trailing edge of the bunch pass rapidly to the walls and produce copious, prompt, secondary emission electrons. The yield depends strongly on factors such as proton beam intensity, secondary emission coefficients, proton beam losses and gas pressure, but it does not appear to be related to the instability thresholds. The secondaries produce tertiaries with a high reflectivity for those in the 2 to 5 eV low energy range, and many

electrons survive until the proton bunch returns. The number surviving corresponds to neutralization levels in the range 1 to 1.5 %, a range that is more in keeping with the observed thresholds. Titanium nitride wall coatings are proposed to reduce the numbers of prompt secondaries, but it remains to establish if the numbers of surviving electrons are also reduced, as this may be of more relevance for the instability.

In contrast to the situation at the PSR, no coasting or bunched beam e-p instability has been found in the ISIS synchrotron [Rees, 1999], despite achieving a higher coasting (but not bunched) beam density. Differences between the rings are thus of interest and these include, for ISIS in comparison with the PSR: proton beam losses confined mainly to the collimation region, larger acceptances, shielded bellows, lower impedance kicker units, and vacuum chamber walls which are profiled at an approximately constant ratio to the beam radii, with rectangular and not elliptical cross- sections. These design features of ISIS are to be included in the ESS rings, together with titanium nitride wall coatings, lower vacuum pressures and special e-p diagnostic devices such as those used at the PSR:

- Biased collector plates, for use inside the magnets [Macek, 2001],
- (RFA) Retarded field analysers [Rosenberg, 2000],
- Electron sweeping detectors for measuring surviving electrons [Macek, 2001]

2.5.5 Profiling of the Vacuum Chamber Wall

There are disadvantages and advantages to profiling the vacuum chamber wall. The disadvantages are the added complexity of construction, including that for shielding the bellows sections, and the increase in the resistive component of the transverse wall impedance, which scales inversely as the cube of the chamber radius. However, it is believed that these disadvantages are outweighed by the following advantages:

- a) The reduced value for the transverse reactive space charge impedance.
- b) The reduced value for the longitudinal space charge impedance, as characterised by the reduced longitudinal g-factor.
- c) The reduced values required for the rf containment due to the reduced g-factor.
- d) The reduction in the external betatron tune spread required to provide coherent transverse stability.
- e) The reduced beam potential, due to the lower g values, for the trapping of the electrons involved in coherent e-p interactions.
- f) The easier escape of the e-p electrons to the walls, due to their closer proximity.
- g) The reduction in the number of prompt secondary electrons produced by primaries due to their reduced velocity when striking the closer proximity walls.

2.5.6 Instability Suppression

There is some partial stabilisation against fast transverse instabilities due to the finite beam momentum spread and the associated betatron tune spreads. Additional methods for providing transverse stability include:

- a) Inclusion of octupole magnets to enhance the beam tune spreads.
- b) Application of fast, low delay, coherent feedback.
- c) Fast variation of the betatron tunes, as used at ISIS [Rees, 1999].
- d) Fast clearing of protons from the beam gap by betatron excitation.

2.5.7 Correction Magnets

It is proposed to include or prepare for correction dipoles (see 2.5.2), quadrupoles, sextupoles and octupoles. Fast trim quadrupoles require ceramic vacuum chambers, and space is reserved for them in the long straight sections.

Sextupoles are required to compensate for sextupole error fields in the lattice dipoles, and are best located adjacent to these magnets. Chromaticity correction sextupoles are not considered necessary because the chromatic and space charge tune spreads are < 0.04 and < 0.07 respectively, operation is below the ring transition energy, and the chromatic tune spreads are considered worth retaining. The situation is different in the 1 GeV, SNS ring where the tune spreads are much larger and the working Q area is limited. Octupoles may provide additional tune spreads, (± 0.1), to combat instabilities, and space is reserved for them in the long straight sections. It is not planned to install them unless other means fail to cure fast instabilities.

2.6 H⁻ CHARGE EXCHANGE INJECTION

Injection is at a point of high ring dispersion as noted in section 2.4. The injection region is shown in Figure 2.4.2, Figure 2.6.1 and Figure 2.6.2, and the choice of field at 0.177 T in the central dipole magnet is important. It is chosen to give negligible pre-stripping of H⁻ ions ahead of the foil, to minimise delayed stripping of H⁰ atoms in the ring, and to provide a bending radius for stripped electrons large enough for direct collection (Figure 2.6.2(c)).

A 540 $\mu\text{g cm}^{-2}$ graphite foil is chosen which strips $\sim 98\%$ of the H⁻ beam to protons, leaving the rest mainly as partially stripped H⁰ atoms in a range of quantum states. The fate of these depends on their Stark state in the injection magnet. Energy levels for states of principal quantum number $n = 4, 5$ and 6 are given in Figure 2.6.2(a) as a function of electric field; the vertical dashed lines are the E-field equivalents for different B-field options with the design value labelled option 2. Atoms of low n (< 4) remain as H⁰ and may be removed from the ring; atoms of high n (> 6) strip rapidly and are accepted as protons; there remain some intermediate states which strip after some delay, so may be accepted or lost or become halo. The atomic physics is discussed in [Damburg, 1983], and a semi-empirical formula is derived for the Stark state lifetimes; those for states $n = 4$ and $n = 5$ are plotted in Figure 2.6.2(b) for 1.334 GeV H⁰ atoms. There is a gap in the graph between the $n = 4$ and $n = 5$ states, and the chosen field of 0.177 T is within this gap. Direct transitions between the two states bordering the gap and the stripped state are forbidden, so the effective gap is enhanced.

Simultaneous ‘painting’ is provided in the longitudinal and both transverse planes. Horizontal and longitudinal painting results from the use of finite normalised dispersion at the foil ($1.6\text{m}^{1/2}$), together with input beam momentum ramping. Vertical painting is obtained by programming the field in four vertical bump magnets, located between the injection cell quadrupoles, so as to separate the ring and injection optics. The excitation currents are reduced to move the vertical orbit bump from 31.5 mm to zero in ~ 1 ms, which is twice the injection interval. The peak and average powers of 14 and 5 MVA, respectively, are inversely proportional to the cube of the length ℓ shown in Figure 2.6.1. The beam cross section at the foil and the associated electron collector are given in Figure 2.6.2(d), with the latter outside the collimator defined acceptances. The entry of H⁻ beam into the ring, and the removal of

unstripped H^- and H^o particles, are both eased by the figure of eight ring quadrupole design. Removal is achieved using a second stripping foil and two downstream 1.2 T septum magnets, as shown in Figure 2.6.3 and Figure 2.6.4.

Injection is the main source of beam loss and hence is a critical item for the rings; it is due to this that the H^- beam is collimated in the injection line. The main ring loss is then caused by H^- and proton traverses of the stripping foil during and after injection. Every effort is made to minimise these by using a foil with two free unsupported edges. Four associated loss mechanisms occur: delayed stripping of excited H^o atoms, inelastic collisions, multiple scattering, and changes in proton momentum. Assuming one H^- and two proton (on average) foil interactions per particle for the ~ 600 turn injection, the first three loss mechanisms are estimated to total 0.005%, and the fourth, 0.008%. The last loss mechanism is due to enhanced horizontal betatron motion, caused by the scattering tail in the momentum distribution and the finite dispersion at the foil. The resulting loss is localised in the collimation section downstream, after a 180° betatron phase shift of the motion.

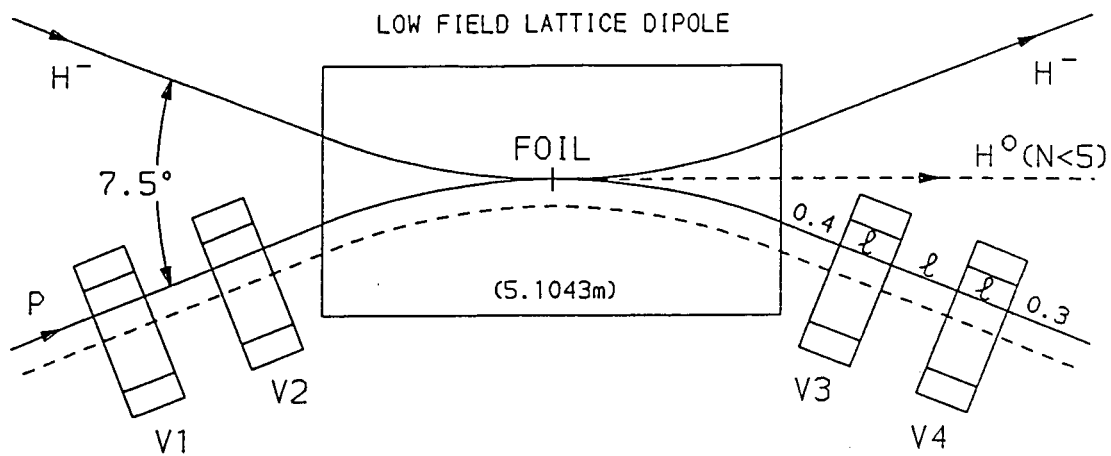
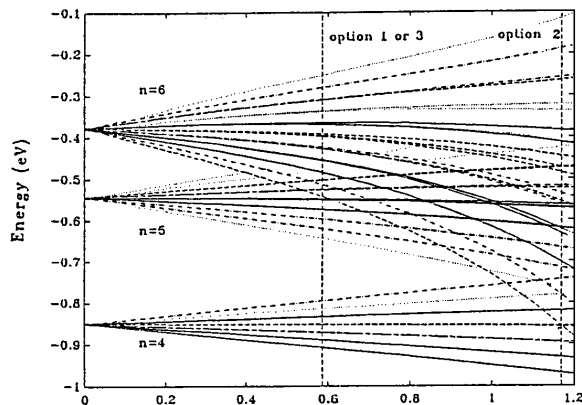
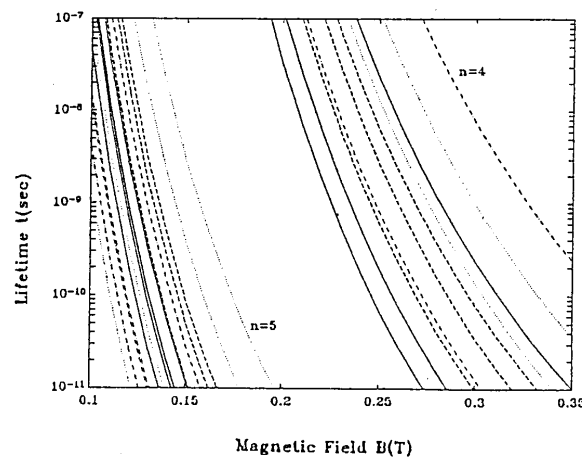


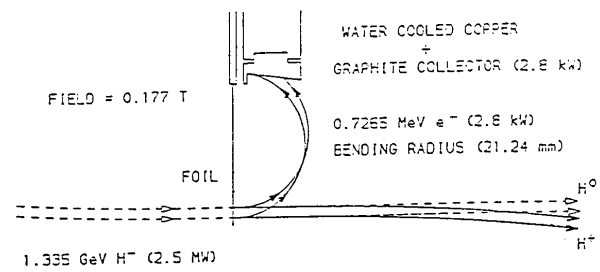
Figure 2.6.1: H^- injection straight section



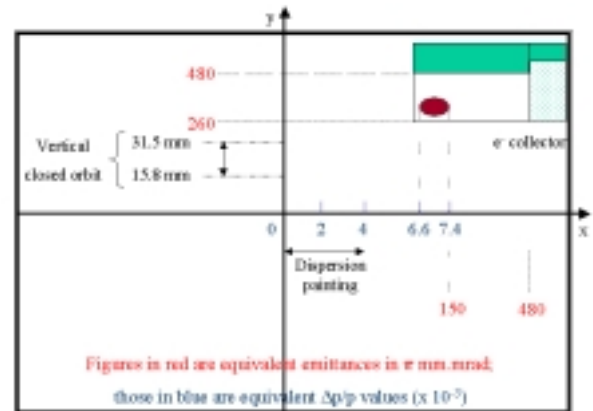
(a)



(b)



(c)



(d)

Figure 2.6.2: (a) Energy levels of Stark states; (b) Stark state lifetimes in laboratory frame; (c) Electron collection following stripping; (d) Cross section at stripping foil

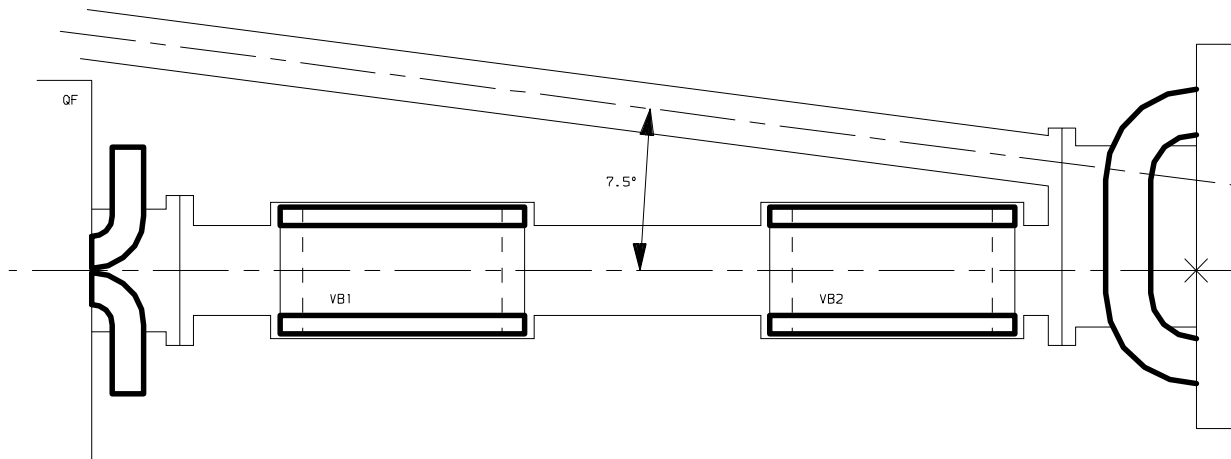


Figure 2.6.3: H^- injection

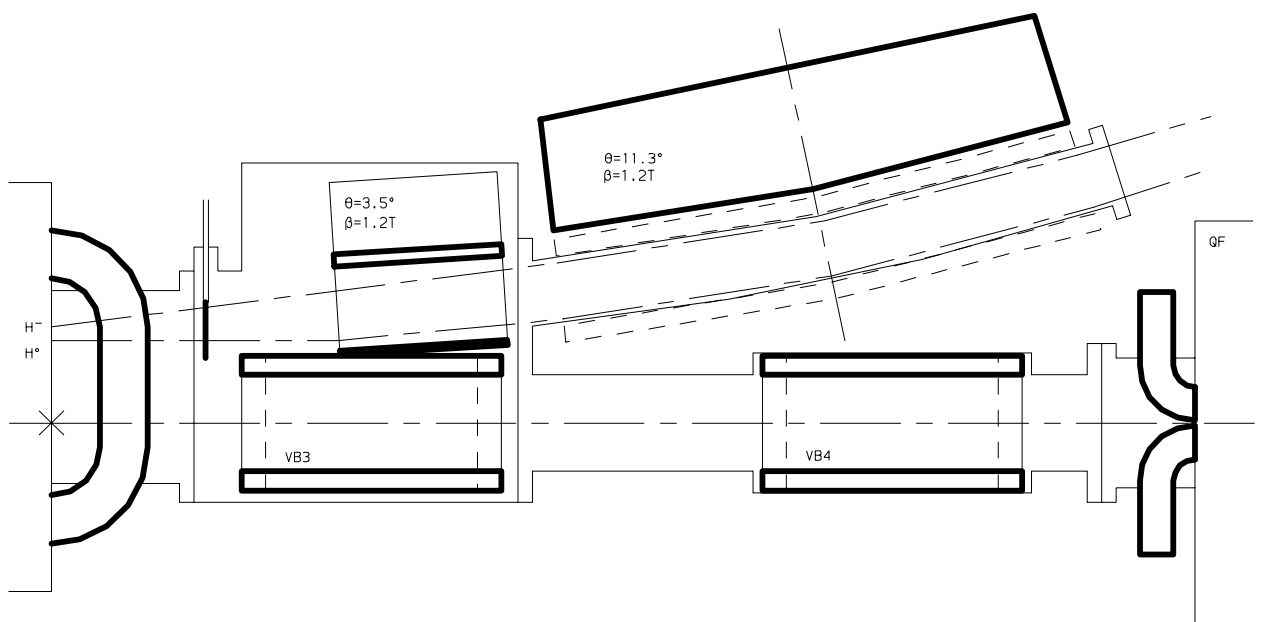
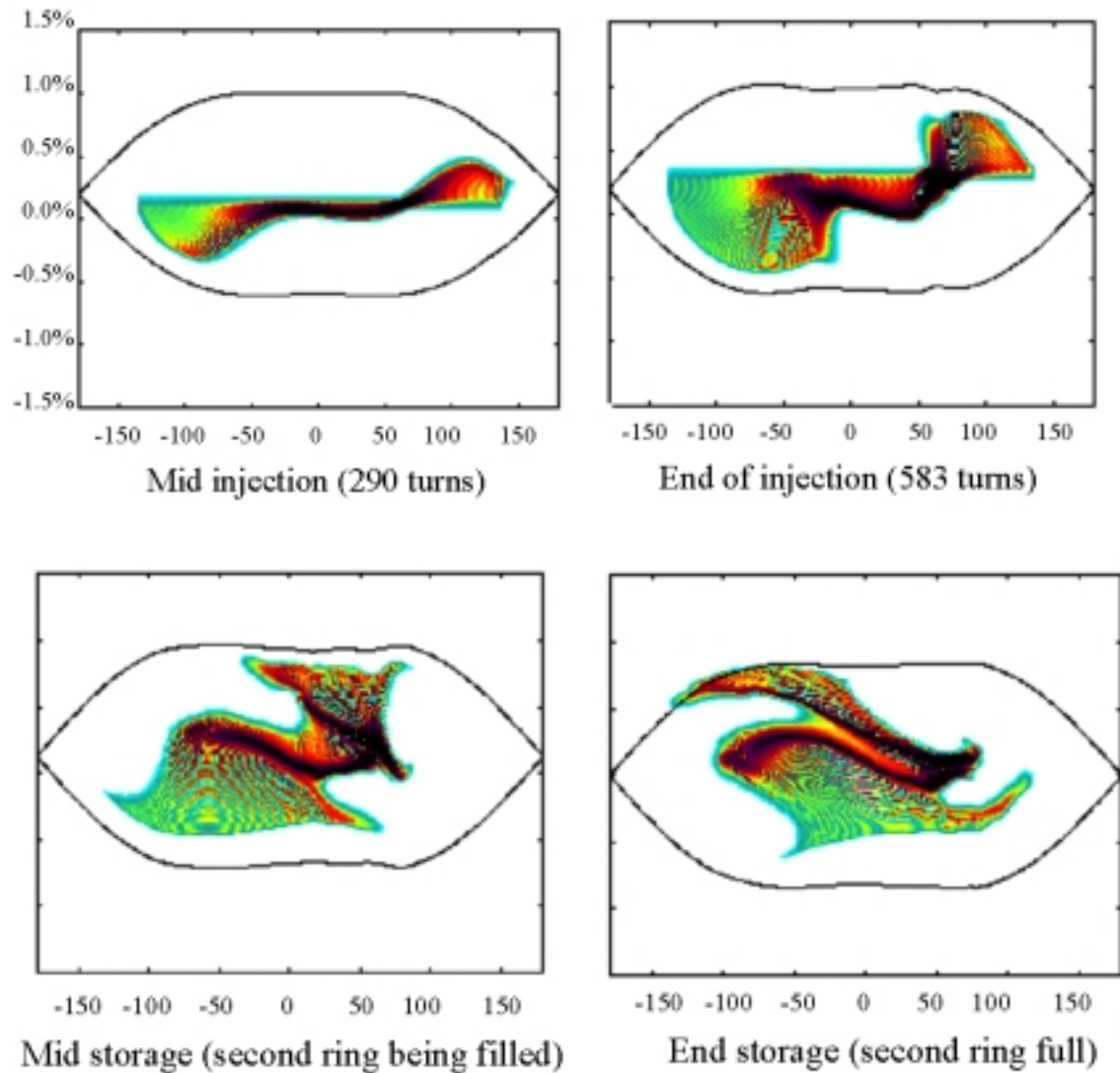


Figure 2.6.4: Removal of unstripped beam



Longitudinal injection. Plots of momentum spread v. phase. A linac momentum spread of $\pm 5 \cdot 10^{-4}$ is assumed

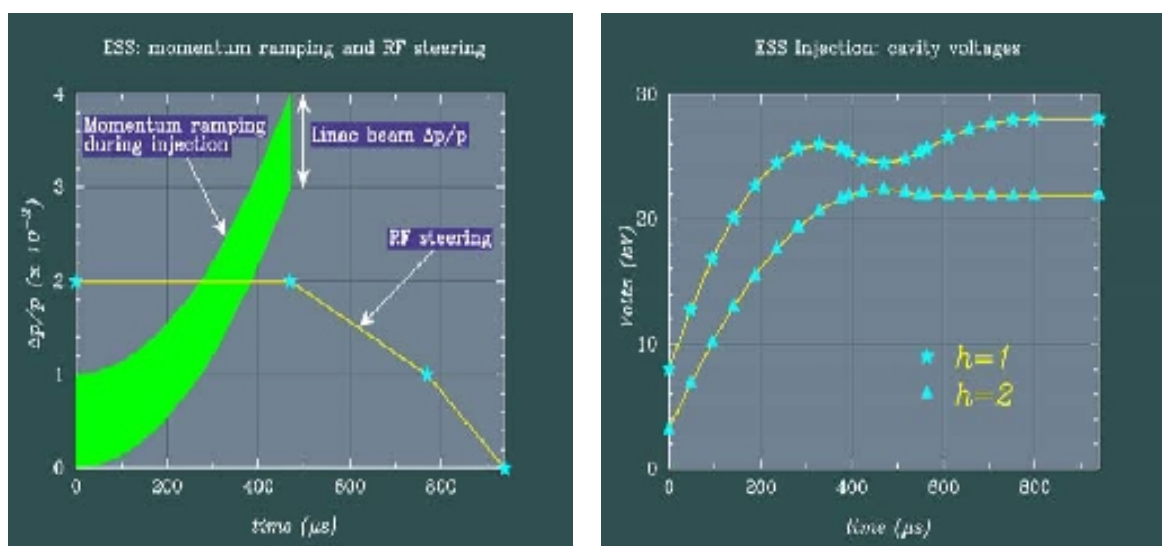


Figure 2.6.5: Longitudinal injection painting

2.6.1 Longitudinal Painting

Longitudinal phase space painting is assisted by the 70 % chopping of the linac beam at the ring revolution frequency and also by amplitude modulation of the dual harmonic RF fields. The preferred parameters for injection are derived by repeated use of modelling codes, which simulate the process using multi-particle techniques taking full account of non-linear space charge in the beam [Prior, 1994]. Injection schemes have been successfully evaluated for a range of linac output emittances and foil spot sizes, but here only the process corresponding to the normal conducting 280/560 MHz linac is described. $2.34 \cdot 10^{14}$ protons must be accumulated in each of the two rings, corresponding to between 580 and 600 injection turns over a period of ~ 0.5 ms. During injection, incoming beam of fractional momentum spread $\pm 0.5 \cdot 10^{-3}$ is ramped linearly from an initial momentum offset $\Delta p/p$ of $0.5 \cdot 10^{-3}$ to $3.5 \cdot 10^{-3}$, as shown in Figure 2.6.5. RF steering is then used, with the injection frequency of 1.2419 MHz (corresponding to a natural particle momentum $\Delta p/p = 2 \cdot 10^{-3}$) reduced linearly to 1.2417 MHz and finally to the synchronous revolution frequency 1.2416 MHz. The effect is to fill the lower half of the stable phase space region during the initial stages of injection and, under momentum ramping, to inject progressively into the upper region during the later stages of the cycle. RF steering finally directs the beam towards the centre of the aperture. Total peak cavity voltages, which rise to a maximum of 28 kV before being reduced and held at 27 kV to contain the beam, are determined from the simulations. The modelling results are detailed in Figure 2.6.5, which shows plots of beam momentum spread against longitudinal phase at the mid-point of injection (0.25 ms), at the end of injection (0.5 ms) and at two subsequent times while the beam is trapped. During the latter phase, the second ring is filled. The choice of voltages enables momentum ‘arms’ emerging from the ends of the bunch to be folded back into the body of the beam and controls the longitudinal distribution. Colour is used in the plots to indicate the levels of charge, ranging from the highest concentration (black) at the centre to the lowest (cyan) at the edge. The resulting bunch does not exceed 600 ns in duration, all injected particles are trapped and both the average and final beam bunching factor (peak:average current) are > 0.4 .

2.6.2 Transverse Painting

Horizontal phase space painting is dictated by the method of filling longitudinal space through momentum ramping, with the dispersion zero for the incoming beam but non-zero for the ring injection point. Four bump magnets are programmed to adjust the vertical closed orbit for vertical painting and to minimise the average number of proton traversals through the foil. This has a bearing on the method of RF steering described above. The resulting oscillation amplitudes vary as injection proceeds from large to small in the horizontal plane and from small to large in the vertical plane. This anti-correlation is the most favourable for reducing foil traversals and helping to minimise the injection dipole acceptances. The process has been modelled using a two-dimensional multi-particle tracking code. Neglecting space charge effects, an incoming beam with 3σ unnormalised emittances of $1.06 \pi \mu\text{rad.m}$ generates a stored beam of $150 \pi \mu\text{rad.m}$. Turns are mismatched into the ring, with $\beta_h = 5.5$ m and $\beta_v = 4.2$ m corresponding to $\beta_h = 13.5$ m and $\beta_v = 6.4$ m in the machine, and with the injection point dispersion at $D_x = 5.88$ m. Under space charge, the ring lattice parameters alter slightly. Modelling indicates that foil traversals may be reduced to below one on average per proton after the initial H^- transit, providing safe operating temperatures for the foil, despite hot spots near the inner corner. Figure 2.6.6 shows how individual turns mix within the beam. Emittances, particularly in the horizontal plane, are correspondingly

increased. The effects of space charge are otherwise not marked, but the tracking simulations continue to be optimised.

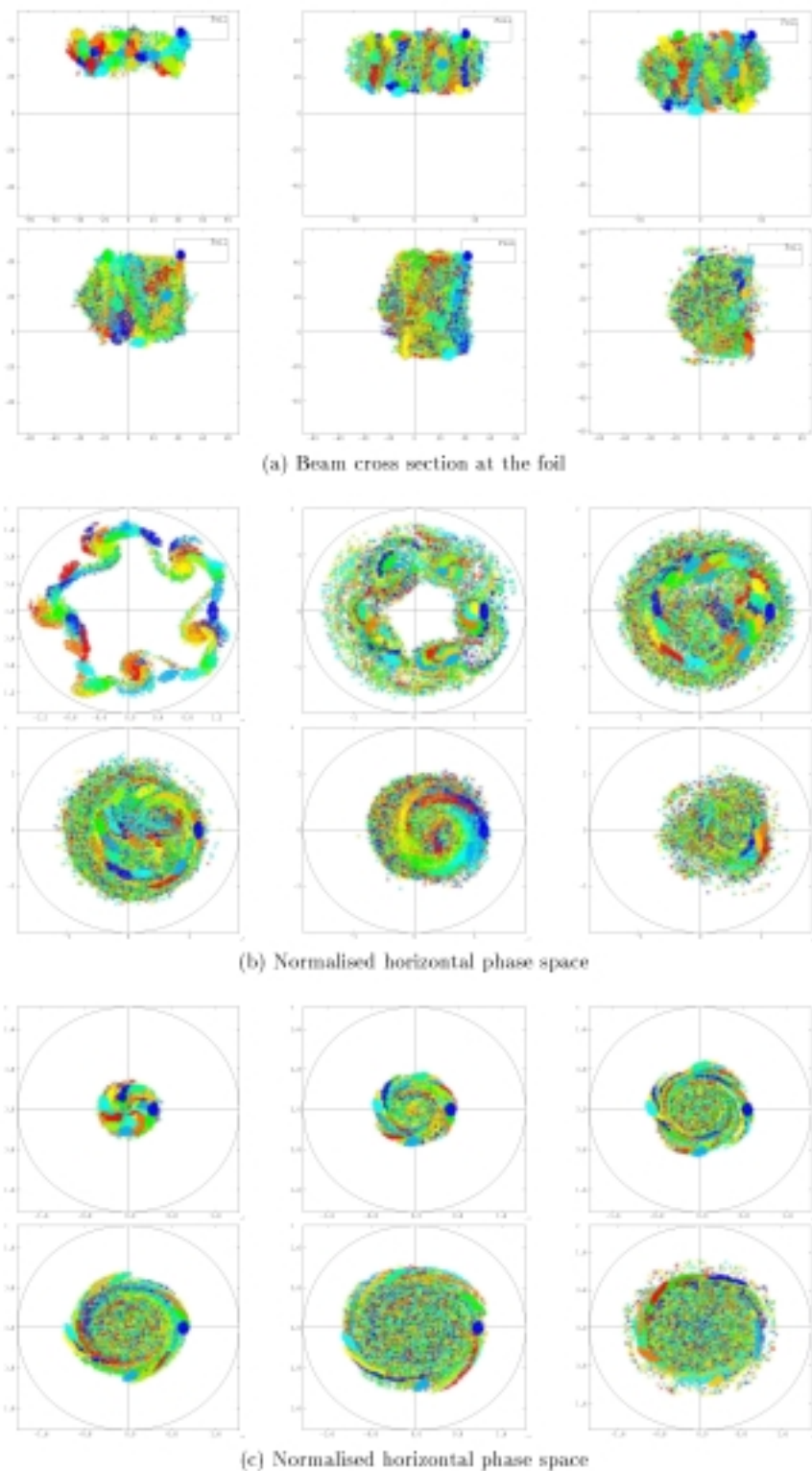


Figure 2.6.6: Transverse injection painting

2.6.3 Stripping Foil Temperatures

Aluminium oxide (Al_2O_3) and graphite have been studied as possible stripping foil materials for the ESS. The foil is to be rectangular, 42.5 mm wide and 14.3 mm high, supported on two sides only to reduce the number of subsequent foil transits by re-circulating protons. A foil mass per unit area of $540 \mu\text{g cm}^{-2}$ is chosen, corresponding to a thickness of $2.0 \mu\text{m}$ for Al_2O_3 and $3.5 \mu\text{m}$ for graphite. The input beam is centred 6 mm from the open foil corner and has an elliptical transverse boundary with radial and vertical beam semi-axis of 2.45 and 2.10 mm, respectively. Other relevant input parameters are a ~ 580 turn injected beam of 2.34×10^{14} particles per pulse at a 50 Hz repetition frequency and a $470 \mu\text{s}$ pulse duration.

Injected H^- ions, stripped electrons and re-circulating protons scatter in the foil and large temperature rises result from atomic excitations and ionisation. The initial rate of temperature rise is inversely dependent on the foil specific heat. The temperature cycles at 50 Hz, with a maximum at the end of injection which is limited mainly by radiation cooling, but with a small foil conduction. A constant peak temperature is reached after approximately five beam pulses. Power losses due to radiation and conduction scale as the fourth and first power, respectively, of the temperature difference from the surroundings, and in proportion to the foil emissivity and thermal conductivity, respectively. The specific heat, emissivity and thermal conductivity are all material and temperature dependent.

Heating and cooling of the ESS foil have been simulated in a program described in [Duke, 1996]. Input H^- beam and re-circulating proton distributions at the foil have been based on the injection tracking studies, and have been entered in the program as the charge incident on each element per turn. Energy deposited in the foil is calculated using charged particle energy loss data, both for protons and stripped electrons. For the H^- ions, one electron is assumed to strip on entry into the foil and the other at the midpoint. High temperature estimates for specific heat have been made by scaling normalised Debye curves in both dimensions to give a best fit with published data. Asymptotes used for the specific heats at high temperatures are 1289.3 and $2125 \text{ J kg}^{-1} \text{ K}^{-1}$ for aluminium oxide and graphite, respectively. Emissivities have been assumed constant at 0.4 for aluminium oxide and 0.825 for graphite. Thermal conductivities have been approximated by:

$$\begin{aligned} 4.765 + 2664470 T^{-1.9496} &\quad \text{for } \text{Al}_2\text{O}_3, \\ 15.0 + 305.958 T^{-1.3091} &\quad \text{for graphite with } T > 573^\circ\text{K}, \text{ and} \\ 217.965 - 0.223325T &\quad \text{for graphite with } T < 573^\circ\text{K}. \end{aligned}$$

Results of the simulations for one proton foil traversal on average after the initial H^- transit show a peak temperature in the Al_2O_3 foil of $< 2400^\circ\text{K}$, with that in the graphite 1880°K , with the difference due to the larger emissivity and specific heat for the graphite. The emissivity of Al_2O_3 may rise with temperature, but even if it reaches 1.0, the peak temperature could still be close to the melting point of 2320°K . Graphite has a melting point of 3823°K and so is a safer material to use for the ESS foils. More careful studies of possible hot spots in the foil are to be made.

2.7 RADIO FREQUENCY SYSTEM

A dual harmonic rf system is proposed for the rings, using the harmonic numbers one and two. This arrangement is preferred to a barrier bucket type system because the peak voltage requirements are significantly less, the beam loading compensation is simpler, and radial beam steering is more readily introduced. Both systems improve the beam bunching factor, but the extra gain for the barrier system is not considered to warrant its extra complexity. The dual harmonic rf voltage, V , is defined for a second to first harmonic amplitude ratio, δ :

$$V = V_0 (\sin \omega_0 t - \delta \sin 2\omega_0 t)$$

The injected beam is chopped at the ring revolution frequency of 1.24 MHz, and the rf system acts to contain the injected protons. The accumulators are filled sequentially, and after each injection interval, the rf system is used to steer the beam to the vacuum chamber centre. In each ring, V_0 is raised from 8 to 26 kV during injection, then increased to 28 kV and subsequently decreased to 27 kV as shown in Figure 2.6.5. The ratio, δ , is adjusted from 0.4 to 0.9 during injection painting and is then kept constant. Extraction is synchronised for a one turn delay between the two rings, 1.1 ms after the start of injection for the first, and 0.5 ms for the second. A time of 200 ns is preserved for each circulating bunch to accommodate the rise time of the fast extraction kicker magnets.

Cavities loaded with capacitors, resistors and ferrite are used to provide the rf fields, and it is proposed to use, for each ring, three single gap, $h = 1$ cavities and one double gap, $h = 2$ cavity. Arrangements of the cavities in the rings, which are separated vertically by 2 m, are shown in Figure 2.7.1, with an isometric projection in Figure 2.7.2. Schematic diagrams are given in Figure 2.7.3 and Figure 2.7.4, respectively, for the $h = 1$ and $h = 2$ cavities. Both cavity types are ferrite loaded, using similar ferrite, having an initial relative permeability of ~ 100 .

The $h = 1$ cavities are 1.4 m long, each with 25 ferrite toroids. A cavity resistance of $1 \text{ k}\Omega$ is obtained by loading the cavity gap with a copper sulphate liquid resistor whose concentration may be changed to vary the resistance. Gap capacitance is added to combat the high reactive loading of the 51.0 A fundamental component of beam current. A value of 4000 pF provides for $Q = 32.0$ and $R/Q = 31.3 \Omega$. To minimise the required generator current in injection and storage, a fixed cavity detuning is used of about 75 % of that needed for full reactive compensation at maximum current. Detuning is obtained by controlling the field in a solenoid winding around the ferrite. The resulting peak current in the power amplifier used with each cavity is < 18 A for the fundamental component, and this may be controlled by feed forward techniques. The use of rf feedback has been assumed unnecessary. The maximum gap voltage required is 9.3 kV peak, and the mean power delivered by the high voltage power supply, for cavity losses and anode dissipation, is < 15 kW per cavity system.

The $h = 2$ cavity is 2.7 m in length and has two sections, each containing 24 ferrite toroids. The design follows that of the ISIS cavities, with liquid resistors and ceramic vacuum capacitors again loading the two gaps. The cavity is tuned by controlling the current through a one turn, figure of eight, bias winding around the two ferrite stacks. The second harmonic component of beam current is small and the cavity is kept on tune. The maximum voltage on each gap is 12.5 kV peak and the generator current is comparable with that for a $h = 1$ cavity. The rf system parameters are summarised in Table 2.7.1.

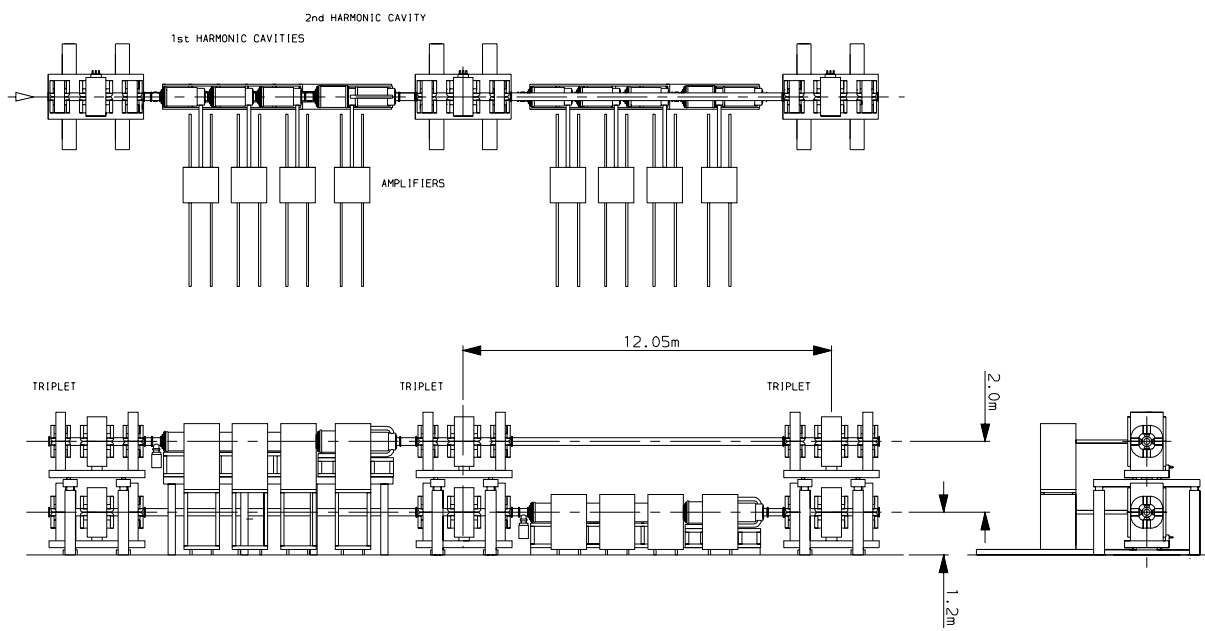


Figure 2.7.1: RF cavity layout

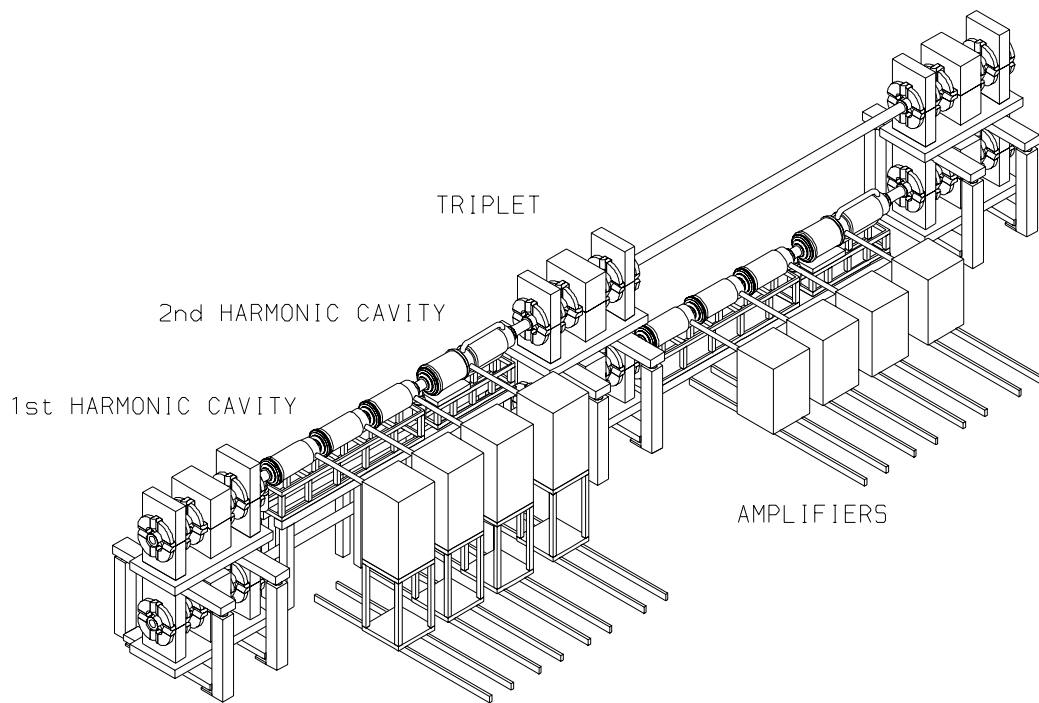


Figure 2.7.2: Perspective of rf cavities

Table 2.7.1: Ring rf system parameters

Dual harmonic numbers, h	1 and 2
Revolution frequency (MHz)	1.2416
Peak kV/turn at injection	8 to 22
Peak kV/turn during storage	28 to 27
Ratio $V(2h)/V(h)$ at injection	0.4 to 0.9
Number of $h=1$ cavities per ring	3
Length of $h=1$ cavities (m)	1.4
Number of ferrite toroids per $h=1$ cavity	25
Q for $h=1$ cavity	32.0
R/Q for $h=1$ cavity	31.3
Number of $h=2$ cavities per ring	1
Length of $h=2$ cavities (m)	2.7
Number of ferrite toroids per $h=1$ cavity	48
Number of circulating protons per ring	$2.34 \cdot 10^{14}$
DC component of beam current (A)	46.55
Beam bunch duration at ejection (μ s)	0.6
Pulse duration at target (μ s)	1.4

Three single gap cavities, one double gap cavity and two vacuum pumps all fit in a 9.72 m straight section between adjacent triplets in one arm of a ring. Upper and lower rings have the cavities displaced as shown in Figure 2.7.2. Crane access to the cavities in the lower ring is provided by removing the beam pipe above them. The power amplifiers are coupled directly to the cavities and are located in housings on the inside of the rings. The amplifier housings are mounted on rails so that they may be easily retracted to facilitate the servicing of both the cavities and amplifiers. The same design of housings is used for both rings, with those for the upper ring raised on plinths.

In the power amplifier housings are water-cooled 250 kW tetrodes and the associated passive circuitry. All the necessary control and diagnostic devices are located in annular service tunnels separated from the rings by shielding walls to protect the electronic units from the operational radiation levels. The use of this arrangement also minimises the cabling costs. The equipment comprises [Barratt, 1996]:

- a) The anode, screen, grid bias and filament supplies for the tetrodes.
- b) The 2 kW solid-state amplifiers for driving the grids of the tetrodes.
- c) The control electronics for tuning the fundamental cavity.
- d) The bias current supplies for tuning the $h = 1$ and $h = 2$ cavities and associated control electronics.
- e) The control electronics for the feedforward beam-loading compensation systems.
- f) The beam control electronics for the frequency, amplitude and relative phases of the cavity voltages.
- g) The controls for varying the concentration of the liquid resistors, and
- h) Diagnostic instrumentation for the rf systems.

Experience with the development and operation of the comparable ISIS synchrotron rf system has provided invaluable guidelines for the design of the system. However, it is proposed that the cavity designs be confirmed by the construction and testing of prototypes and the

performance under beam loading be confirmed by simulation or by measurements using hardware to simulate a full intensity beam.

Suitable power supplies for the high power tetrodes are available from a number of commercial sources, and it is expected that this will also be the case for the driver amplifiers. The cavity tuning systems and the other control electronics, as well as the diagnostic instrumentation, need special design and development but such systems are familiar in accelerator control engineering.

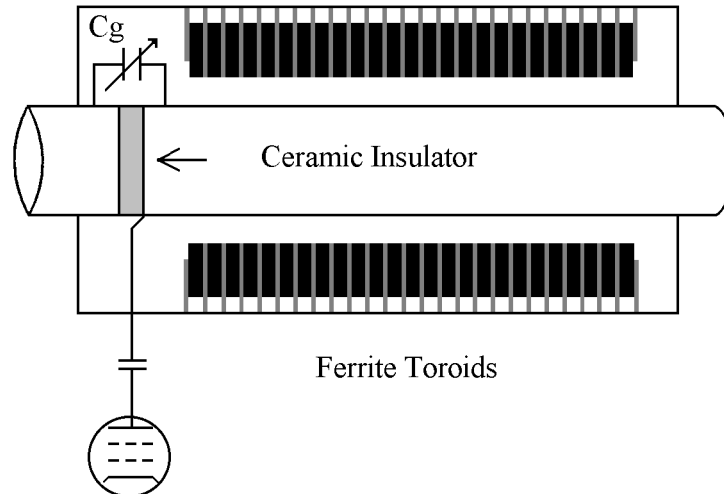


Figure 2.7.3: Schematic diagram of $h=1$ cavity

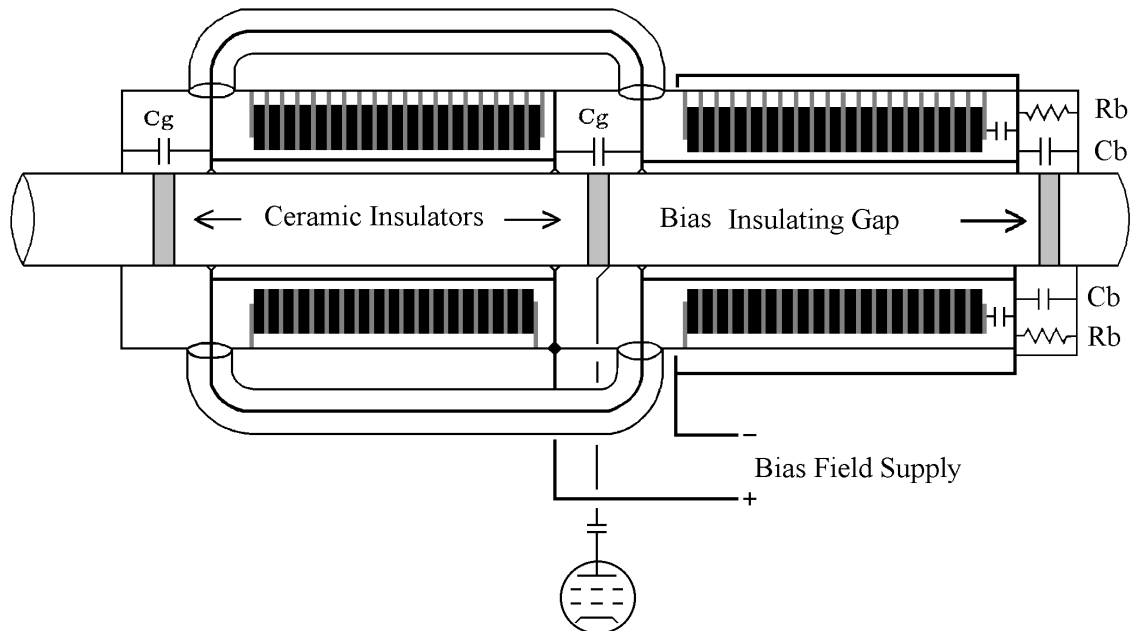


Figure 2.7.4: Schematic diagram of $h=2$ cavity

2.8 FAST EXTRACTION SYSTEM

Each ring has single turn beam extraction in the horizontal plane from a dispersion free region, with fast kicker magnets placed upstream of a quadrupole triplet, and a septum extraction magnet approximately one cell downstream. A perspective of the fast kicker magnets is shown in Figure 2.8.1 and the extraction septum magnets are shown in Figure 2.8.2. Parameters for this arrangement are:

Un-normalised 100 % extraction emittance	260	(π) μ rad m
Total deflection angle	14.1	mr
Required 99 % field rise time	< 190	ns

After optimising the lattice for extraction, a choice has to be made of kicker magnet type to use with the large beam current. High beam induced voltages result if conventional delay line kickers are used; instead, lumped kickers are chosen, in a push-pull configuration, with a central ground plane to limit the induced fields. The same magnet lengths are involved in both types of kicker, but the induced voltages are much reduced for the chosen system. There is the disadvantage, however, that two pulsing systems are required in place of one for each module. Three such push-pull kickers are used at ISIS [Boardman, 1982], together with six pulser systems. These numbers increase to four and eight, respectively, for each ESS ring, assuming similar voltage, current and impedance levels.

Vertical and horizontal apertures for the kickers are set by acceptance conditions, but the horizontal apertures of the downstream kickers are increased to allow for the extraction deflection. Individual kicker lengths are adjusted to give equal kicker inductances, so the pulser systems are the same for all modules, and have the same rise times. The kicker arrangement is shown in Figure 2.8.3(a), and the ISIS pulser system in the upper part of Figure 2.8.3(c). A coaxial thyratron switch connects a lumped pulse forming network (PFN) and speed up network (SUN) with an impedance, Z_0 , in parallel with a feed cable, Z_0 , which passes to a half kicker. The feed cable is then back terminated with respect to the beam passing through the kicker, though there is a doubling of the thyratron current. Voltage levels for the ISIS PFN are 40 kV, the thyratron currents are 5000 A and seven 50 Ω cables are used in parallel for the feeder cable. Similar values are chosen for the ESS but six 50 Ω cables are used in place of seven for the feed cables to give a Z_0 value of 8.33 Ω .

The termination, Z_0 , is removed and the peak thyratron current reduced for an alternative pulser arrangement shown in the lower half of Figure 2.8.3(c). There is a saturating inductor, SI, inserted between the feed cable and half kicker, which has a SUN in parallel. A low beam coupling impedance is retained by the presence of the SUN (1250 pF and 5 Ω) and the SI, which isolates the kicker from the pulser when the thyratron switch is open. The SI also serves to reduce the effect of the thyratron displacement current [Barnes, 1992]. PSpice simulations for the system voltages are shown in Figure 2.8.3(b), for the kicker current in Figure 2.8.3(d), and for the thyratron current in Figure 2.8.3(d). These show improved waveforms in comparison with the ISIS pulser, and the initial thyratron current is halved. The results need to be confirmed on an R&D model, with a dump switch thyratron included, to remove the reflected pulses. Thyratron lifetimes should increase as a result of the halving of the current. Beam induced voltages remain to be evaluated; measurements at frequencies up to a few MHz are needed for the coupling impedances as these are larger than in the ISIS system. Mechanical engineering for the kickers follows the proven ISIS design.

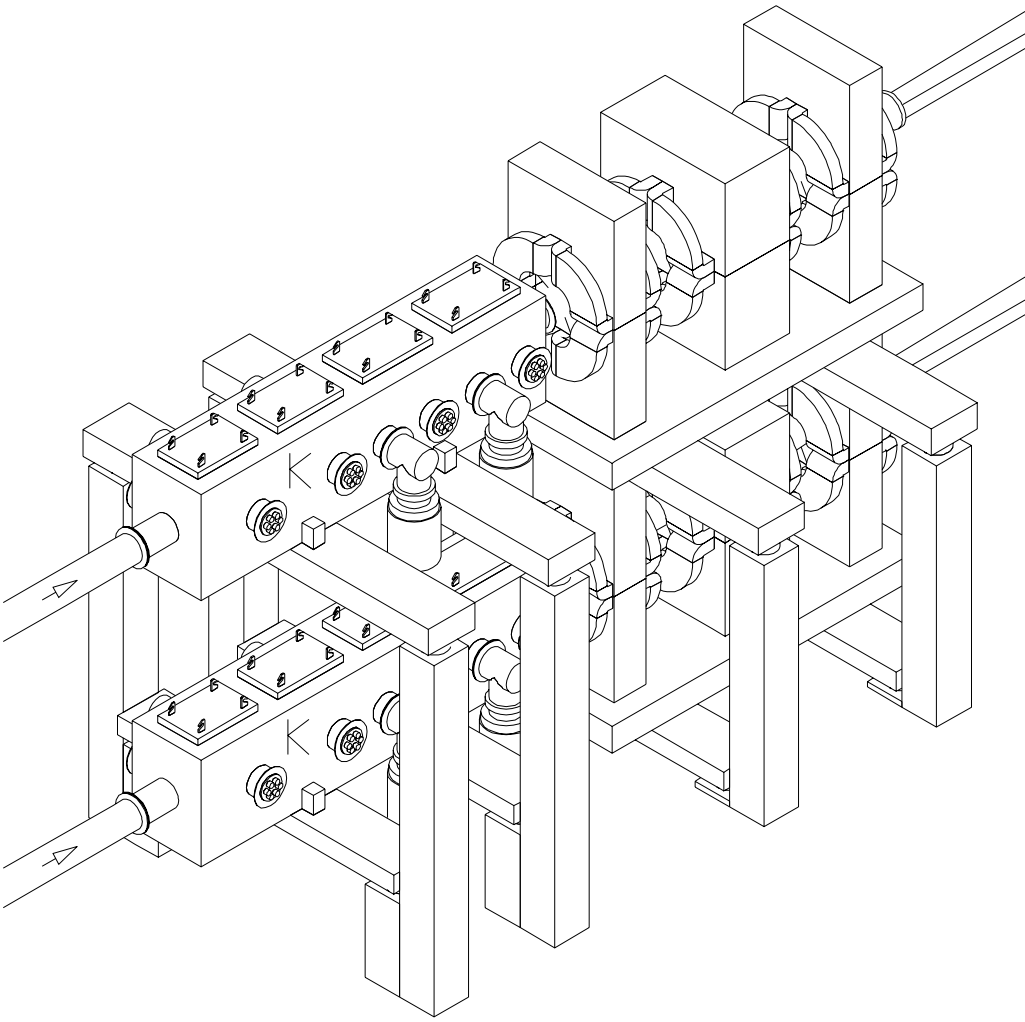


Figure 2.8.1: Perspective of fast extraction kicker magnets, *K*

The bunch in each ring is deflected off-axis horizontally by pulsing the kicker magnets. Downstream, each deflected bunch passes through triplet quadrupoles into a horizontal dc extraction septum magnet that bends the beam out of the ring (see Figure 2.8.1 and Figure 2.8.2). Beam clearances are maintained through extraction at acceptances $> 260 \pi \mu\text{rad m}$. The septum magnet is based on that of the ISIS vertical extraction unit, which has a similar length and field [Boardman, 1982] though a different deflection angle due to the different proton energies.

The ESS septum magnet has a field of 1 T, a bending radius of 6.903 m, an arc length of 1.754 m and a deflection angle of 14.562° relative to the horizontal axis. The location in the 9.72 m long straight section is with the exit point 0.75 m upstream of a set of triplet quadrupoles. At the input of the first F quadrupole of this triplet, the horizontal beam displacement is 560 mm, the beam half width is 62 mm, while the half width of the figure-of-eight F quadrupole is 460 mm, allowing ample clearance. Design objectives for the septum magnet include:

- a) The beam deflection should be constant to within $\pm 0.1\%$ over the aperture;
- b) The operating temperature of the septum conductors must not exceed 90°C ;

- c) It must split around the extracted beam vacuum pipe for ease of removal;
- d) The yoke and coils must be insulated with radiation resistant materials; and
- e) The integrated external field on the ring beam must be < 1 gauss m.

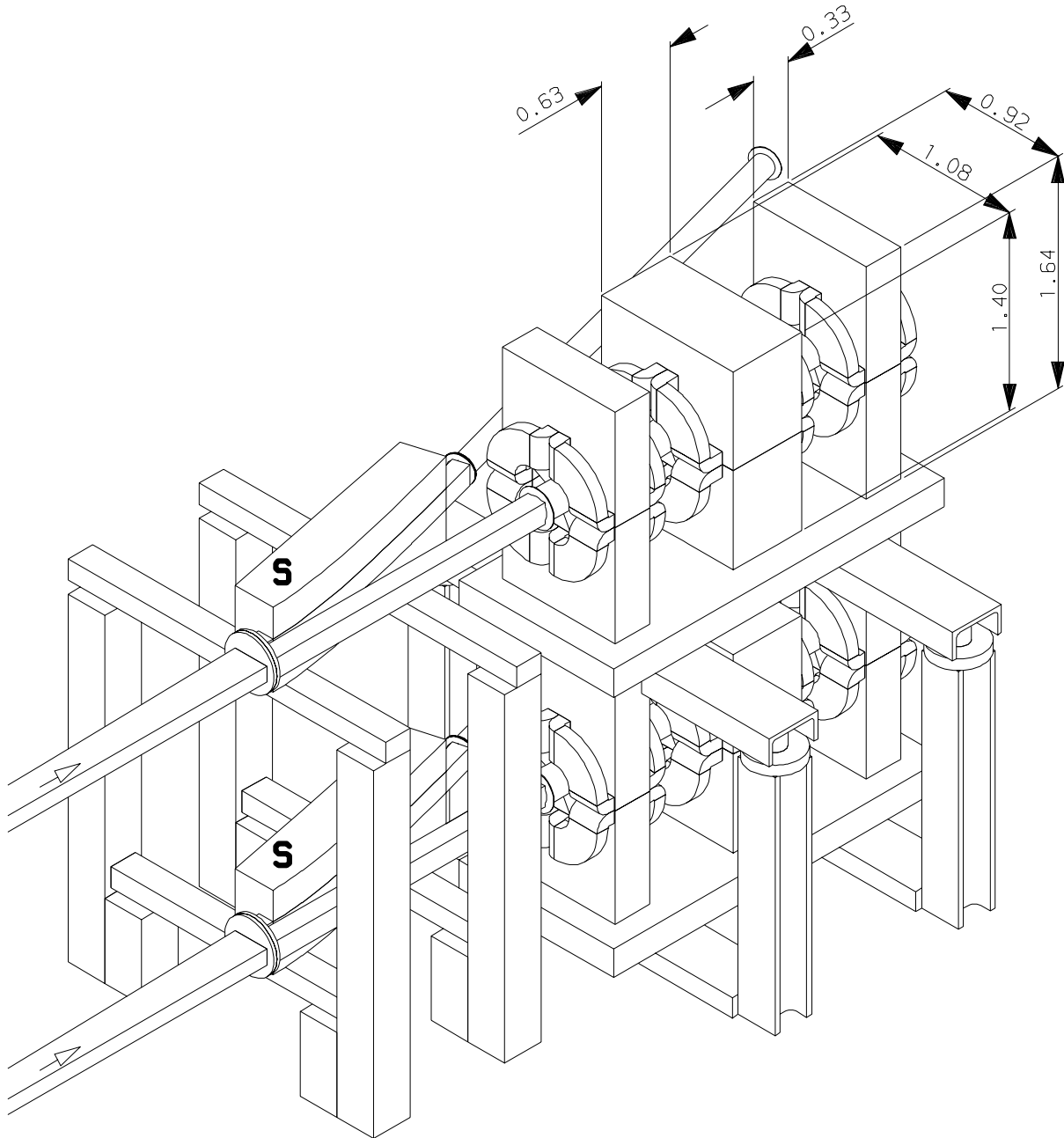


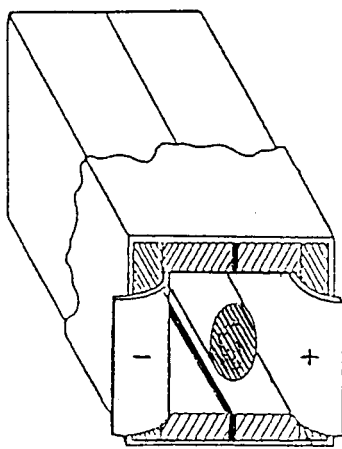
Figure 2.8.2: Perspective of fast extraction septum magnets, S

Magnet codes, GFUN2D and GFUN3D, were used to design the ISIS septum magnet and to study the field effects due to cooling channels in the septum conductors, insulation gaps between the conductors, the use of field clamps, the location of the septum end conductors, and their spacing from the yoke. These are all important in determining the uniformity of the septum fields. The septum coils are made from copper, 10.8 mm square at the input end, but thickened in one plane to 28.6 mm for most of the length to reduce the power dissipation.

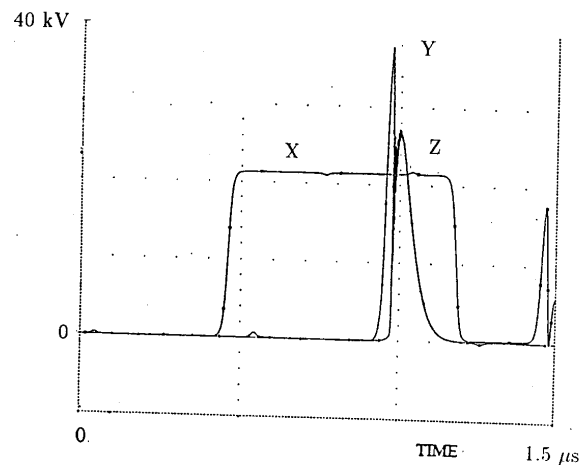
The copper tube has a square water cooling channel of cross-sectional area 4.8 mm^2 . There are two 4-turn coils, one for each half of the magnet, clamped in position. The return conductors are 45 mm by 8.8 mm in section, and both septum and return conductors have a 0.2 mm layer of aluminium oxide, plasma sprayed insulation.

Inside the septum magnet, the stainless steel vacuum vessel is pre-stressed outwards so that it is held firmly in place when clamped by the half yokes. The vacuum vessel for the circulating beam, adjacent to the septum, is made of mild steel to provide some magnetic shielding. The upper, lower and outer walls are 8 mm thick, but the inner wall is thinned to 3 mm at the input end of the septum. The magnetic shielding is important to reduce the effect on the circulating ring beams.

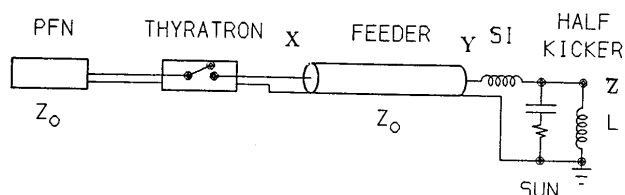
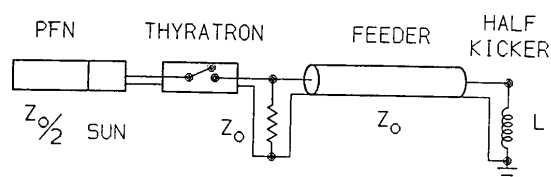
The septum is cooled with demineralised water, using heat exchangers and filters to isolate the components with induced radioactivity. The water flow rate per conductor is 9 litres per minute, with a total of 144 litres per minute for eight septum and eight return conductors in parallel. The septum current is approximately 8500 A, with the exact value depending on the design of the end conductors which link the septum and return conductors, and the use or not of field clamps. The power supply requirements are approximately 350 kW for the dissipation in the septum magnet, buss bars, connections and cables.



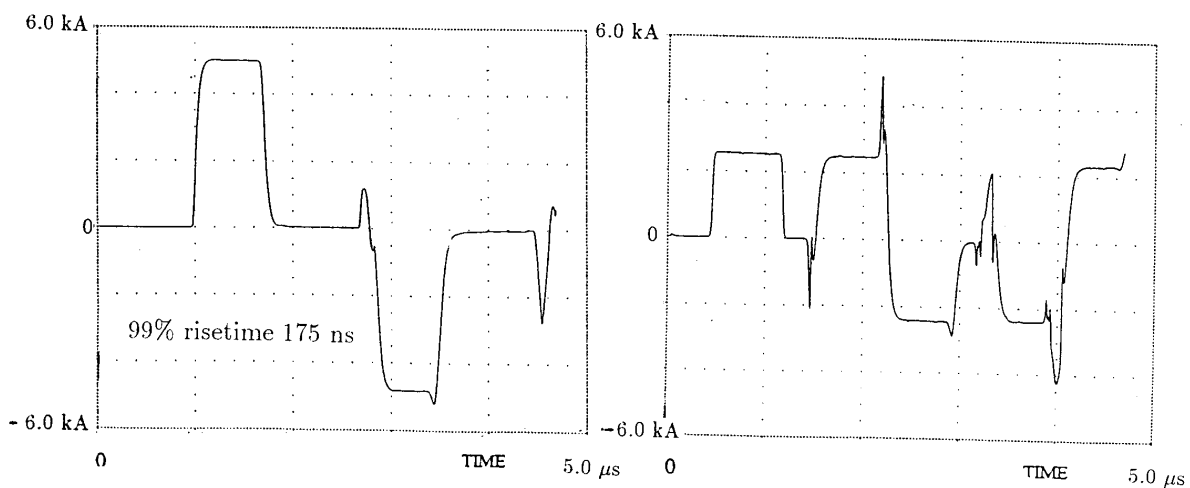
(a) Lumped push pull kicker



(b) Voltage waveforms



(c) Pulser systems



(d) Kicker current

(e) Thyratron current

Figure 2.8.3: Fast extraction details

2.9 BEAM LOSS COLLECTION

Collection systems are designed to control loss under both regular operating conditions and ‘large loss’ fault conditions. The former are the highest priority as they occur for prolonged periods and largely determine activation levels. The latter trigger beam protection systems, leaving up to one full beam pulse which requires efficient removal to prevent damage. The mode of loss, i.e. the plane and magnitude of emittance growth, affects the location and efficiency of interception. It is therefore important to identify the likely loss mechanisms.

Interactions of the input beam with the stripping foil are expected to be the major cause of regular loss. The most important are: delayed stripping of H^0 , elastic scattering, inelastic nuclear interactions and ionisation energy loss. Percentage losses due to the first three are $\sim 0.005\%$, whilst the last is $\sim 0.008\%$. Other possible causes of regular loss include space charge induced transverse emittance growth, instabilities, and particles exceeding the longitudinal acceptance. To deal with fault losses, provision is made for fast removal of particles with large transverse emittance and those with significant momentum errors. Fast removal of any beam exceeding the extraction system transverse acceptance ($260 \pi \text{ mm mr}$), or occupying the longitudinal beam gap, may also be important to prevent extraction loss. Optimisation of the machine beam dynamics means that all losses, except those driven by unavoidable foil interactions, should be at negligible levels. However, some contingency for imperfect machine set up or unexpected behaviour is included in the collector design. Precautions for combating the e-p instability include provision of space for locating electron clearing electrodes, and the possibility of titanium nitride coating of internal surfaces.

To control possible losses, three collimation systems are designed to deal with a range of transverse emittance growth rates and various longitudinal loss modes. Transverse emittance growth is dealt with by a betatron collimation system, situated in a dedicated well shielded dispersionless straight, downstream from the injection region. Low momentum particles generated by the foil are removed with a momentum tail collection system, which is integral with the betatron system. These systems deal with most loss, but as a precaution, general momentum collimation is also provided by jaws near the first dispersion peak downstream from the betatron system. Locations are indicated in Figure 2.4.1 and Figure 2.9.1.

Betatron systems are based on two stage collimation, using double jaws (i.e. both sides of the beam). Acceptance, primary and secondary collimation limits, and the injected beam emittance are set at 480 , 260 , 285 , and $150 \pi \text{ mm mr}$ respectively. Minimisation of the out-scattered halo requires secondary collimators at betatron phases of 90° and 163° with respect to the primary. The long primary jaws are configured to ‘absorb’ incident particles, although additional secondary jaws are included at 20° and 32° to intercept out-scattered cascade products and protons. Primary jaws are as far upstream as possible to achieve the required phase advance for the 163° collimators. Collimation is also required to protect the triplet magnets. Similar transverse phase advances allow most collimation units to be combined, except for the 163° downstream units, where they are split around the final triplet (Figure 2.9.1). This double jawed, two stage collimation system has advantages of efficient single and multi turn collimation, with fast removal of halo before extraction. This system could be used in conjunction with a ‘beam in gap’ kicker, to prevent extraction loss if required.

Particles losing momentum at the foil (a dispersion maximum) undergo an enhanced betatron oscillation, which reaches its first maximum in the collector straight after a 180° phase shift of the motion. The primary horizontal betatron collector on the inside radius of the machine is

near this location (actually 171°), and therefore functions as a momentum tail collector. The jaws constituting the general momentum system are placed near a dispersion (and normalised dispersion) peak. This allows interception of any low momentum particles generated by the betatron system, as well as those due to linac or RF problems. No secondary jaws are provided for this system, as associated loss levels are expected to be very low.

Most collimators combine horizontal and vertical systems, and are double jawed. A tubular box like construction has many advantages, enclosing the most active internal surfaces and combining many jaws in fewer, easily removable units. It is also beneficial for interception of the flux of secondary particles produced by upstream collimators, important for the protection of accelerator components. Rugged materials that allow effective collimation whilst minimising additional radiation hazards are selected: copper for the primary jaws and graphite for the secondaries. Jaws are nominally about 3 nuclear interaction lengths long, i.e. 0.5-1.0 m. The designs draw on extensive experience from the ISIS machine and are optimised for active handling, including measures for quick movement of components and shielding (Figure 2.9.2 and Figure 2.9.3). The collimation regions are fully enclosed in local concrete shielding to minimise surrounding radiation levels, and reduce air activation. This allows hands on maintenance for most ring areas and active maintenance in the designated shielded loss region [Gear, 1996]. Expected heat loads peak at about 1 kW on the primary jaws and water cooling is recommended for all units. Nominally primary jaws will be adjustable and secondaries fixed. For simplicity of design, and to exploit the large rectangular machine apertures, jaws are flat in the transverse and longitudinal directions.

A Monte Carlo simulation code has been developed and used to study the loss collection process [Warsop 2002]. The model includes all the important proton interaction processes with the collector material, treatment of the 3D collector geometry, detailed modelling of beam transport and the ring machine aperture. Studies also included effects of field errors and misalignments. A number of options were studied, including angled jaw geometries, and use of large atomic mass materials. Results with the simple jaws and materials described above were found to give good results, with other options providing minimal advantages. Many loss modes were simulated: a wide range of transverse growth rates, interception of particles with instantaneous large transverse emittances or momentum errors, beam loss due to foil interactions, and removal of halo exceeding the extraction acceptance. Simulations indicated that overall collimation efficiencies (localisation in the collimator regions) exceed 90 %, with typical results $\geq 95\%$. Inclusion of errors had minimal effects on the distribution of loss. Simulations also highlighted the fact that some of the injection loss will unavoidably occur before beam reaches the collimator system, but at the expected levels this is acceptable. Results also indicated that the main effect of errors was to increase the extent of the surviving transverse halo, which was easily accommodated within the machine acceptance.

Representative results obtained from simulations are shown in Figure 2.9.4, which indicates the percentage of the total loss occurring over ~ 0.5 m intervals around the machine. The upper figure shows the distribution of loss around the whole machine circumference, and the lower that in the collimator region. In this case losses are over multiple turns, due to a horizontal growth rate at the primary jaw of $10 \mu\text{m/turn}$. The schematic of the magnet lattice below the histogram indicates the location of quadrupole magnets (green), bending magnets (blue) and collectors (red). For total losses at 1 kW levels, the percentage losses predicted by simulation correspond to loss rates well below the required 1 W/m over most of the machine.

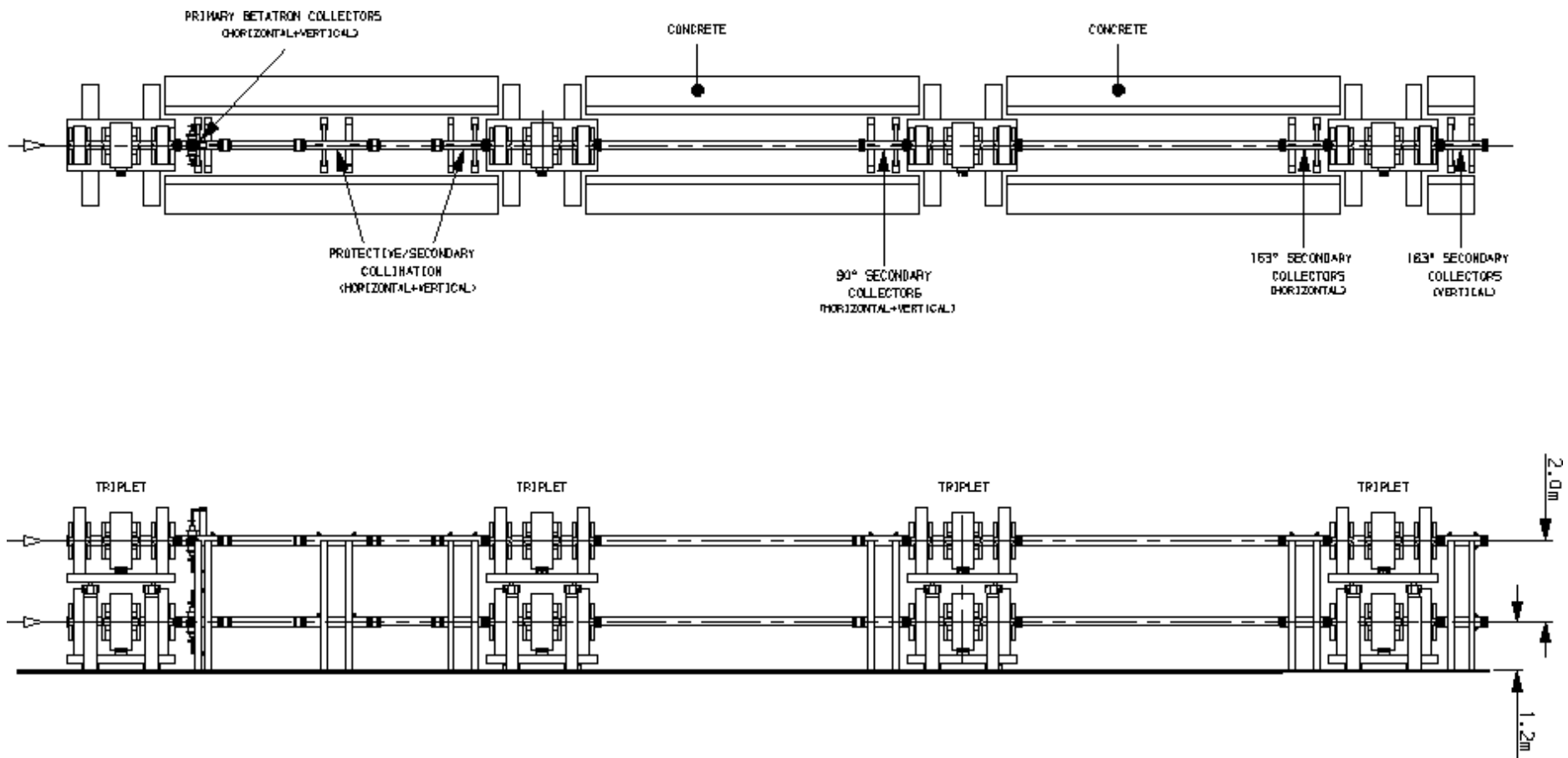


Figure 2.9.1: Layout of Beam Loss Collectors

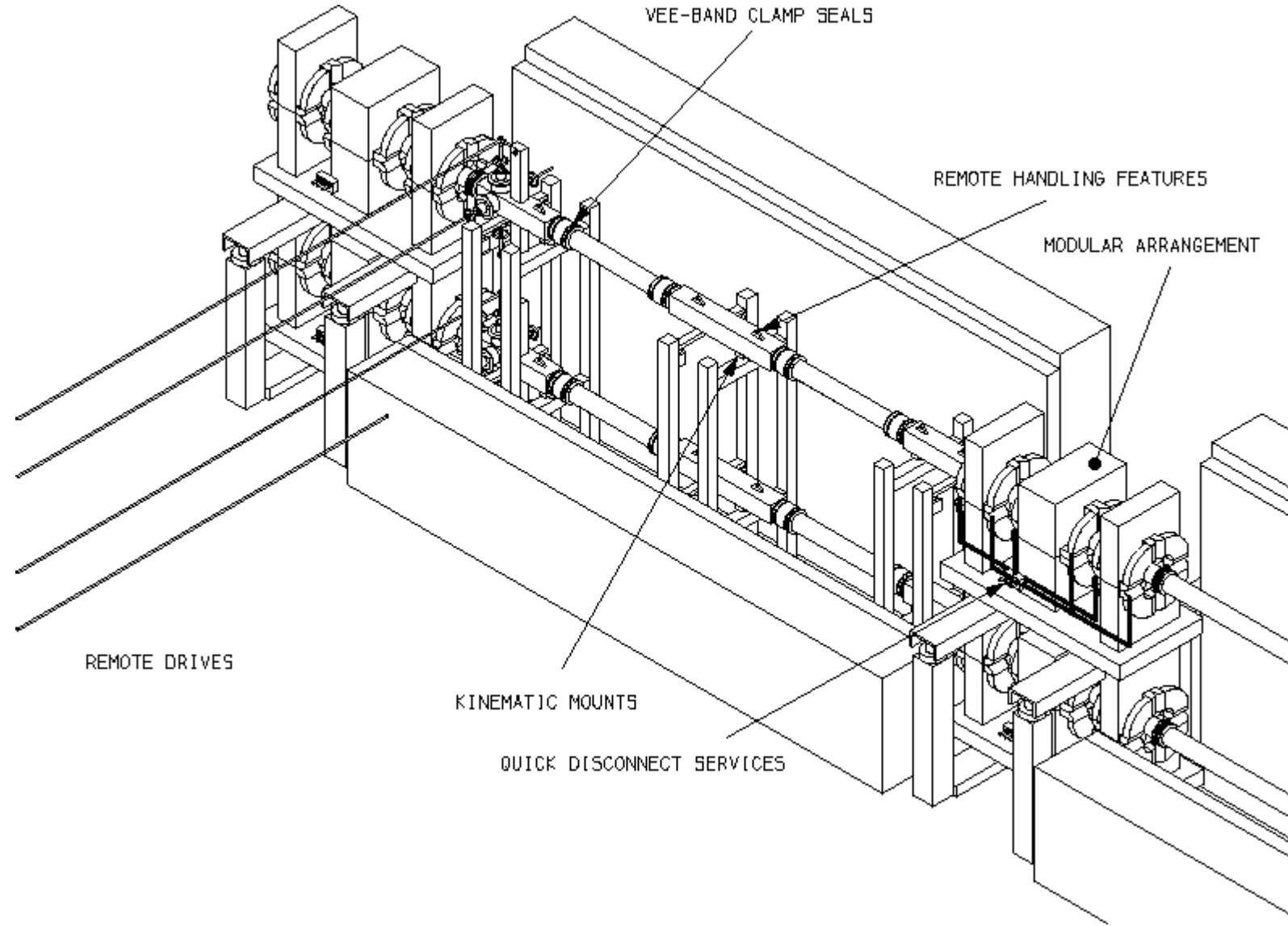


Figure 2.9.2: Active Handling Concept

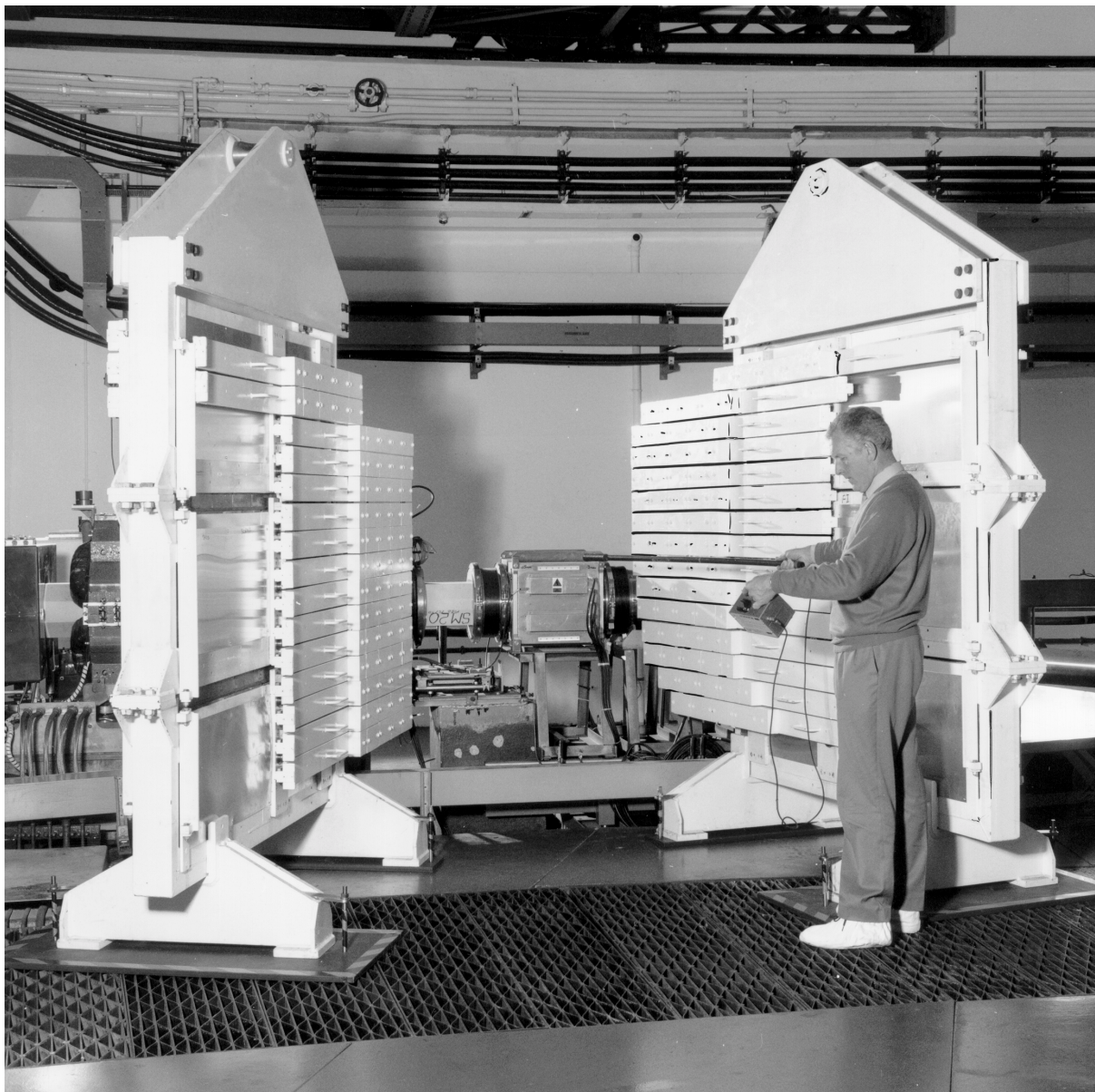


Figure 2.9.3: Adjustable Lead Shielding for Active Handling (as used at ISIS)

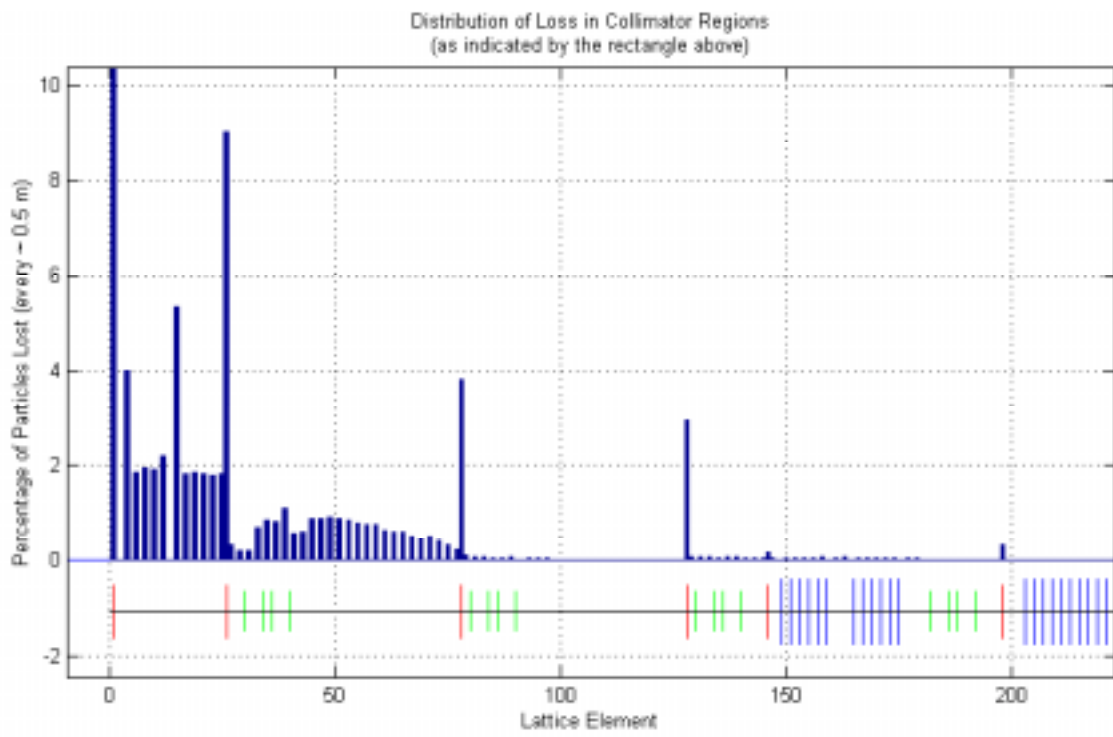
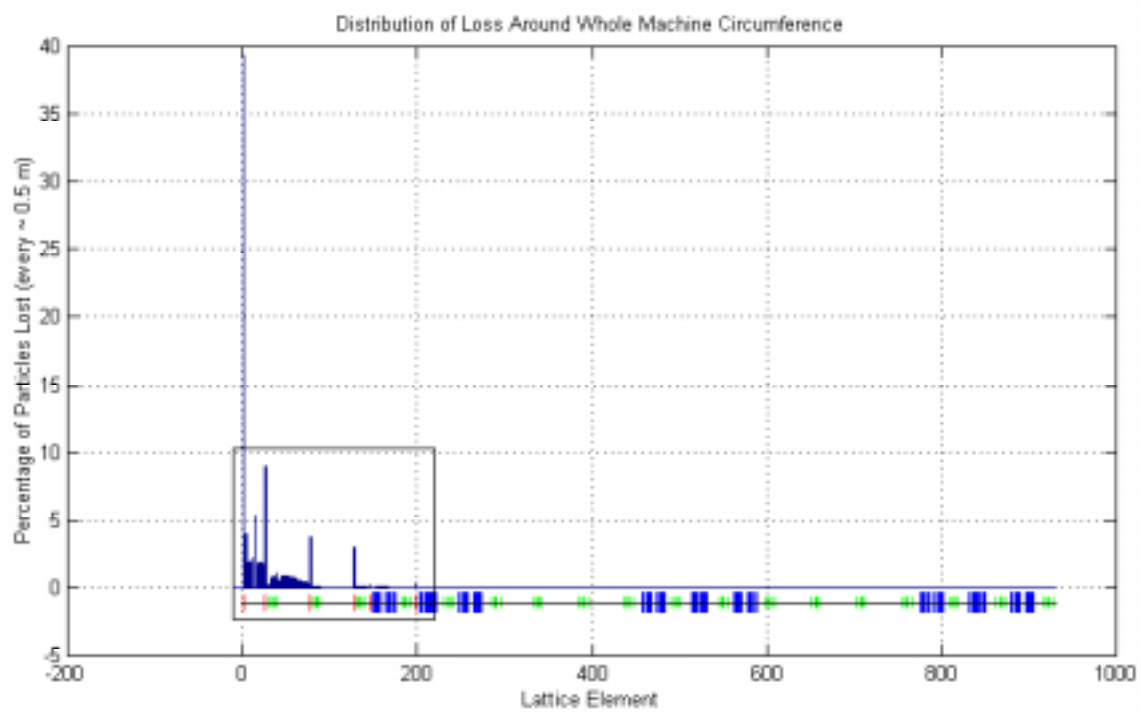


Figure 2.9.4: Representative Beam Loss Distribution from Simulations

2.10 MAGNETS AND POWER SUPPLIES

The magnets for the injection beam line, the rings and the target beam lines have been evaluated using the two and three dimensional codes, POISSON, MERMAID and MAFIA. Requirements for field quality have been met without difficulty apart from in the cases of the septum magnets and the kickers, where some effort has had to be made to obtain the required fields. The main task for the magnet system has been to optimise the magnets and magnet power supplies for minimum cost of manufacture and operation.

2.10.1 Accumulator Ring Bending Magnets and Quadrupoles

Each ring has 12 main dipole magnets, 3 auxiliary dipoles, 15 vertical dipole correctors, 12 horizontal trim windings on the main dipoles, 4 vertical orbit bumper injection dipoles, 2 septum magnets to assist in removing the unstripped beam, 36 focussing quadrupoles and 18 horizontally defocussing quadrupoles. A list of the main magnet parameters is given in Table 2.10.1. The quadrupole magnets are arranged in triplets, $F_a D_a F_a$, $F_b D_b F_b$ and $F_c D_c F_{cc}$ and each triplet has its three quadrupoles mounted on a common support. A figure-of-eight design is adopted for all the quadrupoles, with the central D quadrupole having a height of 1.4 m, a width of 1.08 m and a length of 0.63 m, while the F quadrupoles have a height of 1.64 m, a width of 0.92 m and a length of 0.34 m. This design is adopted to accommodate the special features of injection and single turn extraction. Consideration is also given to the inclusion of trim windings on the quadrupoles of the $F_a D_a F_a$ triplets. The total power for the dc magnets is 8.0 MW.

2.10.2 Injection Beam Line Bending Magnets and Quadrupoles

The initial section of line has seven F and seven D singlet quadrupoles. This is followed by the 180° achromat which has 16 combined function focussing magnets and 16 combined function defocussing magnets, each with an arc length of 3.05 m and a gap height of 50 mm. The third section of line has two vertical bending magnets, one of which is pulsed, an upper and lower horizontal dipole magnet, four matching quadrupoles, and 18 quadrupoles in both an upper and lower injection line. In addition there is a vertical bending magnet and four quadrupoles in the line from the centre of the achromat to the 5 MW beam dump. The total power for dc magnets is approximately 0.4 MW, and parameters are listed in Table 2.10.2.

Table 2.10.1: Bending magnets, quadrupoles and power supplies for the accumulators

Parameter	Magnets	Main B Dipoles	Auxil. Dip. B1	Horiz. Trims	Vertical Correcs.	Septum 1	Septum 2	Vertical Bumpers
Length	m	3.0	5.1	3.0	0.33	0.35	1.14	0.54
Angle	deg	28.125	7.5	0.44	0.10	3.5	11.3	2.00
Field	T	1.13	0.177	0.012	0.089	1.2	1.2	0.40
Gap	mm	130	140	130	200	15	30	192
Weight	t	17	31	0.1	0.1	0.4	3.6	0.2
Current	A	1740	660	50	143	2400	1750	6110
Voltage	V	61	41	10	10	15	50	75
Number		24+1	6+1	24+1	30+1	2+1	2+1	8+1
No in series		12	3	1	1	1	1	4
P/S	A	1840	700	± 50	± 50	2400	1750	6110
P/S	V	775	130	± 10	± 10	504	50	2300
Power	kW	1425	91	0.5	1.4	pulsed	88	Pulsed
Number		2+1	2+1	24+1	24+1	2+1	2+1	2

Note: +1 indicates a spare

Parameter	Magnets	Quadrupoles Fa	Quadrupoles Fb, Fc, Fcc	Quadrupoles Da	Quadrupoles Db, Dc
Length	m	0.36	0.34, 0.34, 0.34	0.70	0.63, 0.63
Gradient	Tm ⁻¹	7.25	7.38, 2.61, 5.08	6.84	7.16, 4.10
Radius	mm	132	132	132	132
Weight	t	5.1	4.8, 4.7, 4.7	8.8	7.9
Current	A	325	325	325	325
Voltage	V	130	129, 46, 88	160	160, 92
Number		24+1	24+1, 12+1, 12	12+1	12+1, 12
No in series		6	6, 3, 3	3	3, 3
P/S	A	344	344	344	344
P/S	V	810	810, 150, 275	500	500, 380
Power	kW	279	279, 52, 95	172	172, 131
Number		4+1	4+1, 4+1, 4	4+1	4+1, 4

Table 2.10.2: Bending magnets, quadrupoles and power supplies for the injection line

Parameter	Magnets	Combin. Fn. BF	Combin. Fn. BD	Vertical Dipole VB1	Vertical VB2	Dipole	Horizontal Dipole B1
Length	m	3.05	3.05	2.55	2.55	(0.74)	2.55
Angle	deg	5.625	5.625	2.95	2.95	(.035)	3.75
Field	T	0.222	0.222	0.14	0.14		0.177
Gap	mm	50	50	32	50	(50)	50
Weight	t	3	3	2	2	(1)	2
Current	A	232	232	1780	95	(24)	95
Voltage	V	27	27	2	27	(7)	27
Number		16+1	16+1	1+1	1+1	(1)	2+1
No in series		16	16	1	1	(1)	1
P/S	A/V	240/460	240/460	1780/680	100/30	(25/10)	100/30
Power	kW	110	110	pulsed	3	(0.25)	3
Number		1+1	1+1	1	1+1	(1+1)	2+1

Note: +1 indicates a spare

Parameter	Magnets	DF	D2F2	D3F3	F,D4,5	F6F7	D6D7	D8	F8
Length	m	0.11	0.11	0.11	0.23	0.23	0.47	0.23	0.47
Gradient	Tm ⁻¹	7.5	9.5	7.5	15.3	15.3	15.3	15.3	15.3
Radius	mm	54	54	54	39	39	39	39	39
Weight	t	0.4	0.4	0.4	0.5	0.5	0.9	0.5	0.9
Current	A	100	100	100	96	96	96	96	96
Voltage	V	22	22	22	25	25	37	25	37
Number		10+1	2	2	4	16+1	8+1	8	4
No in series		5	1	1	1	8	4	2	1
P/S	A	100	127	100	100	100	100	100	100
P/S	V	100	25	20	30	210	160	55	40
Power	kW	10	3	2	3	21	16	6	4
Number		2	2	2	4	2+1	2+1	4+1	4+1

2.11 BEAM DIAGNOSTICS

The purpose of the diagnostics is to bring the facility into operation according to specifications, to monitor and maintain normal operation, to protect the hardware in case of malfunctioning and finally to provide information for trouble-shooting. The diagnostics can be divided into:

- Operational or on-line instrumentation.
- Characterisation instrumentation.

The first is always available during runs and is used to establish and maintain daily operation. This part of the diagnostics is non or minimally interceptive in order to withstand the high current and not increase the beam loss significantly. The characterisation diagnostics may be interceptive and need not withstand full beam power. It is used to characterise the beam fully, or as well as possible, and is used during commissioning, setting-up and trouble-shooting.

The special features of the ESS as compared to other accelerator facilities arise from the very high beam intensity. This has at least two important consequences for diagnostic instruments. First of all a large amount of heat is deposited in material intercepting the beam, and possibly may melt the device. Furthermore, beam losses will be increased above the acceptable levels during normal operation by any intercepting instruments. Also the large electric field from the beam has important implications. Another important design constraint has been to avoid, or minimise, active parts (electronics) of the diagnostics inside the shielding.

The diagnostics should measure the interesting properties of the beam, and, in general, in a way that interferes as little as possible with the beam. The properties of interest are: intensity, beam profile, position, time structure, betatron tunes, emittance, energy spread and beam loss, but also some special parameters may need to be controlled. Several of the instruments used are common to the whole accelerator complex, whereas others are specialised to a specific part, for example, that carried by the rf system.

The current is of obvious interest, not only to provide an accurate measurement, but also to monitor transmissions and current variations. Two Faraday cups measure the current out of the ion sources in the LEBT; these cups also act as beam stops. Current transformers of various kinds are used to measure the current along the accelerators. Low-droop current transformers are used in the LEBT, DTL, CCL, SCL and HEBT to measure accurately the charge in a single macro-pulse; furthermore they provide observations of fast current variations. DC current transformers, or parametric current transformers, are used in the rings. They are also used to complement the low-droop current transformers in the HEBT. In the rings and the EPBL, yet another type of beam transformer, namely the beam charge monitor, is used. This type is specially suited for measurement of total charges in fast pulses.

In a high intensity machine like the ESS, beam losses have to be minimised to keep activation at an acceptable level and to protect the machine. Beam-loss monitors are inherently much more sensitive than comparisons between current transformers. At low energy, where the intensity of secondary neutrons is low, a mobile system of scintillators and photo-multipliers will be used. Coaxial ionisation chambers, 3 m long, are used as beam-loss monitors along the accelerators and beam lines. Up to the end of the DTL, these ionisation chambers have a large diameter and are equipped with amplifiers to increase the sensitivity.

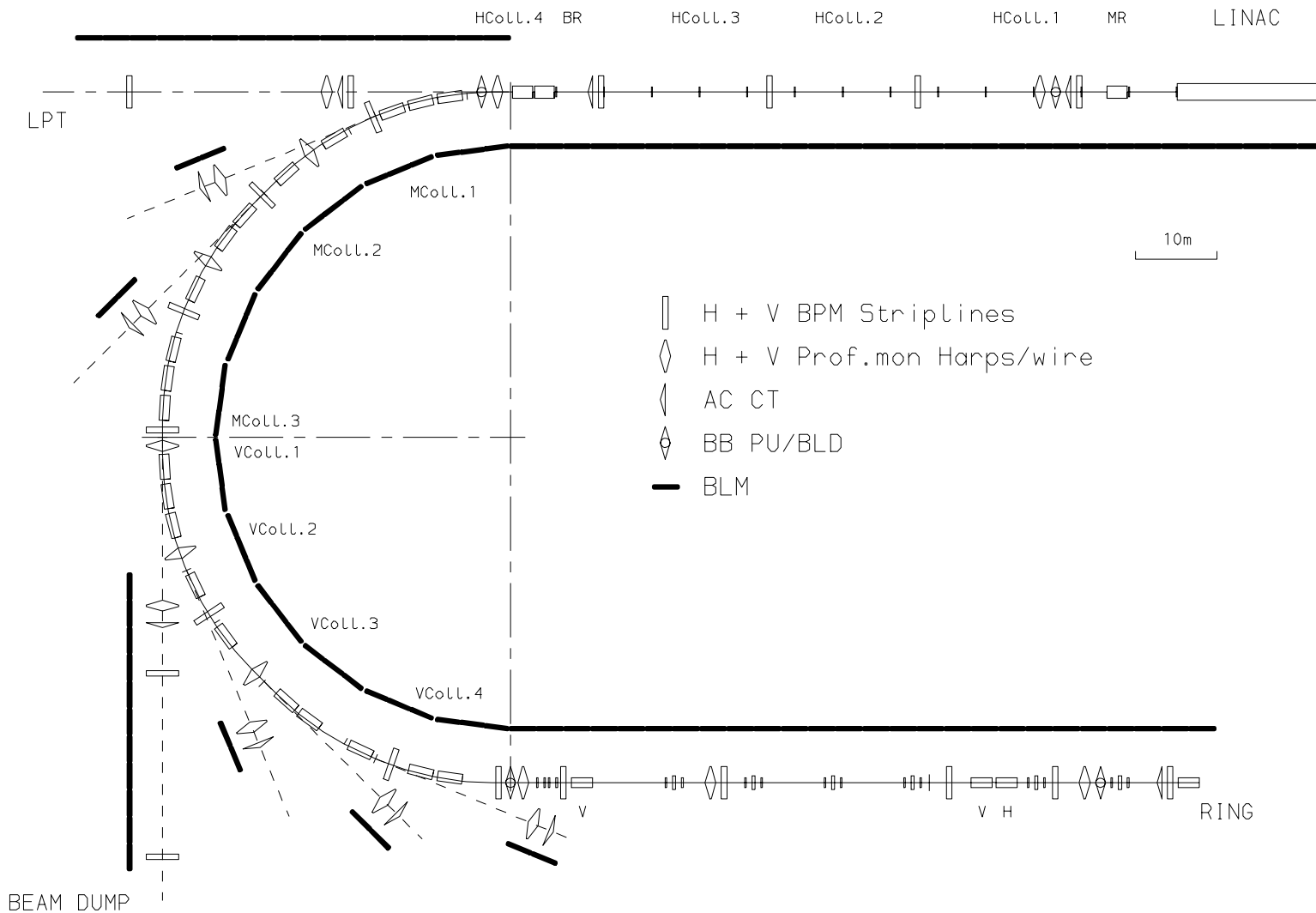


Figure 2.11.1: Injection beam line diagnostic components

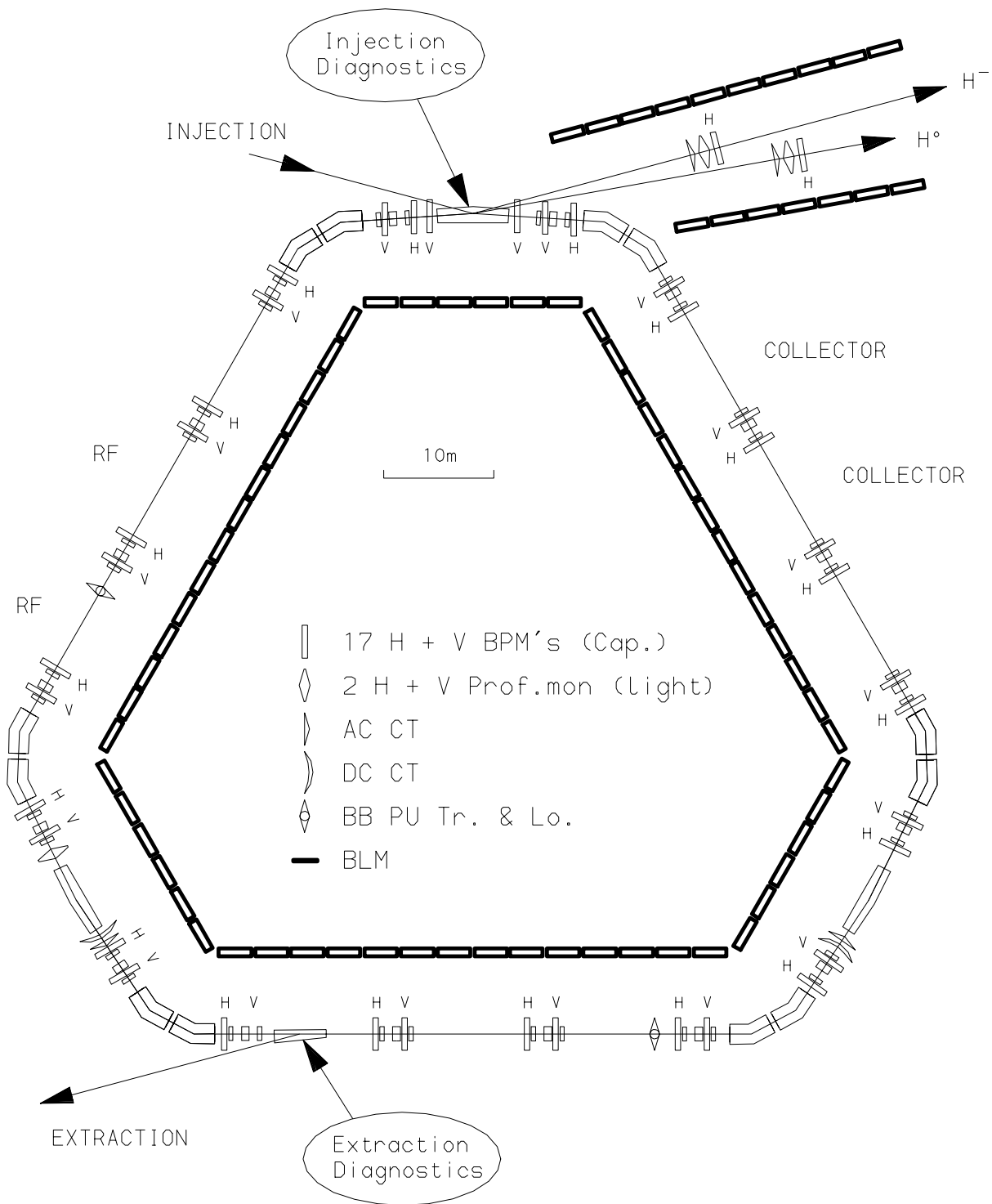


Figure 2.11.2: Accumulator ring diagnostic components

In the rings, a system on the floor and a system on the ceiling will determine which ring is losing beam. This system of beam-loss monitors has the sensitivity to monitor beam-losses much below the level of 1 nA/GeV/m, and has also a dynamic range to detect much larger losses. The beam-loss monitors are also used to switch off the accelerator in cases of excessive losses. Signals from many beam-loss monitors can be added and observed in time-domain. Beam losses, and other interesting parameters, will be logged during operation.

Beam profiles are important measures of emittances and beta-functions; if one is known the other can be extracted. Measurement of more profiles enables extraction of both emittance and beta-functions. True emittance measurements will be done at the output of the ion-sources using the usual slit-and-profile method. Profiles will be measured in the LEBT by observing fluorescent light from the rest gas. This method can only be utilised at low energy, where the excitation cross section of residual gas atoms is large, or at high energy in the rings, where the low cross section is compensated by the large circulating current. Secondary electron emission wire monitors (harps) are used all along the facility, apart from in the rings. They may only be used with the full macropulse (and low rep. rate) after the linac, due to heat problems. In the CCL and HEBT, the harps are complemented with fast-flying wire scanners owing to the mm beam size. Finally some sort of profile observation close to the targets is desirable. Observation of infrared light emitted from the beam line window is envisaged.

Knowledge of the beam position along the accelerators is needed to steer and centre the beam in the aperture. In the LEBT, DTL, CCDTL, CCL, SCL and HEBT, where the rf-frequency is high (280 or 560 MHz), striplines are used. These are normal striplines of length $\beta\lambda$ in the high-energy end of the CCL and the HEBT, but are short micro-striplines at low energy where space is very limited. The stripline system also provides measurement of beam phase, beam intensity and time-of-flight, quantities which are necessary for tuning the linacs. In the rings and the EPBL, capacitive beam position monitors are used, utilising the revolution frequency of 1.24 MHz in the former. In the EPBL, positions can be extracted for each of the pulses from the two rings. A halo-monitor provides information about the beam impact-position on the target.

Bunch lengths and accurate timing information are important quantities. Coaxial pickups with large bandwidth will be installed in the LEBT and linac, and fast, high bandwidth current transformers in the DTL, CCDTL, CCL and SCL. In the HEBT, where there is more space, wall-gap monitors will be installed. Very high resolution (10 ps) bunch-length measurements are obtained in the LEBT, DTL and CCL using a so-called BLVD-detector. In such a detector, the beam is intercepted by a wire, and the secondary electrons, which have the same time-distribution as the primary beam, are detected synchronously with the rf-frequency. Using a slit, the same detector also provides the beam-profile, and hence the 3-D beam.

Several specialised instruments will be used. Electron detectors are needed for e-p studies, and sensing of unstripped beam will be used for ring protection. Observation of the ring stripping foils with an infrared camera will give directly the impact area of the injected beam. Special devices will be used at the septum magnets for the early commissioning. The rings will be able to store a low intensity beam for longer than the 1 ms for normal operation. This means that Schottky-analysis techniques of stored beams may be used to extract detailed information about the ring operation. In addition to the profile and emittance measurements described, the true linac emittance will be measured by photo-detachment of the H^- beam with a narrow laser-beam combined with a profile measurement of the H^0 beam. Photo-detachment of the H^- beam by lasers can also provide longitudinal information. Resonances

in the photo-detachment cross section combined with the Doppler-shift allows one to measure the velocity (and spread) directly. Injection of one turn into the rings and observation on a turn by turn basis give measurements of tunes and tune-spread, betatron amplitudes and momentum spread.

The diagnostic instruments described consist of the monitor and the associated electronics. Whereas the monitor has to be close to the beam, the system is designed so that the first part of the electronics are in all cases at least a few meters from the monitor and the beam, outside the radiation shielding. The signal conditioning in this first part of the electronics allows the signals to be transmitted to local diagnostics electronics, where signals from groups of monitors (typically 8 or 16) are processed before being sent to the local diagnostics control room. Here the data acquisition takes place using a VXI-system. This data will then be available anywhere in the accelerator complex, and in particular in the control room. The individual analogue signals will only be available in these local diagnostic control rooms unless analogue waveform switching and multiplexing is also considered. We envisage four such local diagnostic control rooms, one at the low energy end for the LEBT and DTL, the second at the high energy end of the linac for the CCL, the third in connection to the main control room for the HEBT and rings and the fourth for the EPBL.

The instruments mentioned above, when installed in particular regions of the machine, may provide information of specific beam properties. Obviously, a beam position monitor placed in the middle of the achromat, where the dispersion is large, gives a very precise measurement of the momentum. In the same way a profile monitor in the same position gives the momentum spread. Observation of the intensity and the distribution of the H^+ beam originating from the collimator stripping foils in the achromat provides direct information about the transverse halo of the beam from the linac. Many more examples exist of such measurements, which can not be described here. However, most instruments are included in the above description, and they will allow measurement of most of the important parameters needed for safe commissioning and operation of the ESS.

2.12 THE VACUUM SYSTEM FOR THE RINGS AND BEAM LINES

The vacuum for the accumulator rings and proton beam lines, shown schematically in Figure 2.12.1, are areas of high radiation and hence the design philosophy is to install only essential components; these will be of high integrity, reliability, long life and requiring minimum maintenance. In addition, the components should be easily and rapidly removable. It is assumed that the general radiation levels in the area of the rings and proton beam lines will be similar to the corresponding areas in ISIS [Gear, 1996] allowing hands on maintenance except in a few regions such as the collectors.

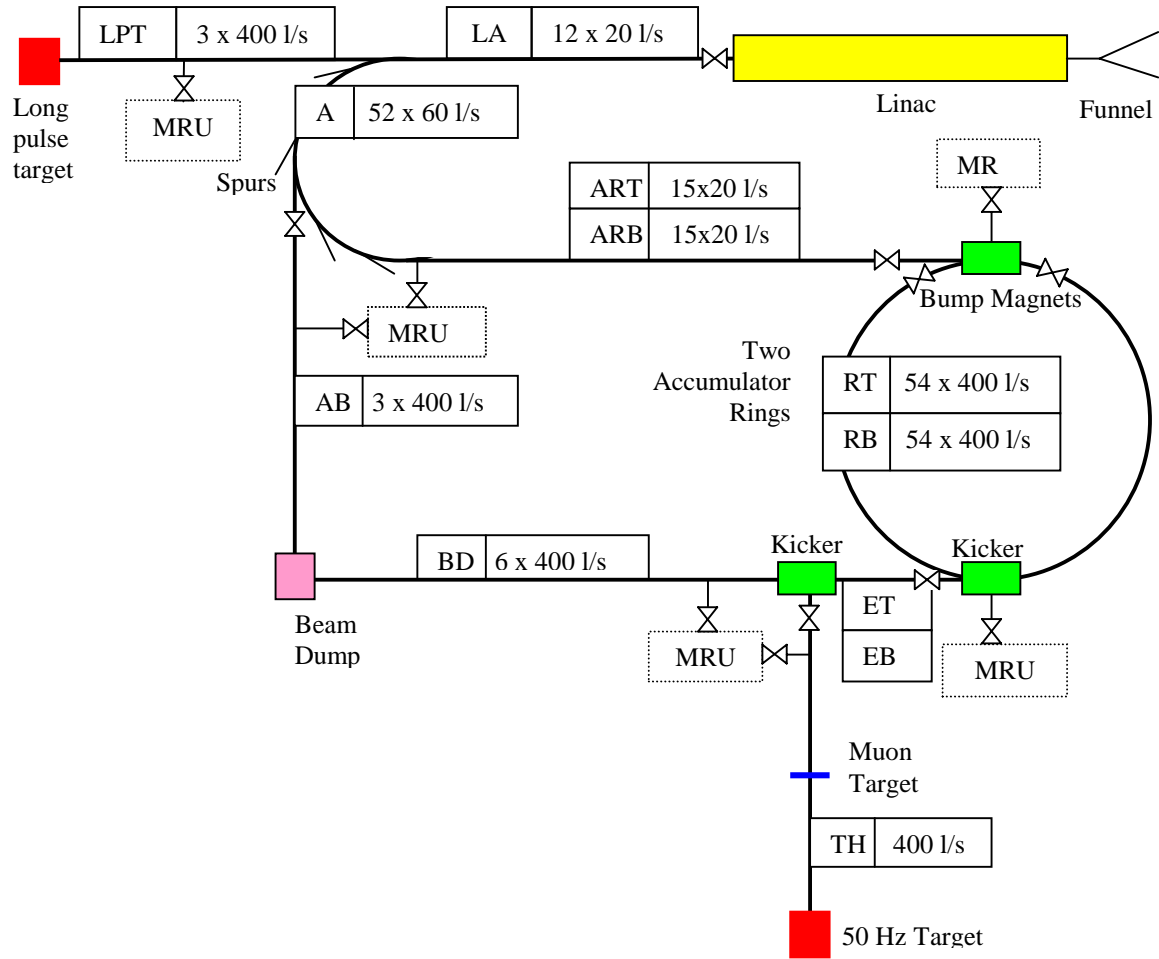


Figure 2.12.1: Schematic diagram of the vacuum system for the rings and beam lines.. Each section is denoted by a letter code. The number and speed of the ion pumps in each section is also given (pumps for BD include the kicker, EB and ET). The mobile roughing units, MRU, are attached by valves where shown. Beam line isolation valves are also shown.

The vacuum system will be built to uhv standards using all metal and ceramic components in the vacuum. Demountable joints will have tapered flanges and chain clamps for quick fitting and removal and will be fitted with aluminium diamond seals. Aluminium vessels will be used in the rings to give the required electrical conductivity for the pulsed proton beam image currents. Aluminium or stainless steel will be used for the vessels in the beam lines. The units

in the beam lines will be carefully cleaned, but not vacuum baked, to achieve a specific outgassing rate of $\leq 5 \times 10^{-10}$ mbar l/s/cm² at 10 hours [Strausser].

The average design pressures in the proton beam lines and the rings is 10^{-7} mbar to avoid excessive beam loss and maintain stability in the rings. However, to avoid the possible e-p (or electron multipacting) instability [Macek, 2001] produced through beam interaction with the residual gas and subsequent secondary electron emission from the chamber walls, it may be necessary to reduce significantly the vacuum pressure. Alternatively, or in addition, coated vacuum chambers may be needed to reduce the secondary emission coefficient. The SNS project has decided on a vacuum pressure of 10^{-9} mbar [Hseuh, 1999]. To reduce the pressure to these low levels will require an increase in the pumping speed or a reduction of the specific outgassing rate. It is impractical to increase the pumping speed by more than a factor of ten before the pumps touch each other. A more practical solution is to give the system a modest vacuum bake at $\sim 100^\circ\text{C}$ for one day. This would reduce the outgassing rate of the aluminium vessels to $\sim 10^{-12}$ mbar l/s/cm² [Elsey, 1977] and would correspondingly reduce the pumping speed requirement. Whilst this is attractive, the disadvantages are the added complexity and cost of baking with heaters and insulation (particularly within the magnets), the inconvenience of removing these items when gaining access to the ring components and the additional time taken for the bake. Until the e-p instability and the possible ways of reducing the temperature of the bake-out and the secondary electron coefficient have been studied, it is not proposed to alter the existing vacuum design pressure of 10^{-7} mbar for the rings.

The minimum number of valves will be installed. Figure 2.12.1 shows the position of the valves; there are no valves in the rings and no fast acting valves in the system. The valves will be of all-metal construction with metal seals. It is assumed that the valves in the 26 cm diameter proton beam lines to the targets need be only 20 cm in diameter by placing them at suitable points in the lines where the beam is small enough to pass through.

Ion pumps will be used giving long life and no maintenance over 20 years at the design pump pressure of $< 10^{-7}$ mbar. It is proposed to use mobile turbomolecular pump units to evacuate the system until the pressure is $\sim 10^{-5}$ mbar and then the ion pumps will be turned on. The mobile turbomolecular pump units (MRU) will be the same as those used for the linac. All-metal valves, with metal seals, will be used to attach the roughing pumps to the system. The mobile units will be removed from the areas when operating the accelerator, since they contain semiconductor devices which are sensitive to radiation.

The control of the vacuum system will be manual from local control areas. Monitoring will also be available in the local control areas with computer links to the central control system. The system will be fail safe, with the system shutting down in the appropriate manner through the hardwired local control systems.

Monitoring of the system pressures will be by inverted magnetron and wide range Pirani gauges strategically located around the system. Simple, inexpensive quadrupole mass analysers heads (mass range 1-100 amu) will be installed around the system for diagnostic and leak detection purposes. Small all-metal right angle valves will also be distributed around the system for attachment of additional diagnostics.

2.13 INSTALLATION AND ALIGNMENT

Beam line components will be modular assemblies, fitted with survey datums, vacuum chambers and all ancillaries. Prior to installation in the tunnel, they are measured and aligned to the kinematic mounts. Vacuum connections to adjacent modules will be made using all-metal seals and ‘v-band’ type clamps. Water connections, made by flexible couplings and ‘easy release’ fittings, and electrical connections will be ‘quick release’, where necessary.

Ring and beam line alignment systems will be similar to those developed and used at CERN. Components are prealigned on special measuring and alignment beds; sockets and level pads allow alignment in the tunnels; stretched wire and 3D theodolite measuring techniques are used with automatic data transfer for computer analysis. Linac alignment and monitoring use laser alignment techniques and may require evacuated sight lines.

The cost of flowmeters, filters, thermal trips, flexible connections, kinematic mounts, alignment sockets, dc cabling (2×45 m per component), cable trays, brackets, and flow and return pipework (2×30 m per component) have been added to beam line component costs. Manpower costs for component measuring, test, alignment, vacuum installation, mechanical and electrical installation and lifting have also been added.

2.14 RESEARCH AND DEVELOPMENT

Two types of R & D may be identified, that which may be deferred until after project approval and that which must be completed ahead of the detailed design. In the former category are prototypes for some components in the beam lines and in the ring injection, rf and extraction systems. The second category comprises the following:

- H⁻ stripping foils lifetimes and foil insertion devices,
- Special diagnostic devices,
- Further beam simulations for the HEBT and for ring injection.

2.15 CONCLUSIONS

Feasible designs have been established for two, large acceptance, 1.334 GeV accumulator rings and the associated injection and extraction beam transport lines.

- The 5 MW, 50 Hz proton beam is accumulated and then transmitted as 1.4 μ s pulses to the 50 Hz target; the specification represents a large advance over existing systems.
- Novel features are the special collimation systems for the injection lines and the very low loss ring injection and containment systems.
- Design aims are loss levels of < 1 part in 10^3 for the achromat collimation and 2 parts in 10^4 for the rings, allowing the use of active handling maintenance procedures.
- Research and Development items have been identified. The most important is the investigation of stripping foil lifetime for the high temperature, thermal cycling.

REFERENCES

- [Barratt, 1996] P Barratt, R Bendall, I S K Gardner, J Hirst and G H Rees
The Radio Frequency Systems for the ESS Accumulator Rings
Report ESS 96-59-R, December 1996
- [Barnes, 1992] M J Barnes et al.
Improving Kicker Systems
Proc. of XVth Int. Conf. on High Energy Acc., Hamburg, 1992, p.191
- [Boardman, 1982] B Boardman, Editor
Spallation Neutron Source: Description of Accelerator and Target
RAL Report RL 82-006, March 1982
- [Damburg, 1983] R Damburg and V V Kolosov
Chapter 3, Rydberg States of Atoms and Molecules
F Stublings, Cambridge University Press, 1983, p. 31-71.
- [Duke, 1994] J P Duke et al.
Dual Harmonic Acceleration
Report ESS 94-12-R, November 1994
- [Duke, 1996] J P Duke
Stripping Foil Temperatures in the European Spallation Source
Proceedings of the 5th EPAC Conference, Sitges, June 1996
- [Elsey, 1997] R J Elsey, J R J Bennett and A J Dossett
A Study of Some Features of the UHV Systems for EPIC
Rutherford Appleton Report, RL-77-038/B, 1977
- [ESS, 1996] European Spallation Source: Volume 3. The ESS Technical Study
Report ESS 96-53-M, November 1996
- [Galluccio, 1996] F Galluccio and V G Vaccaro
Coherent Stability Criteria for the Accumulator Rings of the ESS
Report ESS 96-57-R, December 1996
- [Gardner, 1995] I S K Gardner, H Lengeler and G H Rees
Outline Design of the European Spallation Neutron Source
Report ESS 95-30M, September 1995
- [Gear, 1996] P Gear
Beam Induced Radiation Problems and Cures
Proceedings of the 5th EPAC Conference, Sitges, June 1996
- [Hofmann, 1979] A Hofmann and F Pedersen
Bunches with Local Elliptic Energy Distributions
Proc. IEEE Trans. Nucl. Sci., Vol. NS-26, No. 3, 1979, p. 3526-3528

- [Hseuh, 1999] H C Hseuh, C J Liaw and M Maples
 Proceedings of the 1999 PAC Conference, New York, 1999
 IEEE cat. No. 99CH3666, 1345 (1999)
- [Macek, 2001] R Macek et al
 Recent Experimental Studies of the Electron Cloud at the LANL PSR
 Electron-Proton Instability Workshop, KEK, October 2001
- [Prior, 1994] C R Prior
 Longitudinal Injection for the ESS
 Report ESS 94-7-R, November 1994
- [Rees, 1994] G H Rees
 Important Design Issues of High Current Proton Rings
 Proc. of the 4th EPAC Conference, London, June 1994, p. 241-245
 High Intensity Performance of the ISIS Synchrotron
 Proceedings of the Workshop on Beam Instabilities in Storage Rings
 Hefei, China, July 1994, p. 198-206
- [Rees, 1999] G H Rees,
 Aspects of Beam Stability at ISIS
 Workshop on Instabilities of High Intensity Hadron Beams in Rings
 AIP Conf. Proc. 496, 1999, p. 17-21
- [Rosenberg, 2000] R Rosenberg and K Harkay
 Retarded Field Analysers
 Nuclear Instruments & Methods A 453 (2000), p. 507-513
- [Strausser] Y Strausser
 Review of Outgassing Results
 Varian Report, VR-51
- [Sugai, 1995] I Sugai et al.
 Dev. of Thick, Long-Lived, Carbon, Stripper Foils for PSR, LANL
 Nuclear Instruments & Methods A 362 (1995), p. 70
- [Warsop, 2002] Ph.D. Thesis, Sheffield University,
 To be presented March 2002
- [Ziemann, 1996] V Ziemann
 New Optics of the ESS Target Beam Lines
 Report ESS 96-54-R, December 1996

Chapter 3

Beam Transfer to Targets

Authors and Contributors

Beam Transfer to Targets

A Lehrach¹, J Dietrich¹, R Maier¹, S Martin¹, J Tang¹

¹FZJ

Contents

Beam Transfer to Targets

3 BEAM TRANSFER TO TARGETS.....	3-5
3.1 INTRODUCTION.....	3-5
3.2 BEAMLINE TO THE LONG PULSE TARGET.....	3-5
3.2.1 FAST SWITCHYARD AND H ⁻ STRIPPING.....	3-5
3.2.2 THE 16 2/3 Hz TARGET LINE	3-9
3.2.3 SLOW SWITCHYARD AND DUMP LINES	3-10
3.3 BEAMLINE TO THE SHORT PULSE TARGET	3-10
3.3.1 EXTRACTION AND MATCHING TO THE DOWNSTREAM BEAMLINE	3-10
3.3.2 JOINING SECTION.....	3-10
3.3.3 SWITCHYARD AND DUMP LINE.....	3-11
3.3.4 ADAPTATION TO THE TARGET	3-11
3.4 BEAM DIAGNOSTICS.....	3-15
3.4.1 BEAM PROFILE MONITORING	3-15
3.4.2 BEAM LOSS MONITOR SYSTEM	3-16
3.5 MAGNETS AND POWER SUPPLIES	3-16
3.5.1 BENDING MAGNETS AND QUADRUPOLES	3-17
3.5.2 NON-LINEAR MAGNETS	3-18
3.5.3 SEPTA, SWITCH MAGNETS AND KICKERS.....	3-18
3.5.4 POWER SUPPLIES.....	3-18
REFERENCES	3-20

3 BEAM TRANSFER TO TARGETS

3.1 INTRODUCTION

For the European Spallation Neutron Source (ESS) two target stations are planned [ESS, 1996], a long pulse target station (LPTS) that takes the beam directly from the linac, and a short pulse target station (SPTS) that gets the beam longitudinally compressed from the two accumulator rings. The repetition rate is 50 Hz for the SPTS with a pulse length of about 1.4 μ s and 16 $\frac{2}{3}$ Hz for the LPTS with about 2.0 ms pulse length. The beam footprint on target should be in both cases 200 mm \times 60 mm (h \times v, in 2σ gaussian). The beamlines to these target stations have to be designed to accept 5 MW beam power with different beam characteristics at the entrance. The critical feature for both beamlines is that target design requires quite large beam profile with good stability (centroid variation \pm 2 mm).

3.2 BEAMLINE TO THE LONG PULSE TARGET

Figures 3-1 and 3-2 are showing the beamline layout and beam optics. Two different types of ion sources for the LPTS are under consideration. One could either use the same H⁻ sources as for the SPTS or build an additional proton source. Therefore, the switching scheme to the LPTS has to be designed to accept both types of beams. One special feature for the LPTS beamline design is the small emittance ($\sim 0.1 \pi \cdot \mu\text{m} \cdot \text{rad}$ for 1σ) from the linac. Therefore, few quadrupoles of small aperture are used for the focusing.

The RF cavities in the section between the linac exit and the first achromat magnet, used for the momentum ramping and the bunch rotation for the injection into the rings, are switched off during the transfer of the long pulse beam. The former will decrease the beam stability, and the latter will increase the space charge effect in the beamline by slowing down the lengthening of the beam packet.

With the peak intensity level of 100 mA (107 mA for short pulse beam, 114 mA for long pulse beam), the space charge effect in the beamline from the linac to both the LPTS and the beam dump is not important, but the focusing parameters in the beginning part of the beamline should be adapted to the beam current. In the downstream, it becomes much weaker as the beam length increases with the distance due to the momentum spread of about $\pm 2 \times 10^{-3}$.

3.2.1 Fast Switchyard and H⁻ Stripping

A fast switch magnet and two bumpers are used for fast switching between the long pulse and the short pulse beams, as the former feeds to LPTS and the latter goes to the rings and SPTS. The switch magnet is put just after the bunch rotation cavity, and the space of 2.1 m between the cavity and the first achromat magnet is enough to make the necessary beam separation. In the case of an H⁻ beam for the long pulse, two strippers are inserted just before the first bending magnet of the achromat to convert the H⁻ beam into a proton beam in the line to LPTS, whereas in the case of a proton source for the long pulse no stripper is used. The switch magnet of 30 mrad strength creates a beam separation of 45 mm at the position of the strippers. The bumpers bend the proton beam back into the linac axis.

The two strippers are very important, perhaps as critical as the one for ring injection. They have to assure a nearly 100 % conversion of the H^- ions into protons.

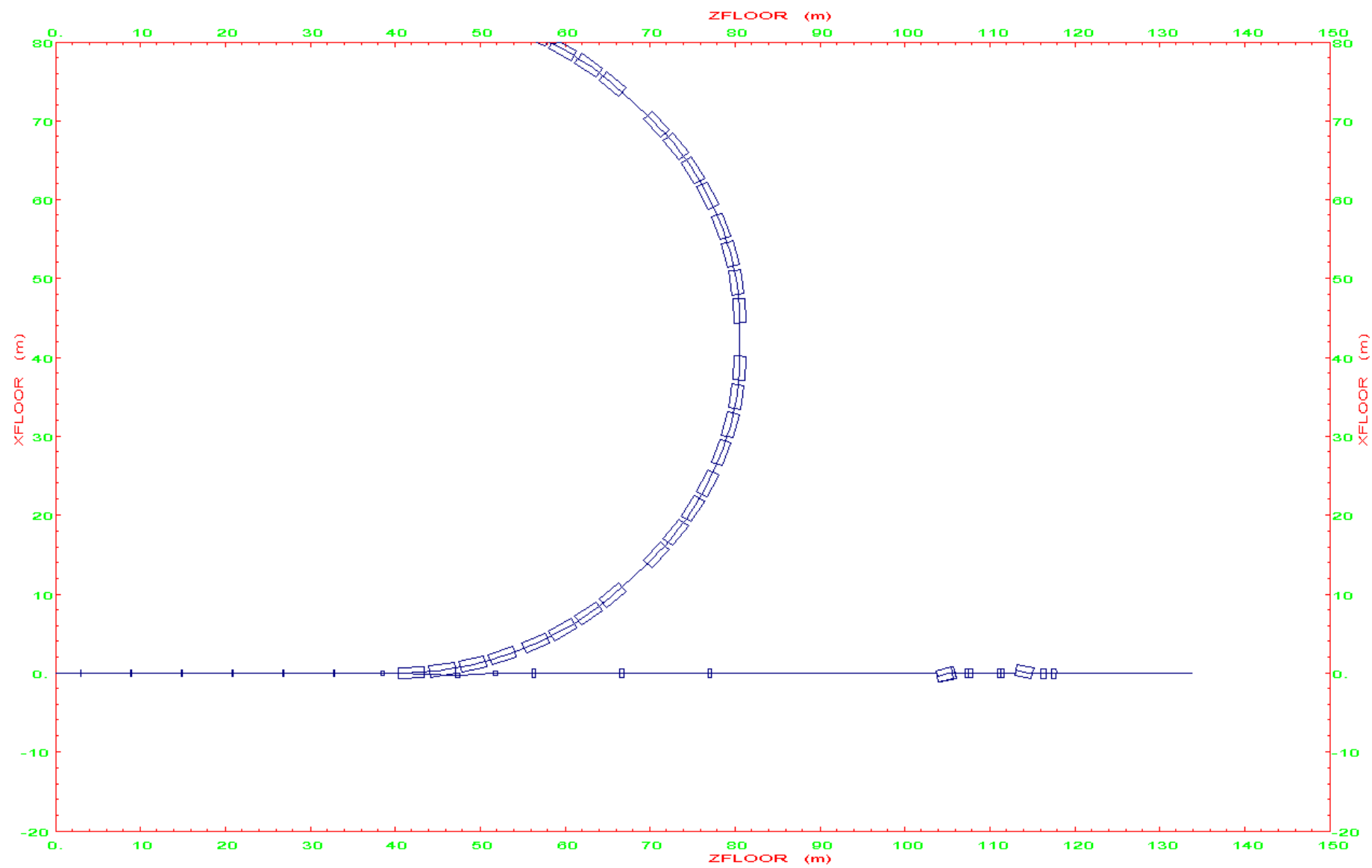


Figure 3-1a: LPTS beamline layout (top view)

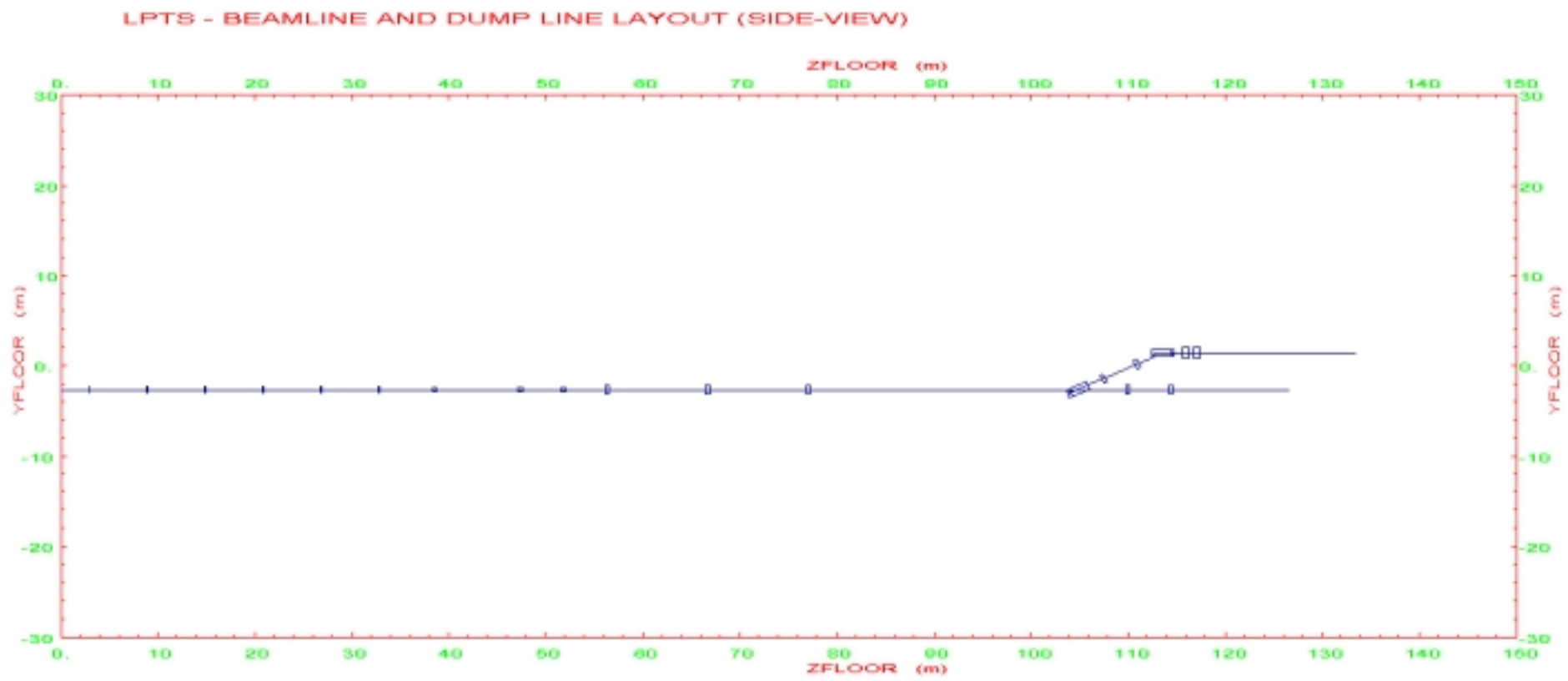


Figure 3-1b: LPTS beamline and dump line layout (side view)

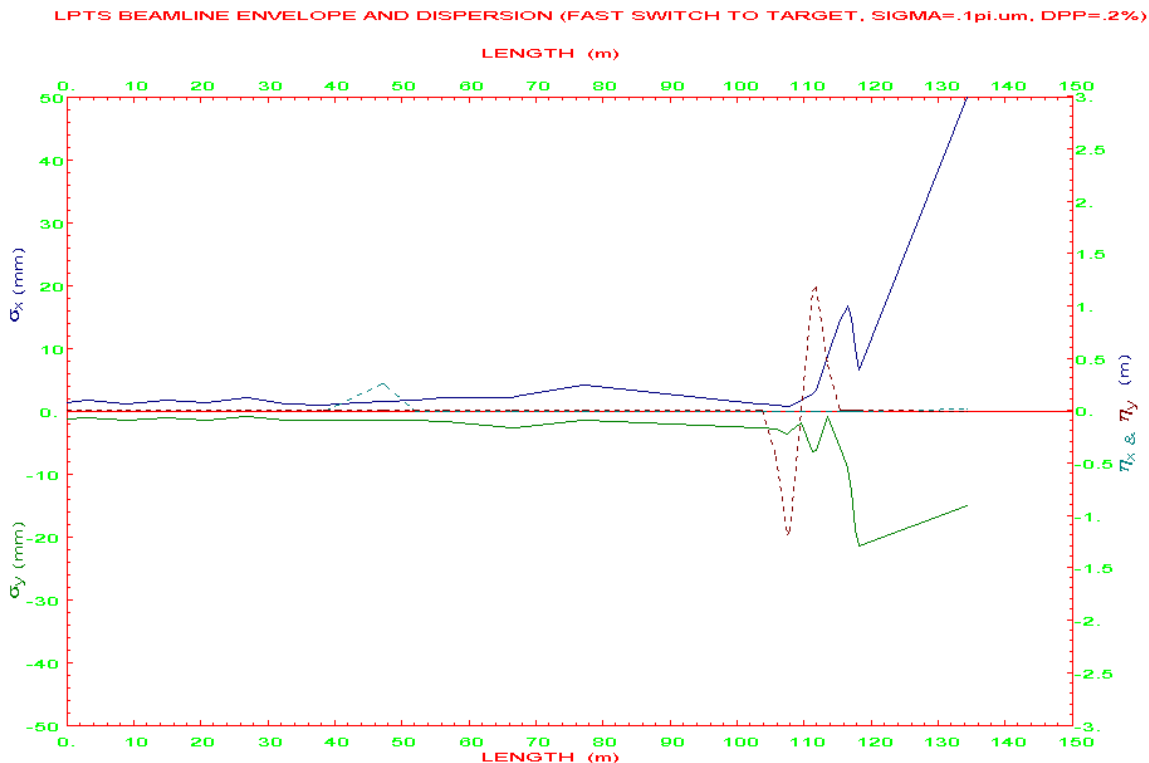


Figure 3-2: LPTS beamline envelope and dispersion

3.2.2 The 16 $\frac{2}{3}$ Hz Target Line

The LPTS is located horizontally along the linac axis but on a different vertical level. The beam is lifted in an achromatic vertical bending section by 4.1 m from the linac level (2.6 m below ground) to the target level (1.5 m above ground). This is an anti-symmetric bending system of two 25° dipoles and two quadrupoles (within 12 m). In order to separate the LPTS building and the achromat building, a transfer section of 50 m and three quadrupoles are inserted between the switch section and the lifting section. The quadrupoles also provide the required phase space adaptation for the envelope control in the vertical bending section.

The last two quadrupoles make the required beam profile at the target (50 mm × 15 mm for 1σ , h × v envelope), assuming that the both transversal planes have a good gaussian-like distribution. The distance of 16 m between the last quadrupole and the target window is reserved for the installation of the collimator before the window, target equipment and for the shielding of backscattering neutrons from the target. In the case of non-gaussian distribution, some multipole magnets in the beamline can make a good gaussian-like distribution in x-y plane at the target.

The design also assures that the energy density does not increase dramatically in the case of failure of one magnet element [Ullmaier, 2001]. The whole transfer system has to work reliably in order not to destroy the target.

3.2.3 Slow Switchyard and Dump Lines

The linac beam dump is along the linac axis on the same vertical level and locates in the LPTS building to share the infrastructure there. This makes the linac commissioning and beam set-up more convenient and safer because the switch magnet and the bumpers are switched off to dump both types of beams (perhaps both H^- beam and proton beam). By switching off the first dipole of the vertical bending section, the both beams go to the beam dump. The quadrupole preceding the dipole and the two quadrupoles afterwards make a round beam ($30\text{ mm} \times 30\text{ mm}$ for 1σ , $h \times v$ envelope) at the dump.

The beamline can transfer the alternate H^- and proton beams to the beam dump without changing the focusing parameters from the linac exit to the dump. If the beam peak intensities from the linac for both the long pulse and short pulse beams are not evidently different, one does not need to switch the focusing parameters in the beamline, as the space charge effect can be seen only in the beginning part of the beamline close to the linac. However in the case of quite different peak intensities for the long pulse and short pulse beams, the beginning part of the beamline should be adapted to the beam current as that has to be done in the linac.

3.3 BEAMLINE TO THE SHORT PULSE TARGET

The design of the beamline from the rings to the SPTS is based on the design in 1996 [Ziemann, 1996] with some modifications. The magnet arrangement and beam optics can be seen in Figures 3-4 and 3-5. Since the emittance is as large as $30\pi\text{ mm.mrad}$ (r.m.s) and nearly equal in the horizontal and vertical planes, the FODO design is a good solution for the main focusing structure, but triplet focusing and doublet focusing are used in the vertical bending sections. The H^- beam pulses of 1.2 ms from the linac are split and sent to the two accumulator rings. After each part of the beam is compressed into 0.6 μs , the two beams are extracted and annexed one after the other to form pulses of 1.4 μs in length.

With the beam peak intensity of 65 A (for one ring), the space charge effect has some minor affect to the focusing. At the matching points, the quadrupoles designed for the phase space matching have to be readjusted to keep good matching. Another important thing is that the beams coming from the two rings may have different distribution, as one of them (lower ring) has to hold up the full intensity for 0.7 ms until the other is fully filled. Space charge effect and other sources may change the beam distribution in the lower ring. Some study should be done later on the transfer of the two slightly different beams to the target.

3.3.1 Extraction and Matching to the Downstream Beamline

The beam extraction from the rings is done by a group of four kickers, a ring quadrupole triplet and a septum magnet. Five quadrupoles are used to match the triplet focusing in the rings to the FODO focusing in the beamline. Together with a 7.5° dipole, they cancel the horizontal dispersion created by the kickers and the septum magnet (15° bending in total).

3.3.2 Joining Section

Joining the two-beams is done by bending down the beam from the upper ring level with a combination of ordinary dipoles, septum and kicker magnets. The nearly anti-symmetric

vertical bending section of two dipoles (one 7.5° ordinary, one 6.18° septum) and a triplet brings the upper beam down about 2.0 m. The final deflection to the beamline axis for the upper ring beam is done by the two quadrupoles and a group of four kickers (18.3 mrad kicking angle in total). The total vertical bending is achromatic. As the bending angle is small, the separation between two branches is quite small for installing the quadrupoles. Special attention is also paid to the beam separation at the septum and the two sharing quadrupoles, as well as the kicker strengths.

3.3.3 Switchyard and Dump Line

Four quadrupoles are used to match the special focusing structure in the joining section to the periodic 90° FODO modules (five quadrupoles, two and half modules). These nine quadrupoles over 30 m also separate the ring building and SPTS building. The beam dump is on the same vertical level as the lower ring, but just below the target assembly to share the infrastructure in the building. An anti-symmetric bending section of two 15° dipoles and two quadrupole doublets (within 17 m) raises the beam 4.1 m vertically to the target level (1.5 m above ground), whereas the beam goes straight to the beam dump by just switching off the first dipole.

The beam dump is important for the ring commissioning and the beam set-up during operation. The quadrupole preceding the dipole and the two additional quadrupoles after it make a nearly round beam (26 mm \times 32 mm for 1σ , h \times v envelope) at the dump.

3.3.4 Adaptation to the Target

Three quadrupoles make the required beam profile (gaussian distribution, 50 mm \times 15 mm for one σ and collimated to 3σ , h \times v envelope) at the target. The distance between the last quadrupole and the target window has to be kept about 16 m in order to allow the installation of target equipment and the collimators in front of the target. A shielding wall separates the magnets from the radiation of backscattering neutrons from the target. The design satisfies the requirement from the target design that the beam should not shrink in the case of failures and variations of any magnet element.

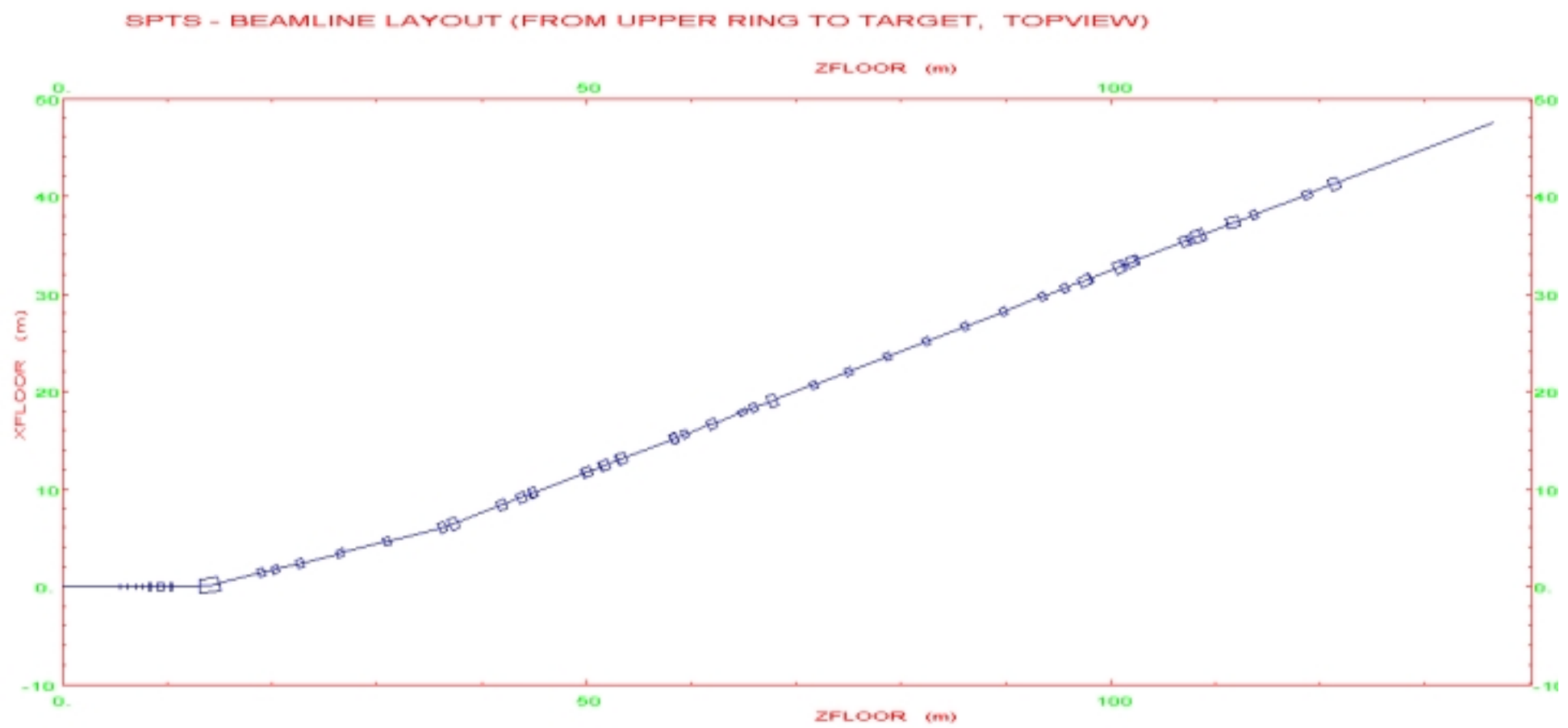


Figure 3-4a: SPTS beamline layout (top-view)

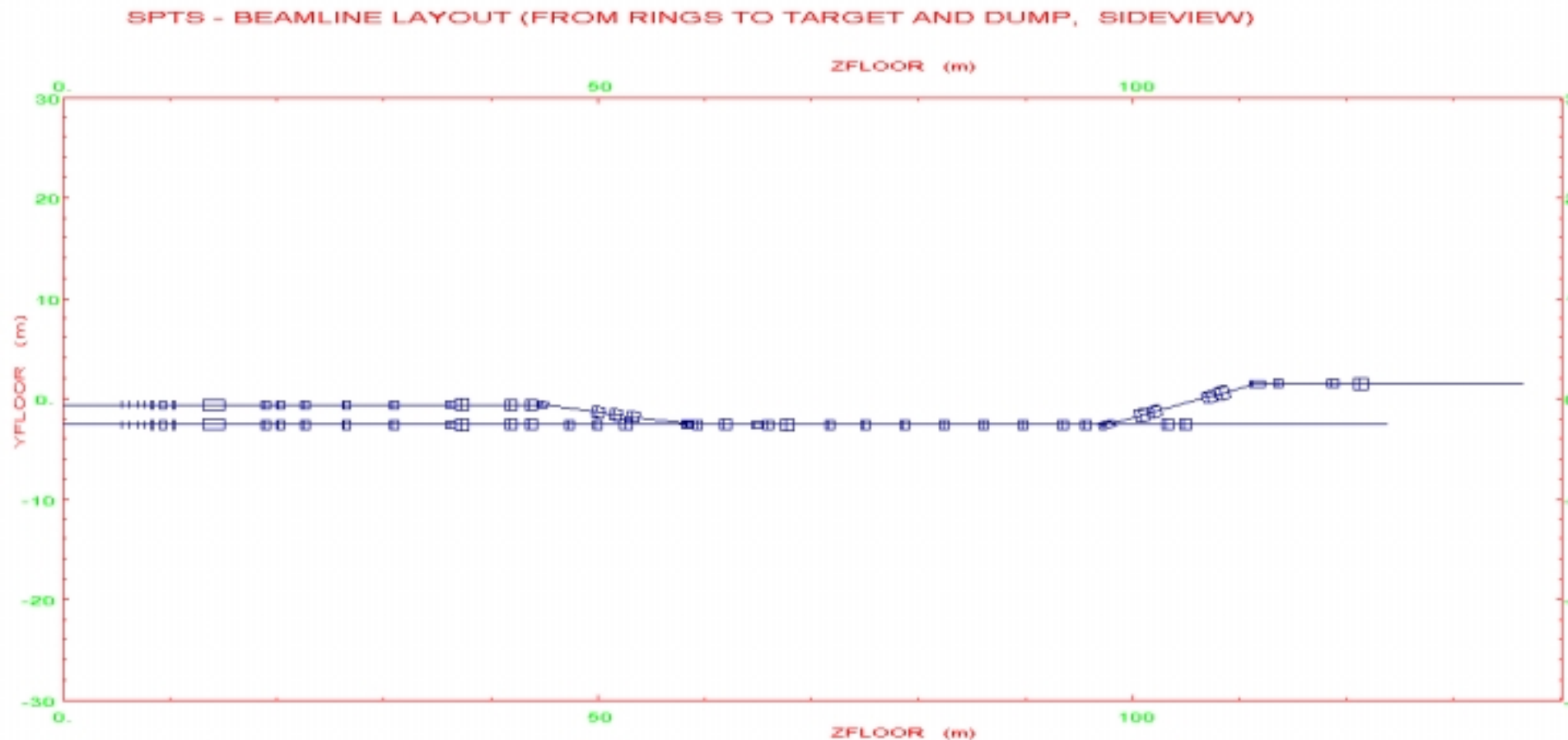


Figure 3-4b: SPTS beamline layout (side-view)

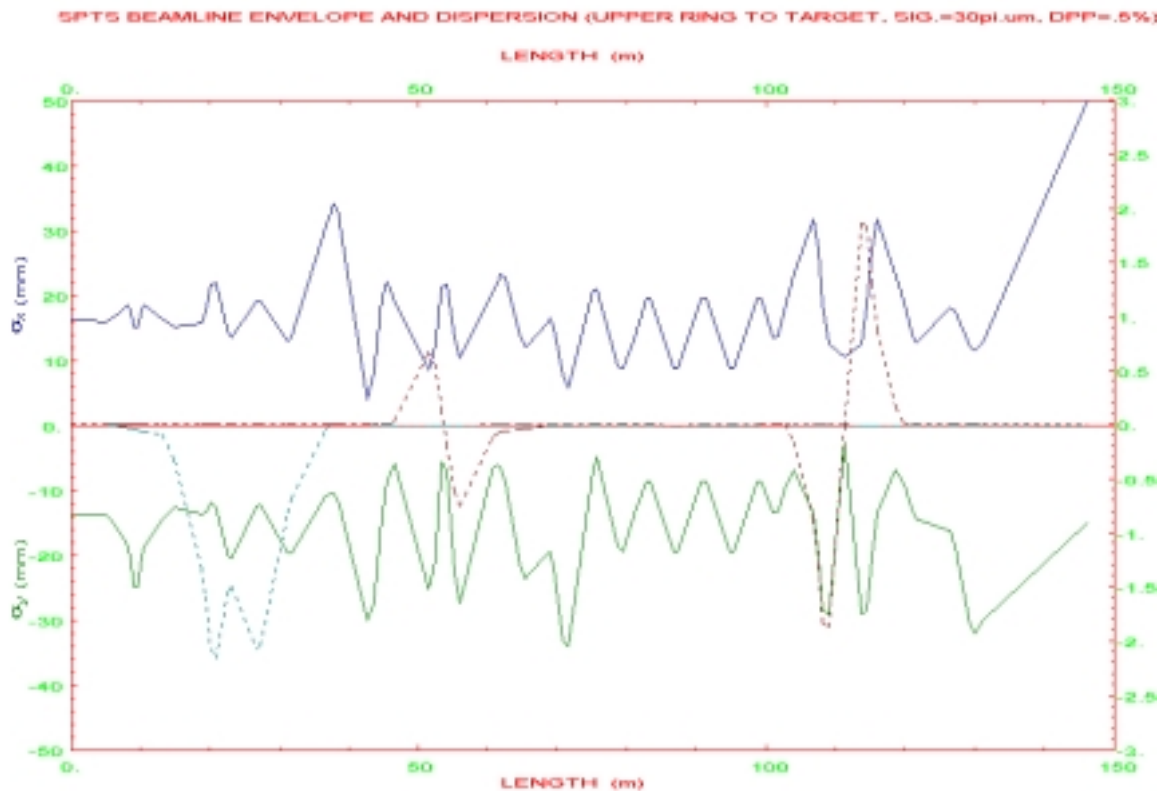


Figure 3-5a: SPTS beamline envelope and dispersion (upper ring to target)

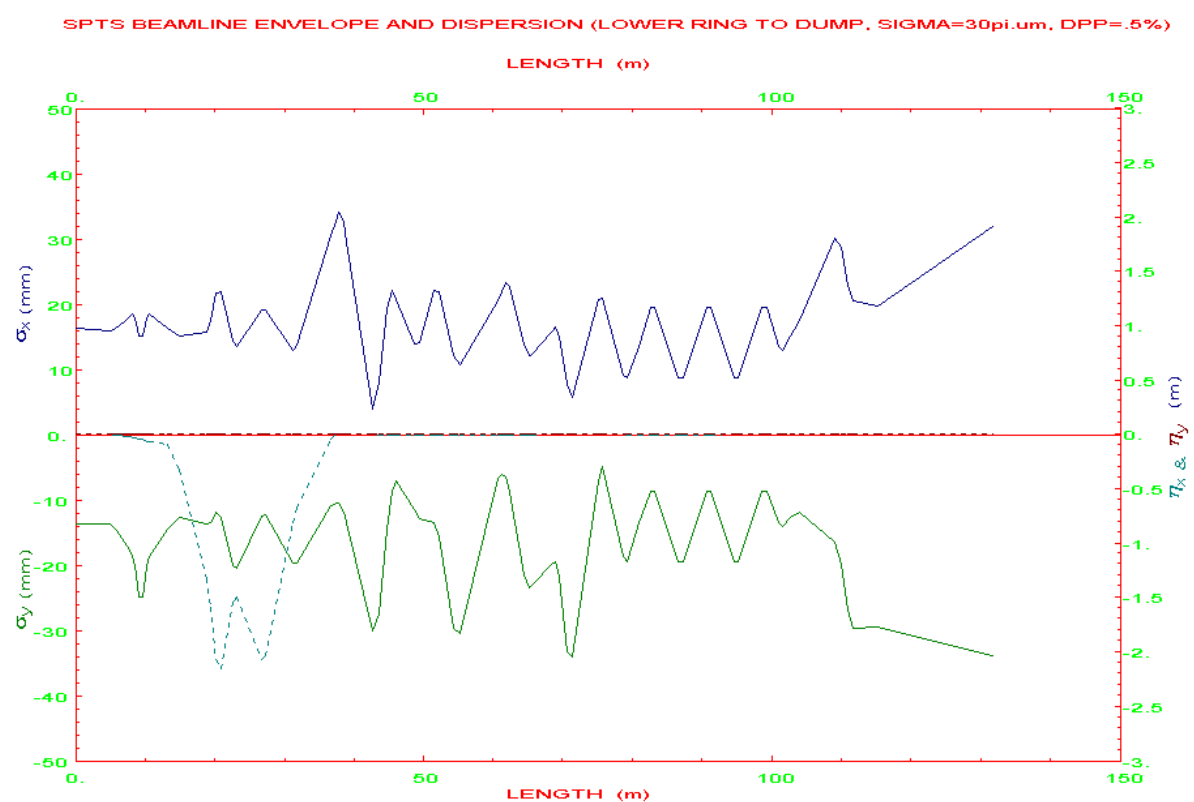


Figure 3-5b: SPTS beamline envelope and dispersion (lower ring to beam dump)

3.4 BEAM DIAGNOSTICS

The beam diagnostics system is very important for machine commissioning and beam set-up but also for the safety control of the whole system. It includes beam position monitors, beam loss monitors, beam profile monitors and beam current monitors. We have to investigate what kind of beam diagnostic devices can work under ESS beam power conditions with reasonable lifetime and low beam interaction to avoid additional radiation.

3.4.1 Beam Profile Monitoring

The big challenge is non-destructive beam profile monitoring, especially those close to the target. Another important point is the beam loss monitoring system around the whole accelerator complex.

There exist several kinds of beam profile diagnostic devices based on registration of particles produced by residual gas ionisation. Usually such devices are used as beam profile monitors that register electrons and/or ions produced in collisions of beam particles with residual gas. Another possibility is H⁻- Laser beam diagnostics, which is now also under development.

Some attempts were made in measuring the light radiation of excited atoms. The scheme proposed by JINR in Dubna [Brovko, 2001] might be used for the ESS beamlines. It has some advantages compared to methods based on registration of particles produced by ionisation, like higher spatial and time resolution, insensitivity to external electric and magnetic fields, as well as to beam space charge fields. The main disadvantage of the registration of photons is its rather lower sensitivity, because the cross-section of excitations

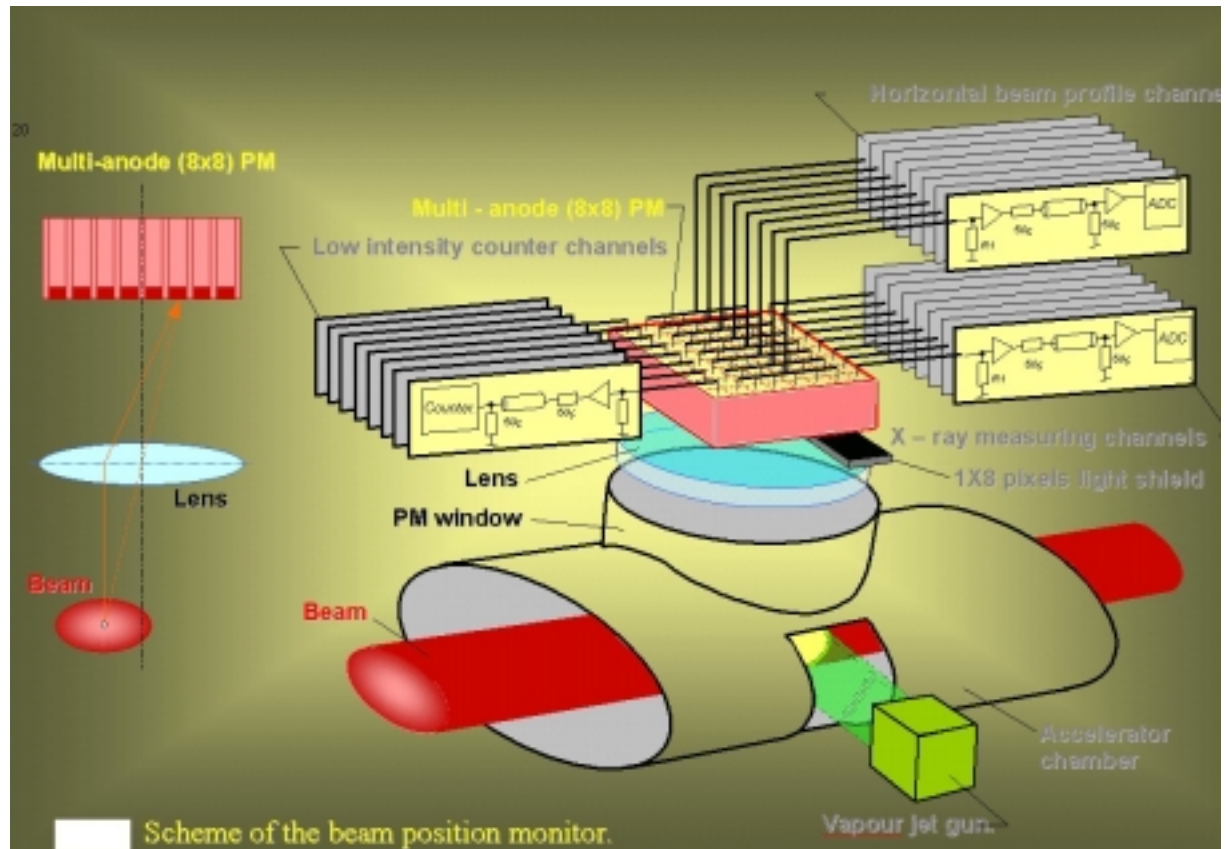


Figure 3-6: Scheme of the beam position monitor for ESS target beamlines

is smaller than in the case of ionisation. However, this disadvantage practically does not at all limit the application under specific conditions like for ESS. This method can be applied both to the beams circulating in rings and to single pass ones.

A schematic drawing of the proposed diagnostic device designed by JINR, Dubna, is shown in Figure 3-6.

The beam image is transported by an optical system (mirrors and/or lenses) onto a photo cathode and is then registered by position-sensitive multi-anode photo multipliers (PMPs). Each of them has 8×8 pixels with a size of 2×2 mm each. It permits to have a space resolution of 1/8 of the aperture. The usage of 2 photo multipliers placed side by side may double this resolution up to 1/16 of the aperture. In each of the 8 strips, it is proposed to use 3 kinds of registration channels oriented along the beam axis.

The first of them is used for light intensity measurement. To increase the sensitivity of the amplitude measurement, 6 parallel anodes of the PMPs are connected together. The 8 signals from these anodes are transferred to the main amplifiers by passing through the buffer preamplifiers placed close to the PMPs. These signals are measured by fast Flash-ADCs and the digital information is stored in a buffer memory.

Secondly, a light shield shades an area of 1×8 pixels of photo cathode. Therefore, just the light generated in the glass of the PMP due to the X-ray radiation of dissipated beam particles is registered. The signals from these anodes will be used to measure the background. The background can be subtracted later from that received from the other analog channels.

The third set of 1×8 channels could be used in counting mode operation to enable single photon registration when dealing with low intensity beams.

In the system proposed by JINR, a vapor jet crosses the vacuum chamber to increase the sensitivity of the device, but for ESS, one might get problems while using such a vapor jet, because the 5 MW ESS beam crossed with the vapor jet may produce a considerable amount of radioactivity. In addition, with the ESS beam there might be enough interaction with residual gas so that there is no need of a vapor jet.

The work is in progress in cooperation with JINR, Dubna. First tests on resolution seem to be successfully.

3.4.2 Beam Loss Monitor System

For the beam loss monitor system Argon filled ion chambers ($70 \text{ nC/Rad} \rightarrow 19 \text{ pA/Rad/h}$) similar to Tevatron and RHIC are useable. For fast loss monitors, Bicron liquid scintillators ($100 \mu\text{C/Rad}$) are taken into consideration.

3.5 MAGNETS AND POWER SUPPLIES

Ordinary rectangular dipoles, septa, kickers, quadrupoles and non-linear magnets are used for guiding, focusing and preparation of the beam. They are listed in tables 3-1, 2, 3 and 4.

Table 3-1: Specification of dipoles and other magnets for the LPTS beamline

Dipole	Angle (radian)	Length (m)	Field (T)	Max (ax/ay) (mm)	Cal./set Gap (mm)	Comment
TSWITCH	0.0300	0.40	0.518	0.99/1.47	17.8/60	$t_r < 100\mu s$
TBUMP1	0.0890	0.50	1.228	1.50/1.52	18.2/60	Two tracks
TBUMP2	0.0590	0.50	0.815	1.79/1.55	18.4/60	Two tracks
LBV01	0.4363	2.00	1.494	1.10/2.92	14.8/120	0° Port
LBV02	0.4363	2.00	1.494	13.94/5.82	117.5/120	

Table 3-2: Specification of quadrupoles for the LPTS beamline

QUAD	Max (ax, ay) (mm)	Cal. Pole Diameter (mm)	Strength K1 (m^{-2})	Remarks
LQ01F	2.17	23.36	0.11	Type A
LQ02D	2.61	26.88	0.21	"
LQ03F	4.15	39.20	0.19	"
LQ04D	3.80	33.40	2.17	"
LQ05F	6.66	59.28	2.17	"
LQ06D	15.93	133.44	1.06	Type B
LQ07D	21.06	174.48	0.99	"
DQ01F	5.33	48.64	0.25	Type A
DQ02D	7.05	62.40	1.31	"
	Max. pole B (T)	Mean pole B (T)	Number, Diameter, Length	
Type A:	0.60		N=7, D=80mm, L=400mm	
Type B:	0.73		N=2, D=200mm, L=600mm	

3.5.1 Bending Magnets and Quadrupoles

Many dipoles and quadrupoles are powered in series to save costs and to increase the availability of the whole system. In the SPTS beamline, there are some quadrupoles that need for high pole fields and large pole diameters. The quadrupoles are grouped into three types. As the emittance is small in the LPTS beamline, the quadrupoles are much smaller than those for the SPTS beamline. They are also grouped into three types. All the quadrupoles have pole field below 1.0 Tesla. The field chosen for the bending magnets is about 1.5 Tesla. Some correctors are needed for beam alignment, and their number will be given later. They are loosely arranged, as the requirement for the alignment is not critical.

Table 3-3: Specifications of dipoles for the SPTS beamline

Dipole	Angle (radian)	Length (m)	Field (T)	max(ax/ay) (mm)	Cal./set Gap (mm)	Comment
BMH01U	0.1309	0.60	1.505	32.7/9.0	78.0/170	7.5deg, A
BMH01L	0.1309	0.60	1.505	32.7/9.0	78.0/170	A
BMV01U	0.1309	0.60	1.505	20.2/7.3	167.6/170	A
BMV02UL	0.1079	0.60	1.241	18.8/6.3	156.4/160	Septum, C
BMV03	0.2618	1.20	1.505	23.1/9.2	190.8/192	B
BMV04	0.2618	1.20	1.505	23.1/9.2	190.8/192	B
KICK	0.0184	2.80	0.045	15.7/23.2	191.6/192	In 4 parts

Note: they are grouped in three types: A, B and C

3.5.2 Non-Linear Magnets

Some non-linear magnets may be needed for better control of the beam distribution both at the SPTS and LPTS targets, as there exist many higher-order sources such as magnet aberration, field imperfection of magnets, space charge effect, non-gaussian distribution from the accelerators and also misalignment of magnets. All these magnets have ordinary design features.

3.5.3 Septa, Switch magnets and Kickers

In the SPTS beamline, septum and kicker magnets are needed to merge the extracted beams from the two accumulator rings, where the kickers are the critical elements (18.5 mrad for four sets, 2.8 m length in total, 200 ns rise-time, similar to the ones for ring extraction). One fast switch magnet and two bumper magnets are also used for the fast switch between the long pulse and the short pulse beams. The switch magnet requires a rise-time of 100 μ s.

3.5.4 Power supplies

The power supplies for the magnets are ordinary except those for the kickers in the SPTS beamline. Many dipoles, quadrupoles and multipoles are powered in series to save costs and to increase the availability of the whole system. Tables 3-5,6 list the power supplies for the magnets in the LPTS and SPTS beamlines.

Table 3-4: Specifications of quadrupoles for the SPTS beamline

QUAD	max(ax, ay) mm	Cal. Pole Diameter (mm)	Strength K1 (m^-2)	Separation Mm
QD01UA, LA	17.55	146.40	0.41	
QF02UA, LA	21.99	181.92	0.73	
QD03UA, LA	20.55	170.40	0.57	
QF04UA, LA	19.11	155.88	0.38	
QD05UA, LA	19.78	164.24	0.39	
QF06UC, LC	34.14	279.12	0.42	
QD07UC, LC	30.19	247.52	0.65	
QF08UB	22.06	182.48	0.71	
QD09UB	25.38	209.04	1.04	
QF10UB	21.66	179.28	0.99	
QD11UB	27.49	225.92	0.98	
QF08LB	22.04	182.32	0.72	
QD09LA	14.19	119.52	0.65	
QF10LA	26.01	214.08	0.62	
QD11LC	30.48	249.84	0.46	
QF01A	8.84	131.02	0.73	54.3
QD02B	23.64	227.72	0.41	32.6
QF03A	22.00	182.00	0.85	
QD04C	34.14	279.12	0.62	
QF05A	20.97	173.76	0.74	
QD06A	19.51	162.08	0.83	
QF07A	19.51	162.08	0.62	
QD08A	19.51	162.08	0.62	
QF09A	19.51	162.08	0.62	
QD10A	19.51	162.08	0.62	
QF11A	19.51	162.08	0.62	
QD12A	13.67	115.36	0.87	
QF13C	31.72	259.76	0.71	
QD14B	29.09	238.72	1.04	
QD15B	29.09	238.72	1.04	
QF16C	31.72	259.76	0.71	
QD17A	14.43	121.44	0.51	
QF18A	18.93	157.44	0.33	
QD19C	32.16	263.28	0.31	
QF01DB	30.00	246.00	0.35	
QD02DB	29.77	244.16	0.31	
	Max. pole B (T)	Mean pole B (T)	Number, Diameter, Length	
Type A:	0.60		(24,D=200mm, L=600mm)	
Type B:	0.90		(10,D=250mm, L=800mm)	
Type C:	0.72		(9, D=300mm, L=800mm)	

Table 3-5: Number of power supplies in LPTS beamline

MAGNET	NO. OF POWER SUPPLIES	REMARKS
SWITCH	1	Single
BUMPER	2	Single
DIPOLE	1	2 in series
QUAD 1	1	2 in series
QUAD 2	7	Single
Total	12	

Table 3-6: Number of power supplies in SPTS beamline

MAGNET	NO. OF POWER SUPPLIES	REMARKS
KICKER	4	Single
DIPOLE 1	2	2 in series
DIPOLE 2	2	Single
QUAD 1	1	5 in series
QUAD 2	9	2 in series
QUAD 3	20	Single
Total	38	

REFERENCES

- [Brovko, 2001] O.I.Brovko, J.Dietrich, V.A. Krasnov, I.N.Meshkov, I.Mohos, A.N.Parfenov, V.N.Pavlov
Proc. of the 6th International Workshop on “Relativistic Nuclear Physics: From Hundreds of MeV to TeV”, Varna, Bulgaria, September 2001 (in printing)
- [ESS, 1996] European Spallation Source: Volume 3. The ESS Technical Study Report. ESS 96-53-M, November 1996
- [Ullmaier, 2001] H. Ullmaier
Some Reflections on the Proton Beam Profile and its Stability Report ESS-108-01-T, March 2001
- [Ziemann, 1996] V. Ziemann
New Optics of the ESS Target Beam Line Report ESS-96-54-R, December 1996

Chapter 4

Target Systems

Authors and Contributors

Target Systems

G.S. Bauer¹, M. Butzek¹, H. Conrad¹, D. Filges¹, F. Goldenbaum¹, P. Jung¹, G. Mank¹, R. Moormann¹

¹FZJ

Acknowledgements to contributors of the ESS study of 1996, Target System Working Group:

ESS-CPT:

F. Carsughi

Risoe National Laboratory:

K. Stendal

FZJ:

H. Cords, K. Doering, B. Guttek, Th. Matzerath, R. Neef, H. Schaal,
H. Stechemesser, H. Ullmaier, J. Wimmer, H. Wyrwich

HMI:

E. Camus, D. Hilscher, F. Jahnke, F. Mezei, L. Pienkowski,
G. Wollenberger

PSI:

Y. Dai, R. Dressler, T. Dury, B. Eichler, L. Ni, B. Sigg, B. Smith, K. Skala, Y. Takeda

RAL:

T. Broome, D. Bellenger, C. Densham, H. Jones, L. Perrott, G. Thomas

University of Birmingham

D. Beynon, D. Picton

Contents

Target Systems

4 TARGET SYSTEMS 4-5

4.2 TARGET STATION TECHNICAL LAYOUT 4-9

4.2.1 INTRODUCTION	4-9
4.2.2 THE OVERALL LAYOUT OF TARGET STATIONS AND EXPERIMENT (USER) AREAS	4-10
4.2.3 THE REFLECTOR AND MODERATOR MODULE	4-12
4.2.4 THE MERCURY LOOP.....	4-12
4.2.5 WATER LOOPS AND SERVICES	4-15
4.2.6 ENCLOSURE SYSTEMS	4-16
4.2.7 PROTON BEAM WINDOW	4-17
4.2.8 REMOTE HANDLING	4-18
4.2.9 SHIELDING	4-19
4.2.10 SHUTTERS AND NEUTRON BEAM LINES.....	4-20
4.2.11 CHOPPERS.....	4-22

4.3 THE MERCURY TARGET 4-23

4.3.1 A LIQUID METAL TARGET	4-23
4.3.2 MERCURY AS TARGET MATERIAL	4-23
4.3.3 STRUCTURE MECHANICS AND DESIGN OF THE TARGET UNIT	4-27
4.3.4 POWER DEPOSITION AND THERMAL HYDRAULICS DESIGN.....	4-29
4.3.5 EFFECTS DUE TO PULSING OF THE BEAM	4-31
4.3.5.1 <i>Effects on the wall from the heated fluid</i>	4-31
4.3.5.2 <i>Effects of direct window heating</i>	4-33
4.3.6 CORROSION, EROSION AND LIQUID METAL EMBRITTLEMENT IN THE TARGET CIRCUIT	4-34
4.3.7 IMPURITY BUILD-UP BY SPALLATION PRODUCTS AND ITS EFFECT ON TARGET MATERIAL QUALITY	4-36
4.3.8 RADIATION EFFECTS IN STRUCTURAL MATERIALS	4-37

4.3.8.1 Radiation Damage

4.3.8.2 *Materials selection and lifetime prediction*

4.3.9 RADIOACTIVITY AND DECAY HEAT.....

4.4 THE MODERATOR-REFLECTOR UNITS 4-43

4.4.1 THE MODERATOR CONFIGURATIONS	4-43
4.4.2 VERTICAL REFLECTOR-MODERATOR-SHIELDING MODULE	4-44
4.4.3 SUPERCRITICAL HYDROGEN MODERATOR SYSTEMS	4-45
4.4.4 CRYOGENIC MODERATOR VESSEL	4-47
4.4.5 PERFORMANCE ESTIMATES.....	4-49
4.4.5.1 Monte Carlo Calculations	4-49
4.4.5.2 Experimental results	4-49
4.4.6 OPTIONS AND ALTERNATIVES.....	4-51
4.4.6.1 Moderator Configuration	4-51
4.4.6.2 Advanced Cold Moderators.....	4-52
4.4.6.3 Systems integration of advanced moderators	4-54

4.5 NEUTRON PERFORMANCE OF THE SHORT PULSE - AND LONG PULSE TARGET STATIONS	4-56
4.5.1 INTRODUCTION	4-56
4.5.2 THE SHORT PULSE TARGET STATION (SPTS).....	4-57
4.5.2.1 Cold Hydrogen Moderator (20K).....	4-58
4.5.2.2 Ambient Temperature Water Moderator (300K)	4-61
4.5.2.3 Moderator Poison Burn-up	4-63
4.5.2.4 "Hot" Neutrons.....	4-64
4.5.3 THE LONG PULSE TARGET STATION (LPTS)	4-64
Cold Hydrogen Moderator	4-66
4.5.4 SUMMARY AND FURTHER INVESTIGATIONS.....	4-68
4.6 BEAM STOPS.....	4-69
4.6.1 LINAC AND RING DEVELOPMENT BEAM DUMPS	4-70
4.6.2 RING (AND LINAC) INJECTION LOSS CATCHERS	4-73
4.6.3 ACHROMAT SCRAPER BEAM CATCHERS	4-74
4.6.4 NEUTRON BEAM COLLIMATORS AND CATCHERS AT PROTON INJECTION INTO THE TARGETS.....	4-74
4.6.5 SUMMARY.....	4-75
4.7 SAFETY ASPECT	4-76
4.7.1 INTRODUCTION	4-76
4.7.1.1 General.....	4-76
4.7.1.2 Overview on the safety concept of the ESS target system	4-77
4.7.2 ESTIMATE OF RADIOTOXIC AND CHEMICAL TOXIC POTENTIALS.....	4-77
4.7.2.1 Radiotoxicity.....	4-77
4.7.2.2 Comparison of (chemical) toxicity and radiotoxicity of mercury.....	4-79
4.7.3 ACCIDENT ANALYSIS BASED ON PSAR (OVERVIEW)	4-80
4.7.4 SAFETY STUDIES BEYOND PSAR.....	4-82
4.7.4.1 System analysis	4-82
4.7.4.2 Iodine volatility	4-82
4.7.5 ADDITIONAL ACCOMPANYING RESEARCH & DEVELOPMENT WORK.....	4-85
REFERENCES	4-87

4 TARGET SYSTEMS

4.1 OVERVIEW

The overall concept of the ESS Target Stations was worked out in the Project Study, for which a report was published in 1997 [Bauer, 1996a]. The report listed a number of R&D issues, most of which have since been or are still being dealt with by the Target Systems Group. The present description of the **reference concept** for the ESS Target Systems takes into account results from this research and new demands coming from the expanding scientific case. The latter is being elaborated under the guidance of the Scientific Advisory Committee (ESS SAC) that was founded after the successful completion of the Project Study. The most important change was triggered by the decision of ESS Council to replace the 1 MW-10Hz short pulse target station (SPTS) by a 5 MW- $\frac{2}{3}$ Hz long pulse target station (LPTS) fed directly from the linac. Furthermore, a superconducting (SC) linac concept is worked and compared to the room temperature (RT) one. Although the final decision on the linac concept (RT or SC) is still pending, the parameters listed in Table 4.1-1 below are valid for both versions. Otherwise the reference concept for Target Systems remained largely unchanged. Some very recent proposals by the Instruments Team relating to combined spectrum beam lines could not yet be incorporated in the concept. Their effect on the technical layout will, however be relatively minor; although some of the figures given in section 4.5 on neutron performance may change slightly due to a new reflector configuration. With this proviso the present account follows closely the description given in [Bauer, 1996a], incorporating new information and results where appropriate and leaving out material which, while not necessarily obsolete, served to justify decisions taken during the Study Phase. For example, materials issues are not dealt with in a separate section anymore, but are incorporated in the descriptions of the subsystems where appropriate. On the other hand, a separate section is devoted to safety considerations, which will play an important role in the technical work ahead. The technical concept for Target Systems described in the present report is a reference concept, which is considered feasible and able to meet the users' needs. Options and modifications that might be dealt with during the optimisation process in order to improve the performance further and to establish a firm project baseline by the end of the year 2003 will be judged against this reference.

The target design developed in the original ESS Study involves a flowing liquid mercury target in a steel container. It was chosen for its ability to cope with the high average thermal power deposition of nearly 3 MW in the target material, its good neutron performance and lowest estimated operating cost of all concepts considered. It is expected to result in acceptable lifetime under the demanding radiation and thermal loads of the 5 MW short pulsed proton beam, although some more development work is required to cope with the high pulse power in this concept: The power delivered by the accelerator system in one single proton pulse to the Short Pulse Target is 100 kJ, about 60 kJ of which are deposited as heat in a volume of a few litres in the target during 1.4 μ s. Due to the much longer relaxation times of the resulting thermo-mechanical loads, special care must be taken to avoid unacceptably large stress on the target container and possible deleterious effects of cavitation. Recommendations on related research given by the Technical Advisory Committee (TAC) at its first meeting have been incorporated in the working programme, but results cannot be reported yet.

Since the considerations that lead to the choice of a mercury target for the SPTS are also valid for the LPTS, the same target concept is foreseen for both. (Although the energy in one pulse for the LPTS is even 3 times higher, the effects on the target structure are considered less serious due to the more than 1000 times longer pulse duration.) Using largely identical target systems for both, SPTS and LPTS, will have positive economic advantages for design, licensing, supply and handling of the targets. It also allows the same basic design for the major components of the two target stations, infrastructure and buildings. A list of parameters is given in Tables 4.1-1, 4.1-2 and 4.1-3.

Table 4.1-1: ESS beam parameters on target

Particles	protons
kinetic energy	1.334 GeV
beam cross section	Elliptical 6 x 20 cm ² 2d-parabolic beam density distribution
average current SPTS / LPTS	3.75 mA / 3.75 mA
average beam power SPTS / LPTS	5 MW / 5MW
peak current SPTS / LPTS	62.5A / 112.5 mA
pulse frequency SPTS / LPTS	50 Hz / 16 ^{2/3} Hz
pulse width on SPTS / LPTS	1.4 µs (two times 600 ns with 200 ns gap) / 2 ms

Table 4.1-2: ESS mercury target system performance parameters

Beam power on targets	SPTS: 5 MW at 50 Hz, 1.4 µs long pulses LPTS: 5 MW at 16 ^{2/3} Hz, 2 ms long pulses
Target material	Mercury
Target type	Liquid flow target
Target container	Martensitic steel
Moderators (reference case)	H ₂ O at ambient temperature, coupled/decoupled liquid H ₂ at 20 K, coupled/decoupled and combinations thereof
Reflector (reference case)	Lead, D ₂ O cooled
Heat deposition in target (time average)	2.80 MW at each of the two targets
Local peak power deposition in target material (time average)	ca. 2.5 kW/cm ³
Induced specific radioactivity at saturation for a 15 tons Hg-system	8 GBq/g at shutdown; 0.8 GBq/g after 1 week:
Specific after heat of the target material	0.67 W/kg at shutdown; 0.12 W/kg after 1 day:

Table 4.1-3: Neutron performance of coupled H₂O-moderators at 5 MW beam power

Average thermal neutron flux density for 5 MW on target	3.1 x 10 ¹⁴ neutrons / (cm ² s)
Peak thermal neutron flux density	SPTS: 1.3 x 10 ¹⁷ neutrons/(cm ² s) LPTS: 1 x 10 ¹⁶ neutrons/(cm ² s)
Decay time of flux density (dominant mode)	150 µs

Although beam input into the target from underneath, as realized in the currently most powerful spallation neutron source, SINQ in Switzerland [Bauer, 2001], has the advantage of offering more shield face to accommodate instruments, horizontal beam input into the targets was selected for a variety of reasons. These include ease of target shell exchange, accessibility to beam transport components, cost and overall complexity. It also allows easier draining of the second enclosure that surrounds the target to retain any spills of liquid metal if the main container develops a leak. The beam transport tunnel within the target building, the target shielding block and target handling area (hot cells) will be serviced from a common high bay area with a 100 tonne overhead crane. This allows to physically separate from the areas accessible to users those rooms in which routine service work on radioactive components will take place. As a consequence, there will be two independent experimental areas at each target station, each featuring twelve beam ports at an angular separation of 11°. Individual rotating shutters designed to stop the high energy component of the neutron radiation when closed while the target is in operation are foreseen for the beam lines, as first proposed in the SNQ project [Bauer, 1982]. The neutron optical inserts (instrument specific and to be provided by the users) can be exchanged from above while the shutters are in closed position, which is considered an important advantage of this concept.

The need to keep the peak proton current density at the target container well below 100 $\mu\text{A}/\text{cm}^2$ for reasons of cooling and radiation damage mandates a rather large beam cross section of the order of 100 cm^2 and correspondingly large target volume with several cm of target material around the beam for good neutron yield. Since neutron coupling between target and moderator depends on the distance of the moderator from the beam axis, an elliptical beam cross section was chosen with 20 and 6 cm major and minor axes. The beam distribution within this footprint is assumed to be roughly 2-d parabolic. Furthermore, it had been shown in earlier work [Bauer, 1982] that a slab type target has a positive effect on the neutron current from small moderators. ESS will feature ambient temperature as well as cryogenic moderators to make a large variety of different beam characteristics available to the instruments according to the users' demands.

The target and moderators will be surrounded by an actively cooled reflector unit, which will be designed to enhance the moderator flux as much as possible without generating unacceptably long tails on the pulses. Currently the reflector material foreseen is lead, but this may be reconsidered in the course of detailed design work, at least for the inner part directly surrounding the moderators. This part of the reflector will also be exchangeable since it will suffer from radiation damage.

Narrow hole collimators are foreseen in the proton beam lines in order to force a focus of the beam at a distance away from the target and thus avoid the possibility of inadvertent beam focussing on the target itself. These collimators will, at the same time limit the cross section and angular divergence of the neutron beam emerging from the target in the direction of the proton beam line in order to minimise activation of beam line components. Neutron beam catchers will be provided behind the last bending magnets in the proton beam line.

Furthermore, several proton beam dumps are included in the scope of Target Systems. One each will serve for test and development operations of the linac and ring without target. Those will be located in the target buildings at the level of the ring and linac beams before their bending upwards to the target level. These beam stops will need to be water-cooled and hence will be designed such that they can be accessed with the high bay area crane for repair and exchange. Significant beam losses are also expected to occur at the positions where the

H^- beams are stripped to protons for injection into the rings and possibly also for onward transport to the LPTS via high field magnets. These dumps will also require active cooling and must be accessible for repair. By contrast, the six beam catchers arranged along the achromat between the linac and the rings are presently assumed to be passively cooled and hence of a somewhat simpler design.

4.2 TARGET STATION TECHNICAL LAYOUT

4.2.1 Introduction

The design for the ESS target stations has developed from the initial work of the study group [Bauer, 1996a]. At this stage in the project it is important that the design is sufficiently flexible to allow the requirements of the users to be accommodated without major changes to the target station concept. At the present stage a single design for both the short pulse and the long pulse target station was adopted. This design takes into account experience at existing spallation sources such as ISIS, SINQ and the SNS and JSNS currently under construction.

The overall layout of the target station is shown in Figures 4.2-1 and 4.2-2. There are twelve neutron channels on each side of the proton beam. Each of these channels can accommodate a neutron beam guide insert up to 230 mm wide and 170 mm high. Rotating disk shutters will allow simple exchange of these inserts. This design allows a high degree of flexibility for different kind of beam extraction systems and provides enough space for new and improved extraction methods still to come.

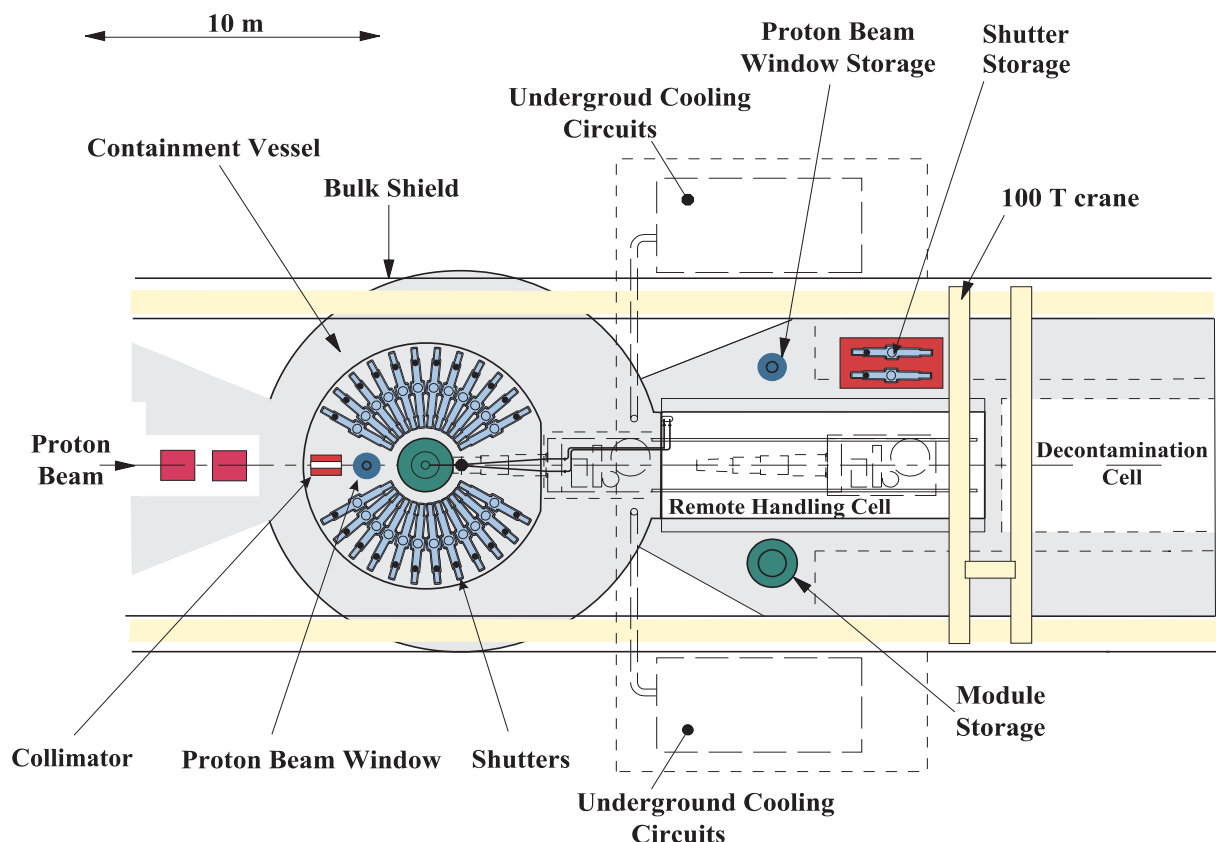


Figure 4.2-1: The overall layout of the target station - plan view

Both target stations will have a liquid mercury target. Since both targets will operate with 5 MW beam power heat removal requirements for the primary cooling loops will be the same. The mercury targets and their associated primary cooling circuits will be mounted on trolleys for transfer to the target remote handling cell. The moderator-reflector assembly, the shutters, the proton beam window and the beam collimator will be removed vertically using

shielded containers. All operations involving the handling of activated and potentially contaminated equipment is performed in a controlled enclosure physically separated from the user areas.

The bulk shield has been designed to reduce the radiation levels to less than $2.5 \mu\text{Sv/h}$ at the shield surface. The inner 1.5 m requires active cooling. An inner enclosure will be used to provide containment of irradiated gases and any fluid leaks in the central region. The shielded active water cooling plant is positioned underground.

The options considered in arriving at this design are discussed in detail in ref. [Broome, 1996].

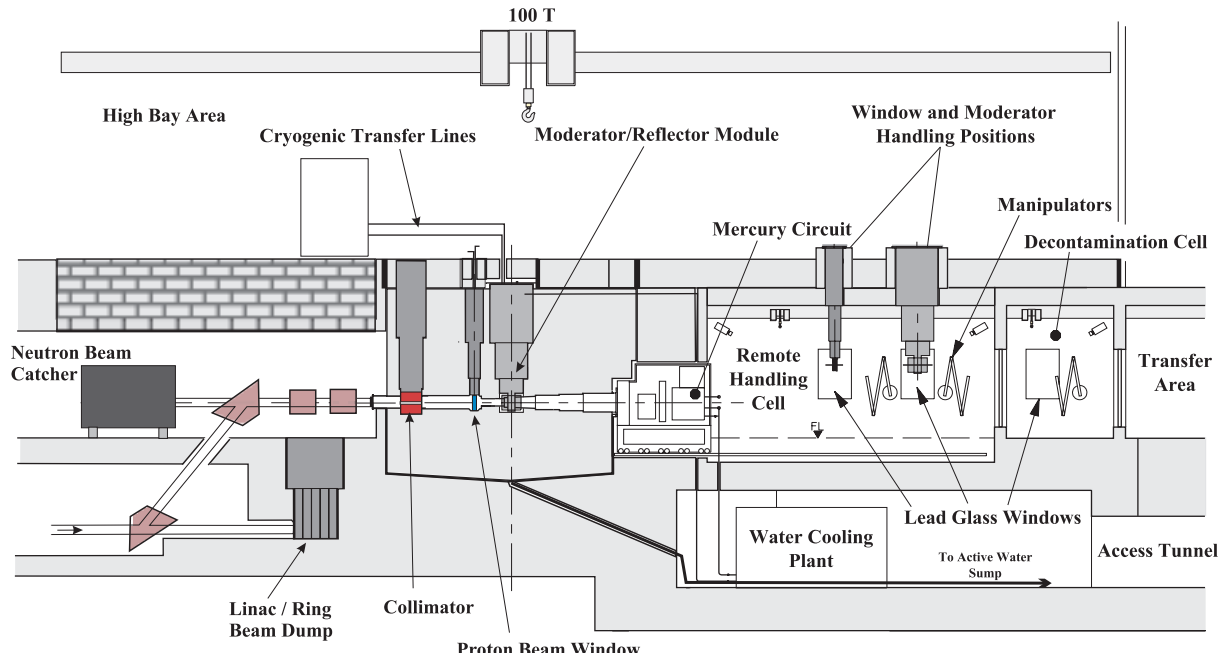


Figure 4.2-2: The overall layout of the target station - elevation

4.2.2 The Overall Layout of Target Stations and Experiment (User) Areas

A cut away view of the target stations and the experimental halls is shown in Figure 4.2-3. The target station will be housed in a hall about 62.5 m long and 75 m wide with extensions, as required, to accommodate the shielded enclosures for the long beam line instruments. The horizontal proton beam and its shielding tunnel, together with the target station and remote handling facilities, effectively occupy the middle section of the building. A 30 tonne crane to install and service the major components of the neutron scattering instruments serves each of the experimental wings.

The proton beam enters the building at a level of -2.6 m below the floor of the experimental hall. It is transferred to a level of $+1.5$ m inside the target building. Since it has been required that test and development runs of the linac and rings should be possible without relying on the targets to be operational, each target station houses a ≥ 200 kW development beam dump. A collimator, together with a neutron catcher, will handle the unavoidable backscattered neutrons from the target (cf. chapter 4.6). Neutron beams axes will be about 0.2 m above and

below the target centre line. A mezzanine floor at about 2.5 m will allow vertical access to the sample areas. Office, laboratory and support rooms will be provided at the sides of the main hall at the mezzanine level. This will allow beam lines to be extended outside the hall, in a straightforward manner under these rooms without major disruption.

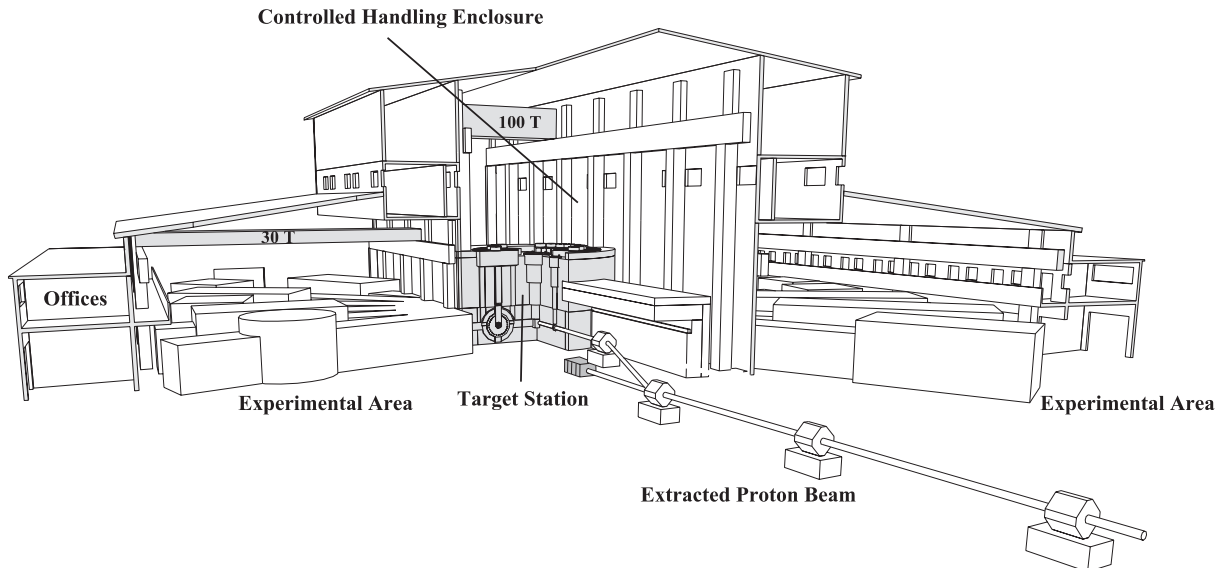


Figure 4.2-3: The target station hall as viewed from the proton beam line

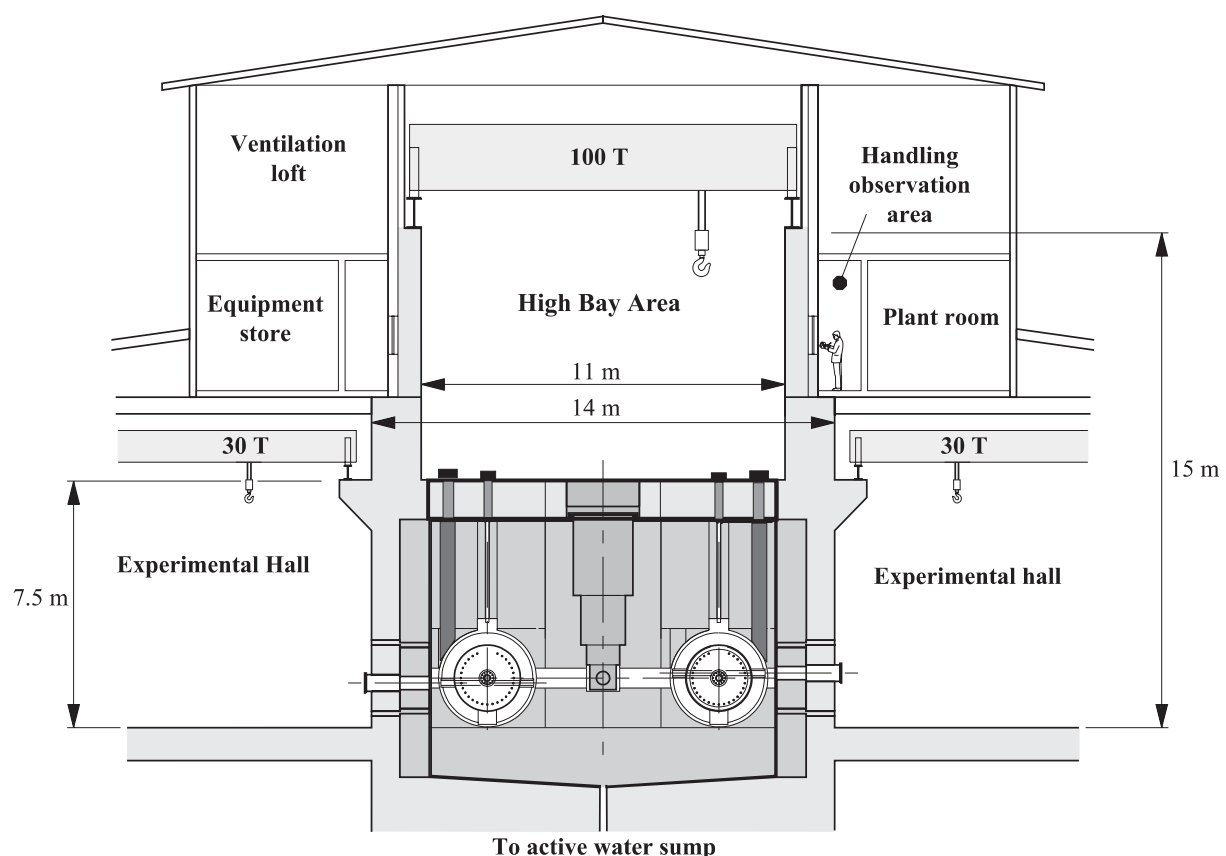


Figure 4.2-4: The target area with controlled handling enclosure above the shielding block

The high bay area above the target station will be equipped with a 100 tonne crane, which can also handle the components of the proton beam line immediately upstream of the target. Plant and equipment rooms for the ventilation systems are positioned at high level along with the high bay area as shown in Figure 4.2-4.

The water cooling systems for the target, reflector, inner shield and the proton beam window will be housed in a shielded underground cavern as shown in Figures 4.2-2 and 4.2-7. This will allow a relaxed layout with provision for shielded corridors or even limited remote handling possibilities as determined in further detailed design work.

The cold boxes for the hydrogen moderators will be located above the proton beam line shielding outside the high bay area. They are supplied with high-pressure helium by feed lines from the compressor building common for both target stations.

4.2.3 The Reflector and Moderator Module

The moderators and the (inner part of the) reflector are suspended from a shield plug inserted and removed vertically from the target station. A view of the whole assembly is shown in Section 4.4.

All instrumentation and cooling pipes for the ambient and cryogenic moderators and the reflector are fitted into stepped slots in the side of the inner shield plug to allow removal and replacement by remote handling. The weight of the whole assembly and its shielded container determines the 100 tonne capacity of the crane in the controlled handling enclosure (high bay area).

4.2.4 The Mercury Loop

The primary target cooling system, i.e. the mercury circuit including the attached helium gas system has to satisfy a number of requirements related to heat removal, gas injection into the target for pressure pulse mitigation, purification of the mercury as well as of the gas, and systems operation and safety. A simplified process diagram of the primary system is shown in Figure 4.2-5

The basic thermal hydraulic design assumes that the heat that needs to be removed from the target by the mercury is transferred to an intermediate cooling circuit via a double walled or single walled straight tube heat exchanger. While the double wall concept makes it possible to detect leaks to an interstitial gap from either the primary or secondary side before Hg can enter the intermediate circuit or vice versa, the preferred solution is a single walled unit. The drawback of the double wall concept is a large heat exchanger that has to be accommodated on the movable trolley unit. A single wall heat exchanger occupies less space but leads to some restrictions in temperature and pressure for both the primary and the secondary circuit. [UTE-ESS]. The system temperatures and pressures on the primary (mercury) side have been chosen to avoid flow induced cavitation in the target region and, at the same time, keep the size of the heat exchanger reasonably small.

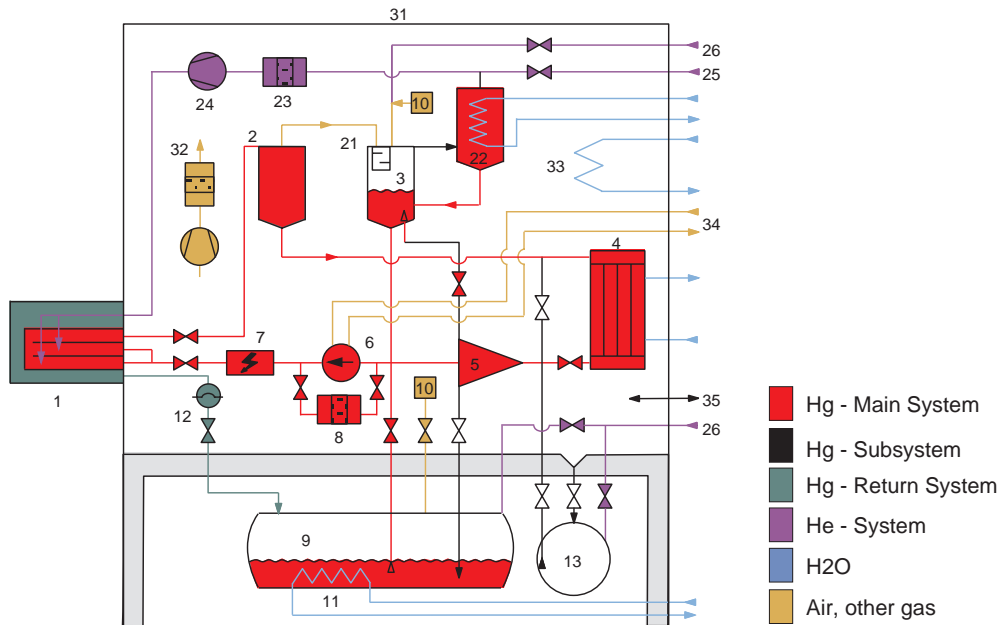


Figure 4.2-5: Mercury target primary circuit process diagram

1 Target	11 Drain Tank Cooling	31 Containment
2 Gas Separator	12 Target Hull Drain	32 Containment Filter (H Recombination)
3 Expansion Tank	13 Containment Floor Drain Tank	33 Containment Cooler
4 Intermediate Heat Exchanger	21 Mist Separator	34 Pump Cooling (if necessary)
5 Impurity Separator	22 Hg Condenser	35 Containment Gas Pressure Control
6 Centrifugal Pump	23 Filter (H Getter)	
7 Preheater	24 He Blower	
8 Filter (Cold Trap)	25 Gas Treatment System	
9 Hg Drain Tank	26 He Supply	
10 Cover Gas Transfer		

The cross section of the main mercury pipes of 125 mm in diameter ensures low friction pressure losses. Average flow velocities below 1 m/s in the mercury part of the loop also eliminate erosion problems. The thermal hydraulic characteristics are summarised in Table 4.2-1. A sketch of the geometric arrangement of the mercury circuit components is shown in Figure 4.2-6. The intermediate cooling circuit and the auxiliary water-cooling loops are closed systems that are cooled by the general plant heat removal system. Alternative designs including a water heat pipe, a mercury-mercury intermediate heat exchanger or other pump types have also been considered but were not judged as advantageous over the present concept.

Table 4.2-1: Thermal-Hydraulic Design Parameters of the Primary mercury circuit

Thermal power	2.8	MW
Hg flow rate	175 - 200	kg/s
Hg temperature at target inlet	60 - 100	°C
Hg temperature at target outlet	167 - 218	°C
Hg pressure at target inlet	5	bar
Hg frictional pressure drop	3-4	bar
Estimated Hg inventory including permanent sump in drain tank	15	t

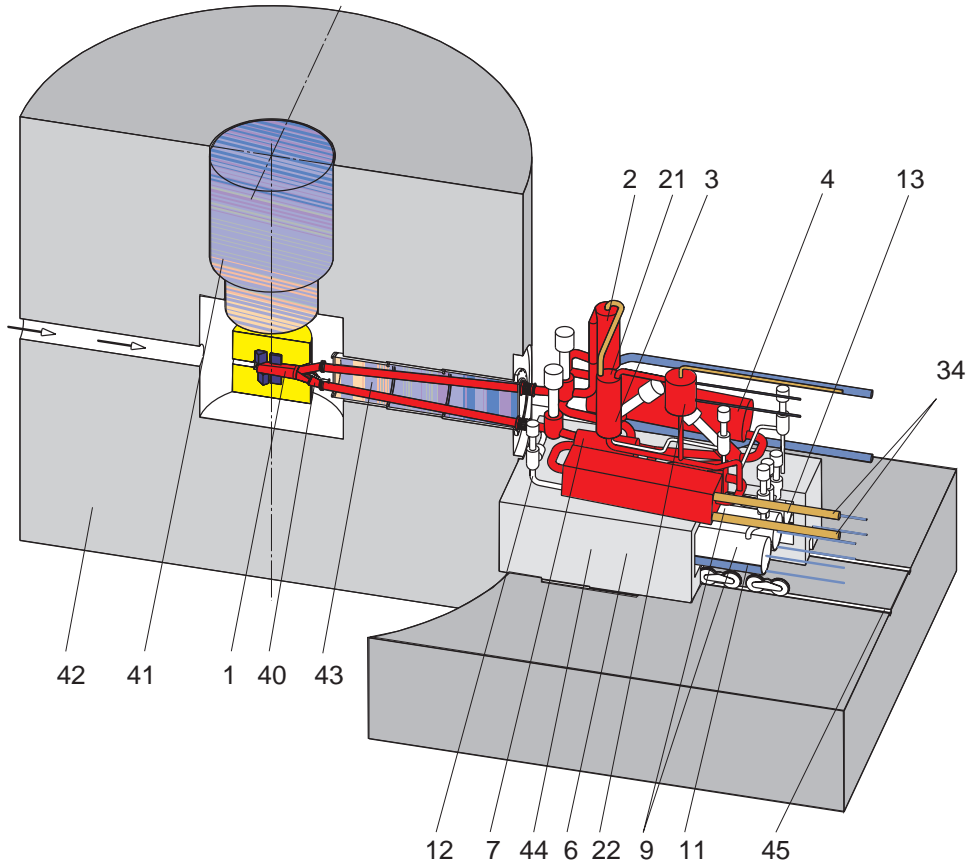


Figure 4.2-6: Sketch of the target trolley with drain tanks and primary target loop. In designing and arranging the components of the liquid metal circuit, care must be taken to ensure that the circuit can be completely emptied by gravity and that no gas pockets can form at any point. (Local shielding of components not displayed)

Components are numbered as in Figure 4.2-5, with the following extras:

40: reflector-moderator-unit

43: horizontal shielding plug

41: vertical shielding plug

44: trolley

42: shutter shielding

45: rail system

It has been estimated [Soltner, 2002], cf. also Section 4.3, that mitigation of the pressure wave effects in the short pulse target will require a volumetric fraction of about 1 % helium of gas in the target fluid. This results in a gas flow rate of about 10^{-4} kg/s. The helium injected into the mercury is removed from the liquid metal in a special gas separator. It is assumed that the separated gas is saturated with mercury vapour and possibly contains small Hg droplets. A large fraction of this mercury can be removed in moist separators and condensers, but some Hg vapour may remain in the gas stream. Besides Hg the gas also contains hydrogen, other volatile spallation/fission products and possibly entrained impurities from spallation. This will be taken into account in the final design of a purification system for this loop.

Although, as discussed in Paragraph 4.3.7, almost all elements that are produced in the mercury target during 10 years of full power operation are well below their solubility limits, some components have been included in the process diagram for on line separation of insoluble impurities. In the separator a small stream of mercury containing light particles is diverted to the expansion tank. Heavy particles, which segregate on the bottom of the

separator, will be periodically drained into the sump tank when the loop is emptied for target shell replacement.

A special gas treatment system is necessary for removing the cover gas before the initiation of maintenance operations requiring exchange, repair or servicing of primary-system components. It includes a vacuum pump, cryo-condensers and a radioactive gas handling system. In addition, it may be necessary to use special cleaning techniques to remove deposits in the primary system, which cannot be expelled by simple gas flushing.

Auxiliary systems will be needed for several functions such as cooling the pump, Hg transfer and drainage and Hg level control. Calculations have shown, that the decay heat removal ($P = 10$ kW right after shut down) for the mercury is possible by relying on passive cooling only.

The process diagram does not include primary system instrumentation and control equipment. Standard techniques for flow, temperature, pressure, level and radioactivity control can be used without additional R&D effort. It may, however, be necessary to install special sensors for bubble injection control and impurity surveillance.

The primary system is installed on a trolley, which can be moved to the maintenance cell after disconnection of the intermediate and auxiliary cooling circuits. Remote access to the system components can be provided from above or, if necessary, from the sides after removing part of the trolley containment and local shielding. In view of a recommendation by the Technical Advisory Committee efforts have been started to adopt a design of the trolley which would eventually also allow to use a rotating solid target if the efforts to mitigate the effect of a pressure wave in the liquid target turns out to be unsuccessful (see also chap. 4.3.5.1).

4.2.5 Water Loops and Services

Scaling from measurements made on the ISIS cooling systems [Broome, 1993] gives general radiation levels around the pipework of the radioactive water cooling systems for the target station of up to 20 Sv/h in operation (no delay tank used) and up to 5 mSv/h even when the radioactive water has been drained into shielded storage tanks. Operation experience at SINQ [Bauer, 1998a] show much lower values of about 1 Sv/h during operation. Unlike ISIS and SINQ, in ESS the proton beam directly hits only a small amount of water and therefore much lower activation can be expected. Nevertheless, all active water services are located in a shielded underground cavern. Shielded (inner) corridors, illustrated in Figure 4.2-7, provide protection from the radiation for personnel entering the plant area. Those components, which require frequent or regular access, such as sensors, flow meters and valves, penetrate through the shield walls into these corridors. They can also be locally shielded if required. In this way the personnel are only exposed to the dose from the component, which requires attention, and are not exposed to the rest of the plant.

The major items such as pumps, heat exchangers, filters and ion exchange columns will all be individually shielded and will be located in the outer corridors where they can be removed and replaced with ‘hands on’ access. All the pipe work installed between the shield walls is fully welded and does not require frequent maintenance.

Access for equipment is via a lift positioned in the floor of the main access area of the target station remote handling facility.

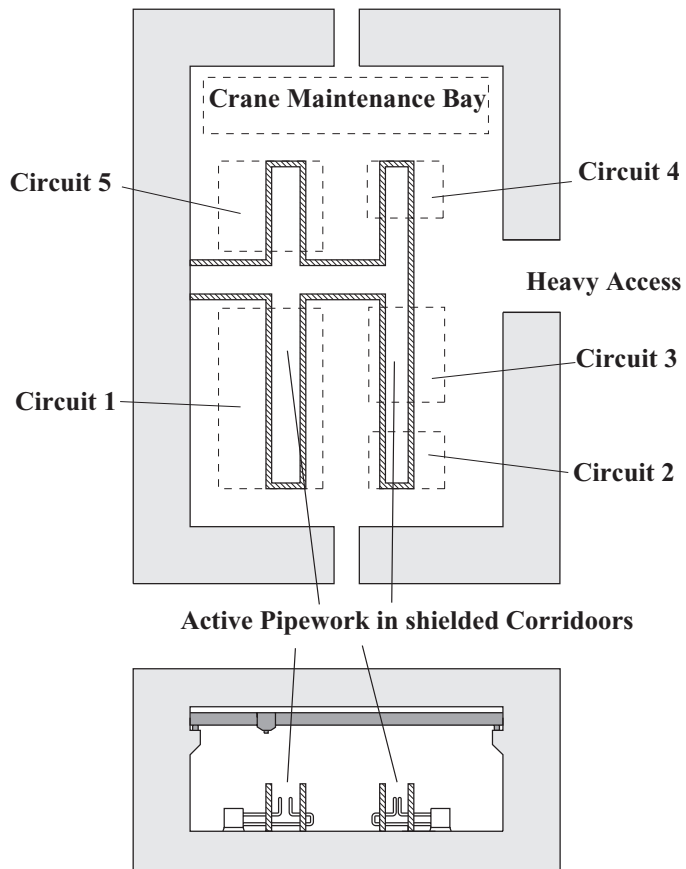


Figure 4.2-7: Schematic layout of the active water systems

4.2.6 Enclosure Systems

During operation components, fluids, gases and unavoidable impurities (e.g.. dust) will be activated. This inventory has to be controlled by a series of physical barriers. The enclosure concept (Figure 4.2-8) for the target stations therefore includes several independent types of barriers.

All hazardous fluids have to be provided with their own containment by either two or more enclosures depending on the potential risk from the fluid itself and on the type of its surrounding controlled enclosure. For example, for the mercury target 3 containments are provided to preventing leakage into the inner target block vessel, while a single containment is sufficient against leakage into the target trolley. Cold moderator material (H_2) at cryogenic temperatures needs to be contained 3 fold all the way from the moderator to the cold box.

In addition to the containment of the fluids themselves, the target station is divided into several separate enclosures. Basically these enclosures are the inner target block vessel, outer vessel, the high bay area, and the hot cell area. Radioactive gases and any spilt fluids are contained inside the inner vessel. A drain is provided for spilled active water and is connected to a collection tank in the active water plant cavern. The mercury circuit will have its own secondary containment in an atmosphere separated from the main containment vessel. A pneumatic, remotely operable seal on the target trolley will complete the containment vessel.

Thin (about 0.5 mm) aluminium alloy foils forming double windows will be positioned in the vessel wall for the neutron beams to pass through. The interspace between the foils will be filled with helium and its pressure will be used to monitor for window failures.

Access to components such as shutters, the reflector/moderator assembly and the proton beam window is provided by removable, sealed flanges at the top of the containment vessel.

It can not be excluded that remote handling operations on the mercury target systems will result in some contamination in the main remote handling cell. A barrier is provided between this cell and a second remote handling area, the ‘decontamination cell’ to control the spread of contamination and to prepare assemblies for transport out of the target station.

As the instrument halls, which will be radiologically controlled areas with low risk of contamination, will be regularly entered by personnel they are completely separated from the target area by an air lock system

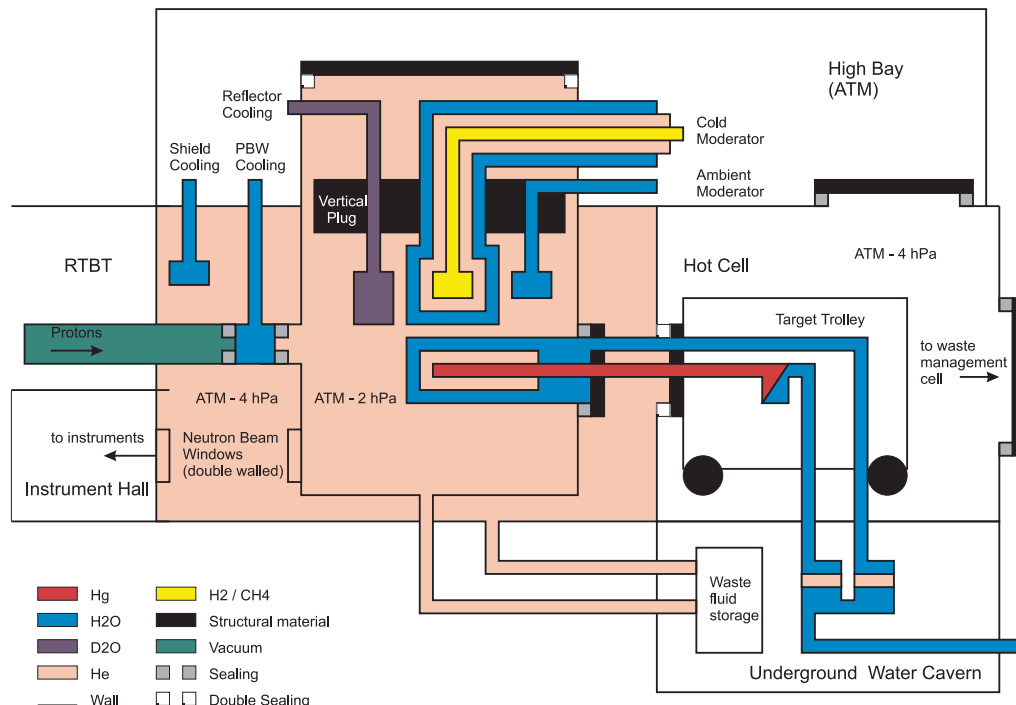


Figure 4.2-8: Enclosure System Concept

4.2.7 Proton Beam Window

The proton beam has a two-dimensional parabolic density distribution with an elliptical footprint of 60 mm by 200 mm at the target with a peak proton current density of $80 \mu\text{A}/\text{cm}^2$. Since this is a divergent beam emerging from the upstream collimator, it will be important to place the beam vacuum window as close as possible to the target to keep the peak current density on the same regime. In the present concept the window consists of two cylindrical plates, which are cooled by water flowing between them (Figure 4.2-9). The maximum temperature in the window material at full beam power has been estimated to be below 230°C [Broome, 1996]. As window material an austenitic stainless steel is the first candidate but the

final decision will be made after the results of ongoing mechanical tests on different materials irradiated under spallation conditions are available.

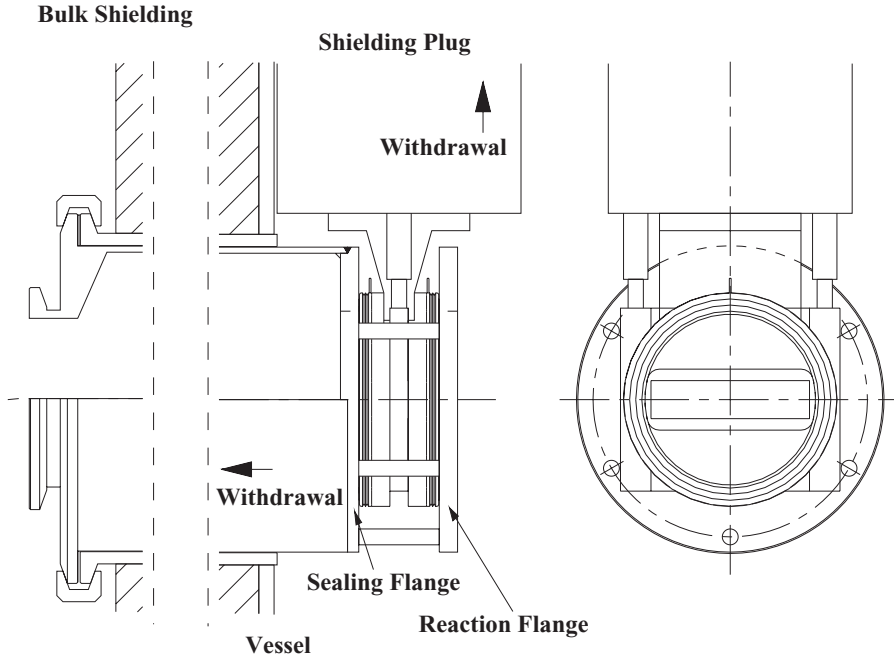


Figure 4.2-9: The proton beam vacuum window.

The window assembly is sealed to the proton beam pipe using gas-pressurised seals. Removal then only requires disconnection of the water services at the top of the shield and depressurising to release the seal. The whole unit, with its shielding plug, is then removed vertically into a shielded container in the controlled handling enclosure.

4.2.8 Remote Handling

The high induced activity in the target, moderator and reflector assembly, collimator, the proton beam window and the neutron beam shutters and guide inserts requires that all maintenance and repair work has to be performed fully remotely. The removal of these assemblies implies the need for control of contamination. This is provided in the design by two controlled enclosures, the high bay area on top of the target station and the hot cell downstream of the target. (Shown in Figure 4.2-2.) While the high bay enclosure acts as a physical barrier, contamination of these areas should still be avoided during normal maintenance work. All handling of hot components in this area must supply local shielding and contamination control. In contrast to that, the hot cell area is supposed to be a fully remote handling area with no personnel access needed during handling. Nevertheless contamination of the hot cell should be kept at a minimum to allow access for certain maintenance or replacement activities when no unshielded active components are present. All handling procedures in the hot cell that may lead to contamination must provide decontamination possibilities.

The proton beam windows as well as the neutron collimator upstream of the target are removed vertically into a shielded flask. This flask will be designed as a universal handling flask, which can also be used for the modules of the proton and neutron beam stops, and possibly some proton beam monitoring equipment, if required.

The moderator-reflector assembly as well as the shutters are also removed vertically and the active modules are placed in local storage pits. The neutron guides located in the shutter wheels are changed vertically with the shutters in “beam off” position. The flanges and joints of the various systems on top of the target station will be worked ‘hands on’. All these operations take place in the high bay area. This is why the cryomodules of the cold moderators that were originally located in this area have been moved to the adjacent rooms.

The target is removed horizontally into the remote handling cell (hot cell) shown in Figures 4.2-1 and 4.2-2. The main cell is equipped with master slave manipulators, a power manipulator and a remotely operated crane. Visual inspection will be possible through lead glass windows and video cameras inserted through the walls of the cell. Due to radiation, local shielding of cameras may be needed while not in use. It has to be anticipated that contamination could well result in very limited personnel access to the cell for servicing the remote handling equipment.

Faulty or spent units and modules (proton beam window, shutter drives, moderator-reflector assembly or the target) are replaced by commissioned spare modules stored at special places in the high bay area. Repair work on individual components can then take place while the source is operational. This can either be done in the remote handling cell constructed as part of the target station, as shown in Figures 4.2-1 and 4.2-2, or the assemblies will be transferred to a cell in the radioactive waste management centre, depending on the activity in question.

Although the general rule is that the time it takes to replace any component should not be longer than 10% of its anticipated life time, certain procedures shall be much faster than this, if they have to be carried out during the scheduled down times of the facility. In particular, the aim is to achieve replacement of the proton beam window in one day and of the target in five days. Replacement frequency of the moderator-reflector assembly will mainly depend on the useful service time of the moderators and is still under evaluation.

4.2.9 Shielding

The bulk shield is designed to give a dose rate at the surface of less than $2.5 \mu\text{Sv/h}$. This requires 5.5 m of iron along the proton beam forward direction, 3.5 m at 90° with an outer concrete layer at least 0.4 m thick. The inner 1.5 m of shielding including the reflector will be water-cooled. The mechanical layout of the shutter system resulted in a somewhat thicker shield than required by the dose rate criterion. The shield thickness is shown schematically in Figure 4.2-10.

To reduce ground shine and soil activation to acceptable levels there will be 3.3 m of iron and 4.0 m of concrete shielding below the target. For details see [Schaal, 1996].

The shield will be constructed from machined iron blocks with poured concrete for the outer layer. The gaps between the blocks outside the shutter area will be filled either with garnet sand or grout depending on the decommissioning philosophy adopted.

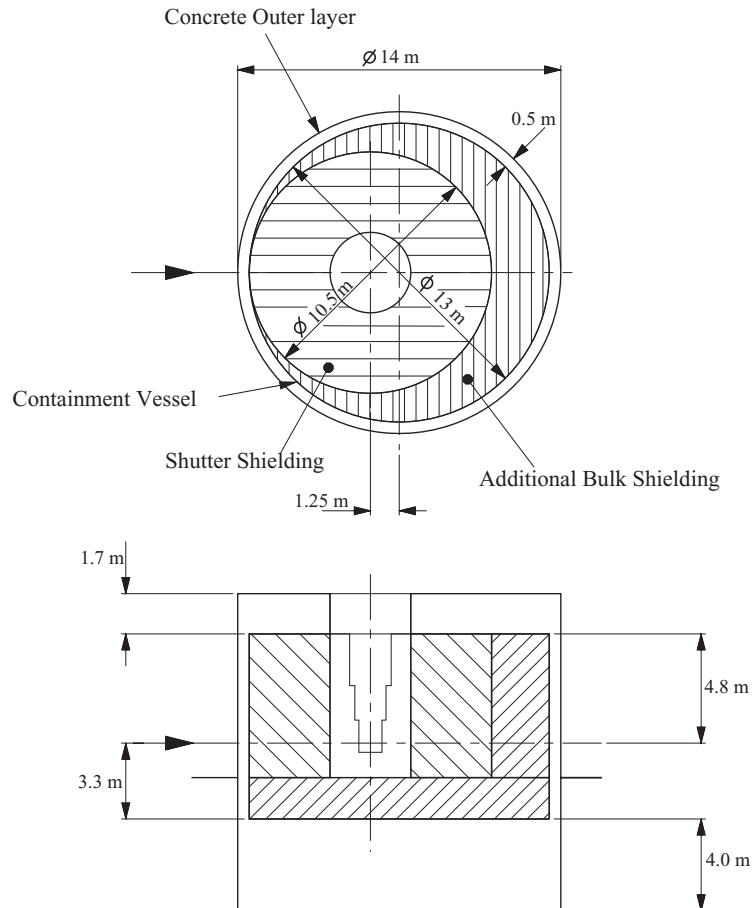


Figure 4.2-10: The shield dimensions

4.2.10 Shutters and Neutron Beam Lines

The goal of the design is to provide as much as 24 neutron beam lines per target station, equipped with shutters to allow sample exchange at the instruments while the source is running. At the same time these beam lines should be able to accommodate neutron optic devices (guides) of various kinds. To keep the flexibility for new and improved neutron guides as high as possible, space for guide inserts of a cross section up to 230 mm x 170 mm outer dimension will be provided. These inserts should start at about 1.5 m from the moderator and have to be aligned with the rest of the neutron flight path.

The current design consists of wheels 2.8 m in diameter that can be rotated about a horizontal axis at right angles to the neutron beam direction. A rotation of 90° moves the beam hole from horizontal (fully open) to vertical (fully closed) position. This operation will take about one minute, but the beam will already be cut off after a few seconds. The section in the shutter wheel facing the moderator or outer guide insert in closed position will be made from tungsten to improve beam blocking. The shutter disk has a hole big enough to allow a guide insert to fit loosely inside. Because of the high alignment requirements, alignment of the guides is assured by adjustable blocks instead of relying on the alignment of the shutter wheels themselves (Figure 4.2-11).

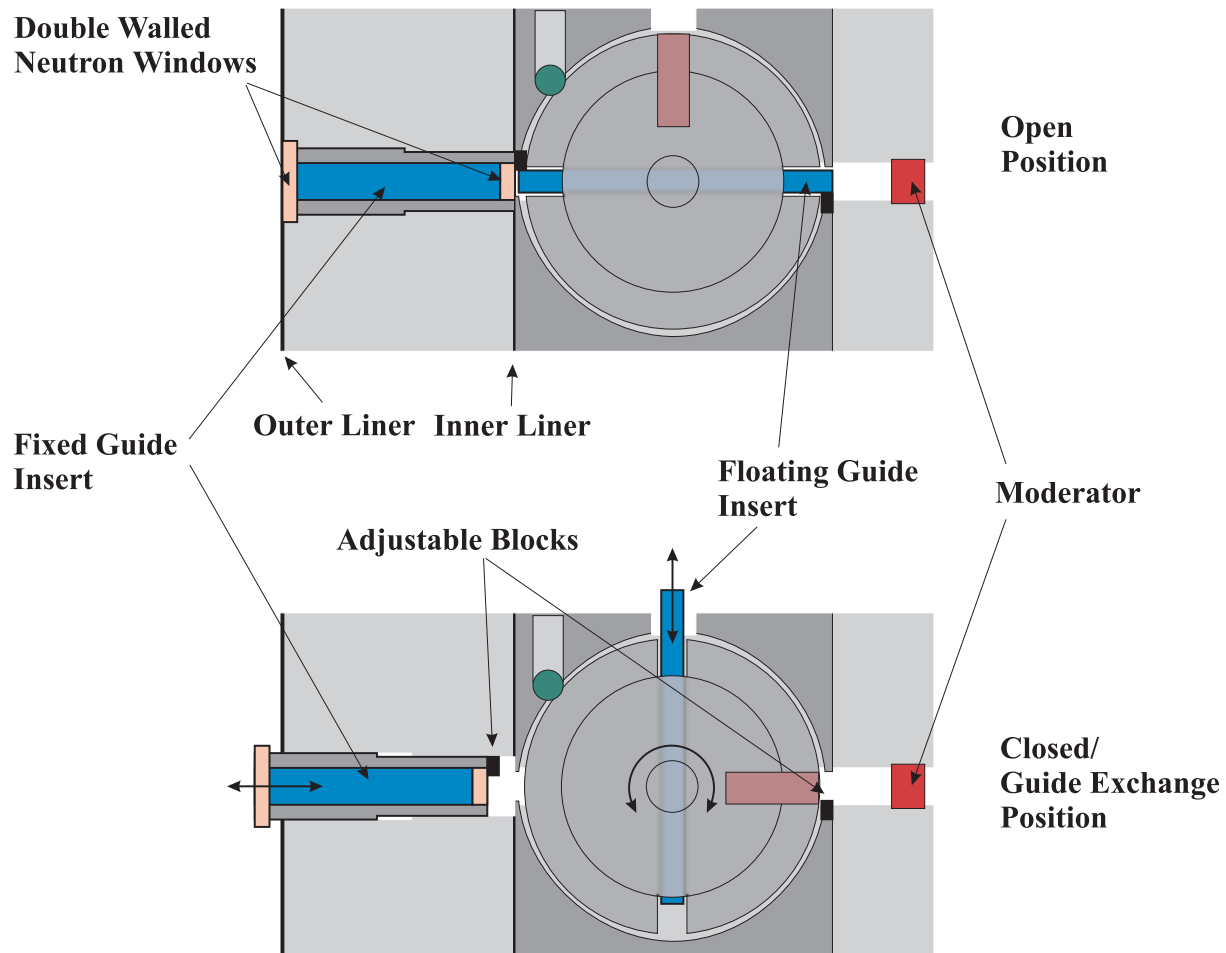


Figure 4.2-11: Schematic arrangement of shutter with exchangeable neutron beam guides and adjustable positioning blocks for reproducible alignment of the guide inserts in open and closed position.

For maintenance and repair of components such as the bearings, the shutter wheel will be removed vertically into a shielded container after removing its upper shielding block (Figure 4.2-12). More frequent maintenance such as changing the neutron guides or collimators or maintaining the shutter drives should be performed without removing the shutter wheel itself. The outer neutron beam windows are part of the stationary (“fixed”) guide insert in the outer shield sector. Their frequency of replacement is expected to be very low.

The shutter is driven by a motor connected by a simple shaft and gearbox on to a gear wheel on the main shutter disk. This drive is positioned in a way not to hinder access to the neutron guides replacement hole.

A schematic view of a sector of the neutron beam shutter arrangement is shown in figure 4.2-12. The shutters operate in a common helium atmosphere of the main containment vessel, thus eliminating the need for windows on the shutters themselves. Abandoning the concept of a separate atmosphere for each shutter allows minimum distance between adjacent guides. Removal of the heat deposited in the shutters is achieved by cooling the surrounding shielding and relying on conduction through the helium to the cooled shielding.

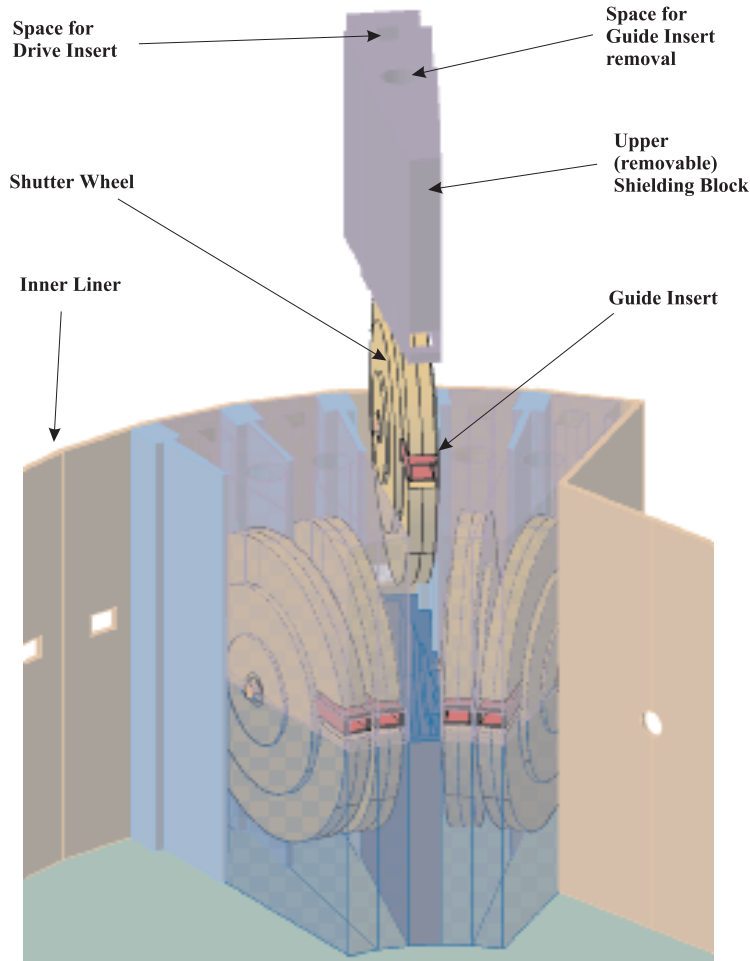


Figure 4.2-12: Arrangement of shutters providing for a small angular separation (11°) between shutters and a short distance (ca. 1.5 m) between guide and moderator

The shutter arrangement is covered by a revolving top plate which is sealed to the inner liner. Flanges in this plate located over each shutter provide access to the shutter drives and the guide inserts by shielded flasks. One big flange will provide access to the shutter wheels. In the very rare case of a shutter wheel exchange the plate will be rotated to position this flange over the faulty shutter wheel to allow its handling by a shielded flask. The close spacing of the shutter units does not permit to have an access flange for every one of the shutters.

4.2.11 Choppers

Access and maintenance requirements for choppers strongly favour a position outside the main biological shield. The current design therefore does not allow choppers closer than 6 m from the moderator. Instrument designs are currently coping with this restriction, although many of them foresee choppers at little over 6 m. According to Figure 4.2-10 this will be possible for most of the angular range. Instruments using beams in the forward direction may need to move their choppers a bit further out. Access to these choppers for maintenance and repair will require substantial amounts of shielding to be moved. It will be possible only when the source is not running due to the radiation from neighbouring beam lines even if the shutter of the one in question is closed.

4.3 THE MERCURY TARGET

The target system is crucial for the feasibility and performance of the whole project. ESS will exceed beam powers of existing facilities with pulsed spallation targets by at least a factor of 30. Also the power of the most powerful spallation target with steady state operation (SINQ at PSI, CH) will be exceeded by a factor of 5. Hence the large step in power for the ESS called for an innovative target design with development potential, rather than extending existing concepts, which might soon approach their limits. Notwithstanding the practical feasibility of a mercury target, several problems, which might affect the viability of the concept, have been identified and require further efforts.

4.3.1 A Liquid Metal Target

The pulsed radiation will cause mechanical and thermal stresses and radiation damage in the ESS-target. While these effects may be deleterious to a heterogeneously cooled solid target, in a liquid metal target they affect “only” the containment. At the same time, by moving the heated target material to the heat sink, it becomes possible to keep the cooling water away from the direct proton beam and thus avoid or at least significantly reduce its radioactive contamination, e.g. by tritium and ^{7}Be from spallation of oxygen. Cooling of a solid target would also require a finer and finer subdivision at the location of high power density, causing reduction of the overall target density. Other arguments in favour of a liquid target are its large mass and hence low specific activity even after many years of service and the fact that no active decay heat removal is required during service and maintenance periods. In view of the above considerations, a liquid metal target has been chosen as the preferred concept for ESS after a viable solution had been worked out.

4.3.2 Mercury as Target Material

Considerations of high atomic number for good neutron yield, reasonably low melting temperature and good availability, leave only a few candidates for a liquid metal spallation target as listed in Table 4.3-1.

Table 4.3-1: Some relevant properties of possible liquid metal target materials [Bauer, 1995]

Property		Pb	Bi	LME *	LBE**	Hg
Composition		elem.	elem.	Pb 97.5% Mg 2.5%	Pb 45% Bi 55%	elem.
Atomic mass A (g/mole)		207.2	209	202.6	208.2	200.6
Melting point (°C)		327.5	271.3	250	125	-38.87
Boiling point at 1 atm (°C)		1740	1560			356.58
Density (g/cm ³)	20°C	11.35	9.75			13.55
	liquid	10.7	10.07	10.6	10.5	
Linear coefficient of thermal expansion (10 ⁻⁵ K ⁻¹)	solid	2.91	1.75			
	liquid	4		4		6.1
Volume change upon solidification (%)		3.32	-3.35	3.3	0	
Specific heat (J/gK)		0.14	0.15	0.15	0.15	0.12
Thermal neutron absorption (barn)		0.17	0.034	0.17	0.11	389

* LME - lead/magnesium eutectic

** LBE - lead/bismuth eutectic

The high thermal neutron absorption cross section of mercury is the main reason for not considering it as a target material for steady state spallation neutron sources, which depend on a long neutron life time in the moderator for high flux densities. In the case of a short-pulsed source like ESS, however, thermal neutron lifetime is not an issue. Furthermore, some moderators are deliberately surrounded by decouplers (neutron absorbers) to prevent neutrons from being moderated in the reflector and target and from returning to the moderator and degrading the pulse shape. In this case, the high absorption cross section of mercury, whose energy dependence is very similar to that of the commonly used decoupler material boron (see Figure 4.3-1), may turn out to be an advantage, because it may avoid the need for the decoupler between the target and the moderator thus further reducing complexity. This question, as well as the effect on a coupled moderator still needs detailed investigation.

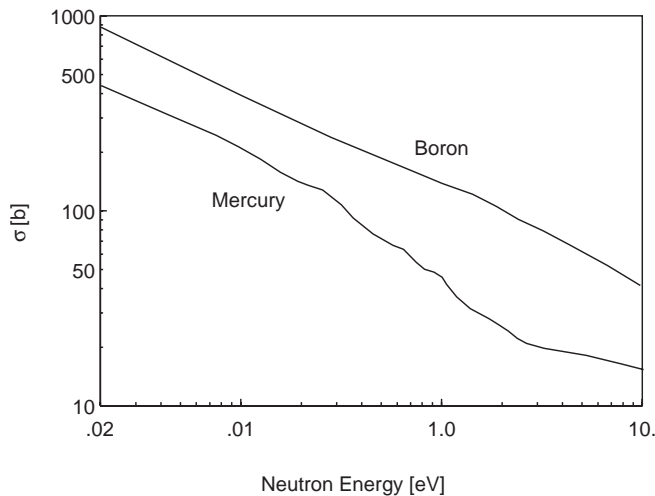


Figure 4.3-1: Thermal neutron total cross sections of mercury and boron.

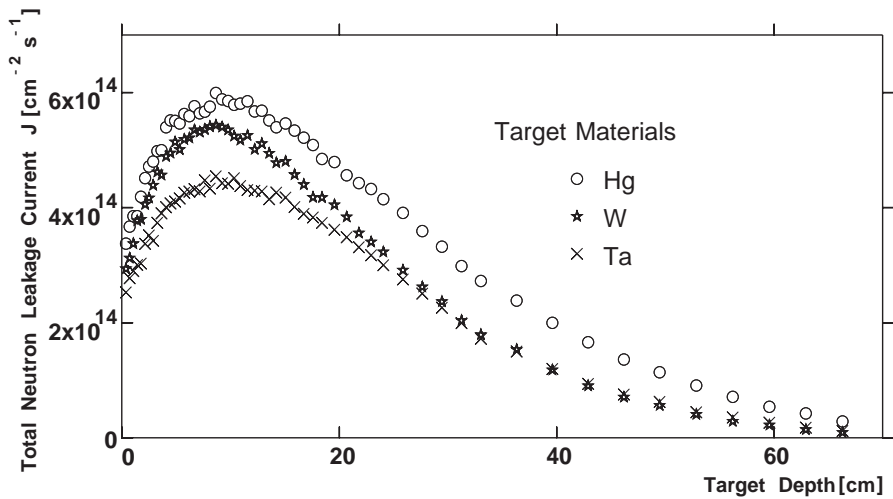


Figure 4.3-2: Comparison of calculated neutron leakage from a lead reflected mercury target and water-cooled tantalum and tungsten targets.

The fact that no water is present in the beam interaction region of a liquid metal target means that there is virtually no moderation taking place in the target volume. This results in a

harder leakage spectrum. There is also a lower probability for resonant absorption of neutrons than in a water-cooled solid target. This is reflected in the calculated neutron leakage distribution from the target surface [Filges, 1995] as shown in Figure 4.3-2. Water-cooled tantalum is inferior to mercury and tungsten because its high resonance integral makes it particularly sensitive to neutron moderation within the target volume. The resulting distribution for the mercury target shows not only higher peak intensity, but also wider downstream extension, making it easier to place two moderators - or a wider one - in a region of high neutron leakage (cf. Section 4.3).

With respect to radioactivity, almost all radioactive isotopes of mercury have half-lives below 50 days, with the exception of ^{194}Hg ($T_{1/2} = 367$ years). Furthermore mercury can be purified relatively easily to reduce activation from impurities.

As mercury is liquid at room temperature, no heating is needed during beam shutdowns. However, special attention is required in the design of the circuit and its surroundings to make sure that no droplets are left behind after draining, which would be difficult to collect, especially when radioactive. Also the low boiling point of mercury requires attention, as it may give rise to cavitation effects, in particular under pulsed heat input.

In summary, mercury was given preference as liquid metal target material for ESS due to its relative advantages compared to the other candidates (highest density, lowest possible operating temperature, no need for auxiliary heating, short neutron pulses)

Despite the fact that not all of the circumference of the target block will be available for neutron beam extraction, horizontal injection was chosen for both ESS target stations for a variety of reasons given in Section 4.1. In addition this allows convenient horizontal removal of the target for maintenance and replacement. The target unit will be moved horizontally on a trolley and positioned in a remote handling cell with suitable equipment for replacement of defective subunits or preventive exchange of highly loaded parts. A schematic vertical cut is shown in Figure 4.3-3. Included in the target system is a shielded storage tank into which all of the mercury can be drained when the circuit needs to be opened, e.g. for preventive replacement of the target shell, see below.

The most critical part of the liquid metal circuit is the vessel (the target shell) which contains the liquid metal in the beam interaction zone and which is exposed to the proton beam and neutron radiation. Its service time will be limited and it will require preventive replacement at intervals yet to be defined. (Present estimates indicate between two to three times per year.) The target shell will be surrounded by an intermediate containment, a separately cooled, double walled, liquid metal return hull (LMRH). This measure was taken in order to make failure of the target container a design base event with no consequences, even though it moves the moderators slightly further away from the target and thus reduces to some extent their neutronic coupling. The function of the LMRH is to prevent the target material from entering the contained atmosphere around the moderator-reflector system in the event of a leak in the target shell. The gas-filled space between the target shell and the return hull is connected to the storage tank via a return pipe, which, under normal conditions, is blocked by a rupture disk. This disk will be destroyed when loaded with target material. The gas pressure has yet to be defined (section 4.3.3).

The liquid metal return hull must be able to hold the target material and to guide it to the storage tank in the event of a failure of the target containment shell. Its material must be compatible with the cooling medium (probably water), and must withstand the liquid mercury long enough to accomplish this task safely, but need not necessarily have long term compatibility with it. This is important because it might allow a material with lower strength and better radiation resistance than the target shell material, which must also resist pressure waves and corrosion in contact with mercury.

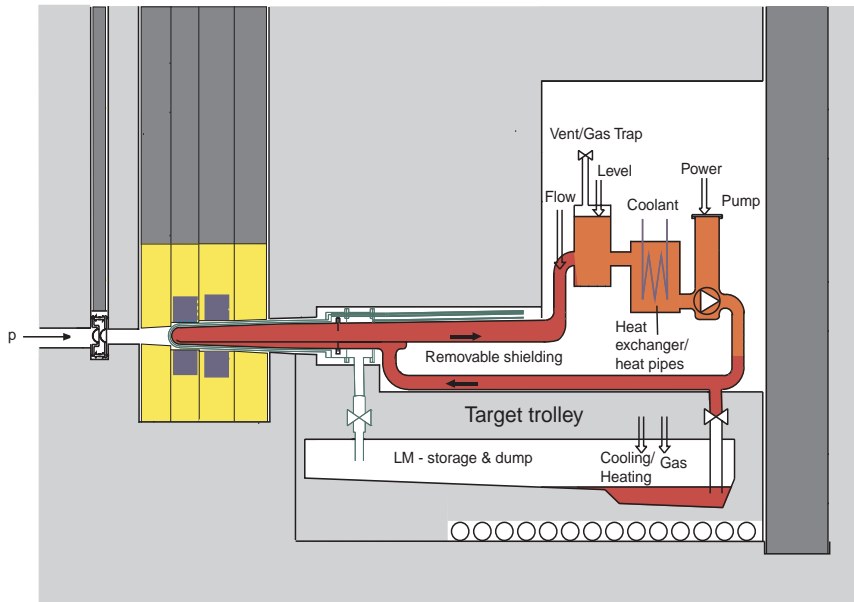


Figure 4.3-3: Schematic representation of the liquid metal (LM) target system. The liquid metal return hull is shown in green, surrounding the target container in the reflector region.

For the target itself, slab-type geometry with an oval cross section was chosen, based on results obtained in conjunction with the SNQ-project [Bauer, 1982]. Apart from the reflecting effect of the wings for fast neutrons, this geometry also offers the advantage of allowing an elliptical beam cross section thus reducing the current density, the associated heat load and radiation damage in the window while keeping the distance between the beam axis and the moderators small. In order to avoid accumulation of gas and to allow complete drainage of the liquid from the circuit, the target is slightly wedge shaped in the proton beam direction. This also reduces lateral losses due to beam broadening along its path through the target and accommodates the expansion of the mercury when it passes through the beam region. Typical outer dimensions of the target in the interaction region are 14 cm (high) and 30 cm (wide), with an elliptic cross section of the beam at the entry window of $6 \times 20 \text{ cm}^2$. The front cover of the target (beam entry window) is curved in two dimensions in order to minimise the stress resulting from thermal gradients and internal pressure. The radius of curvature is constant in the vertical plane and an elliptical contour is used in the horizontal one, (cf. Subsection 4.3.4).

A long lifetime of the target is desirable mainly for two reasons: minimum radioactive waste and maximum availability. For the latter, the replacement time is decisive. It is, therefore crucial that target shell replacement can be accomplished during the scheduled shut down periods of the facility in a matter of a few days. In this context, it is a decisive advantage that no cool-down time for the target material has to be allowed for, because of its low specific

after-heat and because it can be drained from the circuit for reuse after the container shell has been exchanged.

4.3.3 Structure Mechanics and Design of the Target Unit

The choice of the slab target geometry has distinct neutronic advantages, allowing to place the moderators as close to the beam axis as possible in order to optimise neutron coupling and hence the performance of the whole system. Furthermore it avoids flow baffles in the direct proton beam and the tapered geometry ensures that any gas injected will be carried away safely, and that complete draining of the shell can be achieved when the circuit needs to be opened. However its flat top and bottom plates pose a special challenge for the structural design in order to avoid excessive bulging under the internal pressure of the fluid. Any measures to stiffen the structure must take into account the extra nuclear heating, effects on gas retention and draining of mercury, and minimal disturbance of the flow of the target material. Possible effects on heat transfer of gas injected to mitigate the pressure waves from beam pulses must also be accounted for, mainly with respect to cooling of the beam window and effectiveness of the heat exchangers. In view of this large number of difficult boundary conditions and because some of the relevant data required to design the target shell are not yet available, only preliminary studies could be carried out so far, and the design is still being developed and optimised.

Figure 4.3-4 illustrates the design of the target shell: the three feed channels at the sides and at the bottom are connected to a common plenum and are dimensioned such that an optimum flow distribution is achieved in the beam interaction zone. Details of the gas injection system still have to be defined, but will probably be placed outside the target area in the mercury circuit. Since the fluid mechanics calculations show that a pressure difference of about 2 bar must be anticipated between the forward and return flow channels (cf. Subsection 4.3.4), structural optimisation is still required.

Using the results of the thermal hydraulics and fluid mechanics calculations, static structure mechanics calculations were performed to examine the resulting stress levels in the beam window and the rest of the target shell. In an early stage of these calculations, both austenitic and ferritic-martensitic steels were considered. However it was found that the thermal and mechanical properties of austenitic steel lead to unacceptably high stress levels. As precipitation hardened high-nickel alloys (e.g. IN718) may be attacked by mercury, only martensitic steel was retained as a candidate (cf. Chapters 4.3.6 and 4.3.8). Hence in the calculations data for HT9 were used as input parameters. The magnitudes and locations of the stresses resulting from thermal gradients and static pressure were calculated with and without reinforcement fins on the target shell. While unacceptably high stress and deformation levels result from the internal pressure without reinforcement, they can be reduced to acceptable values with fins running across the target shell. Such fins are, however, not easily made compatible with the boundary conditions stated above.

The results of the preliminary stress calculations performed for the target are compiled in Table 4.3-2. While they all refer to the beam window, not all of them occur at the same location and it remains to be determined how they would superimpose to give a value to be compared to the allowable design stress or the endurance limit.

Even if mitigation of the effect of pressure waves can be successfully accomplished, the resulting overall stress may still exceed 100 MPa. Its effect on the mechanical integrity of

the beam window is difficult to assess, because, in general, endurance data are not available for very high frequencies. Investigations of high-cycle fatigue, possibly of pre-irradiated candidate materials in liquid mercury are needed. (cf. also Subsection 4.3.6.) Some reduction of the static and low cycle load on the target shell might be accomplished by pressurising the interspace between the LMRH and the target shell, for example, with 2-3 bar helium. This should also prevent ingress of mercury through small leaks and help to detect any developing cracks by monitoring the pressure level in this space and above the mercury. Such a gas pressure would also reduce the static stress level on both, the target shell and the inner shell of the LMRH. Nevertheless it affects the mechanics of the target structure and will have to be examined carefully.

Table 4.3-2: Causes, approximate levels and relevant frequencies of different contributions to the total stress in the target beam window (preliminary results).

Cause of stress on beam window	Approximate peak value (MPa)	Relevant frequency
Temp. gradients by heat deposition with superimposed static and dynamic hydraulic forces	135	static
Temperature rise at end of pulse	4	50 Hz
Effect of pressure waves in the liquid target without mitigation	400	10 kHz
with 1 vol% gas in the liquid	3	10 kHz
Internal ringing of the window after power pulse	10	1 MHz

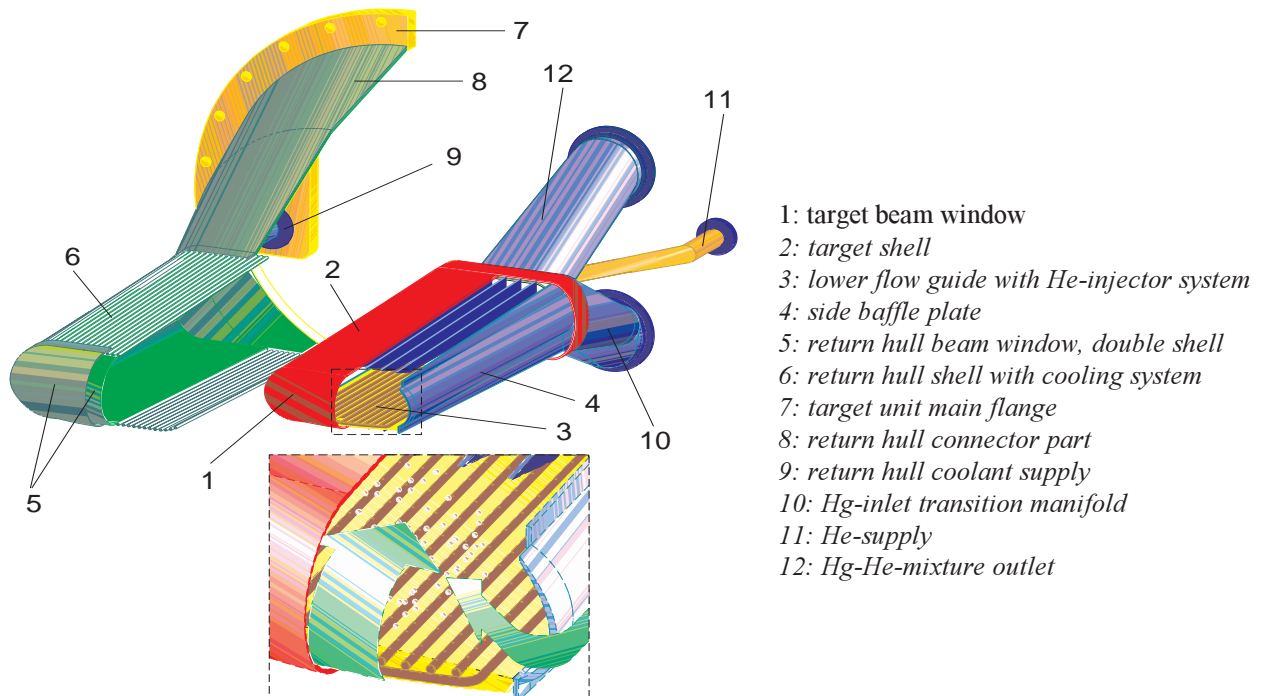


Figure 4.3-4: View of the principal design of the target shell and the liquid metal return hull. The detailed view shows the mixing zone of the bottom and one side Hg-inlet flow. The main flow directions and the injected He-bubbles are indicated schematically

For fabrication of the target structure, tests on laser welding showed promising results for martensitic stainless steels (MANET). In parallel other fabrication methods by casting or by a combined technique are under examination [Koppitz, 2002].

4.3.4 Power Deposition and Thermal Hydraulics Design

The temperature distribution in the window and the target volume was calculated for an elliptical beam crosssection of $20 \times 6 \text{ cm}^2$, constant throughout the target volume. In practice the beam will widen somewhat and hence the power density will be slightly reduced, however with a minor effect in the present context. The axial distribution of the power density in the central cylinder of 1 cm radius as obtained from Monte Carlo calculations [Neef, 1995] is shown in Figure 4.3-5a, together with a fitted curve, giving a total deposited power of 2372 kW i.e. 47 % of the total beam power. The rest of the beam energy is taken away by escaping particles or by binding energy [Neef, 1996]. A 20 % margin is added to give the design value for the total power deposition in the target, i. e. 2800 kW. The curve in Figure 4.3-5.b shows the power density per unit length used for thermal calculations. For the power deposition in the window, the calculations yield a peak power density of 1.4 kW/cm^3 in steel [Guttek, 1997], corresponding to a value of $2.27 \text{ kW/g/(mA/cm}^2\text{)}$ for a beam current density of $79 \mu\text{A/cm}^2$ and a density of 7.8 g/cm^3 .

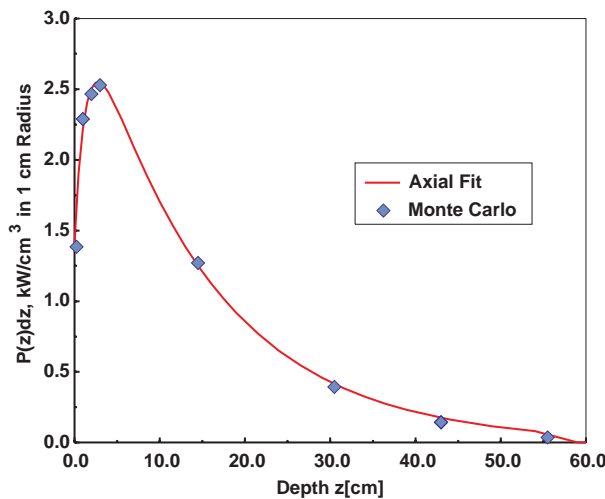


Figure 4.3-5a: Power density in the central cylinder of 1 cm radius of the mercury target for a beam of 5 MW as obtained from Monte Carlo calculations

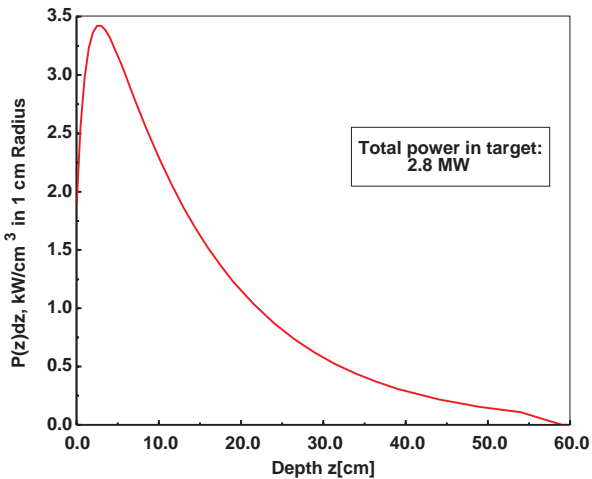


Figure 4.3-5b: Power distribution along the z-axis of the mercury target recommended for thermal calculations

In order to assess the flow distribution and the time average temperature field in the target, the thermal hydraulics codes CFDS-FLOW3D [CFDS-FLOW3D] and ASTEC [Astec, 1992] were used. A model was developed; simulating the tapered, slab type mercury target and its containment shell with its oval cross section normal to the beam imposing forced circulation by a fixed inlet pressure. Two and three-dimensional models were investigated, with different arrangements and designs of internal baffles (flow guides), and different coolant flow distributions in the target. The total inlet mass flow was 175 kg/s and the total heat load 2.8 MW - of which 11 kW was deposited in the window, which was assumed to vary in thickness from 1.5 mm at the centre to 3 mm at the edge. The thermal properties used were those of ferritic-martensitic steel (HT9), as mentioned before.

Results from the 3D model are shown in Figure 4.3-6a. It features a lower inlet channel for adequate window cooling, and two side inlets with return flow through the centre [Dury, 1997]. The side baffles are slightly more recessed from the window, than the bottom baffle. For practical reasons it is desirable to have the same inlet pressure in all three channels. This is the situation the contour lines in Figure 4.3-6a refer to. Shown are contour lines of the temperature field for an arbitrarily chosen target inlet temperature of 100 °C. Even for this high inlet temperature, the mercury temperature will remain well below the boiling point (356.6 °C at 1 atm) everywhere, which makes it possible to operate the system at a modest pressure level. The assumed geometry does not result in the lowest possible peak temperature in the liquid. Achieving this goal requires further optimisation of the channel geometry. Preliminary parameter studies also showed that a certain degree of asymmetry in the inlet pressure, as it might occur in practice, will affect the peak temperature [Dury, 1997], but with a suitably chosen inlet temperature, there exists always sufficient margin to avoid boiling. The pressure drop between the inlet and outlet channels was found to be about 2 bar at the flow rate given above. The region of highest fluid temperature is well downstream from the window and from the point of peak power deposition, which is one of the advantages of the configuration chosen, in which the liquid flows away from the beam entrance window. This is significant for the window temperature and in the light of pulsed operation, because the temperature rise during the pulse is about 20 K at the point of highest power deposition close to the window.

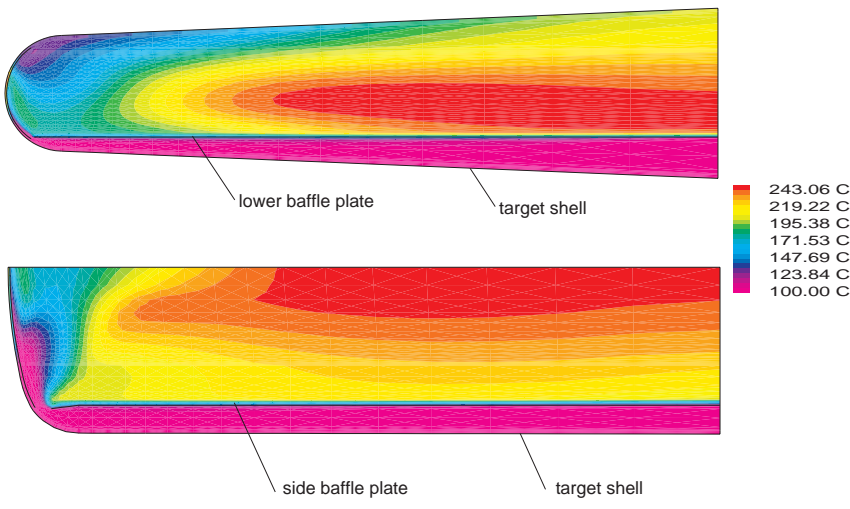


Figure 4.3-6a:
Vertical (top) and horizontal (bottom), sections through the 3-dimensional model of the target shell used to calculate the temperature field. Lines of constant time averaged temperature are shown for an inlet temperature of 100°C. In the bottom figure only one half of the target is shown.

Figure 4.3-6b shows calculated maximum fluid temperatures as a function of the fraction of flow through the bottom channel, with both side channels symmetric. Part of the differences between different codes may arise from different turbulence models used [Wolters, 2002]. Heat transfer rates from CFD calculations, using the FLUENT code were verified by experimental studies in a model mercury loop [Bucenieks, 1998]. Combined experimental [Patorski, 2000] and computational studies on cooling of the beam window are also in progress.

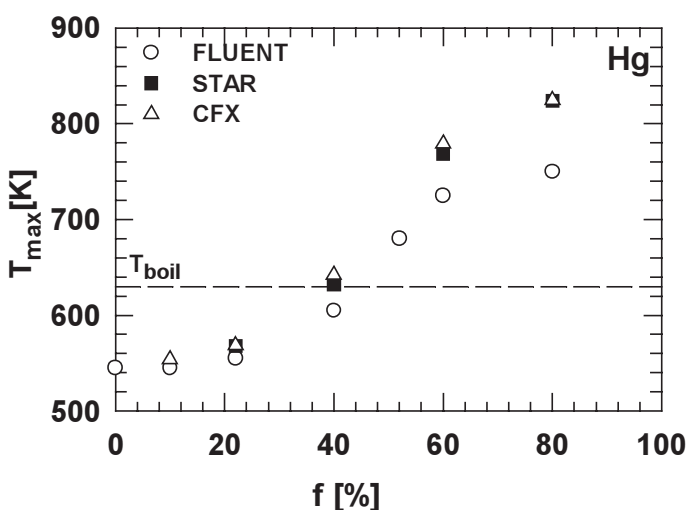


Figure 4.3-6b:
Calculated maximum fluid temperatures as a function of the fraction f of flow through the bottom channel, with both side channels symmetric.

Investigations on alternative target geometries concentrate on a cross-flow target with asymmetric arrangements of inlet and outlet baffles. In 2D calculations also window cooling was studied. So far, preliminary 3D calculations on this target gave too high maximum fluid temperatures.

Studies on the behaviour of gas bubbles indicated the risk of accumulation of bubbles in certain regions for bubble diameters above 0.05 mm. Smaller bubbles would still be suitable for pressure wave mitigation, but may be difficult to produce in reality.

4.3.5 Effects due to Pulsing of the Beam

4.3.5.1 Effects on the wall from the heated fluid

The above temperature estimates were based on the time averaged power input to the system. For a pulsed system, like ESS, it is however important to examine the effects of the time structure of the beam, which deposits nearly 60 kJ of thermal energy within 1 μ s in a few litres of liquid metal. As a consequence, the liquid will heat up very rapidly and will try to expand. Since the low compressibility of the surrounding liquid hinders this expansion, pressure will build up instantaneously and a pressure wave will propagate through the liquid. Depending on the geometry of the system, this may lead to substantial tensile and shear stresses in the walls. In order to investigate the magnitude and temporal behaviour of these stresses, a computer code (FLUSS_MET_TARG), developed for ESS [Skala, 1995] and available codes (ANSYS [ANSYS], KASKA from PSI [Ni, 1997]) were used, which allowed to calculate these stresses in three dimensions. One important result of these calculations was that open surfaces couldn't be sustained in the beam interaction region of a liquid metal target at ESS conditions because the liquid would be expelled at a velocity of about 10 m/s. A beam entry window and sustaining sidewalls are necessary. This excluded several of the target configurations considered at the beginning of the study.

For the case of a cylindrical target of 20 cm diameter and a beam diameter of 11 cm with parabolic intensity distribution (yielding the same peak power density as the elliptic cross section mentioned above), the stress obtained in a 3 mm thick steel wall is as high as 480 MPa. The stress peak travelling down from the apex of the domed cover along the cylindrical wall, gives rise to a complicated oscillatory behaviour with a characteristic time of

the order of 100 μ s [Skala, 1995]. Similar results were obtained for elliptical target and beam geometries, which were also examined. Because of the close proximity of the point of peak power deposition to the window (see Figure 4.3-5), the main effect to be expected for a different geometry results from the curvature of the window. Calculations with different codes for 100 kJ / 1 μ s pulse on a 1.5 mm thick window gave good agreement, yielding maximum stresses of 400 MPa as shown in Figure 4.3-7 [Probst, 2001a; Probst, 2001b].

These results were obtained under the assumption that the liquid cannot go into tension, which is certainly pessimistic, since rather high tensile stresses have been observed in liquids, before cavitation occurs [West, 1969; Hahn, 1963]. On the other hand, nucleation centres, which could be generated by impurity content, high vapour pressure, and intense energy deposition, may severely reduce the tensile strength of a liquid. These effects will have to be investigated. At present it seems safe not to count on tensile strength in the liquid. First results from experimental studies of stresses and damage by 0.8 GeV (LANSCE) and 14 GeV pulses (BNL, ASTE co-operation) are available [SNS, 2001] and are in good qualitative agreement with calculations (Figure 4.3-7b). Quantitative evaluations are still in progress.

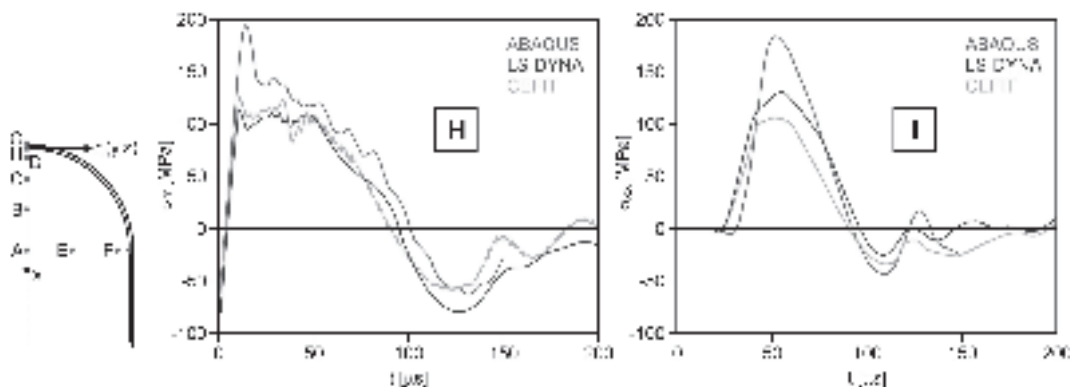


Figure 4.3-7a: Calculated tangential stresses along the wall of a mercury target in point H in radial direction and in point I in axial direction, see insert, as calculated by different codes [Probst2001a; Probst, 2001b]

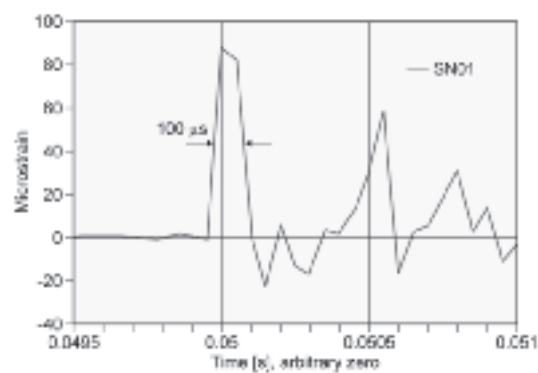


Figure 4.3-7b: Measured tangential strain along the wall of a mercury target near the apex point of a cylindrical target window (ASTE)

The wall load results from the sum of the mechanical stresses generated by the static pressure in the mercury and the superposition of the time averaged temperature gradients (cf. Subsection 4.3.3) and cyclic stresses from the pressure waves in the liquid metal. The stress levels derived for the ESS target are not tolerable, because they already exceed the recommended design stress of the ferritic-martensitic steels considered for the structure material (cf. Subsection 4.3.8). Another possible effect of the pressure waves in a liquid of limited tensile strength may be cavitation, which in turn may induce local erosion damage ("pitting") to the wall [SNS, 2001]. A possible way to circumvent both of these problems may be to maintain a small concentration of helium bubbles in the beam interaction zone. This is expected to increase the compressibility of the target, which may initially accommodate the expansion of the liquid, by compression of the gas bubbles. This results in lower pressures in the system. The computer program mentioned above allows this effect to be included for the general case of a polytropic compression of the gas. It is found, however, that isothermal compression (i.e. simultaneous heating of gas and liquid) is the worst case and so this was used for the computations. Calculations for 3 vol.-% of helium in mercury indicated that the stress rises more slowly, and that the maximum value is lower by an order of magnitude than in the case without gas [Skala, 1995]. Experimental results revealed significantly reduced velocity and enhanced damping of sound in liquid mercury, already by volume fractions of gas bubbles around 0.1% [Soltner, 2002].

It must be emphasised that these results are preliminary and probably on the pessimistic side for the gas free case, neglecting tensile strength of the liquid. Further verification is needed, in particular with respect to the practicality and dynamic response of such a two-phase system. Anyhow, these results show that the development of a viable technique to introduce helium bubbles with a suitable size distribution may be crucial for the feasibility of a liquid metal target under ESS operating conditions. Because of the many advantageous features of the liquid mercury target concept (see chapter 4.1 and [Bauer, 1995]), this work will be pursued with high priority. It should be mentioned, however, that feasible back-up solutions involving a solid target material exist (a rotating rad target [Bauer, 1982] and a plate target [Bauer, 1996a, pp. 4-68]).

4.3.5.2 Effects of direct window heating

Short heat pulses also affect the material of the beam window, although the power density is lower in steel than in mercury. Two computational approaches were taken: Firstly the FEM code FLUSS_MET_TARG was developed to include solid materials, mainly by expressing the bulk modulus by Young's modulus and Poisson's ratio and by allowing the pressure in the volume to assume negative values, corresponding to tensile stresses in the solid. Secondly the commercial code ANSYS [ANSYS] was used to calculate the response of a solid plate to a sudden rise in temperature in its centre. The results from both approaches agree remarkably well in cases where comparisons can be made. FLUSS_MET_TARG needed a fine mesh to resolve the details of the oscillatory behaviour. However, the important features could also be analysed with ANSYS, which was finally used to investigate the behaviour of the domed beam entry window. So far, only a "free" window, i.e. not in contact with liquid metal on its inner side, has been investigated. There are mainly two effects:

Firstly, at the end of the power deposition period, the temperature rise in the window (before cooling becomes effective) leads to thermal deformation and generates a "quasi-static" stress distribution with compressive stresses at the inside and tensile stresses at the outside of the window at levels of about 4 MPa each. These stresses disappear during the pulse-off period and hence repeat themselves with the pulse frequency.

Secondly, as a consequence of the acceleration of the volume elements during the pulse and the elastic properties of the metal, an oscillatory motion is triggered, which is most pronounced in the "axial" direction perpendicular to the window surface and hindered in the plane of the window (radial and azimuthal or hoop stress). The frequency of this oscillation depends on the thickness of the window and is of the order of one MHz. The resulting stress amplitude for a 1 μ s pulse in the mid plane of the 3 mm thick window at the apex of the dome was found to depend strongly on the pulse duration and decreased from almost 80 MPa for a δ -function to 10 MPa, see Figure 4.3-8. While the axial (y) component oscillates between positive and negative values, the radial (x) component always remains negative (in compression). It was found that the oscillations become strongly damped as the pulse duration exceeds the period of the oscillation. This observation needs further investigation. Also the fact that, in the ESS target, one side of the window will be in contact with the liquid metal may cause some asymmetries in the stress, which is not accounted for in the present calculations.

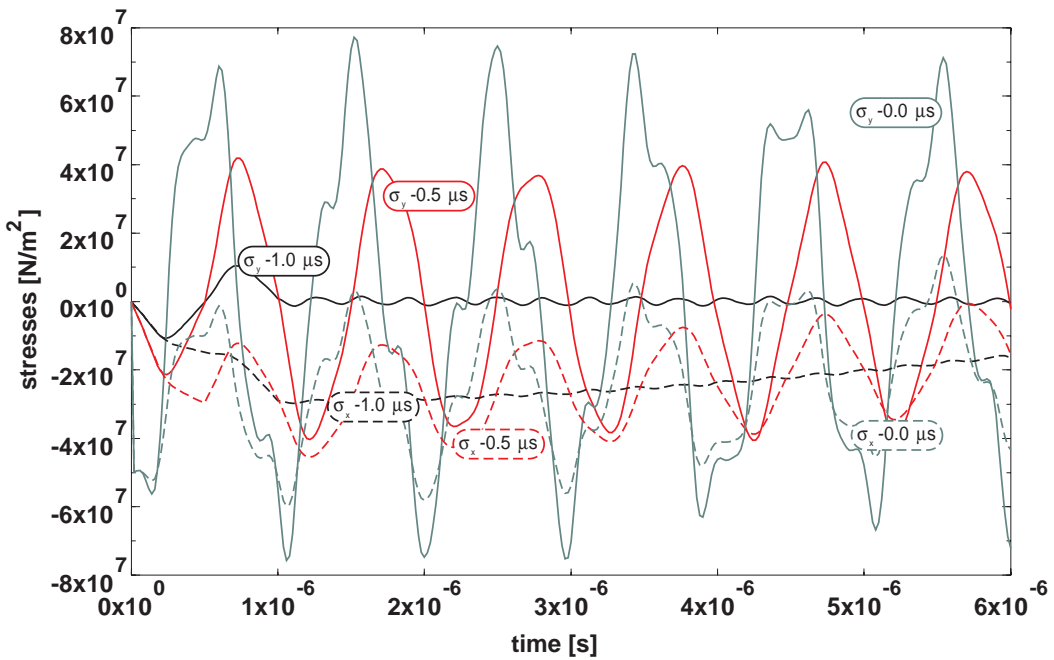


Figure 4.3-8: Elastic stress in the midpoint of the wall for a 3 mm thick hemispherical proton beam entry window following a proton pulse. Data are given for 0, 0.5 and 1 μ s pulse lengths. Their direction is antiparallel to the direction of the proton beam; x direction is normal to it.

From the studies carried out so far, one can conclude that the most significant stress effect in respect of the structural integrity of the window is the thermal cycling from beam trips, provided that mitigation of pressure wave effects is possible (see Table 4.3-2).

4.3.6 Corrosion, Erosion and Liquid Metal Embrittlement in the Target Circuit

Most data on corrosion in mercury circuits pertain to higher temperatures than envisaged for the ESS target circuit and not too many are available at all. A relatively comprehensive summary for iron-based materials [Nejedlik, 1964] shows a clear dependency of the corrosion rate on the content of nickel, chromium and manganese (Figure 4.3-9). Although

not explicitly obvious from these data, it may be suspected that nickel is the most important component because it has the highest solubility in mercury (see Fig 4.3-10) and liquid metal corrosion largely happens by dissolution of the wall material at the hottest points (beam window, return channel) and segregation to the coldest point (heat exchanger). Also the destruction of protective surface coatings, e.g. oxide layers, plays a significant role. The addition of a small amount of Zr to mercury has been found to inhibit corrosion quite effectively, probably forming layers of ZrC or ZrN by reacting with carbon or nitrogen from the steel. On the other hand, the stability of these brittle layers on the surface of the ESS target window may be limited by cyclic stresses (Table 4.3-2). Therefore, instead of relying on a protective coating, a structural material with low corrosion in mercury should be selected. Apart from higher strength and better thermo-mechanical properties (cf. Subsection 4.3.8), this also favours ferritic-martensitic steels over austenitics because their total content of non-iron elements is in the order of 10 - 15 % compared to 30 - 35 %. Some corrosion tests in stagnant (non-pumped) mercury without irradiation have been performed in support of the present study [Dai, 1997; Zalavutdinov, 1999; Zalavutdinov, 2001] and will be extended to a pumped circuit. Opportunities to perform experiments in a spallation situation have been identified and corresponding work is in preparation.

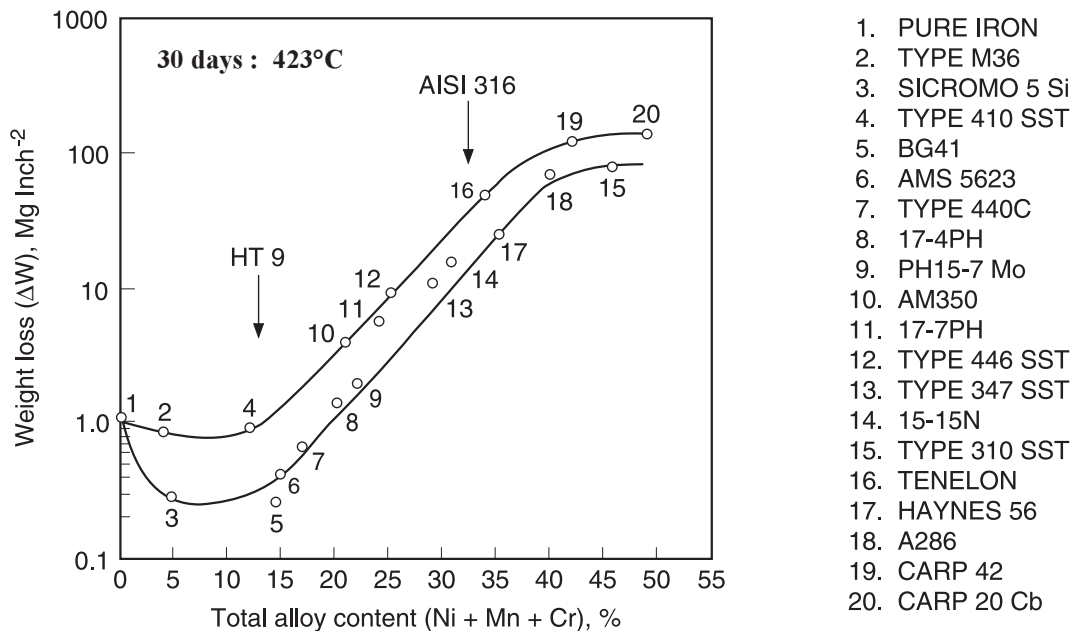


Figure 4.3-9: Dependence of observed corrosion rate in mercury on the total Ni+Cr+Mn content in iron-base materials [Nejedlik, 1964].

Another effect sometimes observed when liquid metals are in contact with solid metals is liquid-metal-embrittlement (LME). Wetting-induced surface roughening as well as solubility and fast diffusion in the liquid metal have been identified as promoting LME. In this context, it is important to note that, according to the MIEDEMA calculations, the chemical potential of Ni in Hg is the same as that of Hg itself [Dressler, 1995]. In principal LME is not an instantaneous process, but is controlled by subcritical crack growth. This often causes extended incubation times and makes it difficult to compare different systems or experimental conditions. Under high-cycle fatigue stresses AISI316 showed virtually no effect of mercury environment [Strizak, 2001], while AISI430 experienced strong reduction of cycles to failure [Levinson]. No information is available on high-cycle-fatigue of ferritic-

martensitic steels in liquid mercury and on synergy effects on LME of cyclic stress and irradiation in mercury.

The structural material of the water cooled LMRH may suffer from irradiation assisted stress corrosion cracking (IASCC). This phenomenon is well known from water cooled power reactors and is closely related to chromium depletion of grain boundaries. While the aggravating effect of tensile stresses is well documented, the possible influence of fast cycling stresses has yet to be examined.

4.3.7 Impurity Build-up by Spallation Products and its Effect on Target Material Quality

Apart from effects on structural materials, corrosion and erosion products are also sources of contamination for the liquid metal circuit. On the other hand, fast fission and spallation processes in the target will produce virtually all elements with mass numbers lower than that of the parent atom. The behaviour and effect of these impurities on the quality of the target material depend strongly on their solubility in mercury, the chemical reaction they undergo with mercury, with structural materials, and with one another. The physical properties of the reaction products are important as for example abrasive and hard compounds in the liquid may lead to erosion of protective surface layers and thus enhance corrosion and also liquid metal embrittlement, cf. Subsection 4.3.6. It is therefore important to be able to predict and possibly control these processes. In view of the large number of elements involved, this is a difficult task, in particular since many of the data needed are not available.

In a first step the known solubilities of the elements in Hg were compiled and reduced to the temperature range of interest. The solubilities of those metallic elements, for which no data were available, were calculated by the MIEDEMA model [Niessen, 1983]. The experimental data and calculated values in Figure 4.3-9 agree reasonably well giving some confidence to those data for which no experimental values could be found. For most of the elements, the solubility limit will not be reached in a target mass of 15 tons, even after 10 years of operation.

As a next step, the tendency to form amalgams needs to be investigated, because this will be the dominant reaction in view of the large degree of dilution of the other impurities. In order to characterise the amalgams, a literature search was carried out and the solubilities were again calculated with the MIEDEMA model [Niessen, 1983]. The most serious problems could, however, arise from the reaction of impurities among each other, because this is where abrasive compounds might be generated. This still needs to be examined.

In general, elements or compounds whose production exceeds the solubility limit, would either float on the mercury or segregate to the bottom. In order to eliminate these products from the circuit, a suitably designed vessel will be incorporated, which will be drained completely into the dump tank whenever the circuit is emptied. In this way, most of the insoluble reaction products should accumulate in the dump tank, where they can do no harm to the sensitive components. Since the total decay heat after a full year of operation is only 10 kW (cf. Subsection 4.3.9), the concentration of a significant fraction of that heat in the dump tank should not be a problem.

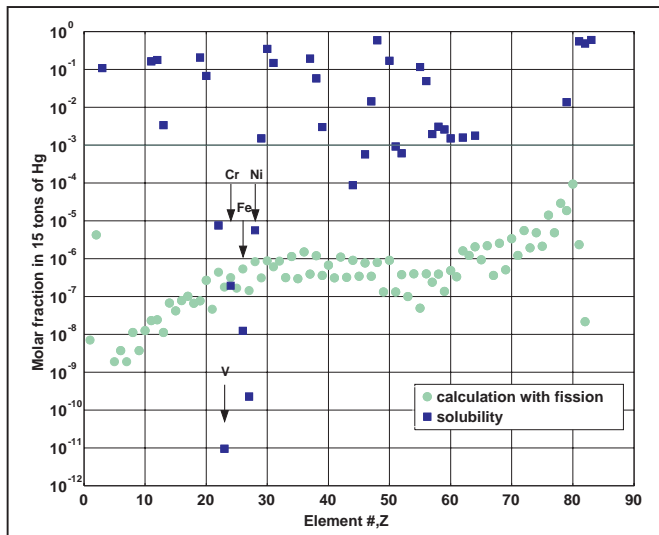


Figure 4.3-10:
Solubility's of
elements in
mercury
compared to their
production in 15
tons of target
material after 10
years of
operation at 5
MW for 6000
hours per year.

4.3.8 Radiation Effects in Structural Materials

In addition to the mechanical and thermal loads resulting mainly from the pulsed energy deposition, the structural materials of the spallation mercury target and the proton beam window will experience radiation effects from the high fluxes of energetic protons and neutrons.

4.3.8.1 Radiation Damage

In solid metallic materials all macroscopically observed radiation effects can be ascribed to two basic interaction processes between the bombarding particles and the target atoms: atomic displacements and production of transmutation products [Ullmaier, 1995; Jung, 2001a]:

- (1) Calculated cross sections σ_d for atomic displacement in Fe as a function of proton and neutron energy are given in [4.3-30]. The concentration of displaced atoms is characterised by the so-called dpa-number (displacements per atom) which is given by the product of the total displacement cross-section σ_d and the particle fluence. It is important to note that only a small fraction of the initially produced defects contributes to the finally observed property changes under irradiation, while the rest is annihilated by recombination. Since the relevant fraction not only depends on material, temperature and recoil energy, but also on the property considered (see Figure 4.3-12), the damage cannot be fully characterised by a single parameter. Nevertheless, the dpa number is a useful measure in correlating results obtained under different irradiation conditions (particles, energies, fluxes and fluences). This is especially important in the case of ESS, as material selection will largely depend on results from irradiations in other environments (reactors, accelerators), performed in previous material programs (fission, fusion etc.).
- (2) Nuclear reactions not only induce radioactivity of the parent nucleus (cf. Subsection 4.3.9) but also lead to the production of foreign elements in the irradiated material. It is known that especially He (produced by (p, α) - and (n, α) -type reactions) and in some cases also H-isotopes can lead to drastic property changes even at concentrations in the ppm-range. Cross sections σ_{He} for He production by protons and neutrons are given in [Filges, 1996a; Filges 1996b]. The resulting concentrations are again derived by the

product of σ_{He} and particle fluence, if all atoms are retained. This is almost quantitatively the case for helium, while some of the hydrogen will escape, unless it is strongly trapped at irradiation defects [Jung, 2001b].

Figure 4.3-11 shows the expected dpa-numbers and helium and hydrogen concentrations as a function of service time in the centre of a steel window of the 5 MW ESS target. For comparison the corresponding numbers in the first wall of a future fusion reactor (ITER) are given. The figure shows that the ESS window will experience about 3 times higher dpa-rates than the first wall of a fusion reactor, but that the production of H and He will be more than two orders of magnitude higher. In a fast fission reactor the dpa values are similar to the fusion case while H and He production are negligibly small. Another difference between fission, fusion and spallation environments are the increasingly harder recoil spectra [Jung, 2001a]. In comparison to other irradiation environments, the outstanding features of the ESS source will be:

- 1) The extremely high instantaneous particle fluxes in the pulses, and
- 2) The unprecedently high transmutation rates.

There is some experimental and theoretical evidence that the first point may generally not cause enhanced damage [Trinkaus, 2001]. On the other hand, there is increasing evidence that high helium and hydrogen concentrations cause severe degradation of mechanical properties, in various materials and temperature regimes [Jung, 2001b].

At the operating temperatures of target components, most irradiation-induced defects or defect clusters are mobile and can react with one another. Such defect reactions lead to changes in the microstructure, which in turn cause (mostly detrimental) changes of the properties of the material. They occur in ranges of homologous temperature (T divided by the melting temperature T_m), which are rather independent of the material (see Figure 4.3-12). Figure 4.3-12 indicates that in the ‘low-temperature’ regime of $T/T_m < 0.3$ austenitic stainless steels are less prone to radiation damage. Irradiation creep is not expected to be a problem since the resulting plastic deformations are small and may even have a positive effect in reducing stress concentrations. On the other hand, at higher temperatures martensitic steels are advantageous.

These statements must still be viewed with some caution. They are derived from fission and fusion materials research but are increasingly confirmed by results obtained in spallation environments [Chen, 1999; Dai, 2001; James, 2001]. The above considerations do not include possible effects of a surrounding medium.

In section 4.3.6 it was mentioned that irradiation may influence the effects of liquid metal embrittlement (in mercury) or stress corrosion cracking (in water). Even transfer of results on irradiation assisted stress corrosion cracking (IASCC), available for steels in light water power reactors [Scott, 1994], is again afflicted with large uncertainties in view of the extremely high impurity generation by transmutation under spallation conditions, combined with cyclic stresses from the pulsed irradiation. Therefore more investigations on high cycle fatigue of irradiated ferritic-martensitic steels in liquid mercury is needed, as the available results obtained under spallation conditions [Marmier, 1994] are limited to less than 10^5 cycles in vacuum.

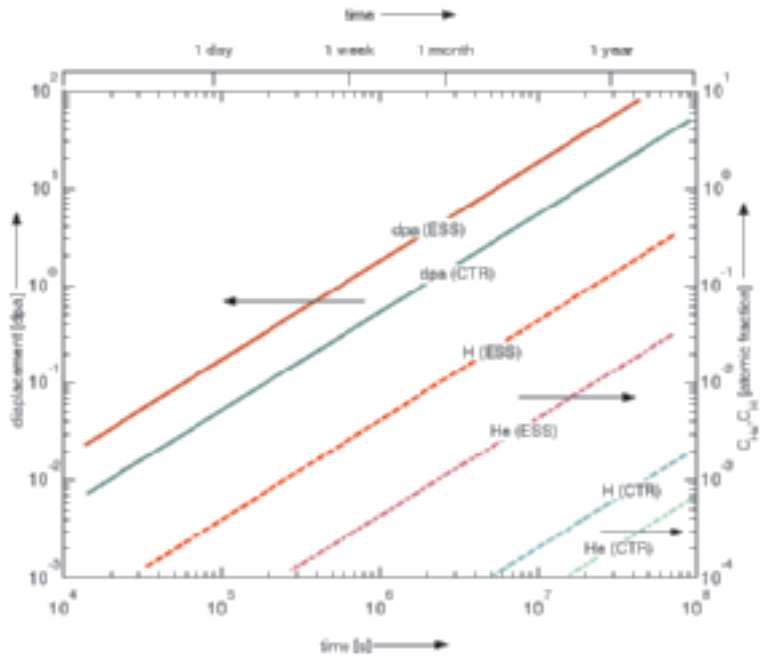


Figure 4.3-11: Number of displacements per atom (dpa), H concentration c_H and He concentration c_{He} as a function of service time t in the centre of stainless steel proton beam entry window in ESS and in the first wall of a fusion reactor (CTR with 1 MW/m^2).

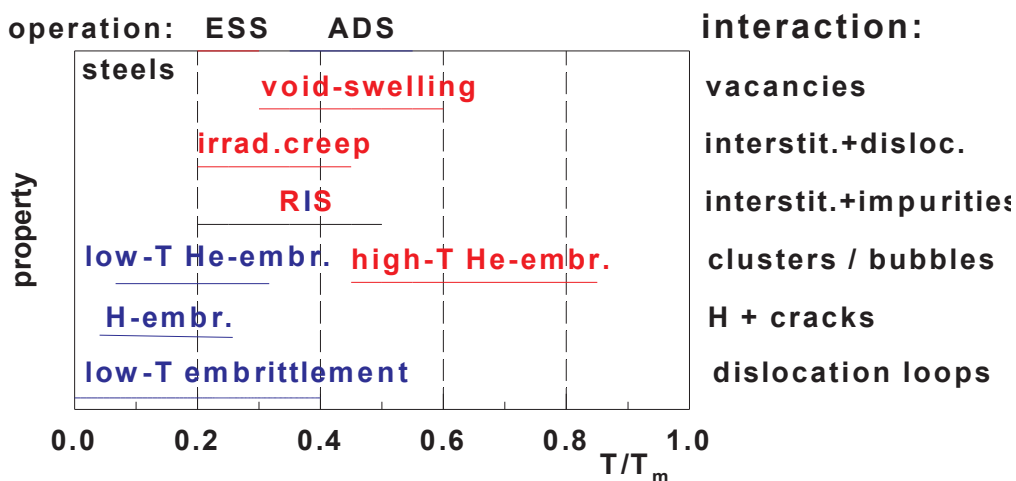


Figure 4.3-12: Approximate ranges of homologous temperatures T/T_m where the major radiation damage effects indicated occur. The blue and red bars indicate effects that are more prominent in martensitic and austenitic steels, respectively. The operation temperature ranges of ESS and ADS (Accelerator Driven Systems) are indicated on the top, while the right hand side column gives the basic mechanism or processes. (RIS: Radiation Induced Segregation).

Another area, which requires further attention, is the effect of irradiation on welds, especially of ferritic-martensitic steels. Limited results on argon arc and electron beam welding of non-irradiated and irradiated martensitic steels is available [Schaaf, 1999]. Especially effects of helium, which even in amounts of a few ppm is prohibitive for re-welding of austenitic steels, must be studied in martensitic steels.

4.3.8.2 Materials selection and lifetime prediction

Starting from a wide variety of candidate structural materials for ESS, including ceramics and composites, most of them were soon discarded for different reasons [Bauer, 1996b]. Considering the short period available for materials development it was concluded that only materials with a sufficient database on their behaviour in nuclear environments should be considered. This leaves only four types of materials:

1. Austenitic stainless steels, preferentially solution annealed, low carbon type 316L.
2. Precipitation hardened high nickel steels, for example Alloy 718.
3. Martensitic stainless steels of the 9% or 12% Cr type.
4. Tantalum or tantalum alloys.

In a preliminary conclusion of the ESS target group, Alloy 718 was selected as prime candidate for the beam window, austenitic 316L for the LMRH and 9%Cr martensitic steel for the target container.

While the austenitics have clear advantages with respect to irradiation damage in the low temperature regime (Figure 4.3-12), their applicability is limited by their low strength and high thermo-mechanical stresses (Figure 4.3-13). Alloy 718 loses some of its strength by dissolution of precipitates and suffers from drastic loss of ductility by irradiation [James, 2001]. Also the ferritic/martensitic steels show embrittlement under irradiation by hydrogen and especially helium production. Their lifetime limit will probably be determined by the accumulation of helium and is still under investigation in experiments at spallation sources and accelerators [Maloy, 2001; Farrell, 2001; James, 2001; Jung, 2002]. For nuclear application these steels are mostly considered in the 9% Cr version, due to their lower irradiation embrittlement. On the other hand, 12% Cr steels are superior with respect to corrosion. In spite of some encouraging results on specimens from a spent target of pure tantalum from ISIS, the development of a sufficient database for this class of materials may not be possible within the time scale for the design of the first ESS target.

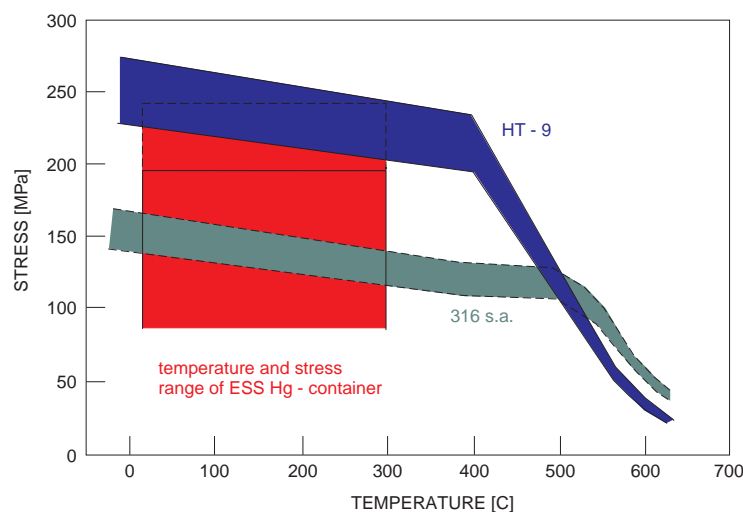


Figure 4.3-13: Comparison of design stresses as a function of temperature for fusion reactor first wall [Rosenwasser, 1984] and [Gordon, 1984] and the anticipated stress temperature range for ESS structural target components (blue: HT-9, green: solution annealed 316).

Figure 4.3-13 shows that the strength of ferritic/martensitic steels is sufficient to withstand the sum of the mechanical stresses given in Table 4.3-2 provided that the effect of pressure waves in Hg can be mitigated, e.g. by the injection of gas bubbles. For austenitic steels the

stress level is higher due to their inferior thermal conductivity and expansion, and the sum of the stresses exceeds the design limit for the non-irradiated, solution annealed material. However, even very low irradiation doses strengthen the material considerably so that also this class of materials could meet the strength requirements if suitable start-up procedures are followed for new target shells.

Of great concern with respect to ferritic/martensitic steels is their transition from ductile to brittle behaviour at low temperatures and especially the increase of this transition temperature (DBTT) under irradiation [Gelles, 1987]. So-called reduced-activation ferritic/martensitic steels (RAFM) which are at present intensively investigated for application in fusion reactors show less increase of DBTT under irradiation, e.g. 9Cr2WVTa [Klueh, 1994]. In terms of activation these materials have no advantages in a spallation environment and might even loose their advantageous fracture resistance under the high H- and He- production rates.

Lifetime estimates for the target structure of ESS will be based on data from existing spallation facilities, and on data from other irradiation facilities, mainly fast reactors. The former will be limited to relatively low doses, while the latter miss the high H and He production rates. Both sets of data cannot include the liquid metal environment, which is only included in some recent experiments employing 1 mAs in liquid Hg (LANSCE) and up to 10 Ah on Pb in austenitic stainless steel (SINQ), where some samples of steel under stress have been irradiated in mercury but still need to be investigated.

4.3.9 Radioactivity and Decay Heat

Although neutron calculations, which also include spallation products, radioactivity and decay heat in the target are reported in section 4.5, we quote here some results in so far as they are of relevance for the target circuit design. Total and specific radioactivity and decay heat for a total inventory of 15 t of target material are shown in Figure 4.3.14 [Filges, 1995]. The large target mass has a considerable dilution effect bringing the specific values down to rather low levels. This will be important in considering how to deal with minor spills.

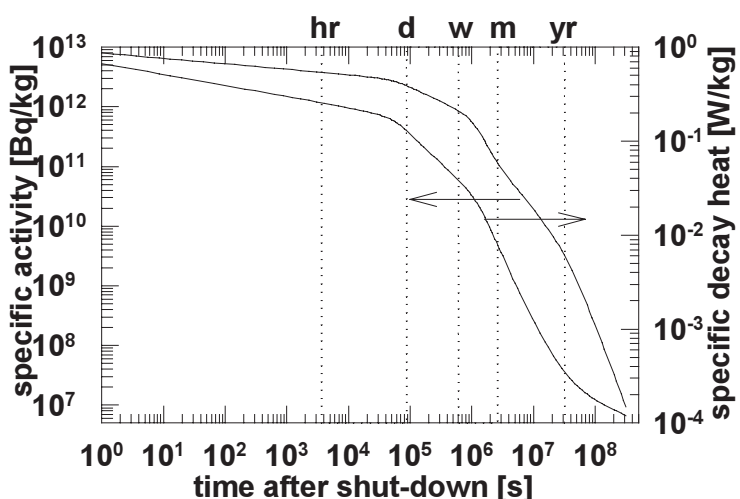


Figure 4.3-14:
Specific radioactivity and specific decay heat after 1 full year of target operation at 5 MW

Since the only radioactive isotope of mercury with a half life of more than 50 days is ^{194}Hg , it is possible, in principle, to purify the target material to reduce its medium term radioactivity to low levels.

The radioactivity of spent target structures, which will accrue from routine exchange, has not yet been estimated. Total activity and decay times will affect the necessary procedures during target exchange and the amount of waste for final deposition.

4.4 THE MODERATOR-REFLECTOR UNITS

4.4.1 The moderator configurations

As mentioned in the Overview (chapter 4.1), recent requirements from the scientific case imposed important changes upon the specifications of the two target stations described in the Technical Study of 1997. In particular, the decision to replace the 1 MW Short-Pulse-Station by a 5 MW Long-Pulse-Target-Station (LPTS) also entailed a different selection of moderators. Both target stations will have thermal and cold moderators, but the number and configuration of the moderators have changed, mainly to have bigger moderators in the peak flux area and to position multi spectrum beam extraction from a cold and a thermal moderator in the same beam tube [Mezei, 2002].

These changes are, however very recent and need to be incorporated in the overall layout during the imminent baselining phase. While this may entail certain alterations in details such as heat loads and positioning of the moderators, the basic concept of having ambient temperature water moderators as well as cryogenic moderators of supercritical hydrogen is the same. For this reason the following discussion still refers to the original moderator concept, for which also the neutron performance calculations presented in Section 4.5 have been carried out. A brief description of the new configuration proposed for detailed evaluation will be given in Paragraph 4.4.6.1 (cf. also Vols. 2 and 4 of this report). Figure 4.4-1 shows a horizontal cut through the “old” moderator configuration of the short pulse target station, which has two moderators above and below the target, two of which are assumed to be cryogenic ones. In order to illustrate the relatively small impact the new configuration will have on the overall design, it has been incorporated in the schematic illustration of Figure 4.4.2:

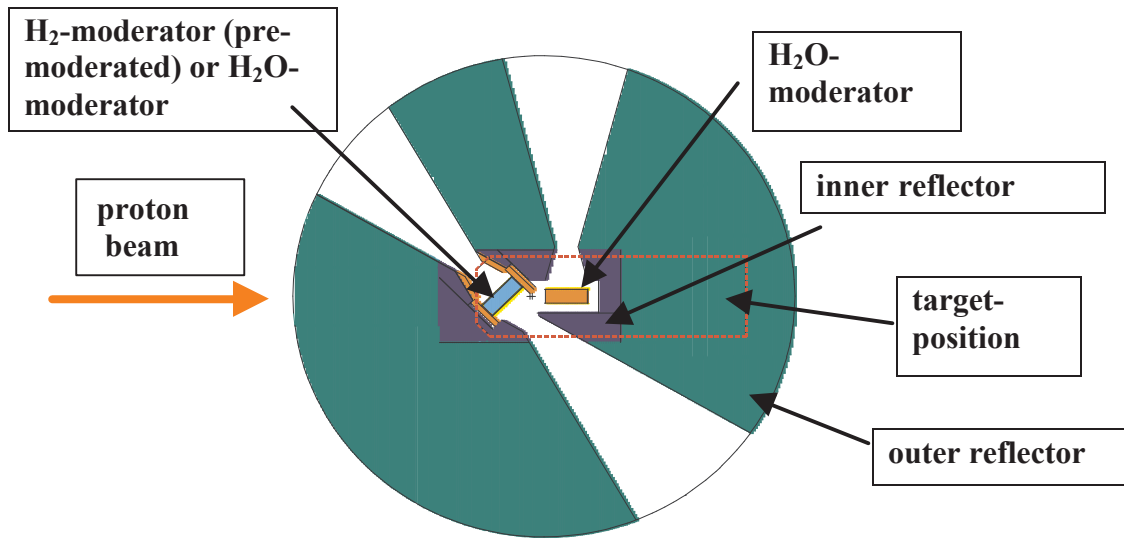


Figure 4.4-1: Cut through the upper moderator plane of the SPTS geometry (cf. Sec. 4.5)

4.4.2 Vertical reflector-moderator-shielding module

Figure 4.4-2 shows a schematic vertical cut through the reflector-moderator-shielding module of the SPTS. The module consists of two concentric parts. This will not only ease the realization of a composite (inner and outer) reflector but will also allow independent exchange of the inner plug, which contains the moderators, and will reduce the crane load for maintenance operations. The target shown in this figure in its operating position is not part of this module and is included for the sake of completeness only. It will be withdrawn from this position prior to lifting either the inner plug or the entire module. The reflector material will be lead and cooled by heavy water. The respective plug of the LPTS will look essentially the same with the exception of a different set of moderators.

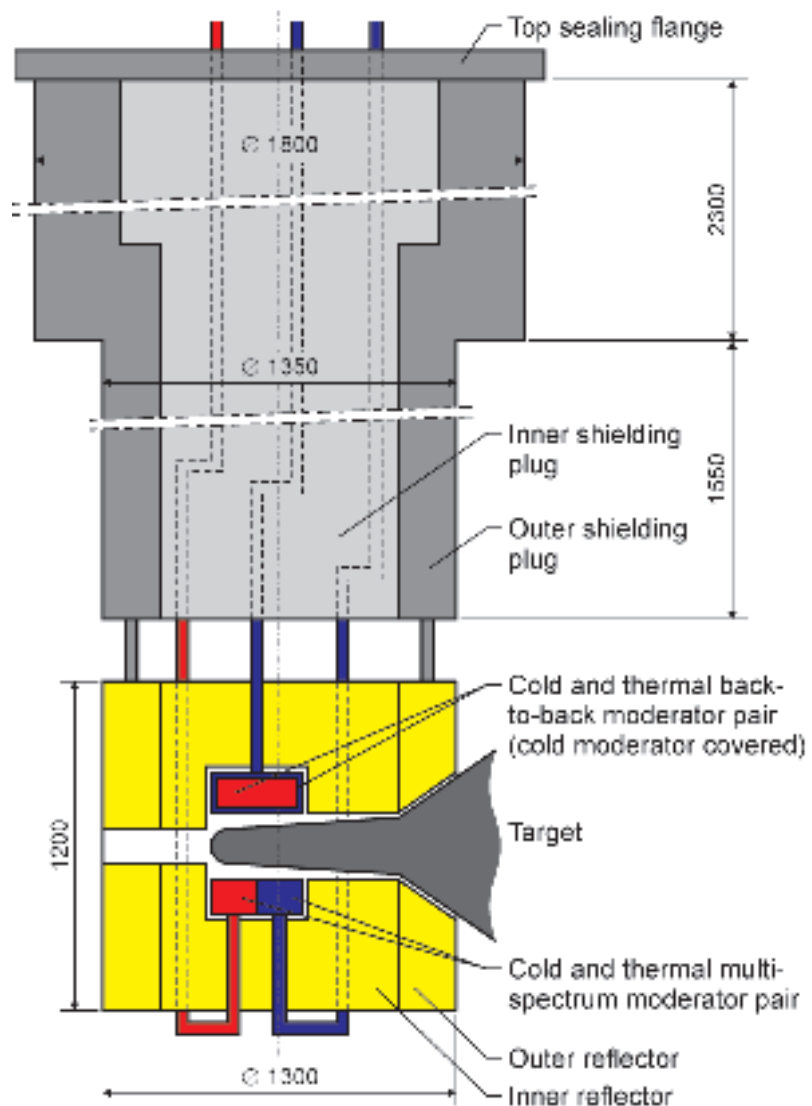


Figure 4.4-2: Schematic representation of a vertical reflector-moderator-shielding module. A horizontally extended upper and a combined lower moderator as proposed recently have been indicated.

4.4.3 Supercritical hydrogen moderator systems

The cryogenic moderators employed in both target stations will be supercritical hydrogen at about $T = 25$ K. Due to the fact that the average beam power dissipated in both targets will not exceed 5 MW, the same estimated cooling capacity of 7.5 kW will be assumed in the present case for any of the individual cold moderators. If, on the other hand, more precise data on the power dissipation will become available or further deliberations of the user community demand more extended cold sources, the capacity of the cooling plant may have to be scaled accordingly. Nevertheless, it is expected that even an increase of necessary cooling capacity of up to 30 % will not influence the total cost very much.

A simplified scheme of the cooling plant can be seen in Fig 4.4-3. The cooling power is generated in a cryo-plant working with helium [Stendal, 1996]. The helium is compressed in a screw compressor. After removal of some of the heat by water-cooling, the low temperature is reached by expanding the helium in turbines. The cold helium is then used to cool the hydrogen circuit including the moderator chamber.

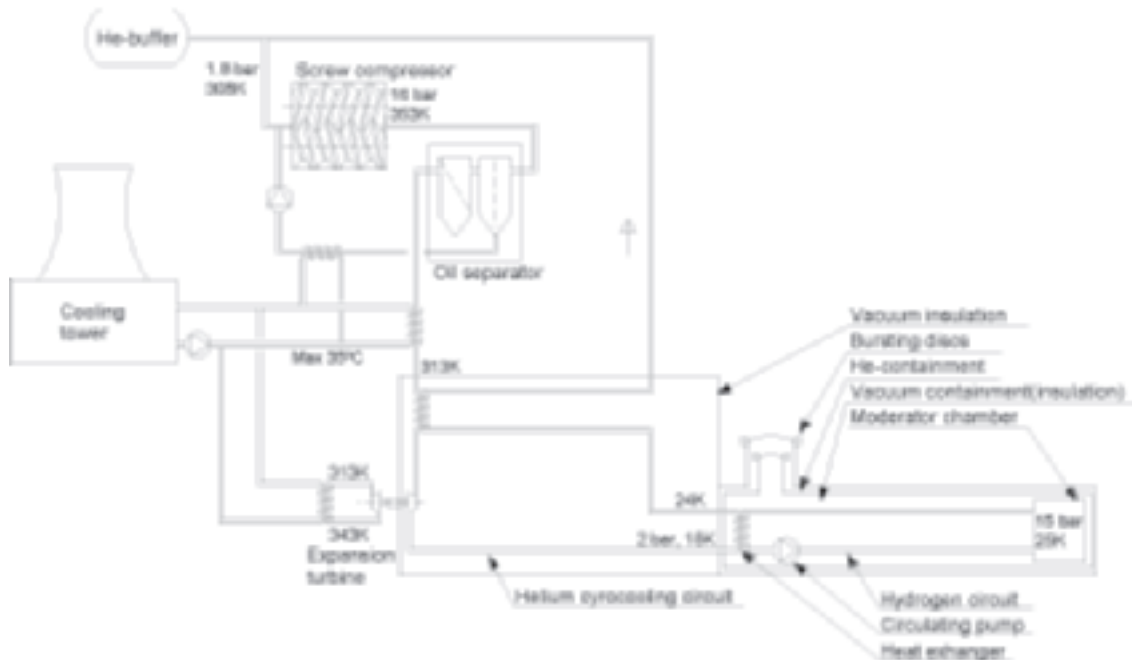


Figure 4.4-3: Schematic diagram of the cooling plant

Insulation of the cold sections of the helium and hydrogen circuits is provided by a vacuum containment system. Furthermore, all hydrogen carrying parts are surrounded by a helium blanket, with the helium at higher pressure than the surrounding atmosphere. This helium blanket serves two purposes. If a leak occurs in the vacuum containment, it can be detected immediately, because helium will penetrate the leak. The other purpose is that the helium blanket prevents other gases from penetrating the vacuum walls through such leaks. This is very important for safety reasons because, if gases other than helium (and hydrogen) get in contact with the hydrogen pipes at 25 K, they will freeze immediately. Solidified gases are difficult to detect as they will not produce a pressure increase, but may generate dangerous mixtures upon warm up, if a hydrogen leak occurs. Even more, if oxygen or nitrogen are irradiated they will form compounds which can explode by self ignition.

The helium blanket prevents this. This system concept is called “triple containment”. It is a crucial feature of the safety philosophy behind these cold neutron sources.

The hydrogen circuit containing the moderator is equipped with circulators and a standby cooling system. The circulators give a large degree of freedom for the geometry of the lines in the hydrogen system since bends are not a problem, because the circulation is forced.

To add further flexibility to the operation of the targets, the supply systems for the four moderators are planned to be completely independent of each other, but as identical as possible. This independence makes it possible to run the individual moderators at different temperatures. Also, because a freon standby system is provided (see below), one of the systems can undergo repair, while the others are in operation. With the four systems as identical as possible, they can profit from the advantages of using common spare parts, handling equipment, tools, operation procedures etc. Furthermore this parallel arrangement makes it possible to use standard equipment, rather than having to design and produce large and expensive special units.

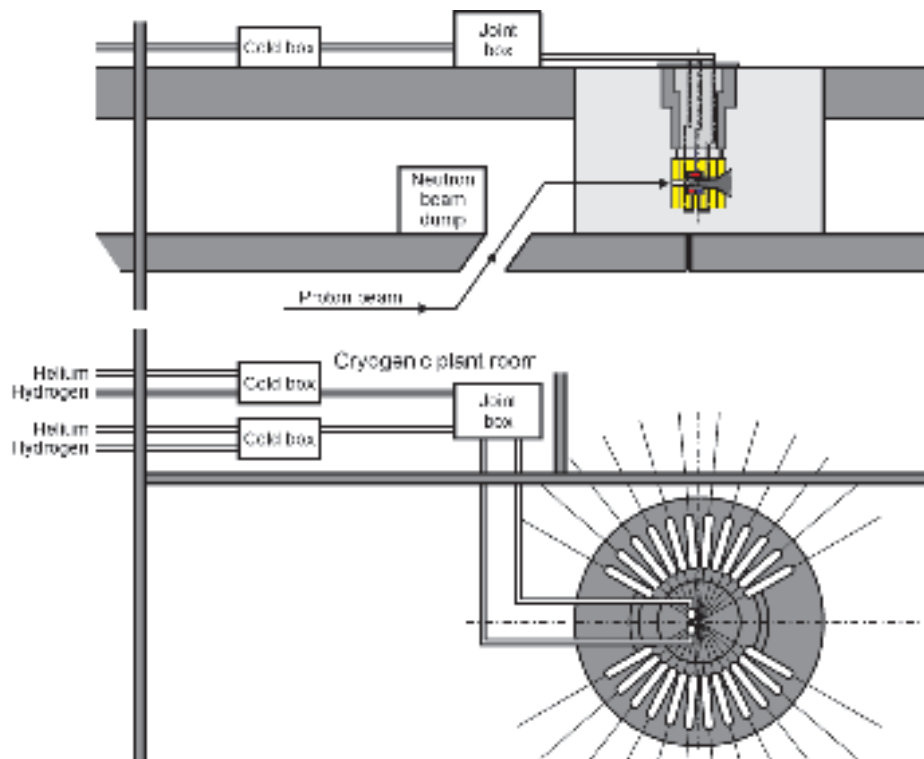


Figure 4.4-4: Schematic representation of the arrangement of components of the cryogenic system in the target halls

The design philosophy of the complete arrangement of the supply systems for both targets is:

- The triple containment liners are as short as possible, to reduce heat losses and complexity.
- In order to minimize heat losses and complexity of connections, the joint boxes and cold boxes are placed as close to the target as possible in a cryogenic plant room adjacent to the high bay area (see Figure 4.4-4 and Figure 4.2-4 of Section 4.2).

- The standby cooling unit and gas handling valve arrangements are outside the target hall, but as close as possible.
- The compressors and filters are in a common hall to limit noise and simplify cooling and power installations.
- It is assumed that both target stations are located in reasonable proximity such that a common compressor hall can be utilized.
- A test location is used for assembling and test runs, before installing units in the target hall. (Later on this location will be used as store and shop area).

The layout is based upon three existing cold neutron sources in service at research reactors and all the components can be produced and delivered with proven technology. As the layout has been taken from reactor installations, also the emergency and safety precautions are as demanded for installations with radiation hazard.

The heat load on each moderator chamber in operating conditions is 7.5 kW. Power requirements of a respective cooling plant are specified in Table 4.4-1. The cooling capacity for the water-cooled outer moderator chambers (see Figure 4.4-5) will be less than 20 kW per target. In a standby situation the hydrogen circuit can be cooled by a freon compressor. The standby system makes it possible to cool the moderators, without having the helium cryo-plant in operation, which can be very useful, for example, during test runs with the target.

Table 4.4-1: Consumption figures for each moderator system at full load

	Electricity (kW)	Cooling water (m ³ /h)	Instrument air (m ³ (STP)/h)
Compressor	560	48	5
Cold box	3	8	5
Standby box	20	8	—
Joint box	2	1	—
In pile part	—	3	—
Instruments	5	—	5
Pumps etc.	20	—	—
Total	610	68	15

4.4.4 Cryogenic moderator vessel

Each moderator vessel (Figure 4.4-5) can feed up to 6 neutron beam channels at the short pulse station. The moderator face viewed by the beam channels has a cross section of 150 mm x 120 mm (inside width x height). The hydrogen thickness perpendicular to the beam channel is 50 mm at its shallowest location. If the thickness has to be increased because there is all para-hydrogen in the vessel (cf. Paragraph 4.5.3), a new assessment of the power deposition will be necessary. The thickness of the vessel walls facing the beam tubes is 3 mm. The concave vessel shape has been chosen in order to minimize geometrical pulse broadening. This geometry is in accordance with the design of the reflector beam ports forming a waist close to the moderators as depicted in Figure 4.4-1. Moreover, the biconcave shape of the moderator vessels helps to stiffen the vessel walls against the substantial inner pressure of about 17 bar of supercritical hydrogen. Despite that shape the concave vessel

walls have to be reinforced. The perforated connecting plates shown in Fig 4.4-5 substantially disturb the hydrogen flow. In Figure 4.4-6 results from 2-dimensional numerical calculations show the differences of the temperature distribution with and without the reinforcement plates [Jahn, 2002]. No attempt has yet been made to optimise the shape of the reinforcement structures with respect to the flow, respectively the temperature pattern and mechanical stress.

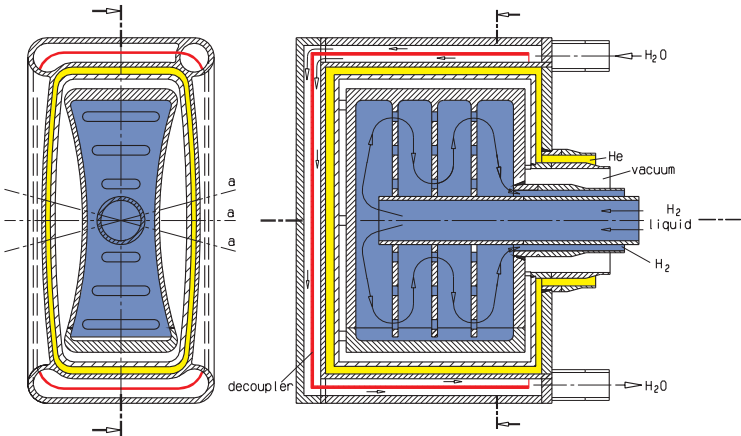


Figure 4.4-5: Schematic horizontal (left) and vertical (right) cuts through the supercritical H_2 moderator vessel (gaps and walls enlarged; a : centre lines of beam tubes). The water jacket serves as a cooling for the vacuum shell and as a pre-moderator as well. The red line inside the water jacket indicates a possible decoupler.
For a quantitative temperature distribution (flow pattern) see Figure 4.4-6.

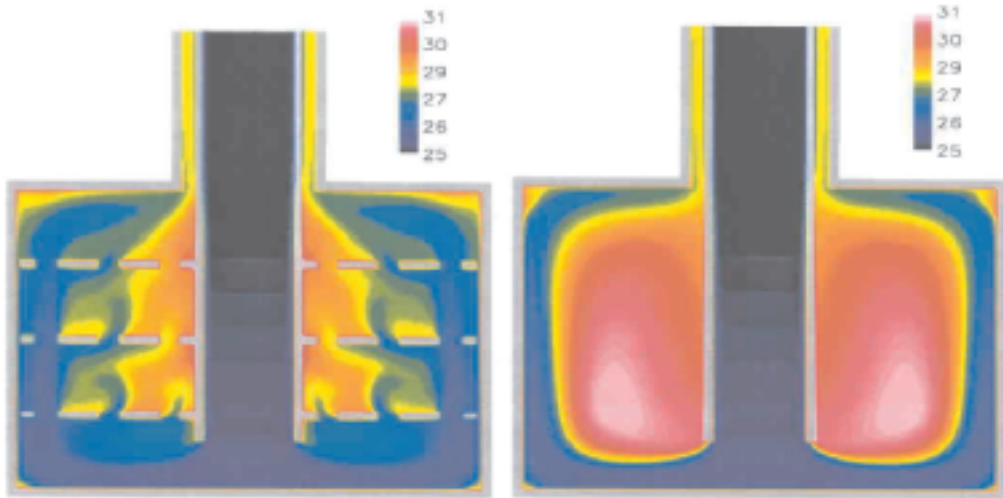


Figure 4.4-6: Results of two-dimensional numerical calculations of the temperature (flow) distribution of the cryogenic moderator vessel of Figure 4.4-5 with (left frame) and without (right frame) perforated reinforcement plates within the vessel [Jahn, 2002]. The temperature is in Kelvin according to the colour scale. Equal flow rate has been assured for both configurations

Up to now the whole chamber design is optimised for a minimum of aluminum (AlMg3)-to-hydrogen mass ratio in order to keep the nuclear heating of the chamber material low. The

same precautions are taken at the supply lines near the chamber. The nuclear heating of the material surrounding the moderator vessel, (vacuum- and helium containment), is not as critical, because these are cooled directly by a cooling water coil on the outside of the helium containment.

4.4.5 Performance Estimates

4.4.5.1 Monte Carlo Calculations

For results of Monte Carlo simulations of the performance of cold hydrogen moderators at $T = 20$ K the reader is referred to Section 4.5.2 of this volume.

4.4.5.2 Experimental results

Experiments with cryogenic moderators were performed using protons of 0.6 GeV from the cyclotron of the Paul-Scherrer-Institut in Switzerland [Bauer, 1985]. Lead and depleted uranium targets were employed as well as lead and graphite reflectors. In addition, a tank with dimensions $1.7 \times 1.7 \times 2.5$ m³ shown in Figure 4.4-7 and filled with up to 5 m³ of D₂O was used as a reflector of a then envisioned long pulse source [Bauer, 1982]. The smaller solid reflectors were piled up on supporting structures in the center of the D₂O tank. With one exception the liquid hydrogen moderators were investigated only in their coupled (high intensity) configuration, i.e. no poisons or decouplers used. On the other hand, a systematic study on the dependence of the neutron leakage currents upon the size and shape (grooves) of the moderator vessels was performed.

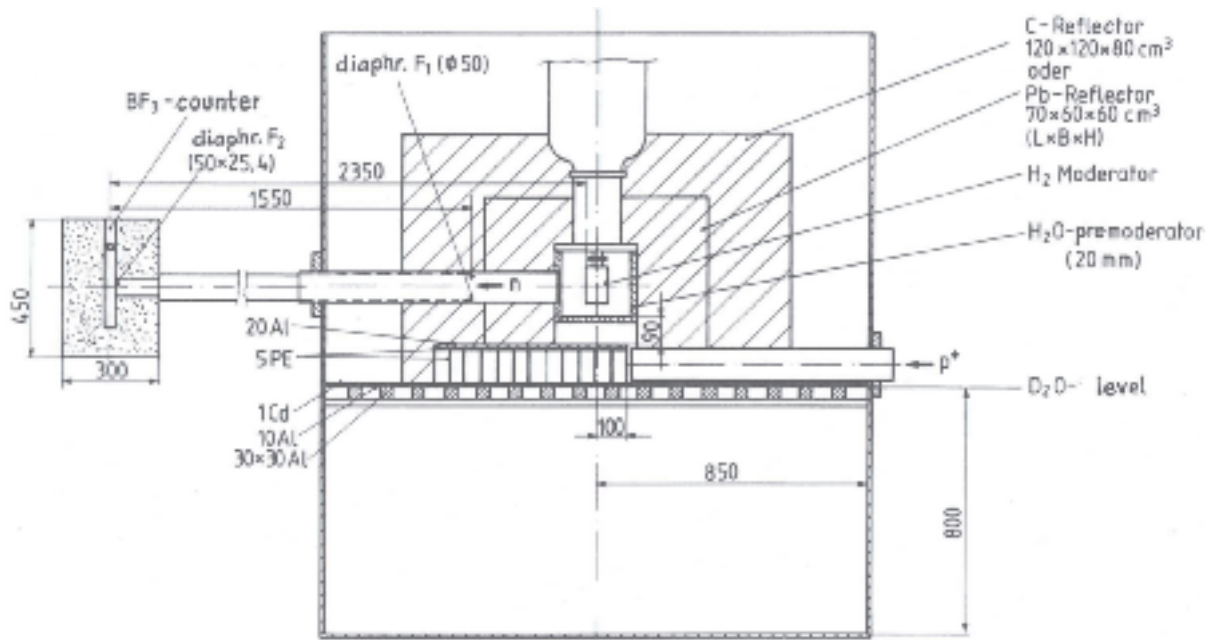


Figure 4.4-7: Target-moderator-reflector configuration for the cold source experiments [Bauer, 1995b]. For sake of simplicity the lead and graphite reflectors are shown in the same drawing. They have not been used together. With D₂O as reflector the tank was filled up to a height of 1.7 m.

In these original pre-moderator studies, the spectral neutron distribution was measured as well, with the surprising result that the neutron temperature of a large series of liquid

hydrogen sources of different sizes and ortho/para ratios were found to be all of the order of 80 K. Although this value might be due to an unfavourable experimental resolution, it may well be that an arrangement has been realized which was later called a composite moderator [Charlton, 1999], i.e. that the hydrogen layer was not thick enough to prevent viewing the water layer (pre-moderator) behind it..

In order to improve the performance of cryogenic moderators a layer of ambient temperature pre-moderator (polyethylene or H₂O) was used enclosing the cold source (with the exception of its viewed face) as depicted in Figure 4.4-7. In fact, an enhancement of the time average cold neutron leakage current by about 50% by this pre-moderator was observed in cases with a solid reflector like lead or graphite. Subsequent optimisation studies by other researchers with respect to the thickness of this pre-moderator resulted in an even more impressive intensity gain of a factor of two [Kiyanagi, 1991].

The experimental results obtained with a liquid H₂ moderator embedded in various reflector materials are shown in Table 4.4-2.

From Table 4.4-2 we deduce the neutron current from a liquid hydrogen cold moderator of a spallation source with a Pb target and D₂O-reflector scaled to 5 MW as $[dj/d\Omega]_{expt} = (1.2 \pm 0.2) \times 10^{13} \text{ cm}^{-2}\text{s}^{-1}\text{sr}^{-1}$. The neutron current from the horizontal cold D₂ source at the ILL is $[dj/d\Omega]_{ILL} = 3.7 \times 10^{13} \text{ cm}^{-2}\text{s}^{-1}\text{sr}^{-1}$ [Ageron, 1989].

Table 4.4-2: Time average leakage currents from a coupled liquid H₂ moderator [Bauer, 1995b]

Target	²³⁸ U	²³⁸ U	²³⁸ U	Pb
Reflector	D ₂ O	Graphite	Pb	D ₂ O
Storage time τ	0.71 ms	0.35 ms	0.23 ms	---
pre-moderator	---	2 cm H ₂ O	2 cm H ₂ O	---
$d^2j/d\Omega dP [\text{cm}^{-2}\text{s}^{-1}\text{sr}^{-1}\text{MW}^{-1}]$	0.53×10^{13}	0.43×10^{13}	0.34×10^{13}	0.23×10^{13}

For comparison, ILL horizontal cold source, liquid D₂ [2.4-8]: $dj/d\Omega = 3.7 \times 10^{13} \text{ cm}^{-2}\text{s}^{-1}\text{sr}^{-1}$, calculated value (Section 4.5) for idealized geometry (one wall, no gaps) $2.1 \times 10^{13} \text{ cm}^{-2}\text{s}^{-1}\text{sr}^{-1}$

In other words, the time average cold neutron current for 5 MW of spallation beam power corresponds to about 1/3 of the neutron current from the horizontal cold source at the ILL reactor with the proviso that the geometry was not optimised in the spallation experiments and that an improvement potential of a factor 1.5 is almost certain. Note, that the calculations reported in Section 4.5 yield an average value of $2.1 \times 10^{13} \text{ cm}^{-2}\text{s}^{-1}\text{sr}^{-1}$ for a rather idealized geometry, in which more structural material and gaps have yet to be introduced to account for the engineering needs discussed above.

With the storage times from Table 4.4-2 we obtain the following ratios of peak to average currents, which is approximately equal to t_{rep}/τ for the SPTS case and $(t_{rep}/t_p) \cdot [1 - \exp(-t_p/\tau)]$ for the LPTS case.

storage time τ [μ s]:	710	350	230
SPTS (50 Hz):	28	57	87
LPTS (16 2/3 Hz, $t_p = 2$ ms):	28	30	30

4.4.6 Options and Alternatives

The layout and performance estimates given in the present reference document are based exclusively on known technologies and proven concepts in moderator design. As mentioned before, there are a number of new ideas that came up recently and which are presently being checked with respect to the performance improvements they might result in for ESS. In the following we give a brief overview of the most important ones and of the consequences their implementation might eventually have on the design of the target system.

4.4.6.1 Moderator Configuration

The essence of the recent proposals to improve beam extraction efficiency is to use horizontally more extended moderators and allow converging neutron guides and a funnelling technique for a cold and a thermal spectrum from two adjacent moderators to be employed, taking advantage of the large openings in the beam shutters that are now provided (cf. Section 4.2). This could eventually lead to the following configuration:

The 5 MW Short-Pulse-Target-Station (SPTS) would house two twin-type moderators, one each above and below the target at the position of maximum fast neutron leakage. On one side there will be a back-to-back pair of a thick thermal and thin cold moderator with a decoupling layer in between. When viewed from one side this will yield a thermal spectrum, while looking on the other side is expected to result in a narrow pulse cold spectrum. On the other side of the target there will be placed in closest lateral proximity a side-by-side pair of thermal and cold moderators, such that both moderators will feed into single neutron beam lines via a neutron guide funnel. The side-by-side moderator pair will enable so-called multi-(dual-) spectral beam extraction [Mezei, 2002]. In order to be able to provide view also on one of the individual moderators of the side-to-side pair only, appropriate collimators can be inserted into the beam shutter apertures.

The 5 MW LPTS would be equipped with only two moderators as well. A side-by-side thermal and cold moderator pair for multi-spectrum beam extraction will be placed on one side of the target and a single cold moderator on the other side. A schematic representation of this concept is depicted in Figure 4.4-8 for both target stations, showing both moderator levels simultaneously and omitting the target.. As indicated by the straight lines in this figure, which give the reflector boundaries, open sectors of about 60° within the reflector will be provided for up to 6 beam holes to view the respective faces of the different moderators.

So far the effect of the large open moderator faces on the surface brightness has not yet been assessed. In order to make such a concept worth while the average gain in extraction efficiency of useful neutrons will have to outweigh the reduction in brightness and the higher fast neutron background in the beams that will have to be dealt with.

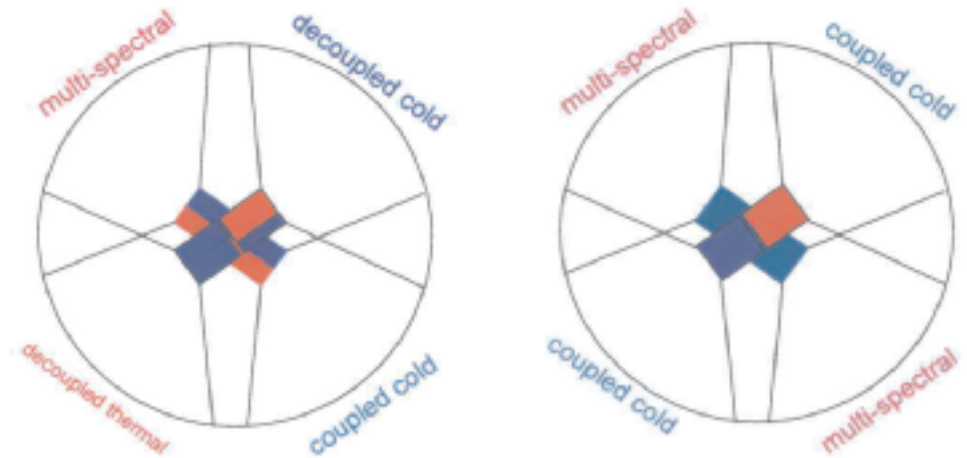


Figure 4.4-8: Schematic plan view of the moderator configurations of the SPTS (left) and LPTS (right). For the sake of simplicity the targets have been omitted and have to be imagined as sitting in between the moderators, which will be located at maximum fast neutron leakage. The circles indicate the inner reflector circumferences and the straight lines the open beam hole sectors. Reflector would be provided at the small faces of the moderators at the respective levels.

4.4.6.2 Advanced Cold Moderators

Liquid – or supercritical – hydrogen is the most convenient cryogenic moderator material to use because

- It is fluid down to 14K and can transport heat by convection
- It has a high scattering cross section
- Collisions with neutrons are very efficient in transferring energy to the “free” atom
- It has reasonable energy transfer properties also at low energies

This is why virtually all cryogenic moderators presently in use at reactors are based on hydrogen or deuterium in elemental form. On the other hand it has been known for a long time that methane is, in principle, a much better moderator, because

- It has a significantly higher hydrogen density than liquid hydrogen,
- It has low-lying modes in the energy region of 1-3meV (5-15K), which the neutrons can excite, if not already thermally occupied.

Unfortunately the use of solid methane as cryogenic moderator is not straight-forward, because

- It has a low thermal conductivity at low temperatures,
- The molecules are destroyed by radiation, which leads to accumulation and eventual spontaneous release of hydrogen in a catastrophic manner and to the formation of waxy residues that tend to stick to the container walls and pipe work.

If a moderator system could be developed which would circumvent these difficulties, substantial gains would be expected in particular at very low energies, as can be deduced from Figure 4.4-9, which shows measured neutron spectra for different materials at temperatures around 20K. Figure 4.4-9 also suggests that water ice at 20 K is a very favourable moderator for neutron energies between 5 and 100 meV, much of which is still in the slowing down regime. Naturally this means that one would expect narrow pulses.

The energy regimes in which methane and water ice give high intensities can be correlated to their respective frequency spectra, or density of states. It turns out that methane hydrate, i.e, ice with methane molecules trapped in cages of the crystal lattice, combines the high density of states of ice above 50 meV with the high density of states of methane below 30 meV (Figure 4.4-10). It may, therefore, be speculated that methane hydrate would make the ideal cryogenic moderator, if a system can be devised that allows heat removal on the one hand and periodic annealing to remove radiation damage on the other.

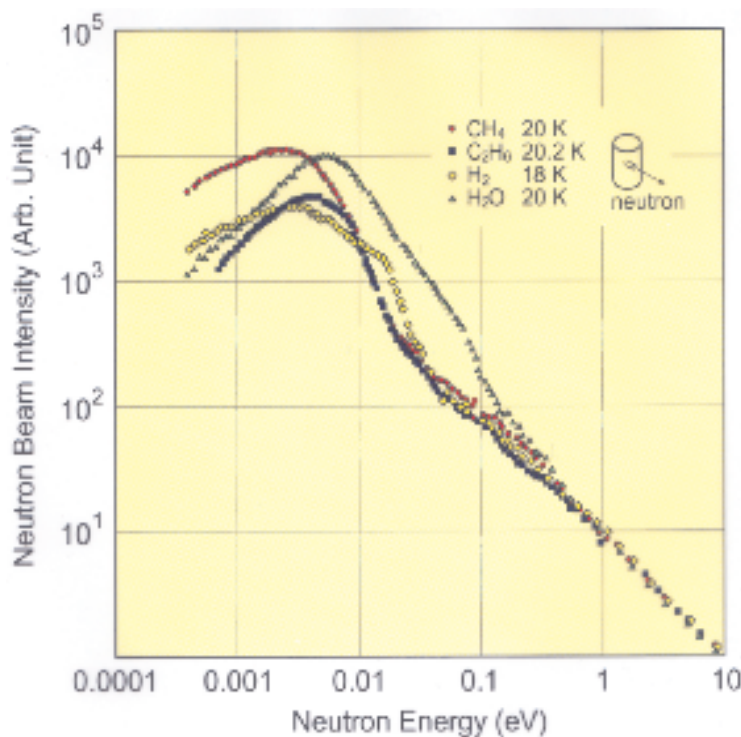


Figure 4.4-9: Measured neutron spectra from different materials at temperatures around 20 K for the same geometry [Inoue, 1979]

In view of this promising perspective efforts are being spent within the ESS Project [Bauer, 1998b] to (a) verify these predictions and (b) develop a system that uses small spherical pellets of either one of the three materials that would be continuously transported through the moderator vessel and would be cooled either by supercritical hydrogen or by liquid helium. For the time being the only promising transport system that would work continuously is based on horizontal transport by mechanical means. This would imply that the moderator-reflector configuration as outlined above would have to be modified in order to accommodate such a system. These efforts met with the strong support of the ESS-TAC at its first meeting and have, as a consequence, been intensified within the available resources.

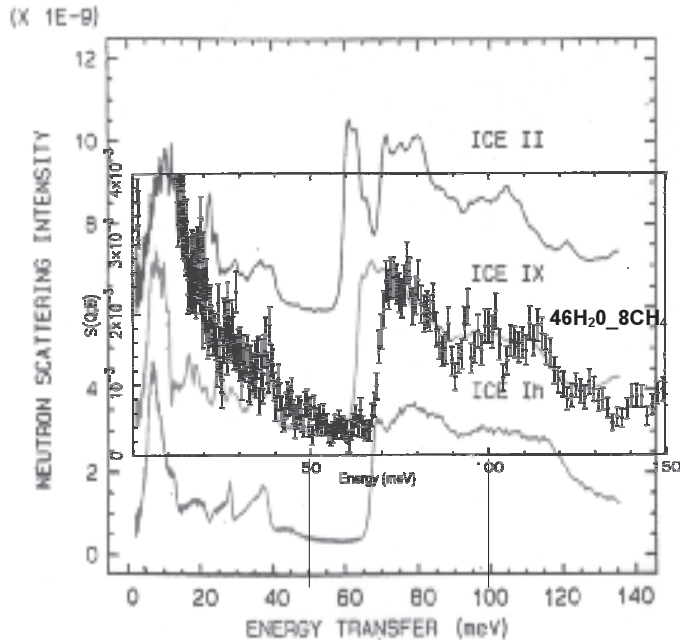


Figure 4.4-10: Frequency spectra from three different modifications of ice (II – blue, IX – red and Ih - green), [Li, 1991], compared to the frequency spectrum of methane hydrate ($46\text{H}_2\text{O}_8\text{CH}_4$) [Trouw, 2002]

4.4.6.3 Systems integration of advanced moderators

According to the concept depicted in Figure 4.4-2, the moderators are embedded in a common reflector-moderator module, which in turn is suspended from a big vertical shielding plug. This design is most likely to prevent a later implementation of an advanced moderator concept based on a bed of small pellets of either solid methane, methane hydrate or water ice. So far, no system for continuous vertical transport of the pellets has been proposed. Up to now only horizontally operating devices have been tested with poly-ethylene pellets at room temperature. In order to enable the change from a conventional cold source to a pelletized one, a combination of a horizontal with a vertical plug is strongly suggested. In order to enable at a later stage of development a change from conventional cold moderators to advanced ones, a horizontal access to the moderator-reflector module will be provided as shown schematically in Figure 4.4-11.

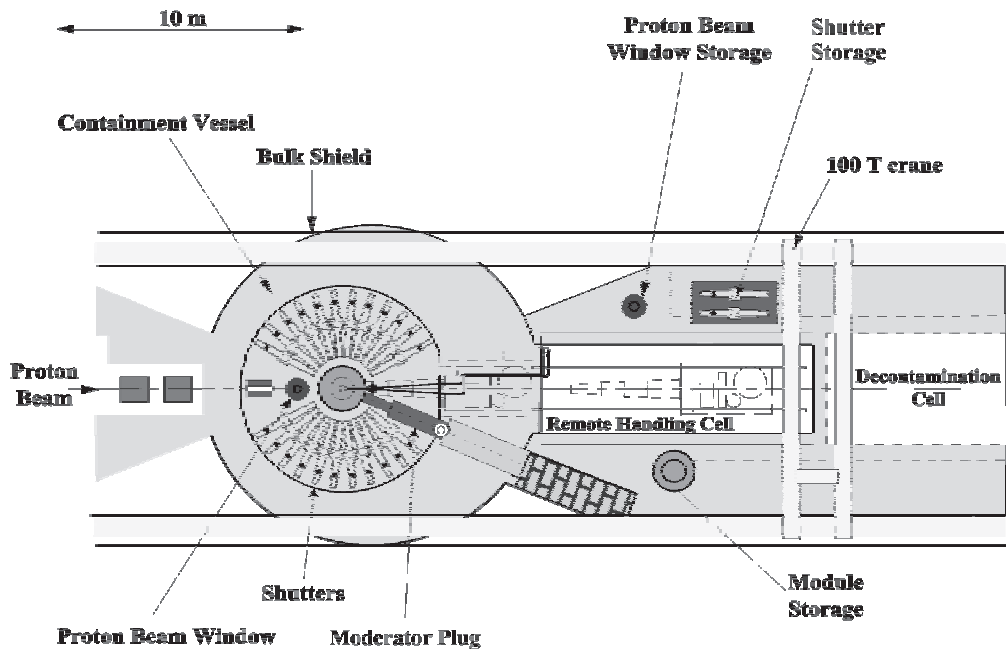


Figure 4.4-11: Plan view of the overall target station layout with a horizontal moderator plug for an advanced cold moderator system.

Such an arrangement, but with a conventional liquid deuterium cold source has already been realized at the Swiss spallation source SINQ [Spitzer, 1997]. An important additional advantage of this solution is that sensitive parts of the installation like the heat exchanger can be safely incorporated in the vertical plug located just outside the inner liner as indicated in Figure 4.4-3.

4.5 NEUTRON PERFORMANCE OF THE SHORT PULSE - AND LONG PULSE TARGET STATIONS

4.5.1 Introduction

Assessing the neutron performance of the ESS target stations is an important task for a variety of reasons:

- The users need orientation with respect to neutron currents, time structure and spectral properties of various moderator options in order to optimise their instrument designs and judge on the feasibility of new and demanding types of experiments.
- Target systems engineering requires input on moderator size, conceptual layout (cryogenic, premoderated etc.), in order to examine technical feasibility and optimise the design.
- Other, more general questions, such as heat deposition, radiation levels energy spectra of the radiation to be shielded effect the whole design of the system.

It is obvious that there exists a close interaction between neutron performance results, new moderator conceptual ideas and the layout of the whole target system including the target as well as the reflector system and also the number of extracted beams and the design of the shutters. ESS went through a first round of such interactions in the phase preceding the publication of the 1997 project study. The moderator-reflector concept presented in this study was the result of several iterations and parameter studies and allowed to predict neutron performance with a certain degree of precision. At that time only short pulse target stations were under consideration and the emphasis was on the performance of a room temperature coupled H₂O moderator in order to provide an indication of the highest thermal neutron flux one could expect for a 5 MW short pulse source.

Input from the users based on detailed instrument considerations first came in 2000, when they proposed to replace the 1 MW short pulse target station by a 5 MW long pulse target station, which is part of the present concept. Nevertheless it took more than another year of intense study and conceptual work on instrument design before a concrete proposal became available, based on neutron performance data that had been generated in the mean time.

The results presented in this chapter refer to the neutron performance of the short pulse target station (SPTS) as described in "The ESS Feasibility Study" Vol. III (1996) [1] and represent more detailed work, which was also extended to the long pulsed target station (LPTS), but retaining, for lack of new information, the SPTS geometry. Further details on results are given in references [Richter, 2001; Seggau, 2001a; Seggau, 2001b]. The goal was to reach highest possible neutron beam intensities for an incident proton beam of 1.334 GeV and average current of 3.75 mA or 2.34×10^{16} protons per second on each target. In extending the work presented in ref [Bauer, 1996a], all values are now calculated for perturbed systems including beam holes and openings. In Table 4.5-1 the main proton beam parameters used for the new calculations are given.

Table 4.5-1: Proton Beam Parameters

Beam Parameter	SPTS	LPTS
beam energy	1.334 GeV	1.334 GeV
beam profile	elliptic footprint with Gaussian distribution, truncated at $x = \pm 10 \text{ cm} = 3\sigma$; $y = \pm 3 \text{ cm} = 3\sigma$	elliptic footprint with Gaussian distribution, truncated at $x = \pm 10 \text{ cm} = 3\sigma$; $y = \pm 3 \text{ cm} = 3\sigma$
average current	$3.75 \text{ mA} = 2.34 \times 10^{16} \text{ p/s}$	$3.75 \text{ mA} = 2.34 \times 10^{16} \text{ p/s}$
protons per pulse	$4.684 \times 10^{14} \text{ ppp}$	$1.404 \times 10^{15} \text{ ppp}$
pulse length/frequency	$1.4 \mu\text{s}/50 \text{ Hz}$	$2.0 \text{ ms}/16.667 \text{ Hz}$

A detailed description of Monte Carlo simulation methods can be found in [Bauer, 1996a]. The calculations here were done using the MCNPX code system [Hughes, 1999] and the revised McFarlane cold hydrogen scattering data based on evaluations by IKE-Stuttgart.

4.5.2 The Short Pulse Target Station (SPTS)

The following moderator configurations were investigated for the SPTS:

- Coupled and decoupled-poisoned ambient temperature water moderator
- Coupled cold (20 K) -, decoupled cold -, and decoupled-poisoned cold liquid hydrogen moderator

The basic geometry concept is as described in the ESS Feasibility study (Vol. III) [Bauer. 1996a]. A moderator size of $5 \times 15 \times 12 \text{ cm}^3$ (thickness times width times height) was assumed for all moderators of SPTS. The distance between the surface of the moderator and the target surface is 7.0 cm. In each simulation the bottom upstream moderator position is considered. The midpoint position of the moderators is 10 cm downstream from the mercury - window interface. H_2O -moderators are placed at the three other moderator positions. The reflector is a cylinder with a height of 180 cm and a diameter of 180 cm. A lead reflector is used with 15 Vol-% of D_2O for cooling. Figure 4.5-1 shows a cut through the moderator plane of the 3-D geometry for the Monte Carlo simulations. In Figure 4.5-2 the geometry of the para $\text{H}_2 / \text{H}_2\text{O}$ moderator is shown. Here the possibility exists to simulate an extended pre-moderator, a Cd-layer for decoupling and a Gd-layer for poisoning.

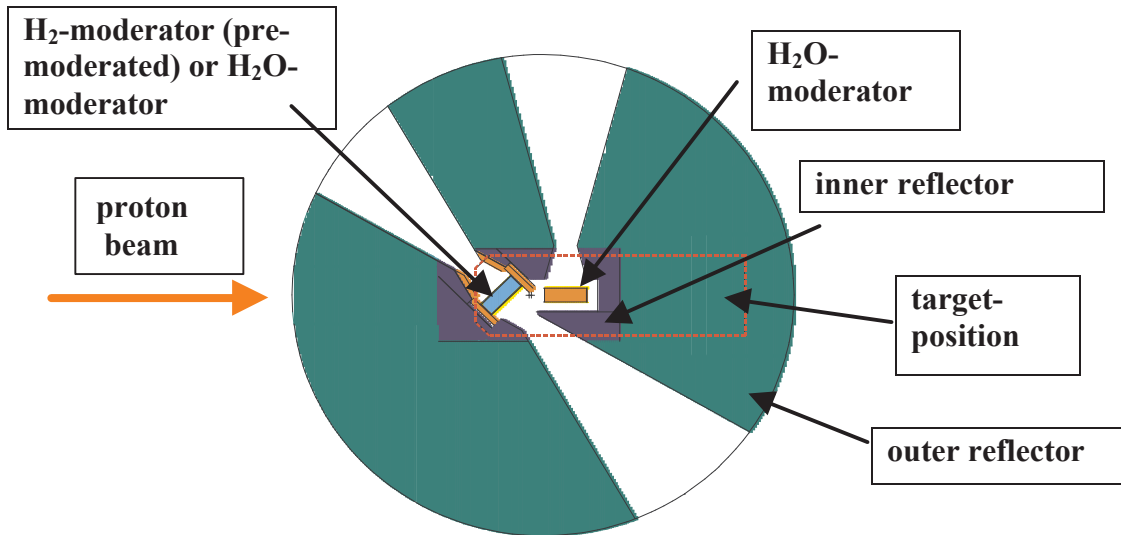


Figure 4.5-1: Cut through the H_2 moderator plane of the SPTS geometry

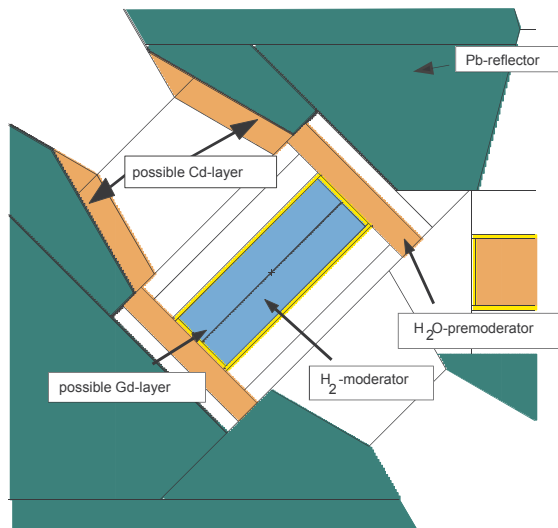


Figure 4.5-2: Geometry of the H_2 (or H_2O) moderator with the possibilities of simulating extended premoderator, Cd decoupler and Gd poisoning

The thermal current densities ($E \leq 0.383$ eV) at the moderator surface were evaluated for a solid angle of 4 degree opening in the direction to the experiments.

4.5.2.1 Cold Hydrogen Moderator (20K)

In all simulations pure para-hydrogen was used as moderator material. An extended H_2O pre-moderator was used, as shown in Figure 4.5-2. The thickness of the water pre-moderator is 2 cm. The length of the extension of the pre-moderator is about 12 cm. The numerical values for the beam current in the direction of the moderators, evaluated over an angular range with 4° opening angle are summarized in Table 4.5-2.

Table 4.5-2a: Peak neutron current density [$n/cm^2/s/sr/\text{\AA}$] of a para H_2 -moderator with extended H_2O pre-moderator for a solid angle of 4 degree opening

$\lambda [\text{\AA}]$	coupled [10¹²]	decoupled [10¹²]	decoupled/poisoned [10¹²]
0.5	19000	19000	18000
1.0	2900	2500	2300
2.0	1600	1200	940
2.5	1300	820	640
2.7	1200	710	480
3.2	820	510	340
3.6	440	230	170
4.0	370	200	140
4.6	280	160	110
5.6	99	51	36
8.3	6.8	3.1	1.7

Table 4.5-2b: Average neutron current density [$n/cm^2/s/sr/\text{\AA}$] of para H_2 -moderator with extended H_2O pre-moderator for a solid angle of 4 degree opening.

$\lambda [\text{\AA}]$	coupled [10¹²]	decoupled [10¹²]	decoupled/poisoned [10¹²]
0.5	7.0	5.8	5.5
1.0	3.5	1.4	1.2
2.0	7.0	1.6	1.0
2.5	7.4	1.6	0.89
2.7	8.3	1.6	0.84
3.2	6.3	1.3	0.66
3.6	3.7	0.72	0.37
4.0	3.3	0.65	0.33
4.6	2.6	0.58	0.29
5.6	1.1	0.23	0.11
8.3	0.1	0.021	0.01

Figure 4.5-3a shows the time distributions of the neutron current densities for different wavelengths (4, 4.6, 5.6, 8.3 Å) for a coupled, a decoupled and a decoupled-poisoned hydrogen moderator. In Figure 4.5b the pulse widths (FWHM) as a function of the wavelength are plotted for each cold hydrogen moderator configuration.

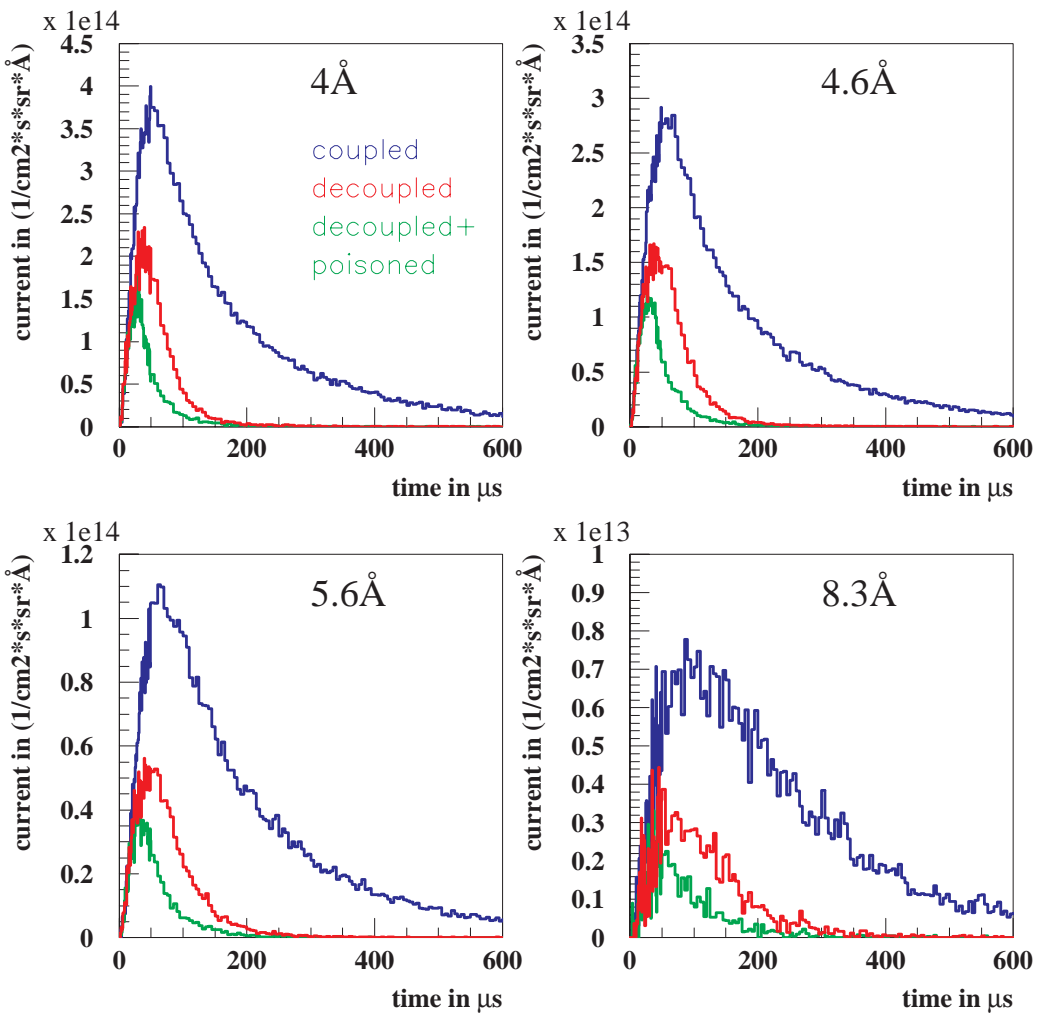


Figure 4.5-3a: Time distributions of neutron current densities as a function of wavelength for the three different hydrogen moderator configurations

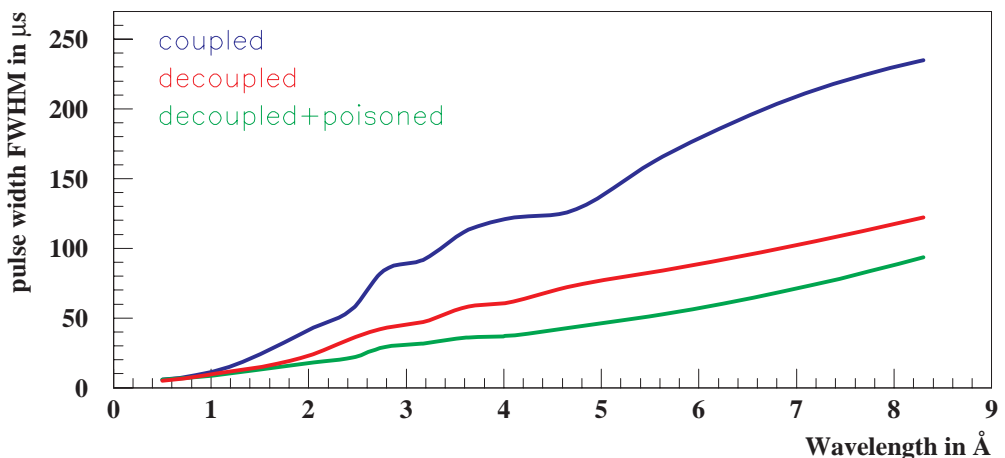


Figure 4.5-3b: Neutron pulse widths (FWHM) as a function of wave length for the three different hydrogen moderator configurations

Decoupling with a 1 mm Cd layer (cf. Figure 4.5-2) causes a decrease of both, pulse widths and peak intensities. An even smaller pulse width can be achieved by poisoning the

decoupled hydrogen moderator with a 0.5 mm thick Gd-layer. In Figure 4.5-4 the peak neutron current densities as a function of wavelength are given for these three cases. An estimate of poison burn-up is given in section 4.5.2.3.

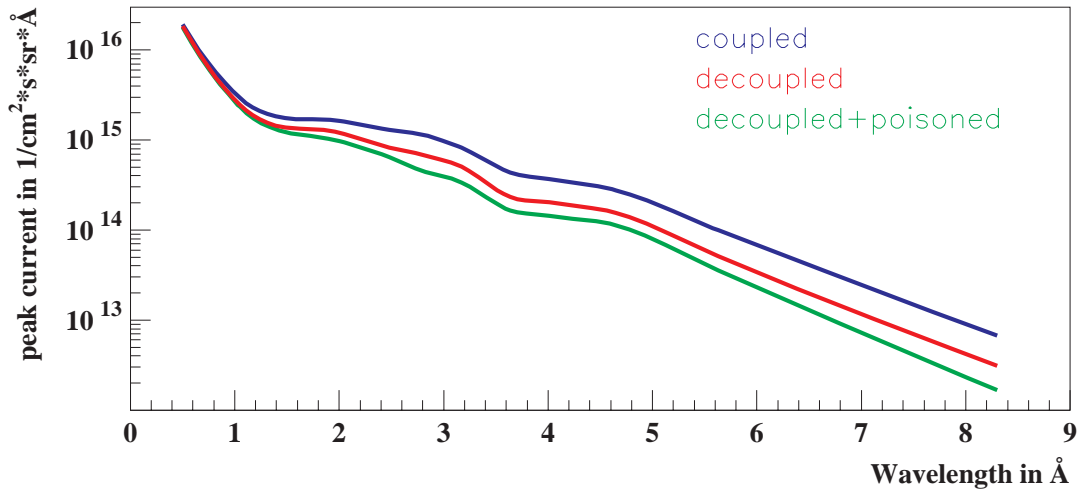


Figure 4.5-4: Peak neutron current densities as a function of wavelength for the three different hydrogen moderator configurations

4.5.2.2 Ambient Temperature Water Moderator (300K)

The geometry of the H₂O moderator is identical to that of the H₂ moderator but without pre-moderator. The pre-moderator volume in the neutron flight path is filled with reflector material. Figure 4.5-5a shows the time distributions of the neutron current densities for different wavelengths (0.5, 1, 2, 3.2 Å) for a coupled and a decoupled-poisoned ambient temperature water moderator. The pulse widths and the neutron current densities as a function of wavelength are given in Figures 4.5-5b and 4.5-6.

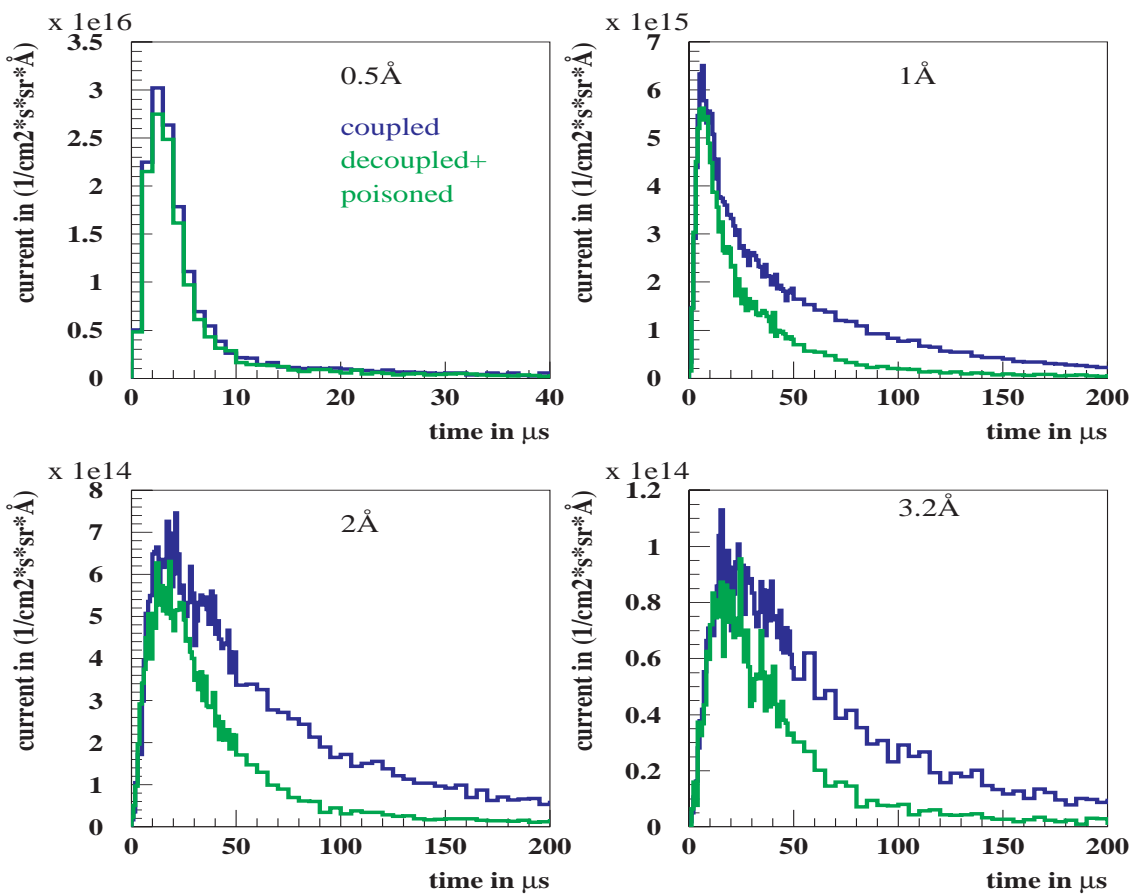


Figure 4.5-5 a: Time distributions of neutron current densities as a function of wavelength for the two different ambient temperature water moderator configurations

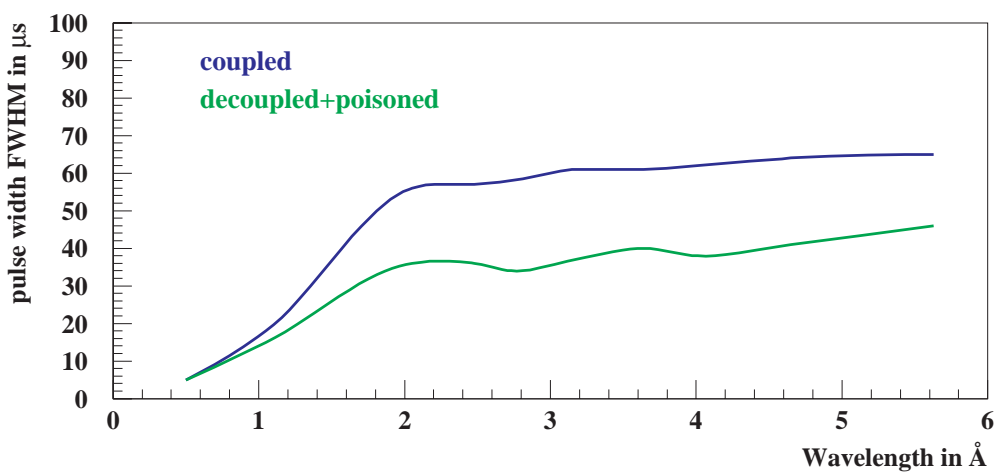


Figure 4.5-5b: Neutron pulse widths (FWHM) as a function of wave length for two different ambient temperature water moderator configurations

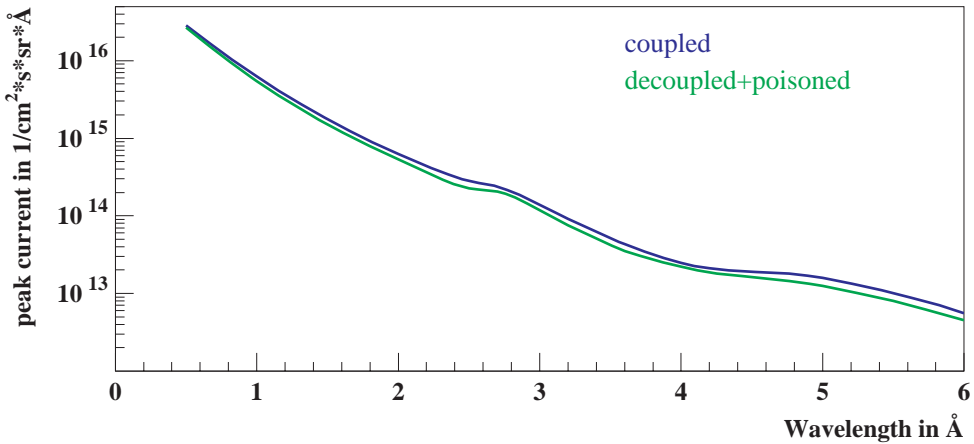


Figure 4.5-6: Peak neutron current densities as a function of wavelength for the two different ambient water moderator configurations

The corresponding numerical values are summarized in Table 4.5-4. When comparing Figures 4.5-3b and 4.5-4 with 4.5-5b and 4.5-6 the differences in peak current and pulse width for the coupled and decoupled-poisoned H₂O moderators are less pronounced than those for the premoderated H₂ moderators. This is partly due to the hard neutron spectrum of the lead reflector in case of the H₂O moderator not allowing for an effective decoupling. On the other hand for the H₂ moderator the H₂O premoderator shifts the spectrum in such way that decoupling is more effective. Secondly the neutron spectrum detected is a superposition of the directly viewed one and the one seen through the poisoning layer (indirect neutrons). The direct neutrons essentially form the peak intensity while the pulse width is governed by the broadening contribution of the indirect neutrons.

Table 4.5-4: Peak and average neutron current densities [$n/cm^2/s/sr/\text{\AA}$] and neutron pulse widths in μs of an ambient temperature H₂O moderator for a solid angle of 4 degree opening.

Wavelength	0.5 Å		1 Å		2 Å		3.2 Å	
	coupled	Decoupled poisoned	coupled	decoupled poisoned	coupled	decoupled poisoned	coupled	decoupled poisoned
peak neutron current density	$2.9 \cdot 10^{16}$	$2.7 \cdot 10^{16}$	$6.3 \cdot 10^{15}$	$5.4 \cdot 10^{15}$	$6.3 \cdot 10^{14}$	$5.4 \cdot 10^{14}$	$9.2 \cdot 10^{13}$	$7.5 \cdot 10^{13}$
average neutron current density	$8.7 \cdot 10^{12}$	$7.6 \cdot 10^{12}$	$1.5 \cdot 10^{13}$	$7.6 \cdot 10^{12}$	$2.8 \cdot 10^{12}$	$1.3 \cdot 10^{12}$	$4.2 \cdot 10^{11}$	$2.1 \cdot 10^{11}$
pulse width FWHM	5	5	18	15	56	36	61	37

4.5.2.3 Moderator Poison Burn-up

The ISIS gadolinium poison plate with a thickness about 40 µm for the cold moderator would burn up in ESS in about three days. Therefore it is important to investigate this problem. For a first estimation a 540 µm thick Gd plate inside the H₂ moderator was assumed. Monte Carlo calculations using such a configuration yield an average thermal neutron flux density at the surface of the poison of $\phi_{th} = 5 \times 10^{13}$ [n/cm²s]. The neutron absorbing isotopes in a

gadolinium plate are Gd-155/Gd-157 with 4.6×10^{20} atoms per cm². Assuming that all neutrons are absorbed in one of these isotopes, the lifetime – accounting also for breeding of Gd-155/Gd-157 of about 3.5% - is about 106 days.

4.5.2.4 "Hot" Neutrons

Neutrons with energies above the thermal spectrum (>100 meV) are produced in very narrow pulses during the slowing down of the primary spectrum from the target. Because the scattering cross section of hydrogen (and most other materials) is fairly constant in the energy range above 1 eV, the time between two collisions, and hence the probability of a neutron to leak from the moderator is inversely proportional to the neutron velocity. This leads to very narrow pulses, which, when used in time of flight, give a constant resolution over the whole slowing down regime. Of course, due to the rapid slowing-down in hydrogenous materials as used in moderators, the total number of slowing-down neutrons in a spallation source is fairly low, although their instantaneous intensity is extremely high.

Recently interest has been expressed by some user groups to use epithermal and hot neutrons in a mode, which requires high time average flux. It can be speculated that the average flux of these neutrons would be increased (by roughly an order of magnitude), if a lead "moderator" would be viewed, rather than a hydrogenous one, because it takes approximately 1500 collisions in lead to slow a neutron down from 2MeV to 1eV, as compared to 15 in water. First Monte Carlo studies investigating a lead reflector demonstrate the importance of large resonances above 1 eV leading to absorption of higher energetic neutrons [Goldenbaum, 2002]. Consequently the abundance of the neutrons in the requested energy range of about 100 meV might be smaller than expected. However, detailed studies including the exact geometry and material composition are necessary. It is an open question if a spallation neutron source can compete with a re-thermalising hot source (graphite at 2400K) on a high flux reactor in terms of hot neutron intensities.

4.5.3 The Long Pulse Target Station (LPTS)

The reference geometry design used for the long pulse target moderator reflector concept is simplified with respect to the one used for the SPTS. It contains only two moderators: a para H₂ (20K) with H₂O extended pre-moderator and an ambient temperature H₂O moderator in wing geometry. A moderator size of 5x15x12 cm³ (thickness times width times height) was used as a standard. The centre of the moderator is located 10 cm downstream from the target window. For some calculations a 10 cm thick para hydrogen moderator was used. The thickness of the pre-moderator is 2.5 cm and the length of the extension was 2.5 cm and 7.5 cm. The distance between the surface of the moderator and the target surface is 7.0 cm. The reflector is again a cylinder with a height of 180 cm and a diameter of 180 cm filled with Pb plus 15 Vol. % D₂O for cooling. For comparison calculations were also done using a Be or a C reflector. The target is identical to the one of the SPTS. In Figures 4.5-8 and 4.5-9 the geometries of the H₂ and H₂O moderators with possible extended pre-moderator are shown.

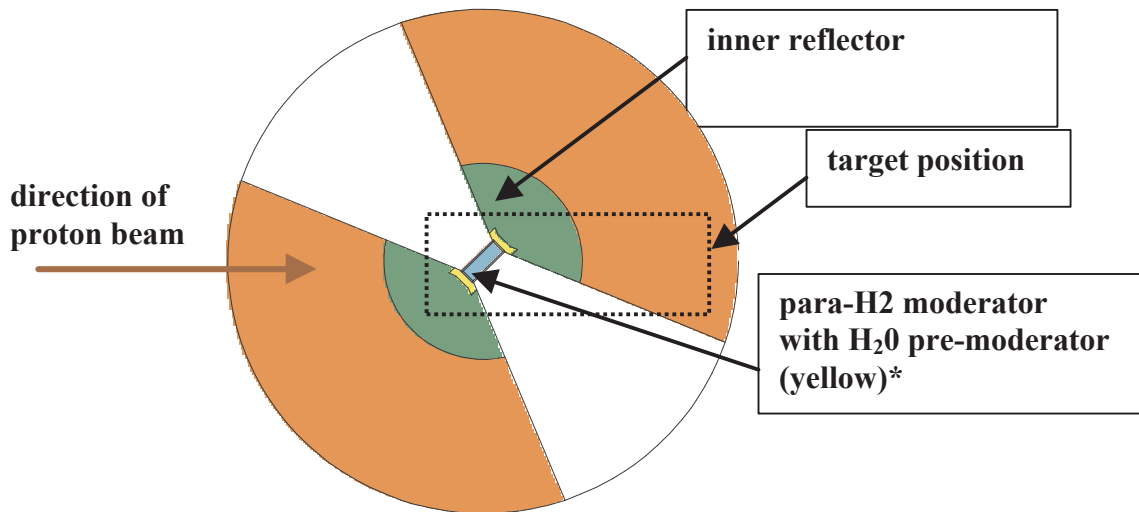


Figure 4.5-8: Cut through the H_2 moderator plane of the LPTS geometry

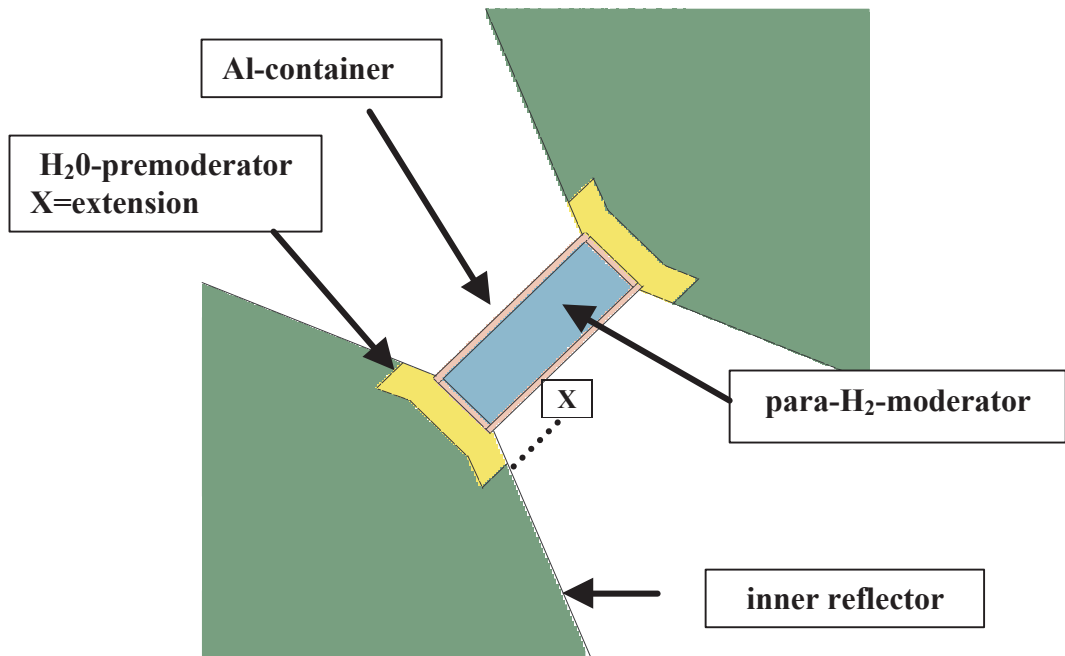


Figure 4.5-9: Geometry of para- H_2 (or H_2O) moderator with pre-moderator

The figures 4.5-8 and 4.5-9 show the geometry for the H_2 moderator. For the H_2O -moderator the yellow part is filled with reflector material. Note that for the H_2 moderator some more structural material will have to be introduced, once the final design has been agreed upon.

Figure 4.5-10 shows the average neutron current densities for different wavelengths for the cold hydrogen moderator for a moderator thickness of 5 and 10cm and two different extensions of the water pre-moderator (2.5 and 7.5cm) for a solid angle of 4 degree opening, as before. A D_2O cooled lead reflector was used.

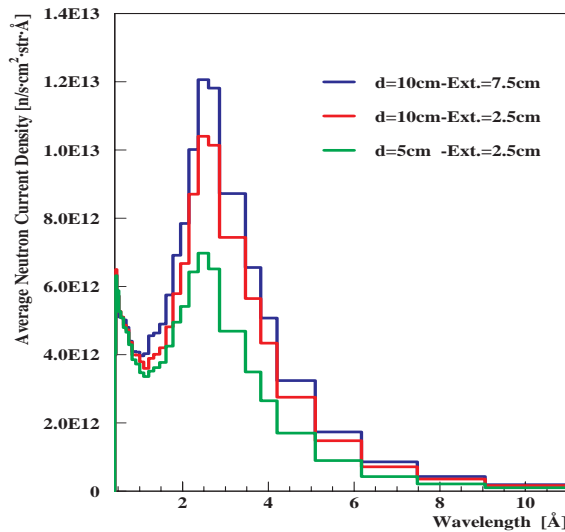


Figure 4.5-10: Average neutron current densities for the cold hydrogen moderator as a function of wavelength for different moderator thickness and extensions of the pre-moderator for a solid angle of 4 degree.

Numerical values of the wavelength dependent peak and average neutron current densities for the cold hydrogen and the ambient temperature water moderator are summarized in Table 4.5-5. For the cold hydrogen moderator the results are given for a moderator thickness of 5cm and 10cm and extensions of the pre-moderator of 2.5cm and 7.5cm respectively. All results are calculated for a solid angle of 4 degree.

Table 4.5-5: Peak and average neutron current densities [$n/cm^2/s/sr/\text{\AA}$] of a cold hydrogen moderator with extended water pre-moderator and of ambient temperature H_2O moderator for a solid angle of 4 degree.

Cold Hydrogen Moderator						
d=5cm, Ext. 2.5cm	0.5 Å	1 Å	2 Å	4 Å	5.6 Å	10 Å
Peak Current	$1.76 \cdot 10^{14}$	$1.03 \cdot 10^{14}$	$1.64 \cdot 10^{14}$	$7.94 \cdot 10^{13}$	$2.65 \cdot 10^{13}$	$3.16 \cdot 10^{12}$
Average Current	$5.97 \cdot 10^{12}$	$3.47 \cdot 10^{12}$	$5.39 \cdot 10^{12}$	$2.70 \cdot 10^{12}$	$9.05 \cdot 10^{11}$	$1.05 \cdot 10^{11}$
d=10cm, Ext. 7.5cm	0.5 Å	1 Å	2 Å	4 Å	5.6 Å	10 Å
Peak Current	$1.72 \cdot 10^{14}$	$1.19 \cdot 10^{14}$	$2.35 \cdot 10^{14}$	$1.52 \cdot 10^{14}$	$5.24 \cdot 10^{13}$	$5.96 \cdot 10^{12}$
Average Current	$5.72 \cdot 10^{12}$	$3.98 \cdot 10^{12}$	$7.86 \cdot 10^{12}$	$5.08 \cdot 10^{12}$	$1.74 \cdot 10^{12}$	$2.00 \cdot 10^{11}$
Ambient Temperature Water Moderator						
d=5cm	0.5 Å	1 Å	2 Å	4 Å	-	-
Peak Current	$2.43 \cdot 10^{14}$	$4.214 \cdot 10^{14}$	$8.18 \cdot 10^{13}$	$3.96 \cdot 10^{12}$	-	-
Average Current	$8.10 \cdot 10^{12}$	$1.41 \cdot 10^{13}$	$2.73 \cdot 10^{12}$	$1.32 \cdot 10^{11}$	-	-

In the following we give figures for the intensity integrated over the energy range below 0.413eV, which we designate as “thermal”, although they refer to the spectral distribution of the cold moderator. Figure 4.5-11 shows the “thermal” ($E \leq 0.413\text{eV}$) neutron current density time distributions in [$n/cm^2/s/sr$] for cold-coupled para hydrogen moderators of thickness 5 and 10 cm with pre-moderator extensions 2.5 cm and 7.5 cm for a viewing angle of 4 degree.

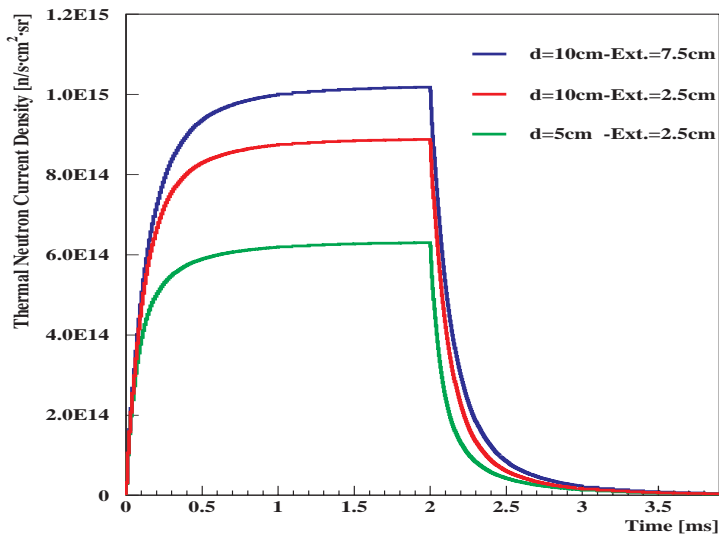


Figure 4.5-11: Time distributions of “thermal” neutron current densities of cold para hydrogen moderator for different moderator thickness and pre-moderator extensions

Table 4.5-6 shows the influence of different reflector materials (Pb, Be, and C) on the time distributions of the “thermal” neutron current densities and their decay behaviour after the 2ms proton pulse.

Table 4.5-6: Results of “thermal” neutron ($E \leq 0.413\text{eV}$) peak current densities [$\text{n/cm}^2/\text{s/sr}$] of the cold hydrogen moderator for different reflector materials for a solid angle of 4 degree.

Reflector Material	Peak Neutron Current Density	Intensity after pulse train $\leq 300\text{\mu s}$		Intensity after pulse train $\leq 1\text{ms}$	
85%Pb, 15% D20 d=10cm, Ext. =7.5cm	$1.1 \cdot 10^{15}$	$1.8 \cdot 10^{14}$	18%	$2.0 \cdot 10^{13}$	2%
100% Be d=10cm, Ext. =7.5cm	$8.1 \cdot 10^{14}$	$3.4 \cdot 10^{14}$	42%	$1.5 \cdot 10^{14}$	18.5 %
85%Pb, 15% D20 d=5cm, Ext. =2.5cm	$6.3 \cdot 10^{14}$	$8.2 \cdot 10^{13}$	13%	$1.2 \cdot 10^{13}$	1.9%
100% Be d=5cm, Ext. =2.5cm	$6.9 \cdot 10^{14}$	$2.7 \cdot 10^{14}$	39%	$1.2 \cdot 10^{14}$	18%
100% C d=5cm, Ext. =2.5cm	$3.9 \cdot 10^{14}$	$1.1 \cdot 10^{14}$	29%	$5.4 \cdot 10^{13}$	14%

The influence of different reflector material compositions on the pulse shapes of “thermal” neutron current densities were also studied. The results plotted in Figure 4.5-12 show the time distributions of “thermal” neutron current densities of cold para hydrogen moderators as a function of different reflector materials. The results for the H_2O moderator are very similar.

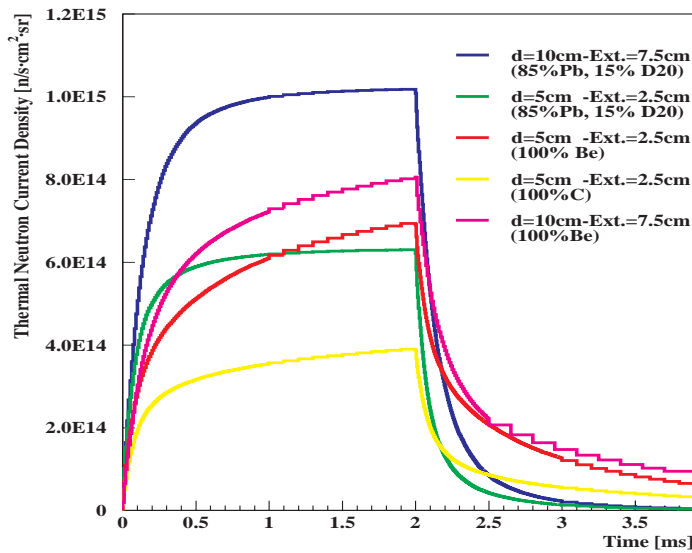


Figure 4.5-12: Time distributions of “thermal” ($E \leq 0.413$ eV) neutron current densities [$n/cm^2/s/sr$] for a cold para-hydrogen moderator for different reflector materials

For the standard configuration ($d=5$ cm, Ext. $x=2.5$ cm) a beryllium reflector gives the maximal intensity and graphite the lowest one. The gain factor of beryllium in respect to a lead reflector is for this case at about 10 %. For the larger dimension ($d = 10$ cm) of the H_2 moderator and the longer extension (ext. = 7.5 cm) a beryllium reflector results in lower peak intensity than lead (about 35 %). With a beryllium reflector the decay constant is larger than for lead. Lead seems to be the best choice for a pre-moderated hydrogen moderator.

4.5.4 Summary and Further Investigations

In Tables 4.5-7 and 4.5-8 a summary of the expected values of integral of the neutron flux densities over the thermal energy range inside the moderators and corresponding neutron leakage current densities are tabulated for different moderators for the SPTS and LPTS. It should be noted that the differences between SPTS and LPTS are due to different pre-moderator settings of the para- H_2 moderator. This results also in minor differences comparing the LPTS values with previously published values [2].

Table 4.5-7: Expected values of “thermal” neutron flux densities inside moderators of SPTS and LPTS moderators for 5 MW proton beam power

moderator type	SPTS		LPTS	
	$\frac{\Lambda}{\phi}$	$\frac{-}{\phi}$	$\frac{\Lambda}{\phi}$	$\frac{-}{\phi}$
	$[n \cdot cm^{-2} \cdot s^{-1}]$		$[n \cdot cm^{-2} \cdot s^{-1}]$	
para H_2 pre-moderated (coupled)	$9.0 \cdot 10^{16}$	$3.2 \cdot 10^{14}$	$7.0 \cdot 10^{15}$	$2.3 \cdot 10^{14}$
ambient water (coupled)	$1.3 \cdot 10^{17}$	$3.1 \cdot 10^{14}$	$9.0 \cdot 10^{15}$	$3.0 \cdot 10^{14}$

Table 4.5-8: Expected values of thermal neutron leakage current densities of SPTS and LPTS moderators for 5 MW proton beam power for a solid angle of 4 degree opening

moderator type	SPTS		LPTS	
	$\frac{\Lambda}{J}$	$\frac{-}{J}$	$\frac{\Lambda}{J}$	$\frac{-}{J}$
	$[\text{n} \cdot \text{cm}^{-2} \cdot \text{s}^{-1} \text{sr}^{-1}]$		$[\text{n} \cdot \text{cm}^{-2} \cdot \text{s}^{-1} \text{sr}^{-1}]$	
para H ₂ pre-moderated (coupled)	$6.8 \cdot 10^{15}$	$2.5 \cdot 10^{13}$	$6.3 \cdot 10^{14}$	$2.1 \cdot 10^{13}$
ambient water (coupled)	$9.8 \cdot 10^{15}$	$1.8 \cdot 10^{13}$	$5.0 \cdot 10^{14}$	$1.7 \cdot 10^{13}$

4.6 BEAM STOPS

Apart from the neutron production targets, which are the only places in the whole ESS facility where the full proton beam power can be accepted, there will be several other locations in which either proton or neutron beams must be stopped in a controlled way in order to avoid undesirable activation of machine components or to allow reduced power operation of the accelerator facilities, mainly for development and machine study work, without making use of the main targets. The general mission of these beam stops is to provide for hazard-free dumping of all waste beams that arise in a controlled manner from the operation and development runs of the accelerator facilities and which cannot be used for scientific purposes,

An overview of the locations of the various beam stops under consideration is shown in Figure 4.6-1.

All beam catchers located in areas which may require personnel access for interventions, service or maintenance of components must be equipped with guillotine type shutters. These must be interlocked with the “ready for operation” and the “access permitted” signals of the overall control system in their open or closed positions respectively.

Connections to the beam lines will be made by inflatable metallic seals of PSI design that can be replaced individually.

Four different types of beam stops are envisaged and presented in the following chapters:

- Linac and ring development beam dumps (chapter 4.6.1)
- Ring (and linac) injection loss catchers (chapter 4.6.2)
- Achromat scraper beam catchers (chapter 4.6.3)
- Neutron beam collimators and catchers at proton injection into the targets (chapter 4.6.4)

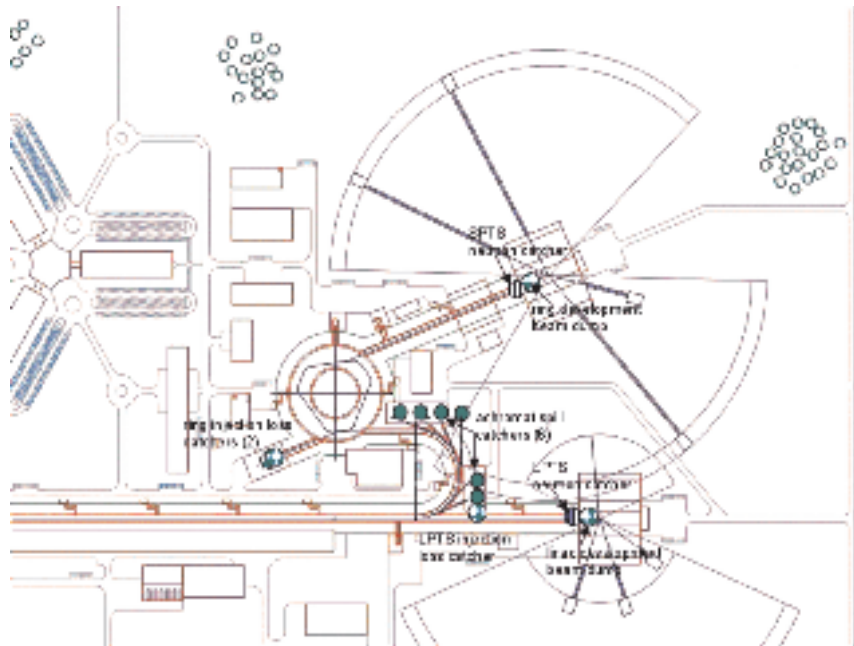


Figure 4.6-1: Types and locations of beam stops in the ESS-facility

4.6.1 Linac and ring development beam dumps

These beam stops will be used to commission and later develop further the linac and compressor rings without directing the beam onto the targets. They will not be in use when there is neutron production for user operation. They must be designed to cope with the scheme of trial runs planned by the linac and ring development teams. This scheme is not yet fully defined. In general, two modes are likely to prevail: (a) operation at full pulse power with reduced pulse frequency and (b) operation at full repetition rate with reduced intensity per pulse. It is postulated that in both modes the average power will be less than 500 kW. The proposed location for these dumps is under the proton beam injection line into the targets at the level of the beam lines before the transition to the above ground level is made as shown in Figure 4.2-2.

So far, no detailed layout studies for these beam dumps have been carried out, but the general design will follow that of the beam dump in use at ‘Paul Scherrer Institut’ (PSI) in Switzerland, which is the result of many years of experience and which, in its present form, has served at a beam power of nearly 1 MW for many years with no problems. Cuts of the PSI beam dump along and perpendicular to the beam are shown in Figures 4.6-2a and 4.6-2b. Photographs are shown in Figures 4.6-2c, 4.6-3a and 4.6-3b.

The design of this beam dump is highly modular with an enclosure tank surrounding four each of inner and outer water-cooled inserts. There is a tapered hole formed by water cooled copper plates which allows to distribute the power in such a way that each plate can transport the heat deposited in it to its outer circumference, where it is carried away by the cooling water.

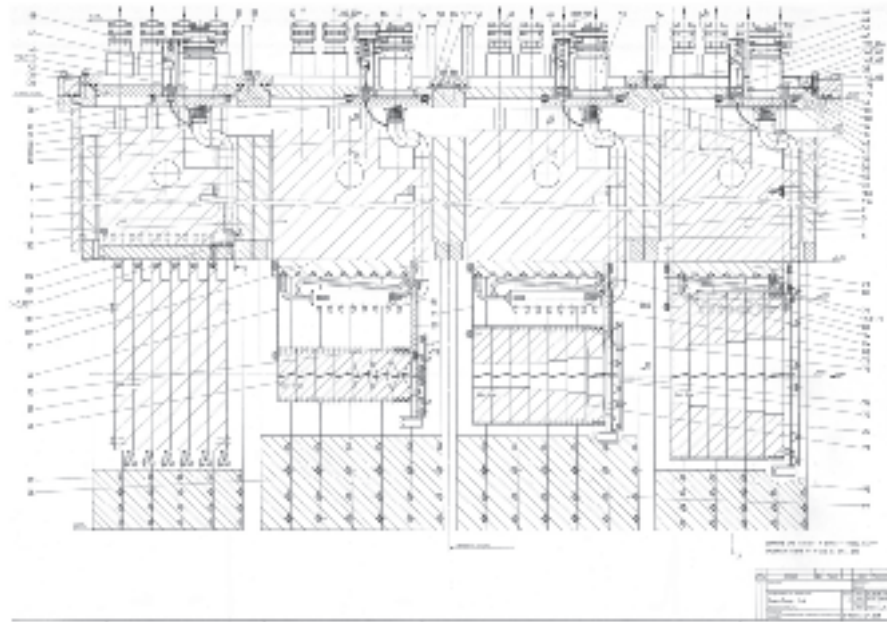


Figure 4.6-2a: Vertical cut through the PSI proton beam dump. The proton beam is incident from the right. The modular design allows replacement of each of the four inner (beam stop) and outer (shielding) water-cooled inserts. (Courtesy PSI)

There are four radial cuts in each disk in order to accommodate the thermal expansion gradient resulting from the temperature gradient.

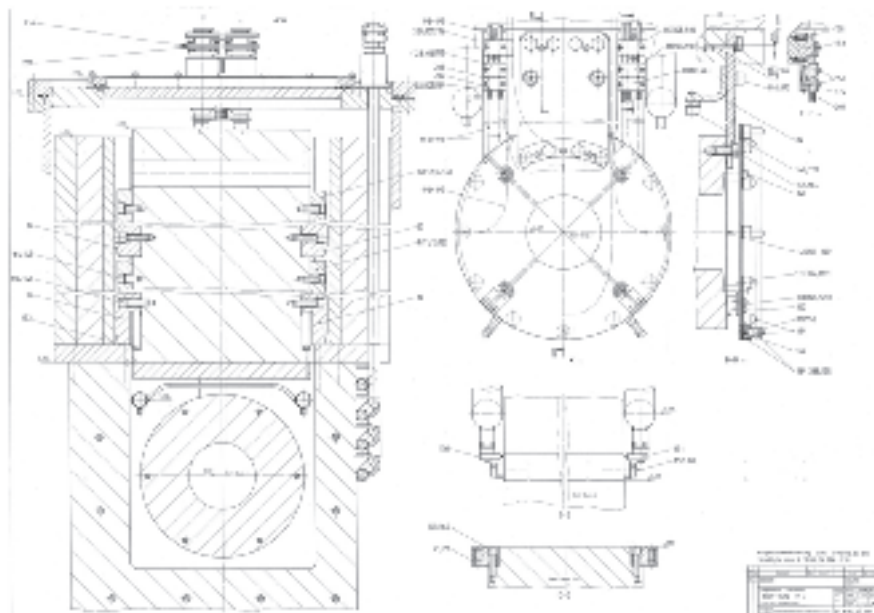


Figure 4.6-2b: Vertical cut perpendicular to the proton beam through the PSI proton beam stop. (Courtesy PSI)

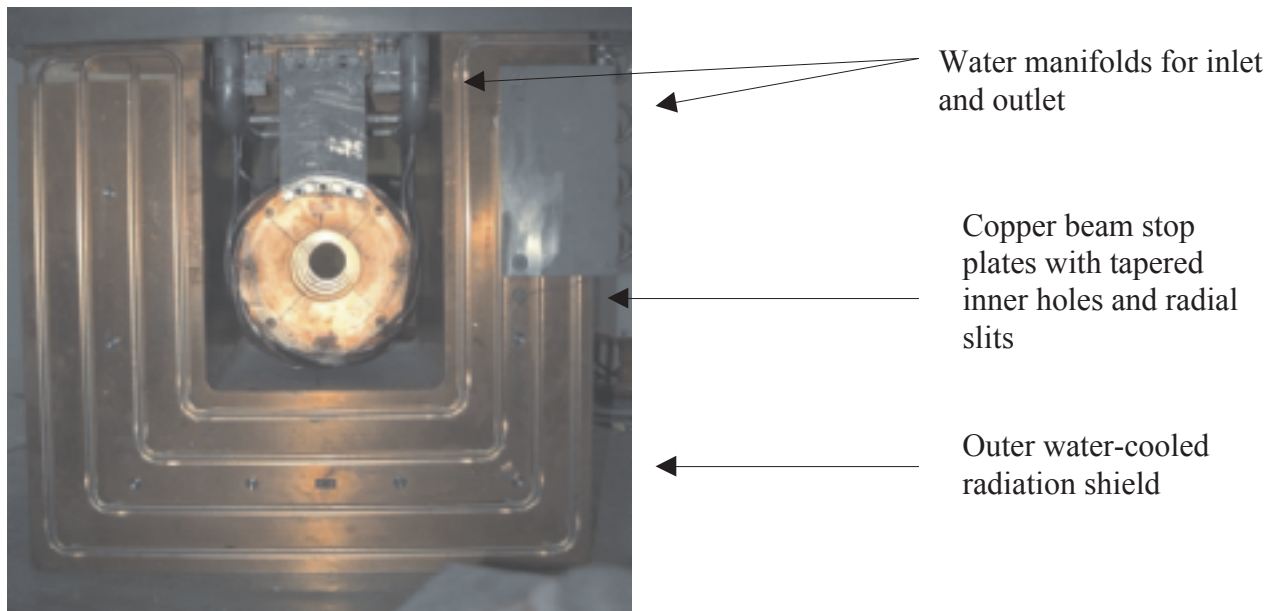


Figure 4.6-2c: Head on photograph of an inner and outer insert of the PSI proton beam dump. The radial slits in the copper plates and the water manifolds for the inner insert are clearly visible. (Courtesy PSI)

Each insert is suspended from a ca. three meters long steel plug (Figure 4.6-3b) and can be removed from its operating position together with this plug by means of a suitably designed transport flask. In this case the connections at the top of the shielding plug (Figure 4.6-3a) can be opened manually. Repair or replacement of the copper parts is possible in a hot cell. There is a sectioned charge monitor in front of the beam catcher to make sure that the beam is steered onto the catcher properly on centre.

Although the cooling water is not directly traversed by the proton beam in this design, it will be a radioactive water loop similar to the cooling water of the magnets in the proton beam transport, possibly even at a somewhat higher level. It is recommended to have a cooling loop for the beam stops, which is independent of the magnet cooling loop(s).

Clearly, the ESS beam stops, while following the same design philosophy as outlined above, cannot be a simple copy of the PSI device. This is obvious from the higher beam energy (1.34 GeV vs. 0.6 GeV at PSI), but also from the fact that high pulse loads must be accommodated. This problem has not yet been studied in detail, because the decision on what exactly these loads would be is still pending and depends on the way in which development runs for the accelerator and rings will be organised.

The three meter long steel plug, from which the beam stops are suspended, is indicative of the shielding requirement around these devices. The main cost for the beam stops will be in their shielding. This is one of the reasons for placing the two most highly rated beam dumps right next to the target blocks.

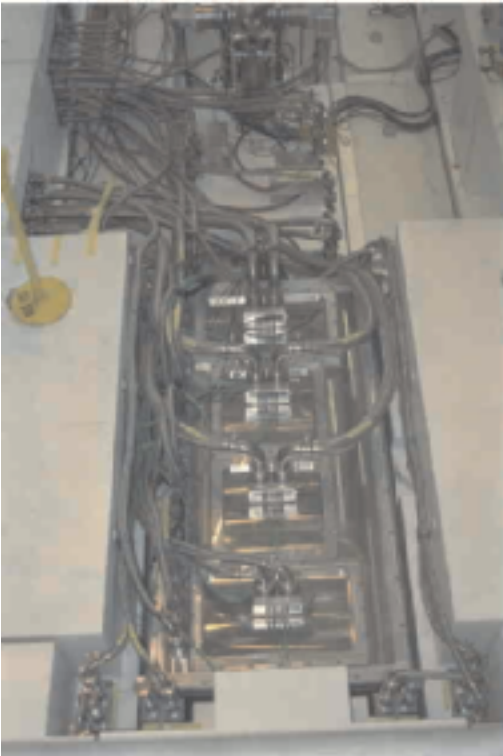


Figure 4.6-3a: Top view of the PSI beam stop with all eight inserts installed.
(Courtesy PSI)



Figure 4.6-3b: The last inner insert of the PSI beam stop with its shielding plug.
(Courtesy PSI)

4.6.2 Ring (and linac) injection loss catchers

Charge exchange from H^- to H^+ at injection into the rings will not be 100% effective. Particles not converted to protons need to be safely collected in beam catchers in order to avoid uncontrolled activation of the ring injection area. There will be one catcher for each of the two rings, located one above the other. The power rating of these catchers has been quoted as 1% of the injected intensity, i.e. ca 25 kW each. While this may in principle allow a somewhat simpler design than the one described above, the power is too high for non-forced cooling. Also the shielding requirements, which are mainly determined by the energy of the protons, will not be too different. It is, therefore, assumed for the time being that these beam dumps will be of a similar design as the ones described above but will have two inner inserts suspended from each plug with their cooling connected in series. This will eventually allow to use the same handling equipment for all actively cooled beam dumps.

Similarly, if H^- will be accelerated for the long pulse target station, they need to be converted into protons for loss free bending in the transition section from the accelerator to the target level (cf. chapter 3.2.3 and 3.3.3) and Figure 4.2-2. Also here a beam catcher is required for the non-stripped fraction of the beam. While it may be possible to use a somewhat thicker stripper foil because it is traversed only once, the non-stripped fraction of the full 5 MW must be dealt with in this case. It is, therefore, assumed for the time being that also this catcher will be actively cooled and will be of the same design as discussed above.

4.6.3 Achromat scraper beam catchers

Preparation of the beam from the linac for clean injection into the ring will be done in a gentle 180° bending section referred to as achromat. Located along this section will be six beam scrapers to remove particles, which are outside the desired phase space volume in all six dimensions. These scraped particles must again be disposed of safely in order to avoid uncontrolled activation of the tunnel. The power rating of each of these beam dumps is ca 5 kW average at a pulse frequency of 50 Hz and a pulse length of 1.2 ms. It will, therefore, be possible to dissipate this heat into the surroundings without active cooling through the large surface of the shielding blocks. Active water-cooling will thus not be provided for these beam stops, but the design will still be such that the most radioactive inner parts can be removed by remote handling if the need arises.

Similar beam dumps have been designed for the SNS-Project (Figure 4.6-4), which are rated at 7.5 kW. The design of the ESS achromat dumps will in all likelihood be very similar.

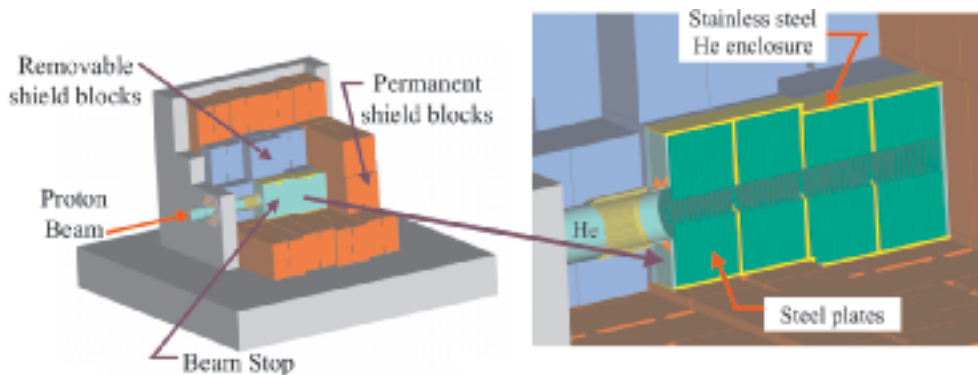


Figure 4.6-4: Sketch of the 7.5 kW beam dumps for the SNS-Project [Gabriel, 2001].

4.6.4 Neutron beam collimators and catchers at proton injection into the targets

An intense beam of neutrons will be emitted from the target in the direction of the proton beam line. In order to avoid undesirable activation of the components and tunnel of the proton beam line, these neutrons must be taken care of by (cf. Fig 4.2-2) (a) inserting a water cooled collimator between the target and the last bending magnet of the proton beam transport line which limits the cross section and angular divergence of the neutron beam in such a way that no beam line components are in the neutron beam line of sight and (b) providing neutron beam catchers behind the last bending magnets in order to safely dispose of the neutrons passing through the collimator

The purpose of the collimator is twofold: On the one hand it limits the divergence and cross section of the high energy neutrons from the target to make sure that no components of the beam transport line are exposed to these neutrons. On the other hand it forces a waist onto the proton beam at this position and a divergent ongoing beam to the target. In this way the target and beam window are protected from inadvertent focussing of the proton beam because this would mean a larger beam cross section at the collimator which will then heat up rapidly and shut off the beam. In order to safely enable this, the collimator must be designed to withstand a substantial heat load at least for a sufficiently long time until the beam is shut off. The exact

amount is difficult to quantify but, since the design shown above for the beam stops can safely handle several hundred kW, the heat handling capacity of the collimators was rated at 500kW.

During normal operation the collimators will only have to take a small heat load from protons but will be exposed to a high neutron flux. Since both, the collimators and the neutron dumps have to handle neutrons with energies up to a few hundred MeV, their design will be similar to that of the proton beam stops and the same handling equipment will be used. It remains to be decided, whether active cooling is required for the neutron catchers. This depends on the size of the opening that will ultimately be left in the collimator and will be determined in the detailed design of the beam transport system.

4.6.5 Summary

Including targets, collimators and neutron beam stops there will be the following locations in which significant amounts of radiation will be stopped and which, as a consequence, will require remote handling in case of maintenance, repair or decommissioning:

Table 4.6-1: Overview of beam stops including neutron production targets and collimators.

	Power rating	Pulse duration	Yearly estim. total charge	Design
SPTS Target	5MW	1.4 μ s	18 000 mAh	Hg-loop, actively cooled
LPTS Target	5MW	2 ms	18 000 mAh	Hg-loop, actively cooled
LPTS Injection dump	100 kW	2 ms	500 mAh	Copper, actively cooled
Ring Injection dumps	2x50 kW	600 μ s	2x250 mAh	Copper, actively cooled
Linac development beam stop	500 kW	2 ms	50 mAh	Copper, actively cooled
Ring development beam stop	500 kW	1.4 μ s	50 mAh	Copper, actively cooled
Achromat scraper beam dumps	6x5kW	1.4 ms	6x20 mAh	Steel, passively cooled
n-p collimator SPTS	500 kW	1.4 μ s	n.a.	Copper, actively cooled
n-p collimator LPTS	500 kW	2 ms	n.a.	Copper, actively cooled
Target neutron beam catchers	tbd			Steel +PE+B, passively cooled

While the targets will have their own dedicated maintenance cells where they can be moved to on their trolleys, all other beam stops will be of a similar modular design that will allow a universal handling flask to be employed for removing them in parts from their operating positions and transporting them to a maintenance hot cell. Such operations are expected to take place very infrequently, which is why it is acceptable to have to dismantle parts of the beam lines to access the development dumps or set up temporary lifting gear to handle the achromat dumps.

Note: The only parts, apart from the target shells, which are expected to require regular replacement, are the proton beam windows in front of the target. Again, their design will be such that the universal flask mentioned above can be used for their transport to the hot cell.

4.7 SAFETY ASPECT

4.7.1 Introduction

4.7.1.1 General

This chapter deals with target specific safety issues. A more general introduction into ESS-safety is found in chapter 8.

Inherent safety features of spallation sources are quite favourable, if compared to fission reactors. This is, partly due to certain design features as outlined in 4.7.1.2 and, with mercury as target material, also to:

- A comparatively small amount of radioactivity,
- The absence of fissile materials, no actinides formed
- No proliferation problems, no criticality issues,
- A low decay heat of spallation products in mercury, no relevant target heat-up by decay heat in case of loss of cooling,
- Significant decay of spallation products already within several centuries (see table 8.4-I), meaning that the waste disposal does not pose serious problems.

The main safety concerns with respect to the ESS targets result from:

- The radiotoxicity of the spallation products (10^5 TBq/target), whose total amount in ESS is however only about 0.1 % of the equilibrium activity inventory of a large fission reactor,
- The chemical toxicity of the mercury (15 t/target),
- The direct radiation penetrating through the shielding which may, among others, result in activation of soil and ground water,
- The condensed, burnable gas (hydrogen), used in moderators, whose explosion might damage the target station.

It should be noted, that the ESS target system is probably the only component of the facility, requiring an accident analysis at all, whereas for the other components safety considerations for normal operation and abnormal events are sufficient.

Compared to the situation described in Vol. III of the ESS Technical Study of 1997:

- the ESS design is now sufficiently detailed for a safety study, and
- there exists a comprehensive safety study for the SNS target [SNS, 2000], which is comparable in many aspects to the ESS target. This work has been documented in the “*Preliminary Safety Analysis Report*” (PSAR) for SNS.

So, there exists a good basis for a safety study of the ESS target. The present chapter deals with:

- The general safety philosophy of the target and moderator systems,
- The radiotoxic and chemical toxic potential within the target system,
- The evaluation of accident behaviour of the target system based on PSAR,
- Extensions of PSAR required for ESS with relevant results, and
- Ongoing and future accompanying R&D work for target safety.

4.7.1.2 Overview on the safety concept of the ESS target system

The ESS safety philosophy is primarily based on defense-in-depth. Main safety features include:

- Containment by multiple barriers to control leakage (see Section 4.2)
 - *target*: target hull, double walled mercury return hull (with connection to the mercury storage tank), inner assembly vessel, target block liner,
 - *target loop*: pipes – vessel - heat exchanger as first barriers; target trolley as second barrier and the target cell as third barrier,
 - *moderator*: moderator vessel, vacuum container surrounding all cryogenic parts of H₂ and He circuits, He blanket with online monitoring of gas composition.
- Safety by design: components to sustain the maximum credible pressure from detonation in hydrogen loop; sufficient buffer tank volumes for moderators; control system with all kinds of abnormal situations leading to proton beam shutdown; sufficient buffer volume on target trolley for mercury in case of primary circuit leakage.
- Quality Assurance: Use of high quality material, design to relevant standards continuous survey and documentation of manufacturing and testing.
- Additional passive safety features (fire walls);
- Simple operation of the facility to reduce probability of human error
- Redundancy and diversity in active safety systems;
- Radiation protection and control system: monitoring of gas borne activities in relevant parts of the target building, monitoring of emissions by air and water, monitoring of activities in the surrounding (air, soil, water), monitoring of doses of the staff and control of dose rates in areas with substantial radiation

4.7.2 Estimate of radiotoxic and chemical toxic potentials

4.7.2.1 Radiotoxicity

The most safety relevant nuclides present in the target were identified based on the nuclide inventory calculated for the SNS target [SNS, 2000] and on similar calculations performed for ESS. Criteria used were yield, dose factors and volatility. Following the classification of PSAR; nuclides were grouped into 3 volatility categories:

- Highly volatile nuclides (tritium, iodine, noble gases)
- Medium volatile nuclides (mercury isotopes)
- Low volatility nuclides (most of the remaining species)

The most relevant nuclides are listed in table 4.7-1 together with their estimated inventories, their half lives, their type of radiation and their boiling points. In order to obtain a figure for the radiotoxic potential of these inventories, dose calculations were performed [Moermann, 2002b], based on German rules for design basis accidents (dba) of light water reactors. These rules are described in more detailed in chapter 8.2.1.3. Short-term emission was assumed, together with worst weather conditions. An emission height of 25 m was considered. This is the approximate height of the target building. (A bigger effective emission height, which would occur in case of fires, will decrease maximum doses). A distance from the emission point (target) to the fence of 250 m was taken into account. Except for low volatile nuclides, emission as gas is assumed, which leads to higher doses for certain pathways compared with release as aerosol. Calculations are performed for a person living near the fence unsheltered for 50 years. Table 4.7-1 contains the estimated doses per emission for the 4 pathways, described in chapter 8.1. It has to be noted, that doses per emission are valid for infants and relate to effective doses except for iodine incorporation, where thyroid doses are presented because of the substantial accumulation of iodine in the thyroid. Thyroid doses are about a factor of 30 higher than effective doses for iodine incorporation. German rules give dba dose limits of 50 mSv (effective dose) and 150 mSv (thyroid dose).

Table 4.7-1: Overview of radiologically most relevant nuclides in one ESS-target (30 y of continuous operation at 5 MW). The colour coding refers to the volatility classes defined above.

nuclide	ESS target inventory [GBq]	half life [d]	boiling point [K]	Type of radia-tion	dose/emission*			
					ground shine	cloud (γ)	inhalation	ingestion
H-3	5.6e5	4500	(14)	weak β	0	0	1.1e-9	**
I-124	3100	4.2	387	β,γ	1.9e-6	1.0e-8	3.0e-5	3.4e-3
I-125	14000	60	„	γ	1.2e-6	1.0e-10	1.8e-5	2.3e-3
I-126	630	13	„	β,γ	2.6e-6	4.2e-9	6.3e-5	7.6e-3
Gd-148	3.5e4	2.72e4	3546	α	0	0	2.2e-3	3.6e-7
Hf-172	7.3e5	683	4875	γ	1.9e-4	7.7e-10	1.3e-5	1.9e-9
Au-195	4.2e6	186	3081	γ	2.1e-6	6.2e-10	2.2e-8	5.9e-10
Hg-193	1.9e6	0.16	629	γ	2.4e-8	1.7e-9	6.5e-9	2.5e-10
Hg-194	2.1e5	1.9e5	„	γ	5.4e-3	1.3e-13	1.3e-6	3.7e-7
Hg-195	3.2e6	0.42	„	γ	5.0e-8	1.7e-9	8.1e-9	6.3e-10
Hg-197	2.2e7	2.67	„	γ	7.4e-8	5.2e-10	2.0e-8	3.0e-9
Hg-203	1.5e7	47	„	β, γ	4.9e-6	2.2e-9	1.8e-7	8.1e-9

* German directives for dba (dose build-up by internal and external irradiation for 50y), infant, effective doses except for iodine incorporation (thyroid), emission height: 25 m, distance emission point – immission: 250 m

**no ingestion model in German rules

Concerning external irradiation it becomes obvious that groundshine is mainly caused by long-lived Hg-194 (associated with a dose/emission value for groundshine about an order of

magnitude larger than that of Cs-137, which is a nuclide well known from fission reactors). This is mainly due to its short-lived daughter nuclide Au-194. A smaller contribution comes from Hf-172. Cloud shine is obviously a less relevant pathway. With respect to incorporation pathways, particularly high doses by inhalation are expected from Gd-148, but iodine nuclides and Hf-172 are also relevant. Substantial ingestion doses may be caused by iodine nuclides. However, it has to be noted, that explicitly accounting for ingestion as in German rules is not required in all European countries. Others rely more on food ban in case of accidents. Comparing the potential doses with the above dose limits and with the inventories for the respective volatility classes, shows that emissions of highly volatile nuclides (iodine) must be limited to about 0.25 % of the total inventory. For mercury this limit is in the range of 0.02 % and for low volatile nuclides at about 0.03 %. These limits will decrease, if simultaneous release of different volatility classes has to be considered.

An additional inventory that might be released in certain accidents is associated with the cooling water of the target system, which contains relevant amounts of ^3H . However, potential doses from this inventory remain much smaller than those from the target inventory.

4.7.2.2 Comparison of (chemical) toxicity and radiotoxicity of mercury

A comparison of the radiotoxicity of the target with the chemical toxicity of mercury relates to the incorporation pathways alone, since external irradiation is not an issue for chemical poisons. Further on, such a comparison can only be done for early consequences because a sufficient dose - consequence relation for late effects is not (yet) available for the chemical toxicity of mercury. A comparison for the (dominating) inhalation pathway was performed for infants, taking into account that

- The LD₅₀ value (lethal dose with 50 % probability) for radiotoxicity for effective lung or red bone marrow dose is 4 Sv, accumulated within 7 d
- The LD₅₀ value for chemical toxicity of mercury is within a range of 5 – 15 mg/kg, applied within a short time period
- The biological half life of mercury in the human body is in average 60 d (necessary for calculation of 7 d doses instead of using the long term dose/emission relations, given in table 4.7-1)

We found [Moormann, 2002b], comparing

$$\frac{\sum [\text{Hg-nuclide activity} * (7\text{d-dose factor}) / \text{LD}_{50}]}{\text{Hg-amount in target} / \text{LD}_{50} / \text{weight of person}}$$

for radiotoxicity, with
for (chemical) toxicity

that the chemical toxicity of mercury is about a factor of 10 – 30 higher than the radiotoxicity of the single nuclide Hg-197. Accounting for the all mercury in the target, this value is reduced by a factor of 2. However, considering the very high dose/emission value of Hg-194 in the groundshine pathway (see table 4.7-1), it becomes obvious, that this does not fully account for the total radiotoxicity of the target mercury. In order to quantify this in a reasonable manner certain assumptions must be made on the external irradiation¹.

¹ In assessing the general consequences rather than individual doses only, ground shine has to be considered very seriously. This is because long term ground shine is the most costly irradiation pathway in radiological accidents due to the fact, that affected areas cannot be used and relocation of population has to take place.

Nuclides other than mercury also contribute significantly to the radiotoxicity of the target. In particular inhalation of Hf-172 and ingestion of iodine isotopes have to be considered. α -emitting Gd-148 is mainly a contributor to late effects by inhalation, but must be taken into account too. Significant other contributors to groundshine are Hf-172, Au-195, and iodine isotopes.

Altogether this means that, while radiotoxicity dominates the overall toxicity of the target, the chemical toxicity must not be neglected. This is particularly true for conditions where the target radioactivity is already reduced by decay. It should be noted again, that the above comparison gives only a very rough figure due to the neglections mentioned. With respect to late effects one may expect, radiotoxicity to be even more relevant than chemical toxicity: an increase of the cancer probability of up to 10%/Sv may be estimated as late radiological consequence.

Concerning the ingestion pathway of mercury it has to be noted, that conversion to organic compounds within the food chain might increase its chemical toxicity and its radiotoxicity alike.

4.7.3 Accident analysis based on PSAR (Overview)

Because of the similarity in design of SNS and ESS, the PSAR for SNS is being reviewed with respect to its applicability to ESS safety studies: We found, that both, the probabilistic and the deterministic part of PSAR are an excellent basis for ESS safety work.

Generally speaking, PSAR points out that substantial release of volatile nuclides may occur already in loss of confinement events, whereas release of mercury by evaporation requires energy intake into the target (fire, proton beam in case of loss of cooling without accelerator shutdown). Low volatility nuclides may be released to a limited extent by mechanical dispersion of mercury only (moderator explosions etc.).

The following design basis accidents were identified in PSAR as being most important:

- Fire (spreading into or starting within the target building)
- Hydrogen explosion with follow-on fire (also as a consequence of seismic events),
- Loss of heat sink accidents without timely shutdown of the proton beam.
- Loss of mercury flow without timely shutdown of the proton beam.

Other accidents identified as relevant and studied in detail in PSAR are:

- Loss of mercury confinement
- Hydrogen explosion without fire (also induced by seismic events)
- Beam mis-steering leading to failure of the target hull
- Crane drop accidents

The main safety relevant features identified in PSAR are a sufficient fire protection and a reliable proton beam shutdown. In general, PSAR comes to the conclusion, that safe operation is possible with adequate safety measures.

Source term estimations in PSAR revealed that the complete target inventory of highly volatile nuclides can be released in the majority of relevant events (except for iodine in loss of confinement events, where only 5 % are released due to low temperatures). For mercury isotopes a complete release was calculated only in the event of unlimited fire, while for other accidents this release stays at < 30 % of the target inventory. For low volatile nuclides the maximum release for worst-case conditions remains at < 1 % of the target inventory.

It has to be noted that the chemical toxicity of mercury was not treated in PSAR. Further on, in order to keep the effort limited, the procedure adopted was to increase stepwise the degree of detail: PSAR started with conservative, rough assumptions on event probabilities and source terms and without consideration of mitigating measures. Only in cases where dose limits were exceeded, analyses were repeated with less conservative assumptions or consideration of selected mitigating measures. This iterative process was stopped when limits given by licensing authorities were reached. Apart from minimising the total effort, this procedure has the advantage that it gives information on the importance of mitigating measures.

Comparing PSAR dose estimations with ESS conditions the following differences were found:

- Greater distance between the SNS facility and the public (1375 m, compared to about 250 m expected for ESS): Doses increase roughly with the inverse square of the distance,
- Larger radiotoxic inventories in the ESS targets due to the higher proton beam power,
- More stringent safety limits in European countries because of higher population densities in most parts of Europe. For example, a 50 mSv effective dose is the maximum allowed for dba in Germany, compared to 250 mSv in the USA,
- Use of a ‘realistic’ consequence models in PSAR instead of a formal, highly conservative dose estimation as required in ESS commissioning,
- Ingestion pathway not included in PSAR consequence estimations.

As a result of these differences, event sequences which remain just below dose limits in PSAR (as is the case for several accident scenarios), will exceed European dose criteria for the ESS: Taking fractional nuclide release values from PSAR and calculating doses for ESS conditions leads to transgression of dose limits by more than 2 orders of magnitude. Accordingly, the depth of safety analyses in PSAR is not sufficient for ESS conditions and additional steps in the iterative safety analysis process described have to be undertaken at least for certain relevant accident events. In general, two options exist in how to meet safety criteria for ESS on the basis of the PSAR study:

- Improved system analysis, leading to a reduction of event frequencies: It has to be shown that the event sequence falls out of the range of design basis accidents due to its low probability.
- Improved deterministic analyses, leading to a reduction of source terms: It has to be shown that the source terms remain so small, that transgression of ESS dose limits does not happen.

Both routes are taken in the ESS safety study. The current status of this study leaves no doubt that the required dose limits can be met without substantial changes of the present design. Relevant results, supporting this statement, are given in the next chapter.

4.7.4 Safety studies beyond PSAR

4.7.4.1 System analysis

System analytical studies lead to the conclusion, that the mitigating effects assumed in later steps of the iteration process in PSAR for events involving fire also apply to ESS conditions. Further on, the analyses indicated, that the assumptions on hydrogen explosions in PSAR are highly conservative and a reduction of this conservatisms is part of the ongoing ESS safety study. Conversely, concerning failure of the target confinement, the assumptions taken in PSAR seem to be quite realistic. This underpins the relevance of the examinations on reduced iodine volatility, presented in the next paragraph.

4.7.4.2 Iodine volatility

One of the conservatisms we found in PSAR concerns the volatility of iodine nuclides. Iodine was classed as a highly volatile nuclide in PSAR like tritium and noble gases, although formation of iodine compounds with lower volatility than the element has to be expected due to the pronounced chemical reactivity of iodine. This lead to a significant release of iodine nuclides into the environment in case that there is a pathway between target and environment (particularly if vaporisation of mercury remains very limited, as in loss of confinement events). As shown in 4.7.2.1, iodine release has to be limited to < 0.25 % of the total inventory for dba in ESS. So, there is an urgent need for a more realistic assessment of iodine sourced terms.

In order to substantiate the arguments for a lower volatility of iodine, thermochemical calculations on the iodine-mercury system were already performed within the JSNS project [Kobayashi, 2000]. These calculations, which concentrate on the condensed state, indicate that iodine exists within the target mainly as mercury iodides. The calculations were extended at FZJ to the gaseous phase in equilibrium with the mercury target [Moormann, 2002a]. The Code SOLGASMIX [Besmann, 1975], developed for examination of thermochemistry in nuclear fission reactors, was applied to the target mercury. This code minimises the Gibbs free enthalpy; input data are the molar amounts of elements in the systems and the compounds to be considered in gaseous, condensed and dissolved state with their respective standard enthalpy and entropy data.

Figure 4.7-1 and -2 give two examples of results from the SOLGASMIX calculations for this problem. Results in Figure 4.7-1 are pertain for a Hg/I system with large Hg surplus at temperatures between 400 K and 629 K (mercury boiling at 1 bar). Apart from gaseous species listed in the figure legend, in the condensed phase the species Hg, I₂, HgI, HgI₂ (2 different solid state phases and the liquid phase) and Hg₂I₂ are taken into account as individual, separated phases. Dissolution of the considered species in mercury is not taken into account. It should be noted, that the vapour pressure of elemental iodine (not shown in figure 4.7-1) is already at 400 K ($1/T=0.0025$) at about 0.2 bar, which is about 4 orders of magnitude higher than the vapour pressure sum of all iodine compounds in figure 4.7-1; the vapour pressure of elemental iodine was assumed in PSAR for release calculations. Comparison of the vapour pressures of the iodine species with the vapour pressure of elemental mercury shows that the total volatility of iodine compounds is smaller than that of mercury for $T < 590$ K. Obviously, HgI₂ is the dominating gaseous iodine species. In the condensed state HgI is the main compound, as already found in [Kobayashi, 2000].

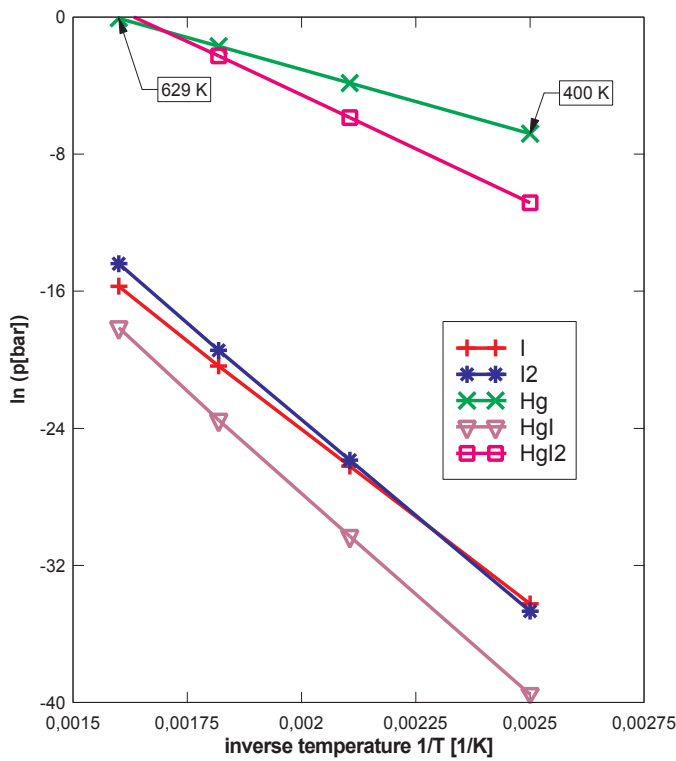


Figure 4.7-1: Equilibrium vapour pressures of iodine and its mercury compounds over a Hg-I system with surplus of mercury

Examination of the influence of other elements formed during spallation concentrated on hydrogen (tritium), because hydrogen iodide HI is highly volatile and might reduce the above trend. Additional SOLGA

SMIX calculations, taking hydrogen and HI into account (total molar amount of hydrogen in the system = 100 fold that of iodine) do not show a substantial increase the total vapour pressure of iodine compounds, which means, that the iodine volatility is still below that of mercury at $T < 590$ K. In addition formation of other, more stable hydrogen compounds (NH_3 , H_2O etc.) might shift the reaction equilibrium away from HI.

Taken together, this means that the volatility classification of iodine within the schema used in PSAR may be changed from high volatile class to at least the mercury (medium volatility) class for loss of confinement events (where boiling of mercury has not to be considered). This will substantially reduce the iodine source terms for this accident: The immediate fractional iodine release of PSAR was assumed to 0.05, whereas under consideration of the above analysis the source term is calculated to 0.0005 (assuming mercury = iodine volatility). For accidents with mercury volume boiling the iodine source term is probably not changed: The reasons are, that the total iodine vapour pressure is slightly higher than that of mercury at 629 K and that the density of mercury iodide HgI is with 7700 kg/m^3 [Kobayashi, 2000] substantially smaller than that of mercury; the latter means, that iodides should swim on top of the mercury, which is favourable for vaporisation. So, for accidents with mercury boiling, as in PSAR a complete release of iodine has to be assumed, even if the mercury is not completely evaporated. The same is true for accidents without volume boiling of mercury but with moderator explosions: Here, by explosion heat the mercury surface becomes evaporated, where - as outlined before - the HgI is probably concentrated.

The assumption of iodine volatility equalling that of mercury does not yet reflect the complete potential of such thermochemical volatility analyses for loss of confinement accidents; Going more in detail does, however require validation experiments as proposed at the end of this paragraph.

Calculation results of calculations that take into account the influence of iron (target loop, assumed as large surplus compared to iodine) on the iodine volatility – in addition to the assumptions described for Figure 4.7-1 are shown in Figure 4.7-2: FeI_2 as solid and as gas is taken into account in the calculations using SOLGASMIX.

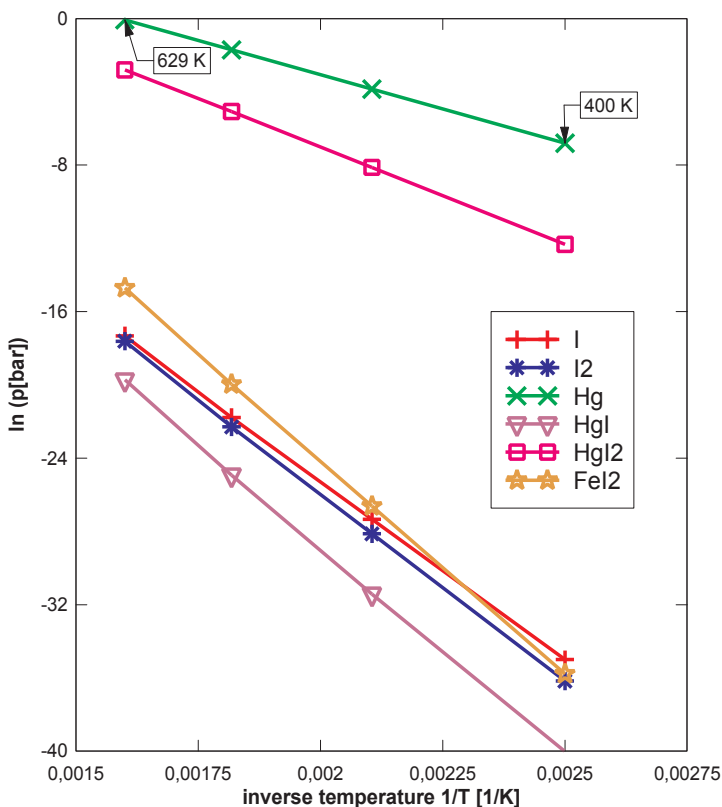


Figure 4.7-2: Vapour pressures over a $\text{Hg}/\text{Fe}/\text{I}$ system (surplus of Hg and Fe).

Accounting for iron leads to an additional decrease of the iodine volatility; main iodine component in the condensed state becomes FeI_2 . Further calculations on the influence of Ni (Ni , NiI_2 in solid, NiI in gas phase) indicated no significant volatility reduction effect as for Fe. If the formation if FeI_2 is assumed, the following iodine source term reduction can be taken into account; on the left of the slash the immediate fractional iodine source term of PSAR / on the right of the slash the expected reduced iodine source term assuming iodine volatility equalling that of mercury, based on the volatility analysis above:

- loss of mercury flow with proton beam shut down failure (1.0 / 0.04-0.3)
- loss of heat sink with proton beam shut down failure (1.0 / 0.3)

For the following explosion events without fire, a substantial retention can only be assumed in the first analysis step, if FeI_2 remains adsorbed on the hull surface and is not transported into the mercury. In the latter case, it might swim up on the mercury surface and a vaporisation by explosion heat cannot be excluded, although the boiling point of FeI_2 is with 1334 K about 700 K higher than that of mercury. Assuming again iodine volatility equalling that of mercury leads to the following source terms:

- seismic events with following explosions, but without following fire (1.0 / 3.e-3)
- hydrogen explosions without fire (1.0 / 0.005-0.015)

Altogether, because the iodine/iron interaction occurs as a surface reaction, the kinetic conditions are not as favourable for a formation of FeI_2 as it is the case for mercury iodides. Accordingly, this effect of the target loop cannot be considered within the first ESS safety analyses without an experimental validation.

Such validation experiments are planned, equilibrating (inactive) mercury with traces of iodine at different temperatures and determination of the gas phase composition over the liquid mercury (sampling by freezing out the gas and measuring the composition by activation analysis). Experiments will be done with and without added target loop material.

Finally, it should be noted that removing volatile spallation products –at least partially- in a bypass loop and trapping them in solid form is part of the ESS concept. In order to assess the degree to which such removal is necessary, studies as outlined above are indispensable.

4.7.5 Additional accompanying research & development work

The following additional safety related R&D work is under way:

- The actual radioactivity content in the target requires some experimental studies. Whereas the total radioactivity in the target during operation and up to 1 y after end of operation is fairly well known, the (calculated) distribution over individual nuclides contains large uncertainties. Relative fractions of certain individual nuclides are uncertain by up to an order of magnitude. Because the toxicity of nuclides varies within a very broad scatter (see dose/emission factors in table 4.7-1), the knowledge on concentrations of individual nuclides has to be improved by experimental investigations. Due to the comparatively small number of long lived nuclides, even the total activity for < 1 y after shutdown becomes uncertain, which is relevant for decommissioning considerations (see chapter 8.4). Concerning these long-lived nuclides the necessary studies have to be done by evaluating a Hg irradiation already performed at SINQ in collaboration with SNS. For measuring short-lived nuclides a corresponding Hg irradiation experiment with protons is still in the planning phase.
- Contamination of soil, surface water and ground water by direct radiation from the target and from the high-energy part of the accelerator has to be considered within the licensing process: It has to be shown that the shielding is sufficient to avoid exceeding allowed activity levels in the ground water. In other words, the ground water contamination has to remain within the drinking water limits outside the ESS area. A detailed examination of this problem is of particular importance for proposed sites with high ground water tables, but ground water contamination may be caused to some extent also by leaching of activated soil by surface water/precipitation. The general tools for examining this problem will be improved, in particular concerning the transport of activity by surface/ground water in soil).
- Safety analyses for the supercritical hydrogen moderator systems of the ESS will need to be performed in due course, too. However, similar installations have been in operation at reactors all over Europe for many years now with no serious faults reported. So, this technology may be considered state of the art and the tools to examine a particular design are, in general, at hand.

- Accident consequence estimations are of particular importance for commissioning and for discussion with the public; besides the formal, conservative dose calculation models, based on diverse rules and directives, these more realistic complex accident consequence models have to be applied in particular in planning of emergency countermeasures. Such consequence models were used in PSAR, too. The COSYMA-model, developed within an EURATOM collaboration, will be used for these purposes [COSYMA, 1994]. However, COSYMA has to be extended to the nuclide vector, emitted in ESS accidents; further on a model for the (chemical) toxicity of mercury has to be implemented in COSYMA, particularly concerning late effects.

REFERENCES

- [Ageron, 1989] P. Ageron, *Nucl. Instr. Meth. A* **284**, 197 (1989)
- [ANSYS] ANSYS Revision 5.1, Swanson Analysis System Inc., USA
- [Astec, 1992] Astec Release 4.2 User Manual, AEA Technology, Harwell, UK (Aug. 1992)
- [Bauer, 1982] G.S. Bauer, H. Sebening, J.-E. Vetter, and H. Willax ,eds., *Realisierungsstudie zur Spallations-Neutronenquelle*, Report JüL-Spez-113 and KfK 3175 Kernforschungsanlage Jülich und Kernforschungszentrum Karlsruhe (1981) and G.S. Bauer, *The general concept for a spallation neutron source in the Federal Republic of Germany*, Atomkernenergie-Kerntechnik 41 (1982) pp.234-242
- [Bauer, 1985] G.S. Bauer, H. Conrad, W.E. Fischer, K. Grünhagen, H. Spitzer; Leakage Flux, Life-time and spectra of cold neutrons from H₂ – moderators with various reflectors, *ICANS-VIII, International Collaboration on Advanced Neutron Sources*. Report RAL-85-110, p. 344 (1985).
- [Bauer, 1995] G. S. Bauer, *Mercury as a Target Material for Pulsed (Fast) Spallation Neutron Sources Systems*, ICANS XIII, Report PSI - Proc. 95-02, Vol.2, p. 518, Nov. 1995.
- [Bauer, 1996a] G.S. Bauer, T. Broome, D. Filges, H. Jones, H. Lengeler, A. Letchford, G. Rees, H. Stechemesser and G. Thomas, eds. "ESS, a Next Generation Neutron Source for Europe ", Vol III, The Ess Technical Study, ESS 96-53-M (1996), ISBN 90 237 6 659 Vol III
- [Bauer, 1996b] G. S. Bauer, Workshop recommendations on materials selection in: L.K.Mansur and H.Ullmaier, Proc. Int. Workshop on Spallation Materials Technology, Oak Ridge 1996, 1-13.
- [Bauer, 1998a] G.S. Bauer, *Operation and development of the new spallation neutron source SINQ at the Paul Scherrer Institut*, Nucl. Instr. Methods B 139 (1998) p. 65-71.
- [Bauer, 1998b] G.S. Bauer, "The ACoM Collaboration – An international Effort to Develop Advanced Cold Moderators", Proc. ICANS XIV,ANL-98/33 (1998), p.101-110
- [Bauer, 2001] G:S. Bauer, Nucl. Instr. Methods A463 (2001) pp 505.
- [Besmann, 19975] T.M.Besmann: SOLGASMIX-PV, a computer program to calculate equilibrium relationships in complex chemical systems; ORNL/TM-5775 (1975)

- [Broome, 1993] T.A. Broome, Operational Consequences of Induced Activity on the ISIS Target Station Proc. ICANS-XII, RAL Report 94-025, May 1993
- [Broome, 1996] T. A. Broome, D.W.J. Bellenger, C.J. Densham, H.J. Jones, L. Perrot, D.J. Picton and G. Thomas, The ESS Target Station Design (Detailed Technical Papers) Report ESS-96-49-T
- [Bucenieks, 1998] I.Bucenieks et.al., *ESS Mercury Target Model Experiments: Investigations on the Heat Transfer*, Report ESS 98-73-T Dec.1998.
- [Carlton, 1999] L. Charlton, Composite Moderator Progress; *4th Meeting of the International Collaboration on Advanced Cold Moderators (ACoM IV)*; Internal report ESS 99-89-T (1999)
- [CFDS-FLOW3D] CFDS - FLOW3D Release 3.3 User Manual, AEA Technology
- [Chen, 1999] J.Chen, Y.Dai, F.Carsughi, W.F.Sommer, G.S.Bauer and H.Ullmaier, *Mechanical properties of 304 stainless steel irradiated with 800 MeV protons*, J.Nucl.Mater. 275 (1999) 115.
- [Dai, 1997] Y.Dai et.al., *Static corrosion experiments on martensitic and austenitic steels in Mercury at 300°C*, in ESS-Mercury Target Development-Progress Report 1996, Report ESS 97-65-T (ISSN 1433-559X) Jul 1997
- [Dai, 2001] Y.Dai, X.J.Jia, W.F.Sommer, M.Victoria and G.S.Bauer, *Microstructure in deformed and undeformed austenitic steel 304L irradiated with 800 MeV protons*, J.Nucl.Mater. 296 (2001) 174
- [Dressler, 1995] R. Dressler, B. Eichler, Verflüchtigung von Kernreaktionprodukten aus geschmolzenen Targets, Report PSI 95-03, 1995
- [Dury, 1997] T.V.Dury et.al., *Design of the ESS liquid metal target using computational fluid dynamics*, in ESS-Mercury Target Development-Progress Report 1996, Report ESS 97-65-T (ISSN 1433-559X) Jul 1997.
- [Farrell, 2001] K.Farrell and T.S.Byun, *Tensile properties of candidate SNS target container materials after proton and neutron irradiation in the LANSCE accelerator*, J.Nucl.Mater. 296 (2001) 129
- [Filges, 1995] D. Filges, R. D. Neef and H. Schaal, *Nuclear Studies of Different Target Systems for the European Spallation Source (ESS)*, ICANS-XIII, Report PSI-Proc., 95-02, Vol. 2, p. 537, (1995).
- [Filges, 1996a] D.Filges, R.D.Neef, H.Schaal, Al.Tietze, U.Weber, W.Breuer, J.Wimmer, *Damage Studies for Structure- and Beam Window Materials for the ESS Mercury Target*, Report ESS 96-47-T, July 1996
- [Filges, 1996b} D.Filges, C.Mayr, R.D.Neef, H.Schaal, Al.Tietze, J.Wimmer, *Development of Cross Sections for Materials Damage and Helium Production for ESS*, Report ESS 96-45-T, July 1996.

- [Gabriel, 2001] T.A. Gabriel, "Beam Profile Monitoring and Safety Considerations for the Mercury Target System and the Three Proton Beam Stops (of SNS)" paper presented at the 7th General Meeting of the European Spallation Source, Seggau, Sept.26-29, 2001
- [Gelles, 1987] D. S. Gelles, *Effects of Irradiation on Ferritic Alloys and Implications for Fusion Reactor Applications*, J. Nucl. Mater. 149 (1987), p. 192
- [Goldenbaum, 2002] F. Goldenbaum, D. Filges, private communication (2002).
- [Gordon, 1984] J. D. Gordon, J. K. Ganer, N. M. Ghoniem and J. F. Parmer, Topical Conf. on Ferritic Alloys for Use in Nuclear Technologies, AIME Warrendale (1984), PA, p. 157
- [Guttek, 1997] B.Guttek, *Present State of the ESS Mercury Target design and its reflector-moderator-region*, in ESS-Mercury Target Development-Progress Report 1996, Report ESS 97-65-T (ISSN 1433-559X) Jul 1997
- [Hahn, 1963] B. Hahn, Nuovo Cimento 28, 339 (1963).
- [Hughes, 1999] H.G. Hughes, MCNPX Version 2.1.5, Los Alamos National Laboratory (1999), LA-UR-99-1995. Disclaimer of Liability: With respect to MCNPX results in this report, neither the United States Government nor the University of California nor any of their employees makes any warranty, express or implied, including the warranties of merchantability and fitness for a particular purpose, or assumes any legal liability or responsibility for the accuracy, completeness, or usefulness of any information, apparatus products, or process disclosed, or represents that its use would not infringe privately owned rights.
- [Inoue, 1979] K.Inoue et al., J. At. En. Soc. Japan 21 (1979) 865
- [Jahn, 2002] W. Jahn and K. Verfondern, Private communication, (2002)
- [James, 2001] M.R.James, S.A.Maloy, F.D.Gac, W.F.Sommer, J.Chen and H.Ullmaier, *The mechanical properties of an alloy 718 window after irradiation in spallation environment*, J.Nucl.Mater. 296 (2001) 139
- [Jung, 2001a] P.Jung, *Radiation effects in structural materials of spallation targets*, J.Nucl.Mater. (2001)
- [Jung, 2001b] P.Jung, C.Liu and J.Chen, *Retention of implanted hydrogen and helium in martensitic stainless steels and their effect on mechanical properties*, J.Nucl.Mater. 296 (2001) 165.
- [Jung, 2002] P.Jung, J.Henry, J.-C.Brachet and J.Chen t.b.p. in 5th Int.Workshop on Spallation Materials Technology, Charleston 2002
- [Kiyanagi, 1991] Y. Kiyanagi et al., Optimization studies on coupled liquid hydrogen moderator; *ICANS-XI International Collaboration on Advanced Neutron Sources*. KEK Report 90-25, (1991)

- [Klueh, 1994] R. L. Klueh and D. J. Alexander, *Impact toughness reduced-activation ferritic steels*, J. Nucl. Mater. 212-215 (1994),
- [Kobayashi, 2000] K.Kobayashi et al.: Physical and thermochemical properties for inorganic mercury compounds; 2nd Int. Workshop on Mercury Target and Cold Moderator Engineering; 13.-15.11.2000, JAERI, Tokai
- [Koppitz, 2002] T.Koppitz, t.b.p.
- [Levinson] D.W.Levinson, L.E.Tanner and J.J.Rausch, Armour research foundation, unpublished.
- [Li, 1991] J.-C. Li et al. J Chem. Phys. 94 **10**,(1991)
- [Maloy, 2001] S.A.Maloy, M.R.James, G.Willcutt, W.F.Sommer, M.Sokolov, L.L.Snead, M.L.Hamilton and F.Garner, *The mechanical properties of 316L/304L stainless steels, Alloy 718 and Mod 9Cr-1Mo after irradiation in a spallation environment*, J.Nucl.Mater. 296 (2001) 119.
- [Marmier, 1994] P.Marmier, *In-beam fatigue of a ferritic-martensitic steel. First results*, J.Nucl.Mater. 212-215 (1994) 594
- [Mezzei, 2002] F. Mezei and M. Russina, Patent applied; Berlin, (2002)
- [Moormann, 2002a] R.Moormann: Thermochemical studies on the mercury/iodine system. ESS-FZJ Technical Note, Jülich, March 2002
- [Moormann, 2002b] R.Moormann: Dose calculations for ESS accidents and comparison of radiotoxicity and chemical toxicity of the target. ESS-FZJ Technical Note, Jülich, March 2002
- [Neef, 1995] R. D.Neef, Private communication, (1995).
- [Neef, 1996] R. D. Neef, Private communication, (1996).
- [Nejedlik, 1964] J. F. Nejedlik and E. J. Vargo, Corrosion, 20 (1964), p. 250
- [Ni, 1997] L.Ni, *On the dynamics of the ESS target under pulsed heating*, in ESS-Mercury Target Development-Progress Report 1996, Report ESS 97-65-T (ISSN 1433-559X) Jul 1997C.
- [Niessen, 1983] A.K.Niessen, F.R.deBoer, R.Boom, P.F.deChatel, W.C.M.Mattes, F.A.R.Miedema, CALPAD 7 (1), 51 (1983)
- [Patorski, 2000] J.A.Patorski et.al., *Liquid Metal Target Experimental Study (Phase 1) of the cooling of a SINQ-Type Mercury Target Window*, Report ESS 00-101-T (ISSN 1433-559X) Mar 2000.
- [COSYMA, 1994] PC COSYMA: An accident consequence assessment package for use on a PC. Report EUR 14916 EN (1994)

- [Probst, 2001a] U.Probst, *Numerische Berechnungen von Spannungspulsen im Quecksilber-Behälter des ESS-Targets und Betrachtungen zur Optimierung*, Report JüL-3900 (ISSN 0944-2952) Aug 2001
- [Probst, 2001b] U. Probst, F. Schubert, C. Byloos, *A Benchmark and Suitability Check on Continuum Mechanical Codes to Reach Calculability in the Pressure Pulse Problem of the European Spallation Source (ESS)*, ESS Report ESS 01-121-T, Nov 2001.
- [Richter, 2001] D. Richter, ESS-SAC / ENSA Workshop on Scientific Trends in Condensed Matter Research and Instrumentation Opportunities at ESS, Engelberg, Switzerland, 03. – 05.05.2001, ESS/SAC/Report/1/01.
- [Rosenwasser, 1984] S. N. Rosenwasser, P. Miller, J. A. Dalessandro, J. M. Rawls, W. E. Toffolo and W. Chen, Proc. Topical Conf. on Ferritic Alloys for Use in Nuclear Technologies, AIME Warrendale, PA (1984), p. 177
- [Schaaf, 1999] B.van der Schaaf, ed., *Weld characterization of RAFM steel*, Report 20027/99.22523/P, Petten, 1999
- [Schaal, 1996] H. Schaal, Shielding Calculations for ESS using the CASL Computer Codes ESS Report 96-43-T (1996)
- [Scott, 1994] P. Scott, *A review of irradiation assisted stress corrosion cracking*, J. Nucl. Mater. 211 (1994), 101
- [Seggau, 2001a] Proc. 7th ESS General Meeting, Seggau 26. – 29.09.2002, 2001, Neutronic Performance of SPTS.
- [Seggau, 2001b] Proc. 7th ESS General Meeting, Seggau 26. – 29.09.2002, 2001, Neutronic Performance of LPTS
- [Skala, 1995] K. Skala and G. S. Bauer, *On the Pressure Wave Problem in Liquid Metal Targets for Pulsed Spallation Neutron Sources*, ICANS-XIII, Report PSI-Proc., 95-02, Vol. 2, p. 559, (1995)
- [SNS, 2000] SNS Preliminary Safety Analysis Report (PSAR), Feb. 28 (2000), US DOE Contract No. AC05-96OR22464
- [SNS, 2001] Third International Workshop on Mercury Target Development, 16-19.Nov.2001, SNS Oak Ridge, TN, USA.
- [Soltner, 2002] H. Soltner, *Effects of Gas Bubbles on Pressure Pulse Propagation in Liquids*, ESS report, to be published (2002)
- [Spitzer, 1997] H. Spitzer et al., First Operation Experience with the Cryogenic Moderator at the SINQ Spallation Neutron Source; *International Workshop on Cold Moderators for Pulsed Neutron Sources*; Argonne, Ill. (1997)

- [Stendal, 1996] K. Stendal, Description of the Moderator Systems for the ESS Project; Risø-R-908 (EN), (1996)
- [Strizak, 2001] J.P.Strizak et.al., *The effect of mercury on the fatigue behavior of 316LN stainless steel*, J.Nucl.Mater. 296 (2001) 225.
- [Trinkaus, 2001] H.Trinkaus and H.Ullmaier, *Does pulsing in spallation neutron sources affect radiation damage?*, J.Nucl.Mater. 296 (2001) 101.
- [Trouw, 2002] F. Trouw, Argonne National Laboratory, private communication
- [Ullmaier, 1995] H.Ullmaier and F.Carsughi, *Radiation damage problems in high power spallation neutron sources*, Nucl. Instr. Methods B101 (1995), 406 and Materials in the Intensive Irradiation Field of Spallation Targets, Report ESS 95-17-T, January 1995
- [UTE-ESS] Mercury Primary Loop Design,
UTE-ESS Report 092-091-F-EA-00201-R
- [West, 1969] C.D. West and R. Howlett, Acustica 21 pp112-117, (1969).
- [Wolters, 2002] J.Wolters, priv.comm., Report in progress
- [Zalavutdinov, 1999] R.K.Zalavutdinov et.al., *Study on the Compatibility of a Target Candidate Steel with Mercury after 300 Days Exposure*, Report ESS 99-97-T (ISSN 1433-599X) Sept.1999
- [Zalavutdinov, 2001] R.K.Zalavutdinov et.al., *Surface analysis of martensitic and austenitic steels after exposure in mercury at 573K up to 5000 hours*, Report ESS 113-01-T (ISSN 1433-559X) May 2001.

Chapter 5

Instruments and Scientific Utilisation

Authors and Contributors

Instruments and Scientific Utilisation

R Eccleston¹, T Gutberlet², F Mezei², H Tietze-Jaensch³

¹RAL/ISIS, ²HMI, ³ESS-CPT

Contents

Instruments and Scientific Utilisation

5 INSTRUMENTS AND SCIENTIFIC UTILISATION.....	5-5
5.1 INSTRUMENTATION: GENERAL ASPECTS.....	5-6
5.1.1 PULSE REPETITION RATES	5-6
5.1.2 PULSE LENGTHS	5-7
5.1.3 NEUTRON BEAM EXTRACTION	5-7
5.1.4 BEAM DELIVERY BY ADVANCED NEUTRON GUIDES	5-8
5.1.5 ADVANCED INSTRUMENT DESIGN	5-8
5.1.6 CHOICE OF MODERATORS	5-9
5.1.7 VIRTUAL INSTRUMENT SIMULATION SUPPORT	5-10
5.1.8 SUMMARY	5-10
5.2 INSTRUMENT SUITE	5-11
5.3 DEVELOPMENT REQUIREMENTS.....	5-14
5.3.1 DETECTORS	5-15
5.3.2 POLARISING DEVICES.....	5-15
5.3.3 DAQ	5-15
5.3.4 SOFTWARE	5-15
5.3.5 GUIDES AND BEAM OPTICS	5-15
5.3.6 CHOPPERS	5-15
5.4 INFRASTRUCTURE	5-16
5.4.1 SAMPLE ENVIRONMENT EQUIPMENT	5-16
5.4.2 INSTRUMENTATION SUPPORT FACILITIES	5-16
5.4.3 SAMPLE PREPARATION LABORATORIES	5-16
5.4.4 DEVELOPMENT LABORATORIES	5-16
5.4.5 USER AREAS	5-16

5 INSTRUMENTS AND SCIENTIFIC UTILISATION

The guiding principle of ESS instrumentation is to combine the highest neutron source power with the most efficient instrument design using highest performance components and state-of-the-art support services. It is this combination that will make ESS a quantum jump in scientific research opportunities with the sensitivity for the detection of small signals enhanced by two – three orders of magnitude in the majority of experiments compared to the best available today at the most advanced neutron sources. Sensitivity is the crucial issue in neutron scattering research. To date a broad spectrum of well established methods have been used to provide resolutions allowing the exploration of microscopic phenomena by neutrons in a vast space – time domain of 0.1 – 1000 nm and 10^{-15} to 10^{-7} s, respectively. At the same time, neutron scattering experiments are in most cases sensitivity limited, i.e. the accuracy of the results or the lower limit of the feasible size of the samples is often determined by the available neutron beam intensities rather than intrinsic limitations of the resolution capabilities. Although the ESS instrument development effort has identified areas where considerable resolution gains will be achieved, the main thrust of the effort is to use the available neutrons most efficiently for the detection of small signals and to enable the investigation of very small samples. Both ways of enhancing sensitivity, namely to provide high neutron intensity beams to impinge on the sample and to simultaneously detect a high fraction of the scattered neutrons, is being pursued in the ESS instrument design and performance assessment effort. A more detailed overview of general instrumentation issues and approaches at ESS is given in ESS Project 2002 Volume II. Volume IV is entirely devoted to an overview of ESS instruments and instrument performances. What follows in this chapter, is a summary of issues, technical solutions, development-needs and support facilities.

Innovation is considered at ESS as the most powerful ingredient in providing the user community with unprecedented performance and scientific opportunities. There is a number of well studied and documented novel approaches, most of which are in the process of being implemented as prototypes at various neutron scattering centres world-wide. Together with well-established techniques, these new developments have also been considered in evaluating the expected performance of ESS instruments. In this process technical risks have been minimised, in particular by the use of extensive computer simulations of detailed, fully realistic instrument models. On the other hand, it is also to be anticipated that new ideas will emerge in the next years, which will substantially extend this potential, and adequate room is reserved in ESS planning to take up and bring to fruition such innovations. However, such assumed developments were not taken into account in evaluating the performance of the instruments.

ESS will also offer research opportunities in areas other than neutron scattering investigations of condensed matter, namely muon spin resonance, particle physics, nuclear physics, irradiation of materials. These applications are not part of the project as planned and costed, however, adequate room is left for their implementation.

5.1 INSTRUMENTATION: GENERAL ASPECTS

At present two basic types of neutron sources cover the research needs of a world-wide community of some 7000 scientists using neutron scattering as a research tool: continuous (or steady state) and pulsed sources. As of today, these two kinds of sources are complementary: some applications are best served by the most powerful steady state sources, others by pulsed sources. In view of future developments, pulsed sources represent a decisive advantage: they allow us to use the produced amount of neutrons in neutron scattering instruments more efficiently. All of these instruments require beams with more or less defined neutron velocities and on a continuous source this requires to throw away from the broad spectrum emitted by the source moderators all those neutrons whose velocity lies outside the desired monochromatic range. In contrast, on a pulsed source, neutrons with different velocities arrive to the sample or detector with different time delays after the pulse, and we are effectively performing a series of experiments with a series of monochromatic beams in the time interval between subsequent source pulses. Therefore a much larger fraction of the produced neutrons is actually used on a pulsed source.

To take full advantage of the higher efficiency of pulsed sources the pulse parameters (namely pulse length and pulse repetition rate) have to be well matched to the requirements of the instrument. On the one hand, accelerator physics, material properties and the nature of neutron propagation and thermalisation processes set strict boundary conditions on the choice of these parameters. On the other hand, the various, very different types of instruments needed to provide a complete spectrum of neutron scattering capabilities set contradictory requirements on the source pulse structure. The main goal of the ESS instrumentation approach is to find compromises, methods and design solutions, which will allow ESS to meet the requirements of all neutron scattering instruments to an unprecedented degree. As a result ESS will move neutron scattering beyond the current paradigm of complementarities between pulsed and steady state sources. Instead ESS as a pulsed source of novel design will vastly enhance the power of neutron scattering in all applications compared to all current sources, steady state or pulsed.

5.1.1 Pulse repetition rates

In various scattering experiments the neutron velocity ranges from a few hundred m/s (cold neutrons) through a few thousand m/s (thermal neutrons) to around 10,000 m/s (epithermal neutrons). Most neutron scattering instruments are sizeable, since they need to be designed for large beam cross-sections (in the range 10 cm^2) for large samples, in order to enhance the total number of neutrons hitting the sample. Radiation shielding also takes up considerable room. Therefore experiments with very different velocity neutrons need very different time intervals between consecutive pulses, which can exceed 50 ms for cold neutrons. Similarly, the pulse length for cold neutrons can be much longer without loss of velocity definition. On the other hand, accelerator, neutron moderation technology and material hardness allow us to produce more neutrons in longer pulses than in short ones. In order to meet broad instrumental requirements ESS will operate, besides the more traditional 50 Hz short pulse target station, a 16.66 Hz target station of equal power with long pulses (2 ms) primarily for cold neutron research. In certain applications of neutron spectroscopy, where the beam intensity is particularly important in view of the weak signals, the novel instrument design concept of Repetition Rate Multiplication will allow to extract several neutron pulses of different velocities from the same source pulse, and deliver pulses with up to 300 to 400 Hz

frequency to the sample. Thus ESS will offer best intensity coverage in an extended pulse frequency range, to meet the individual requirements of different instruments.

5.1.2 Pulse lengths

Various instruments require different pulse lengths, depending on the definition of the neutron velocity needed. While longer pulses offer the advantage of delivering more neutrons per pulse, shorter pulses provide better resolution. ESS will make use of three approaches to supply a broadest variety of pulse length and intensities:

- (a) The long pulse target station for long and most intense pulses
- (b) A choice of different moderators on the short pulse target station and
- (c) Pulse shaping mechanical choppers for the shortest pulses.

In this way for cold and thermal neutrons pulse length will be available over the whole range of velocity from 5 μ s to 2 ms. The shortest pulses will enable ESS to reach unprecedented resolutions e.g. in diffraction studies with cold neutrons, for which the neutron moderation times limit the neutron pulse lengths to not less than about 80 μ s. Pulse length tailoring mechanical choppers also interfere with the neutron velocity band available, for this reason they can be most readily used on the long pulse target station and in some cases also for beams from the longest pulse (coupled) cold moderators on the short pulse target station, with intrinsic pulse lengths of up to 300 μ s. Adding the innovative approaches (a) and (c) to the traditional choices offered by (b) amounts to a substantial extension of capabilities at ESS.

5.1.3 Neutron beam extraction

ESS beam lines will be equipped with advanced neutron optical devices in order to enhance the number of neutrons which make their way through the 6 m thick bulk shielding and further to the sample. State-of-the-art supermirror coated neutron guides can transport neutron beams with enhanced beam divergence. In order to fully illuminate these guides for long wavelength (cold) neutrons, they have to start at a close range from the moderator. The ESS beam shutter design will allow us to put neutron guide inserts into the shutter openings, which will bring the entrance of neutron guides within 1.5 to 1.7 m from the moderators. The shutter design also offers the capability to change the guides relatively easily, if the high radiation field so close to the target would deteriorate the performance of supermirror coatings sooner than the several years estimated today. For short wavelength, neutrons supermirror optical beam extraction will also offer enhanced efficiency at ESS. In this case converging neutron guides will be used in a fashion not to obstruct the direct view of the moderator from the sample. The neutrons reflected on the supermirror coated guide walls come in addition to the direct view and this provides for a substantially enhanced neutron flux on the sample for all incoming neutron energies up to 500 meV.

Another major enhancement of the beam intensity and of the beam quality can also be achieved by placing supermirror optical systems inside the bulk shielding. A supermirror coated neutron transparent Si plate can combine the beams emitted from a cold and a thermal neutron moderator placed side by side in a fashion that most of the two spectra are efficiently added together in the extracted beam. Such a multi-spectral, simultaneously cold and thermal beam will open up novel opportunities by enabling instruments to operate in a very broad

incoming neutron energy range, from 100 meV down to below 1 meV. This latest innovation will allow ESS users to cover a larger dynamical range in a single experiment than it was thought possible by now.

5.1.4 Beam delivery by advanced neutron guides

The distance between source, moderator and sample is an instrument design parameter of central importance. This distance plays a decisive role in determining the monochromaticity of the neutrons impinging on the sample at a given time, and it is therefore a key instrument design parameter. By the use of advanced neutron guides ("Ballistic guides") one can greatly reduce the neutron beam intensity losses with increasing distance, so that source to sample distances of 200 – 300 m or more become feasible. Combined with the potential of making very short pulses with fast mechanical choppers (see chapter 5.1.2). ESS will achieve neutron velocity (wavelength) resolution for cold neutrons in the range of $2 - 4 \times 10^{-5}$, an order of magnitude improvement compared to current state-of-the art.

For thermal neutrons and hot neutrons, up to some 500 to 900 meV the use of neutron guides is a novel feature. By now the $1/r^2$ drop of neutron intensity on the sample in direct view of the moderator was a decisive factor in favour of as short instruments as possible (typically 10 to 13 m). Using converging supermirror coated guides ESS instruments will benefit from essentially the same beam delivery efficiency at considerable larger distances. This can either be taken advantage of by improving the resolution without much effect on beam intensity, or gain in intensity without loss of resolution by using a longer pulse, higher brilliance moderator.

All this amounts to an essential change of paradigm in instrument design. With beam delivery by advanced neutron guide systems the distance between moderator and sample becomes an effectively free parameter in instrument optimisation. This novel freedom will be used at ESS to either enhance beam intensity or to improve resolution compared to current design practice.

5.1.5 Advanced instrument design

The novel approaches discussed in the previous chapters 5.1.1 to 5.1.4 assure highest incoming neutron flux for the instruments, well beyond current state-of-the-art efficiency of turning the high energy neutrons produced in the spallation process into "useful" neutrons actually impinging on samples. ESS instruments will also be designed to detect the scattered neutrons with maximum efficiency. This primarily requires the extensive use of large area position sensitive detectors. The vastly enhanced incoming neutron intensity of ESS will make possible, on the one hand side, to observe small scattering signals and to study very small samples that are not accessible today. For this purpose existing detector technology is satisfactory, and progress over the next decade is primarily expected to lead to price reduction. Currently, about half of the total costs of an instrument amounts to detectors covering a large solid angle of the scattered neutrons. On the other hand, the unprecedented flux of ESS will also allow us to take complete data sets in a ms or shorter period of time and observe fast processes in real time. The instantaneous neutron counting rates expected at ESS will exceed 10^5 counts/s per cm^2 detector area. Such high counting rates are beyond the capabilities of existing neutron detectors, but progress of extensive R&D efforts at ESS

partner laboratories and other centres suggests that the challenge of developing about an order of magnitude faster detectors will be met within this decade.

Another technical challenge not yet fully solved is the phasing of mechanical, fast rotating neutron choppers to the source pulses and in general the stability of the timing of the neutron pulses. The firing of high power accelerators is more economical if it is loosely locked to the phase of the electric power grid, which is far from stable on the scale of precision neutron scattering experiments ($< 0.1 \mu\text{s}$). (In contrast, a quartz clock fires ISIS.) Technical development work at SNS and Los Alamos is on the way to solve this problem. In addition, drifts in moderator temperature lead to small shifts between the effective time of the neutron pulse and that of the accelerator pulse. ESS will offer two additional approaches to overcome timing instabilities:

- (a) To use the long pulse source for experiments that require very high timing accuracy: pulse shaping choppers here will offer the best pulse stability, similar to that regularly achieved by choppers on continuous sources.
- (b) Switching from the conventional histogram data collection mode to "event recording" techniques well established in high-energy physics (so-called list mode). By registering the time of each neutron count together with all system parameters (timing of each accelerator firing, each chopper revolution, data from global system monitoring) instabilities can be checked and corrected for in an off-line data reduction process.

5.1.6 Choice of moderators

The need to meet the requirements of many different kinds of instruments concerning source pulse characteristics will be met at ESS in a novel and more efficient way than on existing and planned other pulsed neutron sources. On the one hand side, the combination of a long pulse and a short pulse target stations allows us to group instruments with similar needs on one or the other target stations, by which we can avoid the necessity to cater for all different instrumental needs on a single type of target.

On the other hand, the novel approaches listed under 5.1.1 to 5.1.4 lead to a novel instrument design paradigm to achieve highest neutron intensity on the sample: use the brightest, longest pulse moderator (and correspondingly longer source to sample distances) compatible with the instrument design goals, instead of using the shortest possible distance and correspondingly a shorter pulse, less bright moderator.

On this basis the ESS choice of moderators needs to favour brightness over minimal pulse length, and it is sufficient to place moderators at the two brightest positions (above and below the targets) instead of using 4 moderator positions per target station, with at least two of them not optimally placed. The reduced number of moderator locations also offers the possibility to enhance the surface of the moderators for higher beam intensity on samples in direct view of the moderator (i.e. for short wavelength). Beams will view two opposite faces of each ESS moderator assembly. On the short pulse target station a thin liquid decoupled H_2 moderator for shortest pulses over the whole neutron energy range will be back-to-back to an equally decoupled, thicker ambient H_2O moderator to provide highest intensity, relatively short pulses in the thermal neutron range. The other short pulse moderator will be a coupled liquid H_2 moderator for highest peak flux and brightness in the cold neutron range, backed by a equally coupled multi-spectral thermal-cold moderator combination on the other side. On the long

pulse target station one of the moderators will be coupled liquid H₂ for highest cold neutron flux, and the other one combined with an ambient H₂O moderator to extend the neutron energy range for multi-spectral thermal-cold beam extraction. Both moderators will be viewed from both sides. Each target station will offer 24 beam lines, with neighbouring beam directions separated by 11°.

The configuration of the moderator is based on established technology, although it presents several innovations in the layout, such as extended moderator surfaces and multi-spectral beams. Beyond liquid H₂ and H₂O solid or liquid methane is being used at lower power spallation sources and it offers clear advantages as de-coupled moderator for a number of instruments. Unfortunately methane is not stable in high radiation fields and as of today there is no proven technical solution to this problem. ESS and its instrument suite is planned in a manner to keep the option free to replace one or both de-coupled moderators on the short pulse target station by a methane or similar advanced cold moderator, once feasibility and performance under high power conditions is established. ESS is part of a broad international collaboration aimed at the development of such advanced cold moderator systems.

5.1.7 Virtual instrument simulation support

The ESS instrumentation development effort makes extensive use of powerful Monte-Carlo computer simulation codes to assess expected instrument performance, to develop and test new techniques and concepts, to optimise instrument layout, etc. Two ESS partner laboratories have developed two advanced program packages for this purpose (McStas and VITESS) in close co-ordination with each other. "Virtual instrument" simulations calculations underpin much of the instrument performance database for establishing the science case and reference instrument suite, presented respectively in ESS Project 2002 Volumes II and IV.

Powerful and in all detail realistic virtual instrument simulation codes are not only developed at ESS as tools for instrument design and development. They will even gain importance once the instruments become operational. Its exact virtual instrument counterparts will accompany each ESS instrument. So experimenters will be able to plan their experiments by the use of the virtual instrument as "flight simulator", optimise the choice of instrument parameters and configuration for the specific goals of their study, take best informed timely decisions on conducting their experiments and use simulation calculations for data reduction, analysis and model refinement. Such an approach will not only largely enhance the efficiency of utilisation of the beam time allocated to each study, but it will also help to rapidly access and interpret the huge quantity of data provided by ESS instruments in a short lap of time, with counting rates exceeding 10⁷ counts/s on many instruments.

5.1.8 Summary

ESS will present an unprecedented leap forward in the power of neutron scattering as a research tool with unique capabilities in condensed matter science and technology in the broadest sense. This will be achieved in a most efficient way, by combining a series of improvements and innovations in every single aspect that is relevant for the ultimate measure of performance of a neutron scattering facility: the data collection rate, which determines the sensitivity in exploring small signals and samples. Thus ESS will not only be the spallation source with the highest accelerator power when it is completed (even compared to the 2 MW

of its strongest competitor at the time of completion, the SNS facility in advanced stage of construction at Oak Ridge, Tennessee), but it also will benefit from a series of innovations leading to enhanced moderator system efficiency, enhanced beam extraction and delivery and most advanced instrument design. This is a very cost effective approach: most often the costs of improved solutions are just marginally increased to the conventional ones, if they are taken into account at a very early stage of design and construction. This was for example also true for doubling the power of ESS by adding a long pulse target station, an extension of extremely low technical risk. On the other hand, this innovation raises the neutron intensity advantage of ESS just as a source in many experiments, particularly important in the study of soft material, nano-structured and biological matter to a full order of magnitude relative to SNS. The sheer source flux advantage of ESS over present day sources in the different neutron scattering applications amounts to factors between 10 and 100. Combining high flux with the novel, improved beam extraction, beam delivery and general instrument design concepts discussed in above, ESS will offer to the scientific and technology development community research capabilities enhanced in most applications by more than two to three orders of magnitude compared with the most powerful existing instruments, either at spallation sources or reactors.

5.2 INSTRUMENT SUITE

A reference instrument suite for the ESS target stations is presented in Tab. 5-1 and Tab. 5-2. Those instruments that would benefit from viewing an advanced cold moderator are written in italics. Detailed descriptions of a subset of these instruments (the reference instruments) are presented in Vol. IV. These instruments were selected by as high priority instruments. The remaining set of instruments represents additional instruments that we would expect to see at the ESS if it was available and fully operational today.

Table 5-1a: *Short Pulse Target Station Instruments. Reference instruments are high priority instruments proposed by SAC and for which a full performance estimate has been made (refer to ESS volume IV, for explanation on port numbers see figure 5-1).*

Instrument on SPTS	Flight Path Length (m) (Primary, Secondary)	Ref.-Instr.	Port No.
Cold Coupled Moderator			
High Resolution Backscattering Spectrometer (0.8 meV)	200 , 3	R	SC19
High λ Resolution (SANS) Instrument	12 , 20		SC21
High Resolution Reflectometer	12 , 3	R	SC22
Cold Chopper Spectrometer (low resolution)	40 , 3	R	SC24

(continued on next page)

Table 5-2b: (continued): Short Pulse Target Station Instruments. Reference instruments are high priority instruments proposed by SAC and for which a full performance estimate has been made (refer to ESS volume IV, for explanation on port numbers see figure 5-1).

Instrument on SPTS	Flight Path Length (m) (Primary, Secondary)	Ref.-Instr.	Port No.
Multi-spectral Moderator			
Particle Physics	40 , x		SM07
High Resolution Protein Single Crystal Diffractometer	40 , 2	R	SM09
Single Pulse Diffractometer	10 , 2	R	SM10
Medium Resolution Backscattering Spectrometer (5 eV)	40 , 2		SM11
High Energy Chopper Spectrometer (high resolution, low Q)	15 , 8	R	SM12
Thermal Decoupled Moderator			
Thermal Chopper Spectrometer (medium resolution)	14 , 2.5	R	ST01
Molecular Spectroscopy (TOSCA)	17 , 1.5		ST02
High Resolution Single Crystal Diffractometer (Chemical Crystallography)	15 , 3	R	ST03
High-Q Powder Diffractometer	40 , 2		ST04
Liquids and Amorphous Materials Diffractometer	11 , 1-6	R	ST06
Decoupled Cold Moderator			
Backscattering Spectrometer (17 meV)	30 , 2		SD13
EV Spectrometer	12 , 1		SD14
Tomography/Radiography Instrument	25 , 4	R	SD15
Engineering Diffractometer	50 , 3	R	SD16
Magnetic Powder Diffractometer	50 , 2	R	SD17
High Resolution Powder Diffractometer	200 , 2	R	SD18

Table 5-2: Long Pulse Target Station Instruments Reference instruments are high priority instruments proposed by SAC and for which a full performance estimate has been made (refer to ESS volume IV, for explanation on port numbers see figure 5-1).

Instrument on LPTS	Flight Path Length (m) (Primary, Secondary)	Ref.-Instr.	Port No.
Cold Coupled Moderator			
Neutron Depolarisation Instrument	12 , 2		LC07
Grazing Incidence SANS Instrument	20 , 8		LC08
Single Peak Diffractometer (CryoPAD)	20 , 2		LC09
Very High Intensity SANS Instrument	21 , 15	R	LC10
Fourier Diffractometer	25 , 2		LC11
Particle Physics Instrument	40 , x		LC19
High Intensity Reflectometer	37 , 3	R	LC21
Focussing Mirror Low-Q SANS Instrument	20 , 8	R	LC22
High Resolution Neutron Spin Echo (NSE) Spectrometer	30 , 6	R	LC24
Multi-spectral moderator			
Variable Resolution, Cold Neutron Chopper Spectrometer	90 , 3	R	LM02
High Intensity SANS Instrument	21 , 30	R	LM04
Ultra-high Resolution Powder Diffractometer	300 , 3		LM05
High Pressure Diffractometer	40 , 6		LM06
Low Resolution Single Crystal Protein Diffractometer	20 , 2		LM13
Coherent Excitations Spectrometer (TAS)	30 , 2		LM15
Wide Angle NSE Spectrometer / Diffuse Scattering Instrument	50 , 4	R	LM16
High Magnetic Fields Instrument	50 , 2		LM17

The individual footprints of the instruments need to be accommodated in accordance with the angular sectors and a given moderator beam-port fan. The result of the presented instrument shuffle is shown in figure 5-1 with corresponding port numbers. For further details of the whole instrument suite layout and target station footprints refer to volume IV, chapter 1.

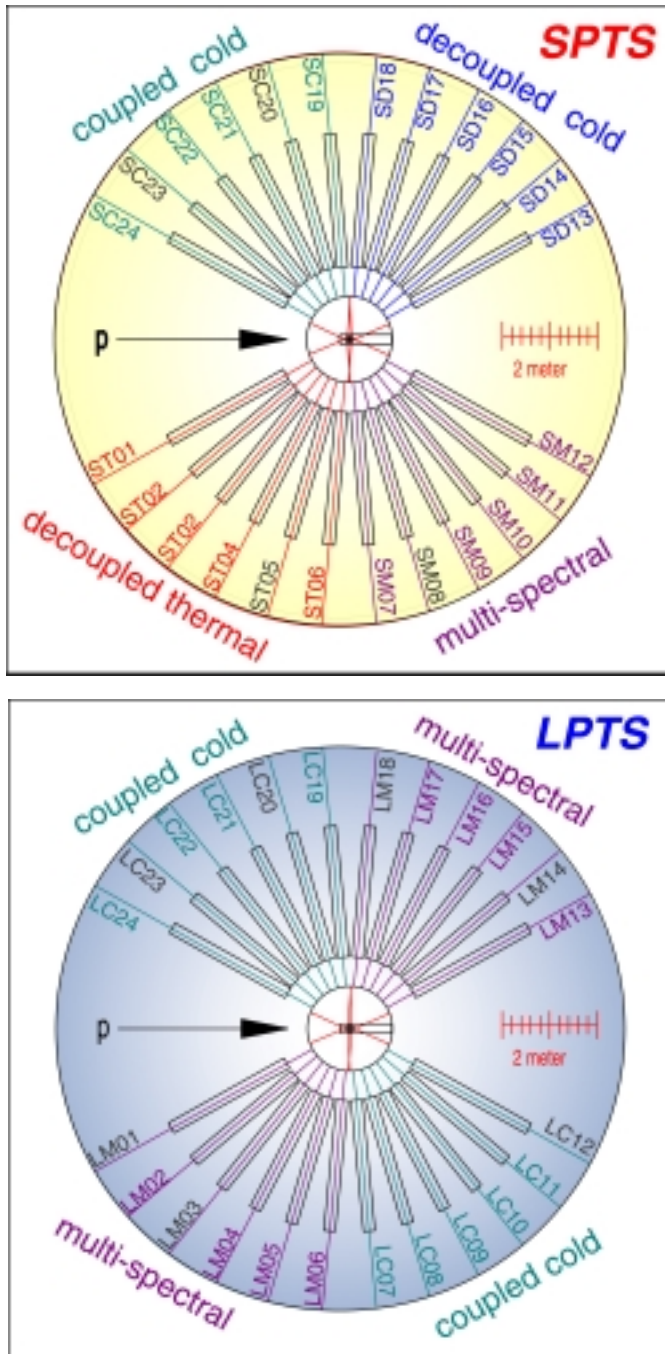


Figure 5-1: Scaled draft of the short pulse target station SPTS (top) and long pulse target station (bottom: reflector vessel (inner circle), set 24 beam shutters of 2.8 m diameter with beam front-end 1.5 m off the moderators, beam port no., size of target shielding (outer circle).

5.3 DEVELOPMENT REQUIREMENTS

The development of new instrument components and instrumentation techniques progress rapidly fuelled by the desire to maximise the efficiency of neutron scattering instruments on existing sources. These developments are certain to continue during the construction phase of the ESS and instruments at ESS will undoubtedly benefit as a result. Indeed the

instrument designs presented in Volume IV of this report have only become possible over the last few years, and further gains in instrument performance might be anticipated between now and the time ESS becomes operational as a consequence of new developments. However, there are some areas where development is essential in order to make optimum use of the intense neutron beams available at the ESS.

5.3.1 Detectors

The high flux available to ESS instruments will require detectors with high count rates, good spatial and time resolution, excellent signal to noise discrimination and cost effective methods for covering large solid angles. The continuing development of gas detectors, particularly, micro strip gas detectors, and the search of more efficient scintillators are of crucial importance. Additionally, new technologies, such as monolithic active pixel sensors (MAPS) particularly for monitors and transition detectors, will play a key role.

5.3.2 Polarising Devices

Polarisation analysis will be a vital component of many of the ESS instruments. In order to deliver this capability, polarising filters and solid-state devices will be required. Recent development on both fronts indicate that the ESS will be able to utilise polarised beams to a far greater extent than pulsed sources have been able to until now.

5.3.3 DAQ

High data rates place stringent demands on the data acquisition (DAQ) system. Considerable expertise exists within Europe that can be brought to bear to provide ESS instruments with an appropriate DAQ system.

5.3.4 Software

Good software is essential for the effective collection, reduction, analysis and visualisation of data, particularly in the volumes that it will be collected at the ESS. Current programmes are in use at the existing facilities and improvements are developed under the umbrella of EC networks.

5.3.5 Guides and beam optics

Neutron guides and beam optics will be key components for many of the ESS instruments.

5.3.6 Choppers

The long pulse target station instruments in particular requires choppers that can operate at high frequencies with good timing accuracy. The demands of the instruments in the reference instrument suite are within what can be achieved with existing technologies.

5.4 INFRASTRUCTURE

The experimental programme will require ancillary equipment to the instruments, particularly sample environment equipment, support laboratories for beam line components, instrumentation development facilities, sample preparation laboratories and facilities available to make the users time at the ESS as effective and comfortable as possible.

5.4.1 Sample Environment Equipment

A wide range of sample environment equipment ranging from cryostats and closed cycle refrigerators to extreme high pressure facilities and complex controlled environment systems will be available for the ESS instruments. Sample environment laboratories will be available close to the experimental halls for the testing and preparation of this equipment.

5.4.2 Instrumentation Support Facilities

Support laboratories for detectors, choppers and polarising filters close to the experimental areas will be required to hold operational spares, test and diagnostic equipment and workshop areas to provide a rapid response to failures.

5.4.3 Sample Preparation Laboratories

General sample preparation laboratories with basic laboratory equipment, will be provided close to the instruments. In addition specialist sample environment laboratories will be required including wet chemistry, biology, crystal growing, surface techniques and engineering laboratories

5.4.4 Development Laboratories

Development of beam line components will continue in the operational phase of the ESS. These activities will take place appropriate development laboratories for guides and optics, detectors, electronics and choppers.

5.4.5 User Areas

Well-designed user areas will make the users' time at the ESS more effective and comfortable and enhance the scientific culture of the ESS. Such areas will include seminar rooms, data analysis centres and rest areas. Each instrument will be provided with appropriate control rooms and preparation areas.

Chapter 6

Conventional Facilities

Authors and Contributors

Conventional Facilities

B Aune¹, G Bauer², D Bellenger³, P Berkvens⁴, D Blouin⁵, F H Bohn⁶, G Bourdelle¹, P Coffin⁵, C Cousin⁵, M Desmons¹, R Eccleston³, P Fabi⁶, R Ferdinand¹, I Gardner³, E Gaultier⁵, P Giovannoni¹, R Gobin¹, J F Gournay¹, J L Jannin¹, H Jones³, J L Laclare¹, J M Lagniel¹, J Lawson⁷ and team, G Le Cann⁵, A Loulergue¹, R Maier², J P Magnien⁴, S Martin², F Mezei⁸, A Morris³, A Mosnier¹, S Palanque¹, J Payet¹, N Pichoff¹, C Prior³, J Tang², H Tietze-Jaensch⁶, J C Treadgold³

¹CEA, ²FZJ, ³RAL/ISIS, ⁴ESRF, ⁵DAM/DP21, ⁶ESS-CPT, ⁷SNS/ORNL, ⁸HMI

Contents

Conventional Facilities

6 CONVENTIONAL FACILITIES	6-5
6.1 INTRODUCTION	6-5
6.2 SITE REQUIREMENTS	6-8
6.2.1 SCIENTIFIC AND INDUSTRIAL ENVIRONMENT	6-9
6.2.2 ADMINISTRATIVE AND LEGAL ENVIRONMENT.....	6-9
6.2.3 ACCESSIBILITY	6-9
6.2.4 SITE REQUIREMENTS.....	6-9
6.2.5 GROUND STABILITY REQUIREMENTS.....	6-10
6.2.6 QUALITY OF ELECTRICITY	6-11
6.2.7 SITE QUALITIES OVER A LONG PERIOD OF TIME.....	6-11
6.2.8 SITE CHARACTERISTICS FOR COST ESTIMATES	6-12
6.3 BUILDING PROGRAMME	6-12
6.3.1 DEFINITION AND CONTENT	6-12
6.3.2 INTERFACES.....	6-12
6.3.3 RADIobiological SAFETY REQUIREMENTS	6-13
6.4 BUILDINGS.....	6-13
6.4.1 THE TWO LAYOUT OPTIONS.....	6-13
6.4.2 DETAILED DESCRIPTION OF MAJOR BUILDINGS	6-14
6.4.2.1 Front end – linac tunnel – klystron hall buildings	6-14
6.4.2.1.1 Front end building	6-14
6.4.2.1.2 Linac tunnel and klystron hall buildings	6-16
6.4.2.2 Ring buildings and tunnels	6-22
6.4.2.3 Long pulse and short pulse target buildings	6-27
6.4.2.4 Central Office and Laboratory (COL) building.....	6-34
6.4.2.5 Central Helium Liquefier (CHL) building.....	6-34
6.4.2.6 Radio Frequency (RF) test facility	6-34
6.4.2.7 Radioactive waste management centre building	6-35
6.4.2.8 Process waste collection system and conventional liquid waste system.....	6-35
6.5 DETAILED DESCRIPTION OF THE MAIN GENERAL SERVICES.....	6-35
6.5.1 ELECTRICITY	6-35
6.5.1.1 Grounding and lightning protection	6-38
6.5.1.2 Raceway system	6-39
6.5.2 WATER COOLING SYSTEMS	6-39
6.5.2.1 Tower water system.....	6-39
6.5.2.2 Chilled water.....	6-42
6.5.2.3 Compressed air system	6-42
6.5.3 HEATING, VENTILATION AND AIR CONDITIONING (HVAC).....	6-42
6.5.4 ROADS, PARKING SPACE, HARD STANDING AND TRENCHES	6-43
6.6 APPENDIX	6-43
REFERENCES	6-53

6 CONVENTIONAL FACILITIES

6.1 INTRODUCTION

The new generation of Research Laboratories of ESS class should provide an attractive working atmosphere, including natural and intensive communication between the users community and the permanent staff. This implies an excellent architectural research, taking into consideration not only technical features, but also the aesthetics of the buildings, as well as an astute distribution of volumes to render the users life on site more comfortable in so far as welcome, housing, feeding, easy communication with close or remote scientific centres.

The ESS will be regarded as an important and spectacular part of European scientific potential. The image projected by the architectural design of the buildings should reflect this concept. Architecture should not be limited to buildings only. The 100 ha site should be landscaped in order to integrate it in perfect harmony with the environment. The architectural concept should also take into consideration the need for a modular, extensible design, so that architectural integrity can be maintained in the event of future extensions and additions.

The technical risks, time scale and costs of the conventional facilities (about 30 % of the construction costs) are of paramount importance. Usually, these are not given sufficient attention, but in the case of the ESS, we have devoted a significant effort to these issues.

First of all, we established a building programme in which all requirements were identified [ESS-BPG, 2002]. It was based on the SNS [SNS-1, 2001] to [SNS-8, 2000], CONCERT [CONCERT, 2001] and updated ESS Vol. III [ESS-VolIII, 1996] & [ESS-1, 1996] programmes, extrapolated to 10 MW. This building programme was used to study possible technical options for each of the conventional facilities' subsystems and to select a reference solution.

Here, we describe reference solutions for buildings and general services such as electricity, water, HVAC etc. and we show their advantages compared to other solutions.

Concerning the linac, we carried out two studies based on a Normal Conducting (NC) and a Super Conducting (SC) high-energy section respectively. They differ principally in accelerator length. Therefore we have two site layouts, given in Figure 6-1 and Figure 6-2.

The targeted level of detail for the main subsystems corresponds to that required for the building permit. Thus, the building dossier will be sufficiently documented to place an Industrial Architect (INA) contract just after the go-ahead and the margin for error of the corresponding cost estimate stands at around 15-20 %.

For cost estimates, we assumed a construction in France. It has to be stressed that the variation of prices between European countries may be of the same order of magnitude as the margin for error. Therefore, we recommend a cost estimate adjustment as soon as the choice of site is known.

Cost estimates also require exact determination of the scope of the programme. The building programme clarifies the dividing lines between conventional facilities and other programmes.

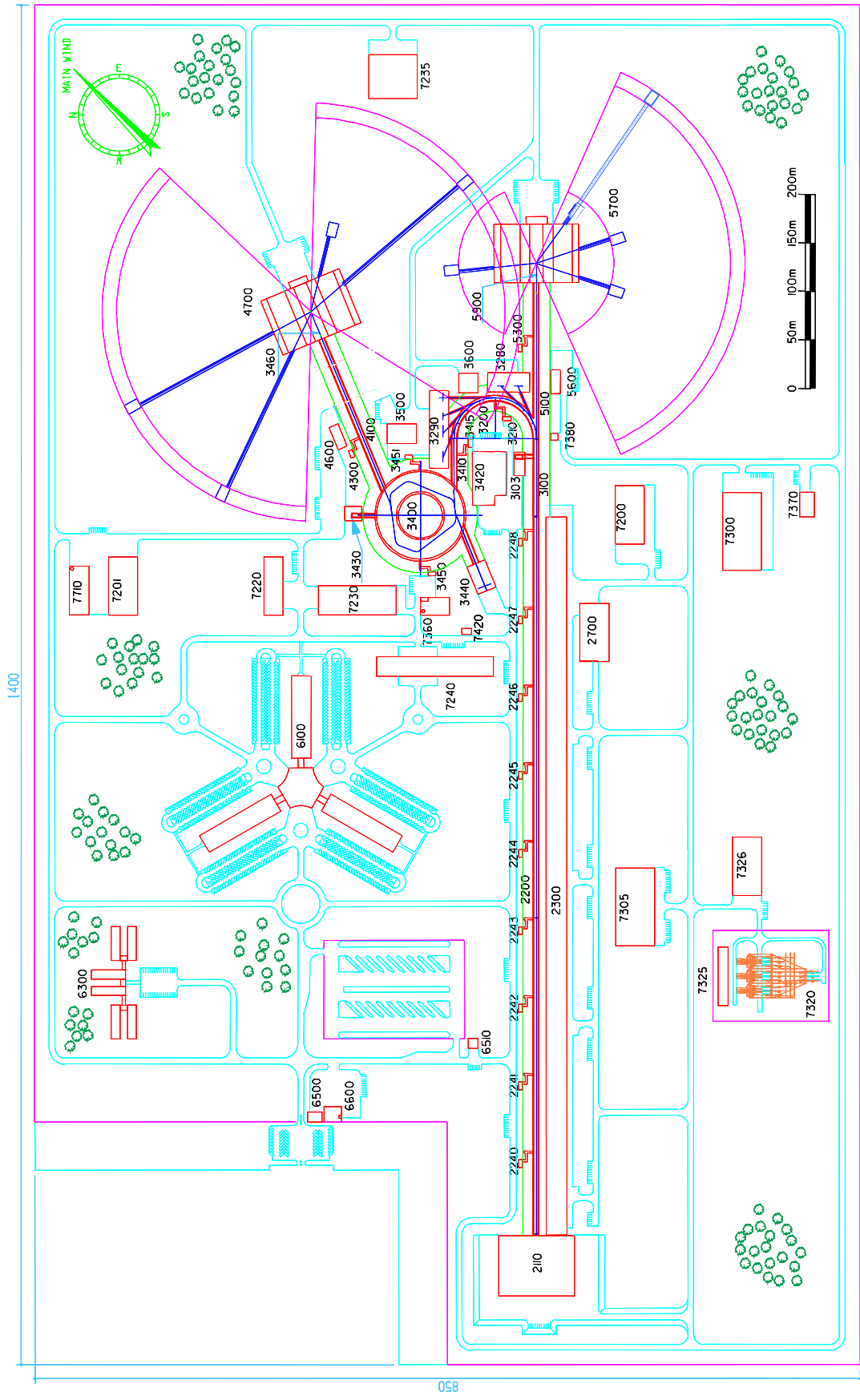


Figure 6-1: Site layout in the normal conducting version

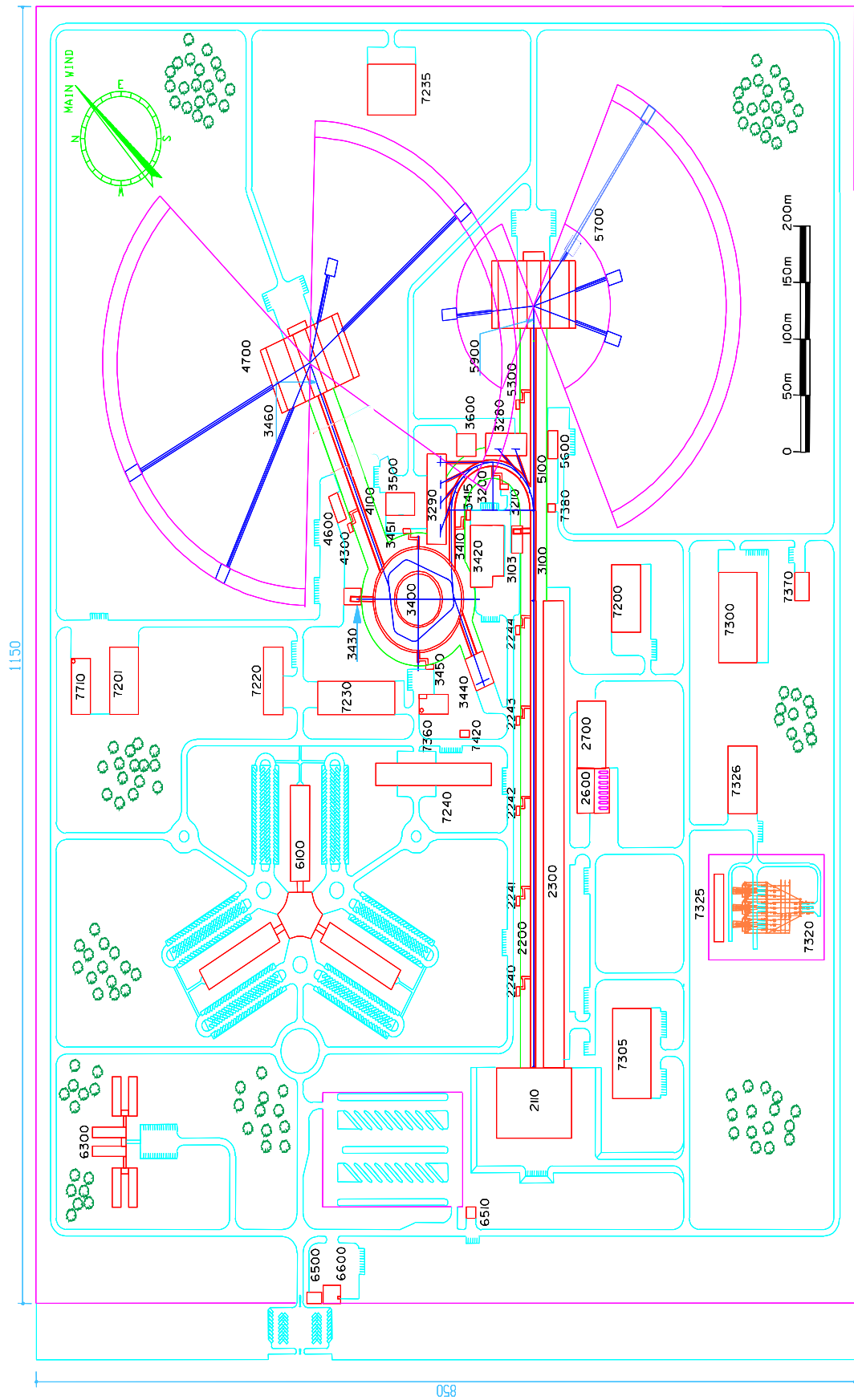


Figure 6-2: Site layout in the superconducting version

Technical risks, extra expense and delays are to be avoided by all means. Very often they have their origin in the interfaces between building contracts. A golden rule is to minimize the number of interfaces under the responsibility of management (ESS management, specific technical assistance and INA) the correct management of this programme is essential. In view of this, we propose to divide conventional facilities operations into three main contracts:

1. All earth works and landscaping. A task that can be started early with a single company on the site.
2. All technical buildings (accelerator tunnels, targets, experimental halls, power plant, cooling plant, other technical buildings, etc). A very large contract to be placed after earth works contract with a consortium of companies having expertise in the key areas (civil engineering, mechanical constructions, electricity, HVAC, piping, etc.).
3. All social buildings (entrance gate, guest house, Central Office and Laboratory (COL) building including auditorium, library, cafeteria, restaurant, etc.). A contract that could be placed after the two others, provided adequate temporary space for the team could be made available late after the decision.

This way of dividing the operations facilitates INA works and avoids having two contracts at the same time at the same place.

The construction of this large facility will have to serve as a model in particular for all works related with the conventional facilities. A contract will be established committing all partners (ESS Management, local authorities, all companies involved, organisms dealing with health, environment, safety at work, employment agency, etc.) to play their role to the full in the implementation of the best quality in the following principles: integrated safety, cleanliness of the site, information of and communication with both workers and the public, reception and training of workers, etc. This approach will contribute to the positive image of the ESS in the public. It is essential to obtain a high level of quality in all areas.

Design and costs of conventional facilities are intimately linked with the site's characteristics. Our 'site-independent' study assumes an ideal reference site 'ready for building' with minimum constraints on the construction. This reference site is defined below.

6.2 SITE REQUIREMENTS

This section describes the specifications of the reference site, which has been used as a basis for the design studies, and costing of the ESS conventional facilities (construction and operation costs).

It is assumed that the site is donated free of charge and that no land taxes will have to be paid. Similarly, access roads, telephone and computer links, electricity lines, water mains etc. would be provided up to the site boundary free of charge by the host country.

Certain sites will not fully meet these specifications, and therefore special measures or design changes will have to be made if the ESS is to be built at such locations. The implications of differences from the reference site in terms of redesign and extra costs will be a factor of selection of the final site. The host country is expected to bear all modifications necessary to restore the initial objectives.

For certain characteristics of the reference site, we used those of the ESRF (European Synchrotron Radiation Facility) in Grenoble.

6.2.1 Scientific and industrial environment

For obvious reasons, it will not be possible to make available on the site, all necessary scientific and technical expertise for optimum operation and later development of the facility. As a first consequence, the facility needs to be surrounded by:

- Universities and research laboratories making use of the facility, with tutors educating students in major fields of science.
- Public or private research laboratories specialised in the fields of metallurgy, microelectronics, chemistry, etc.
- A dense network of active small and medium sized high-tech businesses specialised in domains relevant to the facility, such as cryogenics, fine electronics, ultra-vacuum technology, precision mechanics, control systems, computers, etc.

6.2.2 Administrative and legal environment

After the go-ahead, and until the new installation is constituted as a legal entity in its own right, with statutes and complete regulations for administrative matters, personnel, contracts, etc., the presence nearby of a large scientific institution officially representing and acting on behalf of the future company for recruitment, award of contracts, etc. is considered as a key advantage without which the time scale will not be met.

Furthermore, the new team will need office space, furniture, computers, network and general support. It is logical that the nearby institution mentioned above should provide these facilities.

6.2.3 Accessibility

The site should be easily accessible with high-capacity motorways in the vicinity, and with a large international airport nearby, combined with adequate public transport to and from the site.

6.2.4 Site requirements

In the SC linac option, the site must have a minimum area of about 100 ha and be rectangular in shape. The minimum lengths of the sides of the rectangle should be 850 m and 1,150 m.

In the NC linac option, the site must have a minimum area of about 110 ha. The minimum lengths should be 850 m and 1,400 m.

Two possible site layouts for NC and SC linacs are given in Figure 6-1 and Figure 6-2.

Control by the management of the facility of new constructions in a 200 m band all round the site is considered necessary to avoid any problems in the longer term and to allow for future extension of the facility.

The site must be reasonably flat and have no exceptional geological conditions (compact subsoil, homogeneous layers down to several tens of meters with low compressibility and no water pockets).

The water table of the reference site was assumed to be deep enough to avoid any constraints on the construction.

At the required time, the site should be handed over, ready for construction with existing road access and all services ready to be connected at the site boundary:

- Private road access for heavy goods vehicles (maximum load 100 tonnes) with free passage for a low loader carrying a railway wagon sized load, connected to the motorway network.
- Telephone connections for 1,500 subscribers.
- Fast communication links to international networks and computing centres (> 2 Mbit/s).
- Minimum high voltage power supply of 120 MW in the SC version and 145 MW in the NC version from two well separated lines.
- Gas connection 12,000 MWh/year.
- Water main minimum flow 250 m³/h (to extinguish fire).
- Main sewer connections (rainwater, wastewater, etc.).

The site must be situated in an area with no special restrictions concerning emissions, noise and power lines.

The local storage of activated equipment (or radioactive waste), resulting from the operation of the facility, must be allowable for a period of up to 20 years.

6.2.5 Ground stability requirements

The performance of the accelerator system requires stable, reproducible alignment of the beam along the linac, in the rings and the beam transfer lines up to the targets. Misalignment of the beam is mostly induced by slow drifts in the position of magnetic elements resulting from non-uniform ground settlement.

Complete realignment is a major task requiring a long outage of the ESS facility. A single realignment per year at the very beginning of the operation is acceptable, but the period between realignments should rapidly increase up to 5 years.

The limit of settlement will be set at some 0.1 mm per 10 m per year.

For movement of magnetic elements at higher frequencies, the peak-to-peak horizontal and vertical vibration amplitudes will be in the few micro-metres range.

For the feasibility studies, we assumed that the French Basic Safety Rule 1.2.c with the minimum reference spectrum specified in the corresponding regulations would apply [Regle, 2001]. We did not assume local seismic activity that would require extra specific anti-seismic precautions.

The ground should:

- Be capable of sustaining loads of at least 40 t/m^2 throughout (80 t/m^2 under target stations).
- Not require special civil engineering techniques for buildings.
- Be suitable for cut and fill techniques for the linac, rings and beam transfer lines.

6.2.6 Quality of electricity

Reliability of the operation and exploitation requires high performances in terms of Unscheduled Beam Interruptions (UBIs). Reaching figures as low as a few hundred UBIs per year is the objective. Unwanted fluctuations in grid voltage are one of the main reasons for power supply trips and therefore UBIs.

Stormy regions with a high density of overhead electricity lines will have to be rejected.

The following characteristics are required:

- Maximum amplitude variation of the voltage $\pm 7 \%$
- Maximum frequency variation $\pm 1 \%$
- A maximum of one long complete (duration $> 600 \text{ ms}$) interruption of electricity supply per year on an average, measured over a period of three years
- A maximum of three voltage dips per year, exceeding 400 ms , or with an amplitude larger than $\pm 12 \%$, on two phases
- A maximum of three voltage dips per year, with an amplitude larger than $\pm 8 \%$, on three phases
- Short circuit power higher than 3,500 MVA
- The facility is to operate for about 6,000 hours per year. Consequently, the electricity bill represents a large fraction of the annual budget. We assumed a unit price of approximately €0.040 per kWh at year 2000 rates. Deviation from this unit price can have a significant impact on the operation budget.

Considering the important needs in electrical power, as soon as the choice of site is known, a detailed study will have to be undertaken to search for energy savings and operation cost reduction by optimising the reference temperatures and buildings insulation.

6.2.7 Site qualities over a long period of time

Guarantee of site qualities (and the 200 m band all round) over a period of 40 years; have to be obtained from the host.

6.2.8 Site characteristics for cost estimates

To design building foundations, we have chosen the following characteristics for the subsoil:

- Type of subsoil: sand
- Allowable bearing pressure: 2.5 MPa
- Angle of friction: 35°
- Modulus of compressibility: 50 MPa

6.3 BUILDING PROGRAMME

6.3.1 Definition and content

The building programme [ESS-BPG, 2002] includes collection of all conventional facilities' specification data. The data are expressed in terms of building space, accesses, electricity, cooling, variations of air temperature, loads, handling systems, ground stability, risks and safety, etc. Extensive use was made of SNS [SNS-1, 2001] to [SNS-8, 2000], CONCERT [CONCERT, 2001] and updated ESS Vol. III [ESS-VolIII, 1996] & [ESS-1, 1996] programmes, after extrapolation to 10 MW. We also took into account the extensive experience gained from existing accelerators and neutron scattering facilities, in particular ISIS (RAL), CERN, PSI and FZJ.

6.3.2 Interfaces

For each building housing a part of the process (accelerators, rings, targets etc.), conventional facilities programme included the design of:

- Building structure and foundations.
- Within every building, layout of the process installations and the equipment belonging to the conventional facilities programme.
- HVAC.
- Electrical substation and switchboard excluding electrical cubicles and cable connection to the switchboard.
- Substations for chilled and tower water distribution inside buildings excluding the pipe connections to either heat exchangers or process equipment.

Special services such as helium recovery or liquid nitrogen supply were not included in the conventional facilities programme.

One of the objectives of the building programme [ESS-BPG, 2002] is to describe unambiguously the interfaces between the conventional facilities and the process.

6.3.3 Radiobiological safety requirements

In accordance with the ICPR – 60 recommendations and the 96/29/Euratom directive, all shield wall and earth material thickness have been specified to obtain $0.5 \mu\text{Sv/h}$ dose equivalent rates on contact behind these shields [ESS-16, 2002], a constraint five times more severe than that of last ESS Vol. III ($2.5 \mu\text{Sv/h}$) [ESS-VolIII, 1996] & [ESS-1, 1996].

Under these conditions, the annual dose that a person can receive is below the 1 mSv limit for non-exposed workers.

With the exception of a few specifically protected zones, on an average, we have assumed a continuous beam loss of less than 1 W/m in the linac, rings and transfer line tunnels. This imposes a delay of about 70 minutes for radiation decay before allowing staff intervention.

Monitoring devices will detect unexpected loss and trigger immediate trips when pre-set limits are exceeded.

6.4 BUILDINGS

6.4.1 The two layout options

As stated in other sections, there is still an on-going comparative evaluation of two technical options (SC and NC) for the high-energy end of the linac. Accordingly, we designed two layouts, one for each option. They differ principally in the length of the linac.

The list of buildings specific of these two options is shown in Table 6-3 of the paragraph 6.6. Special requirements for electric power, cooling power, cranes, drainage, etc., are indicated. A single electrical substation is housed in a dedicated building. The other ones are housed inside existing buildings.

Whenever possible, the buildings were designed to allow for future extensions (laboratories, office space, new instruments as well as other potential scientific uses of the facility).

With the exception of the COL building and the guesthouse, all other buildings are steel framed with insulated metal panel cladding. Built-up roofing is planned for roof covering. Floor-mounted units using the chilled water system and hot water heating system will provide air conditioning.

Buildings with no significant potential for airborne contamination are maintained at a slight positive pressure. Otherwise, they are maintained at a slight negative pressure.

6.4.2 Detailed description of major buildings

6.4.2.1 Front end – linac tunnel – klystron hall buildings

6.4.2.1.1 Front end building

The front end building houses sources, RFQs, DTLs, funnel and RF systems, HVAC, cooling, vacuum systems, diagnostics and electronic control racks. We have studied two possible options.

One possible option is to place the sources, RFQs, DTLs and funnel underground, with all other pieces of equipment (RF systems, HVAC) being accommodated in adjacent buildings at ground level. The latter would be conventional steel-framed buildings.

Another option is to have a single steel-framed building at the same level as the linac with a concrete shield enclosing the sources, RFQs, DTLs and funnel for radiobiological protection. The second option has our preference. It is technically simpler and more convenient for operation and maintenance than the first one [ESS-2, 2002] & [ESS-9, 2002]. A 3D view and a cross section of this solution are given in Figure 6-3 and Figure 6-4.

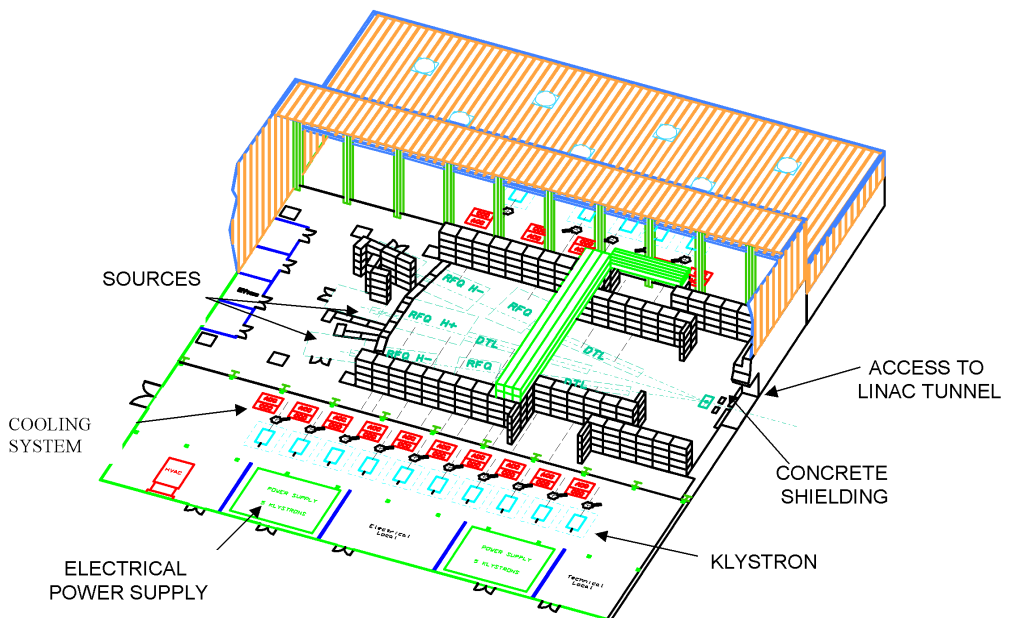


Figure 6-3: 3D view of the front end building

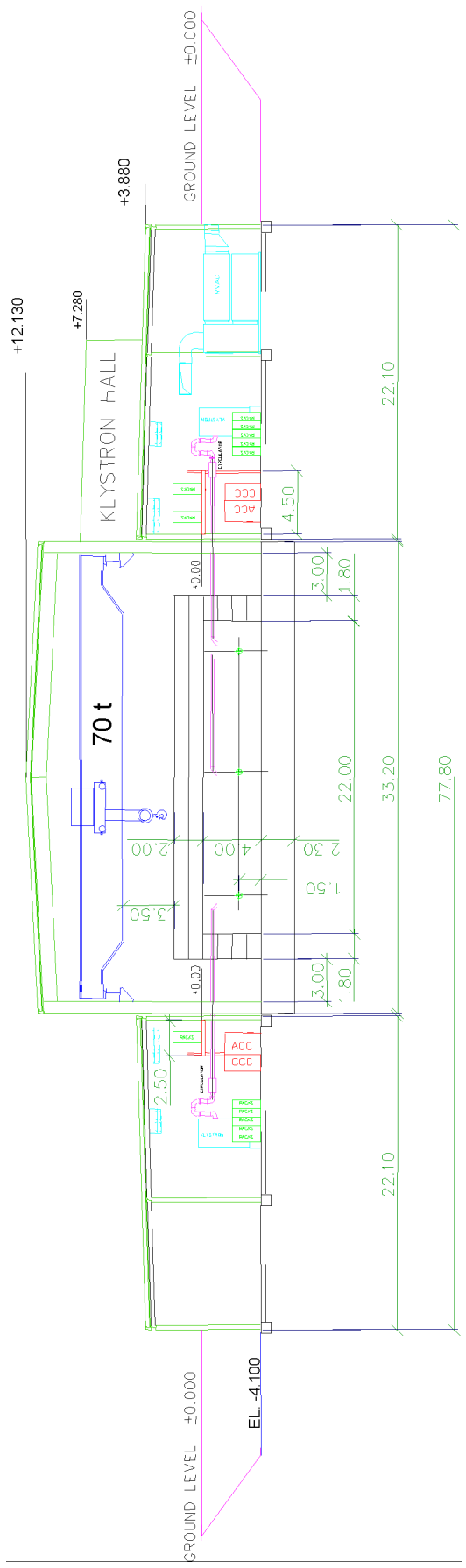


Figure 6-4: Cross section of the front end building

The area of the Front End building is approximately 4,850 m². The beam remains at the same level as in the linac tunnel, i.e. 1.5 m above the finished floor slab.

Access into the linac tunnel is provided through the building by removing concrete shielding blocks.

The floor consists of three separate slabs on grade. The central slab, which supports the concrete shield, sources and associated beam transport elements is independent and isolated laterally from the two adjacent slabs by an expansion joint. This central slab is integrated with the linac tunnel floor slab to behave as a continuous, monolithic unit. The two lateral slabs are standard.

Two lorry doors provide access for goods.

The building also provides a storage area and space for test and development of sources. The atmosphere inside the concrete shield is air conditioned to provide control of both temperature and humidity. The whole building is temperature controlled and ventilated. Year-round requirement is 24 ± 1 °C.

Temperature must be maintained above the dew point.

A first make-up unit air for the linac tunnel is located in the front end building. It is connected with the make-up and exhaust system for the overall tunnel. This unit has High Efficiency Particulate Air filters.

A waste collection system is provided for the building. Drains collect effluents and carry them to the general process waste system.

6.4.2.1.2 Linac tunnel and klystron hall buildings

The linac tunnel houses the majority of the linac structures for beam acceleration (from 20 MeV to 1,334 MeV) and focusing elements.

The klystron building is parallel to the linac tunnel and houses, primarily the RF system (high voltage power supplies, klystrons, wave guides, etc.) but also electromagnet power supplies, cooling system, electronics and vacuum racks as well as conventional facilities items (electrical switchboard, HVAC, etc.).

Many options were considered before making the decision on the reference solution. In all these options, the klystron building is a light building (steel-framed) and the linac tunnel is made of reinforced concrete.

- Option 1: The linac tunnel is buried with the roof just below ground level, and covered with earth. The thickness of the earth covering increases from the beginning to the end of the linac tunnel in order to remain below the limit dose rate of less than 0.5 µSv/h (constant loss of 1 W/m assumed). The klystron building is parallel but distant enough from the linac tunnel to avoid having a retaining wall for the building wall to withstand the pressure of the earth.

With this option, we limit the quantity of earth covering material and associated works and costs. On the other hand, depending on ground compressibility, the difference of vertical pressure at both ends of the linac might create excessive differential settlement.

- Option 2: The linac tunnel is again buried with the roof just below ground level. However, the thickness of earth covering is the same along the entire tunnel. This is satisfactory from the point of view of differential settlement.

The klystron building is nearer to the linac tunnel than in Option 1 and has a retaining wall that can withstand the pressure of the earth.

With this option, we are minimising the length of the wave guides connecting the klystrons to the cavities.

- Option 3: The linac tunnel is buried much deeper underground and the klystron building is directly above it.

This option has two disadvantages. The water table must be deeper than in previous options and from the timescale point of view, it is impossible to build the linac tunnel and the klystron building in parallel.

- Option 4: The linac and klystron building floor are at the ground level.

This makes a high level of the water table less problematical and linac tunnel construction is simplified. However, we would need to bring in more covering material, and furthermore, the connections of the wave guides and pipes between the klystron building and the linac tunnel cause several problems.

After technical and cost analysis, we considered that Options 3 and 4 had too many drawbacks in comparison with Options 1 and 2 and that Option 1 should be preferred, particularly in the matter of ducts between klystron building and tunnel linac (bending, secured supports and tightness).

Therefore, we selected **Option 1** as the reference solution [ESS-2, 2002] & [ESS-9, 2002].

Design cross-sections of linac tunnel, klystron building and earth covering material for both NC and SC linacs are given in Figure 6-5 and Figure 6-6.

In order to reduce the quantity of earth material and the distance between linac tunnel and klystron building, we have selected reinforced earth as covering material, which makes it possible to increase the slopes of the banks on the sides [ESS-6, 2002].

Figure 6-5: Cross section of the linac tunnel and the klystron building

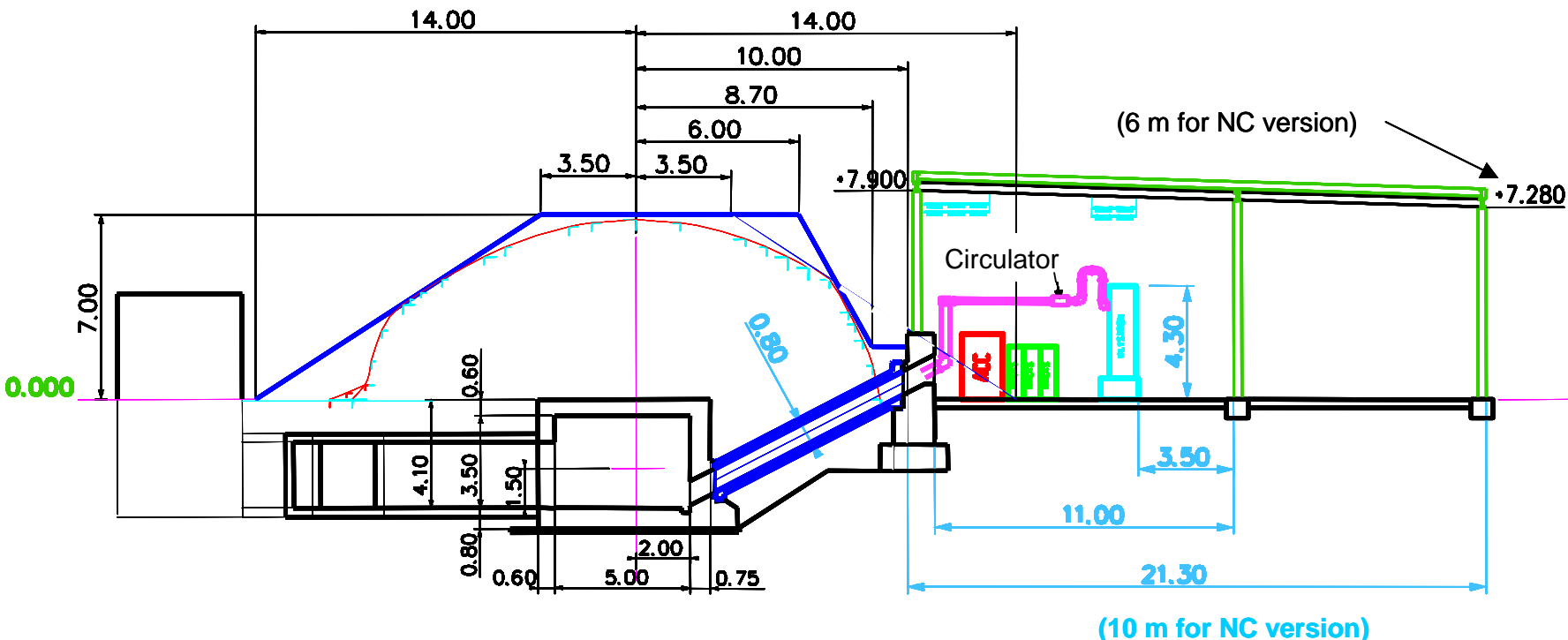
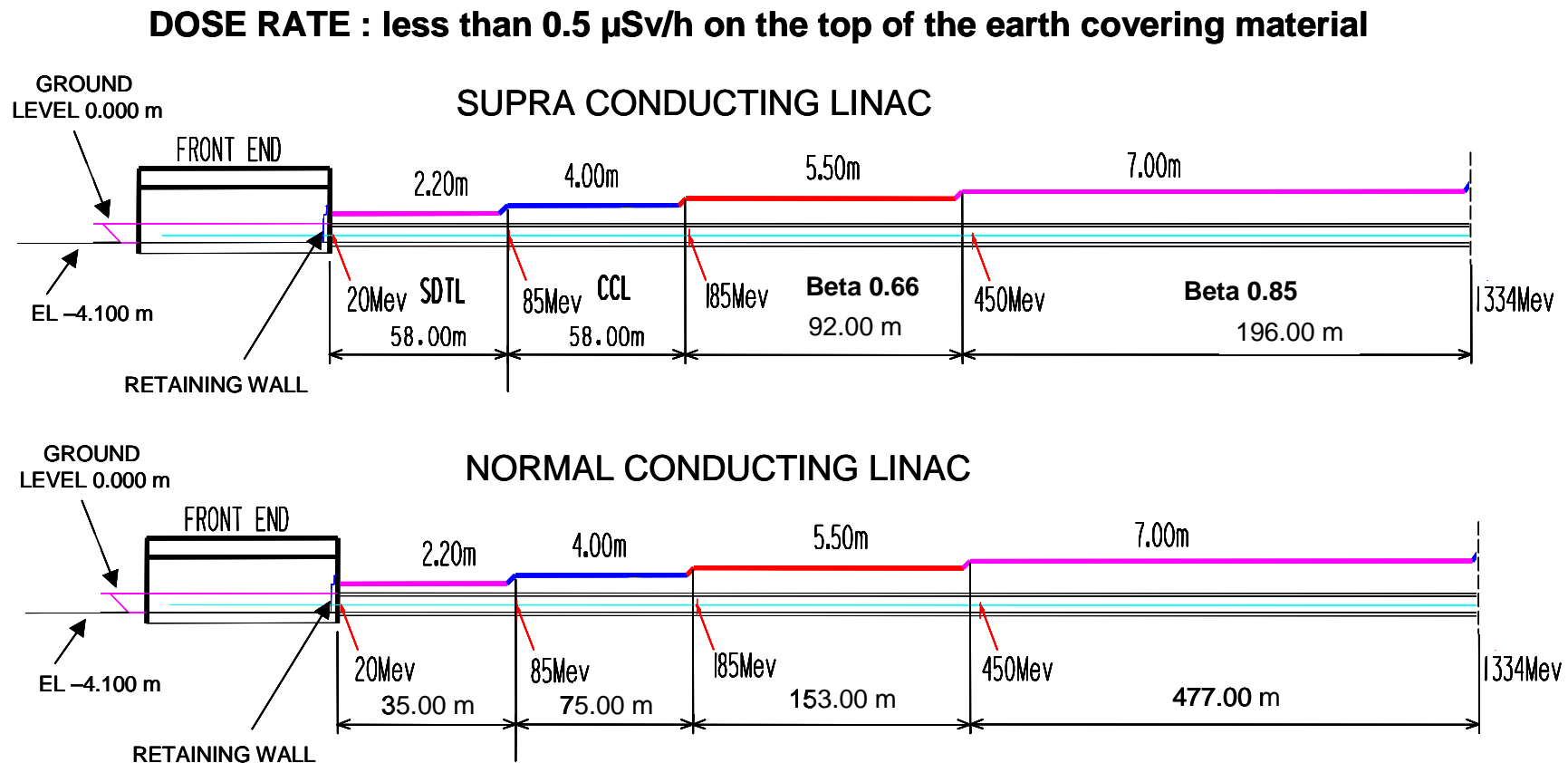


Figure 6-6: Thickness of earth material on top of the linac tunnel



6.4.2.1.2.1 Linac tunnel

The inside of the linac tunnel is 5 m wide by 3.5 m high. The sidewalls, roof and floor are made of reinforced concrete. The length is 740 m in the NC version and 415 m in the SC version. Cross sections of DTL, CCL and SC sectors of the linac tunnel are given in Figure 6-7 and Figure 6-8.

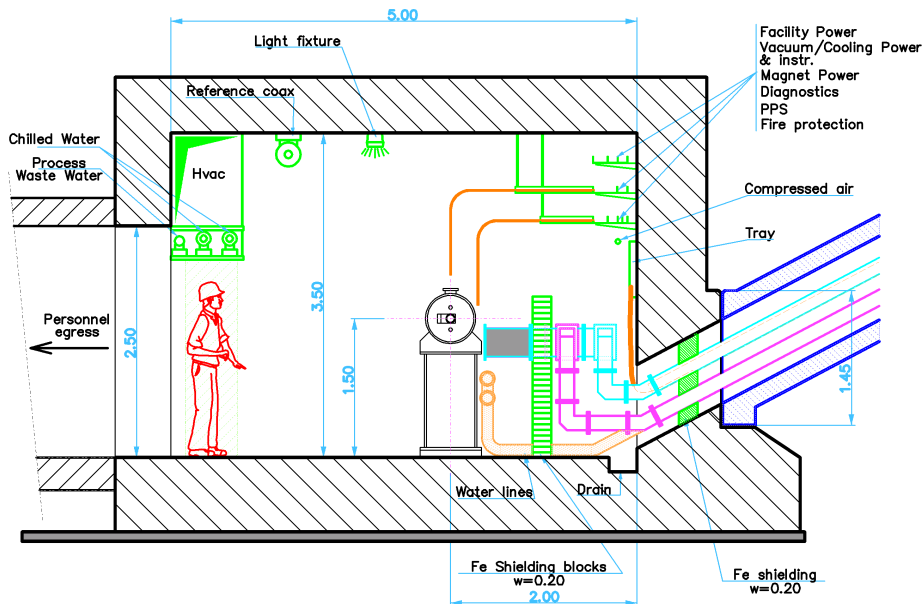


Figure 6-7: Cross section of the linac tunnel (NC sector)

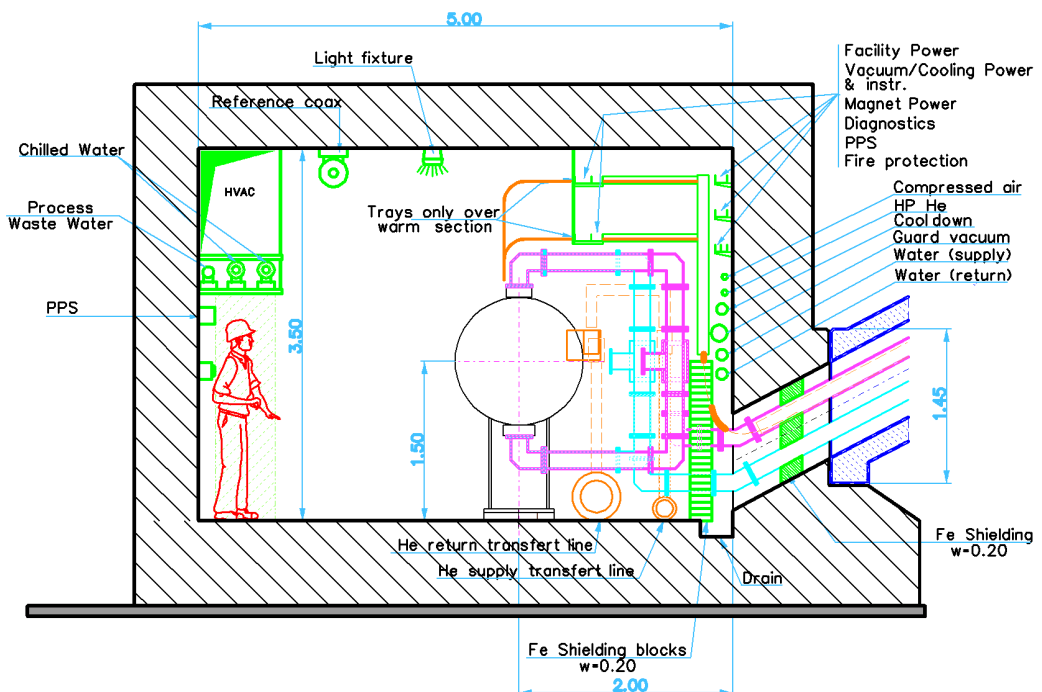


Figure 6-8: Cross section of the linac tunnel (SC sector)

The structure is watertight to prevent water intrusion and to provide containment for any water leaking from the cooling system within the linac tunnel.

Drains are provided around the tunnel foundations to collect and remove any groundwater that could reach the structure.

The beam axis is 1.5 m above the finished tunnel floor and at a 2 m distance from the southern interior wall of the tunnel.

The finished floor is 4.10 m below ground level.

Access to the tunnel for installation and maintenance is provided through the front-end building, four personnel access ways on the north side, and one access way for equipment at the end of the tunnel.

Heavy equipment would be moved through the linac tunnel by means of forklift trucks and wheeled dollies. There are no cranes inside the linac tunnel.

The four personnel access ways to the linac tunnel are designed with chicanes to protect people against radiation in compliance with the limit dose of $0.5 \mu\text{Sv/h}$, and to avoid having heavy doors at both ends of the access ways.

There is one personnel access way every 80 m.

As in the SNS design, wave guides, water pipes and other services pass through ducts between the klystron building and linac tunnel. From a financial point of view, ducts are preferable to large tunnels for both NC and SC options. However, for maintenance, special equipment is required (SNS design).

Ducts are made of thick concrete to accommodate all expected loading conditions including earth covering and differential ground settlement between the klystron building and the linac tunnel.

The tunnel structure, composed of 40 m long modules, has sufficient rigidity to meet the ground settlement limit requirement. Steel connectors are used at the junctions between module floor slabs. In this way, vertical displacement can be reduced and longitudinal expansion can be allowed for.

In the SC version, the tunnel is connected to the Central Helium Liquefier (CHL) building by four circular pipes.

To prevent local variations of temperature along the accelerator, we will use HVAC units regularly spaced along the linac tunnel. A temperature of $30 \pm 3^\circ\text{C}$ is expected when the beam is on and $24 \pm 3^\circ\text{C}$ when the beam is off.

In both cases, temperature must be maintained above the dew point.

The make-up air and exhaust system for the linac tunnel is integrated with that of other tunnels of the complex (ring tunnel, tunnel from linac to ring, tunnel from linac to long pulse target station, tunnel from ring to short pulse target station).

The air of the linac tunnel is scavenged from the front-end building to the central exhaust stack building.

The make-up air and exhaust system is off during operation of the accelerator. At the end of operation, it runs for a period of 70 minutes at a 7 air changes per hour rate, in order to obtain a low level of activation of ambient air and equipment after this period.

Afterwards, it runs at a 2 to 3 air changes per hour rate during the maintenance periods, until accelerator operations resume.

During operation, the linac tunnel is at a slightly negative pressure with respect to both ambient pressure and pressure in the klystron building.

Vessels to collect leakage of cooling water will be placed inside the linac tunnel.

6.4.2.1.2.2 Klystron building

This is a light building with a steel frame and cladding walls. The reinforced concrete floor slab is at ground level.

Inside dimensions are 10 m width x 6 m height and 740 m length for the NC option and 20 m width x 7.5 m height and 415 m length for the SC option.

A cross section of the klystron building is given in Figure 6-5.

Klystrons and other heavy pieces of equipment are moved on air pads and forklift trucks. There are two 3-tonne hoists, each of which covers half of the length of the klystron building. The klystron building is heated and air-conditioned to maintain the same temperature as in the linac tunnel ($30\pm3^{\circ}\text{C}$ when the beam is on and $24\pm3^{\circ}\text{C}$ when the beam is off).

Substations located inside this building will produce De-Ionised (DI) cooling water for the entire linac tunnel and klystron building.

6.4.2.2 Ring buildings and tunnels

This section covers the injection tunnel, achromat-arc tunnel, ring injection tunnel, accumulator ring hall and associated buildings [ESS-3, 2002] & [ESS-10, 2002].

Transfer lines and rings are designed for minimum loss, typically less than 1 W/m, allowing hands-on maintenance. Unavoidable losses will be concentrated in an area designed for active handling. Shielding is calculated for external radiation levels of less than $0.5 \mu\text{Sv/h}$.

The proposed design is based on the RAL's report of December 2001 with the following modifications [ESS-VolIII, 1996] & [ESS-1, 1996]:

- a) Increase in wall, roof and floor slab thickness, for rigidity reasons
- b) Replacement of tunnels by ducts for water pipes and electrical cables in order to reduce construction costs
- c) Addition of new personnel access to meet safety regulations
- d) New design for material access

A top view and a cross section of the accumulator ring hall and associated buildings are given in Figure 6-9 and Figure 6-10.

The ring tunnel and transfer lines are constructed of reinforced concrete. The inside dimensions of the ring tunnel are of 20 m width x 12 m height. The ring mean radius is 35 m.

The mean cross sections of the tunnels upstream of the rings are 5 m width x 5.5 m height allowing for adequate space for services, temporary shielding (during maintenance), personnel and material access. The mean radius of the accumulator ring hall is 42.5 m.

Six beam dumps serving the stripping foils in the achromat are grouped in two adjacent buildings providing all service and handling requirements, as shown in Figure 6-9. A large service building is located in the achromat arc for power, water service, equipment preparation, spares, storage and local service. This building is dedicated to achromat injection, achromat arc, ring injection tunnels and accumulator ring hall.

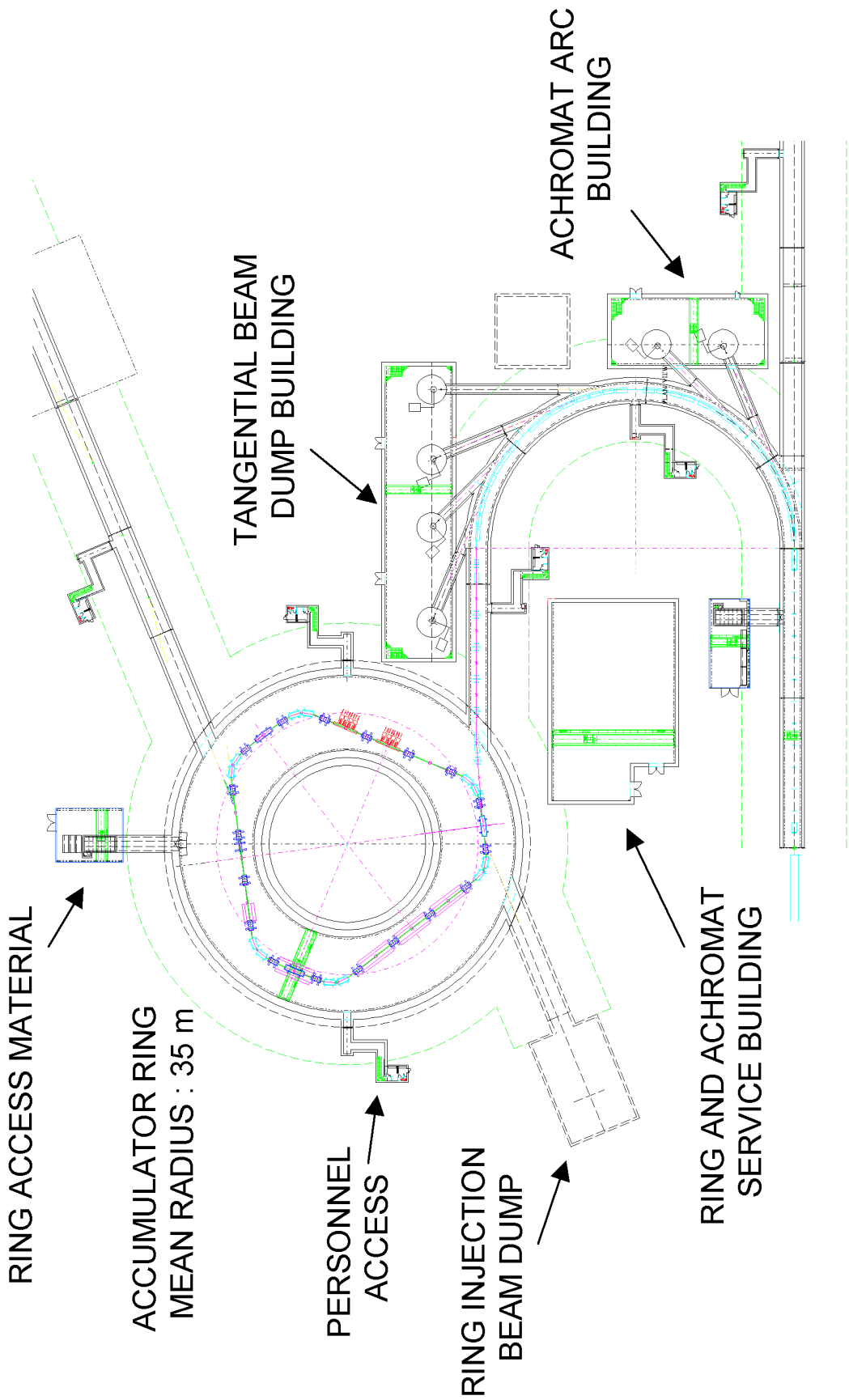


Figure 6-9: Top view of the accumulator ring hall and associated buildings

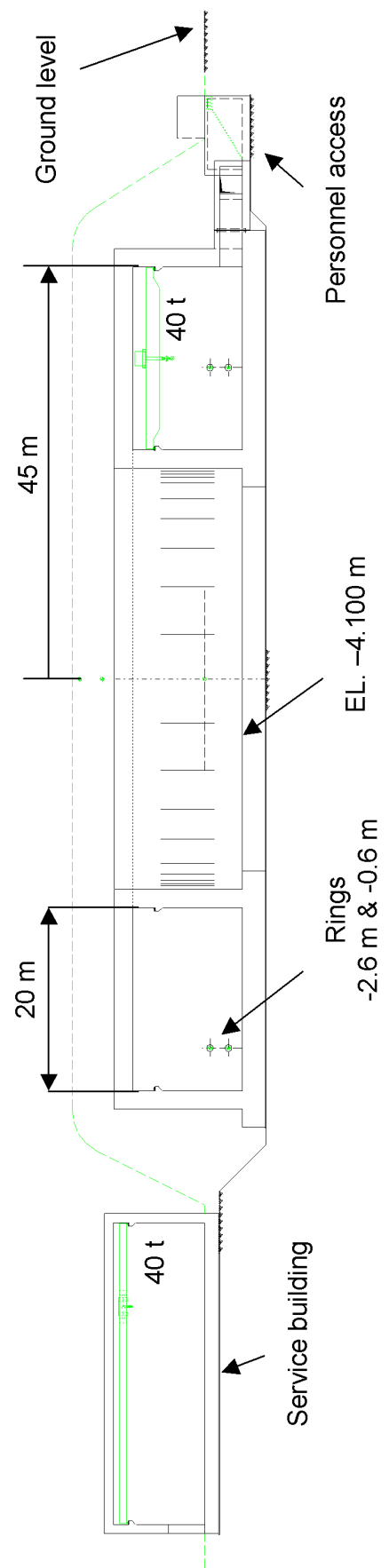


Figure 6-10: Cross section of the accumulator ring hall and associated buildings

All main tunnels have travelling cranes for removal and installation of components and will be accessed by heavily shielded slabs and doors.

The structure of accumulator ring hall is watertight and drains are provided around the tunnel's foundations.

The beam axis is 1.5 m above the finished floor of tunnels and accumulator ring hall and 2.6 m below ground level. The lower ring is at the linac beam height with the upper ring 2 m above.

Material access to the accumulator ring hall is through a light building and tunnel. To meet the $0.5 \mu\text{Sv/h}$ dose rate, we use a removable concrete slab in the building and a removable-shielded door between the tunnel and the accumulator ring hall. A cross section is given in Figure 6-11.

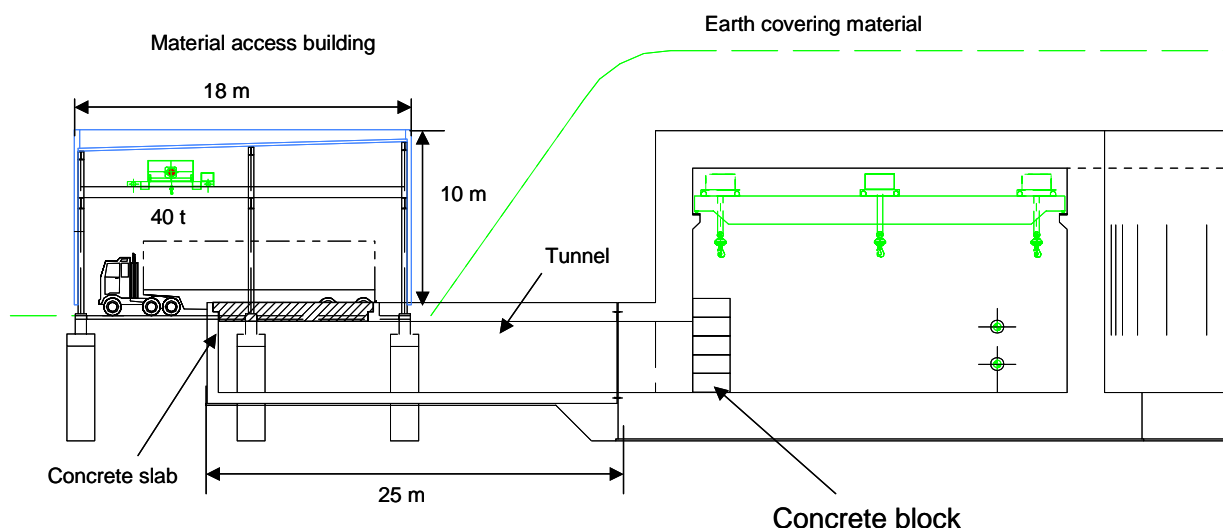


Figure 6-11: Material access to the accumulator ring hall

Equipment will be moved using a 40 tonne crane in the light building, a wheeled dolly (or air pad) in the tunnel and a 40 tonne or 20 tonne radial crane in the accumulator ring. The radial cranes, in the accumulator ring, will be remote controlled to minimize exposure to radiation. The beams left unstripped after the injection foils are transported via a tunnel to the beam dump.

To meet the ground settlement limit requirement, the tunnel structure has sufficient rigidity, and we opted for a reinforced apron.

The ventilation system is calculated for simple temperature and humidity control, no tunnel heating being considered necessary. We have assumed 10 % transfer of heat from the components into the air. Nominal air temperature is $30 \pm 3^\circ\text{C}$ when the beam is on and $24 \pm 3^\circ\text{C}$ when the beam is off.

6.4.2.3 Long pulse and short pulse target buildings

For the conventional facilities associated with the Long Pulse, we will assume a high degree of similarity with the Short Pulse.

Conventional facilities have to provide the target buildings required to support the neutron scattering research programmes. This includes providing the experiment facilities for the scattering instruments, meeting their space and utility requirements, providing proton beam line shielding and hot cell complex used for target system, and housing the electrical, cooling, waste and HVAC systems used to support the proton target, neutron moderators and experimental facilities in an appropriately shielded and serviceable environment.

Conventional facilities also have to provide beam dump buildings to house the beam dump targets.

A 3D view, two cross sections and a top view of the basement of target buildings are given in Figure 6-12, Figure 6-13, Figure 6-14 and Figure 6-15.

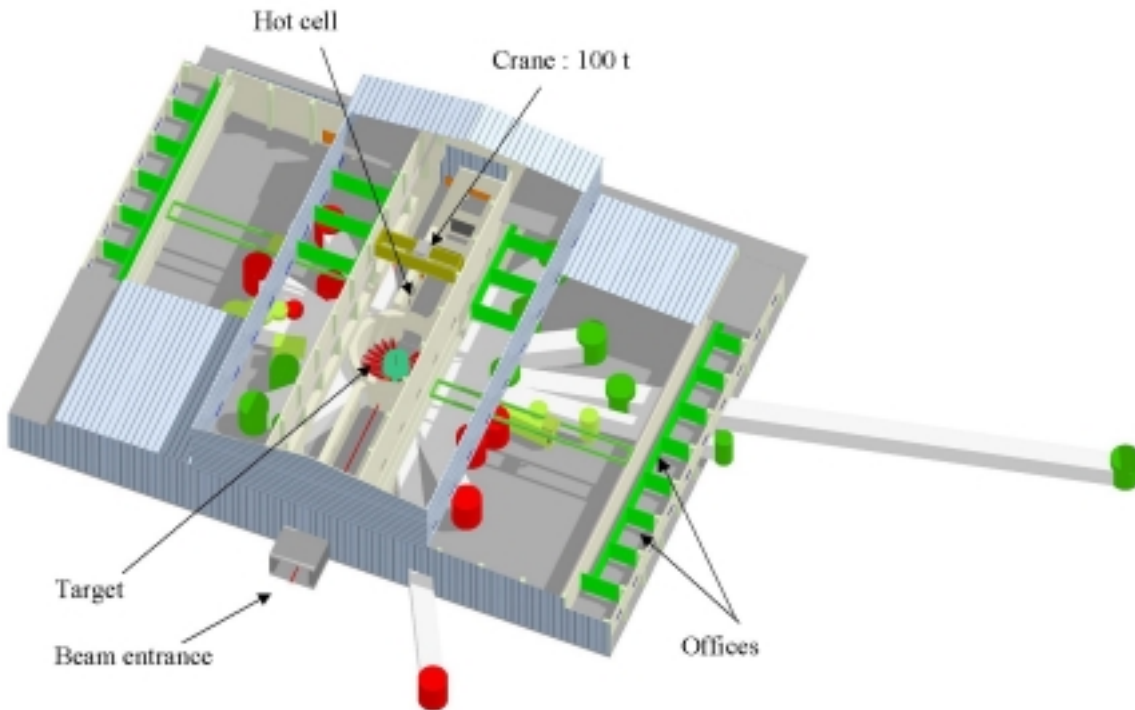


Figure 6-12: 3D view of the target buildings

Each target building consists of three main areas [ESS-4, 2002], [ESS-5, 2002], [ESS-11, 2002] & [ESS-12, 2002]:

- 1) The target systems complex, including parts of the proton beam tunnel, the target monolith (bulk shield) and mercury process loop room, the high bay, the maintenance hot cell complex with the waste handling system and basement and loft areas for the utility systems and storage. These parts of the building will be accessible to operation staff only and will be licensed in accordance with the rules applicable to radiation hazard areas.

- 2) Two experiment halls, one on either side of the target system complex, to house the neutron scattering instruments. These will be controlled areas with a low risk of contamination and accessible to users.

The two target buildings have a large main floor (62 m x 88 m) containing the target and the floor area for instruments.

The two target buildings will be multi-storey buildings.

We are designing the short pulse and long pulse target buildings to house the beam line shielding for 24 instruments each.

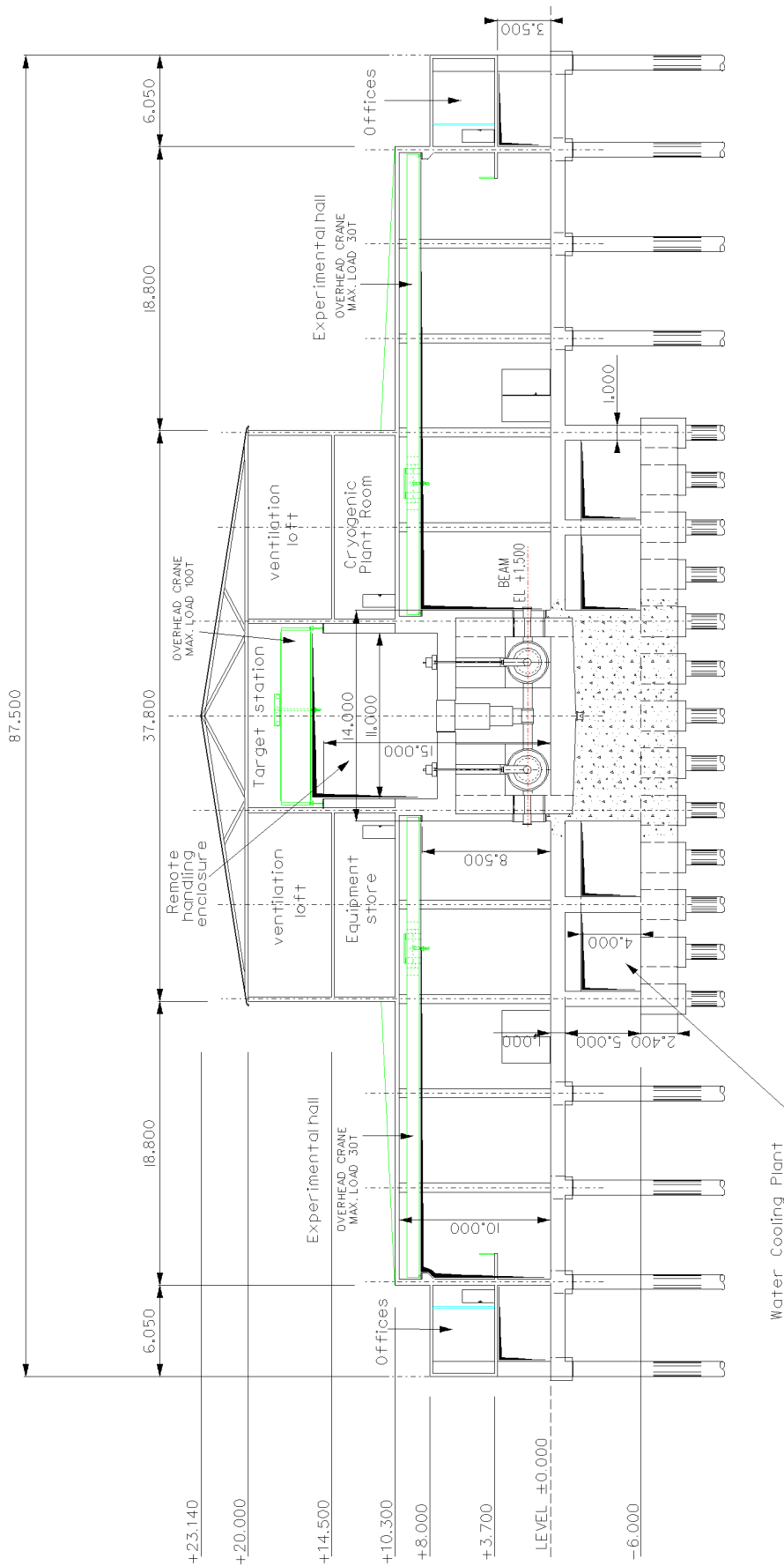


Figure 6-13: *Cross section of the target buildings*

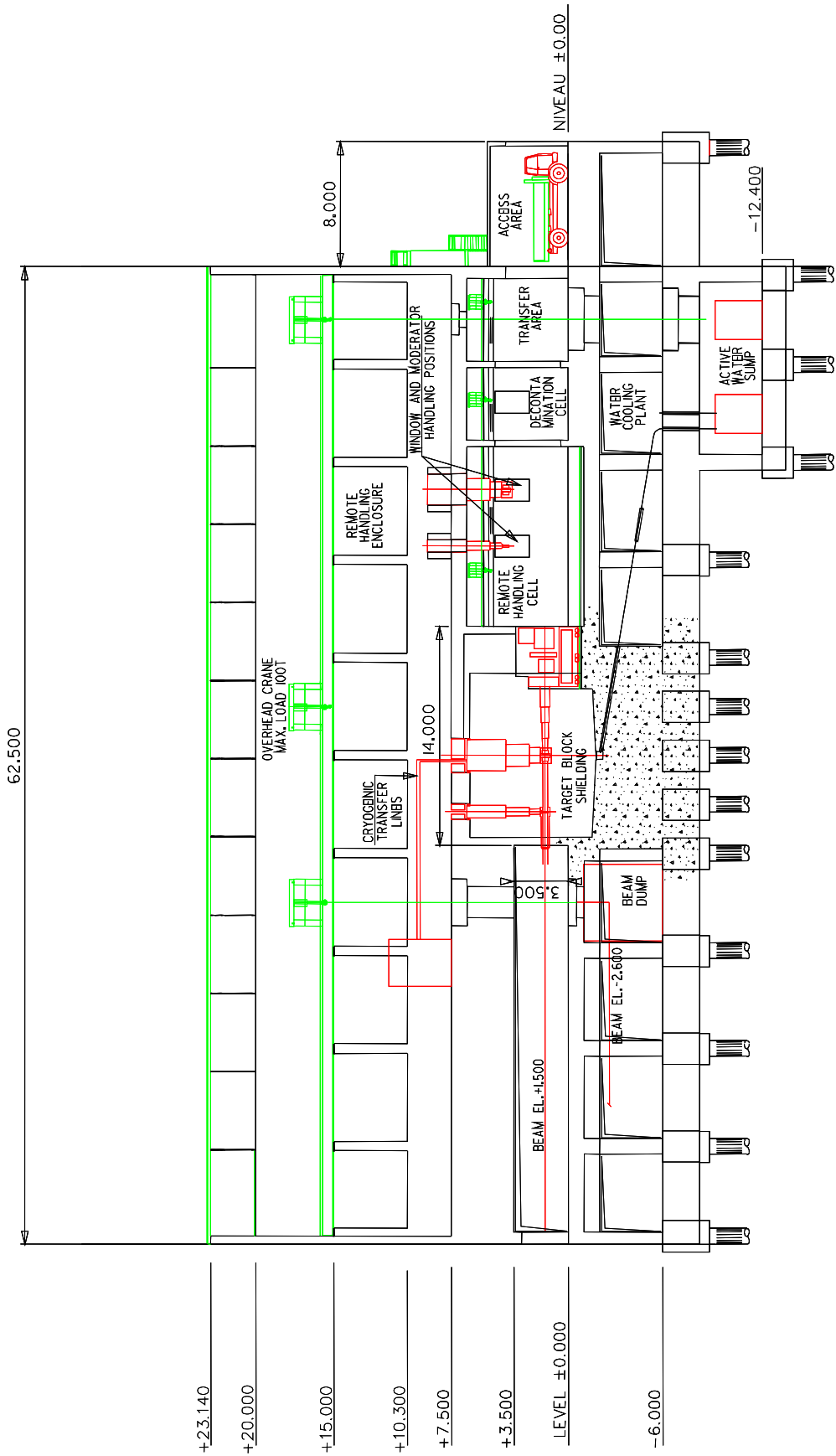


Figure 6-14: Longitudinal view of the target buildings

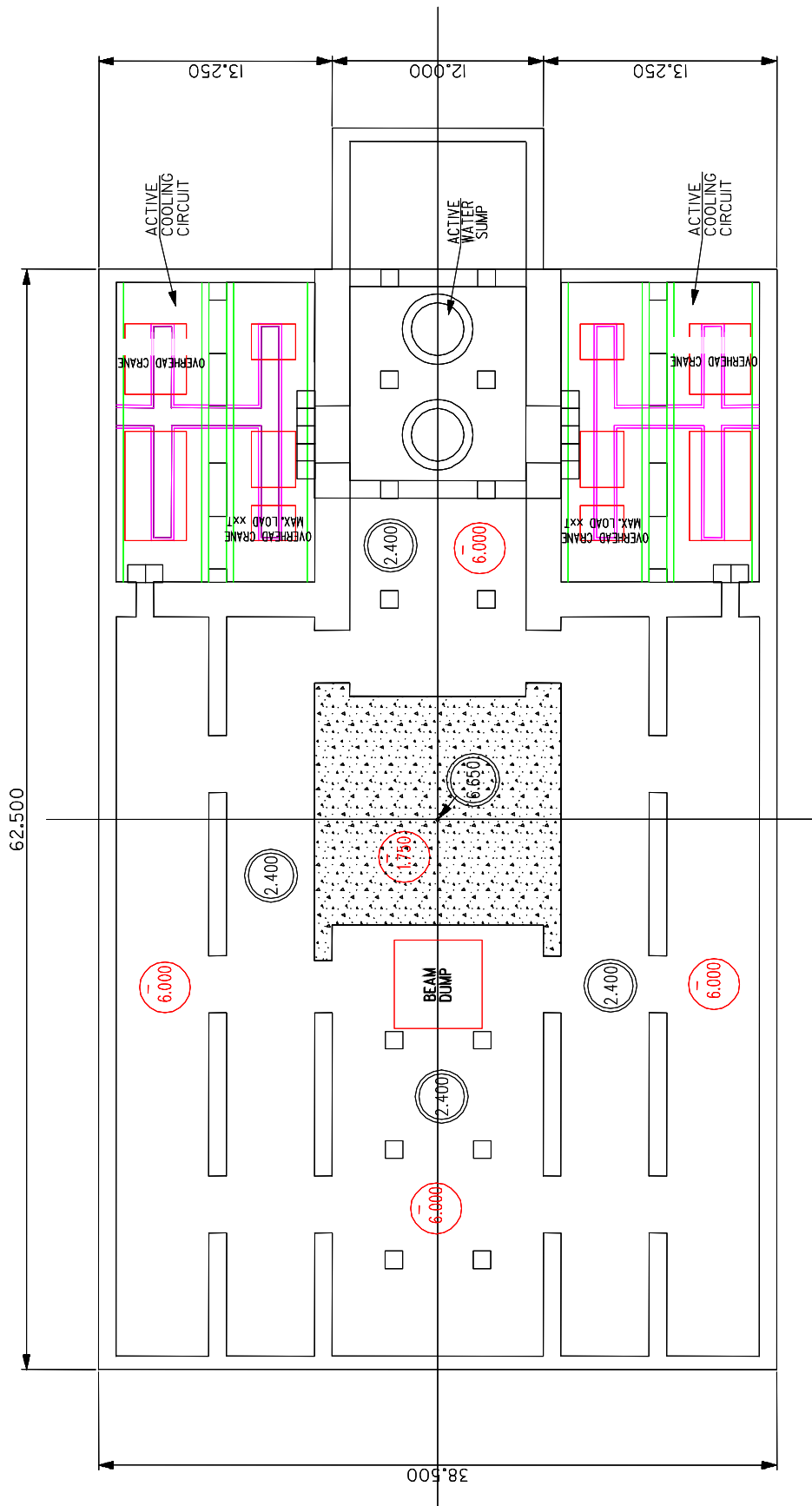


Figure 6-15: Top view of the target building basement

The horizontal proton beam, and its shielding tunnel, together with the target station and remote handling facilities, effectively occupies the middle of the building. A 30-tonne crane is provided on each side to install and service the major components of the neutron scattering instruments and beam lines. Each instrument will have a 1 tonne pillar crane to deal with light components such as sample environment equipment and dewars in the sample enclosures.

The proton beam is at a height of 1.5 m above the hall floor level. Office space, laboratories and support rooms will be provided at the sides of the main hall at the mezzanine level. This will allow beam lines to be extended outside the hall, under these rooms, in a straightforward manner, as required, without major disruption.

The controlled handling enclosure above the target station (high bay) will be equipped with a 100 tonne crane that can also handle the components of the proton beam line immediately upstream of the target. Plant and equipment rooms for the ventilation systems are positioned at high level along with the controlled high bay as shown on the cross-sectional view.

The water-cooling systems for the target, reflector, inner shield and the proton beam window will be housed in a shielded basement.

A drain for receiving active water is provided and is connected to a collection tank in the water plant cavern as shown in the longitudinal view.

Foundation drains will be provided around low-grade areas to intercept the groundwater liable to reach the structure. This water will be discharged after radiobiological analysis.

The target building main floor (62 m x 88 m) that carries the target and the instruments floor area, is configured to transfer the extremely heavy loads to the building foundations. The following scheme (Figure 6-16) shows assumed floor load distributions. We will have to use piles or big apron, depending on the site characteristics, to meet ground settlement requirements.

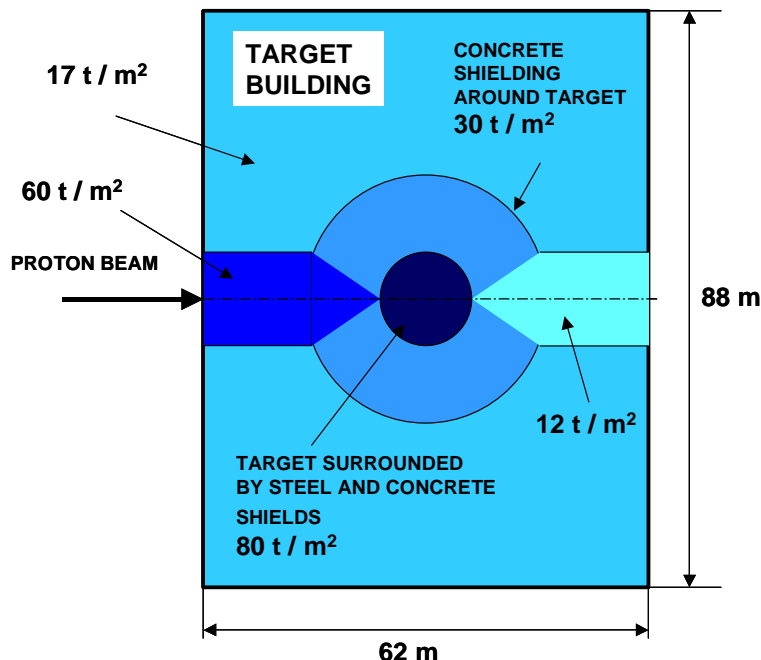


Figure 6-16: Floor load distribution

For cost evaluation, we have considered a soil with the following reference characteristics:

- Sand
- Bearing pressure limit: 2.5 MPa
- Angle of Friction: 35°

and a site with low seismic activity (see above, section on site characteristics).

Small satellite buildings that house the instruments and beam lines which extend beyond the enclosed instrument floor will be included in the scope of instrument systems. These buildings will also provide the concrete base that is to support the neutron beam tube and its associated shielding.

There is a compressor building, located close to the target stations, that houses the He-compressor supplying high-pressure helium to the cryogenics equipment in the loft area of the target buildings.

A target control room includes space for operator workstations, equipment racks and control equipment that is safety class and safety significant.

The HVAC confinement ventilation system will be designed to complement the physical barriers and to provide an integrated containment system to minimize the spread of radioactive contamination.

There will be four separate types of air exhaust systems, one serving the hot cells, one the nuclear portion of the facility, one the non-nuclear portions, and one the low-contamination risk areas of the building such as the instrument floor, operation control room, electrical and mechanical equipment room.

During operation, the nuclear facility area pressure will be at a slight negative pressure with respect to both ambient pressure and pressure of the non-nuclear facility area. A slight negative pressure relative to ambient pressure will result in the continuous exhaust of air from this region.

The ventilation of the hot cells will be connected to high-efficiency filters.

Air-conditioned spaces will be maintained at about $22 \pm 1^\circ\text{C}$.

6.4.2.4 Central Office and Laboratory (COL) building

This building is a multipurpose facility providing offices, reception space, auditorium, restaurant, library, laboratories central control room, central electronic room, telecommunication/alarm systems, etc.

The design allows for future extensions.

The building has approximately $23,500 \text{ m}^2$ of floor space. From the point of view of architecture, it consists in three four-storey wings connected to a five-storey central tower.

There are three entry points, the main entrance, a public entry from the West on the layouts, and two others from the East.

This building houses about 650 people with some extra space for visitors and users [ESS-13, 2002].

6.4.2.5 Central Helium Liquefier (CHL) building

For the building housing the CHL, it was decided to adopt the SNS option. The main features of this installation (electrical power, HVAC, cooling, ground load capacity) were extrapolated from 2.4 to 10 MW.

The CHL will provide liquid helium for the linac. It houses compressors, cold box, local control room and all associated mechanical and electrical systems and equipment necessary to supply cryomodules in the linac. The outside walls will have sound suppressing vents. Closely outside the building, we foresee gaseous helium storage tanks with purifier systems, a liquid helium dewar a nitrogen dewar as well as parking and unloading areas for helium and liquid nitrogen trailers.

This building is 40 m long by 18 m wide and 10 m high. The ground slab under the compressors is decoupled from the other slabs.

6.4.2.6 Radio Frequency (RF) test facility

This building provides an area to test klystrons, RF power components and warm accelerating structures. There is an RF test laboratory, an electrical and instrumentation workshop and a storage area.

We will also be able to perform, in this building, tests of the cryogenic cavity modules used in the linac.

The cryogenic cavity modules will be assembled outside the facility but tested in the building.

This building is 60 m long by 30 m wide and 10 m high.

6.4.2.7 Radioactive waste management centre building

Radioactive waste will be produced in several parts of ESS site, but mostly from the target stations.

We will find the following types of radioactive waste:

- Low level waste : coveralls, overshoes, etc.
- Irradiated water from cooling systems
- Irradiated equipment such as seals, accelerator components, etc.
- Highly active components such as the mercury target vessels and proton beam windows
- Waste from active machining

The building is 80 m long by 40 m wide and 10 m high. It houses equipment and rooms to perform activities such as shredding, compaction, storage and packaging.

It will be serviced by the process waste system.

6.4.2.8 Process waste collection system and conventional liquid waste system

This system will collect wastewater from normal operations and from any anticipated abnormal occurrences.

It consists in diversion tanks, underground piping and manholes, storage tanks and a tanker loading station with single-contained process waste piping.

The piping layout will be designed for gravity flow from collection manholes in the ESS area to the process waste storage tanks.

The conventional liquid waste system will transfer cooling tower blow-down to a storm water basin for retention and stabilization prior to release outside (ditch, river, etc.).

6.5 DETAILED DESCRIPTION OF THE MAIN GENERAL SERVICES

6.5.1 Electricity

The host country's grid system will have to supply at high voltage, 120 MW in the SC version and 145 MW in the NC version with possible extension of several MW for other uses of the facility.

A layout of the electrical distribution network is given in the Figure 6-17. As shown on this layout, there are three 70 MVA transformers. One of them is a spare to avoid being confronted with a very long delivery time in the event of failure.

We have designed 30 electrical substations connected in 10 loops [ESS-7, 2002] , [ESS-8, 2002] & [ESS-14, 2002]. This choice is dictated by maintenance considerations and also to facilitate future extensions.

The loops feeding the process substations are separated from the one feeding utilities or conventional buildings.

One substation uses a dedicated building; the others are housed inside existing buildings.

Distribution voltages are power load dependent: about 20 kV for > 500 kW, about 5 kV between 250-500 kW and 400 V for < 250 kW.

Two well-separated high voltage lines will secure the power supply to the site. In addition to this, several emergency on-site AC power supplies and Uninterruptible Power Supplies (UPS) will be installed to make sure that some sensitive pieces of equipment are always powered.

LOOPS AND SEPARATE ELECTRICAL SOURCES FOR CONVENTIONAL BUILDING USE AND MACHINE / EXPERIMENTAL USE

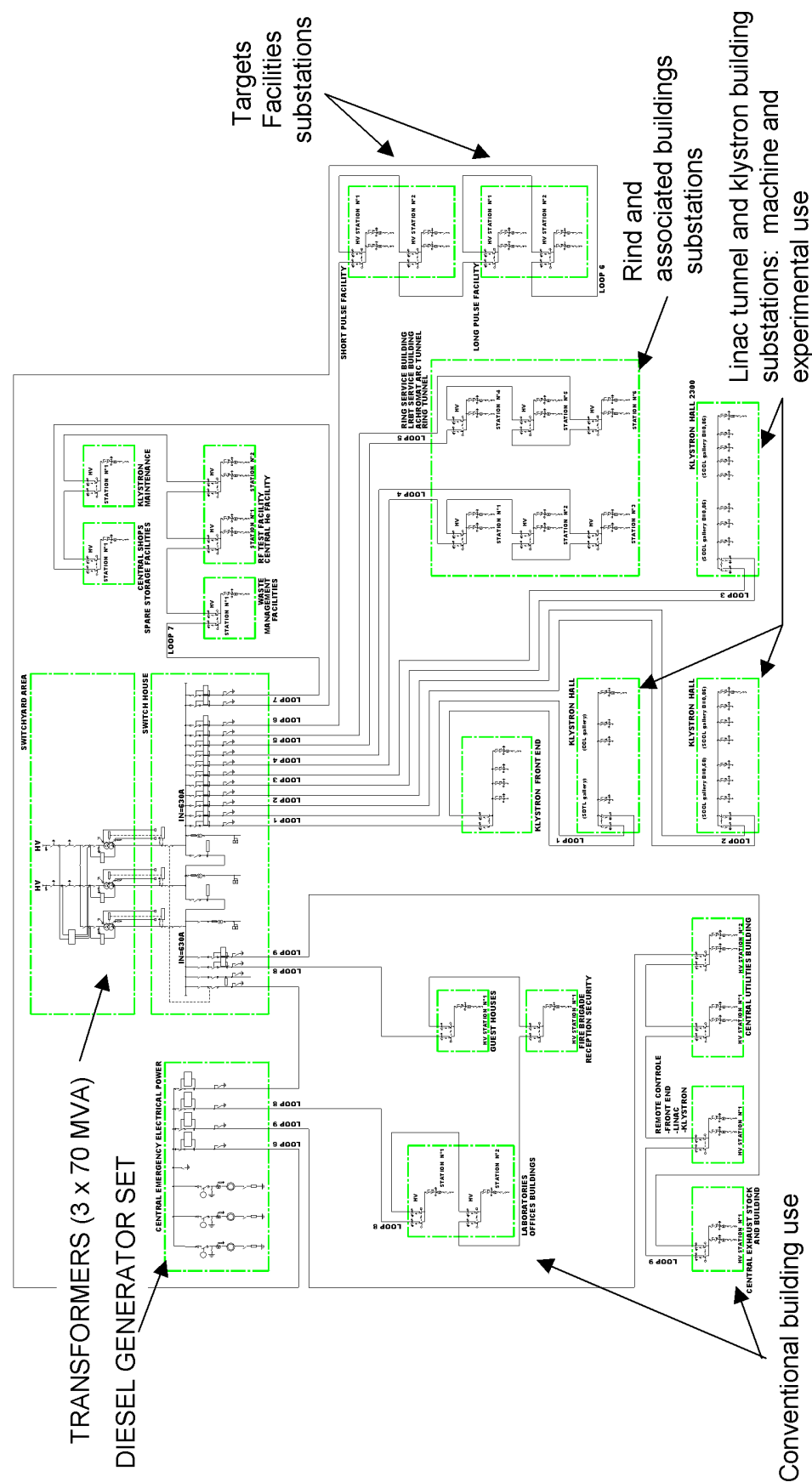


Figure 6-17: Layout of the electrical distribution network

The emergency on-site AC power supply system will consist of nine diesel generators, installed in a building next to the switchyard. These generators will provide 25 % of the total electrical power.

The essential loads supplied are:

- Safety interlock system
- Vacuum system, instrumentation and controls
- Main control room servers and hardware
- Selected telecommunication equipment
- Alarm systems, including fire alarm
- Stand-by ventilation fans in tunnels
- Emergency lighting systems

It will be capable of automatically supplying the connected loads in the event of power failure.

The UPSs distribute their power to loads requiring a continuous source of power. Such loads are considered essential to providing for the personnel safety and/or preventing severe economic loss, due to damaging of equipment, in the event of primary failure. Loads requiring UPS systems include several of the previously listed items:

- Safety interlock system
- Vacuum system instrumentation and controls
- Main control room servers and hardware
- Selected telecommunication equipment
- Alarm systems, including fire alarm
- Critical power supply controls and protection

We anticipate 10 units, 600 kVA each, with 10 minutes autonomy.

The facility electrical power system is designed to mitigate the effects of power harmonics and power factor produced by non-linear loads on both the electrical distribution equipment and other loads on the system.

6.5.1.1 Grounding and lightning protection

The grounding and lightning protection system will provide:

- An electrically safe facility environment for personnel
- A protection against lightning-induced and switching transients to ensure proper operation of electrically energized equipment, and to ensure reliable operation of building systems.

The grounding is made by 10 m x 10 m grids of 30 mm x 2 mm copper strips laid in the concrete basements of the buildings. All buildings are connected together.

The same grids on the walls and roofs with copper lightning points on the top make the lightning protection system.

6.5.1.2 Raceway system

A raceway system including conduits, cable trays, and duct banks, will provide separate cable trays for low level signal, normal signal, fibre optics and computer connections, personnel protection system and power wiring without mixing the various types.

6.5.2 Water cooling systems

Due to the cooling power required, for financial reasons, we have decided that there should be two different central utility buildings, which makes it possible to use smaller, standard items of equipment (pumps, pipes, etc.) which is not the case if there is only one building [ESS-7, 2002], [ESS-8, 2002] & [ESS-14, 2002].

For reliability and maintenance reasons, we have planned for water loop distribution both for the chilled and tower water.

In the event of loss of one central utility building, the other building can provide about 60 % of the total power required.

The central utility buildings house the tower water system, chilled water system, pumps and compressed air system serving the site.

6.5.2.1 Tower water system

The tower cooling water system provides adequate coolant flow and pressure to remove heat from the chilled water system, DI cooling water system as well as other water-cooled equipment throughout the facility.

For cost evaluation, we assumed that the system would have a maximum coolant temperature of 30 °C with external conditions of 32 °C.

A layout showing the tower water location on the site is given in Figure 6-18.

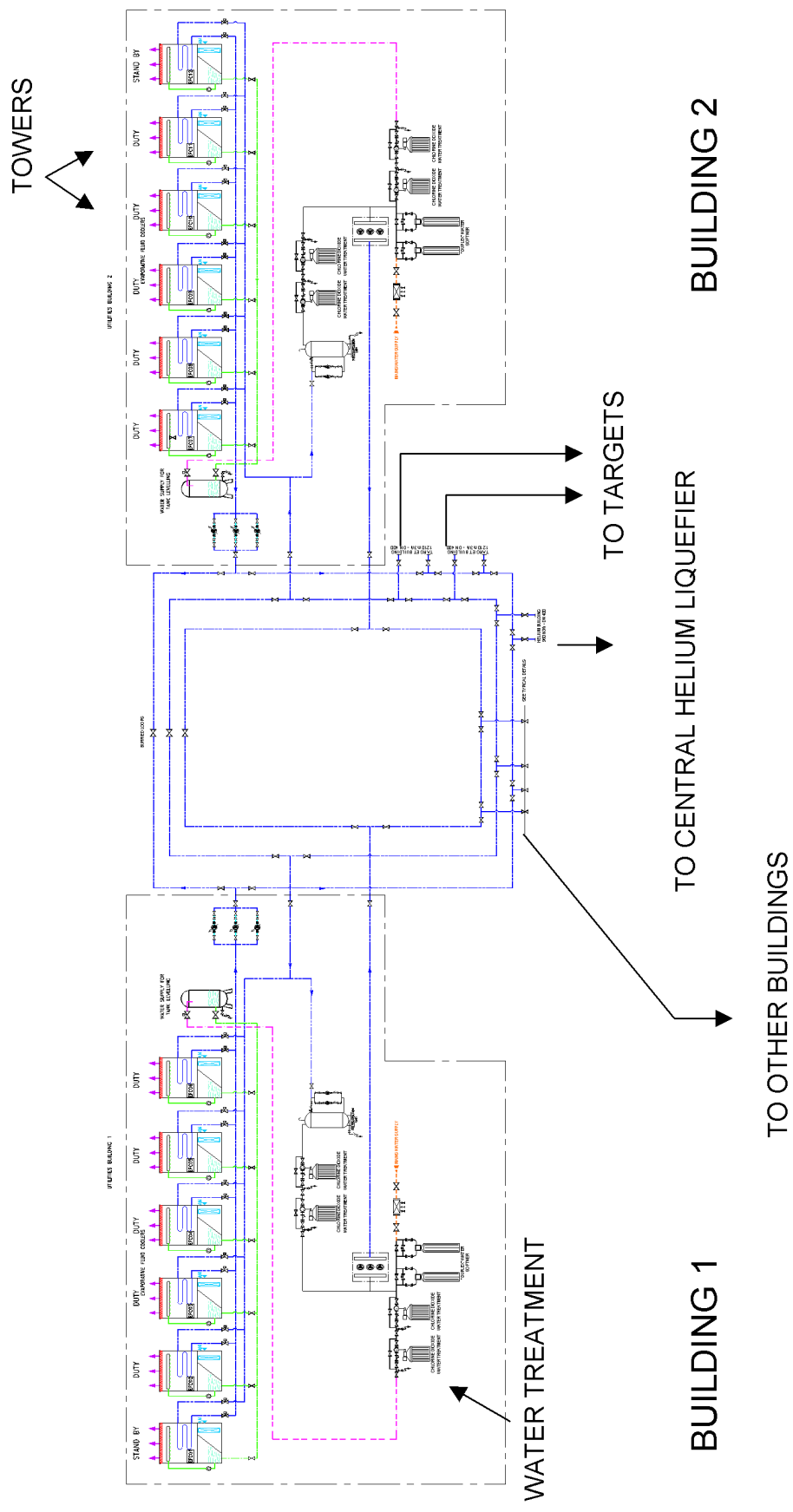


Figure 6-18: Layout of the tower water distribution network

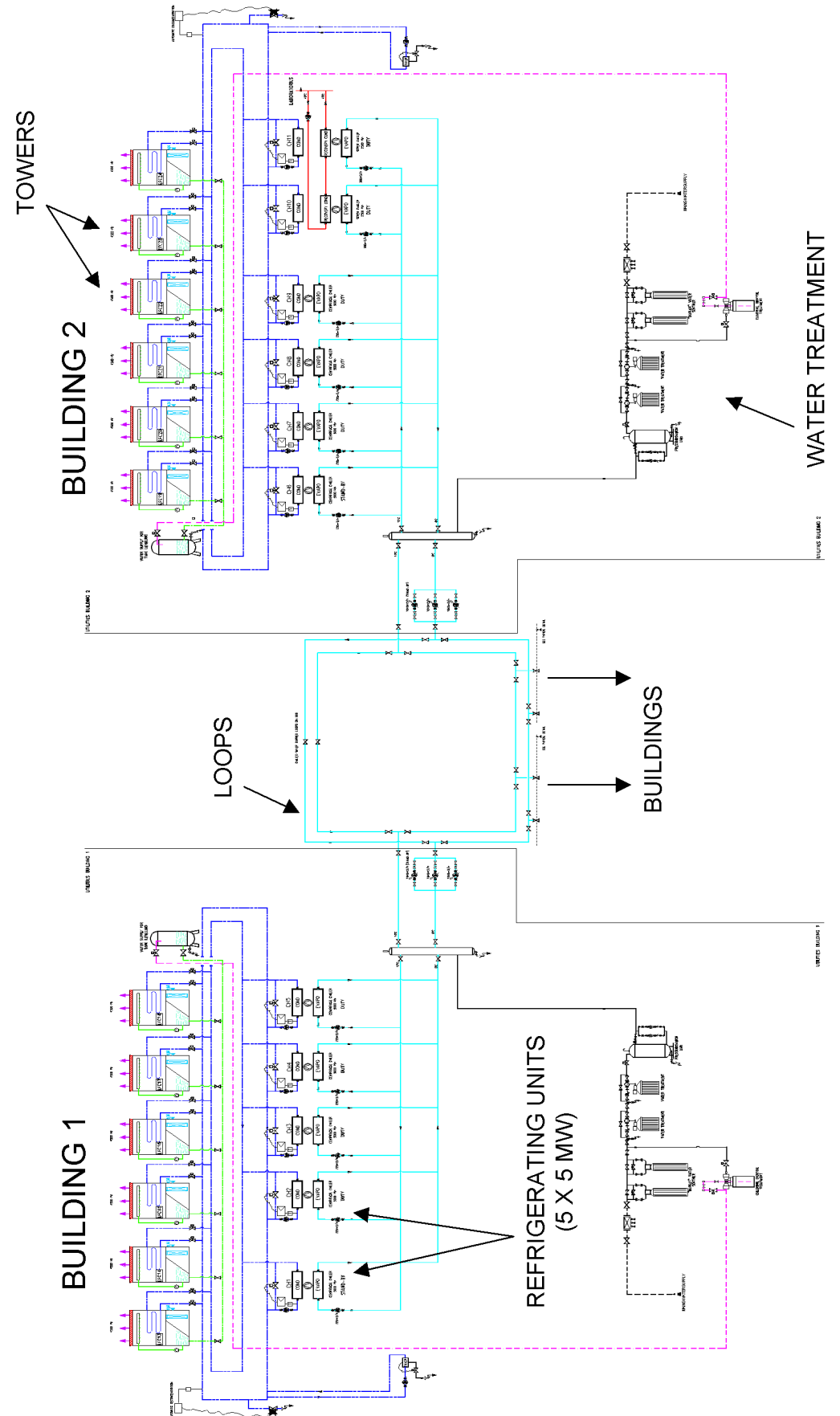


Figure 6-19: Layout of the chilled water distribution network

6.5.2.2 Chilled water

The chilled water cooling system provides adequate chilled water flow and pressure to remove heat from the HVAC air handling units, the activated and inactivated DI chilled water systems and other chilled water users.

The system will be capable of operating all water chillers between 20 % and 100 % of full chiller capacity to meet varying chilled water demands, and will reject heat generated by the chillers to the tower cooling water system.

We plan for 11 chiller units, of 5 MW each including one as a spare.

The chilled water system is designed to have a temperature of 6 °C at the outlet of chiller units and 12 °C on the return.

The evaporative cooling towers for tower water and chilled water will be located on the roof of the central utility buildings and orientated with due regard for the prevailing winds to minimize fogging, icing, noise, etc.

There will be a blow-down subsystem that conveys the blow-down to the conventional liquid waste collection system.

A layout showing the chilled water location on the site is given in Figure 6-19.

6.5.2.3 Compressed air system

The compressed air system provides pressurized air to instruments pneumatic devices, and services air outlets throughout the facility. The source consists of four compressors with a load capacity of 1 000 Nm³/h each. Each of them will provide a 10 bar air supply.

The substations are located inside existing buildings. Each of them will have a capacity of 250 Nm³/h. Air expansion from 10 to 6 bar will take place in these substations.

6.5.3 Heating, Ventilation and Air Conditioning (HVAC)

The HVAC site service includes:

- Above-ground and underground ductwork connecting from individual buildings to appropriate ductwork
- Central air handling units inside existing buildings or shared by several buildings
- Centralized exhaust stack

HVAC requirements associated with process (accelerators, targets, etc.), offices, laboratories and test areas have been allowed for in the separate building specifications [ESS-7, 2002], [ESS-8, 2002] & [ESS-14, 2002].

The centralized exhaust stack is of prefabricated concrete construction. The platform is large enough to provide room for personnel and adequate clearance for maintenance. The stack is sized to handle the maximum simultaneous exhaust airflow from the tunnels and beam dump

buildings. The primary and secondary confinement systems of the target buildings have their own exhaust. The stack will have a minimum size of 25 m.

The boiler house provides hot water with adequate flow, temperature, and pressure for heating COL building, guesthouse, workshops and other parts of conventional buildings. The buildings accommodating the process are heated during the maintenance period by electrical coils.

6.5.4 Roads, parking space, hard standing and trenches

All roads are specified 10 m wide with a load carrying capacity of 100 tonnes [ESS-15, 2002]. Total length of roads is 12 km with a NC and 11 km with a SC linac. Parking for 800 vehicles, 16 buses and adequate extra hard standing for storage of shielding, overflow parking and temporary office location amount to 15 hectares, and this is included for in the estimates. Allowance has been made for pavements, kerbing, drainage and street lighting. Electrical cables, water pipes, sewer, etc. are buried underground in trenches. The total length of trenches is 10 km.

6.6 APPENDIX

Table 6-1: Summary of the AC power requirements for the sc and nc linac

Buildings	Electrical power requirements for the sc linac (MW)	Electrical power requirements for the nc linac (MW)
Front end, linac and klystron buildings	46	75.5
CHL and SRF test buildings	7	0
Ring, associated buildings and transfers to rings and targets	23	23
SP target and associated buildings	8	8
LP target and associated buildings	8	8
COL building	2.5	2.5
Central utilities building and other conventional facilities	12.5	18
TOTAL	107	135

Table 6-2: Summary of the DI and tower water requirements for the sc linac

Buildings	DI water requirements for the sc linac (MW)	Tower water requirements for the sc linac (MW)
Front end, linac and klystron buildings	22	34.5
CHL and SRF test buildings	0.5	6.5
Ring, associated buildings and transfers to rings and targets	20.5	22.5
SP target and associated buildings	0.1	11
LP target and associated buildings	0.1	11
COL building	0.5	6.5
Central utilities buildings	0	
TOTAL	43.7	92

Table 6-3: Summary of the DI and tower water requirements for the nc linac

Buildings	DI water requirements for the nc linac (MW)	Tower water requirements for the nc linac (MW)
Front end, linac and klystron buildings	45	64
CHL and SRF test buildings	0	0
Ring, associated buildings and transfers to rings and targets	20.5	22.5
SP target and associated buildings	0.1	11
LP target and associated buildings	0.1	11
COL building	0.5	6.5
Central utilities buildings	0	
TOTAL	66.2	115

Table 6-4: Main buildings in the conventional facilities programme

No.	Function & Type	Dimensions L (m) x W (m) x H (m)	Remarks	Cranes (tonnes)	Special services
2110	Front End	78 x 62 x 16	Housed sources, RFQs, DTL and funnel (20 MeV) Retaining wall	70	House make-up air unit for the linac tunnel
2200 NC	Linac tunnel for NC	740 x 5 x 3.5 (Inner measurement)	Houses accelerator (CCDTL, CCL1, CCL2A, CCL2B) Concrete and earth	No crane Special handling tooling	Wave guides and service ducts Access without heavy door
2200 SC	Linac tunnel for SC	415 x 5 x 3.5 (Inner measurement)	Houses accelerator (SDTL, CCL, SC β 0.66, SC β 0.85) Concrete and earth	No crane Special handling tooling	Wave guides and service ducts Access without heavy door Space at the end of linac for a spare cryomodule
224X	Personnel access to linac tunnel: Building (1) and tunnel (2)	(1) 8.5 x 4.5 x 4 (2) 24 x 2 x 2.5	Houses radiological control Steel frame for building and concrete and earth for tunnel	No crane	

(Continued on next page)

Table 6-5: Main buildings in the conventional facilities programme (continued)

No.	Function & Type	Dimensions L (m) x W (m) x H (m)	Remarks	Cranes (tonnes)	Special services
2300 NC	Klystron hall for NC	740 x 10 x 6	Houses RF system, power supplies, HVAC etc. Steel frame	No crane Special handling tooling: air pads and 2 x 3-tonne hoists	
2300 SC	Klystron hall for SC	415 x 21 x 8	Houses RF system, power supplies, HVAC etc. Steel frame	No crane Special handling tooling: air pads and 2 x 3-tonne hoists	
2600	Central Helium Liquefier	40 x 18 x 10	Houses cryogenic system and compressors to provide liquid He to linac Steel frame	10	A decoupled slab for compressors
2700	RF test facilities	60 x 30 x 10	Provide space and equipment to process, assemble and test the cryogenic cavity units Steel frame	10	Shop areas in clean rooms
3100	Achromat injection	80 x 5 x 5.5	Concrete and earth Services in the ring service building (3420)	25	Equipment and personnel access (3103) Active drains

(Continued on next page)

Table 6-6: Main buildings in the conventional facilities programme (continued)

No.	Function & Type	Dimensions L (m) x W (m) x H (m)	Remarks	Cranes (tonnes)	Special services
3103	Achromat injection access: Building (1) and tunnel (2)	(57 24 x 11 x 10 (2) 18 x 3.5 x 3.5	Steel frame for building Concrete and earth for tunnel	25	
3200	Achromat arc tunnel	133.5 x 5 x 5.5	Houses dipoles, quadrupoles etc. Concrete and earth	10	Active drains Beam dump tunnel
3210	Personnel access to achromat arc tunnel: Building (1) and tunnel (2)	(57 8.5 x 4.5 x 4 (2) 24 x 2 x 2.5	Steel frame for building Concrete and earth for tunnel	No crane	
3280	Achromat arc building	45 x 20 x 14	Houses dumps Steel frame with retaining wall	25	Active drains
3290	Tangential beam dump building	80 x 20 x 14	Houses dumps Steel frame with retaining wall	25	Active drains
3400	Accumulator rings hall	Diameter: 90	Houses rings Concrete and earth	40 (radial) 20 (radial)	Active drains
3410	Ring injection tunnel	57 x 5 x 5.5 (57 m between end of achromat arc tunnel and entrance of ring building)	Houses dipoles, quadrupoles etc. Concrete and earth	25	Active drains

(Continued on next page)

Table 6-7: Main buildings in the conventional facilities programme (continued)

No.	Function & Type	Dimensions L (m) x W (m) x H (m)	Remarks	Cranes (tonnes)	Special services
3415	Personnel access to ring injection tunnel: Building (1) and tunnel (2)	(1) 8.5 x 4.5 x 4 (2) 24 x 2 x 2.5	Houses radiological control Steel frame for building Concrete and earth for tunnel	No crane	
3420	Ring and achromat service building	55 x 35 x 12	Houses power supplies and all other general services for: rings, ring injection, achromat arc and achromat injection Steel frame	25	Active drains
3430	Ring access hall: Building (1) and tunnel (2)	(1) 18 x 15 x 10 (2) 25 x 3.5 x 3.8	Steel frame for building Concrete and earth for tunnel	40	
3440	Ring injection beam dump	30 x 20 x 15		45	
3450 3451	Personnel access to accumulator rings hall: Building (1) and tunnel (2)	(1) 8.5 x 4.5 x 4 (2) 24 x 2 x 2.5	Houses radiological control Steel frame for building Concrete and earth for tunnel	No crane	
3500	RF power	30 x 20 x 12	Steel frame	10	Active drains
3600	Target helium compressor building	20 x 20 x 10		5	

(Continued on next page)

Table 6-8: Main buildings in the conventional facilities programme (continued)

No.	Function & Type	Dimensions L (m) x W (m) x H (m)	Remarks	Cranes (tonnes)	Special services
4100	RTBT tunnel	170 x 5 x 5.5	Houses equipment for transfer line between ring and SP target Concrete and earth	10	Active drains
4300	Personnel access to RTBT tunnel: Building (1) and tunnel (2)	(1) 8.5 x 4.5 x 4 (2) 24 x 2 x 2.5	Houses radiological control Steel frame for building Concrete and earth for tunnel	No crane	
4600	RTBT service building	25 x 10 x 5	Houses power supplies and all other general services for: rings, ring injection, achromat arc and achromat injection Steel frame	25	Active drains
4700	Target station SP (1) Central Hall (2) Experimental Hall (3) Ventilation loft etc. (two levels)	(1) 62 x 14 x 20 (2) 62 x 37 x 10 (3) 62 x 12 x 10	(1) Houses target, hot cells (nuclear part) Concrete walls (2) Houses instruments and associated equipments; Steel frame (3) Houses services (ventilation etc.) Steel frame	100 (central hall) 2 x 30 (experimental hall)	Piles for foundations

(Continued on next page)

Table 6-9: Main buildings in the conventional facilities programme (continued)

No.	Function & Type	Dimensions L (m) x W (m) x H (m)	Remarks	Cranes (tonnes)	Special services
5100	LTBT tunnel	160 x 5 x 5.5	Houses equipment for transfer line between ring and LP target Concrete and earth		Active drains
5300	Personnel access to LTBT tunnel: Building (1) and tunnel (2)	(1) 8.5 x 4.5 x 4 (2) 24 x 2 x 2.5	Houses radiological control Steel frame for building Concrete and earth for tunnel	No crane	
5600	LTBT service building	25 x 10 x 5	Houses power supplies and all other general services for: rings, ring injection, achromat arc and achromat injection Steel frame	25	Active drains
5700	Target station LP (1) Central Hall (2) Experimental Hall (3) Ventilation loft etc. (two levels)	(1) 62 x 14 x 20 (2) 62 x 37 x 2.5 (3) 62 x 12 x 10	(1) Houses target, hot cells (nuclear part) Concrete walls (2) Houses instruments and associated equipments Steel frame (3) Houses services (ventilation etc.) Steel frame	100 (central hall) 2 x 30 (experimental hall)	Piles for foundations

(Continued on next page)

Table 6-10: Main buildings in the conventional facilities programme (continued)

No.	Function & Type	Dimensions L (m) x W (m) x H (m)	Remarks	Cranes (tonnes)	Special services
6100	COL building	3 wings 85 x 20 x 16 GF+3 Central tower 2800 m ² for offices	Houses laboratories, offices, central control room, restaurant, auditorium and library. Number of permanent people: 650		
6300	Guest house 1	35 x 9 x 8 2 wings, GF+1	60 persons		
6310	Guest house 2	35 x 9 x 8 2 wings, GF+1	60 persons		
6320	Guest house 3	35 x 9 x 8 2 wings, GF+1	60 persons		
6500	Reception and security	15 x 10 x 5 GF+1			
6510	Transport	10 x 10 x 5	3 offices		
6600	Fire brigade	18 x 16 x 23 GF+2			
7200	Central Utility Building 1	60 x 30 x 10	Houses cooling utilities tower water and chilled water	10	
7201	Central Utility Building 2	60 x 30 x 10	Houses cooling utilities tower water and chilled water	10	
7220	Mechanical and electrical engineering workshops	60 x 20 x 6		10	

(Continued on next page)

Table 6-11: Main buildings in the conventional facilities programme (continued)

No.	Function & Type	Dimensions L (m) x W (m) x H (m)	Remarks	Cranes (tonnes)	Special services
7230	Instrument support facility	80 x 30 x 12		3 x 10	
7235	Laboratories for instruments	50 x 45 x 10		2 x 10	
7240	Magnet and vacuum test area	120 x 20 x 6		40	
7300	Waste management facility	80 x 40 x 10	To collect, shred, compact, package and store all kind of radioactive wastes produced on the site	100	Active drains
7305	Spares and stores facility	80 x 40 x 10		40 10	
7320	Switchyard area	120 x 94			
7325	Switch house	60 x 10 x 8			
7326	Diesel generator set	60 x 30 x 8			
7360	Central exhaust stack	30 x 18			
7370	Process waste tank farm	25 x 15 x 10			
7380	Diversion tank building	7.5 x 7.5 x 6			
7420	Electrical substation	10 x 6 x 6			
7710	Boiler house	50 x 20 x 8	To heat buildings		

REFERENCES

- [CONCERT, 2001] CONCERT building programme,
CONCERT/CF/DOC/GN/001, June 2001
- [ESS-1, 1996] The ESS Accelerator and Beam Lines with the 280/560 MHz linac.
ESS-01-1A, November 1996
- [ESS-2, 2002] Front end-linac tunnel-klystron building
Specifications and Calculation Report.
ESS/CF/TCN/2000/001, January 2002
- [ESS-3, 2002] Ring tunnels: Achromat Injection
- Achromat Arc - Accumulator ring - Access - Service building
Specifications and Calculation Report.
ESS/CF/TCN/3000/001, January 2002
- [ESS-4, 2002] Short Pulse Target Building.
Specifications and Calculation Report.
ESS/CF/TCN/4000/001, February 2002
- [ESS-5, 2002] Long Pulse Target Building.
Specifications and Calculation Report.
ESS/CF/TCN/5000/001, February 2002
- [ESS-6, 2002] Industrial equipment for design and cost evaluation of buildings.
ESS/CF/DOC/0000/001, January 2002
- [ESS-7, 2002] Electricity - HVAC - Cooling - Compressed Air
Specifications and Calculation Report.
ESS/CF/TCN/7000/001, January 2002
- [ESS-8, 2002] Industrial equipment for design and cost evaluation of
Electricity - HVAC - Cooling - Compressed Air.
ESS/CF/DOC/7000/001, January 2002
- [ESS-9, 2002] Front end-linac tunnel-klystron building cost calculation report.
ESS/CF/CST/2000/001, January 2002
- [ESS-10, 2002] Ring tunnels: Achromat Injection - Achromat Arc - Accumulator ring -
Access - Service building Cost Calculation Report.
ESS/CF/CST/3000/001, January 2002
- [ESS-11, 2002] Short Pulse Target Building Cost Calculation Report.
ESS/CF/CST/4000/001, February 2002
- [ESS-12, 2002] Long Pulse Target Building Cost Calculation Report.
ESS/CF/CST/5000/001, February 2002

[ESS-13, 2002]	Social Buildings and Workshops Cost Calculation Report. ESS/CF/CST/0000/001, February 2002
[ESS-14, 2002]	Electricity - HVAC - Cooling - Compressed Air Cost Calculation Report. ESS/CF/CST/7000/001, February 2002
[ESS-15, 2002]	External Works: Cost Calculation Report. ESS/CF/CST/1000/001, February 2002
[ESS-16, 2002]	Shielding Calculation for the ESS Accelerator ESS/CF/SAF/0000/001, February 2002
[ESS-BPG, 2002]	ESS BUILDING PROGRAMME, ESS/CF/DOC/0000/001, January 2002
[ESS-VolIII, 1996]	The European Spallation Source Study, Volume III, The ESS Technical Study ESS-96-53-M, November 1996
[Regle, 2001]	Regle fondamentale de surete n° 2002-01 relative a la determination du risque sismique pour la surete des installations nucleaires de base, Ministère de l'économie, des finances et de l'industrie, Ministère de l'aménagement du territoire et de l'environnement, 2001
[SNS-1, 2001]	System requirements document for the spallation neutron source. Land improvements, utility systems and service buildings. Conventional facilities. SNS Doc. 108 000 000 SR 001 R02, August 2, 2001
[SNS-2, 2000]	System requirements document for the spallation neutron source. Target station and beam dump. Conventional facilities. SNS 108 030 700 SR 001 R01, July 2000
[SNS-3, 2000]	Spallation Neutron Source Interface Control Document. Target Systems and Target building. SNS 106 000 000 IC 0001 R01, July 2000
[SNS-4, 2000]	Spallation Neutron Source Interface Control Document. Interfacing WBS Elements - Instrument Systems and Conventional Facilities and Target Building. SNS 107 000 000 IC 0001 R01, July 2000
[SNS-5, 2001]	System requirements document for the spallation neutron source. Ring and transport line. Conventional facilities. SNS Doc. 108 030 500 SR 0001 R02, June 21, 2001

- [SNS-6, 2001] System requirements document for the spallation neutron source.
CHL and RF shop.
Conventional facilities.
SNS. 108 031 600 SR 0001 R01, July 21, 2001
- [SNS-7, 2001] System requirements document Title II design of the front end building, the linac tunnel and the klystron building.
SNS Doc: 108 030 000 SR 0001 R02, June 25, 2001
- [SNS-8, 2000] Preliminary Safety Assessment Document.
SNS Doc: 102 030 103 ES 0003 R00, September 2000

Chapter 7

Control Systems, Network and Computers

Authors and Contributors

Control Systems, Network and Computers

F Gournay CEA

Contents

Control Systems, Network and Computers

7 CONTROL SYSTEMS, NETWORK AND COMPUTERS	7-5
7.1 FOREWORD	7-5
7.2 NETWORK LAYOUT	7-5
7.3 ACCELERATOR CONTROL AND EXPERIMENT AREA SLOW CONTROL	7-5
7.3.1 HARDWARE FOR EQUIPMENT INTERFACING	7-5
7.3.2 CONTROL SOFTWARE	7-6
7.3.3 SYSTEM ARCHITECTURE	7-6
7.4 EXPERIMENTAL DATA ACQUISITION	7-8
7.4.1 ACQUISITION SYSTEMS	7-8
7.4.2 STORAGE AND SCIENTIFIC COMPUTING.....	7-8
7.5 CONCLUSION.....	7-9
REFERENCES	7-9

7 CONTROL SYSTEMS, NETWORK AND COMPUTERS

7.1 FOREWORD

This chapter describes the solutions envisaged for the ESS project concerning networking, control systems for accelerators, targets and experimental areas, acquisition systems for experimental areas, and computer infrastructure. The following is intended to provide the basic elements needed for the final design when the various requirements will be analysed in detail. This analysis is largely based on commercially available products or on solutions developed for similar projects. A detailed document gives a description of all solutions that fulfil the ESS requirements for networking, controls and computing needs [Gournay, 2002].

7.2 NETWORK LAYOUT

The ESS controls network is a 100Mbps switched Ethernet network, with a backbone at 1 Gbps. The number of nodes to be connected to the site network has been estimated for each part of the ESS facility. The total number of nodes is around 2000. The chosen network design will provide enough flexibility for the number of nodes to be increased without difficulty when required.

The ESS network will consist of several networks connecting all the different nodes found on the site: workstations, PCs, disks, printers, accelerator front ends, acquisition systems etc. The major reason for having multiple networks is to provide isolation (logical and physical) between the different subsystems.

The different entities of the facility are mostly independent from each other. Instead of hardware insulation, VLANs will be used. VLANs group individual nodes into logical workgroups whatever their location on the network. The collision domains are restricted to VLANs, thereby addressing the potential problem of unpredictable transfer delays.

Each node will be connected to a switch by a point-to-point link. A switch creates private connections to nodes connected to it and separates the LAN into collision domains. Therefore the traffic on the shared part of the network is dramatically reduced and most collisions are avoided. The switches will also be connected to the site-wide high-speed backbone through 1 Gbps uplinks.

7.3 ACCELERATOR CONTROL AND EXPERIMENT AREA SLOW CONTROL

7.3.1 Hardware for Equipment Interfacing

Although it has been in existence for more than 15 years, the VME standard is still widely used. In the accelerator domain, most new projects (DIAMOND, SOLEIL, NLC, SLS, SNS) still use VME as the main equipment interface. A set of standard VME modules will provide interfaces for analog and digital input and output signals as well as motors, encoders and serial lines connection. In the domain of fieldbuses, there are several systems on the market

and there is no consensus on the use of any particular one in the accelerator community. For ESS, the choice of a standard fieldbus must be a combination of criteria including experience, preference and the availability of solutions from other laboratories. A facility with such varied requirements will also need “non-standard” solutions to interface the control system with some specific equipment: like GPIB to interface high precision multimeters, numerical oscilloscopes, function generators etc., RS232 to interface diverse controllers and fibre optically linked distributed system for HV controls.

Each experiment area will be equipped with appropriate VME systems for managing the control of the devices used for the experiment (motors, counters, analysers). One or two VME will be used for each line for this purpose. In the domain of experiment slow control one cannot rely on a well-defined set of standard modules. In many cases, the hardware will probably be built with specific electronics and therefore it will not be easy to standardize.

7.3.2 Control Software

The basis of the control software for ESS will be EPICS [EPICS, 1991]. There are several reasons for this: the manpower in laboratories is decreasing, users have ever-increasing requirements and the solutions tend to be more and more complex. This analysis has been made by most of the laboratories, which have recognized EPICS as a good toolkit for building efficiently a powerful and scalable control system. Most new projects have opted for EPICS: BEPC2, Diamond, IPHI, NLC, SLS, SNS and SSRF. Today, around 100 facilities worldwide use EPICS. The other very strong point in favour of EPICS is its use for SNS [Gurd, 1999], because several solutions developed there are likely to be directly reusable for ESS.

A facility as large as ESS will have tens of thousands of parameters, so the database is a very important issue. BESSY and KEK have already created a comprehensive, project-wide relational database from which (among other things) the EPICS distributed database is automatically produced. SNS is also following this direction. The database will be based on a consistent, hierarchical, site-wide naming convention.

Several general-purpose software products interface with EPICS such as Excel, Mathematica and IDL visualization software. The accelerator codes Xorbit by ANL (lattice design code for circular accelerators) and ARTEMIS by Jefferson Lab (beam optics simulation package) also interface with EPICS. This means that machine data, such as magnet settings, can be sent to the software to calculate orbits, beam envelopes etc. in “real-time”.

7.3.3 System architecture

The control system for the entire accelerator, the beam lines, the targets and the slow control of the experiment areas will have the same architecture. The hardware architecture supporting EPICS is very simple. It is split into two levels. The first consists of VME crates (so called IOCs) connected to the equipment. The second consists of workstations (so called OPIs), which either play dedicated roles (file server, archiver) or offer a man-machine interface function. These two levels communicate through TCP-IP on Ethernet. This topology is not new and is commonly called “the standard model”.

As shown on Figure 7–1, the following hardware configurations for interfacing the equipment and supported by EPICS will be used:

- VME crate with various standardized IO boards (ADC, DAC, binary IOs, motor controller) and custom boards when needed (diagnostics, power supplies interfacing).
- VME crates with optical links will specific modules used for the control of ion sources. These modules will be used to control all equipment at HV.
- VME crate with serial line connections will also be provided.
- VXI crate with specialised hardware: this will be used for low-level RF control. The solution used for SNS [Regan, 2000] has to be carefully studied to see if it meets the ESS requirements. It consists of three VXI modules (cavity/resonance control, protection and clock distribution) for each cavity.
- GPIB interface: a black box connected to the Ethernet network will provide connection to dedicated appliances.
- Programmable logic controllers will be used to manage functions relating to safety: safety of the accelerator (vacuum, cryogenics, beam inhibit) or safety of personnel. The PLC market is mostly based on proprietary solutions: for the PLCs themselves, their I/O boards, the supported fieldbuses and the actuator/sensor hardware to be connected to these fieldbuses. So care must be taken when choosing a supplier and this choice must be enforced site-wide.

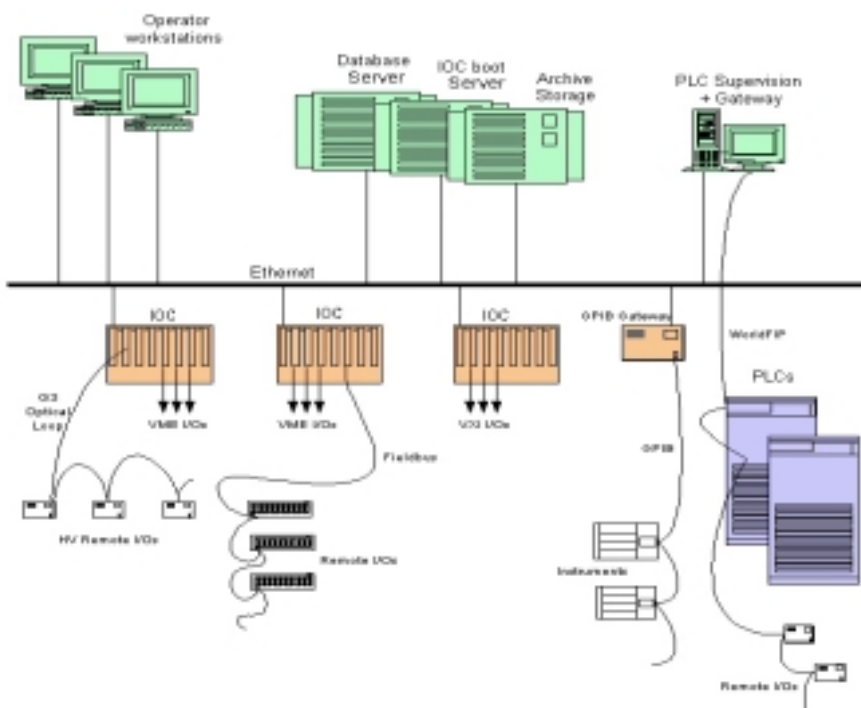


Figure 7–1: System architecture for controls

7.4 EXPERIMENTAL DATA ACQUISITION

7.4.1 Acquisition systems

In general, acquisition cannot be handled directly under software control. For example, for the flying time experiments in condensed matter or for accumulation of spectra in counters, the latency time is far below the microsecond and therefore these acquisitions must be made by specific electronics. The acquisition specific hardware, data flow and processing power will be studied individually for each experiment.

For acquisition software, a generic package such as the ESRF Modular Data Acquisition Software can be proposed for experiments [Epaud, 1995]. It follows a very conventional scheme in this field. An information producer reads the information directly from the detector and stores it in a global memory and a consumer builds events from elementary pieces of information retrieved from this global memory and writes them to disk. This package also has a server that is able to talk to clients located in workstations and controls and monitors the acquisition.

For some experiments, the volume of data can be enormous and impossible to handle directly by software. Large amounts of data such as this must be filtered and pre-processed before being stored on a magnetic device.

7.4.2 Storage and scientific computing

In order to store the experimental data, a solution based on the Networked Attached Storage technology (NAS) will be used. A NAS system can manage an almost unlimited storage space, is easily upgradeable, is easy managed and will continue to evolve in the future. A storage capacity of 1 TByte will be provided for each hall. The data contained on these disks will be mirrored on the large disks in the scientific centre.

For each hall, a computer with adequate power will be provided. There are no plans to run complex codes on this computer. It will be used to perform some run control and quick-look tasks to validate the progress of the experiment.

In the scientific centre, several computer systems will provide the processing and storage power required to work efficiently on data already acquired and stored in the respective experimental halls. These computers will have at least the same power as those in the experimental halls and will be compatible with them. There will be one computer for each experimental hall. This duplication will provide the opportunity to run the same codes in both locations, have the same environment etc.

LINUX clusters will also be provided. These clusters are characterized by an outstanding performance/price ratio. They offer dynamic sharing of resources, parallel processing and batch queuing. There are two obvious choices here: either use of standard high-end PCs with somewhat limited performance and evolution capabilities or use of more powerful and flexible machines based on Ultra-SPARC or Alpha processors. At ESRF, a PC-based solution is available and a solution based on the Sun Ultra-SPARC machine is being studied. For parallel programming, Beowulf software [Beowulf] can be used. With this software and high

performance cluster hardware, the performance level is not far from that reached with expensive massively parallel processors.

Some basic software tools will also be provided and supported by the ESS software team. One example is some commercial graphical packages, already widely used in the condensed matter community (ILL, Grenoble and LLB, Saclay). It is likely that the graphing packages developed at CERN (PAW and ROOT), which are de-facto standards for many physicist communities, will also be used and supported by the ESS software team.

7.5 CONCLUSION

The technical choices made for networking, controls, acquisition and computers are intended to offer the guarantees required for such a facility:

- Reliability and availability
- Scalability
- Performance
- User-friendliness and ease of maintenance.

These choices were made keeping in mind the time-span between this feasibility study phase and the construction phase. Some figures will have to be revised and some minor adaptations made, but the overall architecture is expected to remain as described here.

REFERENCES

[Beowulf]	Beowulf, URL: www.beowulf.org
[Epaud, 1995]	Overview of Beamline Control and Data Acquisition at ESRF, F. Epaud, ICALEPCS'95 Conference
[EPICS, 1991]	EPICS Architecture, L.R. Dalesio et al., ICALEPCS'91 Conference, Tsukuba
[Gournay, 2002]	Control systems, network and computers, J F Gournay, TMT meeting n°4, Juelich, 6 February 2002
[Gurd, 1999]	Plans for a collaboratively developed distributed control system for the spallation neutron source, D. P. Gurd et al., ICALEPCS'99 Conference, Trieste
[Regan, 2000]	Design of the SNS normal conducting linac RF control system, A. Regan et al., LINAC 2000 Conference

Volume III Technical Report

Chapter 8

Safety and Licensing

Authors and Contributors

Safety and Licensing

P Berkvens¹, T Broome², P Fabi³, D Findlay², P Giovannoni⁴, R Lennartz⁵, A Matic⁶,
J Mertens⁵, R Moormann⁵, K Verfondern⁵, P Wright²

¹ESRF, ²RAL/ISIS, ³ESS-CPT, ⁴CEA, ⁵FZJ, ⁶Chalmers Univ .

Contents

Safety and Licensing

8 SAFETY AND LICENSING	8-5
8.1 INTRODUCTION.....	8-5
8.2 LEGAL FRAMEWORK FOR ESS COMMISSIONING IN THE DIFFERENT EUROPEAN COUNTRIES	8-7
8.2.1 RADIOLOGICAL ASPECTS	8-7
8.2.1.1 France	8-7
8.2.1.2 United Kingdom	8-8
8.2.1.2.1 Health and Safety Executive (HSE) Requirements	8-8
8.2.1.2.2 Environment Agency (EA) Requirements.....	8-8
8.2.1.2.3 Nuclear Installations Inspectorate (NII) Requirements	8-9
8.2.1.2.4 Health and Safety Commission (HSC) Requirements.....	8-9
8.2.1.2.5 Department of Transport Requirements	8-9
8.2.1.2.6 Waste Disposal Authorities Requirements	8-9
8.2.1.2.7 Site Specific Requirements.....	8-9
8.2.1.3 Germany	8-9
8.2.1.3.1 Dose calculations for design basis accidents (dba) in Germany	8-11
8.2.1.4 Sweden.....	8-11
8.2.2 TOXIC ASPECTS	8-13
8.2.2.1 European Union	8-13
8.2.2.2 France	8-14
8.2.2.3 United Kingdom	8-14
8.2.2.4 Germany	8-15
8.2.2.5 Sweden.....	8-17
8.2.2.6 USA	8-17
8.2.2.7 Japan	8-18
8.2.3 SELECTED ASPECTS OF CIVIL LICENSING	8-19
8.2.4 CONCLUSION	8-19
8.3 SAFETY ASPECTS OF ESS KEY COMPONENTS.....	8-20
8.3.1 SAFETY CONSIDERATIONS FOR THE ACCELERATOR AND THE RINGS — SHIELDING	8-20
8.3.1.1 Introduction	8-20
8.3.1.2 The model used for the shielding calculations	8-21
8.3.1.3 Measures against local beam losses.....	8-26
8.4 WASTE FROM DECOMMISSIONING AND DISMANTLING	8-29
8.5 GENERAL PROCEDURE OF ONGOING ESS SAFETY WORK.....	8-30
REFERENCES	8-30

8 SAFETY AND LICENSING

8.1 INTRODUCTION

As with any other large facility of its type, the ESS has to be designed for safe operation, commissioned safely, and operated safely. Although, when it is built, the ESS will be the largest spallation neutron source in the world, the important safety issues to be considered are well known and understood. Extensive experience is available from the ISIS and SINQ spallation neutron sources already operating in the UK and Switzerland respectively, and guidance is also available from the safety issues being addressed at the SNS spallation neutron source currently being constructed in the USA.

Nevertheless, the radioactivity generated in the mercury target and in other parts of the ESS together with the chemical toxicity and volatility of mercury require that considerable effort has to be spent on safety examinations, shielding calculations and preparation of the formal safety report to support the procedures required to obtain authorisation to build and operate the ESS.

Throughout the EU (as in most other countries) safety considerations are required for three different categories, distinguished mainly by their frequency of occurrence:

- Normal operation and frequent abnormal events ($>10^{-2}$ per year)
- Design basis accidents, dba ($10^{-6} - 10^{-2}$ per year)
- Hypothetical events ($<10^{-6}$ per year)

Besides event sequences which result from failure within the facility itself, accidents based on external events (earthquakes, gas cloud explosions, aeroplane crashes, *etc.*) have to be part of the safety analyses.

In estimation of radiation doses the following pathways have to be considered:

- External irradiation
 - a) Direct radiation from the facility
 - b) Radiation from radionuclides in an airborne plume (cloud shine)
 - c) Radiation from radionuclides deposited on the ground (ground shine)
- Internal irradiation (by incorporation)
 - d) Inhalation of airborne radionuclides
 - e) Ingestion of radioactivity (nuclides deposited on the ground or in surface water and incorporated via a food chain)

Doses from pathways b) – e) result from emissions in normal operation (H-3, C-11, Ar-41) or in accidents. Pathway a) may contribute via ground water and soil activation to some extent to ingestion doses, too. For mercury absorption via the skin has to be taken into account in addition to inhalation and ingestion.

For all harmful substances “early” and “late” consequences have to be distinguished. “Early” consequences (e.g. acute radiation syndrome) are characterised by a threshold dose and by a

dose-rate dependence of this threshold dose and of the degree of consequences. For “late” consequences (e.g. cancer induced by radiation) no threshold dose and no dose-rate dependence exist, but a linear relationship between consequence and dose is assumed for conservatism.

Whereas normal operation, frequent abnormal events and design basis accidents are considered as part of the commissioning process and require conservative assessments of accident consequences to be made, analyses of *hypothetical events* are necessary for planning of emergency countermeasures and demand that best estimates of consequences be made. Planning of emergency countermeasures means to estimate areas outside the facility, which require evacuating or relocation, sheltering, banning particular foodstuffs or iodine tablet distribution.

Risk limits for workers in a facility and for the general public are usually different. For normal operation and frequent abnormal events, dose limits for workers are higher than for the general public. Further, while in an accident situation extra doses to workers to mitigate the effects of the accident may have to be regarded as acceptable, no such relaxation can be permitted for the general public.

One problem concerning ESS commissioning arises from the fact that regulatory requirements for a facility like ESS are somewhat different in different European countries, and these regulatory differences can give rise to cost differences. In some countries a separate licence to build and to operate is required, whereas in other countries different mechanisms prevail. For convenience, the term “licensing” will be used in the rest of this paper to represent the regulatory process in whatever form it may be. Issues arising from different regulatory regimes in different countries will have to be resolved as part of the process of choosing a site for the ESS, which means, that this is a duty of the local working group. In contrast to that, regulatory issues, which are the same for all sites, will be resolved under auspices of the ESS Central Project Team. Similar problems may result from specific conditions on a proposed site (e.g. high probability of earthquakes or aeroplane crash onto the plant, possibilities of ground water and soil contamination etc.); safety examinations related to these site specific items have also to be handled by the national working group.

In general, safety issues should be addressed as part of the overall design of the facility. It is important to include questions of radiation shielding at the design stage, where differences in shielding requirements can lead to large cost differences. For the same reason it is also important to address issues of decommissioning and waste disposal at the design stage.

Altogether, this paper deals with the legal framework for licensing the ESS in different European countries as regards:

- Radiological protection (including decommissioning and waste disposal issues)
- Requirements following from the (chemical) toxicity of mercury
- Aspects of civil licensing

Also discussed are general safety features for key ESS components (e.g. the target system, accelerator and rings, instruments and beam dumps). A more detailed description of accelerator and ring shielding issues is presented in Section 8.3.1, and information on the safety of the target system is outlined in Section 4.7. Further, some statements on post-decommissioning issues are presented. Finally, plans for future safety work in 2003 are briefly outlined.

8.2 LEGAL FRAMEWORK FOR ESS COMMISSIONING IN THE DIFFERENT EUROPEAN COUNTRIES

8.2.1 Radiological aspects

The formal requirements for licensing with respect to radioactivity are different in different European countries. Several countries (United Kingdom, Germany, Sweden etc.) treat the ESS as a non-nuclear plant, whereas rules in other countries (France, Belgium, Italy etc.) require a nuclear licensing process for ESS. Therefore, the effort to be spent might depend on the local law, which has to be applied on the site of the plant. Accordingly, each country that will propose a site for ESS has to provide a safety study in accordance with the local requirements. As a first step to that, these formal requirements for the radiological licensing process have to be listed for each of the applying countries; as examples, important licensing requirements are outlined in the following chapter for France, UK, Germany and Sweden.

8.2.1.1 France

According to the French decree of the 27th of April 1982 concerning the classification of particle accelerators as Nuclear Installations, ESS will be classified as a nuclear installation (for proton accelerators the criteria is that the energy must be > 300 MeV and the power > 0.5 kW). Both the accelerator (and rings) and the target will be considered a nuclear installation. The licensing of nuclear installations is defined in the decree no. 63-1228 of the 11th of December 1963 (modified by decrees no. 73-405 of 27/03/73, 85-449 of 23/04/85 and 90-78 of 19/01/90).

This decree foresees that the creation of a nuclear installation requires an authorisation covering not only the nuclear installation itself but also all the peripheral installations, which are classified for the protection of the environment (as defined in the French law 76-663 concerning the ICPE (*Installations Classées pour la Protection de l'Environnement*)).

The safety assessment document submitted to obtain the required authorization of the Ministry of Industry must cover the following points:

- a) General information (applicant, short description of the site, site map, etc)
- b) Detailed information of the site and its surroundings (public roads, railways, rivers and lakes, electricity networks, pipelines, ...)
- c) Detailed description of the installation containing a preliminary safety assessment document, describing the risks and the measures foreseen to limit the consequences in case of an accident. This document also includes a study of the final decommissioning of the site.

The request for authorisation automatically includes a public enquiry. This public enquiry is carried out on a departmental level (all departments included in a circle of a radius of 5 km around the site are concerned).

An authorisation decree finally authorises the construction of the installation.

At the latest 6 months after the start-up of the installation (in the sense of first beam in the accelerator) the following documents must be submitted to the Central Service for the Safety of Nuclear Installations (Service Central de Sûreté des Installations Nucléaires):

- a) A provisional safety report including a description of the measures and technical solutions foreseen to comply with the prescriptions of the authorisation decree.
- b) General operation rules and procedures to guarantee the nuclear safety during the operation of the installation.
- c) An emergency plan for the installation defining the organisation and the available means to cope with an emergency situation in case of an accident.

The rules and regulations for the emission of liquid or gaseous effluents into the environment are defined in the decree no. 95-540 of the 4th of May 1995. Depending on the quantities and concentrations again a public enquiry may result from this.

Independent of the nuclear (and environmental) licensing the protection of workers and the public against ionising radiation hazards is defined in the decrees no. 86-1103 of the 2nd of October 1986 and no. 75-306 of the 28th of April 1975. The dose limits defined in these decrees will be modified in the near future to comply with the Euratom Directive 96/29 [EURATOM, 1996]. The general philosophy for ESS used for the shielding calculations is that all personnel should be considered as non-exposed workers, which means that according to the new European limits the integrated dose per year shall not exceed 1 mSv. All other activities (e.g. interventions in the tunnels, remote handling around the target etc.) should whenever possible maintain this general policy.

8.2.1.2 United Kingdom

UK regulatory and administrative requirements for an ESS type project: ionising radiation aspects (Status: May 2001)

In general, the regulatory and administrative requirements for an ESS type project in the UK do not appear to be prohibitive and the operational experience of an accelerator such as ISIS would be important in demonstrating basic competence and standards to the interested authorities, organisations and persons. However there are some special issues for which the regulatory requirements could be limiting; as in the case of the 15 tonne liquid mercury target. Requirements of various authorities are given in the following paragraphs.

8.2.1.2.1 Health and Safety Executive (HSE) Requirements

The HSE is responsible for administering the Ionising Radiation Regulations 1999 (IRR99) which were revised to comply with the European Safety Directive of 1996 and relate to the control of radiation risks in the workplace. Specific attention is given in the regulations to accelerators. However the IRR99 do not require licensing approval for an ESS type project, provided that the project complies with the generic safety requirements issued by the HSE. An ESS type project would of course be expected to fully comply with the IRR99.

The generic requirements detail the conditions for radiation dose control to workers and others at an accelerator. Examples of these controls would be interlocks, shielding, procedures and maintenance schedules. The main, yearly whole body dose limit applied is 20mSv for workers and 1 mSv for members of the public. A comprehensive prior risk assessment, which must also extend to any major experiments proposed for the project, would be needed. The acceptable levels and conditions of risk would be similar to that of the situation in Germany.

8.2.1.2.2 Environment Agency (EA) Requirements

The EA administers the Radioactive Substances Act 1993, which requires justification, registration to use radioactive material and authorisation to accumulate and dispose of radioactive substances. They would require a full environmental impact assessment and the

main limit (member of public dose), from all sources produced by an ESS type project, would be 0.3 mSv per year.

It should be noted that the EA would expect radioactive waste disposal routes to be available and contracts established before granting approval. At decommissioning, the large mass and bulk of active accelerator components and associated structures could be of concern because of the impact on the storage capacity of disposal authorities. Decommissioning strategy would have to be based on the best practical options consistent with radiation safety.

A background environmental radioactivity study would be required by the EA to establish a datum level for comparison of environmental data.

The EA is bound to consult with public and local authorities. Any local council would invoke the relevant planning act (1988) and would also expect an Environmental Impact Assessment.

8.2.1.2.3 Nuclear Installations Inspectorate (NII) Requirements

The NII is a branch of the Health and Safety Commission and administers the Nuclear Installations Act 1990. It is not expected to have a direct interest in an ESS type project in the UK. They could become interested in any major experiment involving fissionable nuclear matter such as Pu239.

8.2.1.2.4 Health and Safety Commission (HSC) Requirements

The HSC would require compliance with the pending Radiation Emergency Preparedness and Public Information Regulations, based on EU Council Directive 96/29 [EURATOM, 1996]. They may impose controls on plant design, similar to those for nuclear reactors, because of the nature of the liquid mercury target. Such controls would extend to the transport of waste mercury.

8.2.1.2.5 Department of Transport Requirements

The Department of Transport administers the Radioactive Material Road Transport Regulations 1996, largely based on the IAEA recommendations. Transportation of a significant mass of active mercury would require special approval and flasks.

8.2.1.2.6 Waste Disposal Authorities Requirements

There could be difficulties with processing active waste mercury, either as target liquid or mixed with other waste, for disposal. Waste disposal authorities would expect conditioning to immobilise mercury and its compounds.

8.2.1.2.7 Site Specific Requirements

The construction of the ESS within an existing campus organisation could be controlled by local policy on such matters as environmental and operational doses. For example, allowance for contributions to dose from other sources is inherent in RAL shielding policy where doses to operators should not exceed 1 mSv per year after inclusion of all sources.

8.2.1.3 Germany

Although ESS is not a nuclear installation in terms of German law, the ESS is covered by the German Radiological Protection Ordinance (Strahlenschutzverordnung, revised version applicable since August 2001 [BGBl-5702, 2001]). The main difference to licensing of nuclear plants is probably the involvement of the public within the licensing procedure, which is not required in case of facilities like ESS.

Construction and operation of ESS have to be licensed. A safety report with the following content has to be submitted to the licensing authority:

- a) General information (applicant, experience of the applicant, short description of the site etc.)
- b) Ecological conditions on the site (actual radiological conditions on the site without consideration of ESS, meteorology, river and ground water systems in the surrounding of the plant, agriculture and use of water around the site area); this chapter is not always required
- c) Objective of ESS
- d) Description of ESS design (detailed information about design)
- e) Description of ESS operation (operation times per year; procedures of operation, maintenance and repair; documentation of operation...; staff: organisation, responsibilities, education; internal operation/maintenance guidelines etc.)
- f) Radiology of ESS (exposition of the staff by external and internal pathways for different areas of the plant: detailed calculations; activation of components; amount of radioactive waste; shielding (maximum doses to staff and public follow EURATOM-guideline 96/29 [EURATOM, 1996]); emissions by air and water (including dose calculations for the public: Dose limits are 0.3 mSv/year effective dose by emissions via air and water, each); activity control systems within ESS and concerning emissions to the environment; systems protecting the staff from radiation/contamination etc.)
- g) Measures relevant to safety and security (fire protection; preparation for countermeasures in case of accidents; security systems: usually a confidential part of the safety report; protection of radioactivity against un-admitted use; protection against sabotage etc.)
- h) Safety considerations (the actual guidelines concentrate on accelerators; however, because completeness is required, target specific safety considerations have to be added; in principle, only the frequency range of down to about 10^{-6} a^{-1} (design basis accidents = dba, this frequency limit is not explicitly written down, but can be evaluated from the frequencies of accidents, usually examined in the licensing process; there is some tendency to decrease these frequency limits) has to be covered for licensing purposes (for emergency countermeasures however see below): It has to be shown, that certain dose limits for the public are met (details see appendix 1), but with general consideration of the ALARA (= as low as reasonably achievable) principle; commissioning practise for nuclear plants indicates, that accidents beyond this frequency limit have also to be considered in the safety report, but without the requirement of meeting the dose limits of dba; a more realistic treatment as for emergency planning (see below) is usual here.
- i) ESS decommissioning (activity of components, proposals on waste disposal etc.)

This list follows the guidelines for ion sources, to which ESS belongs in terms of German law. However, in contrast to such sources, high activities are enclosed within the mercury target. Following the consequence estimations for SNS it is expected, that in addition to the safety report outlined above (and in contrast to usual ion sources) a *report on countermeasures* (evacuation, relocation, foodstuff ban, sheltering) *protecting the public* in case of accidental releases has to be prepared; this report covers accidents beyond the scope of the usual licensing procedure (i.e. accidents with frequencies < about 10^{-6} a^{-1}) and is usually confidential. In contrast to dba analyses (see next paragraph), dose calculations for decision

about emergency countermeasures are performed on a more realistic basis (i.e. consequence models like the EU code system COSYMA [COSYMA, 1994] may be used). A report about emergency countermeasures is not necessary, if it can be shown, that the ICRP-63 [ICRP-63, 1993] respectively EU limits on emergency countermeasures are surely not met down to accident frequencies of about 10^{-8} a^{-1} .

8.2.1.3.1 Dose calculations for design basis accidents (dba) in Germany

It was found out already in the past, that considerable differences to other countries exist with respect to procedure of part h.) (safety considerations) of the safety report required in Germany. These differences are mainly found within rules for dose calculations for dba (as an example a comparison between US and German dose estimation guidelines is found in [Maneke, 1988]), so the German procedure will be outlined here shortly.

A governmental guideline, originally developed for dba of PWRs (pressurised water reactors), but used also for other nuclear facilities, requires dose calculations outside the plant area in the following manner [BA, 1983], [BA, 1994]:

- Exposure pathways: external radiation, inhalation and ingestion (with respect to the latter it is assumed, that the reference person eats/drinks only the highest contaminated food, considering, that within a circumference of 1 km around the plant 1 day after start of radioactive release a complete foodban is declared)
- No shielding by houses etc., worst location of the reference person in the area outside the plant is assumed
- Worst weather conditions have to be selected within a formal procedure
- Dose build-up occurs over 50 y (internal radiation, ground shine)
- Doses added over all exposure pathways must remain sufficiently below 50 mSv (effective dose and doses for radiation sensible organs), 150 mSv (thyroid dose and most other organ doses) and 300 mSv (skin dose and doses for other low sensitive organs).

Particularly *consideration of ingestion* leads to the before mentioned substantial differences to dose calculations in other countries, because in many cases the ingestion dominates the overall dose. It has to be noted here, that transfer factors, which describe the nuclide transfer within a food chain and which are necessary for ingestion calculations, are probably not available with sufficient accuracy for all elements found within the ESS target; accordingly, work in this field is required. With respect to methods of dose calculations for inhalation and external irradiation, results obtained by German guidelines seem to be similar to those obtained by rules of other countries (provided shielding by houses is neglected etc.).

In addition to the described handling of ‘normal’ dba, German law ‘Atomgesetz’ restricts severe consequences of core meltdown accidents in LWRs to the plant area, which probably means, that countermeasures like evacuation and relocation must not be necessary down to accident frequencies of about 10^{-8} a^{-1} . However, detailed guidelines how to handle this part of the ‘Atomgesetz’ are not yet available, because no LWR was licensed since the Atomgesetz was extended in the before mentioned manner.

8.2.1.4 *Sweden*

The Swedish Radiation Protection Institute’s (Statens Strålskydds Institut, SSI) regulations are issued on the basis of the Swedish Radiation Protection Ordinance (1988:293), which

empowers the Institute to issue regulations according to the Radiation Protection Act (1988:220).

According to the Radiation Protection Act (1988:220) a permit is required for the manufacture, import, sale, transfer, lease, acquisition, possession, use, installation or maintenance of technical devices, which are capable of generating ionising radiation (§ 20). SSI issues additional conditions required with reference to radiation protection. The planned activity must also follow the issued regulations on radiation protection for workers and public. For the public, the permissible annual doses are those of [EURATOM, 1996], whereas the permissible doses for workers are not yet those of EU-guidelines, but about a factor of 2.5 higher.

In accordance with the Radiation Protection Ordinance (1988:293) SSI can determine that an Environmental Impact Assessment (EIA) has to be submitted for a particular case (§ 14a). Such an Environmental Impact Assessment should be prepared following chapter 6 of the Environmental Code (1998:808).

SSI has issued Regulations on Radioactive Waste Not Associated with Nuclear Energy (1983:7). The regulations are not however applicable on the highly radioactive mixed waste (chemical/radioactive) arising from the planned activity. There is today no waste system for non-nuclear radioactive waste in Sweden. A Governmental commission of inquiry will in a near future review the situation and suggest a system for handling and storage and final disposal of non-nuclear radioactive waste in Sweden. If the commission of inquiry will cover the waste from ESS is not yet clear.

In order to achieve a permission to construct the ESS facility in Sweden, the following procedure should be followed. A preliminary application is to be forwarded to the Swedish Radiation Protection Institute describing not only the technical aspects of the ESS facility but also the (European) application procedure where localisation to Sweden is asked for. The application can be made in several successive steps having an increasing degree of details, and written in a form suitable for official documentation. The ESS application should present the information in a form that facilitates assessments referring to relevant legal frames, i.e. Radiation Protection Act (1988:220) and additional. As described above an Environmental Impact Assessment most probably has to be performed.

Possible terms for the application are:

- Data on the (calculated/expected) maximum and minimum dose rate values at the border of the facility (both prompt and related to activation).
- Specification of emissions to the surroundings, surface water, ground water and air.
- Specification of doses to the general public.
- Specification of the facility decommissioning procedure, how remaining radioactive material will be taken care of, and what type of economical resources are available that will guarantee the decommissioning to be possible.
- Description of: internal rules applicable to the radiation protection organisation, handling of radiation safety for the staff, measures against incidents, general management and waste disposal.
- Description of the facility in view of radiation protection terms – accelerator, storage rings, beam transport and targets. Description of construction of buildings and their shielding capacity, and the personal access to different parts of the facility. Proof of

integrity of the cooling system and of the function of the ventilation system. Calculations on beam losses during various conditions including influence on construction material and equipment. Description of procedures for handling activated material.

8.2.2 Toxic Aspects

Apart from the radioactivity contained in the target material, the chemical toxicity of mercury represents a major hazard to both people and environment if accidentally released. Not only have large and fast releases to be considered, but also small, continuous releases and minor incidents. An undetected continuous small release of mercury affecting the staff is unlikely to occur because of the easy detection of radioactivity in the target material. It should be checked, however, whether or to what extent such an escape may remain undetected for a still unirradiated target. Furthermore, incidental mercury intake by the staff in course of filling the target has to be considered.

Due to environmental concerns, numerous regulations have been created which have led to a major decrease in the Hg consumption all over the world since the 1980s. Existing restrictions are mainly referring to discharges of various bioaccumulative chemicals or emissions from coal-fired power plants, or to potential exposure at the work place. The rules for treating accidental mercury release (safety guidelines for chemical plants are applicable here) are different to some extent in different countries. Besides for EU and European countries, respective rules are described for USA and Japan, too, which are both countries, developing a spallation source; this was done, because -in contrast to rules for the radiological licensing-the legal framework concerning toxic mercury was not yet part of the preliminary safety analyses for these spallation sources.

8.2.2.1 European Union

The general frame of activities within the European Community related to hazardous materials is given by various EU directives, which are related to the handling of hazardous substances.

The Council directive 67/548/EWG on “Classification, Packaging and Labelling of Dangerous Substances in the European Union” of 1967 [R548, 1967] and 1979, respectively, requires an assessment for the characteristics of chemicals which are categorized hazardous and which are intended to be put professional markets (which, however, is not the case for ESS). The labelling for a hazardous substance must include the chemical detonation, hazard symbols, reference to particular risks (“R-Sentences”), safety advises (“S-Sentences”), and other information. This guideline serves also the correct selection of the necessary R and S sentences. The characterization of mercury is given by the R sentences R23 (poisonous when inhaled), R33 (danger of cumulative effects), R50 (very toxic to aquatic organisms), R53 (may cause long-term adverse effects in the aquatic environment), and by the S sentences S1 (store in containment), S2 (must not be accessible to children), S7 (keep container tightly closed), S45 (consult doctor immediately in case of an accident), S60 (substance and/or container must be disposed as dangerous waste), S61 (avoid release into environment, consult safety data sheet). The EU labelling of mercury is T (toxic) and N (dangerous to environment).

The European Council Directive 98/24/EC of 1998 on the “Protection of Workers from the Risks Related to Chemical Agents at Work” or Chemical Agents Directive [CD98, 1998] regulates what employers should do as a minimum to protect the personnel’s health from the

effect of hazardous chemical agents, covering both toxic hazards and fire hazards arising from an explosive atmosphere. It also sets a new framework for establishing occupational exposure limits. This directive must be implemented in Member States legislation by May 2001. Indicative Occupational Exposure Limit Values (IOELV) are the legal limits for concentrations of a hazardous substance in air proposed by the CEC. Member States are obliged to introduce an occupational exposure limit for these substances in accordance with national legislation and practice that takes the IOELV into account. The CEC list does not include yet mercury.

The EU frame guideline 96/62/EG of 1996 [CD96, 1996] on the Valuation and Control of Air Quality is in force. It demands to lay down limits and alarm threshold values for various substances. The particular daughter guideline for mercury is presently under construction. It is expected that these data be transformed into national law. A harmonized European guideline on general occupational protection is also under construction describing the minimum standards for the handling of hazardous materials at the work place.

The EU Council Directive 96/82/EC, also known as Seveso II directive, of 1996 [Seveso-II, 1996] has become mandatory for both industry and public authorities since February 1999. It aims at the prevention of major hazards and the limitation of the consequences to man and environment at a high level of protection. It is distinguished between lower tier and upper tier establishments depending on whether specified threshold quantities for certain substances are exceeded or not. The difference is given by additional documentation such as Safety Management System, Internal Emergency Plan, Safety Report, required for upper tier establishments. Mercury is not explicitly mentioned in the directive's list of regulated substances. In this case the list of characteristics applies giving the following threshold values for substances labelled toxic: 50 t (lower tier) and 200 t (upper tier). This means that the Seveso II guideline does not apply to the ESS Spallation Source, which has a maximum inventory of 30 t of Hg for two targets plus a presumably small reserve.

The WHO has adopted the range of 10 ppm to 20 ppm mercury in hair as the threshold for the harmful effects of methyl mercury.

8.2.2.2 France

In France, the use of mercury is subject to the law of the protection of the environment (ICPE). In the case of mercury an authorisation is required for quantities above 200 kg. Therefore the ESS target will be subject to authorization. The French ministry in charge of Labour publishes French short-term and long-term exposure limits.

8.2.2.3 United Kingdom

In the United Kingdom, health and safety legislation is made under the power of various Acts of the Parliament. The Health and Safety at Work etc. Act of 1994 requires employers to take all reasonable practical measures to minimize the risk to the health and safety of their employees and other people who may be affected by the work activity. Employers must make sure that any equipment is fit for its intended purpose and that adequate information is supplied to ensure that it can be used safely.

The "Control of Substances Hazardous to Health (COSHH) Regulations" of 1999 apply to all substances defined as hazardous (very toxic, toxic, harmful, corrosive, irritant) and to all places of work. COSHH states in general what standards must be achieved, but places the ultimate responsibility on the employer how these standards shall be met. He must conduct a suitable and sufficient assessment, which identifies the risk to health. So-called Approved

Codes of Practise and Guidance Notes complete Coshh. Maximum Exposure Limits (MEL) are given in one of the appendices.

Mercury is one of the hazardous substances for which health surveillance is required. A typical Threshold Limit Value (TLV), time-weighted average, used in the UK is 0.05 mg/m³; PEL is 0.1 mg/m³ [Mercury, 1996]. In addition, there are Occupational Exposure Standards (OES), which are considered good practise and realistic control criteria. The National Occupational Health and Safety Commission responsible for reviewing, updating, and declaring the “Adopted National Exposure Standards for Atmospheric Contaminants in the Occupational Environment” has proposed in 2000 a change of some exposure standards. The suggestion for (metallic and inorganic) mercury time-weighted average values is now down to 0.025 mg/m³ or 3 ppb.

Emissions of mercury via the stack in normal operation including maintenance etc. (if any) and due to abnormal events have to be estimated within the licensing process, too; the licensing authority in course of the licensing process will define maximum annual emission values.

8.2.2.4 Germany

The legal basis in Germany is, in principle, given by the guidelines of the European Union, which are being transferred into national law. The protection of the environment has the status of a state goal within the Basic Law.

Within the complex system of codes and standards, the Federal Immission Control Act (Bundes-Immissionsschutzgesetz, BImSchG) or in long: “Act for the Protection against Harmful Ambient Air Effects by Air Pollution, Noise, Concussion, and Similar Processes” [BGBl-1, 1990] issued first in 1974 describes the aspects of protection of man and environment against and prevention of harmful environmental influences from the operation of systems containing hazardous substances. It is based on the “principle of origin” or the “causer pays” principle and covers the whole area of immissions. The act is considered a frame law with the details to be defined in separate ordinances and administrative directives.

The fourth Federal Immission Control Ordinance (4th BImSchV) of 1985 [13] contain requirements for the construction and operation of any new plants subject to a license in the general development plan for industrial areas. The Federal Disaster Control Act and the Land Disaster Control Acts and Fire Service Acts detail the requirements for emergency planning in the area surrounding the hazardous facilities.

The Major Industrial Accident Ordinance (12th BImSchV or „Störfallverordnung“ of 2000) [14] contains requirements for on-site and off-site contingency plans which should be agreed with the competent authorities. The ordinance demands the conduction of a safety analysis to allow statements on the consequences of conceivable accident scenarios for public and environment. It also contains the requirements for the provision of information concerning hazardous activities to the public. A new aspect since the year 2000 is that the ordinance is to be applied to a whole operational range; quantities of hazardous substances are valid for all plants, infrastructures, and activities of an establishment meaning that a summation over all substances / categories has to be made.

The Ordinance on Immission Values (22th BImSchV) [15] and the Technical Instructions on Air Quality Control (“TA-Luft”) [16] prescribe the immission limits and measurement procedures. The standards for the air at the work place are 0.1 mg/m³ (elemental Hg), 0.01

mg/m^3 (organic Hg), 200 $\mu\text{g/l}$ (urine), 25 $\mu\text{g/l}$ (blood). The Technical Instructions on Waste Management (“TA-Abfall”) [TAAbfall] regulate the disposal of hazardous substances.

The Chemical Act or Act for Protection against Hazardous Substances of 1980 (“ChemG”) [GSGS, 1980] requires the assessment and characterization of common industrial chemicals which are listed in the Annexes to the Major Industrial Accident Ordinance, and stipulates that hazardous substances be replaced by non-hazardous ones.

The Ordinance for Protection against Hazardous Materials (“GefStoffV”) of 1999 [VSGS] prescribes the employer to take all measures for the protection of life and health of employees and the public as well as of the environment according to the guidelines for workers protection and accident prevention. In addition, an ordinance on mothers’ protection has been issued in 1997 to protect female workers when handling substances, which are deemed reproduction-toxic. Establishments, which handle hazardous materials, have the obligation to list all respective substances within a certain section including classification, hazardous properties, quantities, and the work areas where they are dealt with. This list must be checked and updated at least once a year and has to be made available to the authorities if requested. Further obligations are the control and labelling of these materials, information to the employees, and the issuance of operation instructions.

If a release of hazardous materials cannot be precluded, it has to be determined whether the Maximum Work Place Concentration (MAK), the Technical Standard Concentration (TRK), which is achievable by state-of-the-art technical means and fixed for substances, for which no MAK values exist, or the Biological Work Place Tolerance (BAT) values be exceeded. Respective values are defined in the Technical Rules for Hazardous Substances (TRGS). MAK values are defined in the TRGS 900 on “Limits in the Air at the Work Place” [TRGS 900]; TRGS 903 [TRGS 903] contains the BAT values. MAK values must not be exceeded during an eight-hour shift; they are completed by an “exceeding factor” for short-term exposure. MAK values for Hg are 0.01 ppm or 0.1 mg/m^3 (met., inorg.) with an exceeding factor of 4 and 0.01 mg/m^3 (methyl), respectively. A threshold for initiating protection measures is usually defined at the 25 %, sometimes 10 % level of the MAK value. The TLV of Hg is 0.025 mg/m^3 time-weighted average (skin). The threshold is also considered exceeded, if the surveillance of the MAK value is not guaranteed.

The VDI guideline 2310 provides standard data for Maximum Immission Concentration or MIK values based on a reference time interval between 0.5 h and 1 yr. They are expected to support decisions on the valuation of air pollution. The respective section on mercury is still under construction. Also the Committee of the “Deutsche Länder” on Immission Protection (LAI) has issued proposals for immission limiting values. The respective data for Hg are 0.05 $\mu\text{g/m}^3$ for man and 1 $\mu\text{g/(m}^2\text{ d)}$ for man, fauna, eco system. Both are orientation values based on a 1-yr reference interval. With respect to aquatic systems, mercury is deemed a severely water jeopardizing substance classified as WGK 3.

In case of exceeding MAK and BAT values, technical measures must be taken to mitigate the exposition. An occupation-related poisoning with Hg as well as Hg-induced occupational diseases are subject to mandatory reporting to the Employer’s Liability Insurance Association (“Berufsgenossenschaft”).

Since respective threshold values from the Seveso II directive were taken over, this ordinance would also not apply to the ESS. Nevertheless it is expected, that a (toxicological) consequence estimation regarding accidental mercury release is required at least in course of

the above outlined radiological licensing process, because a complete picture of consequences - including chemical toxicity - is probably required for radiological relevant accidents.

For the public, the permissible annual doses are those of [EURATOM, 1996], whereas the permissible doses for workers are not yet those of EU-guidelines, but about a factor of 2.5 higher.

8.2.2.5 Sweden

The Swedish Environmental Protection Agency is responsible for the monitoring of mercury levels and effects in the environment, the use of Hg in industries and laboratories, release controls, and the final disposal of mercury. All activities involving environmentally hazardous substances must follow the “General Rules of Consideration” of the Environmental Code as legal basis.

Sweden considers mercury as an environmental pollutant and pursues the strategy for risk reduction by phasing out all uses of Hg. The Environmental Government Bill 1990/91:90 of 1990 suggests to abandon Hg use by legislative and voluntary actions, with a few exceptions, by the year 2000. The chloralkaline industry, which currently accounts for the largest annual new addition (= 7 t) of Hg into the national balance, is allowed to continue operation until 2010. The most recent Governmental Bill 2000/01:65 “A Chemical Strategy for a Non-Toxic Environment” [Bill65] demands that Hg may not be used in production processes, unless the producer could prove that neither human health nor the environment would be harmed. The National Board of Health and Welfare has the overall responsibility to evaluate health effects on human beings [Forssell].

The Chemical Products (Handling, Import, and Export Prohibitions) Ordinance (1998:944) issued in 1998 [ChemPro, 1998] includes among other substances mercury regulating commercial import and export, regulating the manufacture of certain Hg containing products, however, granting exemptions from the prohibitions where exceptional reasons exist.

The Municipal Committee, which would be the most likely authority supervising facilities such as the ESS, is entitled to demand for an operation permit even if it would not be compulsory according to the Environmental Code. Notification must be given to the Municipal Committee containing a technical description sufficient for an assessment of the nature, scope, and environmental consequences of the activity considered. The notification must also include an environmental impact assessment.

Data on exposure limits are published in the Ordinance AFS 1966:2 of the Swedish National Board of Occupational Safety and Health. The upper limit of Hg concentration in the air at the work place is 0.05 mg/m³.

8.2.2.6 USA

In the USA, the federal government develops regulations and recommendations to protect public health. The Environmental Protection Agency (EPA), the Occupational Safety and Health Administration (OSHA), the Food and Drug Administration (FDA) and others develop regulations, enforced by law, concerning toxic substances. Recommendations providing guidelines are given, e.g., by the Agency for Toxic Substances and Disease Registry (ATSDR) and the National Institute for Occupational Safety and Health (NIOSH).

The General Industry Permissible Exposure Limit (PEL), i.e., the maximum allowable exposure (“acceptable ceiling concentration”) set by the OSHA code of regulations under

29CFR1910, subpart Z, [CFR] can be defined as “8 hr time-weighted average” or as “ceiling value”, which should not be exceeded any part of the working day. It is 0.1 mg of metallic or inorganic Hg per m³ for mercury and 0.04 mg/m³ (0.01 8h time-weighted average) for organic mercury. The NIOSH Recommended Exposure Limit (REL) corresponding to suggested industrial practices for airborne Hg exposure is half the above value: 0.05 mg/m³ averaged over an 8-hour work shift and 0.01 mg/m³ for organic and alkyl compounds. The ACGIH (American Conference of Governmental Industrial Hygienists) TLV is 0.025 mg/m³. NFPA (National Fire Protection Agency) rating is Health=3, Fire=0, Reactivity=0 (on the scale of 0 - 4). Spill quantities of greater than 1 pound (= 0.453 kg) must be reported, e.g., to the EPA. The EPA has set a limit of 2 ppb of mercury in drinking water.

While many laboratories indicate that only levels above 15 µg/dl should be considered toxic, a value of 50 µg/g urine is proposed by many experts as a biological threshold limit value for chronic exposure to mercury vapour. In 1980 a World Health Organization study group endorsed this. In unexposed individuals, the amount of mercury in blood is usually less than 2 µg/dl. Levels of about 2.8 µg/dl have to be reported to the Health Department. According to some experts, an average airborne concentration of 50 µg/m³ corresponds to a mercury concentration in blood of about 3-3.5 mg/dl. Early effects of mercury toxicity have been found when the blood concentration exceeds 3 µg/dl [EPA]. Management of laboratory and work place health and safety requires the preparation and implementation of a Chemical Hygiene Plan (CHP) in compliance with OSHA standards.

The EPA has established rules and guidelines for the disposal of mercury in manufacturing and other industries. There are currently no regulations restricting the discharge of mercury down the drain at medical institutes and laboratories.

8.2.2.7 Japan

The Japanese public and industries are particularly sensitive to the mercury issue because of several well-publicized disasters of heavy metal pollution of the environment in the 1960s and 70s (e.g., Minamata). They gave rise to Japan setting strict regulations to protect the environment.

The Environmental Agency founded in 1971 established quality standards. Under the Industrial Safety and Health Law of 1972, there are “Guidelines for the Necessary Means to Prevent Health Impairments to Workers due to Chemical Substances”, which include a “Chemical Substances Management Plan” for the work place. In 1974 Japan enacted the Chemical Substances Control Law according to which substances are categorized in Class I or Class II or Designated Substances. Whenever consensus on target values is possible, the Japanese industries regulate voluntarily rather than initiating legislated restrictions. An agreement on a provisional value is reviewed after 5 years.

Long-term (8 h) exposure limits are recommended by the Japanese Society of Occupational Health. The assessment standard for mercury and its inorganic compounds in working environment has been fixed at 0.05 mg/m³; for organic mercury, the limit is 0.01 mg/m³ [Air]. The respective standard for maximum total Hg concentration in ground water, drinking water, and soil is 0.0005 mg/l [Water].

SUMMARIZING TABLE:

The following table 8-1 contains most relevant information concerning concentration limits for mercury and compounds in different countries.

Potable water	EU	0.001 mg/l
	Germany	0.001 mg/l
	Japan	0.0005 mg/l
	USA	0.002 mg/l 2 ppb (EPA, FDA)
Air at work place	France	0.1 mg/m ³ inorganic, skin, long-term limit (8 h)
	United Kingdom	0.05 mg/m ³ long-term exposure limit (8 h) 0.15 mg/m ³ short-term exposure limit (15 min)
	Germany	0.1 mg/m ³ elemental and inorganic Hg 0.01 mg/m ³ organic Hg 200 µg/l urine 50 µg/l blood (*)
	Sweden	NGV 0.05 mg/m ³ , skin
	Japan	0.05 mg/m ³ elemental and inorganic Hg 0.01 mg/m ³ organic Hg
	USA	0.01 mg/m ³ alkyl compounds (organic Hg, 8 h time-weighted average) 0.1 mg/m ³ organic Hg (OSHA) 0.05 mg/m ³ met. Hg vapor for 8-hr shift and 40 h work weeks (OSHA)

(*) This value has been reduced to 25 µg/l blood in 2001.

Table 8-1: Environmental Standards concerning mercury in different countries

8.2.3 Selected aspects of civil licensing

In general, the civil licensing process for ESS will follow an established procedure in all European countries; however, there might be some site-specific items, which have to be addressed on a short-term base, because they may influence the design and may have a remarkable influence on costs. This influence has to be known ready for the overall ESS cost estimation. To these site-specific items for example belong:

- Stability of the ground
- Seismic conditions
- Specific climate conditions, which influence the design

8.2.4 Conclusion

The general conclusion from these descriptions of licensing requirements in different European countries to be drawn is, that main differences between rules of different countries belong to the consequence estimation part for dba and -concerning the procedure- whether the public has to be involved into the commissioning process or not. For normal operation, guidelines and rules concerning radiation protection of the staff and the public are very similar; all are based on EURATOM-directive 96/29 [EURATOM, 1996]; respective maximum permissible doses by direct radiation are outlined exemplarily in 8.3.1.1.

Concerning emissions into the environment in normal operation, for maximum permissible doses to the public holds nearly the same. Despite to differences in handling of dba, a substantial part of the safety analyses also for accidents is probably independent of the particular site, i.e. large parts of the system analysis, of the source term estimation and of dose estimations for emergency planning; further on it is expected, that safety analyses to be performed for planning of emergency countermeasures are similar for all countries; all are based on guideline ICRP-63 [ICRP-63, 1993] of the International Committee on Radiation Protection. With respect to toxicity of inactive mercury, the EU-directive (Seveso-II) guideline [Seveso-II, 1996] has not to be taken into account, because the total amount of mercury in ESS is below a limit of 50 t. The occupational safety concerning mercury and the maximum tolerable drinking water contamination are similar for most countries. Except to UK, where a slightly different commissioning process has to be fulfilled, the toxicity of inactive mercury is handled within the radiological licensing procedure, where a complete picture of the risk of the facility has to be outlined; a separate licensing is not required in most countries.

Site-specific conditions, which may influence the safety situation, remain to be identified for each possible site. It has to be noted, that more restrictive licensing requirements of some countries may increase total costs.

8.3 SAFETY ASPECTS OF ESS KEY COMPONENTS

The following components of ESS have to be considered in safety analyses:

- a) Target system: Concerning safety, the target system is the most relevant component, because -besides its direct radiation- it contains considerable amounts of radiotoxic and chemical toxic materials and also the burnable liquefied moderator, which may form explosive mixtures, if evaporated by failure. The target is the only component of the facility, which requires a detailed accident analysis for dba and hypothetical events (see 8.1). Due to the complex geometry, target shielding is an extensive task, as described in chapter 4.2 [4.2-7]. An overview on target system safety work is presented in chapter 4.7.
- b) Accelerator and rings: The main safety concern is due to direct radiation, which requires a sufficient shielding; mainly workers of the facility may be affected by direct radiation (occupational safety problems), although -via soil and ground water contamination due to direct radiation- the public may also be affected. The actual status on the safety work for the accelerator and the rings (shielding in normal operation and measures against local beam losses) is described in chapter 8.3.1, some statements on ground water and soil contamination are found in chapter 4.7.
- c) Other components (instruments, beam stops): Safety aspects of these components are in principle the same as already described in b) for the accelerator and the rings.

8.3.1 Safety considerations for the accelerator and the rings – shielding

8.3.1.1 *Introduction*

A more detailed description of shielding issues for ESS is found in [Berkvens, 2002]. The radiation protection legislation defines the rules that must guarantee the protection of the personnel against the ionising radiation. These rules are based on the ICRP-60

recommendations, and in the European Community more explicitly on the 96/29/Euratom directive [EURATOM, 1996].

Any radiation protection policy must respect the fundamental ALARA (As Low As Reasonable Achievable) principle. For the ESS project, we define the shielding thicknesses such that people working around the accelerators can be classified as non-exposed workers. We use the annual limits defined in the Euratom directive 96/29 [EURATOM, 1996], namely 1 mSv per year for non-exposed workers. Note that an annual equivalent dose of 1 mSv corresponds to an equivalent dose rate of $0.5 \mu\text{Sv h}^{-1}$, assuming 2000 working hours per year.

All shield wall thicknesses have been designed to obtain dose equivalent rates, at contact behind the shield wall of $0.5 \mu\text{Sv.h}^{-1}$, using conservative, but realistic beam loss assumptions. For the calculations occupancy factors of 100 % are assumed. Under these conditions, we guarantee that the annual dose a person can receive will be far below the 1 mSv limit for non-exposed workers, including doses originating from accidental beam losses.

For proton energies above 1 GeV, the shielding calculations for the ESS accelerator facility have been done using the analytical Moyer model [RSA, 1988]. This model has proven to give very reliable results (see different examples given in reference [FGD, 1966]) and has e.g. recently been used for the shielding design of the SPL project at CERN [Autin, 2000]. Below 1 GeV a similar model is used, with energy-dependent source terms and attenuation lengths [Sullivan, 1992].

8.3.1.2 The model used for the shielding calculations

Analytical shielding models used for high-energy proton accelerators ($E > 1 \text{ GeV}$) are based on two fundamental ideas:

- a) At proton energies above 1 GeV, the dose outside the shield wall will be caused by high-energy neutrons ($E \geq 150 \text{ MeV}$) and low energy neutrons in radiation equilibrium with them. Because of the energy dependence of the inelastic cross sections for neutrons the attenuation in the shield can be described using a single dose attenuation length independent of neutron energy.
- b) The dose equivalent source term ($\text{Sv} \cdot \text{m}^2$ per proton) is approximately proportional to the primary proton energy.

The shielding calculations for the high-energy part of the ESS accelerators ($E > 1 \text{ GeV}$) have been carried out using one of these analytical models, the Moyer model.

For a detailed description of the Moyer model, we refer to reference [RSA, 1988], pp. 282 – 307. We simply recall in what follows the basic ideas of this model.

Figure 8-1 gives the general geometry used for shielding calculations in the case of a proton beam hitting a target.

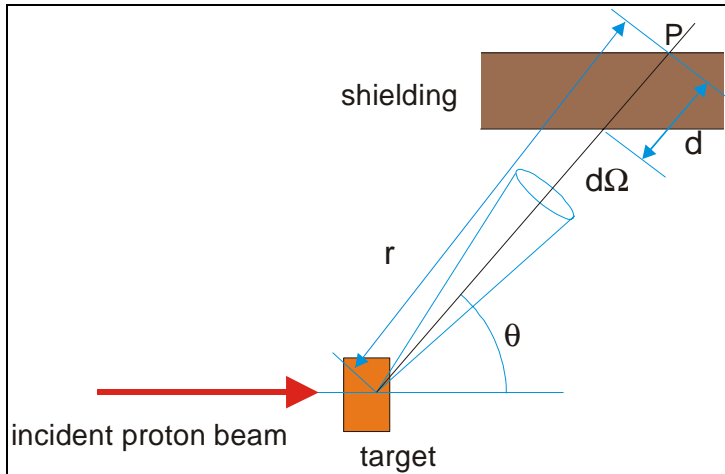


Figure 8-1: Geometry used for shielding calculations

For shielding calculations we can assume that neutrons are the only secondary particles. The gamma component could be one order of magnitude less than neutron dose but should still be considered in some cases, e.g. chicanes and penetrations. Considering the target as an effective point source, we obtain the following expression for the dose equivalent rate \dot{H} at a point P behind the shield wall:

$$\dot{H} = \frac{1}{r^2} \int F(E) B(E, \theta) e^{-d(\theta)/\lambda(E)} \frac{d^2 n(E, \theta)}{dE d\Omega} dE,$$

With:

$F(E)$: fluence to dose equivalent conversion factor,

$B(E, \theta)$: build-up factor,

$\lambda(E)$: effective removal mean free path,

$\frac{d^2 n(E, \theta)}{dE d\Omega}$: differential neutron yield.

In the Moyer model, the above expression is approximated by a single neutron energy group, based on the characteristic variation of neutron attenuation lengths as a function of energy, as shown in figure 8-2 (high energy pions and protons in the hadronic cascade have very similar cross-sections). As shown in this figure the actual variation of the attenuation length with energy may be approximated by a step function:

$$\lambda(E > 150 \text{ MeV}) = \lambda,$$

$$\lambda(E \leq 150 \text{ MeV}) = 0.$$

The essence of the Moyer model, therefore, is that the dose equivalent at any point outside the accelerator shield is largely governed by the simple line-of-sight propagation of the cascade generating particles (> 150 MeV) produced at the target. These particles have an attenuation length that is independent of their energy.

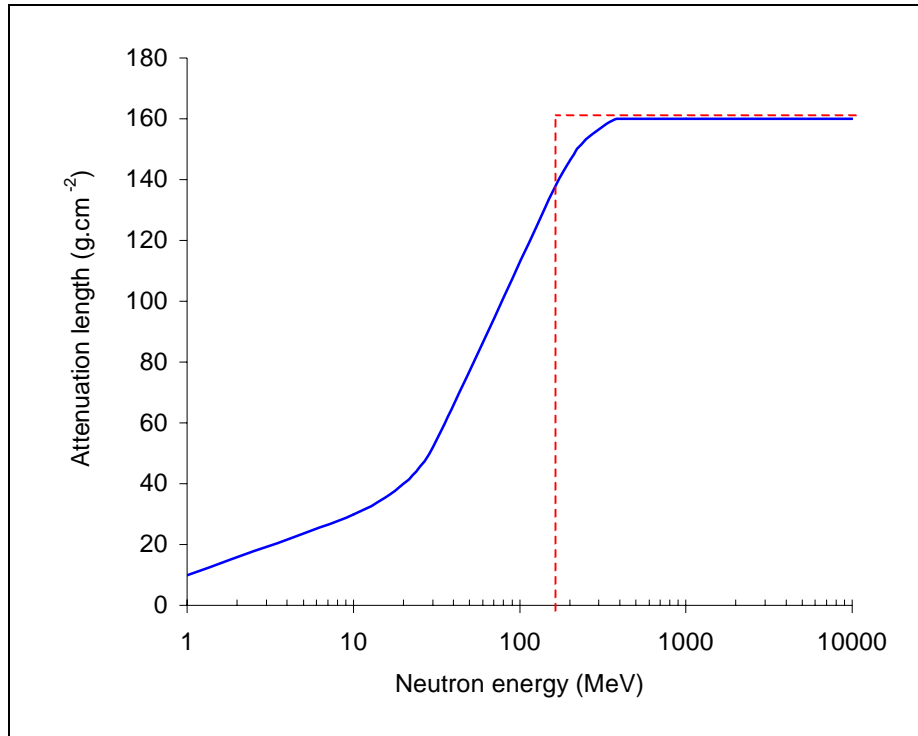


Figure 8-2: Neutron attenuation length as a function of energy. The dashed line shows the step-like function assumed in the Moyer model calculations.

Using experimentally determined values for the source strength and for the angular distributions of the emitted hadrons, finally the following expression is obtained for the transverse shielding calculations for a typical accelerator geometry shown in figure 8-3 [FGD, 1966]:

$$H = \frac{\Psi(E_p)N e^{-\beta\theta} e^{-\frac{D}{\sin\theta}}}{R^2/\sin^2\theta}$$

With:

$$\begin{aligned}
 \Psi(E_p) &= 2.8 \times 10^{-13} E_p^{0.8} \text{ Sv} \cdot \text{m}^2, \\
 \beta &= 2.3 \text{ radians}^{-1}, \\
 D &= \sum \frac{d_i}{\lambda_i} \\
 N &= \text{Number of protons interacting,} \\
 E_p &= \text{Proton energy in GeV}
 \end{aligned}$$

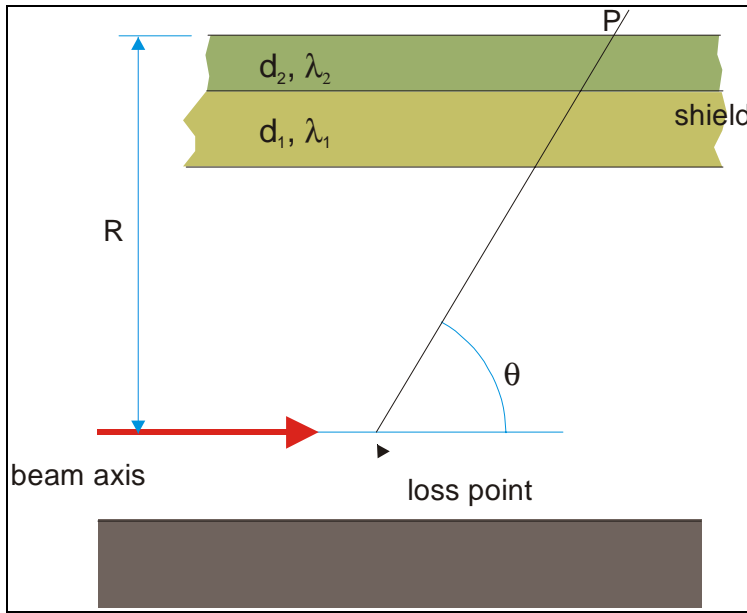


Figure 8-3: Accelerator geometry used in the Moyer model calculations

For our calculations the following values for the attenuation lengths were used [FGD, 1966], densities are given in brackets:

Concrete	(2.35 g cm ⁻³):	50 cm
Soil	(1.8 g cm ⁻³):	69 cm
Iron	(7.4 g cm ⁻³):	20.81 cm

For proton energies below 1 GeV the two basic assumptions for the high-energy shielding model are no longer valid:

1. The average secondary particle energy will be less than 150 MeV and consequently their attenuation mean free path in the shield will change with energy.
2. The ionisation energy losses of both the primary protons and the secondary charged hadrons become important, inhibiting the full development of the hadronic cascade. As a consequence the approximate proportionality of the dose equivalent source term to the incident proton energy will no longer hold.

Analysis of experimental shielding data and results from Monte-Carlo calculations in this energy range show that it is still possible to use a simple analytical model of the form:

$$H = \frac{H_0 e^{-d/\lambda \sin \theta}}{R^2 / \sin^2 \theta},$$

Provided one uses energy dependent values for the dose equivalent source term H_0 and the neutron attenuation lengths λ [Sullivan, 1992].

Figure 8-4 gives the relative variation of the effective source term at 90 degrees with proton energy, and figure 8-5 shows the relative secondary particle attenuation mean free path as a function of primary proton energy.

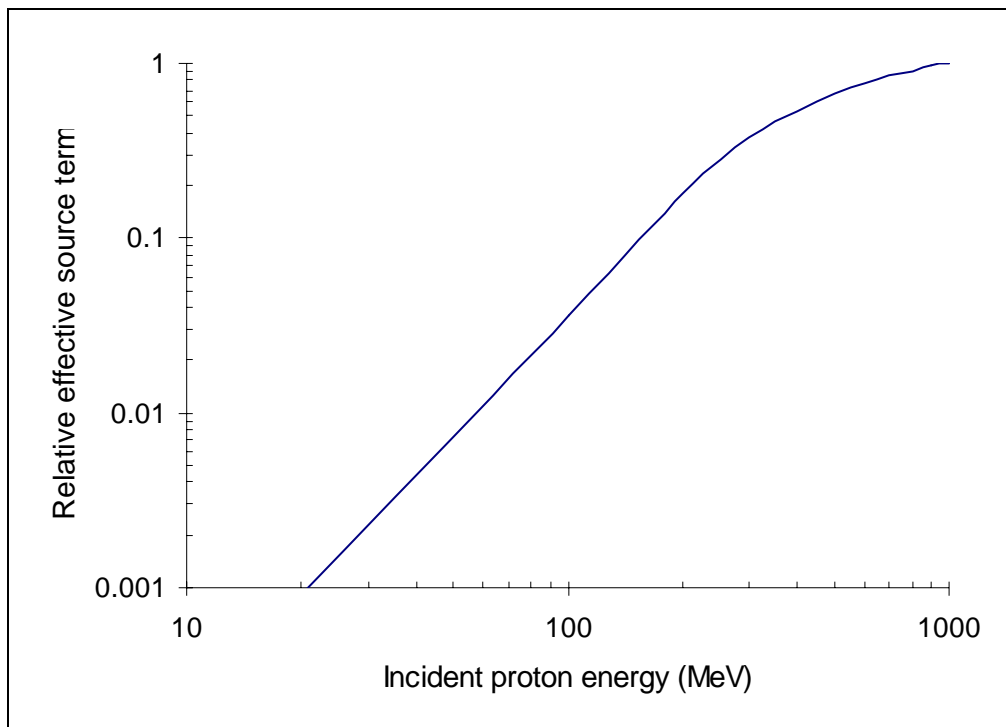


Figure 8-4: Relative effective source term for transverse shielding, as a function of incident proton energy

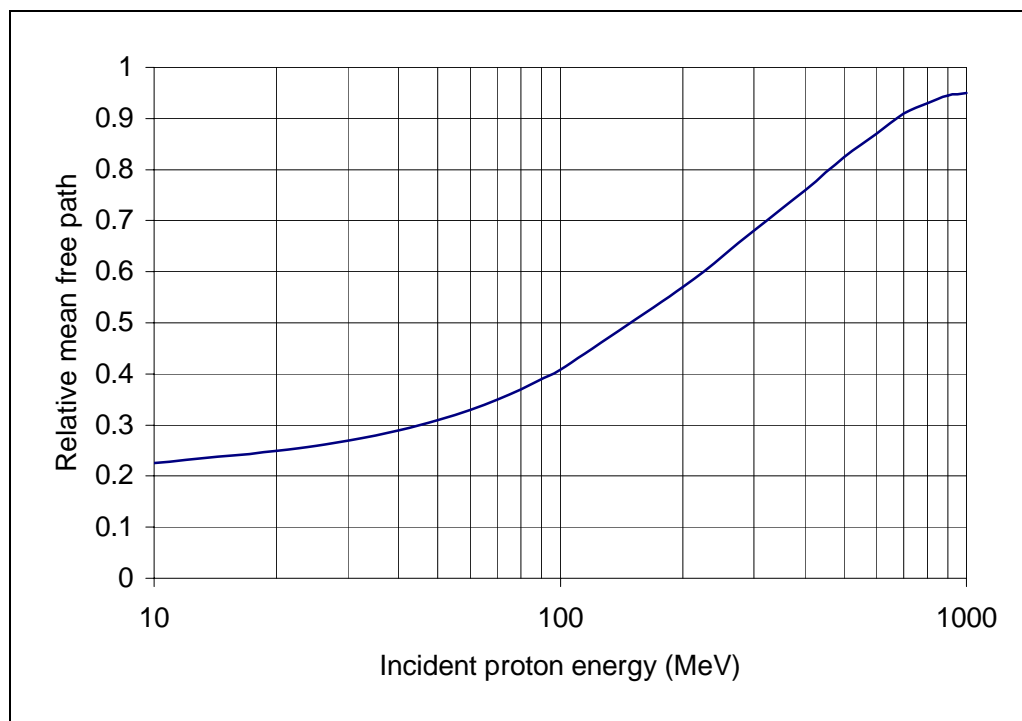


Figure 8-5: Secondary particle attenuation mean free path as a function of primary proton energy

Finally we have multiplied artificially all dose values obtained with the model using the source terms proposed in reference [RSA, 1988] by a factor of 2 to take into account the increased neutron quality factor defined in the directive 96/29/Euratom [EURATOM, 1996].

The dose calculations were done using a computer programme, written in C++ under Windows. This programme allows calculating shielding thickness for point losses, and finite and infinite linear losses. The programme was extensively tested by reproducing the various examples presented in reference [RSA, 1988], as well as the shielding calculations given in reference [Aulin, 2000], and has been successfully compared with results from the Monte-Carlo calculations given in reference [APSAD, 2000].

The main result of application of the methods described before to the ESS accelerator is as follows: Assuming continuous beam losses of $1 \text{ W} \cdot \text{m}^{-1}$ a thickness of soil shielding of about 6.8 m is required for reduction of dose rates to $0.5 \mu\text{Sv}/\text{h}$ on the outside of the shielding [Berkvens, 2002].

8.3.1.3 Measures against local beam losses

In the chapter before the methods to be applied for calculation of a shield wall thickness for the linac, transfer lines and the ring assuming continuous beam losses are described. In this chapter the effect of accidental losses is evaluated. Figure 8-6 shows the dose rate outside the shielding, above a continuous localized loss of 10 MW, as a function of the earth thickness above the 60 cm thick concrete tunnel roof (calculated with Moyer model, at 1.334 GeV). The thickness of 6.8 m of earth required to reduce dose rates to $0.5 \mu\text{Sv} \cdot \text{h}^{-1}$ for a linear loss of $1 \text{ W} \cdot \text{m}^{-1}$ is indicated, too. One sees that a thickness of 15.5 m earth is required to reduce the dose rate to $0.5 \mu\text{Sv} \cdot \text{h}^{-1}$ for a continuous point loss of 10 MW. As expected it is therefore practically impossible to provide enough shielding to allow for continuous full power losses.

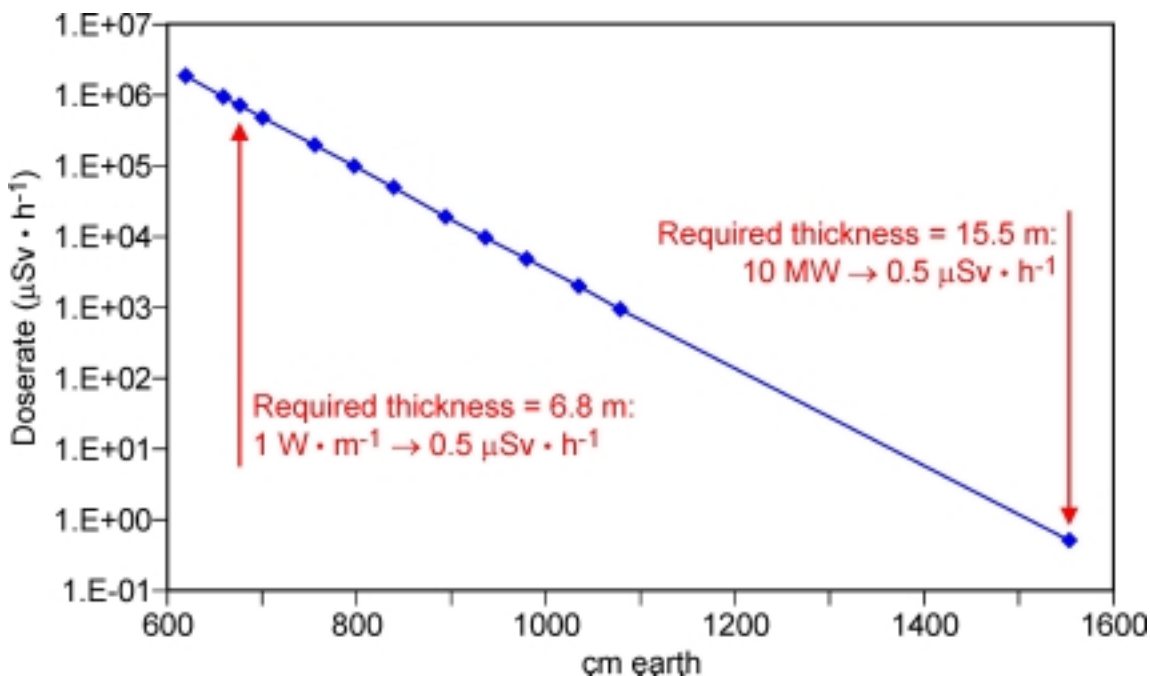


Figure 8-6: Dose rate as a function of earth thickness above 60 cm concrete roof, for a continuous 10 MW local (point) loss.

Accordingly, an interlocked system is needed, combining accelerator diagnostics and radiation monitors which role is to stop the linac as soon as abnormal beam losses occur. From an accelerator point of view such an interlock system must be fast in order to limit equipment damage if the high power beam accidentally hits un-cooled accelerator components. From a radiation protection point of view the behaviour of such an interlocked system must be evaluated for two different aspects:

1. The integrated dose outside the shield wall due to accidental losses must be compared to the dose from the normal $1 \text{ W}\cdot\text{m}^{-1}$ beam losses. With the shielding philosophy used we can accept maximum accidental beam losses resulting in the same integrated dose as the continuous $1 \text{ W}\cdot\text{m}^{-1}$ losses.
2. A $1 \text{ W}\cdot\text{m}^{-1}$ loss rate has been generally accepted as a loss rate that will produce activation levels inside the tunnels allowing hands-on maintenance during the shutdown periods. It is therefore important that the activation level induced from the accidental losses should not strongly increase this activation level.

Figures 8-7a to 8-7c show the requirements of the interlock system for a Mean Time Between Failure (MTBF) of 8 hours, of 2 days and of 20 days respectively. We assume that the accidental beam losses always occur in the same location. The figures contain the number of pulses (5 MW, 50 Hz) an accidental beam loss can last before the integrated dose outside the shield wall from this accidental loss equals the dose from the continuous $1 \text{ W}\cdot\text{m}^{-1}$ loss (e.g. in case of a MTBF = 8 hours, the dose due to an accidental loss shall not exceed $8 * 0.5 \mu\text{Sv}\cdot\text{h}^{-1} = 4 \mu\text{Sv}$). This number of pulses is shown by the vertical red lines for a 6.8 m thick earth shield (which is the shielding calculated for the $1 \text{ W}\cdot\text{m}^{-1}$ loss), for a shield with 1 extra m of earth and for a shield with an extra 2.4 m of earth. In the same figures we have also shown the saturation activation level (calculated at 0.5 m from the local loss point) relative to the activation level from the continuous $1 \text{ W}\cdot\text{m}^{-1}$ loss, for 3 isotopes with half-lives of 5 d, 30 d and 250 d. The 250 d case is typical for the long-lived isotopes that will be found around high-energy accelerators.

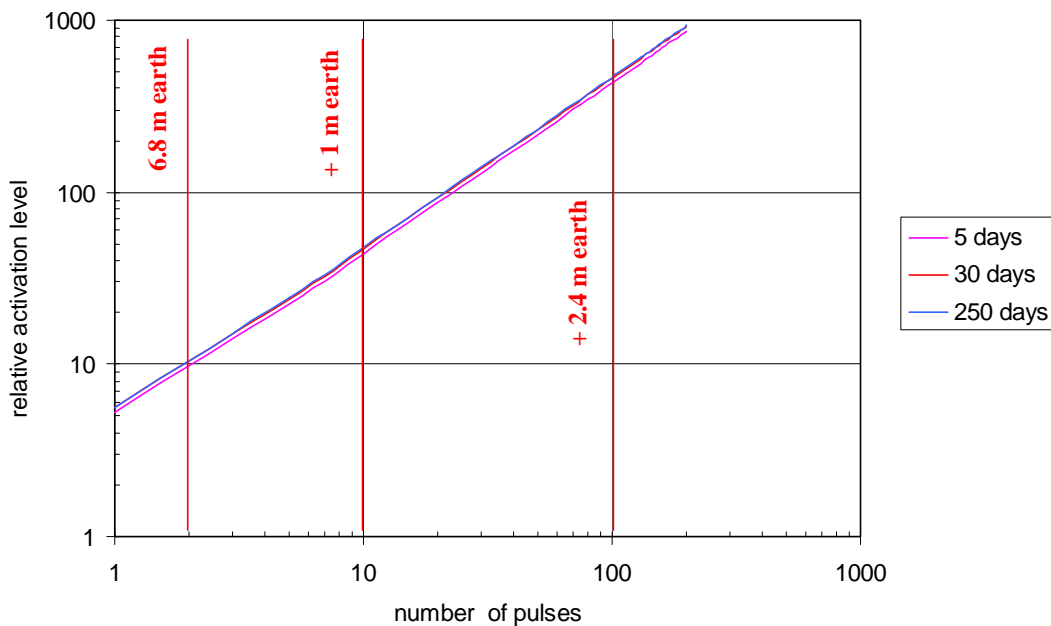


Figure 8-7a: Relative activation levels as function of the duration of an accidental beam loss for a MTBF of 8 h for 3 isotopes with half-lives of 5 d, 30 d and 250 d. The red vertical lines show the number of pulses required to obtain an integrated dose per beam loss outside the shield wall of $4 \mu\text{Sv}$ for an earth shield of 6.8 m, 7.8 m and 9.2 m.

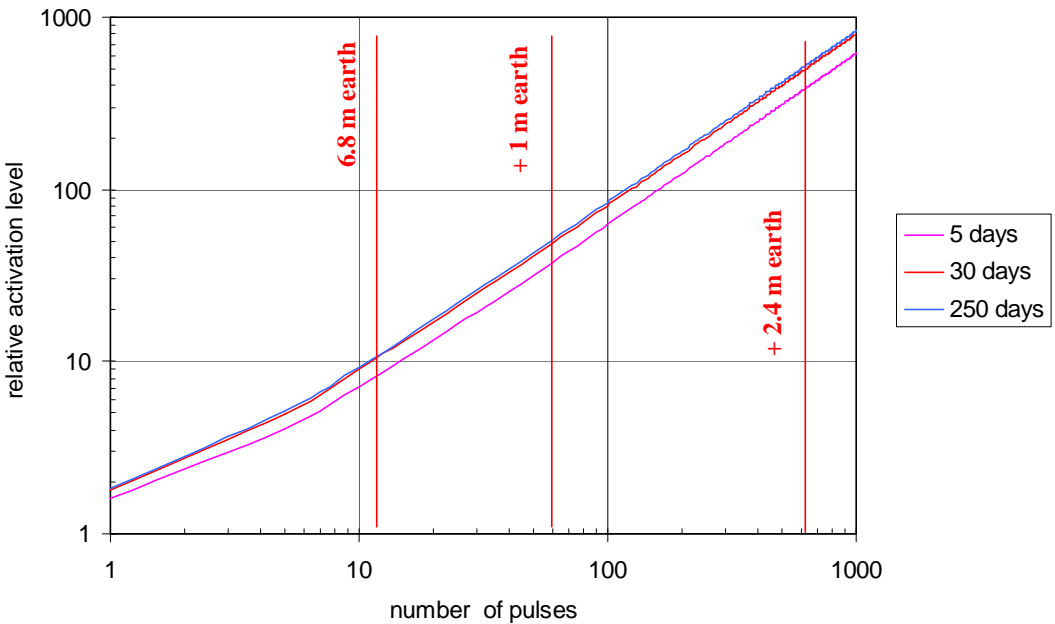


Figure 8-7b: Relative activation levels as function of the duration of an accidental beam loss for a MTBF of 2 d, for 3 isotopes with half-lives of 5 d, 30 d and 250 d. The red vertical lines show the number of pulses required to obtain an integrated dose per beam loss outside the shield wall of 24 μSv for an earth shield of 6.8 m, 7.8 m and 9.2 m.

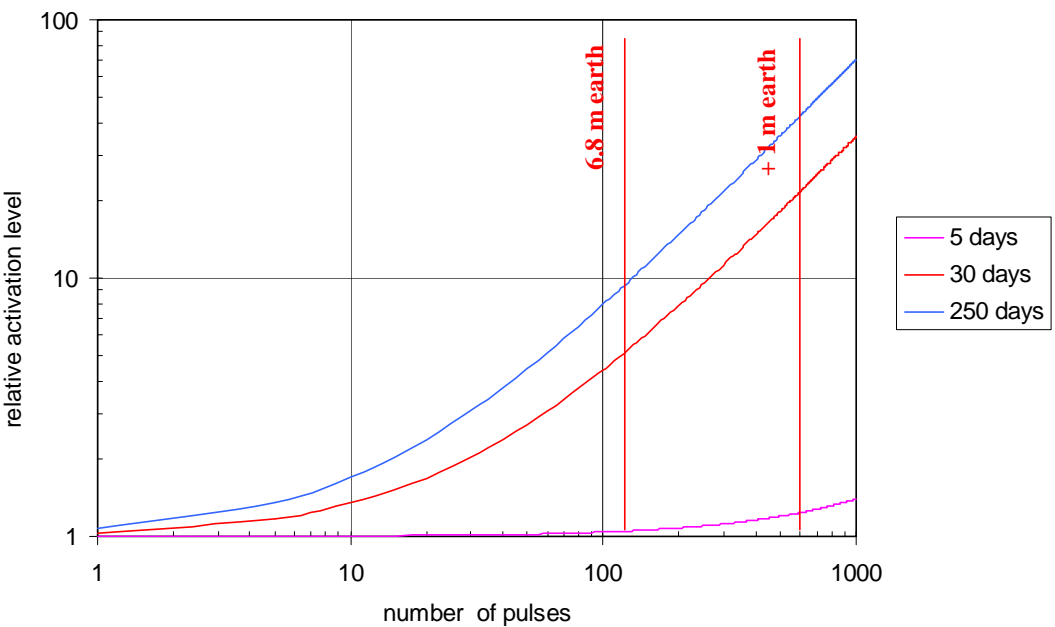


Figure 8-7c: Relative activation levels as function of the duration of an accidental beam loss for a MTBF of 20 d, for 3 isotopes with half-lives of 5 d, 30 d and 250 d. The red vertical lines show the number of pulses required to obtain an integrated dose per beam loss outside the shield wall of 240 μSv for an earth shield of 6.8 m and 7.8 m.

From these figures one sees, that from a radiation protection point of view the highest constraint on the beam loss interlock system comes from the residual activation level inside

the tunnels. With the shielding walls calculated for the $1 \text{ W} \cdot \text{m}^{-1}$ continuous loss we already cope with accidental beam losses that will increase the activation levels by nearly a factor of ten. It is therefore obvious that increasing the shield thickness does not make too much sense, knowing that this will anyhow not allow relaxing on the speed of the interlock system.

8.4 WASTE FROM DECOMMISSIONING AND DISMANTLING

High active waste ($>3.7 \times 10^5 \text{ GBq/m}^3$ following German definitions for liquid waste, shielding and cooling required during storage) is produced mainly in the target system: Mercury ($2 \times 15 \text{ t} = 2.2 \text{ m}^3$) with a starting activity of altogether about $2.5 \times 10^5 \text{ TBq}$ is the main issue. It has to be noted however, that the only nuclide with a half life $> 1000 \text{ y}$ occurring in substantial amounts in the target is Ho-163 ($t_{1/2} = 4570 \text{ y}$), which decays with a very low decay energy of 2.8 keV by electron capture without γ -emission to stable Dy-163, and is accordingly probably of relatively small radiological relevance. The most relevant long lived nuclide within the target are Pt-193 ($t_{1/2} = 60 \text{ y}$), and Hg-194 ($t_{1/2} = 515 \text{ y}$), together with a small amount of La-137 ($t_{1/2} = 60000 \text{ y}$) which dominates the activity of the mercury at $t < 20000 \text{ y}$; there are no actinides or other fissile materials or long lived α -emitters in the waste.

Table 8-2 contains the total activity of the target for 100, 1000 and 10000y after end of a 30 year period of operation (based on [PSAR, 2000]; a second row shows the total activity without the radiologically less important Ho-163:

	Activity [GBq]		
	100y	1000y	10000y
Total activity	2.2e5	5.0e4	7000
Total activity without Ho-163	2.0e5	2.4e4	15

Table 8-2: Activity decay of the ESS mercury targets (30 y continuous operation)

It should be noted, that long-term activities ($>1 \text{ y}$ after shut down) of the ESS target were probably too low in the 1997 version of the ESS technical report.

Considering the comparison of radiotoxicity and chemical toxicity of mercury concerning early consequences, outlined in chapter 4.7.2.2, it becomes obvious, that – taking only incorporation pathways into account - the chemical toxicity becomes dominating after about 500 - 1000 y; the radiotoxicity of the target mercury remains large for this long time period mainly because of the great half life of Hg-194. If external irradiation has to be considered, too, this time period becomes substantial larger, as outlined in 4.7.2.2. It has to be noted, that after already about 100 y the target mercury is no longer high, but medium active waste (no cooling, but shielding required in storage).

Other sources of high active waste are the proton window and other parts of the target hull, which will be exchanged about 2 times per year. Most other target components have to be considered as medium active, as the beam dumps and other highly irradiated areas of the facility like parts of the shielding of target, accelerator, ring and instruments. Large amounts of low active waste ($< 0.37 \text{ GBq/m}^3$) are expected from all components of the facility; this low active waste is at least to some part a possible subject of recycling; storage of low active waste does not require a shielding. There is substantial knowledge available to decommissioning and amount of waste in course of dismantling of particle accelerators [HFW, 2000], [EC, 1999], so details are not given here.

8.5 GENERAL PROCEDURE OF ONGOING ESS SAFETY WORK

A preliminary safety analysis for ESS will be performed until the end of 2003. This analysis will cover all relevant ESS components. The main aims of this analysis are:

- Supporting ESS design work with respect to optimisation of ESS safety features
- Giving sufficient information about safety for the decision about ESS construction
- Collecting arguments for convincing the public about a safe ESS operation
- Acting as basis for a safety report for ESS to be prepared just after the decision for ESS construction

The safety analysis is based on the respective SNS work [PSAR, 2000], [APSAD, 2000] , but will consider the specific ESS conditions concerning design and commissioning; in chapter 4.7.3 it is outlined that, due to differences in commissioning requirements, the ESS safety study for the target has to be more detailed than the respective SNS studies. This safety analysis deals mainly with site independent safety items; site dependent issues (both, legal aspects and physical conditions of the site) will be worked out by national teams and can be added to the documentation of the analysis.

REFERENCES

[Air]	National Institute of Technology and Evaluation and Japan Chemical Industry Association, List of Materials on Laws and Regulations: Air, Internet: http://www.rminfo.nite.go.jp/english/gyousei/kankyo.htm
[APSAD, 2000]	Spallation neutron Source - Accelerator- Preliminary Safety Assessment Document, September 2000
[Autin, 2000]	B. Autin et al., "Conceptual design of the SPL, a high-power superconducting h-linac at CERN, Grenoble (2000)
[BA, 1983]	Störfallberechnungsgrundlagen für die Leitlinien zur Beurteilung der Auslegung von Kernkraftwerken mit DWR gemäß §28 Abs. 3 StrSchV, Bundesanzeiger 35, 31.12.1983, Nummer 245 a

- [BA, 1994] Neufassung des Kapitels 4 „Berechnung der Strahlenexposition“ der Störfallberechnungsgrundlagen für die Leitlinien zur Beurteilung der Auslegung von Kernkraftwerken mit DWR gemäß §28 Abs. 3 StrSchV ; Bundesanzeiger 46, 26.11.1994, Nummer 222a, G1990A
- [Berkvens, 2002] P. Berkvens, Shielding calculations for ESS accelerators, Report ESS/CF/SAF/0000/001, February 2002.
- [BGBI-1, 1990] Gesetz zum Schutz vor schädlichen Umwelteinwirkungen durch Luftverunreinigungen, Geräusche, Erschütterungen und ähnliche Vorgänge (Bundes-Immissionsschutzgesetz) in der Fassung der Bekanntmachung vom 14. Mai 1990 (BGBI. I S. 880), Internet:
http://www.umweltschutzrecht.de/recht/luft/bimschg/bim_ges.htm or
<http://teiresias.umsicht.fhg.de/WebTeiresias/vtdat/bimschg>
- [BGBI-5702, 2001] Verordnung für die Umsetzung von EURATOM Richtlinien zum Strahlenschutz, 20.07.2001, Bundesgesetzblatt G5702 (2001) Nr. 38
- [Bill65] A Chemical Strategy for a Non-Toxic Environment, Govt. Bill 2000/01:65, Internet:
<http://www.chem.unep.ch/mercury/gov-sub/sub28govatt3.pdf>
- [CD96, 1996] EU Council Directive 96/62/EG on the Valuation and the Control of Air Quality of 1996, Internet:
http://www.lua.nrw.de/anlagen/r196_62_eg.pdf
- [CD98, 1998] Council Directive 98/24/EC of 7 April 1998 on the Protection of the Health and Safety of Workers from the Risks Related to Chemical Agents at Work or Chemical Agents Directive, Internet:
http://europa.eu.int/eur-lex/en/lif/dat/1998/en_398L0024.html
- [CFR] Codes of Federal Regulations (CFR), Title 29 Occupational Safety and Health Administration (OSHA), Part 1910 Occupational Safety and Health Standards, Subpart Z - Toxic and Hazardous Substances, Internet:
http://www.osha.gov/OshStd_toc/OSHA_Std_toc_1910_SUBPART_Z.html
- [ChemPro, 1998] The Chemical Products (Handling, Import, and Export Prohibitions) Ordinance (1998:944), Internet:
<http://www.chem.unep.ch/mercury/gov-sub/sub28govatt1.pdf>
- [COSYMA, 1994] PC COSYMA: An accident consequence assessment package for use on a PC. Report EUR 14916 EN (1994)

- [EC, 1999] Evaluation of radiological and economical consequences of decommissioning particle accelerators, European Commission, Report 19151 EN, Luxembourg (1999)
- [EPA] Mercury Use Reduction & Waste Prevention in Medical Facilities, Environmental Protection Agency (EPA), Internet: <http://www.epa.gov/seahome/mercury/src/outmerc.htm>
- [EURATOM, 1996] EU Council Directive 96/29/EURATOM of 13.05.1996, laying down basic safety standards for the health protection of the general public and workers against the dangers of ionising radiation
- [FGD, 1966] French Government: Décret n° 66-450 du 20 juin 1966 relatif aux principes généraux de protection contre les rayonnements ionisants, annexe 2 «classification des radionucléides»
- [Forssell] J. Forssell, E. Gustavsson, H. Parkman, Global Assessment of Mercury and its Compounds, Internet: <http://www.chem.unep.ch/mercury/gov-sub/sub28gov.pdf>
- [GSGS, 1980] Gesetz zum Schutz vor gefährlichen Stoffen in der Fassung vom 16. September 1980, Internet: <http://bundesrecht.juris.de/bundesrecht/chemg/inhalt.html>
- [HFW, 2000] M.Höfert, D.Forkel-Wirth: The decommissioning of accelerator installations, a challenge for radiation protection in the 21th century, Proc. IRPA-10, Hiroshima (Japan), 14.-19.05.2000
- [ICRP-63, 1993] Report ICRP-63: Principles for Intervention for Protection of the Public in a Radiological Emergency, May (1993)
- [Maneke, 1988] J.Maneke et al.: Study of US and FRG criteria for use in HTGR safety evaluation. DOE-HTGR-87102 (1988)
- [Mercury, 1996] Safety Data for Mercury, Internet: <http://physchem.ox.ac.uk/MSDS/ME/mercury.html>
- [PSAR, 2000] SNS Preliminary Safety Analysis Report (PSAR), Feb. 28 (2000), US DOE Contract No. AC05-96OR22464

- [R548, 1967] Richtlinie 67/548/EWG des Rates vom 27. Juni 1967 zur Angleichung der Rechts- und Verwaltungsvorschriften für die Einstufung, Verpackung und Kennzeichnung gefährlicher Stoffe, Internet:
http://www.umwelt-online.de/recht/eu/69/67_548gs.htm or
http://teiresias.umsicht.fhg.de/WebTeiresias/vtdat/r67_548 (in German)
- [RSA, 1988] Radiological Safety Aspects of the Operation of Proton Accelerators, IAEA Technical Reports Series no. 283, Vienna, 1988
- [Seveso-II, 1996] EU-Council Directive 96/82/EC of 9th Dec 1996 on the control of major-accident hazards involving dangerous substances (Seveso-II directive)
- [Sullivan, 1992] A.H. Sullivan, "A guide to radiation and radioactivity levels near high energy particle accelerators", NTP (1992)
- [TAAAbfall] Zweite Allgemeine Verwaltungsvorschrift zum Abfallgesetz („TA Abfall“), Internet:
http://www.bmu.de/sachthemen/abfallwirtschaft/bmu_stadt/pd/taabfall.pdf
- [TALuft] Technische Anleitung Luft („TA Luft“), Internet: <http://www.bmu.de/download/dateien/taluft.pdf>
- [TRGS 900] TRGS 900 - Grenzwerte in der Luft am Arbeitsplatz - Luftgrenzwerte, Internet:
http://www.umwelt-online.de/regelwerk/t_regeln/trgs/trgs900/mak_ges.htm
- [TRGS 903] TRGS 903 Biologische Arbeitplatztoleranzwerte - BAT-Werte, Internet:
http://www.umwelt-online.de/regelwerk/t_regeln/trgs/trgs900/903_ges.htm
- [V4-BISG, 1985] Vierte Verordnung zur Durchführung des Bundes-Immissionsschutzgesetzes, Verordnung über genehmigungsbedürftige Anlagen, Internet:
http://jurcom5.juris.de/bundesrecht/bimschv_4_1985/
- [V12-BISG, 2000] Zwölfta Verordnung zur Durchführung des Bundes-Immissionsschutzgesetzes, Störfall-Verordnung, Internet:
http://jurcom5.juris.de/bundesrecht/bimschv_12_2000/

[V22-BISG]

Zweiundzwanzigste Verordnung zur Durchführung des BundesImmissionsschutzgesetzes, Verordnung über Immissionswerte, Internet:
http://www.umweltschutzrecht.de/recht/luft/bimschg/vo/22bv_ges.htm

[VSGS]

Verordnung zum Schutz vor gefährlichen Stoffen, Internet:
http://www.umwelt-online.de/recht/gefstoff/gefahrst.vo/gfv_ges.htm or
<http://de.osha.eu.int/legislation/verord/gefstoffv.htm>

[Water]

National Institute of Technology and Evaluation and Japan Chemical Industry Association, List of Materials on Laws and Regulations: Water Quality, Soil., Internet:
<http://www.rminfo.nite.go.jp/english/gyousei/kankyo2.htm>

Chapter 9

Project Schedule, Organisation, Personnel and Costs

Authors and Contributors

Project Schedule, Organisation, Personnel and Costs

F H Bohn¹, K Bongardt², M Desmons³, I Gardner⁴, D Findlay⁴, P Giovannoni³, J F Gournay³, H Jones⁴, J L Laclare¹, S Martin², S Palanque³, J R Treadgold⁴

¹ESS-CPT, ²FZJ, ³CEA ⁴RAL/ISIS

Contents

Project Schedule, Organisation, Personnel and Costs

2 PROJECT SCHEDULE, ORGANISATION, PERSONNEL AND COSTS.....	9-4
9.1 OVERVIEW.....	9-4
9.2 PROJECT SCHEDULE.....	9-5
9.2.1 CONSTRUCTION PERIOD	9-5
9.2.2 OPERATIONS PERIOD.....	9-7
9.3 ESS AS AN EUROPEAN ORGANISATION.....	9-8
9.3.1 MODEL FOR THE ORGANISATION.....	9-8
9.3.2 ORGANISATION CHART	9-8
9.3.3 POLICY FOR PERSONNEL AND STAFF MULTI-ANNUAL PROFILE	9-9
9.4 CONSTRUCTION COSTS	9-10
9.4.1 BASIS FOR COST ESTIMATES.....	9-10
9.4.2 CONSTRUCTION COSTS BREAKDOWN	9-12
9.4.3 LONG-TERM OPERATIONS COSTS.....	9-13
9.4.4 ESS MULTI-ANNUAL BUDGET PROFILE	9-14

9 PROJECT SCHEDULE, ORGANISATION, PERSONNEL AND COSTS

9.1 OVERVIEW

The construction of the ESS facility is planned to take 8 years including 2 years for sequential commissioning of the complete chain of accelerators, the 2 targets and the first set of 10 instruments.

Therefore, assuming that all required decisions are made by January 2004, operations could start in January 2012.

During the last year of construction and the first year of operations, the beam power would increase in steps, up to the specified 5 MW to be delivered to each target station. Before starting **routine operations** in User Service Mode (USM) in **January 2013**, with the above assumptions, the full first year of operations will be dedicated to performing calibration and test experiments on the first 10 instruments.

The construction costs, i.e. all the costs during the 8-year construction period, of the ESS facility (1.33 GeV, 5 MW to each target and 10 initial instruments plus the cumulative costs during this construction period of another 18 instruments whose construction will start in this period) amount to

1 552 Million Euro at 2000 prices.

This figure includes not only capital investments for all components necessary for the ESS baseline as described in chapters 1 to 8, but also all the manpower required (in-house and subcontracted staff) at the various stages of the project: detailed design, procurement, construction, testing, installation and commissioning.

A 15 % contingency is included.

With regard to the organisation of the ESS facility, it is proposed to follow the ESRF model with a few optimisations.

For such a highly user-oriented facility operating up to 5 500 hours per year in User Service Mode with 40 instruments, apart from instruments of Collaborating Research Groups (CRGs), a permanent staff of 600 posts plus 50 students is assumed on the long term.
The operations budget amounts to

142 Million Euro at 2000 prices.

This includes a recurrent expenditure for developments and systematic refurbishment/enhancement and replacement of 3 instruments equivalent to 3 new units per year.

9.2 PROJECT SCHEDULE

The construction of ESS will take 8 years, from the decision for the project go-ahead (Milestone 1 or M 1) to the start of operations (Milestone 6). The estimated duration is based on industrial studies and experience gained from the construction of similar facilities like ESRF and SNS.

The conventional facilities programme is one of the most critical from the standpoints of technical risks, schedule and costs (~ 35 % of overall construction costs). Machine parts can generally be ready for installation well before the buildings are completed. Therefore, the conventional facilities dictate the overall construction schedule. Highest priority is required for starting the conventional facilities programme and for placing the Industrial Architect (INA) contract very shortly after the decision for the project go-ahead (M1).

Figure 9-1 shows the summary of the ESS project schedule indicating major activities, which are briefly explained in the following.

9.2.1 Construction period

Milestone 1: The project go-ahead will be the start of 15 months for recruiting the nucleus of the project team, revising the program in accordance with the funding profile, launching the call for tenders and awarding the INA contract. Approximately 1 year after M 1 first procurements will be made.

Milestone 2: (Milestone M 1 + 15 months) is marked awarding the INA contract. Also, it will be the beginning of a period of 6 months dedicated to preliminary design, after which another 12 months are needed for detailed design, both for subsystems on the critical path. Design activities for less critical items will follow this period. As soon as the building permits will be obtained (1 year after M2) the call for tenders for ground breaking and conventional facilities will be issued. The first contracts can be awarded.

Milestone 3: (M 1 + 32 months) is marked by ground breaking. Site preparation can then start, and as soon as contracts have been awarded, conventional facilities construction can begin. The total period for tendering and awarding of contracts for conventional facilities is assumed to be 15 months. Of the total period of conventional construction of 36 months, 24 months will be devoted to construction, commissioning and acceptance of the technical service buildings providing electricity, fluids and HVAC. During this period, in a pre-defined order, the first buildings housing machine subsystems will be made available for Beneficial Occupancy (BO) and installation. That last event defines the next milestone.

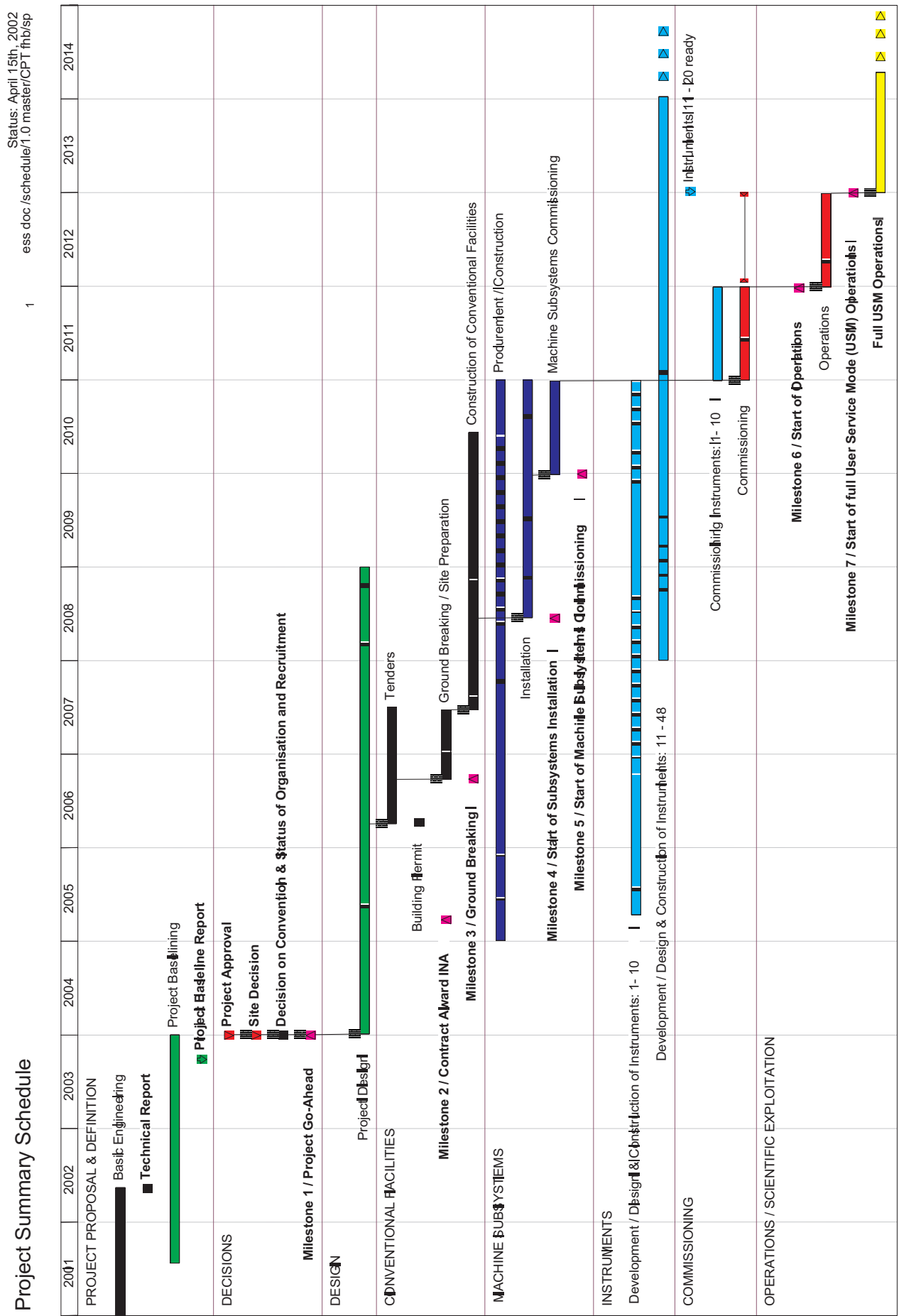
Milestone 4: (M 1 + 54 months) corresponds to the start of the installation of components inside buildings, which have been completed for BO. It is expected that BO of Front End and Linac buildings will occur 12 to 15 months after the start of the conventional facilities construction.

Milestone 5: (M 1 + 72 months) corresponds to the start of the commissioning of machine facilities. This subsequent period will be dedicated to sequential testing and commissioning of the accelerator and targets subsystems and first instruments. Regarding the first 10 instruments, those requiring the longest development and construction, time will have to be started first.



EUROPEAN SPALLATION SOURCE - ESS -

Project Summary Schedule



Milestone 6: (M 1 + 96 months) Assuming that all required decisions have been made by January 2004, the construction period will end in December 2011. Thus, first operations will start in January 2012. The power delivered by the accelerator to the targets will increase step by step up to full performances at 5 MW.

9.2.2 Operations period

The 9th year after project go-ahead will be the first year of operations of the facility producing the first scientific results. To demonstrate that the experimental goals have been achieved, pre-defined calibration experiments specific to each of the first 10 instruments will be performed.

Milestone 7: (M 1 + 9 years) After one year during which routine operations of instruments will be achieved, full USM will start beginning of year 10.

Already during year 9, the commissioning of 5 new instruments has to be started leading to a total of 15 instruments available for users at the beginning of year 11 (see Figure 9-2). At the beginning of year 18, the 40 instruments in USM will be available.

In the subsequent years, a refurbishment/enhancement and replacement, equivalent to 3 new instruments per year is planned.

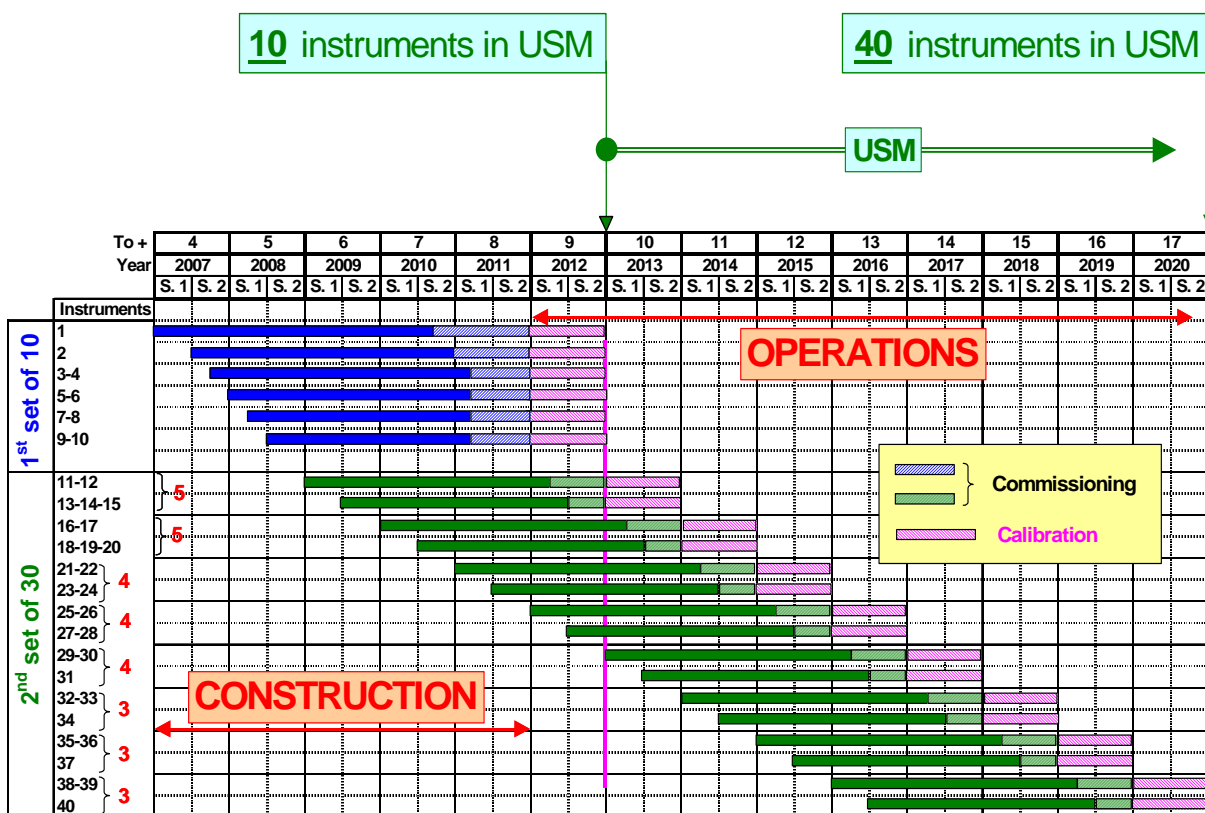


Figure 9-2: Schedule for instruments

9.3 ESS AS AN EUROPEAN ORGANISATION

9.3.1 Model for the organisation

The ESS will be the most innovative neutron source worldwide for all classes of instruments. For several decades, it will operate a high power proton accelerator complex, 2 target systems as dedicated sources (short and long pulses) of neutrons and experimental beam-lines using the most advanced technology in neutron optics, detector design and information technology to push experimental measurements to their practical limits.

In many respects, among them common scientific interest and European partnership, the ESS will be similar in its mission to ILL and ESRF. It is therefore logical to use these institutions as models for the organisation with particular emphasis on the more recent ESRF model based on the many years of experience with ILL.

9.3.2 Organisation chart

The following chart sketches the envisaged organisation:

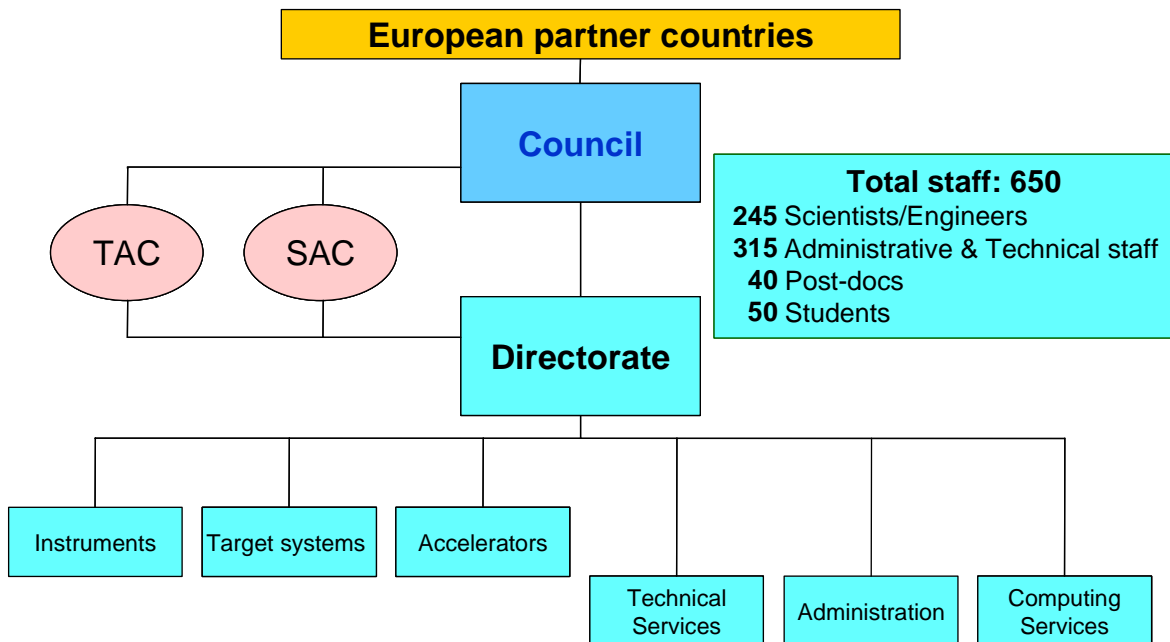


Figure 9-3: ESS organisation chart

- The Council composed of representatives of all contracting parties will rely on the advice of several committees (administrative and finance, purchasing, audit, etc.) to control the management of the facility.
- The director general, chief executive and legal representative of the ESS, leads the directorate. The directors of operational divisions (instruments, target systems, accelerators) assist him.
- A Scientific Advisory Committee (SAC) and a Technical Advisory Committee (TAC) advise the council and the directorate.

- Three support divisions (technical services, administration and computing services) support the operational divisions.

9.3.3 Policy for personnel and staff multi-annual profile

ESS personnel management and salaries policy will depend on the future legal status of the organisation. A private company is assumed subject to host country employment legislation. Salaries, allowances, taxes, employer contributions, etc. are supposed to be similar to those applied at ESRF. When fully operational, ESS will employ 650 staff (560 permanent, 40 post-docs and 50 students).

The ESS will first and foremost be a user-oriented facility operating 24 hours per day for 6 weeks during a typical beam cycle. In view of this, average teams of about 2 scientists, 1 post doc, 1 engineer, 2 technicians and 1 student per instrument, together with all necessary technical infrastructures are foreseen.

During construction, ESS will only recruit people also needed for its long-term operations, improvements and developments. The scientists, engineers and technicians who have worked on the design, construction and commissioning of the facility will have an intimate understanding of it. They are the best people to operate the neutron sources and the experimental equipment efficiently.

A total of 1 800 in-house man years will be required during the 8 years of construction. Figure 9-4 shows the build up of in-house staff, with the average number of people, broken down into divisions.

Additional “peak effort”, needed during construction, will be subcontracted under capital costs.

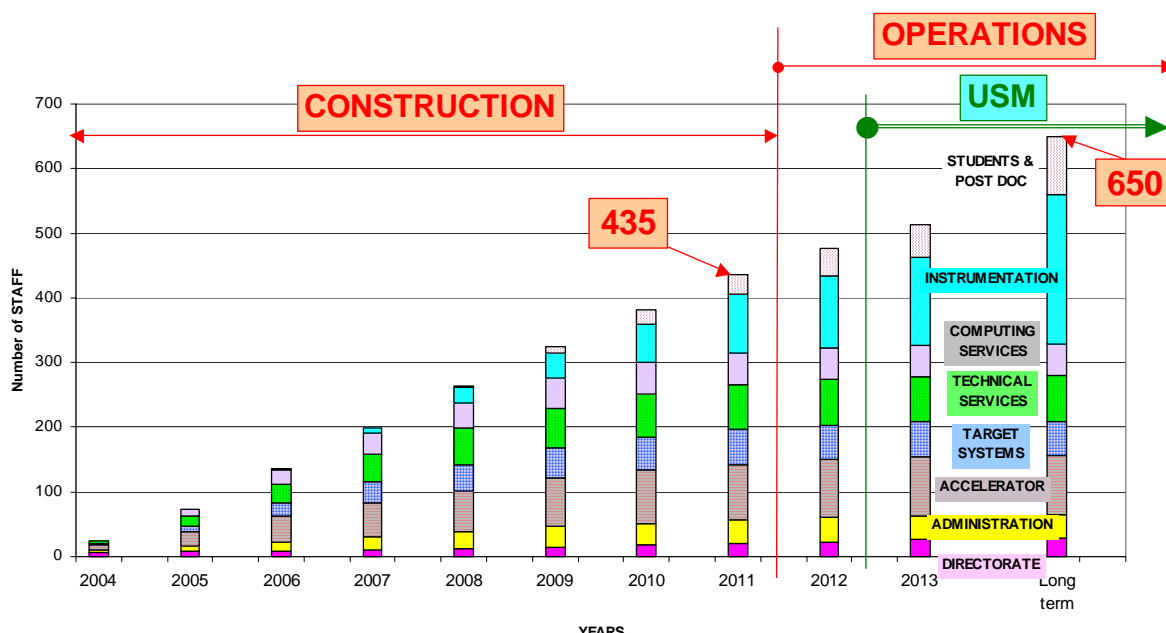


Figure 9-4: ESS in house staff profile

9.4 CONSTRUCTION COSTS

9.4.1 Basis for cost estimates

Construction costs are quoted at 2000 prices, and are exclusive of Value Added Taxes (VAT) and customs duties. They are based on the assumption that ESS is free to choose “best value for money” for offers meeting the technical requirements.

A 15 % contingency is included.

As stated in Chapter 6.2, it is supposed that the site is donated free of charge and that no taxes will have to be paid. Similarly, access roads, telephone and computer links, fire brigades, electricity lines, water mains, etc. should be provided free of charge up to the site boundary by the host country.

Technical and administrative support at the new site should also be provided by the hosting country during the first years of the construction phase while the autonomous ESS legal entity with its own regulations will be implemented.

Finally, the host country will also cover any extra costs arising from local site conditions deviating from the reference site specifications.

The cost estimates are based on the extrapolation to 10 MW of the updated ESS Vol. III (1996), bottom up estimates of the current ESS design and additionally involving industrial expertise. The on-going construction of SNS is being closely followed. Additionally, the experience of other large-scale European facilities has been incorporated.

For additional confirmation, parts of the costing have been cross-checked independently. For example:

- Main conventional facilities through architect engineers on the basis of a building programme.
- Linac RF power (klystrons, power supplies, wave guides, magic T + loads, electronics, etc.) from industrial quotations.
- Cryomodules, cryogenics and controls, networks and computer systems by experts running similar large scale facilities

Overall construction costs plus integrated operations costs for over 20 years are among the key factors to establish the baseline. Nevertheless, there are still a few on-going comparative evaluations.

A good example is the comparison between the two technical approaches for the high-energy part of the linac: Normal Conducting (NC) and Super Conducting (SC). Both options can meet the ESS requirements. For a given acceleration, a SC section is more expensive (contribution to accelerator capital costs) when compared with the equivalent NC version. However, it is significantly shorter, leading to savings on the linac tunnel and adjacent klystron hall (conventional facilities capital costs).

The two options are nearly equivalent (difference much smaller than the error bars) from the point of view of construction costs. The difference in operations costs results from the required electrical power, which is significantly less for a SC linac. A larger number of klystrons to be replaced partly counter balances this. There are also other technical differences to be considered and quantified. This is the reason why both options are still being evaluated.

Regarding the negligible difference in costs and keeping in mind the potential for the SC version to offer a better solution for ESS, costing in this chapter is shown for the SC linac.

Construction costs include the conventional facilities, accelerator complex (1.33 GeV, 10 MW), 2 targets (Short Pulse and Long Pulse) and a first set of 10 instruments as well as cumulative costs during this 8-year period for another 18 instruments (of the second set of 30), which have to be initiated during the construction phase.

Instruments will have a different design and therefore, costs will vary significantly. An average unit price per instrument of 8.5 Million Euro (7 Million Euro capital costs plus 1.5 Million Euro manpower costs) has been estimated, taking into account experience gained at ILL, ISIS and SNS.

For in-house manpower, the average ESRF costs per category at 2000 prices have been considered.

User facilities include a library, restaurant, cafeteria, and a 60-bed hostel (extensible to 180 beds).

A breakdown of the major project tasks into subsystems is shown in Table 9 –1.

Linac	Ion sources & LEPT / RFQ systems / Chopper systems / DTL systems / Funneling systems / CCDTL / SDTL systems / CCL systems / Beam dynamics / RF systems / Power supply Systems / Cyro systems / Diagnostics systems / Beam dumps Development and Injection
Achromat & Rings	HEBT / Achromat / Ring Injection / Accumulator / Extraction / Diagnostics / Ventilation / Development Beam dumps Development / Scraping and Injection
Beam transfer to targets	Beam Line to LP-Target / Beam Line to SP-Target / Beam Diagnostics / Power Supplies / Interfaces to infrastructure
Target systems	Long Pulse Target station / Short Pulse Target station / Target Techn. & Materials / Moderator & Reflector system / Ancillary & Auxiliary systems / Neutron Beam dumps
Instruments & Scientific utilisation	Detector / Chopper and N-Lab / Diffractometers / Spectrometers / Reflectometers / N-Spin-Echo instruments / Engineering.-instruments / spec. sample Env. / Scientific utilisation / Technical support for instruments / Controls & Data acquisition
Conventional facilities	Site preparation / Linac & Front End buildings / Achromat & Rings buildings / Target buildings and Concrete Structures / Laboratory & Office buildings / Beam Transfer buildings / Instrumentation buildings / Controls for buildings / Central utility buildings / Workshops & Gen. site buildings / Interfaces to infrastructure
Control systems and Networks	Integration / Global system incal controls / Achromat & Rings controls / Beam transfer controls / Targets & Beam dumps controls / Instrumentation controls / Conventional buildings interfaces to central control system / CHL & Cryo controls / Safety & interlock systems / Safety control systems
Management & Admin. Support	Project Planning & Control, Configuration Management, Quality Assurance, Information & Documentation Management, Health /Safety & Environment, Assembly & Commissioning, Preparation of operation

Table 9-1: Breakdown of project into major subsystems

Manpower required during the construction phase of the project for design, procurement, contract monitoring, quality assurance, acceptance testing, installation, system testing and

commissioning has been estimated and cross-checked with similar large scale projects. Of the overall manpower of 3 300 man years required during construction approximately 1 800 man years will be in-house staff and approximately 1 500 man years will be subcontracted externally.

9.4.2 Construction costs breakdown

The ESS baseline construction costs of (1.3 GeV; 5 MW delivered to each of the two targets ; 10 instruments at the start of operation) amount to 1 552 Million Euro at 2000 prices, including a 15 % contingency.

Breakdown of construction costs into major subsystems including in-house and external manpower is shown in Table 9-2 and Figure 9-5.

Costing for Beam dumps is included in the relevant sub-systems Linac, Achromat & Rings, and Targets).

Major sub-systems	Construction costs MEuro at 2000 prices
1.1 Linac	370
1.2 Achromat and rings	85
1.3 Beam transfer to targets	20
1.4 Target systems	180
1.5 Instruments & Scientific utilisation	115
1.6 Conventional facilities	465
1.7 Control systems & Networks	55
1.8 Management & Admin. support	60
Total Estimated Costs	1 350
Contingency (15 %)	202
Total Project Costs	1 552

Table 9-2: Breakdown of construction costs into major sub-systems

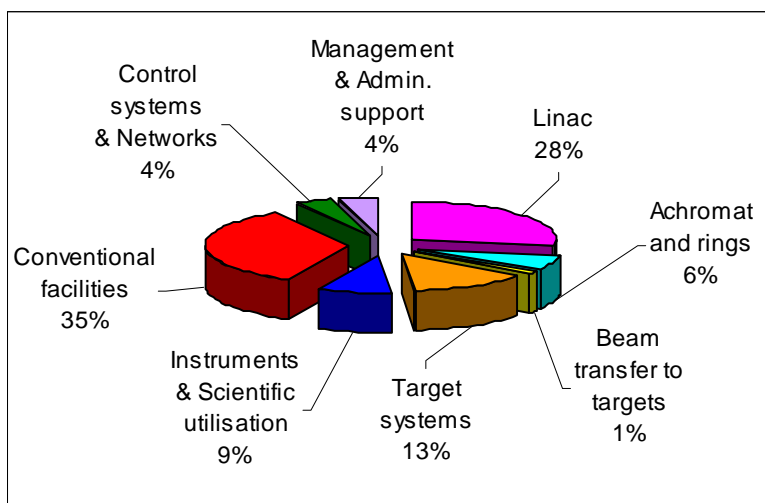


Figure 9-5: Breakdown of construction costs in percentage

9.4.3 Long-term operations costs

The long-term budget for operations is estimated at 142 Million Euro per year at 2000 prices.

Figure 9-6 shows the breakdown of expenditure.

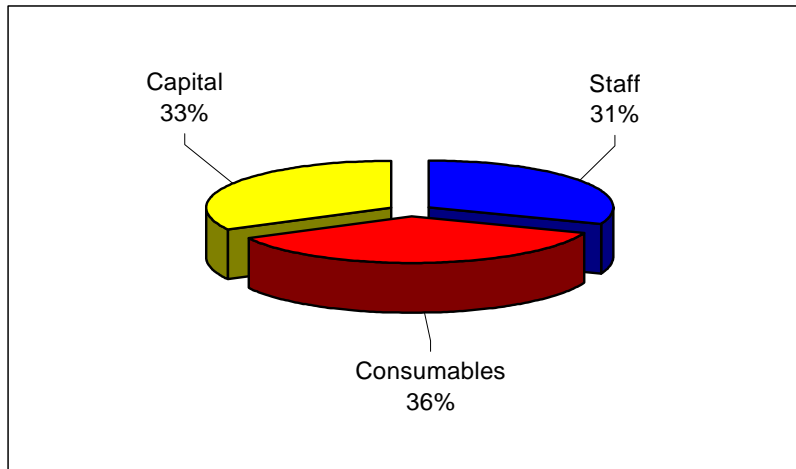


Figure 9-6: Breakdown of long-term operations budget

Staff expenditure, based on the ESRF model, amounts to 31 % of the operations budget. It allows for the financing of 650 posts including 40 post-docs and 50 students (thesis). This staffing is necessary for the operation of the facility with 40 instruments. Additional instruments can be built and be operated by Collaborating Research Groups (CRGs). The staff of 650 does not include posts for :

- Firemen
- Security guards
- Medical support

Staff costs also include a contribution to removal expenses, medical costs, employer's contributions to training, works committees etc.

36 % of the operations budget are “consumables”.

A consumables budget is assigned to each programme. This budget provides the necessary resources for operating the facility (accelerators, 2 targets and 40 instruments) 5 500 hours per year in USM. 1 000 hours distributed over each year will be necessary for light maintenance and “Accelerators and Targets Development Time”.

Consumables expenditure is largely determined by the cost for electricity. Taking into account the electricity unit cost as paid by the ESRF of 0.040 Euro/kWh the ESS electricity expenditure will amount to 28 Million Euro per year.

The capital costs represent 33 % of the annual budget. 54 % of the total capital expenditure is devoted to instruments development, refurbishment /enhancement and replacement (3 instruments per year on the long term). The rest relates to replacements of components for the

"Instruments", "Targets Systems", "Accelerators", and "Control systems & Networks". Provisions are also made for maintenance of conventional facilities and computing services.

9.4.4 ESS multi-annual budget profile

Figure 9-7 shows a suggested budget authority profile over a period of almost 20 years starting from the project go-ahead. Peak payments occur during years 4 to 6 with a value of the order of twice the long-term operations budget. The progression of in-house staff can be followed year after year. The total number of 650 people is reached a few years before commissioning of the 40th instrument.

On the long-term, the capital costs will be constant (about 1/3 of the annual operations budget), a significant part of it being dedicated to the refurbishment of beam-lines and instruments. There is a smooth transition between the start of operations and the long-term equilibrium during which the capital costs decrease while the recurrent costs and the staff costs increase.

All figures are at 2000 prices.

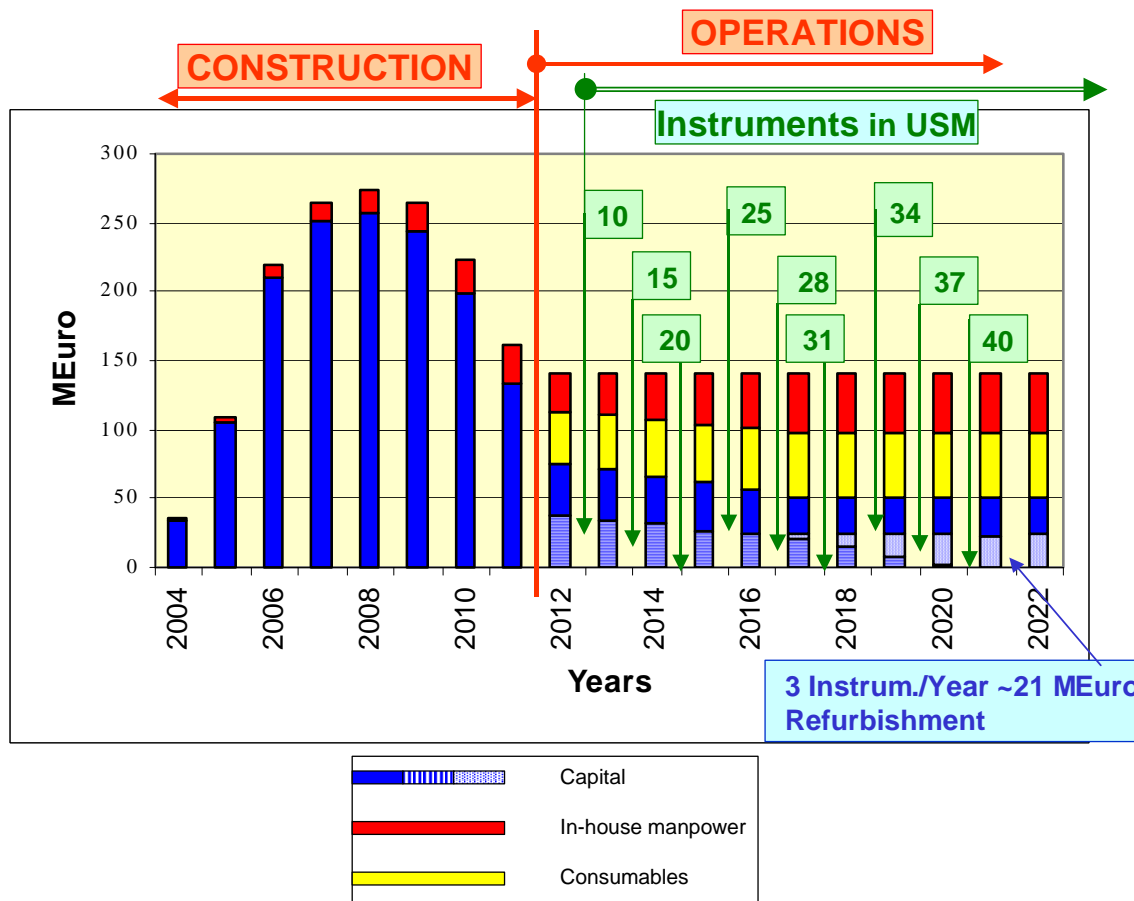


Figure 9-7: Multi-annual budget profile